Visualising and manipulating macrophage phenotypes during mycobacterial infection *in vivo*



University of Sheffield

Zoë Charlotte Speirs

A thesis submitted in partial fulfilment of the requirement for the degree of

Doctor of Philosophy

The University of Sheffield
School of Medicine and Population Health
Faculty of Health

March 2026

Abstract

Tuberculosis, caused by *Mycobacterium tuberculosis* (*Mtb*), remains a global health emergency, heightened by rising antimicrobial resistance. Host-directed therapies (HDTs) are promising strategies by enhancing immune responses. Macrophages, key innate immune cells, polarise along a spectrum from pro- to anti-inflammatory states, yet how these phenotypes arise *in vivo* during infection remains poorly understood. As macrophages serve as the principal intracellular niche for *Mtb* survival, they represent powerful HDT targets. A central unresolved question is how anti-inflammatory macrophages arise in infected tissues: through repolarisation of pro-inflammatory populations or recruitment in subsequent waves.

Using *Mycobacterium marinum*-infected zebrafish larvae, I evaluated the *TgBAC*(*arg2:GFP*) line as an *in vivo* reporter of anti-inflammatory macrophages. Macrophage *arg2:GFP* expression required virulent bacteria and Toll-like receptor signalling. Timelapse imaging revealed that *arg2:GFP*+ macrophages were smaller, rounder and faster than *arg2:GFP*- macrophages, mirroring anti-inflammatory behaviours described in mammalian macrophages. To test whether *arg2:GFP*+ macrophages arise through repolarisation, I combined *arg2:GFP* with a novel pro-inflammatory reporter, *Tg(tnfa:mCherry-F*). I identified a distinct *tnfa+arg2+* population with characteristics of *arg2:GFP+* macrophages. A subpopulation of *tnfa:mCherry*+ macrophages upregulated *arg2:GFP* over time, accompanied by this phenotypic switch, providing the first *in vivo* visualisation of pro-inflammatory macrophages transitioning to an anti-inflammatory-like state.

To manipulate repolarisation, I modulated hypoxia inducible factors (HIFs), key regulators of macrophage function. Genetic Hif-2α stabilisation induced *arg2:GFP* in resting leukocytes, and Hif-2α was partially required for *tnfa*:*mCherry+* cells to become *arg2:GFP*+ during infection, aligning with mammalian studies identifying arginase as a HIF-2α target. Genetic and pharmacological disruption of macrophage arginase impaired bacterial control, indicating that this phenotypic switch is host-protective.

Collectively, this work demonstrates that pro-inflammatory macrophages can repolarise, supporting macrophage plasticity rather than distinct inflammatory subsets. It further establishes *arg2:GFP* as a powerful platform for *in vivo* assessment of macrophage plasticity and bacterial burden, providing an early-stage screening tool for macrophage-targeted HDTs.

Acknowledgements

I would first like to thank my primary supervisor, Dr Phil Elks, for not only providing me with this incredible opportunity to grow as a scientist, but also for his unwavering support throughout my PhD. From challenging me to improve my weaknesses to having confidence in me when I often lacked it myself, I couldn't have asked for a better lab in which to spend the past few years. I would also like to thank Prof Endre Kiss-Toth, my secondary supervisor, for his insightful input and feedback into this project, as well as the many laughs when I have not liked a valid experimental suggestion! Having a perspective outside of the zebrafish world has been exceptionally valuable and has sparked many interesting discussions.

Thank you to the NC3Rs for not only funding my project, but also for providing me with the opportunity to attend workshops and meet others in my cohort. Having such a small cohort meant each of us felt very seen – an experience that I never took for granted. Despite the questionable spaghetti-marshmallow tower team-building activities on a random patch of grass in Liverpool, I thoroughly enjoyed being a part of the NC3Rs community.

I would like to thank all members of the Elks lab, past and present. Firstly, to Amy, for teaching me so much in the lab, providing helpful suggestions in practise talks and for having all lab resources/protocols meticulously documented – the lab was never the same without you. To Jelle and Tom, for being the best lab mates and the best friends, I could have ever asked for. I knew you were both great from the first day I met you after my interview, but I never expected to get this lucky. I gained great colleagues but even better friends for life – thank you for making me laugh even in the most difficult of times. From long coffee breaks and cinema dates, to trips to Alton Tower and The Deep – every activity with you both filled my cup and I can't wait for more of them once we are all on the same side of the world again.

I would also like to thank the ever-growing Johnston lab for keeping me company in the lab – you made the end of my time in the lab a lot less lonely! I am particularly grateful to Dr Simon Johnston, for all his helpful input, both in terms of my project and my wellbeing throughout my time in the lab. From helping me seek the support I needed, to sharing photos of all your animals (especially the goats), I could not be more grateful. To Becca, whether it was a good gossip, help with a stressful protocol or just taking on some of the lab jobs, you kept me sane and I am forever thankful you joined the G floor offices. To everyone in D31, for being such a wonderful and supportive group of people, it has been a pleasure to spend my PhD alongside you all. A special thanks to Cat, for providing me with so many protocols and tips in the lab when everything seemed to be going wrong – a PCR never failed after getting advice from you! A huge thanks to Ada from SITraN, for being such a ray of sunshine and going above and beyond helping me from the first time we were introduced – your insight into the carp

genome was invaluable. Finally, to Ben – for all your help and patience with the scRNAseq– I'm glad our lucky socks let the chip run!

Making friends is always hard as an adult, but I never needed to worry when I moved to Sheffield. To Holly, for being a constant source of funny stories and for being an absolute powerhouse, you are an inspiration to women everywhere. To Dan, for not only being an exceptional source of laughter, but also a fountain of knowledge when I needed help with RNAseq. To Corinna, who started and ended her PhD with me – thank you for all the lunch and pub catch-ups, whether it was talking about Bake Off or debating what snacks were provided at the pub, I always knew I could count on you!

To my friends and family, thank you for always reminding me that I am more than my PhD when arginase was consuming me. A particular thank you to Louisa, for without you I don't think I would have ever had the confidence to pursue a PhD. I can't wait for all the post-PhD catch-ups and wine nights now that you are done globe-trotting – especially with whatever fluffy creature you've currently fostered! To Denis, my longest-standing friend – months can go by without us speaking, but whenever we do it feels just like it did back in secondary school, and I couldn't be more grateful to call you my friend. Thank you to the Durney's for being my second family, with a special thanks to Jim for all the belly laughs and cow photos over the years – it looks like I am finally graduating from apprentice doctor! To my mum, thank you for the support you have given me throughout all my studies and for always standing by me, I promise this is the last degree. To my grandpa, for being my first introduction into science and for ensuring that in a family full of non-scientists, my passion for science continued to burn. To Bailey, for being the cuddliest, friendliest and most emotionally sensitive dog anyone could have asked for. To Sunny, for being the best cat I could have asked for in my final year – you loud purrs, lap cuddles and chatty meows are always a source of happiness. Frankly, you should be co-author of this thesis. Lastly, to my late dad, who never stopped believing in what I could achieve and would have been extremely proud of the person I am today.

Finally, to Thomas. There are not enough thank yous to express how grateful I am for you. This PhD would not exist without you. Thank you for being unbelievably patient with me, for sharing enthusiasm when things went right in the lab and for making me laugh even when all I wanted to do was cry. Thank you for your unrelenting support throughout my PhD journey – both academically and in ensuring I maintained my hobbies out of the lab. You are always a hug away on a bad day. Whether it's running for a pastry, hiking up a mountain or belaying each other, you truly are my constant, and I could not wish for a better person to share my life with.

Abbreviation list

AMR	Antimicrobial resistance
ANOVA	Analysis of Variance
Arg	Arginase
ASPA	Animals (Scientific Procedures) Act 1986
BMDM	Bone marrow-derived macrophage
bp	Base pairs
cAMP	Cyclic adenosine monophosphate
cDNA	Coding DNA
CCR	CC chemokine receptor
CFU	Colony forming units
CHT	Caudal haematopoietic tissue
CRISPR/Cas9	Clustered regularly interspaced palindromic repeats-Cas9
csf3r	Colony stimulating factor 3 receptor
CTCF	Calculated total cell fluorescence
DA1	Dominant active HIF-1α RNA
DA2	Dominant active HIF-2α RNA
DAMP	Damage associated molecular pattern
DEPC	Diethylpyrocarbonate
DMOG	Dimethyloxallyl Glycine
DMSO	Dimethyl sulphoxide
DN1	Dominant negative HIF-1α RNA
DN2	Dominant negative HIF-2α RNA
DNA	Deoxyribonucleic acid
dpf	Days post-fertilisation
dpi	Days post-infection
ESAT-6	Early secretory antigenic target-6
ESX-1	ESAT-6 secretion system-1
FC	Fold change
FDR	False discovery rate
FG4592	Roxadustat
FIJI	Fiji Is Just ImageJ
GFP	Green fluorescent protein
HDT	Host-directed therapy
HIF	Hypoxia inducible factor
HIV	Human immunodeficiency virus
HK	Heat-killed

hpf	Hours post-fertilisation
HSC	Haematopoietic stem cell
IFN	Interferon
IL	Interleukin
IRF	Interferon regulatory factor
ISH	*In situ* hybridisation
iNOS	Inducible nitric oxide synthase
KEGG	Kyoto encyclopaedia of genes and genomes
LMP	Low melting point
LPS	Lipopolysaccharides
MDM	Monocyte-derived macrophage
MDR	Multi-drug resistant
Mm	*Mycobacterium marinum*
MO	Morpholino oligonucleotide
mRNA	Messenger RNA
Mtb	*Mycobacterium tuberculosis*
Myd88	Myeloid differentiation primary response 88
NO	Nitric oxide
OXPHOS	Oxidative phosphorylation
PAMP	Pathogen associated molecular pattern
PBMC	Peripheral blood mononuclear cells
PBS	Phosphate buffered saline
PCR	Polymerase chain reaction
PGE_2	Prostaglandin E2
PHD	Prolyl hydroxylase domain
PR	Phenol red
PVP	Polyvinylpyrrolidone
RD	Region of difference
RNA	Ribonucleic acid
RNAseq	RNA sequencing
ROS	Reactive oxygen species
RPKM	Reads per kilobase million
rpm	Revolutions per minute
scRNAseq	Single cell RNA sequencing
SEM	Standard error of mean
STAT	Signal transducer and activator of transcription
T7SS	Type VII secretion system

TAE	Tris-acetate-EDTA
TB	Tuberculosis
TGF	Transforming growth factor
Th	T helper
TLR	Toll-like receptor
TNF	Tumour necrosis factor
TPM	Transcripts per million
VHL	von Hippel-Lindau
WHO	World Health Organisation
WT	Wildtype

Declaration

I, the author, confirm that this thesis is my own work. I am aware of the University's Guidance on the Use of Unfair Means (www.sheffield.ac.uk/ssid/unfair-means). This work has not previously been presented for an away at this, or any other, university.

Part of the work discussed in this thesis has been published in various publications, listed below and in the corresponding chapters:

- Hammond, F.R., Lewis, A., **Speirs, Z.C**., Anderson, H.E., Sipka, T., Williams, L.G., Nguyen-Chi, M., Meijer, A.H., Wiegertjes, G.F. and Elks, P.M. An arginase 2 promoter transgenic illuminates immune cell polarisation in zebrafish. *Disease Models & Mechanisms.* 2023 Jun 1; 16 (6):dmm049966. doi.org/10.1242/dmm.049966
- **Speirs, Z.C.**, Loynes, C.A., Mathiessen, H., Elks, P.M., Renshaw, S.A. and Jørgensen, L.v.G. What can we learn about fish neutrophil and macrophage response to immune challenge from studies in zebrafish. *Fish & Shellfish Immunology.* 2024 May; 148:109490. doi.org/10.1016/j.fsi.2024.109490
- Bastos T.S.B.*, Loynes C.A.*, **Speirs Z.C.***, de Lima J.D., Junior L.W., de Paula A.G.P., Czaikovski A.P., Luz R.B.S., Paredes L.C., Norris M., Tomlinson G.S., de Rocha W.D., Renshaw S.A., Elks P.M., Braga T.T.. Loss of Cathepsin Z enhances pro-inflammatory macrophage responses and promotes tissue regeneration in zebrafish. **In Press, *Disease Models & Mechanisms***. *Authors contributed equally to this work.

Table of Contents

Abstract ii

Acknowledgements iii

Abbreviation list v

Declaration viii

List of figures and tables xiv

1. Introduction 1

1.1. Tuberculosis 1

1.1.1. Global burden 1

1.1.2. Treatment options and antimicrobial resistance 2

1.1.3. Host-directed therapies 4

1.1.4. TB pathogenesis: early infection and initiation of host immunity 5

1.1.5. TB pathogenesis: granuloma formation and disease progression 6

1.2. Macrophages 8

1.2.1. Macrophages and their ontogeny 8

1.2.2. Macrophage polarisation: the M1/M2 paradigm 10

1.2.3. Macrophage polarisation: challenging the M1/M2 paradigm 13

1.2.4. Macrophage polarisation: phagocytic capacity 16

1.3. Host immune response to mycobacterial infection 17

1.3.1. Early innate immune responses: macrophages and neutrophils 17

1.3.2. Macrophages in *Mtb* infection: early innate responses and cellular heterogeneity 18

1.3.3. Macrophages in *Mtb* infection: subcellular strategies for immune evasion 19

1.3.4. Macrophages in *Mtb* infection: the pro- to anti-inflammatory transition during granuloma development 22

1.3.5. Macrophages in *Mtb* infection: granuloma breakdown and bacterial dissemination 23

1.3.6. Macrophages in *Mtb* infection: unresolved questions 24

1.4. Manipulation of macrophage phenotypes as a host-directed therapy strategy 24

1.5. Hypoxia and Hypoxia Inducible Factors (HIFs) 28

1.5.1. HIF and macrophage function 30

1.5.2. HIF during mycobacterial infection 32

1.6. The zebrafish as an *in vivo* model 35

1.6.1. The zebrafish as an immune model 36

1.6.2. The zebrafish as a model of TB 38

1.6.3. Fish as models of macrophage signalling 41

1.6.4. 3Rs impact: partial replacement 44

1.7. Hypothesis and aims 46

2. Materials and Methods 48

2.1. Ethics statement 48

2.2. Zebrafish work 48

2.2.1. Zebrafish husbandry 48

2.2.2. Embryo maintenance 49

2.2.3. Dechorionation and anaesthetisation 49

2.2.4. Preparation and injection of RNA 49

2.2.5. Morpholino knockdown 50

2.3. Compound treatment of embryos 50

2.4. Immune challenge (injury and infection) 51

2.4.1. Tail fin transection 51

2.4.2. Injection into the caudal vein 51

2.5. Microscopy 52

2.5.1. Stereo microscopy 52

2.5.2. Confocal microscopy 52

2.5.3. Widefield microscopy 52

2.5.4. Spinning disk microscopy 52

2.5.5. Whole body cell counts 53

2.6. Image analysis 53

2.6.1. Measurement and calculation of calculated total cell fluorescence (CTCF) 53

2.6.2. Quantification of cell shape and behaviour using ImageJ 53

2.6.3. Measurement of bacterial burden using ZF4 54

2.6.4. Measurement of granuloma number, granuloma size and bacterial dissemination using QuantiFish 54

2.6.5. Randomisation and blinding 54

2.6.6. Determining gene expression across larval development 55

2.7. *Mycobacterium marinum* culture and injection 55

2.7.1. 7H10 agar plates 55

2.7.2. 7H9 media 55

2.7.3. Preparation of *Mm* overnight culture 55

2.7.4. *Mm* microinjection of larvae 56

Molecular biology 56

2.8. Validating *myd88* morpholino knockdown 56
2.8.1. Total RNA extraction from zebrafish larvae 56
2.8.2. cDNA synthesis 57
2.8.3. Primer sequences and PCR protocol 57
2.9. Raising of a *Tg(ccn1l1:eGFP)* transgenic line 58
2.9.1. Bacterial artificial chromosome (BAC) preparation and injection from glycerol stock 58
2.9.2. DNA linearisation 59
2.9.3. RNA synthesis 59
2.9.4. Generation of a stable transgenic line 59
2.10. Raising of a stable *Tg(mfap4:mCherry-F)* transgenic line 59
2.10.1. Plasmid purification 59
2.10.2. Plasmid sequencing 60
2.10.3. Microinjection of plasmid into the single cell stage 60
2.10.4. Generation of a stable transgenic line 60
2.11. Generation of a *Tg(tnfa:mCherry-F)* transgenic line 60
2.11.1. Plasmid purification and plasmid subcloning 60
2.11.2. Primer design 61
2.11.3. Gradient PCR and PCR protocol 61
2.11.4. PCR purification 62
2.11.5. Restriction digests 62
2.11.6. Gel electrophoresis and gel extraction of digested vector 63
2.11.7. T4 ligation 63
2.11.8. Transformation to competent cells and DNA purification 63
2.11.9. Microinjection of plasmid into the single cell stage 64
2.11.10. Generation of a stable transgenic line 64
2.12. Whole larvae single-cell RNA sequencing 65
2.12.1 Whole larvae dissociation 65
2.12.2 10x Genomics Chromium 65
2.12.3 Data analysis 65
2.13. Published RNAseq data analysis 66
2.14. Statistical analysis 66
3. Characterising macrophage *arginase2* expression during *Mm* infection using an *arg2:GFP* transgenic zebrafish line 67
3.1. Introduction 67
3.1.1. Macrophage phenotypes in TB 67

3.1.2. *In vitro* evidence for macrophage plasticity 68
3.1.2. Arginase expression in infection 69
3.1.3. The *arginase 2* zebrafish transgenic reporter 70
3.1.4. Hypothesis and aims 71

3.2. Results 72
3.2.1. Characterising putative pro-inflammatory macrophages during early *Mm* infection 72
3.2.2. Macrophage *arg2:GFP* expression rises when granulomas begin to form at 3 dpi 82
3.2.3. Developing a more stable macrophage reporter for *Mm* studies 88
3.2.4. *arg2:GFP* expressing macrophages are less branched, more circular and faster 92
3.2.4. Determining signalling mechanisms that lead to macrophages *arg2:GFP* expression in *Mm* infection 99

3.3. Discussion 112

4. Putative pro-inflammatory macrophages upregulate *arg2:GFP* local to the infection site... 122

4.1. Introduction 122
4.1.1. Macrophage activation states: beyond the M1/M2 dichotomy 122
4.1.2. A critical gap: where do polarised macrophages come from? 123
4.1.3. Leveraging the zebrafish model to resolve macrophage polarisation dynamics 124
4.1.4. Hypothesis and aims 126

4.2. Results 128
4.2.1. Generating a *tnfa:mCherry* transgenic line to visualise macrophage *tnfa* and *arg2* expression simultaneously 128
4.2.2. *arg2:GFP* positive macrophages originate from macrophages local to the infection site ... 136
4.2.3. *arg2:GFP* positive macrophages arise from *tnfa:mCherry* positive populations 141

4.3. Discussion 155

5. Manipulating macrophage phenotype to improve infection outcome 162

5.1. Introduction 162
5.1.1. HIF signalling and macrophage polarisation 162
5.1.2. Modulating macrophage phenotype as a potential HDT 163
5.1.3. *In vivo* reporters for pharmacological macrophage polarisation 164
5.1.4. Hypothesis and aims 165

5.2. Results 167
5.2.1. Stabilisation of Hif-2α signalling upregulated leukocyte *arg2:GFP* expression both under resting conditions and in immune challenge 167
5.2.2. Hif-2α is partially required for *tnfa:mCherry+ arg2:GFP-* cells to become *arg2:GFP+* 178
5.2.3. Therapeutic manipulation of macrophage phenotype 193

5.3. Discussion 201

6. Identification of alternative anti-inflammatory macrophage marker genes 210

6.1. Introduction 210

6.1.1. Macrophages polarise on a wide spectrum *in vivo* 210

6.1.2. Conserved cross-species anti-inflammatory macrophage markers 211

6.1.3. The resting state of larval zebrafish macrophages 211

6.1.3. Hypothesis and aims 212

6.2. Results 213

6.2.1. Data mining zebrafish infection RNAseq data for anti-inflammatory macrophage candidate genes 213

6.2.2. *ccn1l1:eGFP* as an alternative anti-inflammatory macrophage reporter 222

6.3. Discussion 232

7. General discussion 240

7.1. Future prospects: targeting macrophage phenotype as a HDT 251

7.2. Concluding remarks 255

8. Bibliography 257

List of figures and tables

Figure 1.1. Tuberculosis pathogenesis. 7
Figure 1.2. Macrophage ontogeny 9
Figure 1.3. Macrophages polarise in response to distinct stimuli and contribute towards macrophage-directed adaptive immunity. 13
Figure 1.4. Macrophages polarise on along a spectrum. 14
Figure 1.5. The macrophage response to *Mtb* and its role in TB pathogenesis. 21
Figure 1.6. Host-directed therapeutic compounds that target macrophage polarisation against *Mtb* infection. 27
Figure 1.7. HIF signalling pathway under normoxic and hypoxic conditions. 30
Figure 1.8. HIF-α isoforms exert opposing effects on macrophage polarisation *in vitro*. 31
Figure 1.9. Summary of neutrophil and macrophage ontogeny in zebrafish. 37
Figure 1.10. Zebrafish macrophages polarise on a continuum in response to different stimuli 42
Figure 1.11. A small subpopulation of zebrafish macrophages upregulate *arg2:GFP* at 1 dpi and 4 dpi. 44
Figure 2.1. Schematic of tail fin transection performed on larvae 51
Figure 2.2. Example of a caudal vein infection in a 30 hpf zebrafish embryo. 52
Figure 3.1. Number of *tnfa:GFP* positive macrophages rises from 1 dpi before falling at 4 dpi. 73
Figure 3.2. Macrophage *tnfa:GFP* brightness increases at 2 dpi, suggesting increased *tnfa* transcription. 74
Figure 3.3. Most *tnfa:GFP+* cells are also *mpeg:mCherry+*. 75
Figure 3.4. *tnfa* is not expressed highly in macrophages during development in unchallenged larvae. 76
Figure 3.5. The proportion of *tnfa:GFP+* macrophages with internalised *Mm* is higher than *tnfa:GFP-* macrophages at 2 dpi. 77
Figure 3.6. Heat killed *Mm* does not grow on 7H10 plates. 78
Figure 3.7. The presence of *Mm* is sufficient to induce macrophage *tnfa:GFP* expression at 1 dpi. 80
Figure 3.8. The proportion of *tnfa:GFP-* and *tnfa:GFP+* macrophages with internalised *Mm* is similar whether alive, heat-killed or avirulent at 1 dpi. 81
Figure 3.9. The number of macrophages expressing *arg2:GFP* is highest at 3 dpi. 83
Figure 3.10. Macrophage *arg2:GFP* fluorescence brightness increases at 3 dpi before falling again, whilst *mpeg:mCherry* brightness remains largely unaffected. 85
Figure 3.11. Morphological differences between *arg2:GFP-* and *arg2:GFP+* macrophage are not identified in confocal images at fixed timepoints. 86
Figure 3.12. The proportion of *arg2:GFP+* macrophages with internalised *Mm* is significantly lower at 3 dpi compared to *arg2:GFP-* macrophages. 87
Figure 3.13. Generating an *mfap4:mCherry* transgenic reporter line. 89
Figure 3.14. The *mfap4:mCherry* transgenic line shows bright mCherry expression of cells with macrophage morphology in the CHT and central nervous system. 90

Figure 3.15. *mfap4:mCherry+* macrophages upregulate *arg2:GFP* expression at 3 dpi and 4 dpi. 91
Figure 3.16. *mpeg:mCherry* and *mfap4:mCherry* fluorescence intensity is similar without *Mm* infection challenge using the same microscope settings. 92
Figure 3.17. Spinning disk timelapse imaging at 3 dpi captures *arg2:GFP-* and *arg2:GFP+* macrophages. 94
Figure 3.18. ImageJ analysis pipeline to determine macrophage morphology and behaviour. 95
Figure 3.19. *arg2:GFP+* macrophages are smaller, less branched and faster than *arg2:GFP-* macrophages. 96
Figure 3.20. Macrophage circularity index does not correlate with speed. 97
Figure 3.21. Single-cell RNAseq identifies a population of *arg2+* macrophages. 98
Figure 3.22. *arg2+* macrophages exhibit a transcriptional landscape reminiscent of anti-inflammatory macrophages. 99
Figure 3.23. Live and virulent *Mm* is required to induce macrophage *arg2:GFP* expression at 3 dpi. ... 101
Figure 3.24. Live and virulent *Mm* is required to induce macrophage *arg2:GFP* expression at 1 dpi. ... 103
Figure 3.25. Live and virulent *Mm* is required to induce macrophage *arg2:GFP* expression at 4 dpi 105
Figure 3.26. The proportion of *arg2:GFP+* and *arg2:GFP-* macrophages with internalised *Mm* is similar whether alive, heat killed or avirulent at 1 dpi. 106
Figure 3.27. Both *arg2:GFP+* and *arg2:GFP-* macrophages contain internalised *Mm* irrespective of whether it is alive, heat killed or avirulent at 3 dpi. 107
Figure 3.28. Example gel for transcript size of successful MyD88 morpholino knockdown. 108
Figure 3.29. Macrophage *arg2:GFP* expression is *myd88*-dependent. 110
Figure 4.1. Two alternative hypotheses for the mechanisms underlying how macrophage phenotypes transitions during mycobacterial infection. 127
Figure 4.2. *tnfa:mCherry* F0 generation expresses the transgene in cells with macrophage morphology at the wound site following tail fin transection. 129
Figure 4.3. A specific subset of macrophages express *tnfa:mCherry* following tail fin transection in F1 progeny. 130
Figure 4.4. Approximately 20% of macrophages upregulate *tnfa:mCherry* at 6 hpA. 131
Figure 4.5. *tnfa:mCherry+* macrophages have a flattened and lobulated morphology. 132
Figure 4.6. *tnfa:mCherry* is not expressed in the gut of F1 progeny under resting conditions. 133
Figure 4.7. Embryos that are *tnfa:mCherry+* express mCherry in the pharyngeal arches under resting conditions. 133
Figure 4.8. Screening embryos for mCherry expression in the pharynx is a reliable way to select *tnfa:mCherry+* larvae 134
Figure 4.9. The *TgBAC(tnfa:GFP)* and *Tg(tnfa:mCherry-F)* transgenic lines have similar expression patterns following a tail fin injury. 135

Figure 4.10. Spinning disk timelapse imaging captures *arg2:GFP-* macrophages that later upregulate *arg2:GFP* 137
Figure 4.11. *arg2:GFP-* macrophages become smaller and more circular following *arg2:GFP* upregulation. 138
Figure 4.12. Changes in behaviour are not captured when tracking arg2:GFP- macrophages that later upregulate *arg2:GFP+.* 139
Figure 4.13. *arg2:GFP-* macrophage morphology remains stable throughout timelapse imaging. 140
Figure 4.14. Immune cells can express both *tnfa:mCherry* and *arg2:GFP* simultaneously in *Mm* infection at 3 dpi. 142
Figure 4.15. Numbers of *tnfa:mCherry+ arg2:GFP+* cells remains similar throughout a 10-hour timelapse of 3 dpi *Mm*-infected larvae. 143
Figure 4.16. *tnfa:mCherry+ arg2:GFP+* immune cells at 3 dpi are smaller, less branched and faster than *tnfa:mCherry+ arg2:GFP-* immune cells. 143
Figure 4.17. *tnfa:mCherry+ arg2:GFP+* immune cells are found at a wide range of distances from the granuloma. 145
Figure 4.18. The spatial distribution pattern of *tnfa:mCherry+ arg2:GFP+* immune cells relative to the granuloma is heterogenous in 2D maximum intensity projections. 146
Figure 4.19. *tnfa:mCherry* fluorescence brightness is similar whether *arg2:GFP-* or *arg2:GFP+* at 3 dpi 147
Figure 4.20. Spinning disk timelapse imaging captures *tnfa:mCherry+ arg2:GFP-* immune cells at 3 dpi that later upregulate *arg2:GFP.* 148
Figure 4.21. *tnfa:mCherry+ arg2:GFP-* immune cells become smaller and more circular following upregulation of *arg2:GFP* at 3 dpi. 150
Figure 4.22. Changes in behaviour are not captured when tracking *tnfa:mCherry+ arg2:GFP-* immune cells that transition to being *arg2:GFP+* at 3 dpi. 151
Figure 4.23. Prior *arg2:GFP* upregulation, *tnfa:mCherry+* transitioning cells become smaller and rounder, but the increase in speed is not captured. 152
Figure 4.24. *tnfa:mCherry+ arg2:GFP-* immune cell morphology remains stable throughout timelapse imaging. 153
Figure 4.25. Schematic illustrating that putative pro-inflammatory macrophages switch behaviours towards an anti-inflammatory phenotype during *in vivo* mycobacterial infection. 155
Figure 5.1. Dominant active *hif-1α* and *hif-2α* RNA induced *phd3:GFP* expression. 168
Figure 5.2. Neutrophils upregulate *arg2:GFP* following genetic stabilisation of Hif-2α under resting conditions. 169
Figure 5.3. Macrophages upregulate *arg2:GFP* following genetic stabilisation of Hif-2α under resting conditions. 171

Figure 5.4. Only genetic stabilisation of Hif-2α, not Hif-1α, increases neutrophil *arg2:GFP* expression in *Mm* infection at 1 dpi. 173
Figure 5.5. Only genetic stabilisation of Hif-2α, not Hif-1α, increases neutrophil *arg2:GFP* expression in *Mm* infection at 4 dpi. 175
Figure 5.6. Neutrophils outside granuloma structures upregulate *arg2:GFP* expression following Hif-1α stabilisation, while neutrophils inside granulomas upregulate *arg2:GFP* following genetic downregulation of Hif-2α. 177
Figure 5.7. Confocal imaging at two timepoints at 2 dpi and 3 dpi suggests most *tnfa:mCherry+* cells transition to also being *arg2:GFP+* overnight. 179
Figure 5.8. *tnfa:mCherry+ arg2:GFP+* immune cells are captured in timelapses at 2 dpi. 180
Figure 5.9. *tnfa:mCherry+ arg2:GFP-* immune cells at 2 dpi are larger, more branched and faster than *tnfa:mCherry+ arg2:GFP+* immune cells. 181
Figure 5.10. Spinning disk timelapse imaging at 2 dpi captures *tnfa:mCherry+ arg2:GFP-* cells that later also express *arg2:GFP*. 183
Figure 5.11. Changes in morphology are captured when tracking *tnfa:mCherry+ arg2:GFP+* immune cells that transition to being *arg2:GFP+*. 185
Figure 5.12. Changes in behaviour are not captured when tracking *tnfa:mCherry+ arg2:GFP-* immune cells that transition to being *arg2:GFP+* at 2 dpi. 186
Figure 5.13. HIF-2α is partially required for *tnfa:mCherry+ arg2:GFP-* cells to transition to double positive. 187
Figure 5.14. *csf3r* morpholino-mediated neutrophil depletion persists for up to 5 dpf. 189
Figure 5.15. Pharmacological inhibition of arginase in neutrophil-depleted larvae leads to an increase in bacterial burden. 190
Figure 5.16. Pharmacological inhibition of arginase in neutrophil-depleted larvae leads to increased granuloma number, size and bacterial dissemination 192
Figure 5.17. Protectin D1 does not upregulate macrophage *arg2:GFP* expression at 2 dpi. 194
Figure 5.18. Systemic injection of PD1 expands the macrophage population in unchallenged larvae... 195
Figure 5.19. Immersion treatment with M2-associated mediators does not significantly upregulate macrophage *arg2:GFP* expression under resting conditions. 197
Figure 5.20. Immersion treatment with pan hydroxylase inhibitors does not upregulate macrophage *arg2:GFP* expression under resting conditions 198
Figure 5.21. Macrophages become more circular following treatment with the pan-hydroxylase inhibitor FG4592 without an immune challenge. 200
Figure 5.22. Arginase inhibition of pro-inflammatory macrophage phenotypic switch is host-detrimental 207
Figure 6.1. Zebrafish macrophage KEGG pathways are most similar to human macrophages polarised towards M2a. 213

Figure 6.2. Zebrafish macrophage KEGG pathways are more similar to circulating monocytes than tissue-resident macrophages. 215
Figure 6.3. IL-4/STAT6 molecular pathway genes are upregulated in zebrafish macrophages under resting conditions. 216
Figure 6.4. Comparison between zebrafish *Mm* infected macrophage and human polarised macrophage RNAseq datasets identified 3 candidate genes. 218
Figure 6.5. Under resting conditions, *ctsz* and *nccrp1* are expressed in larval zebrafish macrophages, with very low expression levels of *ocstamp* in haematopoietic populations 220
Figure 6.6. Zebrafish gene organisation of candidate genes share high homology with human orthologues. 222
Figure 6.7. Human CCN1 protein structure is similar to zebrafish ccn1l1 223
Figure 6.8. Human CCN1 protein has been shown to play a role in tissue repair and macrophage polarisation. 224
Figure 6.9. Zebrafish *ccn1l1* shares homology with human and mouse *CCN1/Ccn1*. 225
Figure 6.10. Carp and zebrafish ccn1l1 sequence and protein alignment indicates gene conservation. 226
Figure 6.11. The *Tg(ccn1l1:eGFP)* transgenic line shows expression of GFP in the otic vesicle and midline under resting conditions, recapitulating *ccn1l1 in situ* hybridisation expression pattern. 227
Figure 6.12. Macrophages do not express *ccn1l1:eGFP* following *Mm* infection. 229
Figure 6.13. Macrophages do not express *ccn1l1:eGFP* following pre-treatment with cAMP and tail fin transection. 230
Figure 7.1. Pro-inflammatory macrophages undergo a phenotypic switch *in vivo*, and this change in phenotype is host-protective. 241
Figure 7.2. Power analysis to estimate how many mice would be required to examine macrophage polarisation dynamics. 250

Table 1.1. *In vitro* polarising stimuli and marker expression of human macrophage subtypes. 15
Table 1.2. Current tools available to visualise and manipulate immune cell populations during *Mycobacterium marinum* infection in zebrafish. 40
Table 2.1. List of zebrafish lines used in this project. 48
Table 2.2. Control and morpholino oligonucleotide sequences. 50
Table 2.3. A list of compounds used to treat zebrafish larvae via immersion in this thesis. 50
Table 2.4. iScript cDNA synthesis reaction protocol 57
Table 2.5. Primer sequences for *myd88* and housekeeping gene *ef1a* 57
Table 2.6. PCR mix reagents and volumes. 58
Table 2.7. Thermocycling touchdown PCR programme for the amplification of *myd88* transcript 58
Table 2.8. Primer sequences to amplify the tnfa promoter region without the sequence of exon one 61
Table 2.9. PCR reaction reagents and volumes for one sample. 62

Table 2.10. Thermocycling PCR programme for the amplification of part of the *tnfa* promoter region. . 62
Table 2.11. T4 ligation reaction of *tnfa:mCherry-F* digested vector and PCR product. 63
Table 2.12. *tnfa:mCherry-F* microinjection mix for single-cell injections. 64

1. Introduction

Some of the text and figures in this chapter (section 1.6) were published in:

Speirs, Z.C., Loynes, C.A., Mathiessen, H., Elks, P.M., Renshaw, S.A. and Jørgensen, L.v.G. 2024. What can we learn about fish neutrophil and macrophage response to immune challenge from studies in zebrafish. *Fish & Shellfish Immunology.* **148**, p109490.
doi.org/10.1016/j.fsi.2024.109490

1.1. Tuberculosis

1.1.1. Global burden

Despite being both preventable and curable, tuberculosis (TB) remains a global health challenge. In 2024, there were an estimated 10.7 million new TB cases worldwide, resulting in approximately 1.23 million deaths (World Health Organization, 2025). For the past three decades, the World Health Organisation (WHO) has classified TB as a global health emergency (World Health Organization, 2025). Airborne infection with *Mycobacterium tuberculosis (Mtb)*, the bacterial pathogen responsible for TB, is the leading cause of death from a single infectious agent – once again surpassing coronavirus disease 2019 (COVID-19) (World Health Organization, 2025). Moreover, TB remains the leading cause of mortality among people living with human immunodeficiency virus (HIV) globally (World Health Organization, 2025).

In immunocompetent individuals, most *Mtb* infections are cleared in the lung when inhaled, without pharmacological intervention and before the adaptative immune response is fully activated (Emery et al., 2021; Verrall et al., 2014). Individuals who do not clear the infection may develop an asymptomatic latent *Mtb* infection, which can persist for years and is estimated to affect approximately one-quarter of the global population (Kiazyk and Ball, 2017). It is estimated that only around 10% of individuals with latent TB progress to activated disease within their lifetime, although the mechanisms driving this transition remain incompletely understood (Kiazyk and Ball, 2017). A recent transcriptomic study found that alveolar macrophages from *Mtb*-resistant individuals – those that remain diagnostically negative for *Mtb* despite exposure to the pathogen – exhibit elevated canonical pro-inflammatory responses compared to those from individuals with latent TB, suggesting that susceptibility to *Mtb* may be at least partly genetically determined (Haynes et al., 2025; Stein et al., 2019). Several risk factors are associated with TB reactivation, including physiological factors such as hormonal changes during puberty and comorbidities likes diabetes; lifestyle factors including smoking, alcohol consumption, and physical inactivity; and socio-economic conditions such low income, malnutrition and overcrowded living environments (Chung et al., 2024; Choi et al., 2023; Rosenthal et al., 2019; Li et al., 2022). A clinically and sociologically significant risk factor is HIV- co-infection, which

increases the likelihood of developing active TB by more than 100-fold (Kiazyk and Ball, 2017). Disseminated TB – where infection spreads to other organs, such as the brain – is rare in immunocompetent individuals (<5%), but occurs more frequently in immunocompromised patients, particularly those with HIV (Meira et al., 2019; Zhang et al., 2025; Huber and Joshi, 2023; Wang et al., 2007). In these cases, TB meningitis (*Mtb* detected in the cerebrospinal fluid) carries an estimated fatality rate of up to 70%, underscoring the severity of disseminated disease in vulnerable populations (Dodd et al., 2021).

Early diagnosis is essential for effective TB treatment; however, identifying individuals with latent TB remains challenging, as they do not exhibit clinical symptoms despite harbouring viable *Mtb*. Although only a small proportion of latently infected individuals will develop active TB, this reservoir represents a major source of future active cases (Ding et al., 2025). Symptoms of active TB vary, but typically include a persistent cough, haemoptysis, fever, night sweats and loss of appetite (Alsayed and Gunosewoyo, 2023). Because latent TB is asymptomatic, public-health strategies focus on targeted screening of at-risk populations. For example, migrants from high–TB–incidence countries are routinely offered latent TB screening shortly after entry as part of national TB-control programmes. In the UK, new entrants from high-burden regions may undergo latent-infection testing following immigration, even if pre-entry screening is limited to excluding active disease (UKHSA, 2014). Similarly, in many European and other high-income settings, experts recommend systematic latent TB screening for immigrants, refugees, and asylum-seekers from high-burden countries, given their elevated risk of reactivation (Braga et al., 2024). In addition to established screening programmes, opportunistic screening – for example during primary-care registration, occupational health assessments or targeted outreach in high-risk communities – can help identify latent infections before symptomatic disease develops. Integrated models combining latent TB screening with other health checks (e.g.: HIV or hepatitis) have shown high feasibility and improved uptake in underserved groups (Hargreaves et al., 2020). Given the size of the latent reservoir and the window before reactivation, systematic identification and preventative treatment of latent TB, especially in high-risk populations, remains one of the most effective strategies for long-term TB control.

1.1.2. Treatment options and antimicrobial resistance

There is currently only one licenced TB vaccine: the Bacillus of Calmette and Guérin (BCG), a live attenuated strain developed over a century ago (Calmette et al., 1921). The efficacy of BCG in preventing TB remains controversial. The vaccine is primarily recommended for infants at high risk or in low-income countries, where it has demonstrated effectiveness in preventing severe forms of TB – such as TB meningitis – and reducing mortality (Mangtani et al., 2014). However, studies indicate that these protective effects begin to wane from around 14 years of age, and reported BCG efficacy in adolescents and adults – the primary demographic responsible for *Mtb* transmission – ranges widely from 0-80%

(Hatherill and Cobelens, 2022; Fine, 1995; Swaminathan and Rekha, 2010). Re-vaccination with BCG has been proposed as a potential strategy to address this variability, but a recent longitudinal trial in Malawi found no additional protection from repeat vaccination, particularly among HIV-positive individuals (Glynn et al., 2021).

Diagnosing TB remains a major obstacle in effective disease management. Distinguishing between latent and active TB is particularly difficult because the diagnostic tools commonly used to detect latent infection – the tuberculin skin test (TST) or interferon gamma release assay (IGRA) – are also positive in individuals with active disease (Jo et al., 2025). As a result, confirmation of active TB therefore requires additional investigations, such as mycobacterial culture and chest computed tomography (CT) (Jo et al., 2025). These challenges in diagnosis complicate clinical decision-making and contribute to delays in treatment initiation, on-going transmission, and inappropriate or incomplete therapy.

The current therapeutic pipeline for active TB relies on prolonged multidrug regimens lasting from 6 to 24 months. Despite the availability of effective antibiotics, treatment success remains challenging due to several factors, including differences between active and latent TB, adverse drug reactions, and lengthy duration of treatment – all of which frequently leads to poor patient adherence (Dartois and Rubin, 2022; World Health Organization, 2025; Kilinç et al., 2021). Poor adherence, in turn, contributes to the emergency of antimicrobial (AMR) resistance, as *Mtb* evolves mechanisms to evade host immunity and antibiotic pressure (Kilinç et al., 2021). Treatment of latent TB aims to eliminate dormant bacilli before they progress to active disease. Preventative regimens typically include rifampicin monotherapy (4 months), isoniazid plus rifampicin or rifapentine (3 months) or isoniazid monotherapy (9 months) (Jo et al., 2025). Drug selection depends on *Mtb* susceptibility patterns, with alternatives such as fluoroquinolones used when resistance is detected (Huaman and Sterling, 2019; Jo et al., 2025; Mase and Chorba, 2019). However, despite latent TB patients representing the largest reservoir for potential future active TB cases, the WHO currently recommends preventative therapy only for individuals at high risk of progression, such as those who are immunocompromised (Dartois and Rubin, 2022). Active TB requires more intensive and prolonged treatment with multiple antibiotics. Regimens and durations vary depending on drug susceptibility. For example, a randomised controlled trial reported that a 4-month course of rifapentine and moxifloxacin was comparable in efficacy to the standard 6-month treatment (Dorman Susan et al., 2021). However, these reduced regimes must be approached with caution, as high relapse-rates in rifapentine-moxifloxacin treated individuals have also been reported, particularly in HIV patients (Jindani et al., 2014).

In cases of multi-drug-resistant TB (MDR-TB), treatment may require up to 5 drugs for at least 18 months, which has been associated with improved relapse prevention but also presents significant

challenges for patient adherence (Cox et al., 2008; Karnan et al., 2024). Non-adherence remains a key issue; for instance, a Ugandan cohort reported that 1 in 10 MDR-TB patients failed to complete therapy (Batte et al., 2021). This, in turn, accelerates the emergence of drug resistance and limits future treatment options. The increasing difficulty of managing antibiotic-resistant TB is underscored by the global rise in MDR-TB and extensively drug-resistant TB (XDR-TB). Both incidence and mortality rates increased in 2021, particularly in low socioeconomic regions such as Somalia (Tan et al., 2025). Similarly, a study in Zambia reported that 35% of TB patients carried strains resistant to both rifampicin and isoniazid (Kangongwe et al., 2024). Furthermore, a meta-analysis found that approximately 13% of previously treated MDR-TB patients had pre-XDR-TB (resistance to rifampicin, isoniazid and fluoroquinolones). This higher prevalence among treated individuals suggests that prior antibiotic exposure – especially when associated with incomplete or inappropriate treatment – may contribute to the selection of additional resistance mutations (Diriba et al., 2023). However, it remains unclear whether this pattern reflects acquired resistance during therapy or reinfection with already resistant strains. To attempt to address the challenges of drug-resistant TB associated with patient non-adherence, the WHO recently endorsed a new oral regimen – BpaL (bedaquiline, pretomanid, and linezolid) – which has demonstrated efficacy against drug-resistant TB within 6 months (Zohaib Ali et al., 2024). However, like all antibiotic-based therapies, BPaL remains vulnerable to the evolution of resistance, highlighting the limitations of pathogen-targeted approaches in TB management.

Taken together, these findings highlight the urgent need for alternative therapeutic strategies and improved treatment adherence programs. The growing burden of drug-resistant TB not only places immense strain on public health systems, but also disproportionately affects low-resource settings, where the economic cost of prolonged and complex treatment further compounds health inequities.

While vaccination offers partial protection, particularly in children, effective control of TB ultimately depends on prompt diagnosis and successful antibiotic treatment. However, treatment is lengthy, complex, and increasingly threatened by the emergency of drug-resistant *Mtb* strains. The growing problem of AMR in TB not only complicates management, but also poses a critical barrier to TB eradication efforts. Understanding TB pathogenesis and the mechanisms underlying resistance is therefore essential to developing more effective therapeutic strategies.

1.1.3. Host-directed therapies

One potential strategy to counter the growing threat of drug-resistant TB is the development of host-directed therapies (HDTs), which aim to modulate the host immune system to enhance *Mtb* clearance, rather than directly targeting the pathogen itself (Kilinç et al., 2021; Tian et al., 2025; Prasanna et al., 2025; Dekkers et al., 2025). HDTs act through multiple mechanisms, such as enhancing phagocytic activity or promoting macrophage activation (Zou et al., 2024). Therefore, understanding

how the immune system responds to *Mtb* infection, how the bacterium manipulates host cell function to evade killing, and the underlying immunopathogenesis of TB are essential for identifying potential immune pathways that can be therapeutically strengthened.

In addition, HDTs have been proposed as adjunctive treatments to complement existing or repurposed anti-TB drugs, with the goal of improving treatment outcomes and shortening therapy duration (Young et al., 2020). Recent experimental evidence supports this approach: for example, meclizine – an anti-emetic drug – was shown to reprogramme macrophages towards a pro-inflammatory metabolic state, thereby reducing antitubercular tolerance in murine macrophages and rendering them more effective (Yadav et al., 2025). Collectively, this suggests that identifying HDT targets, particularly within the innate immune system – the body's first and fastest line of defence against invading mycobacteria – represents an attractive avenue for developing novel therapies to enhance *Mtb* clearance, especially as HDTs are inherently less susceptible to the challenges of AMR.

1.1.4. TB pathogenesis: early infection and initiation of host immunity

Mtb has a defined pathogenic life cycle, ensuring its survival and transmission to other hosts (**Fig. 1.1.**). Initially, a patient with active TB releases aerosolised *Mtb*-containing particles, which are then inhaled by another individual, subsequently reaching the lung (**Fig. 1.1.** – step 1) (Turner and Bothamley, 2015). Once in the lung, alveolar macrophages are the first immune cell to come into contact with the bacteria, and are the primary target of *Mtb* at early stages of infection (**Fig. 1.1.** – step 2). Infected alveolar macrophages exhibit a pro-inflammatory phenotype, evidence by *in vitro Mtb* models, whereby bone-marrow derived macrophages (BMDMs) have elevated mRNA levels of TNF-α and IL-1β (Chacón-Salinas et al., 2005). Additionally, many genes in primary murine macrophages infected with *Mtb* overlap with the transcriptional signature of *in vitro* pro-inflammatory macrophages (Ehrt et al., 2001). At the subcellular level, *Mtb* uses ESX-1-dependent virulence secretion together with host IL-1R-inflammasome signalling to promote early intracellular escape events. These mechanisms enable *Mtb*-infected alveolar macrophages to escape the alveolar space and re-locate into the lung interstitium, initiating early bacterial dissemination (Cohen et al., 2018). In parallel, release of pro-inflammatory cytokines (e.g.: IL-1β) are critical for control of *Mtb* infection, but also for recruitment of other immune cell types – including neutrophils, monocyte-derived macrophages (MDMs), dendritic cells and natural killer cells – to the infection site (Cohen et al., 2018; Mai et al., 2024; Portevin et al., 2012). A crucial next step in establishing protective immunity is the transport of *Mtb* or *Mtb*-derived antigens from the lung to the draining mediastinal lymph node, where antigen-specific T-cells are first activated. Foundational work demonstrated that CD4+ T-cell priming in TB does not occur in the lung, despite high bacterial burdens, but instead requires antigen production within the draining lymph node itself (Wolf et al., 2008). Although dendritic cells have long been considered the primary antigen-transporting cells, evidence now shows that macrophage- and monocyte-derived cells also contribute

to this process. CCR2+ monocytes and monocyte-derived macrophages can carry *Mtb* or bacterial antigens from the lung to the lymph node and participate in initiating T-cell activation (Samstein et al., 2013; Mohapatra et al., 2025). Moreover, recent human studies indicate that many *Mtb*-specific CD4+ T-cell clonotypes recognise antigens presented directly by infected macrophages, highlighting their importance as functional antigen-presenting cells during TB (Stetsenko et al., 2025). Together, these findings position macrophages as key intermediaries linking early innate infection to the activation of adaptive, cell-mediated immunity.

1.1.5. TB pathogenesis: granuloma formation and disease progression

As infection progresses, the recruited immune cells begin to organise around infected macrophages, forming a granuloma – a hallmark structure of TB that aims to contain bacterial spread (**Fig. 1.1.** – step 3) (Ramakrishnan, 2012; Adams, 1974). However, despite its protective intent, the granuloma core may also provide a protective niche that enables bacterial expansion, contributing to latent TB that may lay dormant for decades. *Mtb* actively shapes the granuloma environment by modulating macrophage phenotypes. At later stages of infection, the bacteria promote anti-inflammatory macrophage phenotypes, dampening pro-inflammatory responses and reducing bactericidal capacity (Cronan et al., 2021; El Kasmi et al., 2008). In addition, *Mtb* cell surface lipids can mask pathogen-associated signals, preventing pro-inflammatory macrophage detection and promoting preferential infection of anti-inflammatory macrophages within granulomas (Cambier et al., 2017; Cambier et al., 2014b; Ly et al., 2008). Within granulomas, mycobacteria infection also promotes macrophage differentiation into epithelioid macrophages, lipid-laden foamy macrophages and multinucleated giant cells (Cronan et al., 2016; Puissegur et al., 2007; Ordway et al., 2005; Rhoades, Elizabeth et al., 2005). While some of these cell types have been shown to be host-protective, such as decreased susceptibility to necrosis in foamy macrophages (Agarwal et al., 2020), their formation often provides benefits to *Mtb*. In particular, lipid accumulation in foamy macrophages can support *Mtb* metabolic needs, and the eventual necrosis of these cells contributes to caseation within the granulomas (Kim et al., 2010). As caseous material softens and cavitates, granuloma integrity is lost. This breakdown permits uncontrolled bacterial expansion and can trigger re-activation of latent bacilli (Grosset, 2003) (**Fig. 1.1.** – step 4). Ultimately, granuloma rupture releases *Mtb* into the airways, enabling transmission to new hosts as the infection cycle repeats (**Fig. 1.1.** – step 5).

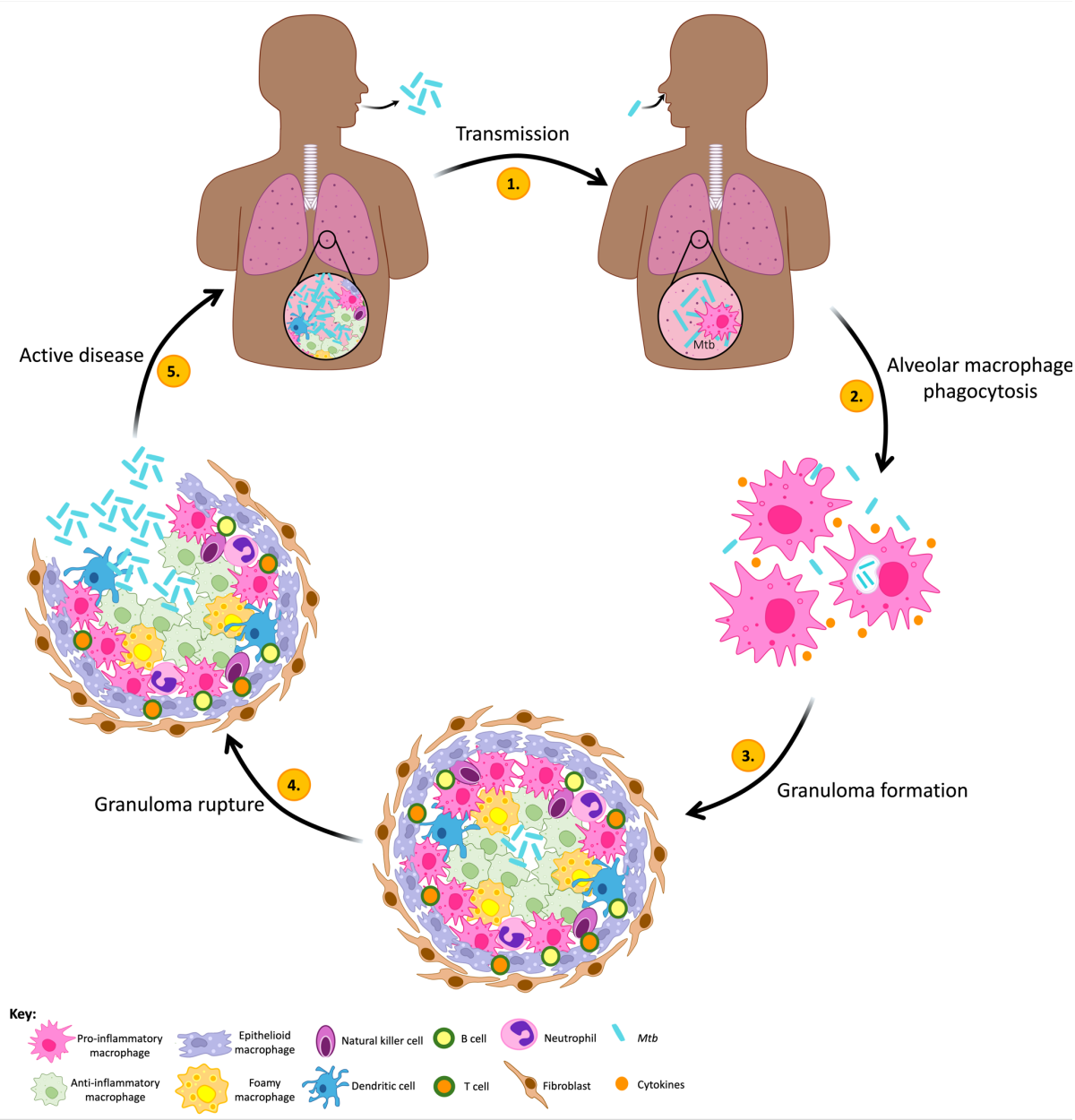


Figure 1.1. Tuberculosis pathogenesis. (**1**) Infection occurs following inhalation of aerosolized *Mtb* (cyan rods) bacilli coughed from the lungs of a patient with active TB. (**2**) *Mtb* is phagocytosed by alveolar macrophages (pink cells) in the lung, the first cells to come into contact with the pathogen. Infected alveolar macrophages engage in a host-protective response, including release of cytokines (orange dots) to recruit additional immune cells to the infection site, including innate and adaptive immune cells. (**3**) Recruitment of immune cells to the infection site results in the formation of a granuloma. Granulomas limit the spread of bacteria, and in healthy patients, the infection may remain asymptomatic at this stage (latent TB). (**4**) In some cases, the infection may be re-activated. Uncontrolled bacterial replication, as a consequence of the granuloma preventing antibiotic delivery within the structure, as well as lipid release from necrotic foamy macrophages (yellow/orange cells) results in the formation of a necrotic core, known as a caseous granuloma. This may result in the granuloma rupturing. This results in the patient having active TB and *Mtb* re-enters the pathogenesis cycle (**1**), as the patient disseminates bacteria and infects others. Key illustrating cell types, pathogens and molecules is illustrated at the bottom of the figure. Adapted from Alsayed and Gunosewoyo (2023).

1.2. Macrophages

1.2.1. Macrophages and their ontogeny

The innate immune system represents the first line of defence against invading pathogens, providing a rapid and non-specific response (Marshall et al., 2018). It employs multiple protective strategies, including physical barriers such as the skin and mucous membranes, physiological mechanisms such as low pH and fever responses, specialised phagocytic and endocytic cells, and the initiation of inflammatory processes (Turvey and Broide, 2010). Among the cellular components of innate immunity, neutrophils and macrophages constitute the two major phagocytic leukocyte populations, responsible for engulfing and eliminating pathogens and cellular debris (Mayadas et al., 2014; Marshall et al., 2018). Together, these cells play crucial roles in orchestrating early immune responses.

Neutrophils are the most abundant leukocyte and the dominant phagocytic cell type within the immune system (Mayadas et al., 2014). They are short-lived, polymorphonuclear cells originating from the bone marrow, typically surviving for up to 5 days (**Fig. 1.2.**) (Mayadas et al., 2014; Marshall et al., 2018). By contrast, macrophages are significantly longer-lived – surviving for months to years – and were formally classified in 1972 as part of the mononuclear phagocyte system (Gordon, 2008; van Furth et al., 1972). Their longevity, functional diversity, and remarkable plasticity have since established macrophages are key regulators of immunity, tissue homeostasis, and development.

Macrophages are distributed throughout virtually all tissues in the body, where they perform roles extending beyond pathogen elimination, including developmental, homeostatic and regenerative functions (Wynn et al., 2013). Macrophages arise from distinct developmental pathways. While early paradigms posited that macrophages were solely derived from bone-marrow-resident haematopoietic stem cells, fate mapping and lineage-tracing studies in mice revealed the existence of two ontogenically distinct populations (Schulz et al., 2012; Yona et al., 2013). Monocyte-derived macrophages originate from bone marrow progenitors and replenish macrophage pools during adult haematopoiesis, similar to neutrophils. Conversely, many tissue-resident macrophage populations – including alveolar macrophages, Kupffer cells and microglia – derive from phagocytes generated in the foetal liver and yolk sac during embryonic development **(Fig. 1.2.**) (Schulz et al., 2012; Yona et al., 2013; Epelman et al., 2014). Tissue-resident macrophages can also replicate, thus self-maintaining their population in the local tissue (Hashimoto et al., 2013). Furthermore, transcriptomic analyses have demonstrated that although foetal liver- and bone marrow-derived macrophages share developmental ancestry, owed to foetal liver progenitors later colonising the bone marrow, they also exhibit distinct gene expression signatures, reflecting functional specialisation (Coşkun et al., 2014). These ontogenetic differences have significant biological implications, as macrophage origin can determine function even within the same tissue. For instance, monocyte-derived liver capsular macrophages, rather than tissue-resident Kupffer

cells, play a critical role in preventing bacterial dissemination (Sierro et al., 2017). Furthermore, contrary to early assumptions that tissue-resident macrophages are sessile, emerging evidence demonstrates that they can actively respond to infectious challenge. In murine models, tissue-resident alveolar macrophages have been shown to respond dynamically to both bacterial and viral infections (Neupane et al., 2020; Yao et al., 2018). Collectively, these observations illustrate that macrophage origin influences both functional diversity and the capacity for dynamic adaptation during immune challenge.

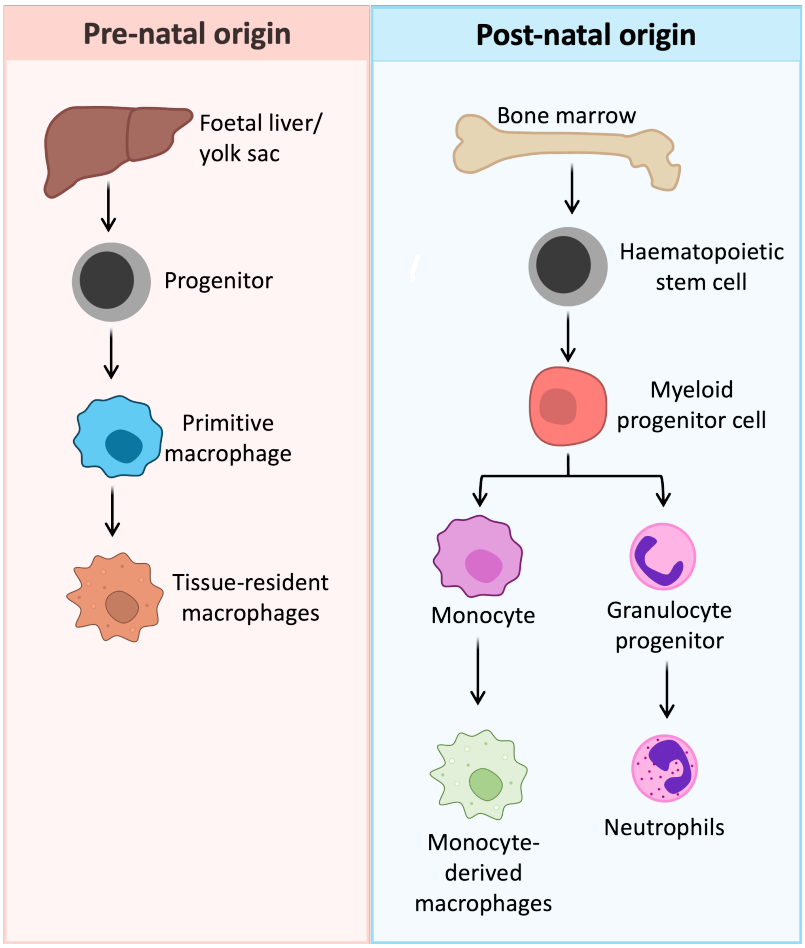


Figure 1.2. Macrophage ontogeny. Tissue-resident macrophages, such as microglia and Kupffer cells, arise from primitive macrophages from the foetal liver and yolk sac prior to the initiation of haematopoiesis. These tissue-resident macrophages are then self-renewing throughout life. Foetal-derived progenitors seed the bone marrow; whereby haematopoietic stem cells are then produced during post-natal haematopoiesis to replenish and maintain leukocyte populations. Myeloid progenitor cells can differentiate into either monocytes, giving rise to monocyte-derived macrophages, or granulocyte progenitors, which can differentiate into granulocytes such as neutrophils. Adapted from Rosales (2018); Galli et al., (2011); Park et al., (2025)

Macrophages play an essential role in maintaining tissue homeostasis through constant surveillance of their microenvironment, enabling rapid detection and response to pathogenic threats. Upon recognition of danger signals, they can eliminate pathogens or initiate tissue repair and remodelling processes (Neupane et al., 2020; Chen et al., 2023). This sentinel function is mediated by a

variety of pattern recognition receptors (PRRs), including toll-like receptors (TLRs), C-type lectin receptors (CLRs) and NOD-like receptors (NLRs), which detect pathogen-associated and damage-associated molecular patterns (PAMPs and DAMPs), and subsequently activate immune signalling (Takeuchi and Akira, 2010). Upon engagement with PAMPs or DAMPs, such as bacterial lipopolysaccharides, PRRs initiate a cascade of intracellular defence mechanisms. These include phagocytosis, followed by phagosome maturation and fusion with lysosomes to facilitate enzymatic pathogen degradation (Pandey et al., 2022; Chen et al., 2025). In addition to lysosomal processes, macrophages employ antimicrobial effectors, such as inducible nitric oxide synthase (iNOS), which is recruited to the phagosome to generate reactive nitrogen species, including nitric oxide, what contribute to microbial killing (Davis et al., 2007; Miller et al., 2004).

Macrophages exhibit remarkable phenotypic plasticity, enabling them to adapt their functional state depending on the nature of the PRR stimulus. For example, activation of the murine TLR4 pathway induces chromatin remodelling, resulting in a pro-inflammatory macrophage phenotype characterised by enhanced aerobic glycolysis (Lauterbach et al., 2019). This metabolic and transcriptional reprogramming underpins the ability of macrophages to tailor their responses to distinct immune challenges, thereby enabling context-dependent roles in inflammation, repair and homeostasis (Beyer et al., 2012; Ashley et al., 2016; Schnitzerlein et al., 2025).

1.2.2. Macrophage polarisation: the M1/M2 paradigm

Macrophage polarisation refers to the capacity of macrophages to dynamically alter their phenotype in response to cues within their microenvironment, both in homeostasis and disease. The concept was originally introduced through *in vitro* studies in which human monocytes were stimulated to adopt distinct functional states, broadly categorised as pro-inflammatory (M1) or anti-inflammatory (M2) (Mackaness, 1962; Nathan et al., 1983; Stein et al., 1992; Martinez et al., 2009). In this classification, M1 macrophages are associated with initiating inflammatory responses, whereas M2 macrophages are involved in tissue repair and restoration of homeostasis. Early work defining these activation states primarily relied on murine and human macrophages stimulated with T helper type-1 type-2 (T_H1/T_H2) cytokines, such as IFNγ or IL-4, leading to the terms ‘classically activated’ (M1) and ‘selectively/alternatively activated’ (M2) macrophages (Pace et al., 1983; Celada et al., 1984; Nathan et al., 1983; Doyle et al., 1994; Stein et al., 1992). However, the traditional view that adaptive immune signals are required to drive macrophage polarisation has been increasingly challenged. There is evidence suggesting that the innate immune system can independently initiate pro- or anti-inflammatory macrophage states, with T_H1/T_H2 responses serving instead to amplify, stabilise and co-ordinate these programmes in a positive feedback system (**Fig. 1.3.**) (Khan et al., 2019; Noël et al., 2004; Mills and Ley, 2014; Wiegertjes et al., 2016). This evolving perspective reflects a more nuanced understanding of macrophage activation beyond the binary M1/M2 paradigm.

Transcriptomic profiling from *in vitro* polarisation experiments has identified characteristic gene expression signatures and metabolic programmes associated with M1- and M2-like macrophages in humans and mice (Raes et al., 2002; Scotton et al., 2005; Martinez et al., 2006; Martinez et al., 2013). For example, M1 macrophages typically favour aerobic glycolysis, whereas M2 macrophages predominantly rely on oxidative phosphorylation (OXPHOS) (**Fig. 1.3.**) (Beyer et al., 2012; Galván-Peña and O'Neill, 2014). However, attempts to associate macrophage phenotype with cellular morphology have produced inconsistent results. Although some studies report that M1-polarised macrophages (IFNγ + LPS) adopt a more elongated shape and M2-stimulated macrophages (IL-4 or IL-10) appear rounder (Vogel et al., 2014), other investigations do not reproduce these patterns. These discrepancies likely reflect substantial variation in the *in vitro* systems used to assess morphology – including macrophage source (e.g.: BMDMs, peritoneal macrophages, MDMs, alveolar macrophages), culture medium (e.g.: RPMI, DMEM) and polarisation stimulus (Antonsen et al., 2023; Aldo et al., 2013; Schnitzerlein et al., 2025; Hind et al., 2016; Hourani et al., 2023; Rey-Giraud et al., 2012). The growing use of label-free approaches may help address some of these inconsistencies. Recent *in vivo* studies using label-free metabolic imaging demonstrate that macrophage populations are metabolically heterogeneous within tissues (Heaster et al., 2021), and mitochondrial-dynamics imaging has shown promise for identifying macrophage phenotypes based on organelle behaviour (Li et al., 2020). Accordingly, within *in vitro* settings and mammalian *in vivo* models, morphology alone cannot reliably define macrophage phenotype and generally must be interpreted alongside transcriptional, metabolic, or stimulus-based markers.

Early frameworks of macrophage polarisation were shaped by observations that inflammatory cues such TNF-α and anti-inflammatory cytokines, such as IL-10, drive divergent macrophage activation states. TNF-α is a key pro-inflammatory cytokine produced by M1-polarised macrophages and is essential for antimicrobial defence, promoting NF-κB activation, cytokine secretion, and microbicidal activity (Wesemann and Benveniste, 2003; Yarilina et al., 2008; Magez et al., 2007). In contrast, IL-10 is a central regulator of anti-inflammatory macrophage phenotypes: it suppresses pro-inflammatory cytokine production, inhibits antigen presentation, and limits tissue damage during chronic inflammation (Stumpo et al., 1999; Deng et al., 2012; Avdic et al., 2013). IL-10 signalling through STAT3 promotes genes associated with wound healing and immunoregulation, thereby contributing to what later became classified as 'M2-like' programmes (Hutchins et al., 2013). These cytokine-driven polarisation patterns laid the conceptual foundation for recognising that macrophages adopt distinct functional states in response to pathogenic or tissue-derived signals.

The M1/M2 model gained further traction following observations that macrophages differentially regulate nitric oxide metabolism, leading to the formulation of the iNOS/arginase axis

(Mills et al., 2000). In several experimental systems, such as in mice and carp, inducible nitric oxide synthase (iNOS) and arginase utilise L-arginine as a substrate but produce distinct products linked to macrophage function (Mills et al., 2000; Wilkins-Rodríguez et al., 2024; Wiegertjes et al., 2016). iNOS generates antimicrobial nitric oxide (NO) and reactive oxygen species (ROS), characteristics of pro-inflammatory macrophages (Nathan and Hibbs, 1991). Conversely, arginase catalyses the production of L-ornithine and polyamines, which supports tissue repair and resolution of inflammation (**Fig. 1.3.**) (Dzik, 2014). However, simple competition for L-arginine does not fully explain the balance between these pathways (Rath et al., 2014). A recent study demonstrated that under constant extracellular L-arginine conditions, arginase does not outcompete iNOS activity (Momma and Ottaviani, 2022), although the relevance of this observation *in vivo* remains uncertain. Instead, regulatory metabolites downstream of arginase, such as the polyamine spermine, can suppress iNOS (or NOS2) mRNA expression in macrophages (Cheng et al., 2005), and spermine has also been shown to inhibit macrophage L-arginine uptake by downregulating expression of the CAT-2B transporter in *in vitro* rat macrophages (Mössner et al., 2001). Together, these data suggest that, at least in rodent and carp systems, the iNOS/arginase axis may be governed less by direct substrate competition and more by the regulation of L-arginine transport and intracellular feedback mechanisms.

Importantly, the iNOS/arginase paradigm does not translate well to human macrophages. In contrast to murine cells, human macrophages generally express minimal *iNOS* and produce limited levels of NO when stimulated with M1-polarising agents (e.g.: LPS, IFNγ) (Muijsers et al., 2001; Gross et al., 2014). Consequently, the reciprocal iNOS/arginase axis that underpins the M1/M2 framework in rodents and carp is attenuated or absent in human cells. These species-specific differences highlight the need for caution when extrapolating L-arginine-centred macrophage polarisation models across systems and underscore the value of *in vivo* models to unravel the mechanisms which underpin this pro- and anti-inflammatory balance.

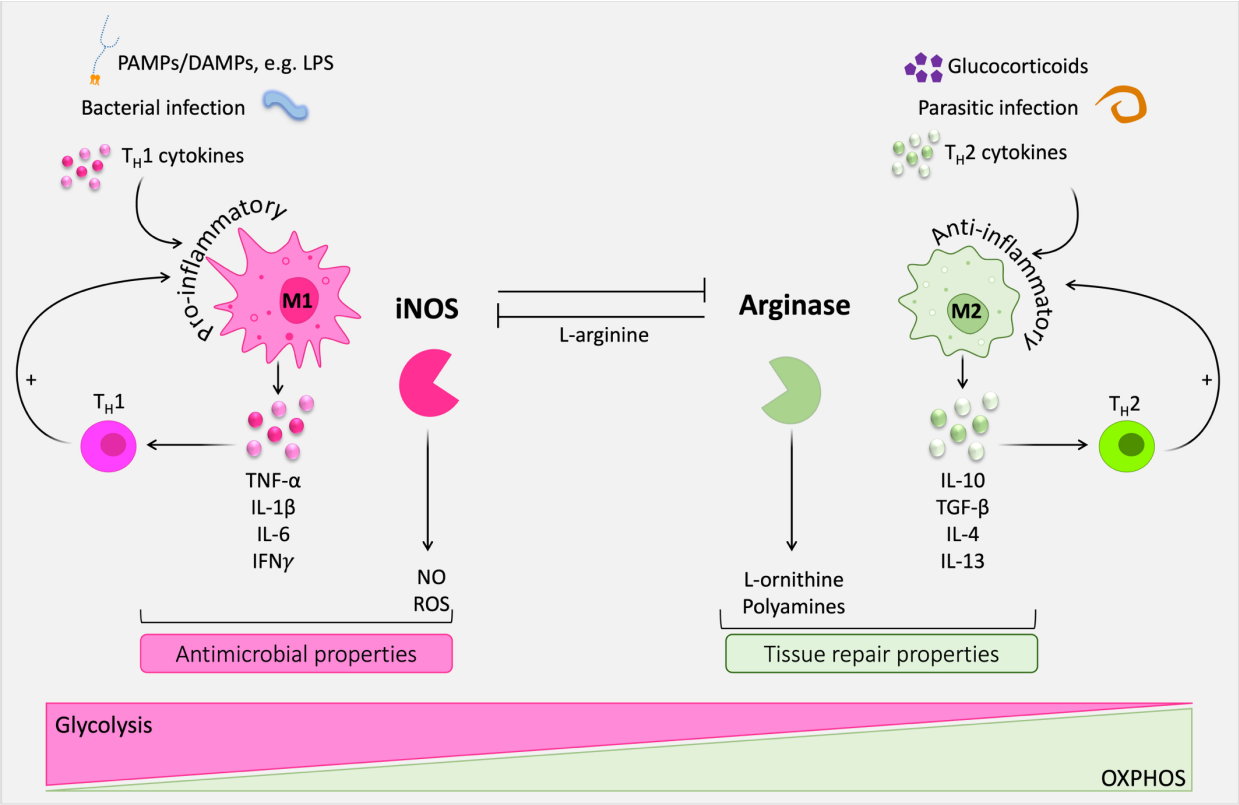


Figure 1.3. Macrophages polarise in response to distinct stimuli and contribute towards macrophage-directed adaptive immunity. Macrophages adopt a pro-inflammatory (M1) phenotype in response to various stimuli, including bacterial pathogens, LPS and T helper 1 effector cell (T_H1) cytokines (Anders and Ryu, 2011). These M1 macrophages release pro-inflammatory cytokines such as TNF-α, IFNγ, IL-1β and IL-6, which promote T_H1 activation and amplify antimicrobial immune responses. A hallmark of this phenotype is the enzyme iNOS, which converts L-arginine into antimicrobial NO and ROS (Nathan and Hibbs, 1991). This glycolytic metabolic programme supports enhanced phagocytic activity and efficient pathogen killing. Conversely, exposure to parasitic infections, glucocorticoids, and T helper 2 effector cell (T_H2) cytokines induce an anti-inflammatory (M2) phenotype, characterised by increased OXPHOS (Bianchini et al., 2019; Anders and Ryu, 2011). M2 macrophages secrete anti-inflammatory cytokines, including IL-4, IL-13, IL-10 and TGF-β, which drive T_H2 activation and reinforce this 'healing' phenotype. Arginase, a robust M2 marker, competes with iNOS for L-arginine to produce L-ornithine and polyamines – key metabolites in wound healing and tissue remodelling (Dzik, 2014). Collectively, these anti-inflammatory functions promote inflammation resolution and restoration of homeostasis. Abbreviations: PAMPs/DAMPs, pattern-/damage-associated molecular patterns; LPS, lipopolysaccharides; iNOS, inducible nitric oxide synthase; NO, nitric oxide; ROS, reactive oxygen species; OXPHOS, oxidative phosphorylation. Adapted from Speirs et al., (2024); Wiegertjes et al., (2016).

1.2.3. Macrophage polarisation: challenging the M1/M2 paradigm

Although *in vitro* frameworks describe macrophage polarisation as a reversible process depending on cytokine exposure *in vitro* (reviewed by Sica and Mantovani, (2012); Yellanki et al., (2024)), it remains unclear how macrophages transition between inflammatory states *in vivo*. Canonical M1/M2 markers (e.g.: iNOS, ARG1, MRC1, CD86) frequently co-localise within the same macrophages in human and non-human primate TB lesions, as well as in other chronic inflammatory environments

(Baidžajevas et al., 2020; Flynn et al., 2015; Kocsy et al., 2025; Mattila et al., 2013). This mixed-marker expression challenges binary macrophage classifications and raises a fundamental unresolved question: do these cells represent macrophages actively re-polarising in response to local cues, or do they reflect stable mixed-phenotype states with specialised functions? Similar hybrid phenotypes have been observed across diverse disease contexts. For example, Rückerl and colleagues demonstrated that macrophages derived from mice previously infected with *Heligmosomoides polygyrus bakeri* displayed co-expression of classical M1 and M2 markers – nitric oxide synthase (NOS) and RELM-α, respectively – following stimulation with the potent M1 agonist lipopolysaccharides (LPS) (Rückerl et al., 2017). Similarly, human macrophages from multiple sclerosis lesions simultaneously express M1 and M2-linked molecules such as CD40 and CD163 (Vogel et al., 2013). Such observations underscore that mixed phenotypes are not rare anomalies but are a consistent feature of macrophages responding to complex inflammatory environments. Collectively, these data challenge the canonical M1/M2 dichotomy and instead support the view that macrophages occupy a dynamic polarisation spectrum, with M1 and M2 representing extremes rather than mutually exclusive endpoints (**Fig. 1.4**) (Mills and Ley, 2014; Xue, Jia et al., 2014; Martinez and Gordon, 2014). Despite this, current experimental systems lack the temporal resolution to determine whether hybrid phenotypes arise from sequential re-polarisation events or represent inherently stable mixed phenotypes. Addressing this gap will require longitudinal *in vivo* imaging approaches capable of tracking individual macrophages over time and across dynamically evolving tissue microenvironments, particularly during chronic infections such as TB, where macrophage plasticity shapes disease outcomes.

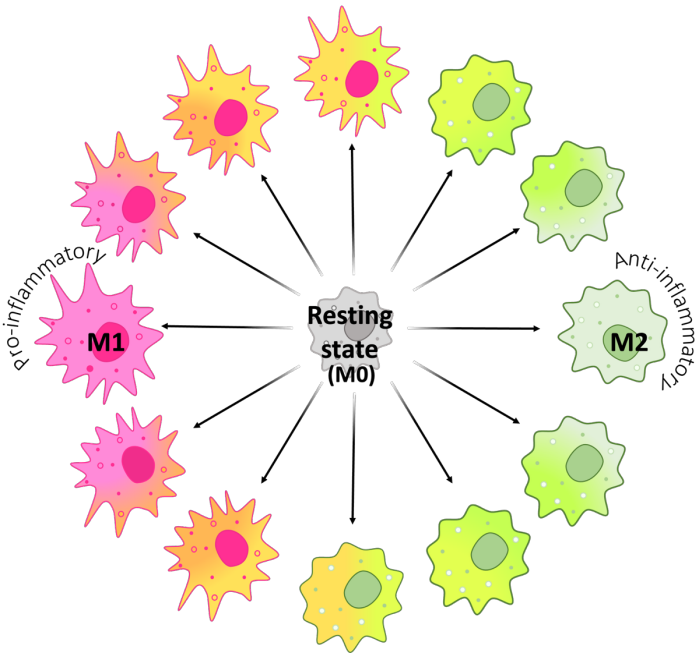


Figure 1.4. Macrophages polarise on along a spectrum. *In vitro*, macrophages are often polarised using defined M1 or M2 stimuli to study pro- and anti-inflammatory macrophages phenotypes. However, this binary classification does not accurately reflect macrophage phenotypes *in vivo*. Instead, macrophages exhibit a continuum of activation states, integrating both M1- and M2-associated functional characteristics to respond effectively to diverse immune challenges. Adapted from Guilliams and van de Laar, (2015).

To better reflect this complexity, the M2 phenotype was subdivided into M2a-d subtypes, based on distinct markers and stimuli (**Table 1.1.**) (Martinez et al., 2008). However, many of these markers overlap across these group, and intriguingly, some M2-like phenotypes (e.g.: M2b, M2d) arise in response to traditionally 'M1-type' stimuli such as LPS and can express M1-associated markers, including TNF-α and IL-1R (Strizova et al., 2023; Gharavi et al., 2022). Transcriptomic analyses further indicate that human macrophages respond to diverse stimuli by adopting unique transcriptional states that extend the binary model into a continuum (Xue et al., 2014). Nevertheless, recent quantitative proteomics in polarised human THP-1 macrophages revealed that although each M2 subtype exhibited subtype-specific proteins, their overall expression profiles were highly similar (Li et al., 2022). These insights support the modular spectrum model proposed by Guilliams and van de Laar (2015), emphasising functional attributes rather than rigid marker-based categorisation.

Table 1.1. *In vitro* polarising stimuli and marker expression of human macrophage subtypes.

Macrophage subtype	Polarising stimuli	Marker expression
M1	IL-6, TNF-α, LPS	iNOS, TNF-α, IL-10 (low)
M2a	IL-4, IL-10, IL-13	IL-10, Arg1 IL-1R
M2b	IL-1β, LPS	IL-10, CCL1, CD86
M2c	IL-10, glucocorticoids	CD163, IL-10, TGF-β
M2d	LPS	TGF-β, VEGF, TNF-α

Adapted from Strizova et al., (2023); Gharavi et al., (2022). Abbreviations: IL, interleukin; TNF-α, tumour necrosis factor-α; LPS, lipopolysaccharides; iNOS, inducible nitric oxide synthase; Arg1, arginase 1; CCL, C-C chemokine ligand; CD, cluster of differentiation; TGF-β, transforming growth factor-β; VEGF, vascular endothelial growth factor.

Importantly, markers defined *in vitro* may not reliably correspond to macrophage phenotypes *in vivo.* Human alveolar macrophages, for instance, express both CD86 (M1) and CD206 (M2) under steady-state conditions (Mitsi et al., 2018). Similarly, human bronchoalveolar lavage samples revealed macrophage subsets expressing exclusively M1 markers, exclusively M2 markers, a combination of both, or neither – highlighting substantial phenotypic variability *in situ* (Takiguchi et al., 2021). Such heterogeneity likely reflects the diverse environmental cues encountered in tissues and the need for macrophages to integrate multiple signals to fulfil context-dependent functions. Consistent with this, transcriptomic comparison of *ex vivo* murine peritoneal macrophages and differentiated murine BMDMs revealed discordance in marker expression following M1/M2 stimulation (Orecchioni et al., 2019), a finding mirrored when comparing stimulated human alveolar macrophages and monocyte-derived macrophages (Orecchioni et al., 2019).

1.2.4. Macrophage polarisation: phagocytic capacity

Phagocytosis is a defining function of macrophages and underpins their roles in host defence, tissue homeostasis, and immune regulation (Hirayama et al., 2017). Through receptor-mediated recognition of opsonised or non-opsonised targets, macrophages internalise pathogens, apoptotic cells, and cellular debris into phagosomes, which subsequently mature and fuse with lysosomes to enable degradation and antigen processing (Flannagan et al., 2009; Gordon, 2016). Beyond microbial killing, phagocytosis contributes to resolution of inflammation by facilitating efferocytosis – the clearance of apoptotic cells – thereby limiting secondary necrosis and promoting tissue repair (Schilperoort et al., 2023).

Importantly, phagocytic capacity is not uniform across macrophage activation states. While M1-like macrophages are optimised for microbial killing through production of ROS and pro-inflammatory cytokine secretion, several studies demonstrate that M2-like macrophages exhibit enhanced phagocytic and efferocytic capacity, particularly for apoptotic cells and particulate material (Kirchhoff et al., 2025; Jaggi et al., 2020; Kumar et al., 2024). In murine systems, M2-polarised macrophages show increased uptake of pathogens, beads and apoptotic cells compared with M1-polarised counterparts, a phenotype associated with elevated expression of scavenger receptors, C-type lectins, and opsonic receptors (e.g.: MRC1, MARCO) (Jaggi et al., 2020; Moss et al., 2024; Kirchhoff et al., 2025; Liebold et al., 2024). Recent work also highlights that macrophage phagocytosis is influenced by mechanical and adhesion cues in the microenvironment, with integrin-mediated phagocytic engagement altering cytoskeletal dynamics and force generation during engulfment, further emphasising that phagocytic capacity is regulated by both cellular state and extracellular context (Depierre et al., 2025). These functional attributes support roles for M2-like macrophages in debris clearance, TB granuloma organisation, and restoration of tissue homeostasis.

Differences in phagocytic capacity between macrophage activation states are linked to cytoskeletal organisation, membrane dynamics and metabolic programming. M2 polarisation has been associated with increased actin remodelling, augmented endocytic trafficking and reliance on OXPHOS, all of which support sustained engulfment and processing of phagocytic cargo (McWhorter et al., 2013; Mendoza-Coronel and Ortega, 2017; Tarique et al., 2015; Zhang et al., 2024). Conversely, M1-like macrophages prioritise rapid inflammatory signalling and antimicrobial effector functions, which may constrain prolonged phagocytic activity despite efficient pathogen killing (Kroner et al., 2014; Antonsen et al., 2024; Xiang et al., 2024). These observations further highlight that macrophage polarisation reflects functional specialisation rather than simple gain or loss of phagocytic capacity. Instead, distinct activation states alter phagocytosis to meet local tissue demands. In the context of chronic infection, such as TB, differences in phagocytic behaviour between macrophage activation states may have important consequences for bacterial containment, granuloma architecture and resolution, versus

bacterial dissemination. Understanding how phagocytic capacity is dynamically regulated across macrophage phenotypes therefore represents an important dimension of macrophage plasticity that complements transcriptional and metabolic frameworks of polarisation.

1.3. Host immune response to mycobacterial infection

1.3.1. Early innate immune responses: macrophages and neutrophils

The innate immune system forms the first line of defence against invading pathogens, including *Mtb*, mounting a rapid response upon pathogen entry (Wang et al., 2024). Following inhalation, alveolar macrophages are the first immune cell to recognise and internalise *Mtb*, initiating early host-pathogen interactions that shape subsequent immune responses (Cohen et al., 2018). Nonetheless, other innate immune cells also play crucial roles during these early stages of infection. Infected macrophages release pro-inflammatory cytokines and chemokines, such as TNF-α, which recruit additional immune cells, most notably neutrophils, to the site of infection (Vieira et al., 2009). Neutrophils employ several antimicrobial effector mechanisms, including phagocytosis, degranulation, neutrophil extracellular trap (NET) formation, oxidative activity and co-ordinated swarming behaviour (Kienle et al., 2021; Oskam, 2024; Morelli et al., 2025; Braian et al., 2013; Kroon et al., 2018; Jobe et al., 2025). Neutrophil-mediated monocyte recruitment and subsequent macrophage differentiation can potentiate neutrophil recruitment; however, recent work has shown that *Mtb*-stimulated primary MDMs can activate neutrophils whilst simultaneously reducing their migratory capacity, thereby retaining them at infection sites (Murphy et al., 2024; Kumar et al., 2018).

The contribution of neutrophils to *Mtb* control is therefore complex. Activated neutrophils have been associated with improved bacterial clearance in TB patients, attributed to increased ROS and NET production (Morelli et al., 2025; Murphy et al., 2024). Conversely, there is also evidence to suggest that an activated neutrophil phenotype may promote *Mtb* survival, and is associated with increased bacterial burden (Andrews et al., 2024). Moreover, neutrophil activation must be tightly regulated. For example, *Mtb*-induced NETs can activate macrophages and stimulate pro-inflammatory cytokine production that aids in bacterial clearance (Braian et al., 2013). Yet in later disease stages, particularly within granulomas, persistent NET-driven inflammation contributes to tissue pathology. The pro-inflammatory activity of NETs has been implicated in granuloma caseation, associated with *Mtb*-induced host lipid dysregulation and renders the granuloma vulnerable to degradation (Zlatar et al., 2024; Elkington et al., 2011).

As the infection progresses, the recruitment of additional immune populations, including T and B lymphocytes, facilitates the development of adaptive immunity (Huang et al., 2025; Stewart et al., 2023). While many immune cell types contribute to host defence against *Mtb*, this thesis focuses on

macrophages, the primary cells that first encounter the pathogen and can be subsequently subverted by *Mtb* to promote its intracellular survival and persistence (Cohen et al., 2018; Bo et al., 2023).

1.3.2. Macrophages in *Mtb* infection: early innate responses and cellular heterogeneity

Macrophages are the primary innate immune cells involved in defence against TB infection, phagocytosing *Mtb* very rapidly; however, they also serve as a critical niche for *Mtb* growth, survival and dissemination (Cohen et al., 2018). The early macrophage response to *Mtb* infection has largely been defined as pro-inflammatory based on observations from traditional *in vitro* macrophage models, and this transient activation following phagocytosis is essential for initial infection control (Arredouani et al., 2005; Huang et al., 2018; Pisu, D. et al., 2020; Chacón-Salinas et al., 2005). However, these models do not typically reflect the behaviour of tissue-resident lung macrophages encountered during the earliest stages of infection. Alveolar and interstitial macrophages are not only ontogenetically different, but also display divergent transcriptional programmes and activation status following mycobacterial infection (Pisu et al., 2020; Pisu et al., 2024). This distinction is particularly important for understanding early host-pathogen interactions, as alveolar macrophages are the first cells infected with *Mtb in vivo*, whereas interstitial macrophages are recruited later to the lung (Huang et al., 2018).

Recent transcriptomic analyses in murine TB models challenge the prevailing view of a uniformly pro-inflammatory early macrophage response by demonstrating cell-type-specific behaviour. These studies show that alveolar macrophages initially adopt an anti-inflammatory programme that creates a permissive environment for bacterial replication, characterised by increased availability of fatty acids and iron (Pisu et al., 2020; Pisu et al., 2024). In contrast, interstitial macrophages develop a pro-inflammatory phenotype that restricts *Mtb* growth (Pisu et al., 2020). This functional divergence has significant consequences for infection control: depletion of alveolar macrophages results in an >80% reduction in bacterial burden, whereas depletion of interstitial macrophages leads to an approximately 10-fold increase (Huang et al., 2018). Nevertheless, alveolar macrophages can generate a pro-inflammatory response, although this capacity is initially constrained. In early infection, the majority of alveolar macrophages in *Mtb*-infected mice are CD38- and exhibit transcriptional signatures associated with anti-inflammatory activity, including lack of *Nos2* (iNOS) expression (~70% at 2 weeks post-infection) (Pisu et al., 2024). By 4 weeks post-infection, however, ~90% of alveolar macrophages are CD38+ and acquire an enhanced capacity to control bacterial growth (Pisu et al., 2024). Increased chromatin accessibility at promoter regions of pro-inflammatory genes, such as *Nos2*, further supports the ability of CD38+ alveolar macrophages to mount a protective inflammatory response as infection progresses (Pisu et al., 2024).

Despite the well-established differences between alveolar and interstitial macrophage responses during TB infection, most historical studies have relied on BMDMs or MDMs (Via et al., 1998;

Clemens and Horwitz, 1995; Mancino et al., 1997; Deretic and Fratti, 1999). These models have nevertheless provided foundational insight into macrophage-*Mtb* interactions. For example, *in vitro Mtb* infection of BMDMs induces early pro-inflammatory responses, characterised by elevated mRNA expression of canonical M1-associated markers such as TNF-α, IL-1β and iNOS (Chacón-Salinas et al., 2005). Similarly, the transcriptional profile of primary murine macrophages infected with *Mtb* resembles that of IFNγ-polarised macrophages (Ehrt et al., 2001). ESAT-6, a key component of *Mtb*'s ESX-1 type VII secretion system, has also been shown to be required for NLRP3 inflammasome activation and IL-1β secretion in THP-1 macrophages (Mishra et al., 2010). Moreover, knockdown of the macrophage scavenger receptor Marco in a zebrafish model of TB not only reduced mycobacteria phagocytosis, but also reduced the pro-inflammatory cytokine profile (e.g. *il1b*) which led to an increase in bacterial burden (Benard et al., 2014). However, despite multiple reports emphasising the host-protective effects of early pro-inflammatory macrophage activation, increasing pro-inflammatory signalling alone – such as through canonical TLR stimulation – was insufficient to eliminate *Mtb* in human macrophages (Yang et al., 2016; Huang et al., 2018; Solomon and Bryson, 2023). This finding underscores a key limitation of *in vitro* TB models: focusing solely on specific pathways, such as TLR and TNF signalling, fails to replicate the complex and multifactorial immune cues present within infected lung tissue (Solomon and Bryson, 2023).

1.3.3. Macrophages in *Mtb* infection: subcellular strategies for immune evasion

In healthy individuals, the macrophage response is often sufficient to clear (or contain) *Mtb* infection (Emery et al., 2021; Ahmad et al., 2022). However, despite the antimicrobial properties of pro-inflammatory macrophages, *Mtb* has evolved numerous ways to evade killing at early stages of infection. Following phagocytosis, *Mtb* survives within the phagosome in part due to the acid-buffering activity of mycobacterial acid resistance protein (MarP) (**Fig. 1.5. A** – step 1) (Levitte et al., 2016). *Mtb* also prevents phagosome maturation through multiple mechanisms. For example, the secreted effector Rv2347c suppresses expression of early phagosome markers, such as *RAB5* (Jiang et al., 2024), while lipoamide dehydrogenase promotes retention of Coronin-1 at the phagosome membrane, thereby maintaining an immature phagosomal state (Deghmane et al., 2007). In addition, *Mtb* inhibits phosphatidylinositol 3-phosphate (PI3P) accumulation, thereby blocking phagolysosome fusion by disrupting vesicular trafficking modulation (**Fig. 1.5. A** – step 2) (Fratti et al., 2003). Beyond inhibiting maturation, *Mtb* can also escape into the cytosol to replicate and disseminate, mediated by host cytosolic phospholipase A_2 activation, Rv2347c-dependent phagosomal rupture and ESAT-6-driven membrane perforation (**Fig. 1.5. A** – step 3) (Jamwal et al., 2016; Jiang et al., 2024; Lienard et al., 2020; Houben et al., 2012).

Following these early evasion strategies, it has become clear that *Mtb's* ability to manipulate phagosomal trafficking, autophagy and cytosolic access lays the foundation for later macrophage

reprogramming. While these processes occur within mammalian macrophages, many of the mechanistic principles were first uncovered using reductionist phagocyte models. In particular, *Dictyostelium discoideum* (Dd) (a social amoeba) infected with *Mycobacterium marinum* (*Mm*) (see section 1.6.2) has been instrumental in defining conserved subcellular events underlying mycobacterial intracellular survival. Dd are soil-dwelling, prey on bacteria, and share key phagocytic behaviours analogous to macrophages (Bozzaro and Eichinger, 2011). As such, the Dd-*Mm* system provides a tractable platform for dissecting early phagocyte-mycobacterial interactions (Martín-González et al., 2021). For example, *Mm* infection of Dd revealed ESX-1-dependent inhibition of autophagy to promote intracellular survival, mirroring observations in human dendritic cells (Cardenal-Muñoz et al., 2017; Romagnoli et al., 2012). Similarly, Dd studies identified *Mm*-induced expression of the zinc efflux pump gene *ctpC*, reflecting the ability of *Mtb* to resist zinc toxicity via ATP-driven metal export in human PBMCs (Hanna et al., 2021; Botella et al., 2011). These findings underscore the evolutionary conservation of key mycobacterial survival pathways across phagocytes. At the same time, the Dd-*Mm* model has highlighted mechanistic divergence between *Mm* and *Mtb*. While *Mtb* utilises host fatty acids, induces foamy macrophage formation and can enter a dormancy-like state *in vitro* (Daniel et al., 2011), *Mm* infection in Dd leads to host lipid utilisation without reduced bacterial growth or metabolic quiescence (Barisch and Soldati, 2017). Such differences reinforce the need to validate Dd-derived insights in mammalian macrophage systems. Nevertheless, Dd has proven valuable for identifying *Mm* virulence factors relevant to macrophage infection; deletion of *mmar_2318/2319*, encoding lipooligosaccharide biosynthesis enzymes, attenuated virulence without impairing entry or proliferation in Dd, a phenotype subsequently confirmed in human THP-1 macrophages (Chen et al., 2016). Collectively, the Dd-*Mm* model has been essential for elucidating conserved mechanisms of phagosome maturation arrest, autophagy inhibition and cytosolic escape – processes that precede and shape macrophage plasticity during *Mtb* infection.

While the type VII secretion system remains the best-characterised *Mtb* virulence system, emerging evidence highlights additional mechanisms by which *Mtb* modulates macrophage function to support its survival. For instance, Rv1804c, a conserved secretory protein, induces a pro-inflammatory macrophage phenotype via NF-κB activation, resulting in elevated TNF-α and IL-6, and reduced *Mtb* survival *in vitro* (Zheng et al., 2024). Importantly, virulent clinical isolates exhibit markedly lower Rv1804c expression and low Rv1804c levels correlated with high bacterial burden in sputum (Zheng et al., 2024). This suggests that mycobacteria has evolved to promote its survival, by downregulating secretion of effector proteins to enhance *Mtb* survival by limiting macrophage-mediated killing (Zheng et al., 2024). Another example is *Mtb* curli pili (MTP), a surface adhesin required for macrophage entry (Menozzi et al., 2006). Recent work showed that MTP suppresses glycolysis in THP-1 macrophages, contributing to the metabolic quiescence characteristic of *Mtb*-infected macrophages and associated with enhanced pathogen survival (Ashokcoomar et al., 2025; Cumming et al., 2018). These studies

highlight a growing paradigm in TB biology: *Mtb* promotes its persistence not only by resisting intracellular killing (e.g. through phagosomal buffering and maturation arrest), but also by actively reprogramming macrophage phenotypes and metabolism to create a permissive niche for intracellular survival.

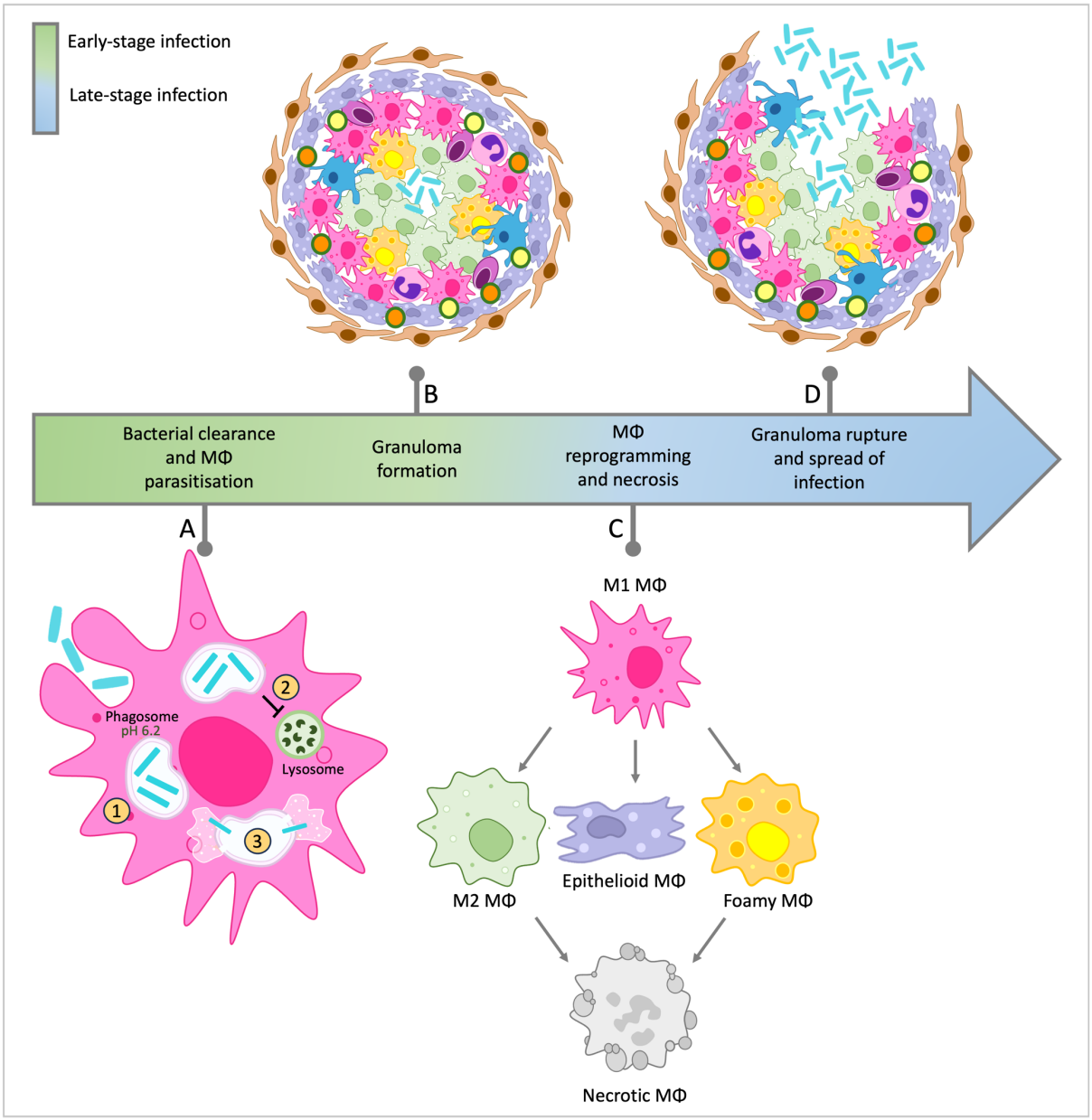


Figure 1.5. The macrophage response to *Mtb* and its role in TB pathogenesis. (**A**) Following *Mtb* inhalation, alveolar macrophages phagocytose the pathogen. *Mtb* parasitises macrophages, using a range of survival strategies within the macrophage phagosome, including (1) suppressing phagosome acidification (Levitte et al., 2016), (2) preventing phagosome maturation and phagosome-lysosome fusion (Asrat et al., 2014; Tan and Russell, 2015; Zhai et al., 2019), and (3) permeabilization of the phagosome using the *Mtb* secretion system to enable escape into the cytosol (Houben et al., 2012; Gao et al., 2004; Lienard et al., 2020). (**B**) Macrophages recruit additional immune cells to tackle the infection, which may result in granuloma formation if *Mtb* is not readily killed. Bacteria can remain alive in granulomas for years, as latent TB (Carranza et al., 2020). (**C**) At later stages of infection, *Mtb* modulates macrophage phenotypes, such as re-programming macrophages towards epithelioid-like cells (Cronan et al., 2016). Additionally, *Mtb* biases pro-inflammatory M1-like macrophages towards an anti-

inflammatory phenotype and differentiation into foamy lipid-laden macrophages. Necrosis of these macrophage cell types within the core results in a 'cheese-like' structure, known as a caesium (Sarathy and Dartois, 2020). (**D**) Caseation of the granuloma can render it vulnerable, and a trigger, such as the patient becoming immunocompromised, can result in granuloma rupture and subsequent spread of infection. Abbreviations: Mϕ, macrophage.

1.3.4. Macrophages in *Mtb* infection: the pro- to anti-inflammatory transition during granuloma development

As infection progresses and granulomas form (**Fig. 1.5. B**), macrophage phenotypes become increasingly complex, reflecting a shift from early bactericidal responses to a dynamic balance between host-driven containment and pathogen-mediated immune modulation. Granuloma formation initially contributes to control by recruiting diverse immune cells and physically containing *Mtb* (Ramakrishnan, 2012; Adams, 1974); however, sustained pro-inflammatory signalling at this stage becomes detrimental, and simply promoting a pro-inflammatory macrophage phenotype is no longer host-protective. For example, promoting an anti-inflammatory macrophage phenotype through pharmacological inhibition of hypoxia inducible factor (HIF)-1α in late TB was found to be host-protective in mice, with reduced pulmonary bacterial loads and tissue damage (Baay-Guzman et al., 2018). Consistent with this, recent single-cell RNA sequencing (scRNAseq) identified a population of *granulin a, tandem duplicate 2* (*grna.2+)* macrophages in granulomas from zebrafish TB models, where depletion of these cells increased pro-inflammatory cytokine expression (*tnfa*, *il1β*), exacerbated tissue pathology and reduced survival (Luo et al., 2025). GRN+ macrophages are also enriched in human TB granulomas, with higher proportions of GRN+ macrophages associated with reduced pulmonary inflammation (Luo et al., 2025). Collectively, these studies highlight the context-dependent nature of macrophage phenotypes during infection, and show that a shift from pro- to anti-inflammatory macrophage states in chronic stages is essential in to limit pathology while maintaining bacterial control.

During macrophage transition, *Mtb* progressively reprogrammes granuloma-resident macrophages (**Fig. 1.5. C**) toward an M2-like phenotype and preferentially infects these more permissive cells (El Kasmi et al., 2008; Cambier et al., 2014; Cambier et al., 2017; Ly et al., 2008). One mechanism involves induction of *arginase 1*, a hallmark of anti-inflammatory macrophages, which decreases NO production (El Kasmi et al., 2008). *Mtb*-infected macrophages can also drive *arginase 1* induction in uninfected macrophages through autocrine-paracrine signalling *in vitro* (Qualls et al., 2010), and increased *ARGINASE 1* expression has been detected in human TB granulomas (Pessanha et al., 2012). *Ex vivo* guinea pig studies further demonstrated preferential *Mtb* infection of M2 macrophages and a switch from pro- to anti-inflammatory transcriptional profiles during granuloma maturation (Ly et al., 2008), while ESAT-6 can directly promote M2 polarisation in human monocyte cultures (Refai et al., 2018). Thus, *Mtb* exploits both intrinsic macrophage plasticity and the evolving

granuloma microenvironment to reinforce anti-inflammatory programmes and limit bactericidal function.

Concurrent tissue-specific cues further reinforce macrophage reprogramming. Type-2 cytokine signalling drives epithelialisation of macrophages, inducing epithelial-associated transcriptional programmes and diminishing inflammatory capacity, while another subset differentiates into lipid-laden foamy macrophages that support bacterial persistence (Cronan et al., 2016; Puissegur et al., 2007; Ordway et al., 2005; Rhoades et al., 2005). In addition to *Mtb*-driven immune modulation, other granuloma-resident immune cells contribute to establishing an anti-inflammatory niche. For example, S100A9-expressing neutrophils were recently shown to induce M2 polarisation in BMDMs and co-localise with Arg1+ macrophages in BCG-infected guinea pig granulomas (Mizutani et al., 2023). Moreover, recent transcriptomic analysis of non-human primate granulomas revealed that a subset of *Mtb*-infected macrophages undergo an epithelial-to-mesenchymal transition, characterised by upregulation of genes involved in cell adhesion and extracellular matrix interactions (Pisu et al., 2025). Mesenchymal cells exert well-documented anti-inflammatory functions; and thus this transition further supports an *Mtb*-driven shift toward regulatory macrophage states (Bernardo and Fibbe, 2013). Collectively, these reprogramming events generate specialised macrophage states that suppress protective inflammation while promoting bacterial persistence and tissue remodelling, with necrosis of these cells setting the stage for granuloma caseation.

1.3.5. Macrophages in *Mtb* infection: granuloma breakdown and bacterial dissemination

Caseation within the granuloma core marks a critical turning point in disease progression (Kim et al., 2010). In resolved granulomas, necrotic debris often becomes calcified (Yedgarian et al., 2025); however, in non-resolving lesions, ongoing necrosis weakens granuloma integrity and further progresses tissue pathology (Grosset, 2003). Notably, *Mtb* can readily proliferate within early necrotic macrophages, underscoring how macrophage death facilitates intracellular bacterial expansion and subsequent dissemination (Lerner et al., 2017). Beyond enabling bacterial escape, multiple host-pathogen interactions further drive late-stage immunopathology. For instance, *Mtb* suppresses the PI3K regulatory pathway in primary human macrophages, resulting in elevated pro-inflammatory cytokine production and matrix metalloproteinase-1 (MMP-1) deposition, which together promote fibrosis and facilitate transmission (Brace et al., 2017). In addition, emerging evidence suggests that *Mtb* can induce macrophage-to-myofibroblast transformation, further contributing to pulmonary fibrosis (Evans et al., 2020). Under conditions of immune suppression – for example during immunosuppressive therapy – structurally compromised, caseating granulomas may rupture, leading to bacterial dissemination, active TB disease, and onward transmission (**Fig. 1.5. D**) (Grosset, 2003).

There is conflicting evidence regarding whether pro- or anti-inflammatory macrophages drive TB granuloma formation. *In vitro*, M1-polarised peripheral blood mononuclear cells (PBMCs) were reported to form granuloma-like aggregates following *Mtb* infection, whereas M2-polarised macrophages failed to do so (Huang et al., 2015). However, this system models granulomas based solely on cellular aggregation within a single-cell-type culture, and therefore lacks the cellular diversity and environmental cues that are essential for granuloma development *in vivo*. In contrast, studies in other granulomatous diseases suggest a role for M2 macrophages in promoting cellular aggregation. For example, in sarcoidosis, integrin Mac-1 was shown to regulate IL-13-mediated M2 polarisation and promote macrophage aggregation in mice (Podolnikova et al., 2016; Cao et al., 2015). Consistent with this, *in vivo* imaging in the zebrafish TB model demonstrated that IL-4-dependent M2-like signalling is required for granuloma formation, with inhibition of the IL-4 pathway resulting in impaired macrophage-to-epithelial transition and disrupted granuloma architecture (Cronan et al., 2021). Taken together, these findings suggest that while pro-inflammatory macrophages may initiate early immune aggregation in simplified *in vitro* systems, anti-inflammatory and epithelializing macrophage states appear essential for the maturation and organisation of TB granulomas *in vivo*.

1.3.6. Macrophages in *Mtb* infection: unresolved questions

Although much has been learned about macrophage behaviour during TB, major gaps remain in understanding how *Mtb* reshapes macrophage phenotypes as granulomas develop. *Mtb*-driven cues, including bacterial lipids, hypoxia, and type 2 cytokine signalling, progressively bias granuloma-resident macrophages toward regulatory or M2-like programmes that limit microbicidal activity while supporting bacterial persistence (Huang et al., 2015; Marín Franco et al., 2020; Cronan et al., 2021). This shift underlies the emergence of anti-inflammatory macrophage states such as foamy, epithelialized, and Arg1+ macrophages, all of which contribute to granuloma maturation and the creation of permissive niches for *Mtb* survival (Cronan et al., 2016; Cronan et al., 2021; Luo et al., 2024; Seto et al., 2022; Mattila et al., 2013; Pisu et al., 2025). Defining the dynamics, regulation, and functional consequences of macrophage phenotype switching remains a central challenge in TB immunology. To determine how these phenotypic states contribute to granuloma function and pathology, *in vivo* longitudinal imaging approaches are required. The *Mycobacterium marinum*-zebrafish model, discussed in section 1.6., provides a uniquely powerful platform to address this gap.

1.4. Manipulation of macrophage phenotypes as a host-directed therapy strategy

As well as *Mtb* repolarising infected macrophages towards an anti-inflammatory phenotype, first-line antibiotics against *Mtb* that act directly on the bacterium (e.g. rifampicin) can also attenuate pro-inflammatory macrophage response through anti-inflammatory and immunosuppressive side-effects (Cho et al., 2020). As an antibiotic, rifampicin inhibits *Mtb* RNA synthesis by targeting DNA-dependent RNA polymerase (Wehrli et al., 1968). Yet its off-target effects on host cells includes

suppression of pro-inflammatory cytokine production (e.g.: TNF-α) and inhibition of NF-κB activation in tissue-resident macrophages (Bi et al., 2011; Kim et al., 2017). Pyrazinamide, which primarily targets non-replicating persistent *Mtb* bacilli, has a less clearly defined mechanism of action, with *in vitro* findings not fully aligning with *in vivo* observations (Zhang et al., 2013; Santucci et al., 2022). Notably, immunohistochemical staining of lung tissue from pyrazinamide-treated *Mtb* patients found a higher proportion of *ARGINASE 1+* macrophages, and this elevated M2-like ratio was associated with increased drug-resistant *Mtb* (Cho et al., 2020).

One potential way to circumvent the rising issue of multi-drug resistance is by targeting host macrophages to bolster the immune response and improve *Mtb* clearance – an approach less likely to drive drug resistance. Host-directed therapies (HDTs) aim to therapeutically manipulate host pathways to enhance bacterial clearance (Kilinç et al., 2021). Moreover, HDTs have been proposed as adjunctive therapies alongside current and repurposed drugs to improve TB outcomes (Young et al., 2020; Li et al., 2025).

HDTs can act on various mechanisms (e.g. increasing phagocytosis or autophagy) and cell types (e.g. neutrophils) involved in *Mtb* infection, but this thesis focuses on compounds that augment macrophage responses to reduce *Mtb* load. A wide range of HDTs that modulate macrophage activation or function have recently been comprehensively reviewed by Li et al., (2025). Most HDTs for TB remain in preclinical stages, with many studies testing repurposed drugs in combination with existing antibiotics to shorten development timelines (**Fig. 1.6.**). The vast majority of macrophage-targeting HDTs aim to promote a pro-inflammatory programme, thereby enhancing host bactericidal activity. For example, Biapenem (a carbapenem antibiotics) and Withaferin A (a steroidal lactone) both activate the p38 MAPK pathway to drive M1 macrophage polarisation, synergising with rifampicin and isoniazid, respectively (Pahuja et al., 2023; Kumari et al., 2023). However, *in vitro* studies such as these do not address potential off-target consequences – including tissue damage or excessive inflammation – that may accompany enhanced pro-inflammatory activation (El Kasmi et al., 2008; Lundahl et al., 2022; Roca and Ramakrishnan, 2013; Piñeros et al., 2017; Finotto et al., 2002; Dall'Asta et al., 2012).

The effect of HDTs on macrophage polarisation are not straightforward. For example, metformin (an antidiabetic drug) was shown to promote an M1 phenotype in *Mtb*-infected THP-1 macrophages, characterised by increased ROS production and phagolysosome fusion (Singhal et al., 2014). In combination with anti-TB drugs, metformin reduced bacterial burden and limited lung pathology in *Mtb*-infected mice – the latter typically associated with anti-inflammatory macrophage phenotypes (Singhal et al., 2014). However, in a phase 2b clinical trial, metformin did not reduce sputum bacterial load when used as an adjunctive therapy, but did reduce circulating pro-inflammatory cytokines, including TNF-α, IL-1β and IFNγ (Padmapriydarsini et al., 2022). Together, these findings

highlight the challenges of classifying HDTs solely as 'M1-' or 'M2-promoting', particularly when translating *in vitro* results to human studies, where systemic effects complicate interpretation. For example, the antibiotic azithromycin promotes an M2-like phenotype in murine and human macrophages *in vitro*, associated with impaired mycobacterial killing (Yadav et al., 2023; Renna et al., 2011). Yet in a randomised phase 2 trial, azithromycin combined with anti-TB drugs reduced markers of lung damage in patient sputum (e.g.: TGF-β), apparently through reduced neutrophilic rather than macrophage-driven inflammation (Dekkers et al., 2025).

Pravastatin is another repurposed drug being explored as a potential HDT for TB. In THP-1 macrophages, pravastatin enhanced efficacy of first-line antibiotics by promoting a pro-inflammatory phenotype and improving phagosome acidification (Dutta et al., 2020). Moreover, adjunctive pravastatin improved bacterial clearance in a murine TB model (Dutta et al., 2020). However, its safety in humans remains uncertain: a phase 2 clinical trial reported toxicity leading to early termination of the two higher-dose arms (120 mg and 160 mg) (*Statin Adjunctive Therapy for TB (StAT-TB)*, 2018).

HDTs that promote anti-inflammatory macrophage phenotypes are much rarer, despite their potential to minimise tissue damage while supporting bacterial clearance (**Fig. 1.6.**). For example, the phosphodiesterase-4 inhibitor CC-11050 dampened macrophage pro-inflammatory responses in *Mtb*-infected rabbits, enhancing isoniazid-mediated bacterial clearance while reducing lung pathology (Subbian et al., 2016; Subbian et al., 2016). Similarly, dexamethasone remains the only WHO-approved adjunctive HDT for TB meningitis (Thwaites et al., 2004). A recent study found that dexamethasone reduced glycolysis in *Mtb*-stimulated human alveolar macrophages stimulated – a hallmark of M1 macrophages – without impairing bactericidal capacity, leading to reduced bacterial loads even when used alone (Thong et al., 2025). Collectively, these studies illustrate the nuanced challenge of identifying HDT targets that modulate macrophage phenotype for TB therapy. Effective approaches may be needed to balance pro- and anti-inflammatory features, tuning cytokine release, transcriptional programmes, and metabolic states to optimise bacterial clearance while limiting pathology.

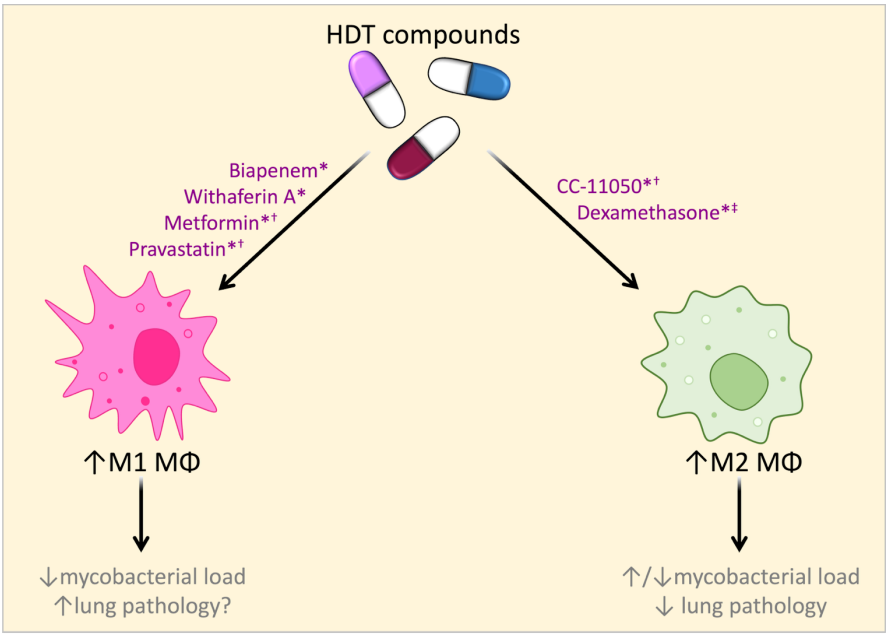


Figure 1.6. Host-directed therapeutic compounds that target macrophage polarisation against *Mtb* infection. The vast majority of HDTs that target macrophage polarisation do so my promoting a pro-inflammatory M1-like phenotype. Biapenem and Withaferin A both activate p38 MAPK signalling to promote M1 macrophage polarisation, working synergistically with antibiotics (Pahuja et al., 2023; Kumari et al., 2023). Metformin promotes a pro-inflammatory phenotype by activating AMP-activated protein kinase, having an additive effect alongside antibiotics (Singhal et al., 2014; Naicker et al., 2023). Metformin has shown positive effects in TB patients in clinical trials (Padmapriydarsini et al., 2022). Pravastatin inhibits HMG-CoA, with evidence of promoting a pro-inflammatory macrophage phenotype and working to reduced bacterial burden through adjunctive activity (Dutta et al., 2020). Pravastatin has completed phase 2 clinical trials and is in the data analysis stage to determine its effectiveness as an adjunctive therapy for TB (*Statin Adjunctive Therapy for TB (StAT-TB)*, 2018). HDTs that target and promote pro-inflammatory macrophage phenotype are often characterised by decreased bacterial burden, but despite the increased inflammatory profile, there are mixed reports on the effects of these compounds on lung pathology. There are some HDT compounds that aim to promote an anti-inflammatory M2-like phenotype. CC-11050 is a phosphodiesterase-4 inhibitor that has shown to reduce *Mtb* burden and lung pathology when used as part of adjunctive therapy (Subbian et al., 2016; Subbian et al., 2016). Phase 2 clinical trial for CC-11050 found that the drug was well tolerated and enhanced lung function in TB patients (Wallis et al., 2021). Dexamethasone is the only HDT adjunctive treatment currently approved for use against TB by the World Health Organisation (Thong et al., 2025). When used alongside antibiotics, dexamethasone leads to reduced mycobacterial load and reduced inflammation. *Additive/synergistic combination; †Clinical trials; ‡Approved for use.

While macrophage-targeted HDTs hold promise, their timing and context are critical, as macrophage functions shift dynamically across different stages of *Mtb* infection. For example, stabilisation of the transcription factor hypoxia inducible factor (HIF)-1α at early stages of infection improves mycobacteria clearance by promoting an M1-like macrophage phenotype (Lewis and Elks, 2019; Baay-Guzman et al., 2018). However, during established granuloma stages, sustained HIF-1α-driven inflammation can exacerbate infection and tissue pathology (Baay-Guzman et al., 2018;

Domingo-Gonzalez et al., 2017). Conversely, promoting an M2-like macrophage phenotype by blocking or reducing HIF-1α expression at this later stage has been shown to decrease bacterial burden, partly through induction of macrophage apoptosis (Baay-Guzman et al., 2018; Domingo-Gonzalez et al., 2017). Thus, although pro-inflammatory macrophage production of NO is a well-characterised antimicrobial mechanism, other bactericidal pathways may operate independently of classical M1 activation (Yang et al., 2016). For instance, systemic treatment with the M2-polarising cytokine IL-33, or adoptive transfer of M2-polarised BMDMs into *Mtb*-infected mice, ameliorated advanced disease despite reduced *iNOS* expression (Piñeros et al., 2017). Similarly, pre-treatment of murine BMDMs and human MDMs with IL-4/IL-13 prior to mycobacterial stimulation skewed cells towards an M1-like transcriptional profile (e.g.: elevated TNF-α, increased *NOS2* and decreased *Arg1* expression) and enhanced bacterial killing, while maintaining an M2-associated OXPHOS metabolism (Lundahl et al., 2022). These findings highlight that simplistic 'M1 equals killing' and 'M2 equals healing' frameworks overlook the metabolic and functional plasticity of macrophages. Together, they underscore the therapeutic potential of HDTs that reprogramme *Mtb*-skewed macrophages towards bactericidal yet tissue-protective states – balancing antimicrobial efficacy with control of host-driven pathology.

1.5. Hypoxia and Hypoxia Inducible Factors (HIFs)

Hypoxia – defined as a state of reduced oxygen availability – is a hallmark of many immune challenges, including infection and inflammation (Krzywinska and Stockmann, 2018). It has broad pathophysiological relevance, contributing to the progression of diverse diseases such as cancer, chronic kidney disease, atherosclerosis and endometriosis (Di Giovannantonio et al., 2025; Faivre and de Seigneux, 2024; Ajoolabady et al., 2024; Hoffmann-Młodzianowska et al., 2024). Under conditions of chronic hypoxia, cells face sustained metabolic stress that can lead to necrosis, tissue fibrosis and organ dysfunction, largely due to a shift from OXPHOS towards glycolysis as an adaptive but energetically inefficient response (Choudhury, 2018; Chen et al., 2020). For example, in TB granulomas, restricted vascular supply and dense cellular organisation can create a hypoxic core, generating metabolic stress that shapes immune cell function and pathogen persistence by activating hypoxia-responsive pathways and altering cellular respiration (Qualls and Murray, 2016). Conversely, transient or moderate hypoxia can trigger beneficial physiological adaptations, including angiogenesis to restore oxygen delivery and enhanced stem cell differentiation (Richard et al., 2000; Pimton et al., 2015). Importantly, hypoxia signalling also plays critical roles in immune regulation. Activation of hypoxia-responsive pathways can enhance neutrophil phagocytic capacity, promote pro-inflammatory macrophage activation and support regulatory T cell differentiation (Lodge et al., 2020; Krzywinska and Stockmann, 2018; Shi et al., 2011).

Central to the cellular response to hypoxia are the hypoxia-inducible factors (HIFs) – master transcriptional regulators that coordinate adaptive gene expression under low-oxygen conditions

(Wang and Semenza, 1995). HIFs are heterodimeric transcription factors composed of an oxygen-sensitive α-subunit and a constitutively expressed β-subunit. Three isoforms of the HIF-α subunit have been identified – HIF-1α, HIF-2α and HIF-3α – which exhibit distinct patterns of expression and regulation across cell types (Taylor and Colgan, 2017). Stabilisation of HIF-1α and HIF-2α profoundly influences innate immunity, with HIF-1α being the best-characterised isoforms since its discovery as the key mediator of the hypoxic response during immune challenge (Wang and Semenza, 1995). In contrast, HIF-2α exhibits more restricted expression, and a more nuanced understanding of its immune functions is now emerging (Steinberger and Eubank, 2023). Importantly, in immune cells, HIF-1α activity dominates during acute hypoxia, whereas HIF-2α signalling becomes more prominent under chronic hypoxic conditions (Jaśkiewicz et al., 2022). While both HIF-1α and HIF-2α act as transcriptional activators, the less well-understood HIF-3α appears to function as a negative regulator of the other α-subunits, though its mechanisms remain poorly defined (Zhang et al., 2014).

Under normal oxygen levels (normoxia), newly synthesised HIF-α proteins are rapidly hydroxylated by the oxygen-sensing enzymes proly hydroxylase domain (PHD) and factor inhibiting HIF (FIH) (Krzywinska and Stockmann, 2018). Hydroxylation promotes binding of HIF-α to the von Hippel-Lindau (VHL) E3 ubiquitin ligase complex, resulting in ubiquitination and proteasomal degradation (Huang et al., 1998; Kallio et al., 1999; Elks et al., 2015). In hypoxic environments, such as those encountered during infection, PHD and FIH activity are impaired due to limited oxygen availability, preventing hydroxylation and allowing stabilisation of HIF-α protein (Krzywinska and Stockmann, 2018). The HIF-β subunit, which is constitutively expressed and predominantly nuclear, then dimerises with stabilised HIF-α, forming an active transcriptional complex (Depping et al., 2008; Krzywinska and Stockmann, 2018). This HIF heterodimer binds to hypoxia- responsive elements (HREs), activating a broad transcriptional programme that includes genes regulating angiogenesis, erythropoiesis, and inflammation (**Fig. 1.7.**) (Lee et al., 2004; Zenk et al., 2021).

Beyond its canonical role in oxygen homeostasis, HIF signalling plays a pivotal role in regulating immune function. In macrophages, HIFs integrate hypoxic and inflammatory signals to coordinate metabolic reprogramming, cytokine production, and antimicrobial responses. The next section discusses the functional implications of HIF activation in macrophage biology.

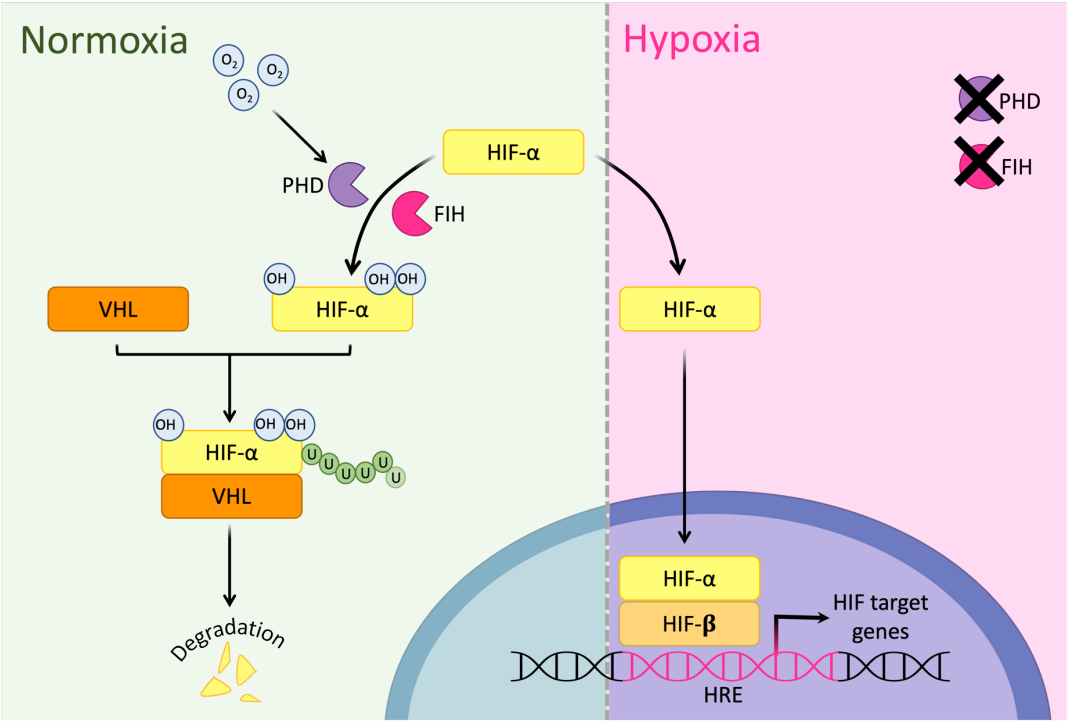


Figure 1.7. HIF signalling pathway under normoxic and hypoxic conditions. Hypoxia Inducible Factor (HIF) is the master regulator of the hypoxia signalling pathway. In normoxia, the oxygen sensing enzymes prolyl hydroxylases (PHDs) and factor inhibition HIFs (FIHs) hydroxylate the HIF-α subunit, triggering the subunit to bind with the von Hippel-Lindau (VHL) protein. This recruits a ubiquitin ligase, resulting in ubiquitination and subsequent proteasomal degradation of HIF-α. During hypoxia, PHD and FIH enzymes are unable to hydroxylate HIF-α due to loss of their oxygen-dependent function. Instead, HIF-α is translocated to the nucleus, where dimerises with the HIF-β subunit and bind to hypoxia-responsive elements (HREs). This results in transcription of downstream HIF target genes. Adapted from Hammond et al., (2020).

1.5.1. HIF and macrophage function

The three HIF isoforms elicit different cellular responses, and while the role of HIF-3α remains poorly characterised, the functions of HIF-1α and HIF-2α in leukocyte biology are well established, particularly in the context of macrophage polarisation (Lombardi et al., 2022). HIF-1α and HIF-2α exert opposing effects on NO homeostasis in murine BMDMs, thereby influencing macrophage polarisation (Takeda et al., 2010). During M1 polarisation with LPS or IFNγ, HIF-1α stabilisation leads to *iNOS* upregulation – a canonical marker for pro-inflammatory macrophages – resulting in enhanced antimicrobial NO production from L-arginine catabolism (**Fig. 1.8.**) (Takeda et al., 2010; Wang et al., 2017). Conversely, stimulation with the M2-polarising cytokine IL-4 promotes HIF-2α stabilisation and accumulation, driving *Arginase 1* upregulation and diverting L-arginine metabolism towards the synthesis of tissue-repair molecules such as polyamines (**Fig. 1.8.**) (Takeda et al., 2010).

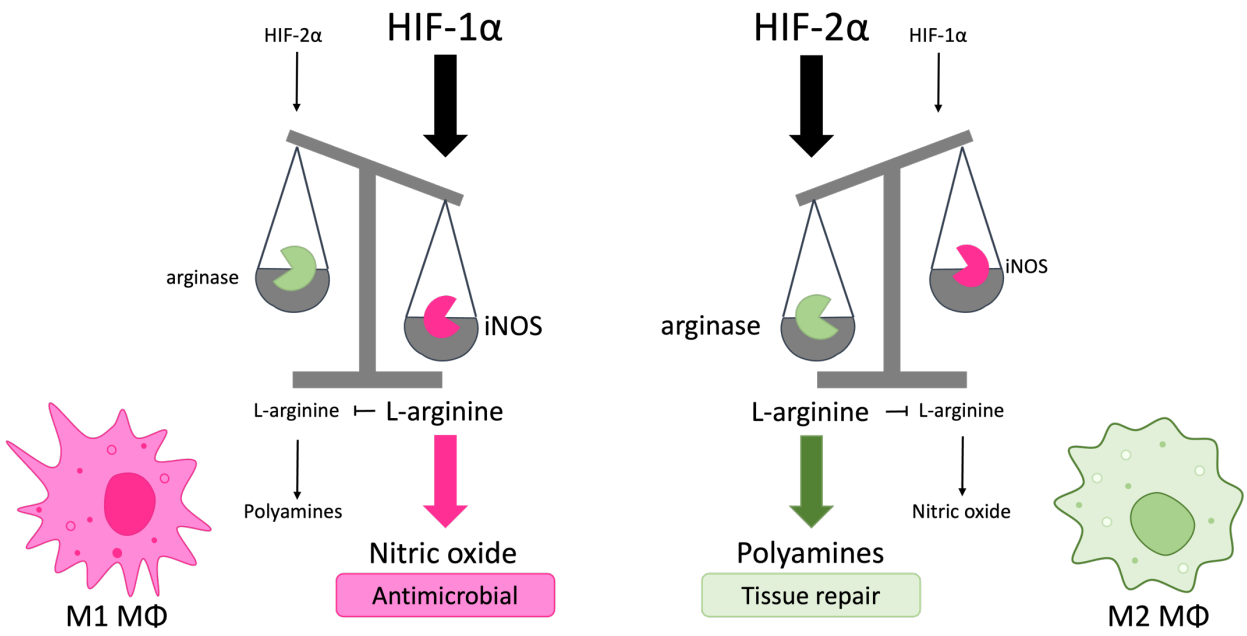


Figure 1.8. HIF-α isoforms exert opposing effects on macrophage polarisation *in vitro*. M1 polarisation of BMDMs (LPS, IFNγ) induces HIF-1α stabilisation, leading to increased *iNOS* expression and enhanced L-arginine catabolism to antimicrobial nitric oxide. Conversely, M2 polarisation (IL-4) promotes HIF-2α stabilisation, resulting in upregulation of *arginase 1*, suppressing nitric oxide production and diverging L-arginine metabolising toward polyamine synthesis for tissue repair. Adapted from Takeda et al., (2010).

Despite *in vitro* evidence that HIF-1α and HIF-2α contribute to macrophage plasticity – with the switch from HIF-1α to HIF-2α dominance often associated with acute versus chronic stages of immune challenge – their roles are far from clear-cut (Jaśkiewicz et al., 2022; Corrado and Fontana, 2020). For example, deletion of either *Hif-α* or *Hif2-α* in murine macrophages did not alter their ability to polarise in response to sterile skeletal muscle injury (Gondin et al., 2015). In a murine myocardial infarction model, Hif-2α stabilised more rapidly than Hif-1α in cardiac macrophages during the acute ischemic phase, challenging the proposed temporal 'HIF switch' (DeBerge et al., 2021). Moreover, Hif-2α has been shown to regulate pro-inflammatory cytokine expression in murine cardiac and tumour-associated macrophages – including *Il6*, *Il1b* and *Tnf* – contributing to tissue damage (DeBerge et al., 2021; Imtiyaz et al., 2010). Conversely, in a murine obesity-induced insulin-resistance model, macrophage-derived Hif-2α reduced adipose tissue inflammation by suppressing NO and pro-inflammatory cytokine production (Choe et al., 2014). Similarly, Hif-2α-deficient hepatic macrophages displayed significantly lower levels of IL-6, a traditionally pro-inflammatory cytokine with hepato-protective functions (Gao et al., 2020). In primary murine macrophages, Hif-2α induction suppressed mitochondrial ROS and MARCO-dependent phagocytic activity, traits typically associated with IL-4-polarised anti-inflammatory macrophages (Dehn et al., 2016; Varin et al., 2010). Collectively, these studies underscore the complexity of HIF signalling in macrophage biology. Rather than acting as simple pro- or anti-inflammatory determinants, HIF-1α and HIF-2α appear to mediate context-dependent

adaptations that enable macrophages to balance inflammatory and reparative functions across different immune challenges (e.g.: infection vs. injury) and tissue environments.

HIFs also play important roles in regulating macrophage function beyond polarisation, including cell migration and proliferation. For instance, the glycolytic metabolic programme driven by HIF-1α promotes macrophage recruitment to sites of infection and inflammation (Marelli-Berg and Jangani, 2018; Doedens et al., 2010). Once within tissue, HIF-1α upregulated expression of netrin-1, a secreted chemotropic cue that inhibits further macrophage migration, thereby retaining cells at inflammatory sites where they can exert effector functions (Ramkhelawon et al., 2013; Gopal et al., 2016). In contrast, Hif-2α appears dispensable for macrophage motility under certain inflammatory conditions (Kerber et al., 2020), yet it is essential for the migration of for tumour-associated macrophage (TAMs) into the tumour microenvironment – cells typically regarded as M2-like (Imtiyaz et al., 2010; Wang et al., 2024). M1-mediated upregulation of Hif-1α in LPS and IFNγ stimulated BMDMs was found to suppress macrophage proliferation by shifting metabolism towards glycolysis (Liu et al., 2016). Conversely, terminally differentiated human MDMs and murine peritoneal macrophages can re-enter the cell cycle under hypoxic conditions in a HIF-2α-dependent manner, a phenotype reminiscent of TAMs (Meng et al., 2024). Together, these findings underscore that HIF-1α and HIF-2α shape macrophage behaviour through distinct, microenvironment-specific mechanisms – co-ordinating their localisation, persistence, and proliferative capacity to match the metabolic and microenvironmental demands of immune challenge.

1.5.2. HIF during mycobacterial infection

HIF signalling exerts profound effects on macrophage function during mycobacterial infection, influencing antimicrobial activity, metabolism and survival in response to *Mycobacterium* challenge. The temporal pattern of HIF expression can determine whether its effects are host-protective or host-detrimental, depending on the stage of *Mtb* pathogenesis and the extent of *Mtb*-mediated macrophage reprogramming. Macrophage Hif-1α-dependent pro-inflammatory polarisation is essential for early control of *Mtb* growth, with increased NO production and IFNγ activation limiting intracellular replication in murine BMDMs (Osada-Oka et al., 2019). This protective effect has also been translated *in vivo*, with *Hif-1α*-deficient mice failing to control *Mtb* infection, with only 25% of mice surviving beyond 30 dpi (compared to 100% survival by ~75 dpi), emphasising the importance of early Hif-1α-mediated macrophage bacterial control (Braverman et al., 2016). Moreover, Hif-1α stabilisation also leads to a glycolytic shift in metabolism, which along with the concomitant increase in ROS production, results in reduced intracellular *Mtb* survival in murine macrophages (Matta and Kumar, 2016; Marín Franco et al., 2020). In addition to these canonical host-protective bactericidal mechanisms, Hif-1α upregulates lactate dehydrogenase-A to promote the conversion of pyruvate to lactate, thereby depleting the

pyruvate pool in *Mtb*-infected BMDMs and restricting *Mtb's* access to this carbon source for growth (Osada-Oka et al., 2019).

The zebrafish has played a pivotal role in defining how Hif-1α enhances early innate resistance to mycobacterial infection, providing mechanistic and real-time insights that are challenging to obtain in mammalian systems. Early work showed that genetic or pharmacological stabilisation of Hif-1α increases resistance to *Mm*, driven by enhanced recruitment of macrophages to infection sites and upregulation of pro-inflammatory reporters such as *tnfa:GFP* and *il1b:GFP* (Elks et al., 2013; Lewis and Elks, 2019; Ogryzko et al., 2019). Notably, zebrafish studies further revealed that Hif-1α increases macrophage pro-inflammatory markers even before infection occurs, enabling a faster and more coordinated inflammatory response upon encountering mycobacteria (Zhang et al., 2023; Dang et al., 2023; Lewis and Elks, 2019; Ogryzko et al., 2019). Importantly, zebrafish studies have also helped define the convergence between Hif-1α signalling and Il-1β-mediated antimicrobial pathways. Both human alveolar macrophages and zebrafish macrophages show improved mycobacterial clearance following HIF-1α stabilisation, associated with increased IL-1β production, highlighting a conserved mechanism of HIF-driven immunity (Marín Franco et al., 2020; Ogryzko et al., 2019). Complementing the zebrafish data, in primary human macrophages, pharmacological HIF-1α stabilisation using the PHD inhibitor Molidustat reduces intracellular *Mtb* viability by boosting antimicrobial peptide expression (Zenk et al., 2021). Interestingly, the host-protective effects of Molidustat on bacterial burden was also found to reduce *Mtb*-mediated TNF-α and IL-10 secretion in human macrophages, emphasising how the protective effects of HIF-1α stabilisation may act through several different mechanisms across species (Zenk et al., 2021). More broadly, the zebrafish provides a unique platform for tracking HIF-responsive macrophages *in vivo* within infected tissues, thereby defining the cellular dynamics of early HIF action during mycobacterial challenge.

Although transient Hif-1α activation promotes early bacterial control, at granuloma stages, however, Hif-1α appears to have detrimental effects due to the increased pro-inflammatory leukocyte profile. For example, pharmacological Hif-1α stabilisation increased bacterial burden and inflammation in a murine progressive TB model (Baay-Guzman et al., 2018; Domingo-Gonzalez et al., 2017). Some evidence suggests that Hif-1α activity can limit inflammation in murine TB, although whether this effect is neutrophil- or macrophage-dependent remains unclear due to the use of myeloid-deficient Hif-1α mice (Resende et al., 2020). HIF-1α is strongly expressed in both murine and human hypoxic granulomas, and recent spatial transcriptomic analyses of non-human primate TB granulomas revealed that bacteria-laden macrophages and impaired immune signalling were present in hypoxic regions of the granuloma (Osada-Oka et al., 2019; Domingo-Gonzalez et al., 2017; McCaffrey et al., 2025). Similarly, in a rabbit model, Hif-1α activation was found to exacerbate progressive *Mtb* infection through NLRP3 inflammasome activation in rabbit and human macrophages, leading to increased

mitochondrial stress and necrosis (Kumar et al., 2025). Moreover, stabilisation of Hif-1α through IL-17 neutralisation was in a necrotic TB murine model increased *Mtb* burden and led to severe pulmonary inflammation (Domingo-Gonzalez et al., 2017). The negative impact of Hif-1α stabilisation at granuloma stages goes beyond its effects on innate immune cell function, with the host detrimental effects also attributed to its role in adaptive immunity. For example, CD4 T cell-specific Hif-1α stabilisation through conditional VHL knockout increased *Mtb* susceptibility in mice, with TB lesions affecting larger areas of the lungs compared to controls (Liu et al., 2022). Collectively, these studies show that HIF-1α exerts stage-specific and context-dependent effects during TB pathogenesis. While early, transient HIF activation may enhance antimicrobial functions of macrophages, sustained or granuloma-stage HIF-1α stabilisation is detrimental. These findings suggest that HIF-targeted HDTs may be most beneficial when applied during early infection to boost macrophage bactericidal activity, or when selectively modulating specific HIF isoforms, while avoiding broad or prolonged HIF-1α stabilisation during established granulomatous disease.

At physiological levels, HIF-1α may exert host-protective effects during the later stages of TB infection by promoting the recruitment of bactericidal lymphocytes through CXCR4 induction and by potentially limiting inflammation via modulation of NF-κB signalling (Schioppa et al., 2003; Bandarra et al., 2015). However, active modulation of the HIF pathway at advanced stages of infection is more complex, as elevated Hif-1α activity has been associated with increased bacillary load and exacerbated pulmonary inflammation at granuloma stages in murine TB models (Baay-Guzman et al., 2018; Domingo-Gonzalez et al., 2017). Moreover, HIF-1α expression was recently found to be higher in patients with active TB than those with latent TB, illustrating the potential for heightened HIF-1α signalling to contribute to disease progression (de Oliveira Rezende et al., 2022). Collectively, these studies underscore the nuanced role of HIF signalling during infection and the caution required when designing HDTs.

HIF-2α represents an especially intriguing therapeutic target, as its opposing effects on macrophage NO homeostasis may be exploited to modulate inflammatory tone during infection. By promoting arginase activity while suppressing iNOS, HIF-2α shifts macrophages towards an anti-inflammatory phenotype, which can limit collateral tissue damage (Takeda et al., 2010). Conversely, inhibiting Hif-2α enhances macrophage and neutrophil NO production, boosting bactericidal capacity while potentially preserving the balance between pathogen clearance and inflammation (Elks et al., 2013). This duality suggests that selective HIF-2α modulation could allow stage-specific interventions: inhibition may be beneficial during early infection to enhance bacterial killing, whereas activation could promote resolution of inflammation during later or granuloma stages. Inhibition of HIF-2α signalling has already shown promise in cancer biology, where decreased HIF-2α activity in M2-like TAMs correlates with improved prognosis, including enhanced tumour cell apoptosis and reduced angiogenic signalling

(Wallace et al., 2016; Susen et al., 2019). Furthermore, specific HIF-2α inhibitors such as PT2385 and belzutifan have progressed to clinical trials, both as monotherapies and in combination with other anti-cancer agents (Courtney et al., 2018; Jonasch et al., 2021). These findings highlight the potential of targeting HIF-2α as an HDT strategy in other diseases, such as TB, where dysregulated macrophage metabolism and lipid accumulation are hallmarks of pathogenesis (Singhal et al., 2021). Indeed, genetic downregulation of Hif-2α (using dominant negative *hif-2α*) was found to reduce *Mm* burden to levels comparable to those observed following Hif-1α stabilisation during early infection in zebrafish larvae (Elks et al., 2013). This protective effect is attributed, at least in part, to enhanced neutrophil NO production, supporting the potential of HIF-2α inhibition as an HDT approach that enhances *Mtb* clearance while limiting collateral tissue damage (Elks et al., 2013). However, it is important to note that pharmacological inhibition of HIF-2α can yield distinct outcomes from genetic silencing approaches, such as those involving VHL knockdown, underscoring the need for careful evaluation of inhibitor specificity and downstream effects when translating these findings to clinical contexts (Arnaiz et al., 2021). Taken together, these studies emphasise that stabilisation or inhibition of HIFs as HDTs must be approached with precision, ensuring enhanced bacterial clearance without provoking excessive inflammation across the stages of TB pathogenesis.

1.6. The zebrafish as an *in vivo* model

The zebrafish (*Danio rerio*) is a valuable *in vivo* vertebrate model that enables investigation of diverse biological processes, including development and immune responses. Compared with other mammalian models such as mice and non-human primates, zebrafish models offer several key advantages, including high fecundity (hundreds of embryos per clutch), ease of adult and larval maintenance, and rapid development (Choi et al., 2021; Mastrogiovanni et al., 2024). The zebrafish genome is also highly conserved with that of humans, sharing orthologues with approximately 70% of human protein-coding genes and 84% of genes associated with human disease, underscoring its value for modelling human pathophysiology (Howe et al., 2013; Liu et al., 2024).

Since sequencing of the zebrafish genome, advances in genetic engineering have greatly expanded the model's utility, allowing for faster and more accessible genetic modification compared with mammalian systems (Choi et al., 2021). For instance, CRISPR-Cas9 can be readily applied to generate stable mutant lines and fluorescent proteins can be inserted to create transgenic reporter lines for specific cell types or proteins of interest (Kim and Zhang, 2020; Kimura et al., 2014; Soroldoni et al., 2009; Kemmler et al., 2023). Zebrafish embryos develop externally, and their optical transparency enables non-invasive, high-resolution *in vivo* imaging of fluorescent reporter lines (Elks et al., 2015). Moreover, imaging of transgenic reporters can be extended into adulthood using pigment-deficient lines such as nacre and casper (Lister et al., 1999; White et al., 2008). The zebrafish also serves as a robust platform for high-throughput screening of pharmacological compounds, with behavioural

responses or transgenic reporter expression providing quantitative readouts (Lee et al., 2021; Zhang et al., 2021). Taken together, these features establish the zebrafish as a powerful *in vivo* vertebrate model for identifying and characterising potential HDT targets.

1.6.1. The zebrafish as an immune model

The zebrafish immune system, like humans, consists of both innate and adaptive arms of the immune system (Speirs et al., 2024). In zebrafish, myeloid cell precursors originate from the anterior lateral plate mesoderm, where they migrate to the yolk sac before extravasating and tissue colonisation (**Fig. 1.9.**) (Torraca et al., 2014; Herbomel et al., 1999; Herbomel et al., 2001). This primitive wave occurs as early as 20 hours post-fertilisation (hpf), prior to the presence of other leukocytes, such as neutrophils (Herbomel et al., 1999). At 24 hpf, with the onset of blood circulation, the transient definitive wave of haematopoiesis occurs in the posterior blood island (PBI), where primitive erythromyeloid progenitors differentiate and primitive macrophages begin to circulate in the blood flow (Torraca et al., 2014; Herbomel et al., 1999; Herbomel et al., 2001; Bertrand et al., 2007; Murayama et al., 2006; Shiau et al., 2015; Stachura and Traver, 2011). The PBI transitions into the caudal haematopoietic tissue (CHT) at 48 hpf, by which point primitive neutrophils are produced and the progenitor population is replaced by haematopoietic stem cells (HSCs), enabling the second wave of definitive haematopoiesis (Torraca et al., 2014; Herbomel et al., 1999; Herbomel et al., 2001; Bertrand et al., 2007; Murayama et al., 2006; Shiau et al., 2015; Stachura and Traver, 2011). During the second wave, HSCs differentiate into macrophage precursors which invade and seed tissues throughout the zebrafish, differentiating into tissue-resident macrophages, including microglia, the specialised macrophages that patrol the central nervous system (Bertrand et al., 2007; Murayama et al., 2006; Ferrero et al., 2018; Ranawat and Masai, 2021). The pronephric kidney marrow develops from 4 dpf and becomes the adult haematopoiesis site from approximately 7 dpf. Migration of HSCs to the developing kidney results in the gradual replacement of the embryonic haematopoietic system (Torraca et al., 2014; Shiau et al., 2015; Jagannathan-Bogdan and Zon, 2013).

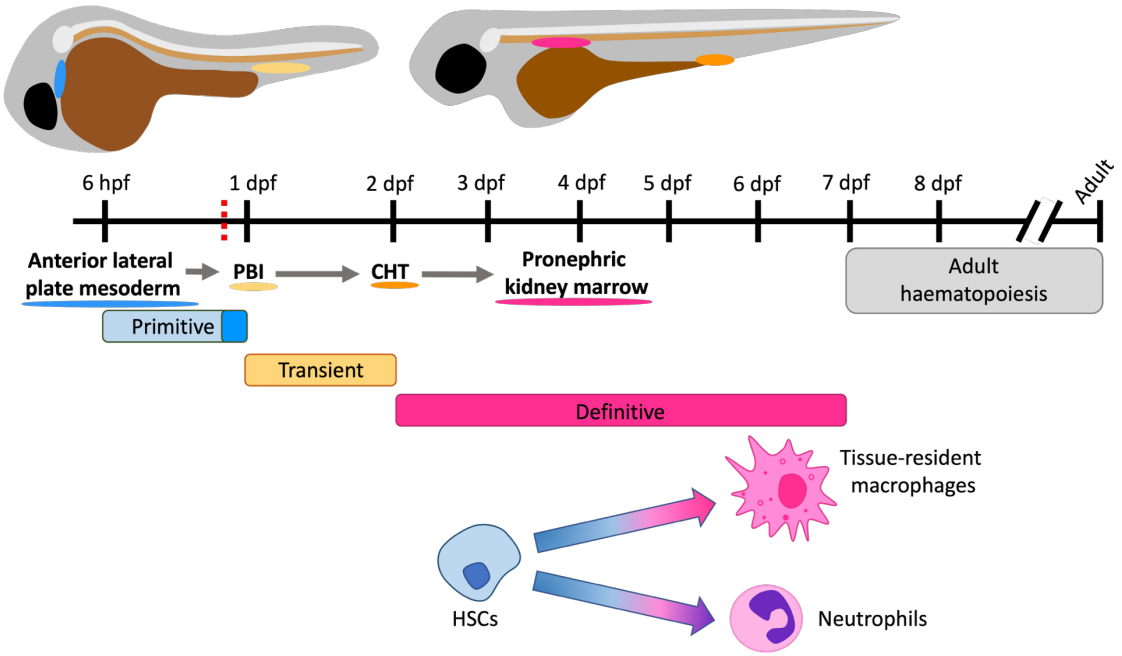


Figure 1.9. Summary of neutrophil and macrophage ontogeny in zebrafish. The anterior lateral plate mesoderm (blue) develops at 6 hpf, where myeloid cell precursors originate. At 20–22 hpf, the primitive wave of haematopoiesis occurs. From 24 hpf and onset of circulation, the PBI (yellow) develops, and the transient wave of haematopoiesis begins. The PBI then transitions into the CHT (orange) at 2 dpf, marking the start of the definitive wave of haematopoiesis, with HSCs differentiating into tissue-resident macrophages and mature neutrophils. From 4 dpf, the pronephric kidney marrow (pink) begins to develop, resulting in a gradual replacement of the embryonic haematopoietic system and onset of adult haematopoiesis at 7 dpf. Abbreviations: hpf, hours post-fertilisation; dpf, days post-fertilisation; PBI, posterior blood island; CHT, caudal haematopoietic tissue; HSCs, haematopoietic stem cells. From Speirs et al., (2024) with permission.

A mature adaptive immune system in zebrafish develops approximately 4 weeks post-fertilisation, at which point lymphocyte responses can be mounted (Trede et al., 2004). This delay between the maturation of the innate and adaptive immune systems allows for the independent interrogation of early innate immune responses. Moreover, as zebrafish embryos and larvae only become legally protected under UK legislation at 5.2 dpf – the point at which they are capable of independent feeding – research on innate immune responses prior to this stage contributes to the principles of the 3Rs in research (see section 1.6.4) (*Animals (Scientific Procedures) Act*, 1986).

The zebrafish innate immune system is highly conserved, with neutrophils and macrophages exhibiting strong morphological and functional similarity to their human counterparts (Speirs et al., 2024; Rosowski, 2020; Varela and Meijer, 2022). These similarities include shared phagocytic activity, cytokine production and inflammatory activation (Speirs et al., 2024; Nguyen-Chi et al., 2015; Muir et al., 2025). In addition, cell-type-specific behaviours such as neutrophil swarming and macrophage polarisation closely resemble those observed in mammals (Isles et al., 2021; Oskam, 2024; Nguyen-Chi et al., 2015). Collectively, the evolutionary conservation of leukocyte function and the absence of an

adaptive immune system before 5 dpf highlight the zebrafish as a powerful *in vivo* model for examining, interrogating, and manipulating innate immune responses.

1.6.2. The zebrafish as a model of TB

Zebrafish have been leveraged as a model of TB using *Mm*, a natural fish pathogen that is genetically related to *Mtb* and induces granuloma structures that closely recapitulate the cellular architecture and immunopathology of human TB (Davis et al., 2002; Subbian et al., 2015; Cronan et al., 2016). *Mm* offers substantial practical and biosafety advantages, replicating approximately 2.5-fold faster than *Mtb* (~8 h vs. ~20 h) and can be handled under biosafety level 2 rather than level 3, thereby accelerating experimental throughput and accessibility (Menon Aruna et al., 2025; Davis and Ramakrishnan, 2009). Unlike single-phagocyte systems (e.g.: *in vitro* macrophages, Dd), the zebrafish-*Mm* model offers a whole-organism platform in which innate immune dynamics, tissue context and mycobacterial virulence strategies can be studied in real-time. This model has transformed our understanding of TB pathogenesis – from the earliest macrophage-pathogen encounters and phagocyte recruitment, through granuloma initiation and organisation, to the emergence of pathogen-driven immune evasion mechanisms (Cambier et al., 2014a; Tobin and Ramakrishnan, 2008; Kumar et al., 2025).

Although murine models dominate TB research, mice are not a natural host for *Mtb*, and disease pathogenesis differs substantially, with most strains failing to develop caseating necrotic granulomas and instead forming loosely organised lesions (Cyktor et al., 2013; Via et al., 2008; Silva Miranda et al., 2012). In contrast, guinea pigs, rabbits and non-human primates develop histopathological granulomas that more closely resemble those in humans, exhibiting cavitary pulmonary TB and extrapulmonary disease (Dharmadhikari and Nardell, 2008). However, these models are limited by significant ethical considerations, high maintenance costs, and a relative lack of immunologic reagents to characterise host immune responses in *Mtb* infection (Dharmadhikari and Nardell, 2008). Despite differences in infection route (i.e.: zebrafish are not exposed to aerosolised *Mm*), the zebrafish-*Mm* model provides a cost-effective and pathologically relevant system for studying TB. In larvae, *Mm* is rapidly phagocytosed by macrophages, leading to neutrophil recruitment and the formation of early innate granulomas (Myllymäki et al., 2016; Davis et al., 2002). In adult zebrafish, *Mm* infection gives rise to mature, caseating granulomas with necrotic cores composed of both innate and adaptive immune cells, and recapitulates *Mtb*-mediated immune cell phenotypes, such as foamy and epithelioid macrophages (Cronan et al., 2016; Ramakrishnan, 2012; Swaim et al., 2006; Johansen et al., 2018). Recent transcriptomic analyses further revealed a shared core of differentially expressed genes between *Mtb*- and *Mm*-infected zebrafish larvae, including *irg1* (immunoresponsive 1) and several matrix metallopeptidases, both of which contribute to inflammation and tissue pathology (Sanderson et

al., 2015). Collectively, these findings reinforce the power of the zebrafish as a surrogate model for TB pathogenesis.

While defining and tracking anti-inflammatory macrophages *in vivo* remains an emerging area, the zebrafish models has already revealed key conserved principles of macrophage-*Mm* interactions. For example, *Mm* cell surface lipids serve as a physical barrier to dampen TLR-mediated pro-inflammatory macrophage recognition (Cambier et al., 2014b). Instead, *Mm* phenolic glycolipids (PGLs) preferentially target anti-inflammatory macrophages and induce Ccl2 chemokine production to recruit putative Ccr2+ monocytes which support bacterial expansion and dissemination (Cambier et al., 2014b; Cambier et al., 2017). PGL-mediated CCL2 induction has also been observed in human alveolar macrophages *in vitro*, although whether CCL2 recruits permissive or inflammatory monocytes remains debated, given the traditional association of CCR2 with inflammatory monocyte subsets (Cambier et al., 2017; Antonelli et al., 2010; Qian et al., 2011). Comparisons across model systems highlight the importance of studying immune responses *in vivo*. For example, prostaglandin E_2 (PGE_2) suppresses TNF-α production in *Mtb*-stimulated human PBMCs (Pellegrini et al., 2021), whereas *Mm*-infected zebrafish require cyclooxygenase/PGE_2 signalling to sustain macrophage *tnfa* expression (Lewis and Elks, 2019). Such contrasts likely reflect both species-specific differences in mycobacterial pathogenesis and the complex, context-dependent roles of PGE_2 in regulating inflammation, underscoring key discrepancies between *in vitro* and whole-organism systems (Martínez-Colón and Moore, 2018; Nakanishi and Rosenberg, 2013).

The zebrafish also offers an extensive experimental toolbox for visualising and manipulating immune responses, including transgenic reporter lines, fluorescently tagged *Mm* and immune cell depletion or enrichment strategies (**Table 1.2.**) (Buchan et al., 2019; Bojarczuk et al., 2016; Bernut et al., 2014). The availability of these tools enables non-invasive, real-time imaging of immune dynamics and facilitates high-throughput screening with translational relevance to mammalian systems. Taken together, the zebrafish-*Mm* model provides an unparalleled opportunity to interrogate macrophage behaviour, immune dynamics and granuloma biology *in vivo*. Its combination of genetic tractability, real-time imaging capacity and strong pathological parallels to human TB positions it as a powerful platform for mechanistic discovery and for identifying HDT targets.

Table 1.2. Current tools available to visualise and manipulate immune cell populations during *Mycobacterium marinum* infection in zebrafish.

Tool	Mechanism	Citation
Transgenic reporter lines		
Tg(*mpeg1:mCherry-CAAX*)	Macrophage reporter (membrane bound)	(Bojarczuk et al., 2016)
Tg(mpeg1:nlsClover)	Macrophage reporter (nuclei)	(Bernut et al., 2019)
Tg(mpeg1:Gal4-VP16)	Macrophage reporter (cytoplasmic; UAS system)	(Ellett et al., 2011)
Tg(mfap4:mCherry-F)	Macrophage reporter (membrane bound)	(Phan et al., 2018)
Tg(mpx:GFP)	Neutrophil reporter (cytoplasmic)	(Buchan et al., 2019)
Tg(*lysC:NTR-mCherry*)	Neutrophil reporter (cytoplasmic)	(Buchan et al., 2019)
Tg(zpu.1:eGFP)	Myeloid cell reporter (cytoplasmic)	(Hsu et al., 2004)
Tg(coro1a:eGFP)	Neutrophils and macrophage reporter (cytoplasmic)	(Liet al., 2012)
Tg(tnfa:eGFP-F)	*tnf-*α expressing cell reporter (membrane bound)	(Nguyen-Chi et al., 2015)
TgBAC(tnfa:eGFP)	*tnf-*α expressing cell reporter (cytoplasmic)	(Marjoram et al., 2015)
TgBAC(il-1β*:GFP)*	*il-1*β expressing cell reporter (cytoplasmic)	(Ogryzko et al., 2019)
Tg(irg1:eGFP)	*irg1* expressing cell reporter (pro-inflammatory macrophages)	(Sanderson et al., 2015)
TgBAC(*arg2:eGFP*)	*arginase2* expressing cell reporter (cytoplasmic)	(Hammond et al., 2023)
Tg(UAS:Kaede)	Kaede expression (when used with Gal4 reporter) – photoconvertible for tracking	(Davison et al., 2007)
Tg(-3.2tnfb:eGFP-F)	*tnfb* expressing cell reporter (membrane bound)	(van Dijk et al., 2025)
Tg(-6.2tnfb:mCherry-F)	*tnfb* expressing cell reporter (membrane bound)	(van Dijk et al., 2025)
Immune cell depletion/expansion		
Tg(UAS:nfsb-mCherry)	Nitroreductase/metronidazole cell depletion (when used with Gal4 reporter)	(Ellett et al., 2011)
Clodronate liposomes	Macrophage depletion	(Bernut et al., 2014)
MO-*irf8*	Macrophage depletion, neutrophil expansion	(Li et al., 2011)
mRNA-*irf8*	Macrophage expansion	(Li et al., 2011)
MO-*csf3r*	Neutrophil depletion	(Ellett et al., 2011; Liongue et al., 2009)
mRNA-*gcsfa/b*	Neutrophil expansion	(Stachura et al., 2013)
MO-*pu.1*	Neutrophil and macrophage depletion	(Galloway et al., 2005)
M. marinum		
M. marinum strain M	Fluorescent bacteria (vectors for different fluorescent proteins)	(van der Sar et al., 2009)

ΔRD1 *M. marinum* strain M	Fluorescent bacteria with attenuated virulence (vectors for different fluorescent proteins)	(Volkman et al., 2004; van der Sar et al., 2004)

Abbreviations: *Tg*, transgenic; *mpeg*, macrophage-expressed gene; *mfap*: microfibril-associate protein; *mpx*, myeloid-specific peroxidase; *lysC*, lysozyme; *pu.1*, spi-1 proto-oncogene; *coro1a*, coronin actin binding protein 1A; *tnfα*, tumour necrosis factor-α; *il*, interleukin; *irg*, immunoresponsive gene; UAS, upstream activating sequence; nfsb, nitrofuran sensitive B; MO, morpholino; mRNA, messenger RNA; *gcsf/csf3r,* colony stimulating factor 3; ΔRD1, delta region of difference 1.

1.6.3. Fish as models of macrophage signalling

Much of our understanding of dysregulated macrophage phenotypes in *Mtb* comes from *in vitro* studies or animal models, such as mice, which are not natural hosts for *Mtb* (El Kasmi et al., 2008; Whittington et al., 2023; Pisu et al., 2024; Hackett et al., 2020). Consequently, the zebrafish-*Mm* model provides an excellent alternative platform to study host-pathogen interactions and dissect macrophage activation states during *in vivo* mycobacterial infection.

Macrophage plasticity is conserved in fish, with carp monocytes able to polarise towards M1 (pro-inflammatory) or M2 (wound healing) phenotypes from monocytes (M0) *in vitro*, with pro- and anti-inflammatory marker expression akin to mammals (**Fig. 1.10.**) (Nguyen-Chi et al., 2015; Forlenza et al., 2011; Wentzel et al., 2020). Due to the large blood volume of larger fish such as carp, they have proven useful models for examining macrophage polarisation in fish, as monocytes can be isolated and cultured to obtain macrophages *in vitro* (Wentzel et al., 2020; Lu et al., 2017; Hu et al., 2018). Canonical markers for M1 and M2 activation states have been identified in macrophages from various teleost fish species, including the common carp, grass carp, ayu and spotted green pufferfish (Wentzel et al., 2020; Hu et al., 2018; Lu et al., 2017). Furthermore, qPCR analyses have found that fish macrophages express M2-associated genes following glucocorticoid exposure (zebrafish) and infection with the parasite *Lepeophtheirus salmonis* (Atlantic salmon), like human macrophages (Xie et al., 2019; Skugor et al., 2008).

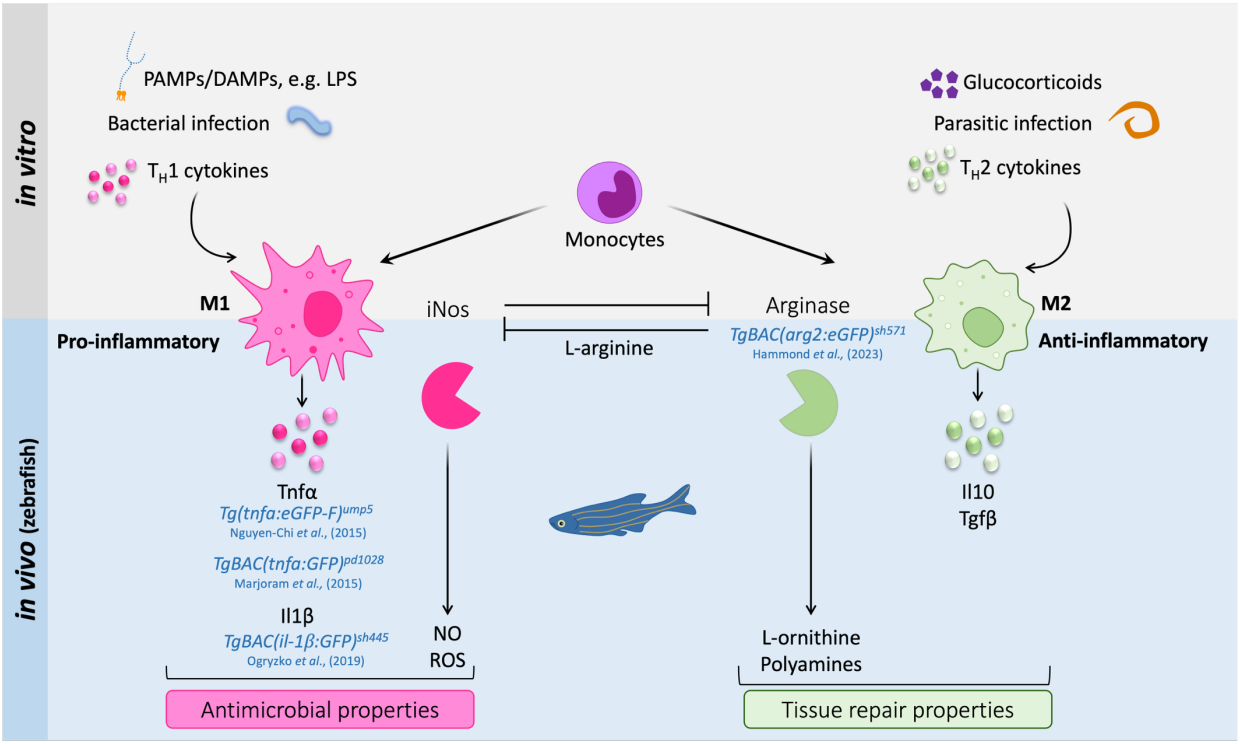


Figure 1.10. Zebrafish macrophages polarise on a continuum in response to different stimuli. Macrophages polarise towards an innate-activated pro-inflammatory phenotype following a range of stimuli, including bacterial pathogens (e.g.: *Mycobacterium marinum*) and PAMPs/DAMPs such as LPS (Anders and Ryu, 2011; Lewis and Elks, 2019). Pro-inflammatory macrophages express and release pro-inflammatory cytokines such as tumour necrosis factor-α (Tnf-α) and interleukin 1-β (Il-1β) (Lewis and Elks, 2019; Ogryzko et al., 2019). A hallmark of pro-inflammatory macrophages is the enzyme iNos, which uses L-arginine as a substrate to produce antimicrobial NO (Nathan and Hibbs, 1991). The antimicrobial immune response of pro-inflammatory macrophages is essential for increased phagocytic activity and consequent pathogen killing. Alternatively, stimuli such as parasitic infection (e.g. Lepeophtheirus salmonis) and glucocorticoids can induce anti-inflammatory macrophages (Bianchini et al., 2019; Anders and Ryu, 2011; Xie et al., 2019; Skugor et al., 2008). They express and release anti-inflammatory cytokines such as Il-10 and transforming growth factor β (Tgf-β) (Harjula et al., 2018; Nguyen-Chi et al., 2015). The enzyme arginase is an anti-inflammatory macrophage marker, also using L-arginine as a substrate to produce 'healing' factors such as L-ornithine and polyamines (Dzik, 2014). These anti-inflammatory properties enable this macrophage activation state to promote tissue repair and return of homeostasis. References for zebrafish transgenic lines currently in use included within the figure. Abbreviations: PAMPs/DAMPs, pattern-/damage-associated molecular patterns; LPS, lipopolysaccharides; iNos, inducible nitric oxide synthase; NO, nitric oxide; ROS, reactive oxygen species. From Speirs et al., (2024) with permission

Zebrafish are too small to obtain sufficient blood to culture monocytes, thus examining zebrafish macrophage polarisation largely depends on transgenic lines and imaging/transcriptomics analysis (Hammond et al., 2023; Nguyen-Chi et al., 2015; Ogryzko et al., 2019). Isolation and RNAseq analysis of macrophages from transgenic zebrafish (*mpeg1:mCherry*) confirmed that the genetic signature of pro-inflammatory and anti-inflammatory macrophages is broadly conserved with humans (Rougeot et al., 2019). Similar to mammalian macrophages, infection or injury results in macrophage

expression of pro-inflammatory markers such as Tnf-α, Il-1β and iNos in zebrafish (Lewis and Elks, 2019; Elks et al., 2013; Ogryzko et al., 2019).

Pro-inflammatory macrophage activation has become well characterised in larval zebrafish, and zebrafish models have shed light on their activation *in vivo*. Several zebrafish reporter lines have been generated that have allowed examination of macrophage polarisation over the time course of injury and infectious pathogenesis. To enable real-time visualisation of pro-inflammatory macrophages, promoter driven tumour necrosis factor (Tnf)-α transgenic lines have been generated and are now well-characterised reporters that robustly label pro-inflammatory macrophages (Nguyen-Chi et al., 2015; Marjoram et al., 2015). *tnfa:GFP* reporters can be crossed with macrophage reporters (e.g.: *mpeg1:mCherry*), enabling direct visualisation of putative pro-inflammatory macrophage activation during infection and sterile injury (McWhorter et al., 2013; Lewis and Elks, 2019; Ogryzko et al., 2019; Bojarczuk et al., 2016; Nguyen-Chi et al., 2017). Using *tnfa:GFP* lines to examine macrophage dynamics *in vivo*, it was found that pro-inflammatory macrophages (Tnf-α+) arrive at wound and infection sites, later switching phenotype to a potential anti-inflammatory phenotype characterised by changes in macrophage shape (amoeboid to elongated) and behaviour (direct to reverse/circular) (Nguyen-Chi et al., 2015; Nguyen-Chi et al., 2017; Sipka et al., 2022). Additional pro-inflammatory transgenic lines which have been used to visualise and characterise pro-inflammatory macrophages in zebrafish include *il-1β:GFP* (Ogryzko et al., 2019). Moreover, expression profiling of *tnfa:GFP*+ macrophages confirmed enrichment of canonical pro-inflammatory genes such as *il1b* and *il6* (Nguyen-Chi et al., 2015).

Macrophage pro-inflammatory NO balance is governed by two enzymes, iNOS and arginase (that both use L-arginine as a substrate), and they are often used as dichotomous markers for mammalian M1 and M2 phenotypes respectively *in vitro* and were found to mark carp M1 and M2 populations in a similar way (Takeda et al., 2010). In zebrafish, the activity of iNos (Nos2) has been measured using an antibody against tyrosine nitrosylation as an indirect measure of macrophage NO (Elks et al., 2013; Madigan et al., 2017). As these experiments rely on fixed larvae, the spatial and temporal dynamics of polarised macrophages is lost. Observing anti-inflammatory macrophages in zebrafish *in vivo* is in its infancy, as characterising the anti-inflammatory response has, until recently, relied on analysis of macrophage morphology and extrapolation from data obtained from these pro-inflammatory reporter lines (e.g.: *tnfa*-expressing macrophages vs. *tnfa*-negative macrophages) (Nguyen-Chi et al., 2015; Nguyen-Chi et al., 2017; Sipka et al., 2022).

Defining anti-inflammatory macrophage states *in vivo* remains challenging, as these states are still largely inferred from *tnfa*-negative macrophage populations and morphological criteria rather than dedicated lineage reporters (Xie et al., 2019; Sipka et al., 2022). To begin addressing this gap, our group recently developed a novel anti-inflammatory transgenic reporter line (*arg2:GFP*), enabling real-time

characterisation of the anti-inflammatory macrophage responses following *Mm* infection (Hammond et al., 2023). While further validation is required to confirm its specificity for anti-inflammatory macrophage signalling, preliminary findings are promising: a small subpopulation of macrophages upregulate *arg2:GFP* at both early and late stages of infection, indicative of anti-inflammatory macrophages during mycobacterial pathogenesis (**Fig. 1.11.**) (Hammond et al., 2023). Additionally, although the correlation between macrophage shape and activation state remains debated, recent data provides convincing evidence for an association between morphology and activation status (Sipka et al., 2022). In a zebrafish wound-healing model, Sipka and colleagues demonstrated that an initial wave of circular macrophages arrives at the wound site, later transitioning to a branched morphology (Sipka et al., 2022). This temporal change coincides with upregulation of anti-inflammatory genes such as *tgfb1* (Sipka et al., 2022; Nguyen-Chi et al., 2015). Notably, treatment of zebrafish embryos with protectin D1, a specialised pro-resolving mediator, accelerated this morphological and behavioural switch towards a predicted anti-inflammatory phenotype, underscoring the potential of the zebrafish as a model for identifying macrophage-specific HDTs (Sipka et al., 2022).

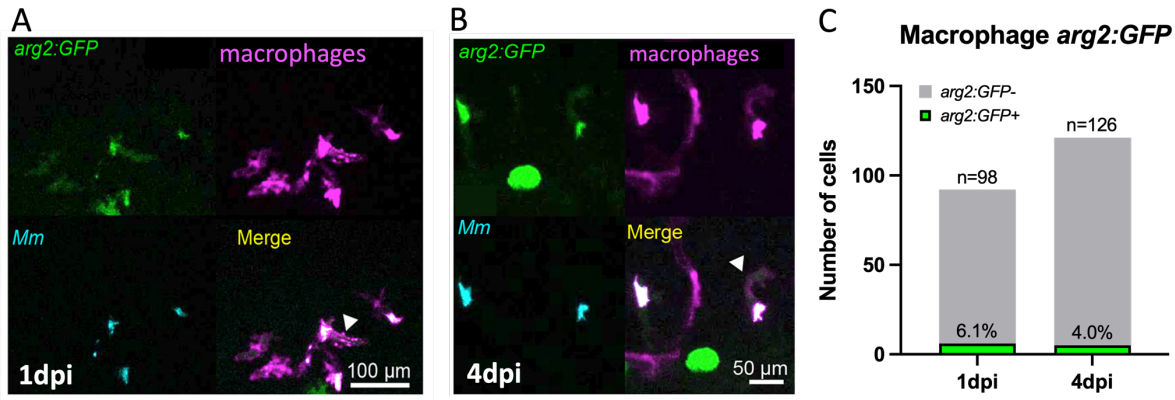


Figure 1.11. A small subpopulation of zebrafish macrophages upregulate *arg2:GFP* at 1 day post-infection (dpi) and 4 dpi. (**A-B**) Representative confocal image of (**A**) 1 dpi and 4 dpi (**B**) *mpeg:mCherry+ arg2:GFP+* larvae, with a single *arg2:GFP* expressing macrophage at each timepoint, indicated by filled arrowheads. (**C**) Graph illustrating the percentage of *arg2:GFP+* and *arg2:GFP-* macrophages at 1 dpi and 4 dpi. Figure obtained and adapted from Hammond et al., (2023) with permission.

Taken together, these studies highlight the zebrafish as a powerful system for investigating macrophage polarisation and its role in mycobacterial pathogenesis, providing both mechanistic insight and translational opportunities for macrophage-targeted HDT development in TB.

1.6.4. 3Rs impact: partial replacement

In TB research, there remains a reliance on protected species to examine macrophage phenotypes both *in vitro* and *ex vivo*. In addition to being costly, this presents ethical challenges due to the need to use and cull these animals. *Ex vivo* experiments, such as those examining tuberculous

granulomas in guinea pigs and macaques, require animals to be culled at defined timepoints post-infection, followed by necropsy and tissue collection (e.g.: lungs) for downstream analyses such as immunohistochemistry (Ly et al., 2008; Mattila et al., 2013). Although some macaque studies use non-invasive approaches, such as computed tomography (CT) imaging to track granuloma formation *in vivo*, there remain significant ethical concerns surrounding the use of higher animals like non-human primates in biomedical research (Lin et al., 2014).

Similarly, to study macrophage responses to *Mtb* infection in isolation *in vitro*, BMDMs are harvested from mice. This process involves culling the animals and dissecting the tibia and femur to extract bone marrow (Bailey et al., 2020). Moreover, while rodents are the most widely used model for TB, they are not a natural host for *Mtb* and typically fail to develop the organised , caseating granulomas characteristic of human disease (Cyktor et al., 2013; Via et al., 2008; Silva et al., 2012). Correspondingly, *in vitro* models cannot fully recapitulate the complex host-pathogen interactions that occur in infected tissues (Tsai et al., 2006; Rhoades et al., 1997; Vogel et al., 2014). Although careful experimental design – such as the application of statistical power calculations – can reduce the number of animals used, this does not necessarily align with the principles of the 3Rs (replacement, reduction and refinement) of animal research, as alternative models could be used in their place.

The use of zebrafish larvae represents a partial replacement strategy, directly reducing the number of protected animal species required for TB research. While adult zebrafish are protected under the Animals (Scientific Procedures) Act (1986), their care and use are continuously refined to ensure high welfare standards (Andersson and Kettunen, 2021; Sabrautzki et al., 2021; Lee et al., 2022). A key refinement is the non-invasive collection and use of zebrafish embryos, which develop *ex vivo*. Zebrafish embryos (<5.2 dpf) are not legally protected, as current scientific consensus holds that they lack the capacity for suffering before the onset of independent feeding. Importantly, zebrafish embryos possess a functional innate immune system, including macrophages – the key immune cell in TB pathogenesis – and their optical transparency enables non-invasive *in vivo* imaging of infection dynamics. Infection with the genetically related fish pathogen *Mm* leads to the formation of granulomas that closely resemble those observed in human TB patients. Collectively, the zebrafish-*Mm* model not only closely mirrors hallmarks of human TB pathogenesis but also supports the principles of the 3Rs by providing a scientifically robust and ethically refined alternative to studies using protected animal species, which often require invasive techniques with higher severity classifications.

1.7. Hypothesis and aims

Mycobacterial infection is characterised by the parasitisation of macrophages, which suppresses their pro-inflammatory, bactericidal phenotypes and skews them towards an anti-inflammatory phenotype that facilitates granuloma formation (Cronan et al., 2021; El Kasmi et al., 2008; Mattila et al., 2013; Luo et al., 2025). However, the mechanisms driving these phenotypic shifts, and how they are regulated within the infected *in vivo* environment, remains poorly understood. Although promoting a pro-inflammatory macrophage phenotype can improve bacterial clearance during early infection, this often leads to excessive inflammation and host tissue damage (El Kasmi et al., 2008; Lundahl et al., 2022). Conversely, at later stages of infection, sustained pro-inflammatory macrophage activity has also been shown to be detrimental to the host (Benoit et al., 2008; Bertolini et al., 2016; Marino et al., 2015). These observations underscore the need to develop HDTs that achieve a balanced pro- and anti-inflammatory response, targeting macrophages in a temporally regulated manner according to the stage of disease pathogenesis.

Recent work from our group using a newly developed *arginase 2* transgenic reporter line (*arg2:GFP*) identified a subset of macrophages that upregulated *arg2:GFP* expression following immune challenge, potentially representing an anti-inflammatory macrophage population (Hammond et al., 2023). Characterising whether these cells phenotypically resemble *in vitro*-defined anti-inflammatory macrophages, and leveraging this model to dissect the mechanisms underpinning macrophage plasticity *in vivo*, may facilitate the identification of novel therapeutic targets for the development of HDTs against *Mtb* infection.

I hypothesise that macrophage pro- and anti-inflammatory signalling is dysregulated during mycobacterial infection in zebrafish, and that this polarisation can be modulated to improve infection outcome.

To test this hypothesis, four key aims were addressed:

1. Determine whether *arg2:GFP*-expressing macrophages represents an anti-inflammatory macrophage population.
    - Characterise macrophage *arg2:GFP* expression in *Mm* infection.
    - Determine whether *arg2:GFP*-expressing macrophages phenotypically resemble *in vitro* M2-polarised macrophages.
    - Identify the signalling mechanisms used by *Mm* uses to modulate macrophage *arg2:GFP* expression.

2. Examine the dynamics of macrophage phenotypes during *Mm* infection.
    - Generate a *tnfa:mCherry* transgenic reporter line to visualise putative pro-inflammatory macrophages in combination with the *arg2:GFP* line.
    - Determine whether *arg2:GFP*-expressing macrophages polarise locally within the infected tissue microenvironment or migrate to the infection site.
    - Assess whether *tnfa:mCherry*-positive cells can become positive for *arg2:GFP* and undergo a phenotypic switch.

3. Manipulate macrophage phenotypes to improve infection outcome
    - Examine whether modulation of the Hif-α pathway influences macrophage phenotype *in vivo* (Takeda et al., 2010; Lewis and Elks, 2019).
    - Explore whether macrophage phenotype can be therapeutically manipulated *in vivo.*

4. Investigate alternative *in vivo* anti-inflammatory macrophage marker genes.
    - Define the resting-state transcriptional profile of larval zebrafish macrophages using published RNA sequencing datasets.
    - Identify candidate anti-inflammatory macrophage marker genes conserved between zebrafish and humans using comparative transcriptomic analyses.
    - Characterise the expression of an alternative anti-inflammatory macrophage transgenic reporter line (*ccn1l1:eGFP*) following immune challenge.

2. Materials and Methods

2.1. Ethics statement

Experiments were authorised by the UK Home Office project licence PP7684817 (to PME) and personal licence I77410835 (to ZCS) under the Animals (Scientific Procedures) Act 1986. All experiments were carried out in up to 5.2 dpf (days post-fertilisation) larvae, before the fish were protected by the A(SP)A 1986, thus contributing to the 3Rs by replacing experiments on adult zebrafish and reducing numbers of mice used in TB research.

2.2. Zebrafish work

2.2.1. Zebrafish husbandry

Zebrafish (*Danio rerio*) were raised in the Biological Services Unit (BSU) aquarium at the University of Sheffield and maintained at 28°C on a 14/10 hour light/dark cycle, in accordance with standard protocols and UK Home Office regulations (Westerfield, 2000). Adult shoals of fish were bred via either marbling or pairing. Marbling involved placing a mesh-bottomed container with a layer of marbles into a collection container and placed within the adult fish tank overnight. For outcrossing zebrafish lines and single-cell injections, individual fish were bred in pair-mating tanks, with a divider placed between them overnight and removed the following morning at the start of the light cycle. Using a strainer, eggs were collected the following morning and placed into fresh aquarium water. A list of all zebrafish lines used in this project are detailed below (**Table 2.1.**).

Table 2.1. List of zebrafish lines used in this project.

Zebrafish line	Allele #	Labelling	Reference
Tg(*mpeg1:mCherry-CAAX*)	sh577	Macrophage reporter (membrane bound)	(Bojarczuk et al., 2016)
Tg(mpeg1:nlsClover)	sh436	Macrophage report (nuclei)	(Bernut et al., 2019)
Tg(mfap4:mCherry-F)	sh699/sh700	Macrophage reporter (membrane bound/farnesylated)	(Phan et al., 2018)
TgBAC(*arg2:eGFP*)	sh571	*arginase2* expression	(Hammond et al., 2023)
Tg(*lysC:NTR-mCherry*)	sh260	Neutrophil reporter (cytoplasmic)	(Buchan et al., 2019)
TgBAC(mpx:GFP)	i114	Neutrophil reporter (cytoplasmic)	(Renshaw et al., 2006)
Tg(phd3:GFP)	i144	*phd3* expression	(Santhakumar et al., 2012)
TgBAC(tnfa:eGFP)	pd1028	*tnfa* expression	(Marjoram et al., 2015)
Tg(tnfa:mCherry-F)	sh716-sh717	*tnfa* expression (membrane bound/farnesylated)	This project
TgBAC(ccn1l1:eGFP)	sh697/sh698	*ccn1l1* expression	This project
Nacre (wild type)	N/A	N/A	N/A
London wild type (LWT)	N/A	N/A	N/A

2.2.2. Embryo maintenance

Zebrafish embryos were maintained at 28°C in 1X E3 solution diluted in distilled water (E3 60X stock: 5mM NaCl, 0.17 mM KCl, 0.33 mM MgSO4, 0.33 mM CaCl2, pH 7.2) with 10^{-5} % (v/v) methylene blue (Sigma-Aldrich). Methylene blue is added to prevent fungal growth. All embryos following experimentation and approaching 5.2 dpf that were not being raised were culled, firstly by anaesthetising with 0.168 mg/mL 3-amino benzoid acid ethyl ester (tricaine, Sigma-Aldrich) via immersion, then exposure to bleach for 24 hours. Infected embryos were also exposed to Virusolve (Amity International) for 24 hours.

2.2.3. Dechorionation and anaesthetisation

Zebrafish embryos that were being subjected to experimentation (e.g. immune challenge) or screened for the presence of a transgene were dechorionated at 1-2 dpf using jeweller's forceps (Sigma-Aldrich). The tip of the forceps was used to pierce and open the chorion without damaging the embryo. For all experimental procedures, embryos were anaesthetised using 0.168 mg/mL tricaine via immersion.

2.2.4. Preparation and injection of RNA

Glass capillaries (World Precision Instruments, WPI) were pulled using a P1000 micropipette puller (Sutter Instruments) and loaded with 2.5-3 μL of injection mix using a gel loading tip (Eppendorf). Needles were placed and tightened into the micromanipulator's needle holder attached to a Pneumatic PicoPump PV820 (WPI). Using a Nikon microscope SMZ 745, the tip of the needle was broken at an angle using jeweller's forceps to achieve a bevelled tip. With a pressure of 40 psi, a graticule with a droplet of mineral oil was used to measure the size of the broken needle's droplet and adjusted to achieve 1 nL.

The mMESSAGE mMACHINE SP6 transcription kit (Ambion) was used to synthesise dominant active/dominant negative Hif-α isoform RNAs. Briefly, 1 μg of linearised DNA was used for *in vitro* transcription using the acid:phenol:chloroform extraction protocol and RNA collected using Amicon Ultracel 100k filter tubes (Millipore). Concentration was measured using ND1000 NanoDrop (~4000 ng/μL stock), aliquoted into 2 μL and stored at -80°C.

At the single cell stage of zebrafish embryos, 50 ng/mL of dominant active/dominant negative HIF-α isoform RNA was diluted in 1:10 phenol red in DEPC-treated water (PR; in MilliQ, Sigma-Aldrich) and injected into the yolk. 1 nL of 1:10 diluted PR was used as a vehicle control.

2.2.5. Morpholino knockdown

To deplete neutrophils, 1 nL of *csf3r* (Gene Tools) morpholino oligonucleotide at a concentration of 500 μM was injected at the single cell stage as described in section 2.2.4. Morpholino was validated using whole body neutrophil counts (see section 2.5.5.). For experiments assessing the role of toll-like receptor (TLR) signalling in macrophage *arg2:GFP* expression, 1 nL of *myd88* (Gene Tools) morpholino at a concentration of 500 μM was injected at the single cell stage. *myd88* knockdown validation is described in section 2.8. A standard control morpholino (Gene Tools) was also injected as a negative control. Antisense oligonucleotide sequences are detailed below (**Table 2.2.**).

Table 2.2. Control and morpholino oligonucleotide sequences.

Morpholino	Sequence	Citation
Control	5'-CCTCTTACCTCAGTTACAATTTATA-3'	Gene Tools
myd88	5'-GTTAAACACTGACCCTGTGGATCAT-3'	(Bates et al., 2007)
csf3r	5'-GAAGCACAAGCGAGACGGATGCCAT-3'	(Ellett et al., 2011)

2.3. Compound treatment of embryos

For compound treatment of zebrafish larvae via immersion, 15 dechorionated embryos aged 1 dpf were placed in 6-well plates with the compound diluted in 3 mL of E3 solution without methylene blue. All compounds used to treat embryos via immersion are listed below (**Table 2.3.**). The following compounds were resuspended in DMSO and stored at -20°C: dimethyloxalylglycine (DMOG; 100 mM stock), FG4592 (25 mM stock), prostaglandin E2 (PGE_2; 284 mM stock), 16, 16-dimethyl PGE_2 (10 mg/mL stock) and nor-NOHA (5 mg/mL stock). The same volume of dimethyl sulfoxide (DMSO) was used as a negative control. Dexamethasone was dissolved in methanol to 63.7 mM stock concentration, and the same volume of methanol was used as a negative control. Sodium butyrate was reconstituted in MilliQ to achieve a stock concentration of 100 mg/mL. Cyclic adenosine monophosphate (cAMP) was dissolved in MilliQ to a stock concentration of 100 mg/mL. For infection experiments, 1 dpf embryos were pre-treated for 4 hours with the compound prior to infection and returned to the compound-treated E3 solution until imaging.

Table 2.3. A list of compounds used to treat zebrafish larvae via immersion in this thesis.

Compound (immersion)	Concentration	Solvent	Supplier	Citation
DMOG	100 μM	DMSO	Enzo	(Elks et al., 2011)
FG4592 (or Roxadustat)	5 μM	DMSO	Selleckchem	(Schild et al., 2020)
PGE_2	10 μM	DMSO	Sigma-Aldrich	(Loynes et al., 2018)
16, 16-dimethyl-PGE_2	10 μM	DMSO	Cayman	(Evans et al., 2019)
nor-NOHA	100 μM	DMSO	Cayman	(Gobert et al., 2000)
Dexamethasone	10 μM	Methanol	Sigma-Aldrich	(Tsarouchas et al., 2018)

Sodium butyrate	6 mM	MilliQ water	Fluorochem	(Cholan et al., 2020)
cAMP	100 μM	MilliQ water	Sigma-Aldrich	(Elo et al., 2007)
DMSO	<1%	N/A	Sigma-Aldrich	N/A
Methanol	<1%	N/A	Fisher Scientific	N/A

For Protectin D1 (PD1; Cayman) experiments, embryos were injected with the compound into the caudal vein as previously described (Sipka et al., 2022). PD1 was dissolved in ethanol (Fisher Scientific) to achieve a stock concentration of 0.1 mg/mL. Following systemic infection with *Mm* (see section 2.4.2 and 2.7.4), embryos were left to recover for 1 hour. Larvae were re-anaesthetised and injected with 200 pg/nL of PD1 or the same volume of 50% ethanol (dissolved in water).

2.4. Immune challenge (injury and infection)

2.4.1. Tail fin transection

The tail fin transection model was used as an injury model (Renshaw et al., 2006). Zebrafish larvae of 2-3dpf were anaesthetised and a sterile scalpel blade was used to cut the tail fin, avoiding the notochord (**Figure 2.1.**). Following injury, larvae were transferred to fresh E3 solution for recovery.

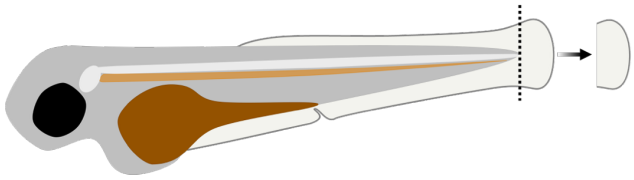


Figure 2.1. Schematic of tail fin transection performed on larvae. Dashed line indicates site of transection, avoiding the notochord and circulation.

2.4.2. Injection into the caudal vein

For systemic infections, *Mm* was injected into the caudal vein of 30-32 hours post-fertilisation (hpf) embryos. Firstly, embryos were dechorionated (see 2.2.3) and anaesthetised. Using a Pasteur pipette, embryos were placed on 0.9% agarose (Bioline) plates made with E3 solution with methylene blue, and excess E3 media aspirated. Using a gel loading tip, 10-20 embryos were aligned on the plate ready for injection into the posterior blood island (PBI), the haematopoietic tissue that develops into the caudal vein (**Figure. 2.2.**).

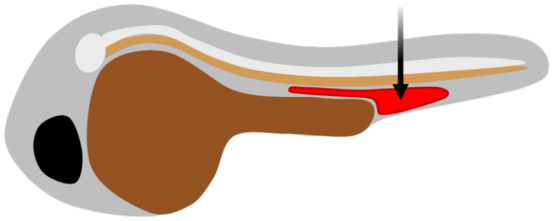


Figure 2.2. Example of a caudal vein infection in a 30 hpf zebrafish embryo. Black arrow indicates the posterior blood island, the site of injection. When successfully injected with phenol red, the dye fills the vein.

2.5. Microscopy

2.5.1. Stereo microscopy

Zebrafish embryos were anaesthetised using 0.168 mg/mL by immersion and placed on a FluoroDish Cell Culture Dish (WPI). Transgene expression (of zebrafish and *Mm*) was screened using a Leica MX10F stereo microscope and images taken using with a GXCAM-U3 series 5MP Camera (GT Vision).

2.5.2. Confocal microscopy

Zebrafish embryos were anaesthetised using 0.168 mg/mL tricaine by immersion and mounted in approximately 500 μL of 1% low melting point agarose (Sigma-Aldrich) containing 0.168 mg/mL Tricaine (Sigma-Aldrich) in 15μ-Slide 4-well glass bottom slides (Ibidi). Whilst the agarose was warm, zebrafish were positioned laterally with the head to the left using a gel loading tip (Eppendorf). Agarose was covered in ~0.5 mL of E3 medium with tricaine. For imaging of *tnfa:mCherry* F1 embryos, zebrafish were placed on a FluoroDish Cell Culture Dish (WPI). Confocal images were taken using a Leica DMi8 SPE-TCS microscope using either a HCX PL APO 40x water immersion lens or a 20x dry objective, with Leica LASX (Leica Microsystems) software. Z-stacks of 2 μm in size were taken using bidirectional imaging, with speed of acquisition set to 600. All images displayed are maximum projection images, unless otherwise stated.

2.5.3. Widefield microscopy

For widefield imaging, zebrafish embryos were anaesthetised and placed on a FluorDish Cell Culture Dish (WPI). Brightfield and fluorescent widefield images of transgenic or infected embryos were taken using a Leica DMi8 SPE-TCS microscope fitted with a Hammamatu ORCA Flash 4.0 camera using a HC FL PLAN 2.5x0.07 dry lens.

2.5.4. Spinning disk microscopy

For time-lapse imaging, zebrafish embryos were anaesthetised and mounted in approximately 500 μL of low melting point agarose as described in section 2.5.2. Embryos were placed in a 28°C heated chamber and imaged on the Nikon W1 spinning disk confocal microscope (Wolfson light

microscopy facility, University of Sheffield) using a 20x/0.75NA dry objective (additional 1.5x magnification manually adjusted on the microscope; total 30x) and 50 μm pinhole-sizes (green, orange and far red). Images were taken every 3 minutes for 10 hours overnight, with 2 μm z-steps. Brightfield image was taken at the middle z-step. ND files generated were processed using the NIS Elements software (Nikon), creating maximum projections of each embryo and splitting multi-points into separate files.

2.5.5. Whole body cell counts

Whole body cell counts were carried out to determine the effect of compounds or morpholino knockdown on leukocyte populations. Larvae from *Tg(mpx:GFP)* were used for neutrophil counts and *Tg(mpeg1:mCherry-CAAX)* for macrophage counts. Briefly, larvae were anaesthetised and experimental groups blinded. A cell counter was used to count leukocyte numbers from the caudal vein to the posterior end under a fluorescent stereo microscope (see section 2.5.1) in 10-15 fish per experimental group in fish up to 5 dpf.

2.6. Image analysis

2.6.1. Measurement and calculation of calculated total cell fluorescence (CTCF)

TIFF images of transgenic zebrafish lines (e.g.: *Tg(arg2:GFP*) were measured for mean fluorescence intensity using ImageJ (also named FIJI). All *mpeg:mCherry+* cells (for initial 1-4 dpi macrophage experiments), 6 of the brightest neutrophils/macrophages (for all other experiments) or a subpopulation of *tnfa:mCherry+* cells were drawn around with the free hand selection tool and measured. Background areas were also measured for each image. As previously described, calculated total cell fluorescence (CTFC) was then calculated (Elks et al., 2013; Burgess et al, 2010). The calculation used for CTCF is described below:

$$\text{CTCF} = \text{Intensity Density} - (\text{Area} \times \text{Mean Background Value})$$

2.6.2. Quantification of cell shape and behaviour using ImageJ

Manual analysis of macrophage shape from confocal images was carried out using ImageJ as previously described (Sipka et al., 2022). Firstly, maximum projection of LIF images obtained from the Leica confocal microscope (see section 2.5.2) were converted to binary format, and threshold set using triangle algorithm. Next, the free hand selection tool was used to draw around individual macrophages. Lastly, area (μm^2), perimeter (μm) and circularity index (4π*area/perimeter^2) were measured.

For analysis of macrophage morphology from timelapse data obtained from the spinning disk (see section 2.5.4), the free hand selection tool was used to draw around individual macrophages/*tnfa:mCherry+* cells in each frame of the ND2 file. Perimeter (μm) and circularity index (4π*area/perimeter^2) were measured, with averages taken for the duration of 1 hour for experiments

comparing cells to their nearest neighbour. For assessment of cell behaviour in these datasets, the manual tracking plugin on ImageJ was used to track speed (μm/sec). The manual tracking plugin also measures location (XY) and distance travelled (μm), allowing for calculation of meandering index (MI), whereby a MI of 1 is the most direct route and <1 is less direct. The calculation used for MI is described below:

$$MI = Distance\ between\ first\ and\ last\ position\ \div\ total\ pathlength$$

The XY coordinates for *tnfa:mCherry+ arg2:GFP+* cells obtained above were also plotted on a scatter plot to determine the spatial distribution of these double positive cells. All coordinates acquired were normalised so that the origin (0,0) equated to the centre of the granuloma in each fish.

For *arg2:GFP-* cells that later express *arg2:GFP*, macrophages/*tnfa:mCherry+* cells were tracked for the duration they are in frame, measuring perimeter, circularity index, MI and speed. To statistically compare differences, averages were taken 1 hour before *arg2:GFP* expression and 1 hour after. As a control, *arg2:GFP-* cells were tracked in the same manner for the duration they were in frame.

To measure cell distance from the granuloma, the line selection tool was used to draw a line from the cell highest fluorescent density to the centre of the granuloma, measuring distance (μm) and migration pattern (towards or away from the granuloma). An average over the duration of 1 hour was taken.

2.6.3. Measurement of bacterial burden using ZF4

Bacterial burden was calculated using ZF4 fluorescent pixel count software on TIFF images as previously described (Stoop et al., 2011). Bacterial pixel count values were then input to GraphPad Prism software to generate plots and perform statistical analysis.

2.6.4. Measurement of granuloma number, granuloma size and bacterial dissemination using QuantiFish

Granuloma number (foci number), granuloma size (large foci) and bacterial dissemination (grid analysis) was calculated using QuantiFish on TIFF images as previously described (Stirling et al., 2020). Threshold for large foci was set to 20 as the minimum area to be considered as a focus. Foci number; large foci number and spatial distribution values were input to GraphPad Prism software to generate plots and perform statistical analysis.

2.6.5. Randomisation and blinding

To avoid bias when doing whole body cell counts (see 2.5.5), experimental groups were blinded by an independent individual and unblinding of experimental groups was only done after data

collection. For experiments where blinding was not possible, all measurements were taken and plotted following complete analysis to minimise bias.

2.6.6. Determining gene expression across larval development

Daniocell is a published online resource that was generated following single-cell RNA sequencing of whole zebrafish embryos from 3.3 hours post-fertilisation (hpf) to 120 hpf. The resource was used to determine expression of genes in macrophages/haematopoietic tissue across larval development (Sur et al., 2023).

2.7. *Mycobacterium marinum* culture and injection

2.7.1. 7H10 agar plates

Glycerol stocks of *Mm* (100 μL) were streaked on fresh 7H10 plates, then re-streaked after two days. *Mm* is re-streaked every 10 days and grown at 28°C, with a new glycerol stock being spread following the sixth re-streak. Agar plates are made by using 3.8 g Difco Middlebrook 7H10 agar (7H10, Sigma-Aldrich), 1 mL glycerol (Thermo Fisher Scientific) and MilliQ to 180 mL, followed by sterilisation via autoclaving. Following sterilisation, agar was allowed to cool to ~50°C before addition of 1:10 final volume of Middlebrook OADC growth supplement (Sigma-Aldrich) and 50 μg/mL of hygromycin (stock 50 mg/mL, Sigma-Aldrich). Approximately 20 mL of supplemented agar was poured into petri dishes, allowed to set and stored at 4°C.

2.7.2. 7H9 media

Overnight cultures of *Mm* were grown in supplemented 7H9 media. 7H9 broth base was made by using 1.04 g Middlebrook 7H9 (7H9, Sigma-Aldrich, 444 μL glycerol (Thermo Fisher Scientific) and MilliQ up to 200 mL, followed by sterilisation via autoclaving. Following sterilisation, 7H9 broth was supplemented with 1:10 final volume of Middlebrook ADC (Sigma-Aldrich) and 50 μg/mL of hygromycin (stock 50 mg/mL, Sigma-Aldrich). 7H9 media was stored at 4°C.

2.7.3. Preparation of *Mm* overnight culture

All experiments (using live and virulent bacteria) were performed using *Mycobacterium marinum* strain M (ATCC #BAA-535) containing the pSMT3-Crimson vector (van der Sar et al., 2009) and overnight cultures prepared from a working 7H10 plate. 10 mL of supplemented 7H9 media was inoculated with *Mm* culture to an OD_{600nm} of 0.2 and incubated overnight at 28°C. The following day, OD_{600nm} should be between 0.6-1. In sterile conditions, overnight cultures were then washed three times with sterile PBS (Oxoid) and OD_{600nm} was measured to resuspend *Mm* in 2% polyvinylpyrrolidone40 (PVP, Sigma-Aldrich, w/v in PBS) to achieve desired colony forming units (CFU)/nL. For heat-killed experiments, half of the resuspended *Mm* culture at desired CFU/nL was

incubated at 80 °C for 30 minutes and vortex prior to injection as previously described (Elks et al., 2014).

For experiments using avirulent *Mm*, ΔRD1 *Mycobacterium marinum* strain M containing the pSMT3-mCherry vector were cultured as above (Volkman et al., 2004; van der Sar et al., 2004).

2.7.4. *Mm* microinjection of larvae

For all infection experiments, zebrafish embryos were infected systemically via injection into the caudal vein at 30-32 hpf (see section 2.4.2). Embryos were injected with 100 CFU/nL or 1 nL of 2% polyvinylpyrrolidone 40 (PVP) as a mock infection, into the caudal vein and incubated at 28°C. To validate infection dose, 1 nL of diluted *Mm* culture was injected onto 7H10 agar plates and incubated at 28°C. Colonies formed were counted after a week.

Molecular biology

2.8. Validating *myd88* morpholino knockdown

2.8.1. Total RNA extraction from zebrafish larvae

To validate *myd88* morpholino (MO) knockdown, 20 embryos injected with *myd88* and control MO were anaesthetised and placed in 1.5 mL reaction vials at 2 dpf. Liquid was removed and fish snap frozen on dry ice for 10 minutes. Next, 500 μL TRIzol (ThermoFisher Scientific) was added and fish were homogenised via pipetting, firstly with a 1000 μL pipette tip, followed by 200 μL tip. Homogenate was allowed to stand for 5 minutes at room temperature before placing in a QIAshredder column (Qiagen) and centrifuged at full speed for 2 minutes. 100 μL of chloroform (Sigma-Aldrich) was added to the tube with a lid before shaking vigorously for 15 seconds and then incubated at room temperature for 3 minutes. Sample was then centrifuged at full speed for 5 minutes. The aqueous phase was transferred to a fresh 1.5 mL reaction vial before adding 250 μL of isopropanol (Sigma-Aldrich). Sample was vortexed for 1 minute and incubated at room temperature for 10 minutes. Next, sample was centrifuged at full speed for 15 minutes at 4°C and supernatant removed. RNA pellet was resuspended in 1 mL of 75% ethanol (v/v in DEPC-treated water) and centrifuged at 8000 rpm for 5 minutes at 4°C. Supernatant was removed using a pipette and briefly centrifuged again. Any additional liquid was carefully removed using a 1 mL syringe (BD PlastiPak) and 21G needle (BD Microlance 3) before being left to air-dry for up to 10 minutes. Pellet was resuspended in 20 μL DEPC-treated water and concentration determined using a ND1000 Nanodrop spectrophotometer (Labtech). RNA was stored at -20°C until required to synthesise complementary DNA (cDNA) for PCR.

2.8.2. cDNA synthesis

cDNA was synthesised from isolated RNA using the iScript cDNA synthesis kit according to manufacturer's instructions (Bio-Rad). Briefly, 4 μL of 5x iScript reverse-transcription reaction mix, 1 μL iScript reverse transcriptase, 1 μg total RNA and up to 20 μL total sterile nuclease-free water were added to a 0.2 mL PCR tube on ice. Samples were placed in the PCR machine and the programme in **Table 2.4.** was run. Concentration of cDNA was determined using a ND1000 Nanodrop spectrophotometer (Labtech) and stored at -20°C until required for PCR.

Table 2.4. iScript cDNA synthesis reaction protocol

Step	Temperature (°C)	Time (minutes)
Priming	25	5
Reverse transcription	46	20
Enzyme inactivation	95	1
Hold	4	∞

2.8.3. Primer sequences and PCR protocol

Synthesised cDNA was used to confirm successful *myd88* knockdown using RT-PCR. Briefly, previously published *myd88* primers were used alongside primers for the housekeeping gene *ef1α* (**Table 2.5.**) (Bates et al., 2007; Gaines, 2022). Primer sequences were ordered from Integrated DNA Technologies (IDT). Samples for PCR were prepared in PCR tubes using the volumes and reagents described in **Table 2.6.** Primers for the *ef1α* housekeeping gene were included for control and *myd88* MO injected RNA as positive controls, and no cDNA control for *myd88* MO injected RNA was included as a negative control. To increase specificity of PCR reaction, touchdown PCR was run as described in **Table 2.7**. Samples were run on a 2% agarose gel at 100V for 45 minutes with a 100 bp DNA ladder (NEB). Control MO injected samples had a 543 bp band, whilst successful *myd88* knockdown was confirmed with a 598 bp band (**Fig. 3.28** – see chapter 3).

Table 2.5. Primer sequences for *myd88* and housekeeping gene *ef1α*

Gene	Forward primer	Reverse primer	Reference
myd88	TCTTGACGGACTGGGAAACTCG	GATTTGTAGACGACAGGGATTA GCC	(Bates et al., 2007)
ef1α	CAGCTGATCGTTGGAGTCAA	TGTATGCGCTGACTTCCTTG	(Hamilton et al., 2020)

Table 2.6. PCR mix reagents and volumes. Volumes for 1 PCR reaction for both control MO and *myd88* MO injected fish cDNA, including a positive control (*ef1a* primers), a negative control (no cDNA) and myd88 (*myd88* primers).

Reagent	Volume (μL)				
	ef1a		***myd88***		**no cDNA**
	Control MO	***Myd88* MO**	**Control MO**	***Myd88* MO**	***Myd88* MO**
5X Firepol	2		2		2
Forward primer (10 μM)	0.5 (*ef1a*)		0.5 (*myd88*)		0.5 (*myd88*)
Reverse primer (10 μM)	0.5 (*ef1a*)		0.5 (*myd88*)		0.5 (*myd88*)
cDNA	1		1		0
Nuclease-free water	6		6		7

Table 2.7. Thermocycling touchdown PCR programme for the amplification of *myd88* transcript. First stage involves a higher annealing temperature (above primer T_m) that is reduced by -0.5°C per cycle for 9 cycles until required annealing temperature is reached. The second stage involves amplification using the desired annealing temperature for an additional 24 cycles.

	Step	Temperature (°C)	Time (seconds)
First stage	Initial denaturation	98	300 (5min)
	Variable cycles (9 cycles)	(1) 95	30
		(2) 60	30
		-0.5°C/cycle	
		(3) 72	50
Second stage	Variable cycles (24 cycles)	(1) 95	30
		(2) 58	30
		(3) 72	50
	Final extension	72	300 (5min)
	Hold	4	∞

2.9. Raising of a *Tg(ccn1l1:eGFP)* transgenic line

2.9.1. Bacterial artificial chromosome (BAC) preparation and injection from glycerol stock

BAC transgenesis to drive eGFP expression under the control of *ccn1l1* promoter was generated and provided as glycerol stocks by Amy Lewis (previous Research Assistant in the Elks group). The glycerol cultures were streaked on LB agar (Sigma-Aldrich) plates supplemented with 10 μg/mL of kanamycin (stock 50 mg/mL, Sigma-Aldrich) and incubated overnight at 32°C. The following day, a single colony was used to inoculate 150 mL sterile LB Broth (Sigma-Aldrich) and placed in the shaking incubator overnight

at 37°C, 200 rpm. BAC DNA was purified using the Nucleobond PC100 Midi AX 100 Kit (Macherey-Nagel) according to manufacturer's guidelines. Concentration was measured using ND1000 NanoDrop spectrophotometer (LabTech) and stored at 4°C for up to a week.

BAC DNA was injected into the embryo at the single cell stage a concentration of 34.88 ng/μL, along with 1 μL Tol2 RNA and 1 μL of 1:10 diluted PR (in MilliQ, Sigma-Aldrich).

2.9.2. DNA linearisation

To synthesise Tol2 transposase RNA, 20 μg of pCS2FA-transposase plasmid MIDIprep (a kind gift from the Renshaw lab) was linearised using NotI-HF (New England Biolabs, NEB) for 2 hours at 37°C. Product was purified using QIAquick PCR purification kit (Qiagen) according to manufacturer's guidelines. Purified linearised DNA was eluted into 30 μL buffer EB (Qiagen). To check successful linearisation, 0.5 μL DNA was run on a 1% (w/v in 1x TAE buffer, Bioline) agarose gel at 100 V for 1 hour alongside a 1kB DNA ladder (Bioline). Concentration was measured using ND1000 NanoDrop and stored at -20°C.

2.9.3. RNA synthesis

To synthesise Tol2 mRNA for injection, 1 μg of linearised DNA was used for *in vitro* transcription using the phenol:chloroform extraction and isopropanol precipitation protocols according mMESSAGE mMACHINE SP6 Transcription Kit (Ambion) and eluted in 10 μL of DEPC treated water. Concentration was measured using ND1000 NanoDrop and stored at -80°C.

2.9.4. Generation of a stable transgenic line

Briefly, injected F0 generation adults were outcrossed with wildtype zebrafish (LWT) and housed individually during the screening process. F1 offspring were screened for specific expression of GFP within the otic vesicle to identify F0 founder fish, indicating germline integration of the transgene. F1 embryos were raised to adulthood and outcrossed to again to wildtype zebrafish (nacre). Embryos were screened for up to 50% GFP expression to ensure single-copy insertion of the transgene. Positive F2 embryos were raised to adulthood to ensure a stable transgenic line which could then be incrossed to generate F3 offspring for future experiments.

2.10. Raising of a stable *Tg(mfap4:mCherry-F)* transgenic line

2.10.1. Plasmid purification

The *mfap4:mCherry-F* and *tnfa:eGFP-F* plasmids were a kind gift from the Nguyen-Chi group (University of Montpellier). Plasmids were received on filter paper and were eluted in 50 μL TE buffer (1:10 diluted in DEPC treated water) by Dave Drew (Research Assistant previously in the Renshaw

group). Both plasmids were transformed to competent cells, spread on carbenicillin plates (50 μg/mL, Sigma-Aldrich) and incubated at 37°C by Dave Drew. From here on in, protocol was continued by me. The following day, a single colony was used to inoculate 150 mL sterile LB Broth (Sigma-Aldrich) supplemented with 50 μg/mL carbenicillin, and placed in the shaking incubator overnight at 37°C, 230 rpm. DNA was purified using the Qiagen MIDIprep kit according to manufacturer's instructions. Concentration was measured using ND1000 NanoDrop. NotI-HF (NEB) and SacI-HF were incubated with 1 μL of the DNA (diluted 1:10 in DEPC treated water) overnight as a diagnostic digest. Digest products were mixed with 6X gel loading dye (NEB) and run on a 1% (w/v) agarose gel for 1 hour at 100 V alongside a 1kB DNA ladder (Bioline). Samples were stored at -20°C.

2.10.2. Plasmid sequencing

Whole plasmid sequencing was performed by Plasmidsaurus using Oxford Nanopore Technology with custom analysis and annotation. Plasmid maps used in this thesis were generated using BioRender (BioRender.com), with publication licences SE271K8TC9 (*mfap4:mCherry-F*) and CG271K8BA0 (*tnfa:mCherry-F*).

2.10.3. Microinjection of plasmid into the single cell stage

A volume of 1 nL of *mfap4:mCherry-F* plasmid DNA was injected into the embryo at the single cell stage at a final concentration of 12.5 ng/μL, along with 1 μL Tol2 RNA, 1 μL PR (1:10 diluted in MilliQ) and nuclease-free water (Qiagen) up to a volume 10 μL. Embryos were screened for macrophage mCherry expression within the caudal haematopoietic tissue at 2 dpf and raised to adulthood.

2.10.4. Generation of a stable transgenic line

Generation of a stable line was carried out as described in section 2.9.4, screening for specific macrophage farnesylated mCherry expression, particularly in the CHT and brain (microglia) to raise the next generations of adult fish.

2.11. Generation of a *Tg(tnfa:mCherry-F)* transgenic line

2.11.1. Plasmid purification and plasmid subcloning

A single t*nfa:eGFP-F* colony (see section 2.10.1) was used to inoculate 150 mL sterile supplemented LB Broth (Sigma-Aldrich) and placed in the shaking incubator overnight at 37°C, 230 rpm. DNA was purified using the Qiagen MIDIprep according to manufacturer's instructions. Concentration was measured using ND1000 NanoDrop. NotI-HF and SacI-HF were incubated with 1 μL of the DNA (diluted 1:10 in DEPC treated water) overnight as a diagnostic digest. Digest products were run on a 1% (w/v) agarose gel for 1 hour at 100 V alongside a 1kB DNA ladder.

In the first instance, subcloning via restriction digest was performed. NotI-HF and SacI-HF were used simultaneously to digest 5 μg of *tnfa:eGFP-F* and 10 μg of *mfap4:mCherry-F.* Digest products were mixed with 6X gel loading dye (NEB) and run on a 1% (w/v) agarose gel for 1 hour at 100 V alongside a 1kB DNA ladder. Gel extraction, ligation reaction, transformation and DNA purification (MINIprep and MIDIprep) were performed as described in sections 2.11.6 - 2.11.8. EcoRV-HF and ApaI-HF (NEB) were incubated with 1 μL of the plasmid (diluted 1:10 in DEPC treated water) overnight as a diagnostic digest. A restriction digest with EcoRV-HF alone to linearise the plasmid was also performed as a secondary test. Whole plasmid sequencing was performed by Plasmidsaurus (see section 2.10.2). Samples were stored at -20°C.

2.11.2. Primer design

To remove the *tnfa* ATG sequence of the ligated *tnfa:mCherry-F* plasmid to ensure the mCherry sequence was in-frame, primers to clone out the *tnfa* promoter via PCR were designed using SnapGene software (www.snapgene.com). Forward and reverse primers included a NotI and EcoRV site, respectively. Primer pairs within 1°C melting temperature (Tm; **Table 2.8.**) range and a GC content less than 30% (excluding restriction sites) were selected. Primer sequences were then ordered from Integrated DNA Technologies (IDT).

Table 2.8. Primer sequences to amplify the *tnfa* promoter region without the sequence of exon one. Restriction site sequences included within the primer are in bold.

Forward primer	TT**GCGGCCGC**TAATTGCTGTATGTCTTAAAG	Tm= 54°C
Reverse primer	**ATC**AACATAAAATGAATCAATG	Tm=53°C

2.11.3. Gradient PCR and PCR protocol

Samples were prepared using the reagents described in **Table 2.9.**, alongside a no template control. To identify the optimal annealing temperature of the primers, a temperature gradient PCR was performed using a T100 Thermal Cycler (BIO-RAD) (**Table 2.10.**).

Table 2.9. PCR reaction reagents and volumes for one sample.

Reagent	Volume (μL)
5X Q5 reaction buffer - vortex	5
dNTPs (10 mM)	0.5
Forward primer (10 μM)	1.25
Reverse primer (10 μM)	1.25
Plasmid DNA (5 ng)	0.33
Q5 high-fidelity DNA polymerase	0.25
Nuclease-free water (up to 25 μL)	16.42

Table 2.10. Thermocycling PCR programme for the amplification of part of the *tnfa* promoter region.

Step	Temperature (°C)	Time (seconds)
Initial denaturation	98	30
35 cycles	98	10
Annealing (optimisation)	(1) 52	30
	(2) 52.7	30
	(3) 53.9	30
	(4) 55.8	30
	(5) 58	30
Extension	72	20 per kb (30s)
Final extension	72	300 (5min)
Hold	10	∞

PCR product was run on 1% (w/v) agarose gel for 1 hour at 100 V alongside a 1kB DNA ladder to identify which annealing temperature resulted in the best PCR product. The best amplification was achieved at Tm 52.7°C, thus an upscaled PCR using the annealing temperature was performed. To ensure successful PCR reaction, 10 μL of PCR product and undigested *tnfa:mCherry-F* was run on a 1% (w/v) agarose gel for 1 hour at 100 V alongside a 1kB DNA ladder.

2.11.4. PCR purification

PCR product was purified using the NucleoSpin Gel and PCR Clean-up Kit (Macherey-Nagel), according to manufacturer's instructions. Concentration was measured using ND1000 NanoDrop.

2.11.5. Restriction digests

Restriction enzymes were selected based on which restriction enzyme sequence was included in the primers (section 2.11.2, **Table 2.8.**). NotI-HF and EcoRV-HF (NEB) were used to digest 1.5 μg of

the *tnfa:mCherry-F* vector, and NotI-HF to digest 1 μg of the PCR product. Reaction mixes were incubated overnight at 37°C to ensure complete digestion. Digested PCR product was purified using the MinElute PCR Purification Kit (Qiagen). Concentration was measured using ND1000 NanoDrop.

2.11.6. Gel electrophoresis and gel extraction of digested vector

The plasmid digest was mixed with 6X gel loading dye (NEB) and run on a 1% (w/v) agarose gel for 1 hour at 100 V alongside a 1kB DNA ladder. Using a sterile scalpel blade, the band of correct molecular weight was excised using a low UV gel transilluminator to visualise bands. Digested vector was extracted using the QIAquick Gel Extraction Kit (Qiagen). Concentration was measured using ND1000 NanoDrop.

2.11.7. T4 ligation

A 3:1 molar ratio ligation reaction (calculated using NEBioCalculator) of PCR insert and vector was used. A list of reagents used and the order in which they were added to the reaction are listed below (**Table 2.11.**). Reaction was incubated overnight at 16°C, before being heat inactivated at 65°C for 10 minutes the following morning. A vector only control was also included.

Table 2.11. T4 ligation reaction of *tnfa:mCherry-F* digested vector and PCR product. A 3:1 molar ratio of insert:vector was used.

Reagent	Volume (μL)
T4 ligase buffer (NEB)	2
Vector	8.03
PCR insert	2.31
Nuclease-free water (Qiagen)	Up to 20
T4 ligase (NEB)	1

2.11.8. Transformation to competent cells and DNA purification

10-beta low efficiency competent cells (*Escherichia coli*, NEB) were thawed from -80°C on ice and 22 μL of cells split across two reaction vials. 3 μL of *tnfa:mCherry-F* ligation reaction and 3 μL of vector-only control were added to each vial and kept on ice for 30 minutes. Cells were heat shocked at 42°C for 45 seconds in a water bath and immediately returned to ice, before adding 100 μL of Super Optical broth with Catabolite repression (SOC) media (Thermo-Fisher Scientific). Supplemented cells were incubated at 37°C in a shaking incubator for 1 hour before being spread on carbenicillin agar plates and further incubated at 37°C overnight. The following day, a single colony was used to inoculate 2 mL of supplemented LB Broth (Sigma-Aldrich) and placed in the shaking incubator overnight at 37°C, 230 rpm. Agar plates were stored at 4°C. DNA was purified using the Qiagen MINIprep kit according to manufacturer's instructions, keeping approximately 500 μL of starter culture. HindIII (NEB) was

incubated with 1 μL of the plasmid (diluted 1:10 in DEPC treated water) and 1 μL of r2.1 buffer (NEB) at 37°C for 1.5 hours as a diagnostic digest. A restriction digest with XmnI-HF (NEB) to linearise the plasmid was also performed as a secondary test. Digest products were run on a 1% (w/v) agarose gel for 1 hour at 100 V alongside a 1kB DNA ladder. Remaining starter culture of clones with bands of the correct molecular weight was used to inoculate 150 mL supplemented LB Broth for an upscaled MIDIprep as describe in section 2.9.1. Whole plasmid sequencing was performed by Plasmidsaurus (see section 2.10.2). Samples were stored at -20°C.

2.11.9. Microinjection of plasmid into the single cell stage

Cloned *tnfa:mCherry-F* plasmid was injected into the single cell stage according to published I-SceI meganuclease transgenesis protocol (Soroldoni et al., 2009). Briefly, microinjection mix was stored on ice and I-SceI meganuclease (stored at -80°C) was added last (**Table 2.12.**). Microinjection needle was loaded and calibrated as described in section 2.2.4. Injection needles were changed with fresh microinjection mix stored on ice every 30 minutes.

Table 2.12. *tnfa:mCherry-F* microinjection mix for single-cell injections. I-SceI meganuclease was added last and gently mixed without vortexing.

Reagent	Volume (μL)
DNA	100 ng/μL (final concentration)
CutSmart buffer (without $MgCl_2$) – NEB	2
$MgCl_2$ (50 mM) – Bio-Rad	2
Phenol red 0.5% (in MilliQ) - Sigma-Aldrich	1
Nuclease-free water - Qiagen	Up to 18
I-SceI meganuclease – NEB	2

2.11.10. Generation of a stable transgenic line

Generation of a stable line was carried out as described in section 2.8.4. A tail fin transection was performed (avoiding the notochord) on 3 dpf embryos to identify specific *tnfa:mCherry-F* expression at the wound site that had macrophage morphology at 20 hours post-amputation (hpA). To ensure expression was macrophage specific, F0 adult fish were first outcrossed to *mpeg1:nlsClover* adults. Founders identified were then crossed to nacre, injured and screened *for tnfa:mCherry-F* expression. Subsequent embryos were screened for mCherry expression in the pharynx using the stereo microscope, as previously described (Nguyen-Chi et al., 2015). Positive embryos were raised to adulthood for the next generations, as described in section 2.9.4.

2.12. Whole larvae single-cell RNA sequencing

2.12.1 Whole larvae dissociation

Nacre larvae were injected with either PR, dominant active HIF-1α (DA1) or dominant active HIF-2α (DA2) at the single cell stage. Embryos injected from 2 batches, meaning that they were obtained from different tanks and the needle changed between batches to obtain 2 biological repeats. 2 batches of uninjected embryos were also collected. The following day, uninjected embryos were infected with 100 CFU of *Mm*-Crimson into the CHT (as described in section 2.7). Embryos injected with PR, DA1 and DA2 (for both biological replicates) were injected with PVP into the CHT as a control.

Embryos were dissociated the following day (at 1 dpi) using protocols adapted from the Yi Feng, Sofia de Oliveira and Merlin Lange groups (Elliot et al., 2025; de Sena-Tomás et al., 2024; VijayKumar et al., 2024). Briefly, anaesthetised fish were placed in reaction vials pre-coated with 1xPBS (Fisher) and 2% BSA (Sigma) with dissociation solution (2.5 mg/mL collagenase IV [Gibco], 15 mM HEPES [Sigma], 25 mM D-Glucose [Sigma], 2% FBS [Gibco] in HBSS without magnesium or calcium [Gibco]). Samples were incubated at 28°C shaking at 300 rpm for 7 minutes. Larvae were mechanically dissociated using a pipette. Incubations were repeated twice more for 5 minutes each, vigorously pipetting after each incubation. 50 μL DMEM + GlutaMAX (Gibco) and 1% BSA were added to each sample until all replicates were dissociated. Subsequently, samples were centrifuged at 500g for 5 minutes at 4°C. Cells were resuspended in non-enzymatic cell dissociation solution (Sigma) and filtered through a 40 μm filter. Samples were centrifuged at 400g for 5 minutes at 4°C, and pellet washed in 1 mL 1xPBS and 1% BSA. Sample was stained for viability using 0.4% trypan blue at room-temperature for 10 minutes. Approximately 120,000 cells were removed, centrifuged at 400g for 5 minutes at 4°C and resuspended in 1xPBS and 1% BSA. Sample was centrifuged again and resuspended in 100 μL of 1xPBS and 0.5% BSA.

2.12.2 10x Genomics Chromium

All following steps were completed by Dr Benjamin Lindsey. Samples were loaded on to a Chromium GEM-X 3' OCM Chip (10x Genomics). Library preparation and final tapestation QC was performed, with a mean read length of approximately 1,300 base pairs. Similar total complementary DNA was obtained between the two pools (1,636 ng and 1624 ng).

2.12.3 Data analysis

FASTQ files were processed using the Parse Biosciences Pipeline (v1.5.0, Parse Biosciences) by Dr Benjamin Lindsey and Trailmaker™ (Parse Biosciences) was used to complete data analysis (www.app.trailmaker.parsebiosciences.com). To bioinformatically identify the population of *arg2+* macrophages, a custom cell set of double-positive *mfap4+ arg2+* genes were sub-clustered from the whole larvae UMAP plot. Dot plots were generated for this cluster using the Trailmaker™ gene

expression plots for custom selected genes based on published teleost macrophage RNAseq datasets (Rougeot et al., 2019; Cronan et al., 2021; Wentzel et al., 2020).

2.13. Published RNAseq data analysis

A Microsoft Excel formula (see formula below, alphanumerics in bold are example cells) was used to identify mutual significantly upregulated genes between IL-4/IL-10 polarised human monocyte-derived macrophages (MDMs) and zebrafish macrophages infected with *Mm* RNAseq datasets. As only one gene was originally identified, genes upregulated in the human MDM dataset were also compared to non-significantly upregulated zebrafish genes to broaden the search.

$$= \mathrm{IF}(\mathrm{ISERROR}(\mathrm{MATCH}(\mathbf{A1}, \$\mathbf{B}\$\mathbf{1}{:}\$\mathbf{B}\$\mathbf{1000}, 0)), "", \mathbf{A1})$$

The MDM RNAseq dataset used to datamine candidate genes and for KEGG pathway comparisons in this project can be accessed at doi.org/10.17632/j2hmt7k9fh.1 (Baidžajevas et al., 2020). The human peripheral blood mononuclear cell (PBMC) RNAseq dataset can be found under accession number GSE154347 (He et al., 2021). Zebrafish macrophage RNAseq datasets are deposited on the NCBI Gene Expression Omnibus (http://www.ncbi.nlm.nih.gov/geo). The datasets for uninfected and *Mm* infected macrophages can be found under accession numbers GSE78954 and GSE68920, respectively (Rougeot et al., 2019). Single-cell RNAseq of adult zebrafish leukocytes can be accessed at https://www.sanger.ac.uk/tool/basicz/basicz (Athanasiadis et al., 2017). To identify KEGG pathways for comparisons between human and zebrafish, genes were input into ShinyGO V.0.80 (Ge et al., 2020; Kanehisa et al., 2021).

2.14. Statistical analysis

All statistical analysis and all graphs were generated using GraphPad Prism version 9 and 10 (San Diego, CA, USA). Data was first checked for normal distribution visually using GraphPad Prism (e.g. histograms and Quantile-Quantile plots). Statistical significance was calculated using either an unpaired *t*-test for experiments with 2 experimental groups or a one-way ANOVA with Bonferroni's multiple comparisons post-hoc test if there were 3 or more experimental groups. For timelapse experiments, a paired *t*-test was used to compare *arg2:GFP+* cells (*mfap4:mCherry+* or *tnfa:mCherry+*) to its nearest *arg2:GFP-* neighbour. For categorical data (e.g. number of *arg2:GFP+* cells), if there were 3 or more groups, a chi-squared test was initially used to determine whether a statistical significance was present, and a Fisher's exact test used on individual groups to determine where the significance lay. If there were 2 experimental groups, only a Fisher's exact test was used. Individual statistics and P values are provided in the figures and/or figure legends.

3. Characterising macrophage *arginase2* expression during *Mm* infection using an *arg2:GFP* transgenic zebrafish line

Some of the data in this chapter (section 3.2.2) was published as:

Hammond, F.R., Lewis, A., **Speirs, Z.C**., Anderson, H.E., Sipka, T., Williams, L.G., Nguyen-Chi, M., Meijer, A.H., Wiegertjes, G.F. and Elks, P.M. An arginase 2 promoter transgenic illuminates immune cell polarisation in zebrafish. *Disease Models & Mechanisms.* 2023 Jun 1; 16 (6):dmm049966. doi.org/10.1242/dmm.049966

3.1. Introduction

3.1.1. Macrophage phenotypes in TB

Although the pathogenesis of human TB remains difficult to fully resolve due to complex host-pathogen interactions, a growing body of evidence illustrates how *Mtb* alters macrophage activation states to favour an anti-inflammatory phenotype at later stages of infection, creating a permissive intracellular niche that facilitates bacterial expansion (Davis et al., 2007; Miller et al., 2004; Guo et al., 2016).

There are several reports describing an early biphasic immune response during mycobacterial infection, whereby the pathogen initially suppresses pro-inflammatory macrophage activation to promote intracellular survival and replication. For example, pro-inflammatory IL-12 secretion by *Mtb*-infected human THP-1 macrophages followed an inverted U-shaped pattern, with elevated secretion at 3 hpi, a decline at 6 hpi, and a resurgence by 9 hpi; IL-10 displayed the opposite pattern (Roy et al., 2024). Similarly, murine BMDMs infected with *Mm* showed elevated *tnf* and *il6* mRNA expression at 4 hpi, which dropped substantially by 36 hpi (Wumaier et al., 2025). Transcriptomic profiling of *Mm*-infected zebrafish larvae further supports this pattern, revealing an early wave of pro-inflammatory cytokine induction at 4 hpi followed by a secondary wave at 3-5 days dpi, highlighting this early mycobacteria-mediated biphasic effect (Benard, 2014). A similar temporal pattern was observed in *Mycobacterium abscessus*-infected alveolar macrophages, where early induction of TNF, IL-1α and IL-1β at 6 hpi diminished markedly by 24 dpi (Gilliland et al., 2025). The dampening of the pro-inflammatory response between waves, termed the lag phase, has been attributed to increased anti-inflammatory signalling. For instance, immunohistochemical detection of IL-4 in lung tissue from mice infected with a virulent recombinant BCG strain showed a gradual increase from 4 to 16 dpi, followed by a decline at 21 dpi to levels comparable to those at 4 dpi (Peng et al., 2022). This lag phase has also been observed in granulomas obtained from human patients with active TB, where it appears essential for establishing organised granuloma formation (Huang et al., 2015).

During granuloma maturation, macrophage phenotypes become more heterogenous. Although there is a broad shift toward anti-inflammatory programmes, pathogenic pro-inflammatory macrophages persist within granulomatous lesions and contribute to tissue damage (Wang et al., 2020; Pisu et al., 2025). Recent single-cell analyses of adult zebrafish *Mm* granulomas identified a granulin+ anti-inflammatory macrophage subset (*grna.2+*) that limits excessive inflammation; depletion of these cells led to denser necrotic granulomas and heightened pro-inflammatory signalling (Luo et al., 2025). At the same time, macrophage expression of inflammatory mediators such as *irg1* (immunoresponsive 1) and matrix metallopeptidases is enriched in both *Mtb* and *Mm* infection and contributed to tissue destruction (Dirks et al., 2024; Subbian et al., 2016). Together, these findings highlight that TB granulomas contain a dynamic mixture of macrophage states, balancing antimicrobial activity with regulation of immunopathology

3.1.2. *In vitro* evidence for macrophage plasticity

It is increasingly clear that macrophages are highly heterogenous and exist along a broad activation spectrum rather than discrete M1 or M2 states (Mills and Ley, 2014; Xue et al., 2014; Martinez and Gordon, 2014). *In vitro* stimulation systems have further subdivided the M2-like category into M2a, M2b, M2c and M2d, each defined by unique transcriptional signatures following exposure to specific polarising stimuli (Mantovani et al., 2004). However, while these categories are useful for mechanistic studies, they do not map cleanly onto macrophage phenotypes *in vivo*, where activation states are shaped by complex and dynamic microenvironmental signals (Orecchioni et al., 2019).

A major unresolved question in TB immunobiology is not simply whether pro-inflammatory and anti-inflammatory macrophages exist, but how their phenotypes evolve over time within infected tissues. *In vitro*, macrophages polarised to M1 or M2 states can be repolarised by switching stimuli, demonstrating that their phenotypes are not terminally fixed (Kalish et al., 2015; Vidyarthi et al., 2018; Carvalho et al., 2021). However, determining whether similar transitions occur *in vivo* has been challenging, largely due to technical limitations in mammalian TB models. Most studies rely on static immunohistochemistry or flow cytometry, which capture only a single time-point and cannot distinguish whether a double-positive macrophage represents a stable hybrid phenotype or a cell caught transitioning (Kocsy et al., 2025; Mattila et al., 2013; Le et al., 2020). For example, macrophages co-expressing M1- and M2-associated markers have been identified in human disease tissue, such as CD68+ CD86+ MRC1+ macrophages in carotid atherosclerotic plaques and double-positive macrophages in the bronchoalveolar lavage fluid of patients with lower respiratory infections or *Mycobacterium avium* complex disease (Kocsy, 2021; Kocsy et al., 2025; Ikegami et al., 2022). However, without temporal resolution, these observations cannot distinguish lineage-specific recruitment from dynamic re-polarisation – leaving a central question in TB immunobiology unanswered: do double-positive

macrophages represent individual cells transitioning between activation states, or are distinct macrophage populations sequentially recruited and retain fixed phenotypes *in vivo*.

3.1.2. Arginase expression in infection

Arginase is widely recognised as a hallmark of alternatively activated (M2-like) macrophages, typically upregulated in response to IL-4 and IL-10 stimulation *in vitro* (Pesce et al., 2009; Dowling et al., 2021). While arginase is often discussed in the context of its competition with iNOS for L-arginine, its biological significance extends well beyond NO homeostasis. Arginase hydrolyses L-arginine into L-ornithine and urea, and these downstream metabolites profoundly influence macrophage behaviour and tissue microenvironments (Nathan and Hibbs, 1991; Dzik, 2014). L-ornithine serves as a precursor for polyamines (via ornithine decarboxylase) and proline (via ornithine aminotransferase), which are essential for cell proliferation, extracellular matrix remodelling and collagen synthesis – key components of wound repair and fibrosis (Szondi et al., 2021; Caldwell et al., 2018). Polyamines such as putrescine and spermidine regulate macrophage proliferation, efferocytosis, cytokine secretion and resolution-phase functions, further linking arginase activity to tissue repair and immunomodulation (Latour et al., 2020). Thus, arginase expression reflects broader immunoregulatory and tissue-repair programmes rather than simply opposition to iNOS.

Correspondingly, arginase expression is well documented during tissue repair, where it promotes wound closure, extracellular matrix deposition and restoration of tissue integrity (Shosha et al., 2023; Campbell et al., 2013). Arginase is also strongly induced during infection. Upregulation occurs in macrophages responding to helminths, protozoa and bacteria (El Kasmi et al., 2008; Iniesta et al., 2005; Chen et al., 2018; Yamada et al., 2018; Brigo et al., 2021). Some intracellular pathogens exploit the arginase pathway to subvert host immunity: *Cryptococcus neoformans* drives Arg1 expression in murine interstitial macrophages *in vivo* via the CPL1 virulence factor (Gibson et al., 2022; Dang et al., 2022); *Candida albicans* induces Arg1 activity in human M1-polarised MDMs to promote persistence (Wagener et al., 2017). *Helicobacter pylori* disrupts host NO production both via its own arginase (rocF) and by inducing host Arg2, shifting metabolism toward polyamine-driven macrophage apoptosis (Lewis et al., 2010; Gobert et al., 2002; Gobert et al., 2001).

Despite extensive study, it remains unclear whether arginase-expressing macrophages in TB lesions represent newly recruited cells or re-polarised cells transitioning from an early pro-inflammatory phenotype. Much of our current understanding of M2-like macrophage dominance at granuloma stages derives from *in vitro* polarisation systems and *ex vivo* analyses of fixed granuloma tissue (Ly et al., 2008; Qualls et al., 2010; Mattila et al., 2013; Huang et al., 2015; El Kasmi et al., 2008). These approaches rely on static endpoint measurements and therefore cannot distinguish whether cells co-expressing M1 and M2 markers represent true hybrid states or macrophages transitioning along a

temporal axis of activation. Likewise, conventional murine and non-human primate models lack tools that allow real-time tracking of macrophage phenotype during infection, making it difficult to determine whether M2-like macrophages are recruited *de novo*, repolarised from earlier M1 states, or arise from multiple parallel lineages. This limitation is highly relevant because temporal regulation of macrophage activation is crucial for TB control: excessive inhibition of early pro-inflammatory responses (e.g.: via iNOS inhibitors or early HIF-1α inhibition) worsens disease, whereas late-stage hyper-inflammation also drives pathology (Baay-Guzman et al., 2018; Chan et al., 1995). Interrupting arginase signalling is similarly nuanced. Systemic arginase inhibition early in infection exacerbates inflammation and lung damage without reducing bacterial burden, whereas macrophage-specific *Arg1* deletion worsens infection outcomes (Chauhan et al., 2024; Jiang et al., 2025; Duque-Correa et al., 2014). These complexities highlight the need to resolve when and where anti-inflammatory macrophage programmes are induced *in vivo*.

Notably, murine and human macrophages differ markedly in their reliance on the iNOS/arginase axis: murine macrophages robustly induce *Arginase 1*, whereas human macrophages express minimal *ARG1* under equivalent stimuli to regulate inflammatory tone (Munder et al., 2005). Nevertheless, the downstream functions of arginase-derived metabolites remain biologically conserved, underscoring the importance of studying arginase regulation across models (Caldwell et al., 2018).

3.1.3. The *arginase 2* zebrafish transgenic reporter

Zebrafish larvae provide a powerful model for visualising immune cell dynamics *in vivo* due to their optical transparency and the availability of transgenic lines labelling leukocytes, including neutrophils and macrophages (Elks et al., 2015). Pro-inflammatory reporter lines such as *tnfa:eGFP* have enabled examination of putative pro-inflammatory macrophages during injury and infection (McWhorter et al., 2013; Lewis and Elks, 2019; Ogryzko et al., 2019; Bojarczuk et al., 2016; Nguyen-Chi et al., 2017). However, tools to visualise anti-inflammatory macrophages in real-time have been lacking, limiting our ability to resolve how macrophage phenotypes evolve during infection. Indeed, we have had to rely on extrapolation from data obtained from these pro-inflammatory reporters to identify anti-inflammatory populations (e.g.: *tnfa*-positive macrophages vs. *tnfa*-negative macrophages) and analysis of cell morphology (Xie et al., 2019; Sipka et al., 2022).

To address this gap, our group developed an *arginase 2* promoter zebrafish transgenic line (*arg2:GFP*), allowing *in vivo* visualisation of a hallmark *in vitro* anti-inflammatory marker (Hammond et al., 2023). *arginase 2* was one of the most strongly upregulated genes expressed in M2-polarised *ex vivo* carp monocytes, suggesting it may serve as a conserved marker of anti-inflammatory programming in fish (Wentzel et al., 2020). Its relevance in TB is supported by single-cell RNA sequencing (scRNAseq) of adult zebrafish granulomas, showing *Mm*-induced type 2 transcriptional programmes, including *arg2*

upregulation in epithelioid macrophages, consistent with ARG1+ CD68+ epithelioid macrophages in human and macaque TB granulomas (Cronan et al., 2016; Cronan et al., 2021). Initial observations using the *arg2:GFP* line identified a small population of macrophages that upregulated *arg2:GFP* early after infection (~6.1%), but whether these cells represent bona fide anti-inflammatory macrophages remains unknown (Hammond et al., 2023).

In chapter 6, the top upregulated gene identified in M2 polarised carp macrophages was explored in zebrafish using a novel transgenic line (*ccn1l1:eGFP*). However, no upregulation of the transgene was identified in macrophages following immune challenge, thus the *arg2:GFP* line represents the strongest available tool for interrogating anti-inflammatory macrophage polarisation *in vivo*.

3.1.4. Hypothesis and aims

In addition to *arg2* being highly upregulated in M2-polarised carp macrophages, Arginase 1 is a canonical M2 marker of mammalian macrophages *in vitro* (Wentzel et al., 2020; El Kasmi et al., 2008; Fitzsimons et al., 2023). Upregulation of *arg2:GFP* expression in macrophages indicates that there may be a subpopulation of anti-inflammatory macrophages during early *Mm* infection (Hammond et al., 2023). Because anti-inflammatory macrophage programming has been implicated in mycobacterial immune evasion but remains poorly defined *in vivo*, I hypothesise that *arg2:GFP* expression is dynamically regulated during early *Mm* infection and that its induction reflects pathogen-mediated modulation of macrophage phenotype.

To address my hypothesis, I will use zebrafish transgenic reporter lines to investigate several research aims:

- To characterise putative pro-inflammatory macrophages during *Mm* infection using the *tnfa:eGFP* reporter transgenic.
- To characterise *arg2:GFP* expressing macrophages during *Mm* infection and determine whether they phenotypically resemble *in vitro* M2-polarised murine macrophages.
- To determine the signalling mechanisms by which *Mm* induces macrophage *arg2:GFP* expression, including RD1-dependent virulence pathways and MyD88-mediated innate signalling.

3.2. Results

3.2.1. Characterising putative pro-inflammatory macrophages during early *Mm* infection

Over the last decade, transgenic zebrafish reporters for pro-inflammatory cytokines have been developed, including *tnfa* and *il-1β* (Nguyen-Chi et al., 2015; Marjoram et al., 2015; Ogryzko et al., 2019). There are currently two *tnfa* reporter lines: *Tg(tnfa:eGFP-F)* (Nguyen-Chi et al., 2015) and *TgBAC(tnfa:GFP)* (Marjoram et al., 2015). The promoter driven *tnfa:eGFP-F* is the most well characterised reporter for putative pro-inflammatory macrophages, with their transcriptional signature resembling M1-like macrophages (Nguyen-Chi et al., 2015). However, despite availability of these reporters, in-depth characterisation of the macrophage *tnfa* expression in *Mm* infection has not been carried out (Lewis and Elks, 2019). At the University of Sheffield, the *TgBAC(tnfa:GFP)* (hereon in termed *tnfa:GFP*) was available and contains a larger promoter region than the *tnfa:eGFP-F* line conferring more accurate reporting; therefore, I aimed to characterise these putative pro-inflammatory macrophages from 1-4 dpi post *Mm* infection.

At 1 dpi, over half (59.5% of n=185) of *mpeg:mCherry+* cells were *tnfa:GFP* positive (**Fig. 3.1. Ai, Aiii**). At this time-point, all fish had examples of *tnfa:GFP+ mpeg:mCherry+* cells (out of 19 larvae) (**Fig. 3.1. Aii**). The proportion of *tnfa:GFP+* macrophages remains similar at 2 dpi, with all fish (19/19 larvae) having examples of *tnfa:GFP+ mpeg:mCherry+* cells, with one fish only having examples of double positive cells (fish 9) and several larvae only having 1 *tnfa:GFP* negative cell (fish 1, 6, 8) (**Fig. 3.1. Bi, Bii**). Collectively, 54.5% (of n=244 macrophages) were *tnfa:GFP+* at 2 dpi, with the proportion of double positive cells impacted by the very high numbers of macrophages captured in some fish (e.g. 27 *mpeg:mCherry+* cells in larvae 14) (**Fig. 3.1. Biii**). The overall number of macrophages identified falls at 3 dpi (173 *mpeg:mCherry+* cells), yet a higher proportion of cells are *tnfa:GFP+* macrophages (68.2%) at this timepoint when granulomas begin to form (**Fig. 3.1. Ci, Ciii**). Only 1 larvae (out of 18) had no examples of *tnfa:GFP* positive macrophages, yet several fish (4) only had examples of *tnfa:GFP+ mpeg:mCherry+* cells (fish 1, 4, 5, 12) (**Fig. 3.1. Cii**). Unlike at 2 dpi, the larvae with more macrophages had more double positive cells, with one fish having 20/23 *tnfa:GFP+* macrophages (fish 14) (**Fig. 3.1. Cii**). At 4 dpi, the proportion of *tnfa:GFP+ mpeg:mCherry+* cells falls by nearly 25%, with 44.8% (of n=181 macrophages) being double positive (**Fig. 3.1. Di, Diii**). Although fewer macrophages were double positive at this time-point, 17/18 larvae had examples of at least 1 *tnfa:GFP+* macrophages (**Fig. 3.1. Dii**). Together, this data demonstrates robust recruitment of putative pro-inflammatory macrophages at the early stages of *Mm* infection, with *tnfa* expression falling at later stages of infection (4 dpi).

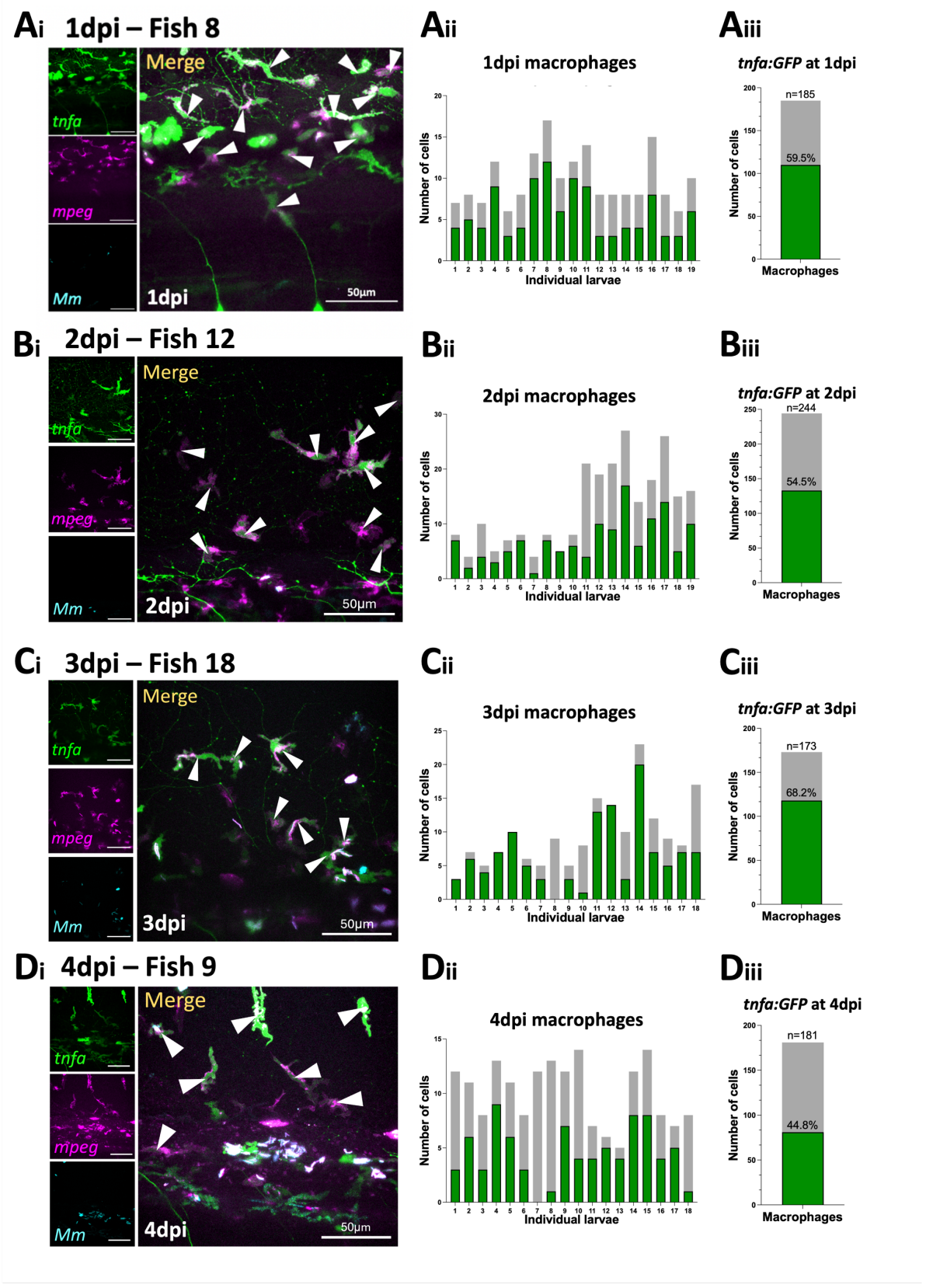


Figure 3.1. The number of *tnfa:GFP* positive macrophages rises from 1 dpi before falling at 4 dpi. (Ai) Representative confocal image of 1 dpi *tnfa:GFP* crossed to *mpeg:mCherry*. **(Aii)** Graph illustrating the number of *tnfa:GFP*+ and *tnfa:GFP*- macrophages counted for each individual larvae at 1 dpi. **(Aiii)** Graph illustrating the percentage of *tnfa:GFP*+ and *tnfa:GFP*- macrophages at 1 dpi. N=2 independent experiments **(Bi)** Representative confocal image of 2 dpi *tnfa:GFP*+ *mpeg:mCherry*+ larvae. **(Bii)** Graph illustrating the number of *tnfa:GFP*+ and *tnfa:GFP*- macrophages counted for each individual larvae at 2 dpi. **(Biii)** Graph illustrating the percentage of *tnfa:GFP*+ and *tnfa:GFP*- macrophages at 2 dpi. Counts from N=2 independent experiments. **(Ci)** Representative

confocal image of 3 dpi *tnfa:GFP+ mpeg:mCherry+* larvae. (**Cii)** Graph illustrating the number of *tnfa:GFP+* and *tnfa:GFP-* macrophages counted for each individual larvae at 3 dpi. (**Ciii)** Graph illustrating the percentage of *tnfa:GFP+* and *tnfa:GFP-* macrophages at 3 dpi. Counts from N=2 independent experiments. (**Di)** Representative confocal image of 4 dpi *tnfa:GFP+ mpeg:mCherry+* larvae. (**Dii)** Graph illustrating the number of *tnfa:GFP+* and *tnfa:GFP-* macrophages counted for each individual larvae at 4 dpi. (**Diii)** Graph illustrating the percentage of *tnfa:GFP+* and *tnfa:GFP-* macrophages at 4 dpi. Counts from N=2 independent experiments. All counts were taken from a 40x field of view near the caudal vein (site of infection) or around clusters of bacteria within the fish. Arrowheads indicate *arg2:GFP+ mpeg:mCherry+* cells. Total number of cells stated on graphs (n).

Macrophage *tnfa:GFP* expression brightness was also quantified (**Fig. 3.2.**). Despite the highest number of *tnfa:GFP+* macrophages being at 3 dpi, the fluorescence brightness of the GFP significantly increases at 2 dpi. GFP brightness then remains high at 3 dpi, before falling again at 4 dpi (**Fig. 3.2.**). This data indicates that, whilst the number of *tnfa:GFP+* macrophages is highest at 3 dpi, *tnfa* transcription rises at 2 dpi.

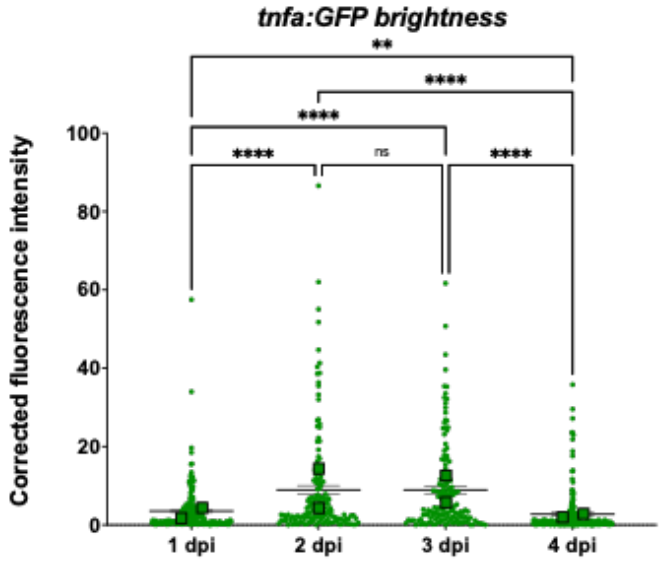


Figure 3.2. Macrophage *tnfa:GFP* brightness increases at 2 dpi, suggesting increased *tnfa* transcription. Corrected fluorescence intensity of individual *tnfa:GFP+* macrophages was calculated using ImageJ software at 1-4 dpi. Error bars depict SEM. Statistical significance was calculated using a one-way ANOVA with Bonferroni's multiple comparisons post hoc test. **P ≤ 0.01, ****P ≤ 0.0001.

Previous work using the smaller, promoter driven membrane-bound Tg(*tnfa:GFP-F)* transgenic line demonstrated that most, but not all, *tnfa:GFP+* cells were also *mpeg:mCherry+* following a tail fin transection (Nguyen-Chi et al., 2015). Thus, the number *mpeg:mCherry+* and *mpeg:mCherry-* cells (cells with immune cell-like morphology) that were also positive for TgBAC(*tnfa:GFP)* were quantified across all infection time-points (**Fig. 3.3.**). Most *tnfa:GFP+* cells were also *mpeg:mCherry+* (442 out of 525 macrophages). Yet 18.8% of *tnfa:GFP* positive cells with immune cell-like morphology were found to be

negative for *mpeg:mCherry* (**Fig. 3.3.**). It is plausible that these *tnfa:GFP+ mpeg:mCherry-* cells represent macrophages not labelled by the *mpeg:mCherry* reporter. Indeed, the *mpeg:mCherry* transgenic line does not label the entire macrophage population – an observation which is evidenced by discrepancies in transgene co-localisation between two macrophage-specific reporters driven by different promoters (*mpeg* and *mfap4*) (Walton et al., 2015).

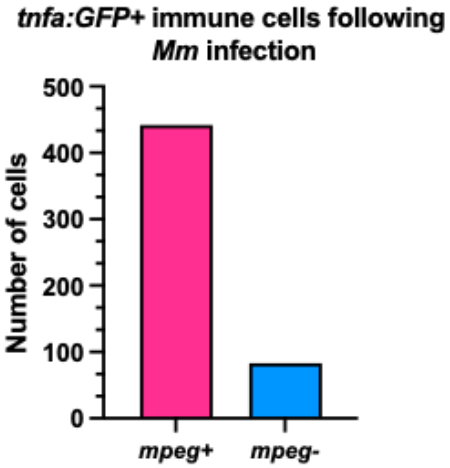


Figure 3.3. The majority of *tnfa:GFP+* cells are also *mpeg:mCherry+*. (**A**) Graph illustrating the number of *tnfa:GFP+* cells with immune cell morphology that were *mpeg:mCherry+* and *mpeg:mCherry-* across all infection time-points (1-4 dpi). N=2 independent experiments.

In zebrafish, the definitive wave of haematopoiesis begins at 2 dpf following the development of the caudal haematopoietic tissue (CHT) (Speirs et al., 2024). Therefore, to determine whether the rise in macrophage *tnfa* transcription (2 dpi) and number of *tnfa:GFP*+ macrophages (3 dpi) identified is due to the larvae being a developing system, macrophage expression of *tnfa* across different stages of development was assessed using Daniocell, a published single-cell gene expression resource (Sur et al., 2023). Expression of *tnfa* was negligible across all developmental stages up to 5 dpf in unchallenged larvae, with expression only slightly rising at 36-46 hpf (**Fig. 3.4. B**). UMAP of the haematopoietic system highlights very low expression of tnfa in macrophages (**Fig. 3.4. A**). This suggests that the increased number of *tnfa:GFP*+ macrophages and increased *tnfa* transcription is not due to the larvae being a developing system, but rather a true reflection of recruitment/polarisation of putative pro-inflammatory macrophages post *Mm* infection.

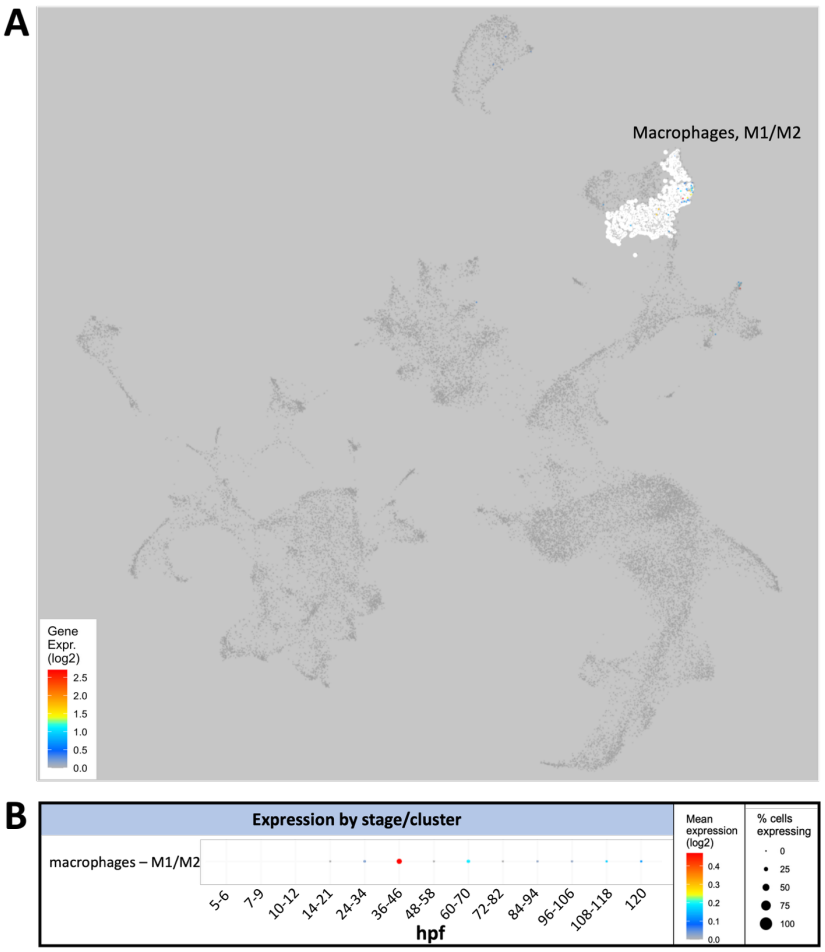


Figure 3.4. *tnfa* is not expressed highly in macrophages during development in unchallenged larvae. (**A**) UMAP of the larval haematopoietic system illustrating expression of *tnfa* in the macrophage cluster. (**B**) Expression of *tnfa* in macrophages across zebrafish development up to 5 dpf. Expression data was obtained from Daniocell (Sur et al., 2023). Abbreviations: hpf, hours post-fertilisation.

To determine if the increase in *tnfa:GFP* expression could be due to whether a macrophage has successfully phagocytosed *Mm*, the proportion of *tnfa:GFP+* and *tnfa:GFP-* macrophages with internalised *Mm* was quantified (**Fig. 3.5. A-B**). The proportion of macrophages with internalised *Mm* was similar whether they were *tnfa:GFP+* or *tnfa:GFP-* at 1, 3 and 4 dpi (**Fig. 3.5. C, E, F**). However, at 2dpi, there were significantly more *tnfa:GFP+* macrophages with internalised *Mm* when compared to proportion of *tnfa:GFP-* macrophages with internalised *Mm* (**Fig. 3.5. D**). This observation could account for the increased levels of *tnfa* transcription detected at 2 dpi (when quantifying macrophage GFP fluorescence), with higher levels of internalised *Mm* resulting in a stronger pro-inflammatory response.

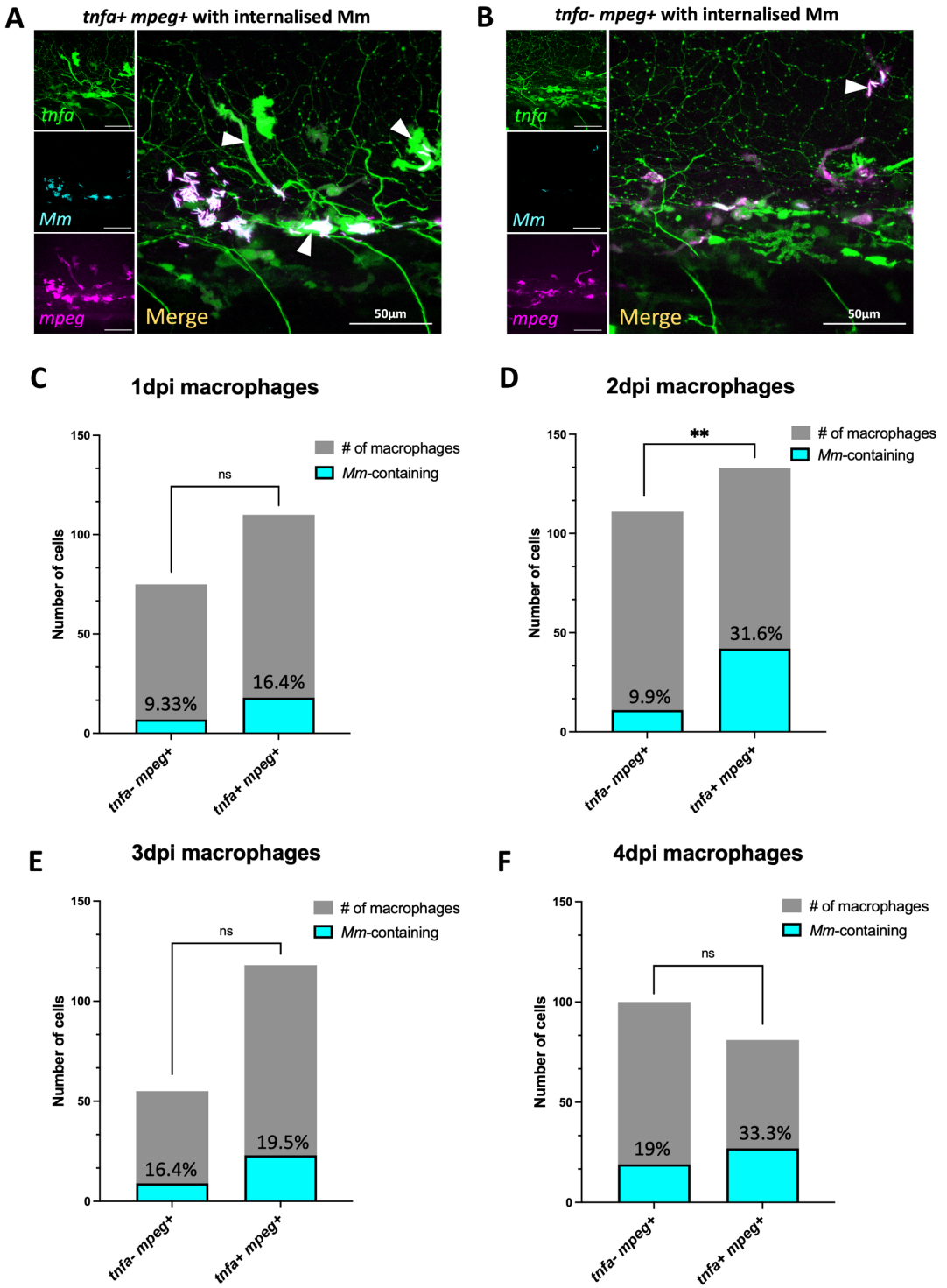


Figure 3.5. The proportion of *tnfa:GFP+* macrophages with internalised Mm is higher than *tnfa:GFP-* macrophages at 2 dpi. (**A**) Representative confocal image of *tnfa:GFP+ mpeg:mCherry+* cell with internalised *Mm*, indicated by filled arrowheads. (**B**) Representative confocal image of *tnfa:GFP- mpeg:mCherry+* cell with internalised *Mm*, indicated by filled arrowhead. (**C**) Graph illustrating that the proportion *of tnfa:GFP+ mpeg:mCherry+* and *tnfa:GFP- mpeg:mCherry+* cells with internalised *Mm* at 1 dpi is similar. (**D**) Graph illustrating that the proportion of *tnfa:GFP+ mpeg:mCherry+* cells with internalised *Mm* is significantly higher than *tnfa:GFP- mpeg:mCherry+* cells at 2 dpi. (**E**) Graph illustrating that the proportion of *tnfa:GFP+ mpeg:mCherry+* and *tnfa:GFP- mpeg:mCherry+* cells with internalised *Mm* is similar at 3 dpi. (**F**) Graph illustrating that at 4 dpi, the proportion of *tnfa:GFP+ mpeg:mCherry+* and *tnfa:GFP- mpeg:mCherry+* cells with internalised *Mm* is similar.

Counts from N=2 independent experiments. Scale bar stated on the image. Graph legends stated on the graphs. Statistical significance was calculated using a Fisher's exact test. **P ≤ 0.01.

Infection with heat killed (HK) *Mm* and *Mm* with a deleted RD1 virulence locus (ΔRD1 *Mm*) resulted in increased α-nitrotyrosine immunostaining in leukocytes, an indirect readout of nitric oxide production, and consequently an indirect readout of increased iNOS activity (Elks et al., 2013; Elks et al., 2014). The RD1 virulence locus encodes genes associated with the ESX-1 secretion system, thus ΔRD1 mutant *Mm* can replicate and grow within larval macrophages, but fails to escape the macrophage phagolysosome (Cosma et al., 2006; Solomon. et al., 2003). This suggests that the presence of *Mm*, not its pathogenicity, is sufficient to induce a pro-inflammatory response. However, the macrophage pro-inflammatory response to HK *Mm* and ΔRD1 *Mm* has not been examined using transgenic zebrafish reporter lines such as the *tnfa:GFP*.

Firstly, to confirm HK *Mm* used in this chapter's experiments was successfully killed, a 100 CFU injection dose of both live and HK *Mm* were plated and CFU counts performed (**Fig. 3.6.**). Following a week of incubation, live *Mm*-Crimson successfully grew on bacterial plates, with colonies visible both under bright field and fluorescent stereo microscope (**Fig. 3.6**. – top). Meanwhile, HK *Mm* failed to grow on bacterial plates, with no colonies visible under either brightfield or fluorescent stereo microscope (**Fig. 3.6**. – bottom).

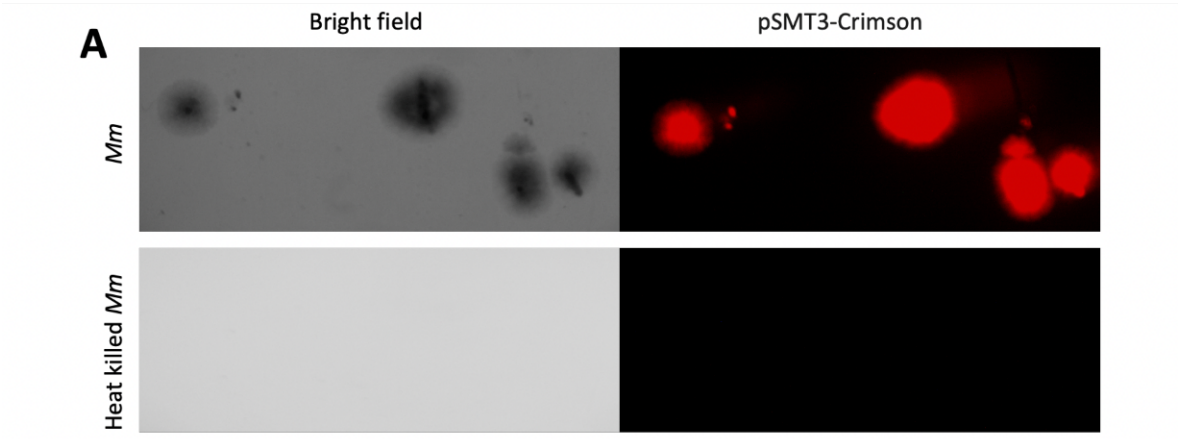


Figure 3.6. Heat killed *Mm* does not grow on 7H10 plates. (**A**) Injection dose of live *Mm*-Crimson and HK *Mm* were plated on 7H10 bacterial plates to perform CFU counts following a week of incubation. Top: Live *Mm*-Crimson successfully grows on 7H10 bacterial plates, visible under bright field and under fluorescent stereo microscope. Bottom: Heat killed *Mm* failed to grow on bacterial plates, with no colonies visible under bright field or fluorescent stereo microscope.

As the macrophage *tnfa:GFP* response is robust at early stages of infection, expression following infection with HK *Mm* and ΔRD1 *Mm* was examined at 1 dpi. Mock infection (PVP) resulted in negligible *tnfa:GFP* expression in macrophages within the imaged field of view (**Fig. 3.7. A**), with only

1.8% (out of 193 macrophages) being *tnfa:GFP*+ (**Fig. 3.7. E**). Measurement of *tnfa:GFP* fluorescence brightness also indicates that PVP does not induce macrophage *tnfa:GFP* expression (**Fig. 3.7. F**). As previously identified, approximately 60% of macrophages (128 out of 191) were *tnfa:GFP*+ following infection with live *Mm* (**Fig. 3.7. B, E**). Infection with HK *Mm* resulted in a similar proportion of *tnfa:GFP*+ macrophages (58.4% out of 191 macrophages) (**Fig. 3.7. C, E**). Meanwhile, infection with ΔRD1 *Mm* resulted in 36% of macrophages (out of 177) being *tnfa:GFP*+ (**Fig. 3.7. D, E**). Despite significantly more *tnfa:GFP*+ macrophages visually identified in HK *Mm* and ΔRD1 *Mm* groups compared to the PVP group, only live *Mm* induced the brightest GFP fluorescence brightness (**Fig. 3.7. F**). Both HK *Mm* and ΔRD1 *Mm* resulted in significantly elevated macrophage GFP brightness compared to PVP, with HK *Mm* producing the higher GFP signal of the two groups. These data confirm that the presence of *Mm* is enough to induce *tnfa:GFP* expression in putative pro-inflammatory macrophages.

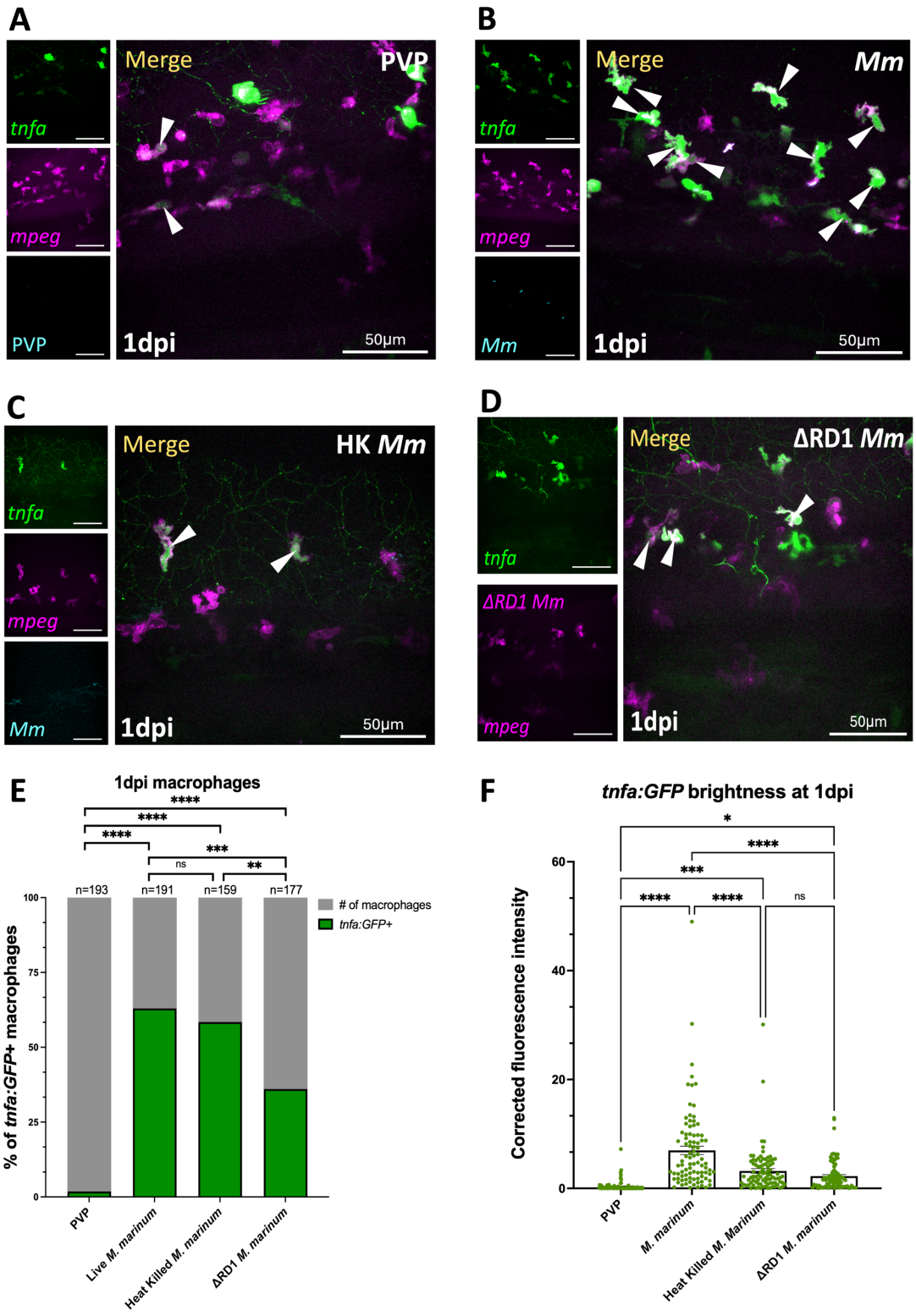


Figure 3.7. The presence of *Mm* is sufficient to induce macrophage *tnfa:GFP* expression at 1 dpi. (**A-D**) Representative confocal image of 1 dpi *tnfa:GFP* crossed to *mpeg:mCherry* infected with (**A**) PVP, (**B**) live *Mm*, (**C**) HK *Mm* or (**D**) ΔRD1 *Mm*. (**E**) Graph illustrating the percentage of *tnfa:GFP+* macrophages at 1 dpi. (**F**) Corrected fluorescence intensity of *mpeg:mCherry+* macrophages in the GFP channel to assess *tnfa:GFP* fluorescence brightness. N=3 independent experiments, with 5 larvae per group imaged per experiment. All counts were taken from a 40x field of view near the caudal vein (site of infection) or around clusters of bacteria within the fish. Up to 6 macrophages were measured for fluorescence intensity. Error bars depict SEM. Statistical significance in (**E**) was calculated using a Chi squared test, followed by Fisher's exact test to determine where significant differences are.

Statistical significance in (**F**) was calculated using a one-way ANOVA with Bonferroni's multiple comparisons post hoc test. *P ≤ 0.05, ***P ≤ 0.001, ****P ≤ 0.0001. Scale bars are stated on the images.

To confirm that the lower macrophage *tnfa:GFP* brightness seen in the HK *Mm* and ΔRD1 *Mm* group is not due macrophages failing to phagocytose the bacteria, the proportion of *tnfa:GFP-* and *tnfa:GFP+* macrophages with internalised *Mm* was quantified.

The proportion of macrophages that had internalised live *Mm* was slightly higher in *tnfa:GFP+* macrophages (44.5% out of 128) compared to *tnfa:GFP-* macrophages (27% of out 63) (**Fig. 3.8. A, D**). When infected with HK *Mm* (**Fig. 3.8. B**) or ΔRD1 *Mm* (**Fig. 3.8. C**), the proportion of macrophages with internalised *Mm* was similar whether *tnfa:GFP-* or *tnfa:GFP+* (**Fig. 3.8. D**). These observations illustrate that the reduced macrophage *tnfa:GFP* brightness is not due to macrophages failing to phagocytose the bacteria, but rather the reduced need for a pro-inflammatory response.

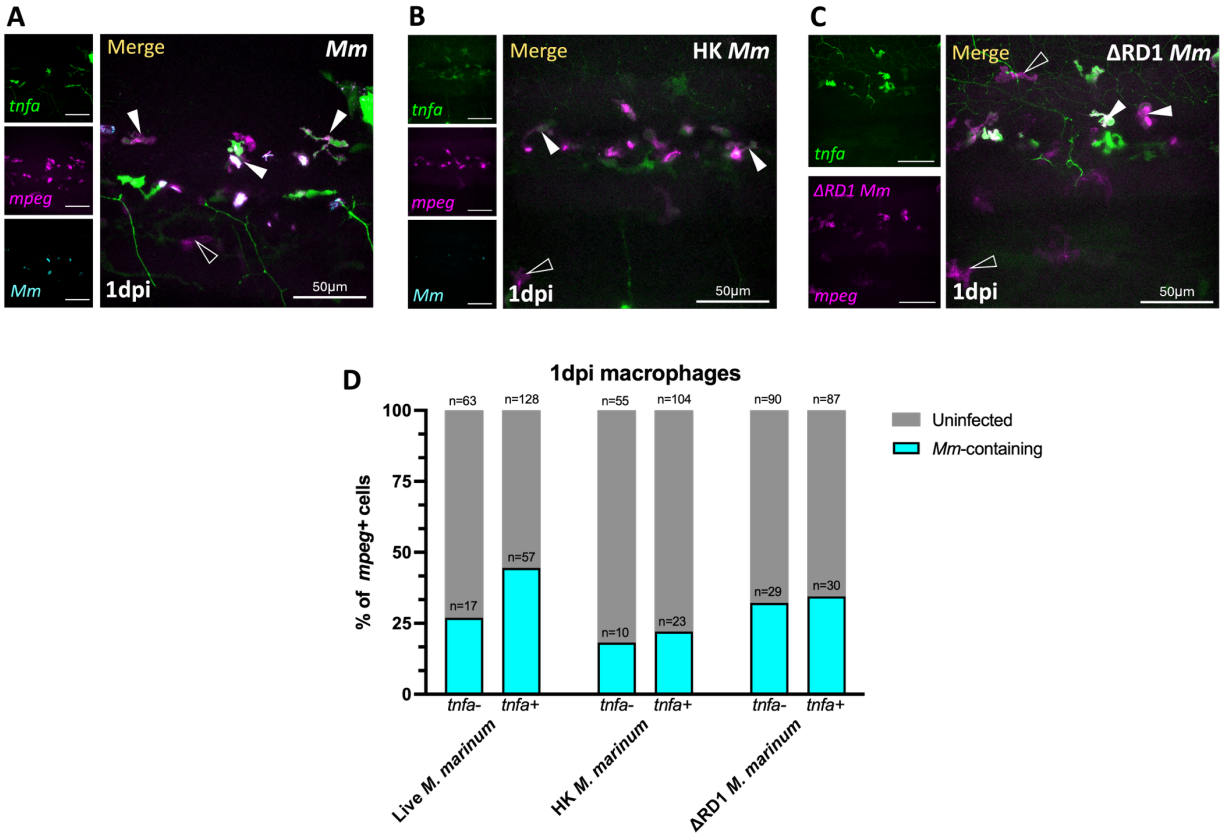


Figure 3.8. The proportion of *tnfa:GFP-* and *tnfa:GFP+* macrophages with internalised *Mm* is similar whether alive, heat-killed or avirulent at 1 dpi. (**A**) Representative confocal image of *tnfa:GFP+* macrophage (filled arrowhead) and *tnfa:GFP-* macrophage (hollow arrowhead) with internalised live *Mm*. (**B**) Representative confocal image of *tnfa:GFP+* macrophage (filled arrowhead) and *tnfa:GFP-* macrophage (hollow arrowhead) with internalised HK *Mm*. (**C**) Representative confocal image of *tnfa:GFP+* macrophage (filled arrowhead) and *tnfa:GFP-* macrophage (hollow arrowhead) with internalised ΔRD1 *Mm*. (**D**) Graph illustrating that the proportion of *tnfa:GFP-* and *tnfa:GFP+* macrophages with internalised *Mm* at 1 dpi is similar for live, HK and ΔRD1 *Mm*. N=3 independent experiments, with 5 larvae per group imaged per experiment. Scale bar stated on the image. Graph legend stated on the graph.

To conclude, a proportion of macrophages robustly upregulate *tnfa:GFP* expression following *Mm* infection, rising significantly from 2 dpi before falling again at 4 dpi. Furthermore, whilst live *Mm* elicits the strongest response, infection with HK *Mm* and ΔRD1 *Mm* emphasises that the presence of *Mm* is sufficient to induce a pro-inflammatory response. This data presents the first thorough characterisation of these putative pro-inflammatory macrophages during early *Mm* infection using a transgenic reporter line.

3.2.2. Macrophage *arg2:GFP* expression rises when granulomas begin to form at 3 dpi

Our group previously characterised macrophage *arginase 2* expression at 1 dpi and 4 dpi (Hammond et al., 2023). Therefore, I aimed to characterise macrophage *arg2:GFP* expression throughout infection pathogenesis (1-4 dpi) and validate the group's previous findings using confocal microscopy. *mpeg:mCherry+ arg2:GFP+* embryos were systemically infected via the caudal vein with 100 CFU of a fluorescent *Mm* strain at 1 dpf. Using confocal microscopy, infected larvae were imaged at 1-4 dpi in the region of the caudal vein or around clusters of bacteria within the fish, checking for *arg2:GFP* ionocyte expression pattern over the yolk to screen for GFP+ larvae as previously described (Hammond et al., 2023).

At 1 dpi, there was a small population (8% of n=125) of macrophages that were *arg2:GFP* positive (**Fig. 3.9. Ai, Aiii**). The majority of *mpeg:mCherry+* cells at this time-point were *arg2:GFP* negative, with only 8/20 larvae possessing *arg2:GFP+ mpeg:mCherry+* cells, of which most fish (7/8 larvae) only had 1 example of an *arg2:GFP+* macrophage (**Fig. 3.9. Aii**). Macrophage *arg2:GFP* expression appears to fall at 2 dpi, with only 4/26 fish showing a single example of an *arg2:GFP+ mpeg:mCherry+* (**Fig. 3.9. Bii**), amounting to only 2.77% (of n=144 macrophages) of double positive cells (**Fig. 3.9. Bi, Bii**). Interestingly, at 3 dpi the proportion of *arg2:GFP+ mpeg:mCherry+* cells rises substantially at 3 dpi, corresponding to a pre-granuloma stage of infection (**Fig. 3.9. Cii, Ciii**). At this time-point, 17/31 larvae had examples of *arg2:GFP+ mpeg:mCherry+* cells, with some larvae (fish 2, 5, 26, 28) only having examples of double positive cells (**Fig. 3.9. Cii**). At 3 dpi, 25.8% (of n=124 macrophages) were *mpeg:mCherry+ arg2:GFP+*, corresponding to over a 9-fold increase in the proportion of this population compared to 2 dpi. At 4 dpi, the proportion of *arg2:GFP+* macrophages falls again, with only 3.6% (of n=196 macrophages) *mpeg:mCherry+* cells also being positive for *arg2:GFP* (**Fig. 3.9. Di, Diii**). Only 7/29 larvae had an example of an *arg2:GFP+* macrophage, each of which only had a single double positive cell (**Fig. 3.9. Dii**). Together, these results identify an interesting time-point (3 dpi) in which the numbers of macrophages expressing *arg2:GFP* is highest, before it falls again at 4 dpi.

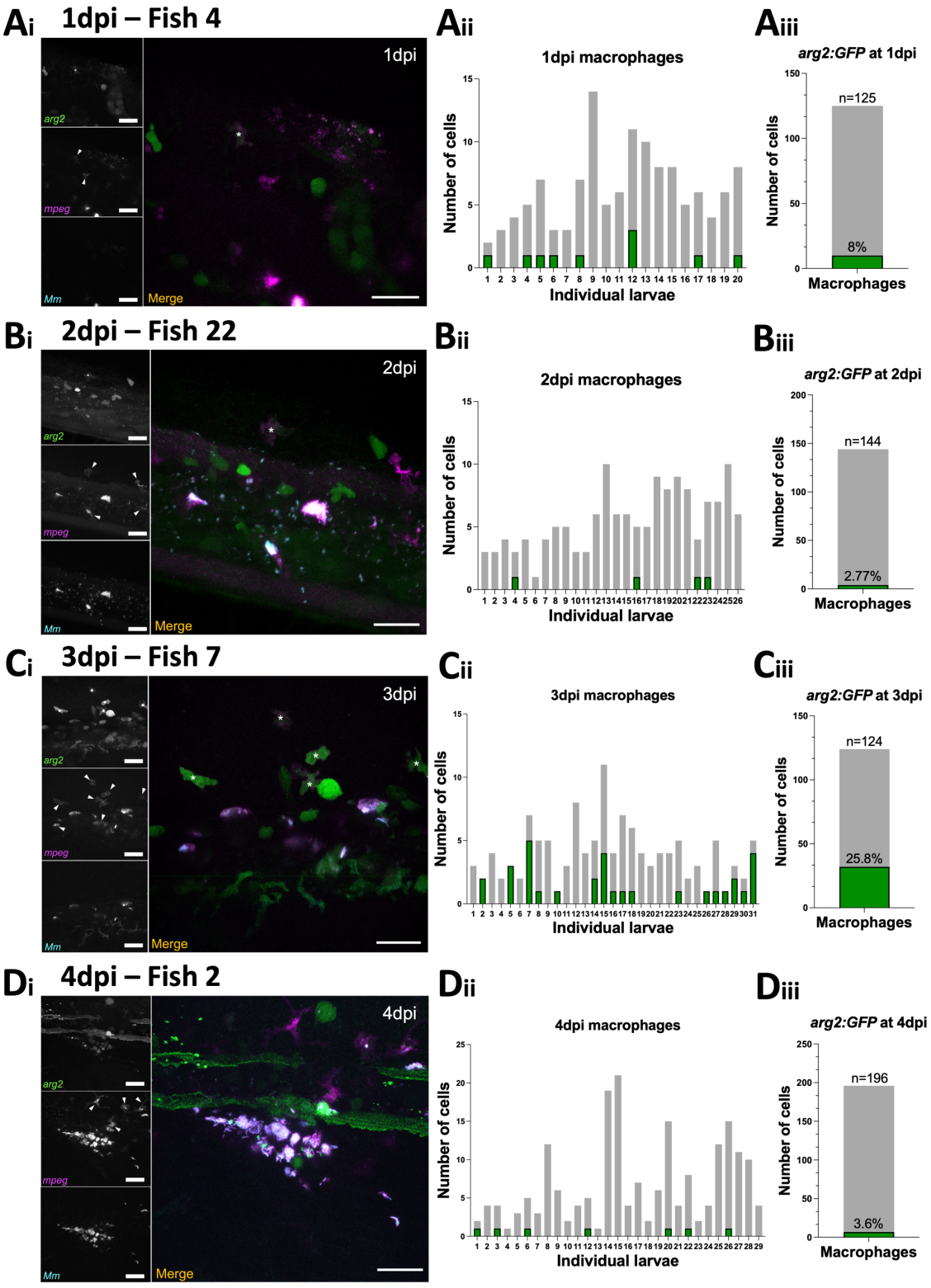


Figure 3.9. The number of macrophages expressing *arg2:GFP* is highest at 3 dpi. (Ai) Representative confocal image of 1 dpi *arg2:GFP* crossed to *mpeg:mCherry*. **(Aii)** Graph illustrating the number of *arg2:GFP*+ and *arg2:GFP*- macrophages counted for each individual larvae at 1 dpi. **(Aiii)** Graph illustrating the percentage of *arg2:GFP*+ and *arg2:GFP*- macrophages at 1 dpi. Combined with data (N=3 experiments) from Dr Ffion Hammond (former PhD student in the Elks group), counts from N=4 independent experiments. **(Bi)** Representative confocal image of 2 dpi *arg2:GFP*+ *mpeg:mCherry*+ larvae. **(Bii)** Graph illustrating the number of *arg2:GFP*+ and *arg2:GFP*- macrophages counted for each individual larvae at 2 dpi. **(Biii)** Graph illustrating the percentage of *arg2:GFP*+ and *arg2:GFP*- macrophages at 2 dpi. Counts from N=3 independent experiments. **(Ci)** Representative confocal image of 3 dpi *arg2:GFP*+ *mpeg:mCherry*+ larvae. **(Cii)** Graph illustrating the number of *arg2:GFP*+ and *arg2:GFP*-

macrophages counted for each individual larvae at 3 dpi. (**Ciii)** Graph illustrating the percentage of *arg2:GFP*+ and *arg2:GFP*- macrophages at 3 dpi. Counts from N=3 independent experiments. (**Di)** Representative confocal image of 4 dpi *arg2:GFP*+ *mpeg:mCherry*+ larvae. (**Dii)** Graph illustrating the number of *arg2:GFP*+ and *arg2:GFP*- macrophages counted for each individual larvae at 4 dpi. (**Diii)** Graph illustrating the percentage of *arg2:GFP*+ and *arg2:GFP*- macrophages at 4 dpi. Combined with data (N=3 experiments) from Dr Ffion Hammond, counts from N=5 independent experiments. All counts were taken from a 40x field of view near the caudal vein (site of infection) or around clusters of bacteria within the fish. White asterisks indicate *arg2:GFP*+ *mpeg:mCherry*+ cells. Arrowheads indicate *mpeg:mCherry*+ cells. Total number of cells stated on graphs (n). Scale bar = 30 μm.

A previous study found that the *mpeg1* promoter is downregulated by *Mm* at 4 dpi (Benard et al., 2015). Therefore, the fluorescence brightness of *mpeg:mCherry* was determined to control for possible *mpeg* downregulation over time (**Fig. 3.10. A**) (Hammond et al., 2023). The fluorescence intensity of *mpeg:mCherry*+ macrophages was overall not affected through the infection time-course, with no significant differences found at 4 dpi, the time-point whereby we would expect to see *Mm*-mediated downregulation of *mpeg* (**Fig. 3.10. A**). Whilst there is a significant decrease in *mpeg:mCherry* fluorescence intensity between 2 and 3 dpi, this is likely due to brighter reporter expression in the larvae used from a clutch of eggs for one of the 2 dpi experimental repeats (**Fig. 3.10. A** – blue dots). Thus, this data shows that the *mpeg:mCherry* line is suitable for examining *Mm*-macrophage interactions.

Macrophage *arg2* expression brightness in the GFP channel was also assessed (**Fig. 3.10. B**). Interestingly, there was a significant increase in fluorescence brightness between 1 dpi and 3 dpi, corresponding to the increased number of *arg2:GFP*+ macrophages identified at 3 dpi (**Fig. 3.10. B**). This data indicates, that in addition to there being more *arg2:GFP+* macrophages at 3 dpi, there are also increased levels of *arginase 2* transcription at this time-point.

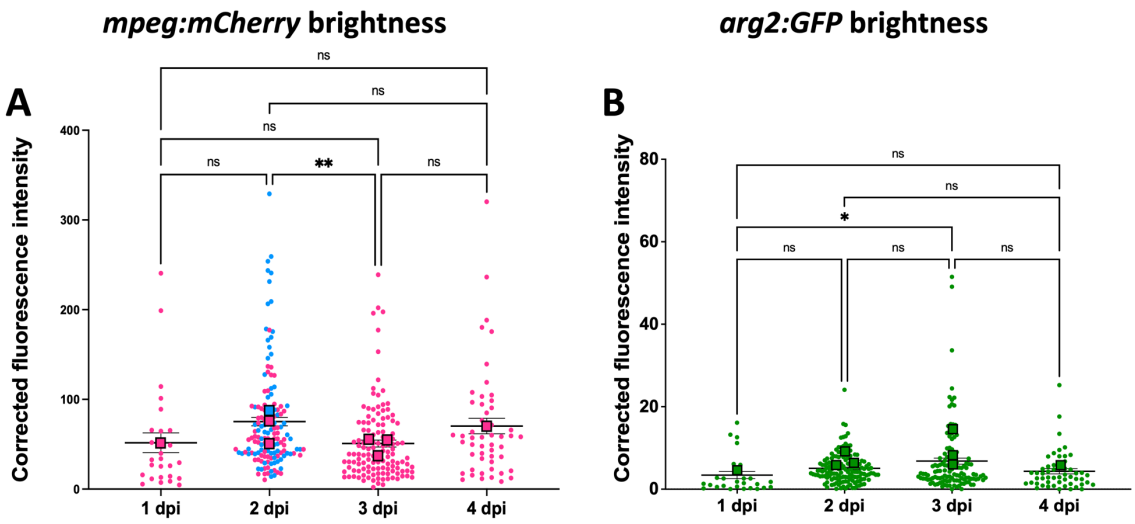


Figure 3.10. Macrophage *arg2:GFP* fluorescence brightness increases at 3 dpi before falling again, whilst *mpeg:mCherry* brightness remains largely unaffected. (**A**) Corrected fluorescence intensity of *mpeg:mCherry*+ cells was calculated using ImageJ software at 1-4 dpi. Blue dots at 2 dpi indicate experimental repeat that resulted in the brightest mCherry expression, likely due to brighter reporter expression in that clutch of eggs. (**B**) Corrected fluorescence intensity of *mpeg:mCherry*+ macrophages was also quantified in the GFP channel to assess *arg2:GFP* fluorescence brightness. Data for 1 and 4 dpi is from N=1 independent experiment each. Data for 2 and 3 dpi was accumulated from N=3 independent experiments. Error bars depict SEM. Statistical significance was calculated using a one-way ANOVA with Bonferroni's multiple comparisons post hoc test. *P ≤ 0.05 , **P ≤ 0.01.

Macrophage shape has been associated with its polarisation status *in vitro*, with different stimuli resulting in different phenotypic appearances (McWhorter et al., 2013; Hourani et al., 2023). In a larval zebrafish model of inflammation, changes in macrophage shape during wound healing (including area, perimeter and circularity) were found to correlate with previous data showing a shift in macrophages from a pro-inflammatory (*tnfa, il1b*) to an anti-inflammatory (*tgfb1, ccr2*) genetic profile (Nguyen-Chi et al., 2015; Sipka et al., 2022). Thus, the same morphometric parameters were used to compare *arg2:GFP*- and *arg2:GFP*+ macrophages.

Analysis of area, perimeter and circularity index of 261 *arg2:GFP- mpeg:mCherry+* and 42 *arg2:GFP+ mpeg:mCherry+* cells found no significant differences in any of the three morphometric descriptors (**Fig. 3.11**). For all descriptors, the mean measurement across all analysed cells was very similar between *arg2:GFP*- and *arg2:GFP*+ macrophages. However, compared to *arg2:GFP*+ macrophages, snapshot confocal images of *arg2:GFP*- macrophages had slightly smaller average area (189.8 μm^2 vs. 184.1 μm^2; **Fig. 3.11. A**) and perimeter (88.3 μm vs. 86.6 μm; **Fig. 3.11. B**), and a slightly higher circularity index (0.37 CI vs. 0.39 CI; **Fig. 3.11. C**).

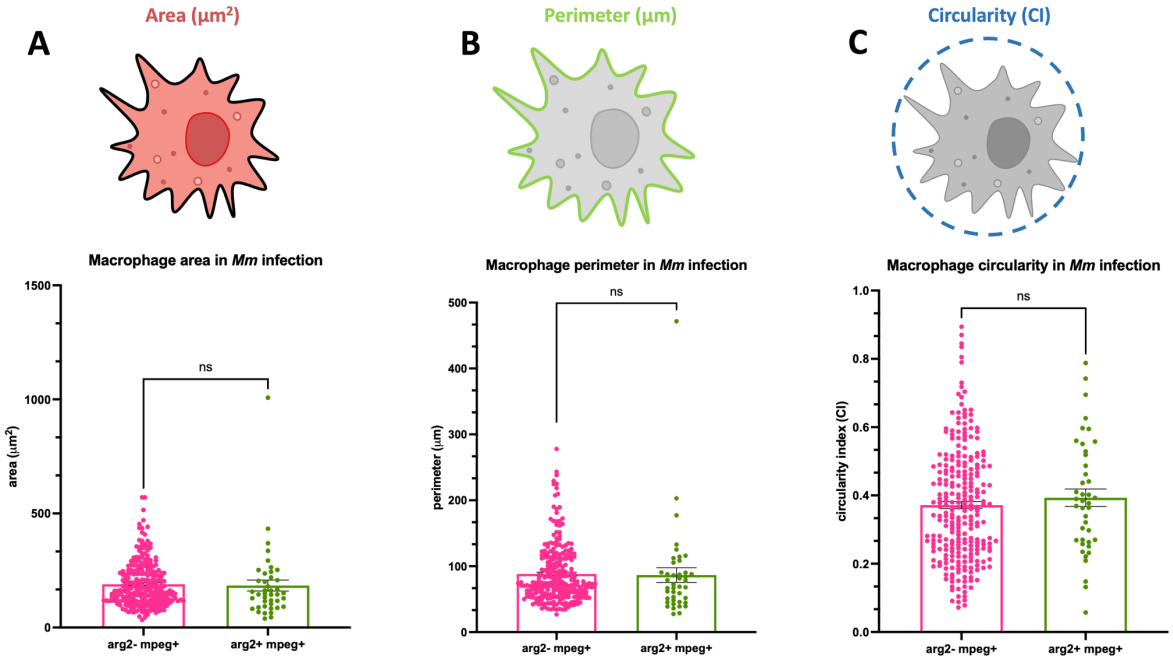


Figure 3.11. Morphological differences between *arg2:GFP*- and *arg2:GFP*+ macrophage are not identified in confocal images at fixed timepoints. (**A-C**) Up: Representation of morphometric descriptors (area, perimeter, circularity index) determined in ImageJ to analyse macrophage shape. Down: Graphs illustrating that the area (**A**), perimeter (**B**) and circularity index (**C**) between *arg2:GFP*- and *arg2:GFP*+ macrophages are similar. Data obtained from 1-4 dpi infection experiments. A total of 261 *arg2:GFP*- and 42 *arg2:GFP*+ macrophages were analysed. Error bars depict SEM. Statistical significance was calculated using an unpaired t-test.

Dr Ffion Hammond (previous PhD student in the Elks lab) found that at 4 dpi, neutrophils can upregulate *arg2:GFP* expression when they have internalised *Mm* (Hammond, 2022). Therefore, the proportion of *arg2:GFP+* and *arg2:GFP*- macrophages with internalised *Mm* was quantified (**Fig. 3.12. A-B**). Whilst the proportion of macrophages with internalised *Mm* was similar whether they were *arg2:GFP+* or *arg2:GFP*- at 1, 2 and 4 dpi (**Fig. 3.12. C, D, F**), there were significantly fewer *arg2:GFP+* macrophages with internalised *Mm* at 3 dpi when compared to the proportion of *arg2:GFP*- macrophages with internalised *Mm* (**Fig. 3.12. E**). This observation could be due to the low number of double positive cells observed at the other time-points, skewing the infected:uninfected ratio for 3 dpi. However, this data could also suggest that *arg2:GFP+* macrophages are either failing to phagocytose *Mm* or they are better at killing the bacteria compared to their *arg2:GFP*- counterparts.

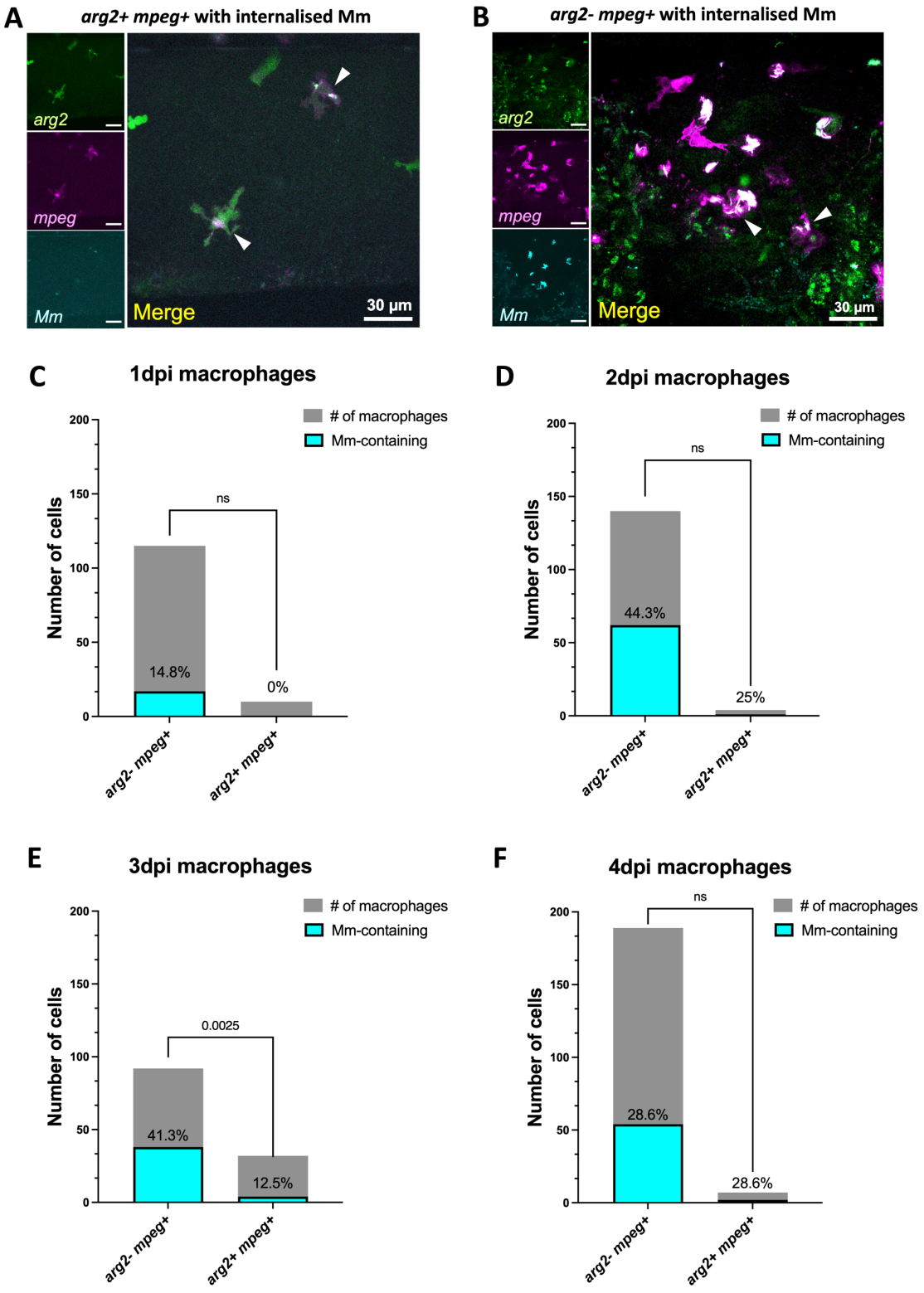


Figure 3.12. The proportion of *arg2:GFP+* macrophages with internalised *Mm* is significantly lower at 3 dpi compared to *arg2:GFP-* macrophages. (**A**) Representative confocal image of *arg2:GFP+ mpeg:mCherry+* cell with internalised *Mm*, indicated by filled arrowheads. (**B**) Representative confocal image of *arg2:GFP- mpeg:mCherry+* cell with internalised *Mm*, indicated by filled arrowheads. (**C**) Graph illustrating that the proportion of *arg2:GFP+ mpeg:mCherry+* and *arg2:GFP- mpeg:mCherry+* cells with internalised *Mm* at 1 dpi is similar. Combined with data from Dr Ffion Hammond, counts from N=4 independent experiments. (**D**) Graph illustrating that the proportion of *arg2:GFP+ mpeg:mCherry+* and *arg2:GFP- mpeg:mCherry+* cells with internalised *Mm* is similar at 2 dpi. Counts from N=3 independent experiments. (**E**) Graph illustrating that the proportion of *arg2:GFP+ mpeg:mCherry+* with

internalised *Mm* is significantly lower than *arg2:GFP- mpeg:mCherry+* cells with internalised *Mm* at 3 dpi. Counts from N=3 independent experiments. (**F**) Graph illustrating that at 4 dpi, the proportion of *arg2:GFP+ mpeg:mCherry+* and *arg2:GFP- mpeg:mCherry+* cells with internalised *Mm* is similar. Combined with data from Dr Ffion Hammon, counts from N=5 independent experiments. Scale bar stated on the image. Graph legends stated on the graphs. Statistical significance was calculated using a Fisher's exact test. Statistically significant P value is stated on the graph.

To conclude, macrophages upregulate *arg2:GFP* expression at 3 dpi, a point at which early granulomas are beginning to form (Davis and Ramakrishnan, 2009; Cronan et al., 2016). Quantification of macrophage morphology and infection status (on an individual macrophage level) from snapshot confocal images did not elucidate whether *arg2:GFP+* macrophages phenotypically resemble an anti-inflammatory macrophage population. By identifying that the highest proportion of *arg2:GFP+* macrophages are found at 3 dpi, it provides a time-point in which to focus future experiments on in order to decipher the phenotype of these cells.

3.2.3. Developing a more stable macrophage reporter for *Mm* studies

Analysis of the fluorescence intensity of *mpeg:mCherry* determined that *Mm*-mediated *mpeg* downregulation did not overall affect reporter brightness over the course of 1-4 dpi in our hands (**Fig. 3.10. A**). However, *mpeg* is a weak promoter and a strong significant *Mm*-mediated reduction in fluorescence has been reported at 5 dpi, whilst fluorescence of an *mfap4* reporter (an alternative macrophage reporter), remained stable (Walton et al., 2015). Though this PhD project only relies on under 5 dpf larvae (up to 4 dpi), the availability of an *mfap4* transgenic reporter at the University of Sheffield would be a useful tool for other researchers using juvenile/adult zebrafish. Thus, I chose to generate a *Tg(mfap4:mCherry-F)* (hereon in termed *mfap4:mCherry*) transgenic report line, where farnesylated mCherry is strongly expressed in macrophages (Phan et al., 2018; Nguyen-Chi et al., 2020).

Following injection of the *mfap4:mCherry* plasmid (**Fig. 3.13. A**; plasmid gifted from Nguyen-Chi group, Université de Montpellier), F0 injected larvae were screened at 2 dpf around the CHT for bright and specific mCherry expression of cells with macrophage morphology. (**Fig. 3.13. B**).

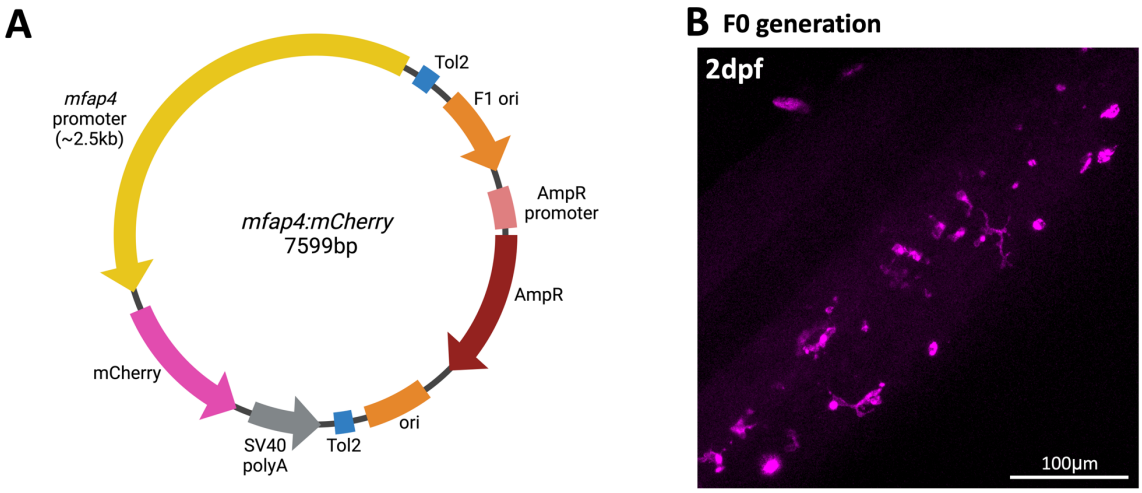


Figure 3.13. Generating an *mfap4:mCherry* transgenic reporter line. (**A**) Plasmid map of *mfap4:mCherry*, including the promoter region, farnesylated mCherry, tol2 sites and antibiotic resistance. Created using BioRender.com (publication licence agreement number SE271K8TC9). (**B**) Representative confocal image (20x magnification) of mCherry+ cells with macrophage morphology at the CHT in 2 dpf larvae. Scale bar is stated on the image.

To generate a stable transgenic line, the F0 generation was outcrossed with a wildtype zebrafish (nacre) line and the F1 offspring screened for bright mCherry expression in cells that had macrophage morphology in haematopoietic tissues (**Fig. 3.14. A** – top right; CHT) and central nervous tissues (**Fig. 3.14. A** – bottom right; microglia). Several founders were identified, but two were carried forward for subsequent generations due to bright mCherry expression. Positive F1 embryos were raised to adulthood and outcrossed again with a wildtype nacre line. mCherry is brightly and specifically expressed in the CHT of F2 progeny, which can be easily screened under a stereo fluorescent microscope (**Fig. 3.14. B**). F2 larvae were raised to adulthood to be used as a stable transgenic line.

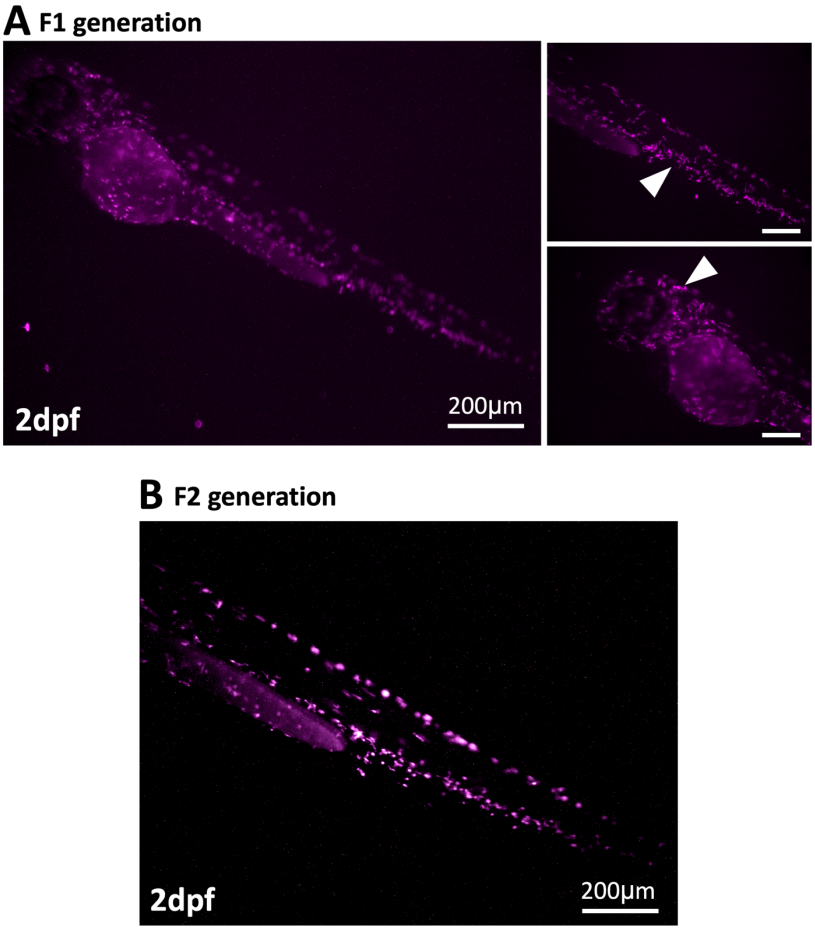


Figure 3.14. The *mfap4:mCherry* transgenic line shows bright *mCherry* expression of cells with macrophage morphology in the CHT and brain. (**A**) Representative stereo fluorescence image of F1 generation *mfap4:mCherry*. Bright mCherry expression in cells with a macrophage morphology in the CHT (top right) and the brain (microglia; bottom right). (**B**) Representative stereo fluorescence image of F2 progeny of *mCherry+* macrophages in the CHT. Scale bars are stated on the images.

As the *mfap4:mCherry* reporter is easier to screen for and the promoter is not attenuated by *Mm* (Walton et al., 2015), I chose to primarily use this transgenic line for subsequent experiments. Thus, I aimed to confirm whether the proportions of *arg2:GFP+ mfap4:mCherry* macrophages were similar to that observed in *mpeg:mCherry* macrophages at 3 dpi and 4 dpi.

At 3 dpi, 36.6% (of n=186 macrophages) were *mfap4:mCherry+ arg2:GFP+* (**Fig. 3.15. Ai, Aiii**). At this time-point, 19/21 larvae had examples of double positive cells, with 14 of these fish having more than 2 examples of *arg2:GFP*+ macrophages and one larvae (fish 7) only having examples of double positive cells (**Fig. 3.15. Aii**). As with the *mpeg:mCherry* reporter, the proportion of *arg2:GFP+* macrophages falls again at 4 dpi, with 16.5% (of n=212 macrophages) *mfap4:mCherry+* cells also being *arg2:GFP+* (**Fig. 3.15. Bi, Biii**). Fewer than half of larvae had an example of *arg2:GFP+* macrophages (10/21 larvae), of which 5 fish had more than 2 examples of *arg2:GFP+* macrophages and a couple of larvae (fish 4, 18) only showing a single example of a double positive cell (**Fig. 3.15. Bii**).

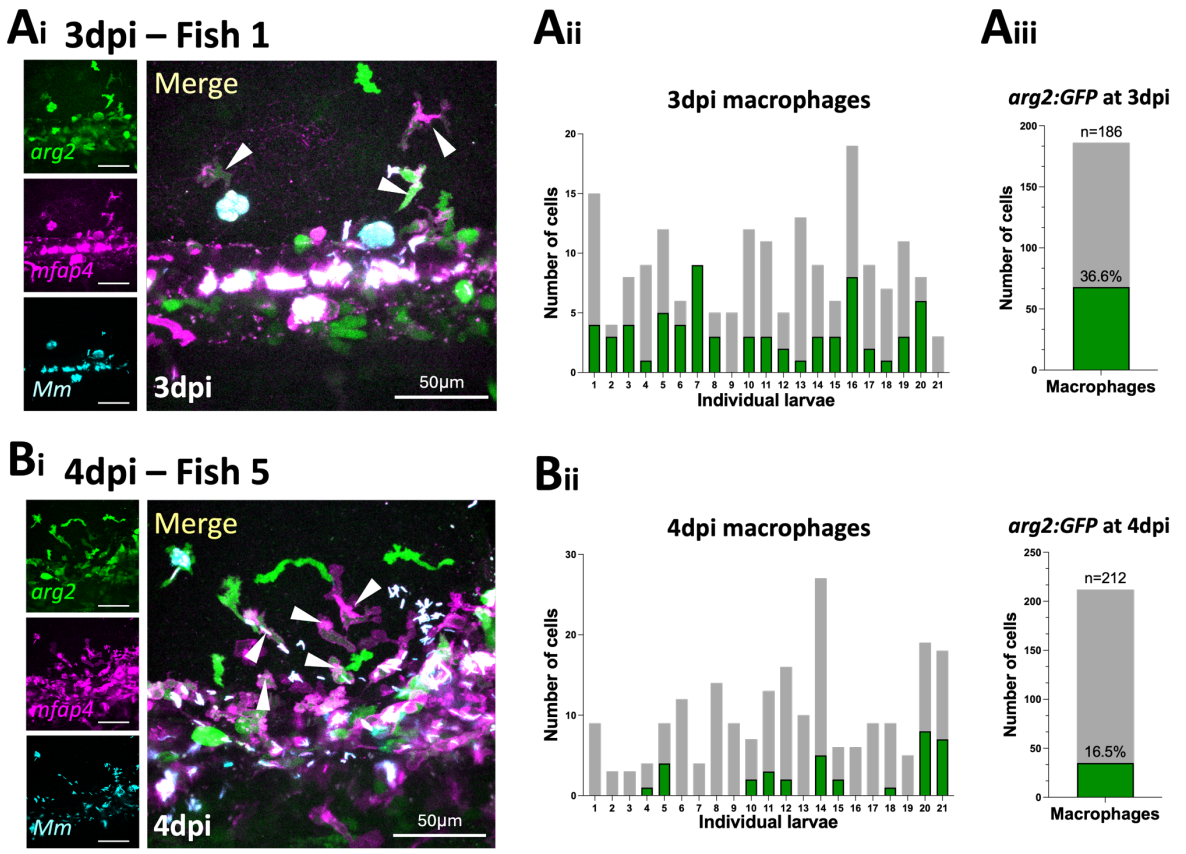


Figure 3.15. *mfap4:mCherry+* macrophages upregulate *arg2:GFP* expression at 3 dpi and 4 dpi. (**Ai**) Representative confocal image of 3 dpi *arg2:GFP* crossed to *mfap4:mCherry*. (**Aii**) Graph illustrating the number of *arg2:GFP+* and *arg2:GFP- mfap4:mCherry* macrophages counted for each individual larvae at 3 dpi. (**Aiii**) Graph illustrating the percentage of *arg2:GFP+* and *arg2:GFP- mfap4:mCherry* macrophages at 3 dpi. Counts from N=3 independent experiments. (**Bi**) Representative confocal image of 4 dpi *arg2:GFP* crossed to *mfap4:mCherry*. (**Bii**) Graph illustrating the number of *arg2:GFP+* and *arg2:GFP- mfap4:mCherry* macrophages counted for each individual larvae at 4 dpi. (**Biii**) Graph illustrating the percentage of *arg2:GFP+* and *arg2:GFP- mfap4:mCherry* macrophages at 4 dpi. Counts from N=3 independent experiments. All counts were taken from a 40x field of view near the caudal vein (site of infection) or around clusters of bacteria within the fish. Filled white arrowheads indicate *arg2:GFP+ mfap4:mCherry+* cells. Total number of cells stated on graphs (n). Overexposed cells are not of interest, as they are cells that express GFP more strongly (e.g. neutrophils and ionocytes). Scale bars are stated on the images.

As the proportion of *arg2:GFP*-positive *mfap4:mCherry* macrophages was higher to that observed using the *mpeg:mCherry* transgenic line, it was hypothesised that the *mfap4:mCherry* reporter may be brighter compared to *mpeg:mCherry* larvae, resulting in easier visualisation of *arg2:GFP+* macrophages. Thus, the fluorescence brightness of *mpeg:mCherry* and *mfap4:mCherry* was assessed without infection at 3 dpf using the same confocal microscope settings (**Fig. 3.16. A-C)**. There were no significant differences found between the mCherry fluorescence intensity of the *mpeg* and *mfap4* reporters without infection challenge (**Fig. 3.16. C**). Fluorescence brightness of the reporters was

not assessed following *Mm* infection due to the difficulty in accurately comparing measurements as *Mm* is autofluorescent, resulting in bleed-through in the mCherry channel.

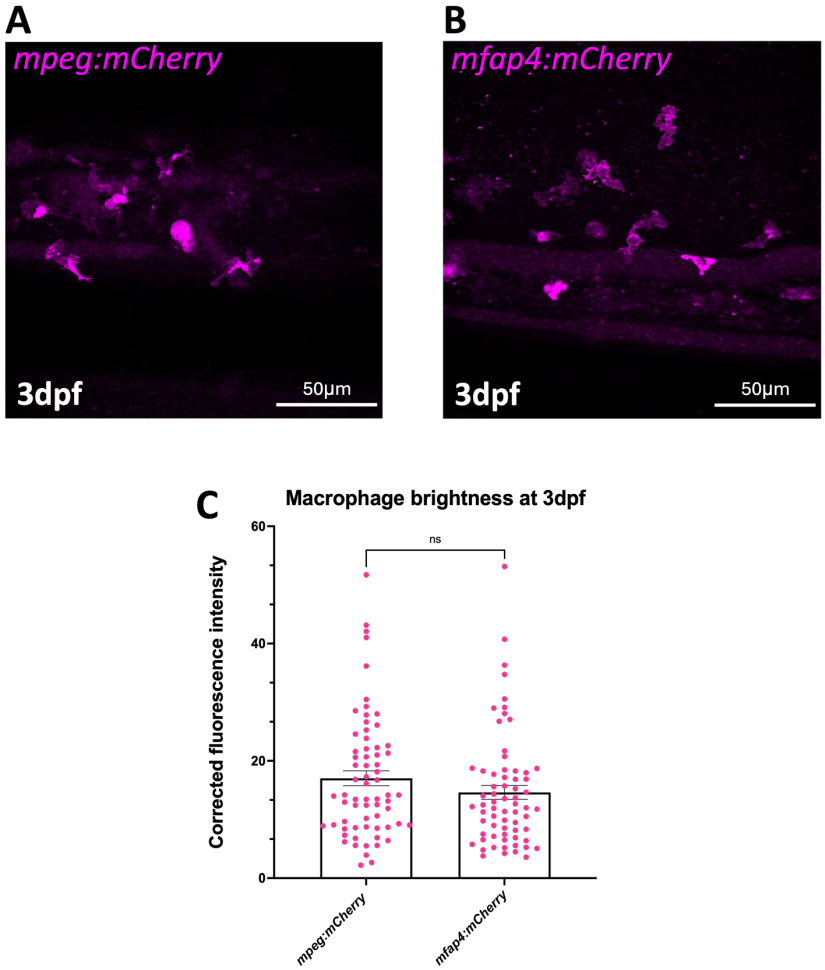


Figure 3.16. *mpeg:mCherry* and *mfap4:mCherry* fluorescence intensity is similar without *Mm* infection challenge using the same microscope settings. (**A**) Representative confocal image of 3 dpf *mpeg:mCherry* larvae. (**B**) Representative confocal image of 3 dpf *mfap4:mCherry* larvae. (**C**) Corrected fluorescence intensity of *mpeg:mCherry+* and *mfap4:mCherry+* macrophages was quantified using ImageJ software at 3 dpf. Data for *mpeg:mCherry* is from N=1 independent experiment (13 larvae). Data for *mfap4:mCherry* is from N=2 independent experiments (14 larvae in total). Up to 6 of the brightest macrophages were measured. Error bars depict SEM. Statistical significance was calculated using an unpaired t-test.

3.2.4. *arg2:GFP* expressing macrophages are less branched, more circular and faster

In vitro and *in vivo* vertebrate data suggests that macrophages exhibit dynamic responses following infection, with M1- and M2-like markers/cytokine profiles fluctuating over the course of infection (Leiba et al., 2023; Sun et al., 2022; Renson et al., 2017).Therefore, I aimed to examine morphology and behaviour of *arg2:GFP* expressing *mfap4:mCherry+* macrophages over time. Using spinning disk confocal microscopy, a 10-hour overnight timelapse was set up using 3 dpi larvae in order to capture the highest number of *arg2:GFP+* macrophages.

Over the course of the timelapse experiments, *arg2:GFP*+ macrophages were successfully captured (**Fig. 3.17.**). In order to quantify phenotypic differences, *arg2:GFP*+ macrophages (**Fig. 3.17. C** – green box) were compared to their nearest *arg2:GFP*- neighbour over the course of a 1-hour window (**Fig. 3.17. B** – pink box). The nearest neighbour was chosen to account for the closest microenvironment match, enabling paired comparisons (Ellett et al., 2015).

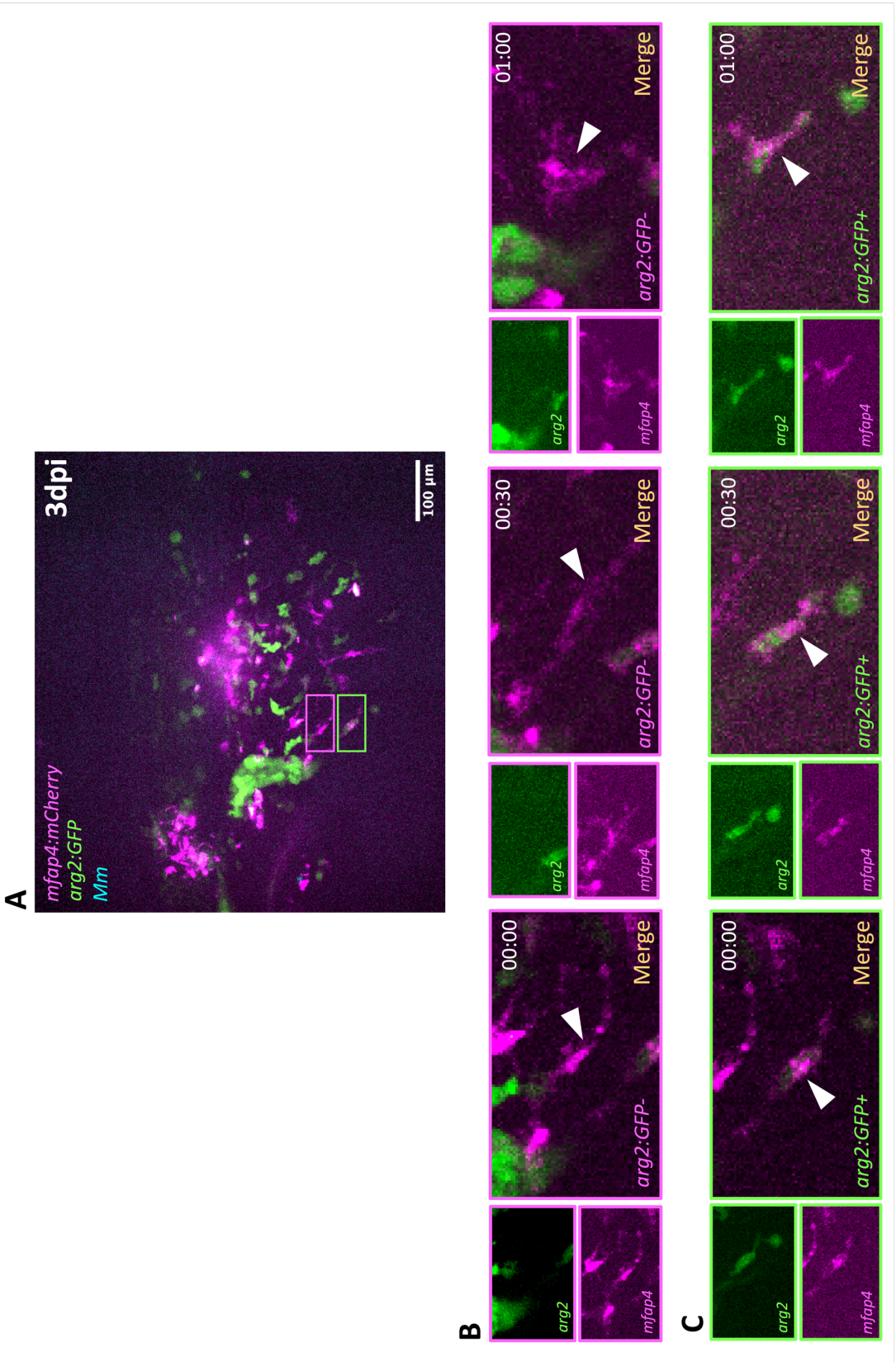


Figure 3.17. Spinning disk timelapse imaging at 3 dpi captures *arg2:GFP-* and *arg2:GFP+* macrophages. (**A**) Representative frame (maximum projection) of a timelapse of 3 dpi *arg2:GFP* larvae crossed with *mfap4:mCherry*. Pink box highlights *arg2:GFP-* macrophage. Green box highlights nearest *arg2:GFP+* macrophage. (**B**) Zoomed area of the *arg2:GFP-* macrophage (white arrowhead) highlighted in the pink box in (**A**), spanning from when it is in the field of view (00:00), 30 minutes and at 1 hour. (**C**) Zoomed area of the *arg2:GFP+* macrophage (white arrowhead) highlighted in the green box in (**A**), spanning from when it is in the field of view (00:00), 30 minutes and at 1 hour. Timelapse time steps were 3 minutes. Scale bar stated on still image in (**A**).

To assess macrophage phenotype, a two-stage approach was adopted. Firstly, macrophages (*arg2:GFP+* vs. nearest *arg2:GFP-* neighbour) were manually drawn around using the free hand selection tool in ImageJ to quantify perimeter (μm) and circularity index (CI) as morphometric descriptors in each frame (3-minute intervals) over the course of a 1-hour window (**Fix. 3.18. A**). Higher perimeter indicates macrophage branching, whilst higher CI suggests a more amoeboid morphology (Sipka et al., 2022). Secondly, the manual tracking plugin on ImageJ was used to track macrophages over the 1-hour window, allowing for speed (μm/sec) and meandering index (MI) measurements to quantify behaviour (**Fig. 3.18. B**).

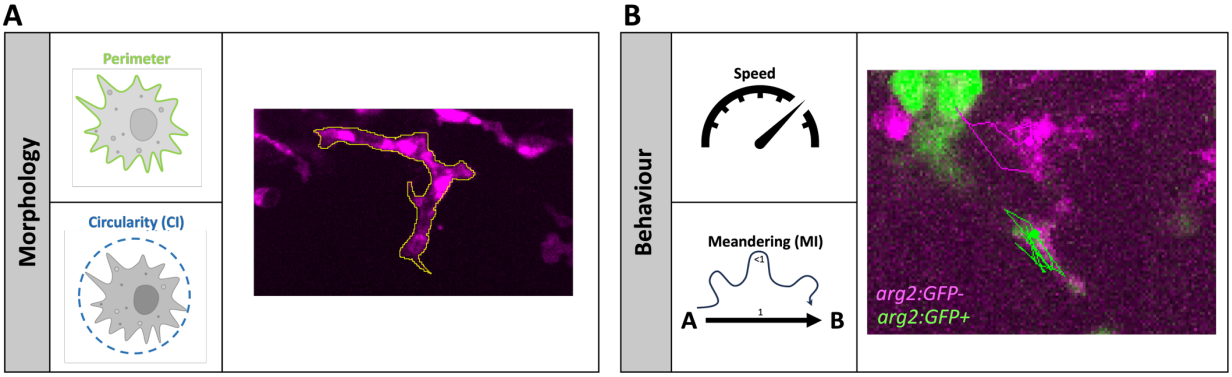


Figure 3.18. ImageJ analysis pipeline to determine macrophage morphology and behaviour. (**A**) To quantify macrophage perimeter (green outline) and circularity index (blue circle; takes into account area and perimeter), macrophages were manually drawn around using the free hand selection tool (yellow outline) in the mCherry channel (*mfap4:mCherry* labels farnesylated membrane) for each frame over the course of a 1-hour window (20 frames). (**B**) The manual tracking plugin was used to track macrophage speed over the course of a 1-hour window (*arg2:GFP-* depicted by the pink line, *arg2:GFP+* depicted by the green line). Meandering index (MI) was manually calculated using the location (XY) and distance travelled (μm) obtained from the manual tracking plugin, whereby a MI of 1 is the most direct route and <1 is less direct.

In terms of morphometric descriptors, compared to *arg2:GFP-* macrophages, *arg2:GFP+* macrophages had a significantly smaller average perimeter (143.6 μm vs. 106 μm; **Fig. 3.19. A**) and a significantly higher CI (0.3 vs. 0.49; **Fig. 3.19. B**) over the course of 1 hour, suggesting *arg2:GFP+* macrophages are less branched and rounder in shape. Examination of behavioural descriptors found no significant differences between average MI of *arg2:GFP-* and *arg2:GFP+* macrophages (0.49 vs. 0.57, respectively; **Fig. 3.19. D**). However, *arg2:GFP+* macrophages had a significantly higher average speed compared to their nearest *arg2:GFP-* neighbour (1.37 μm/sec vs. 1.63 μm/sec; **Fig. 3.19. C**) during the 1-hour window.

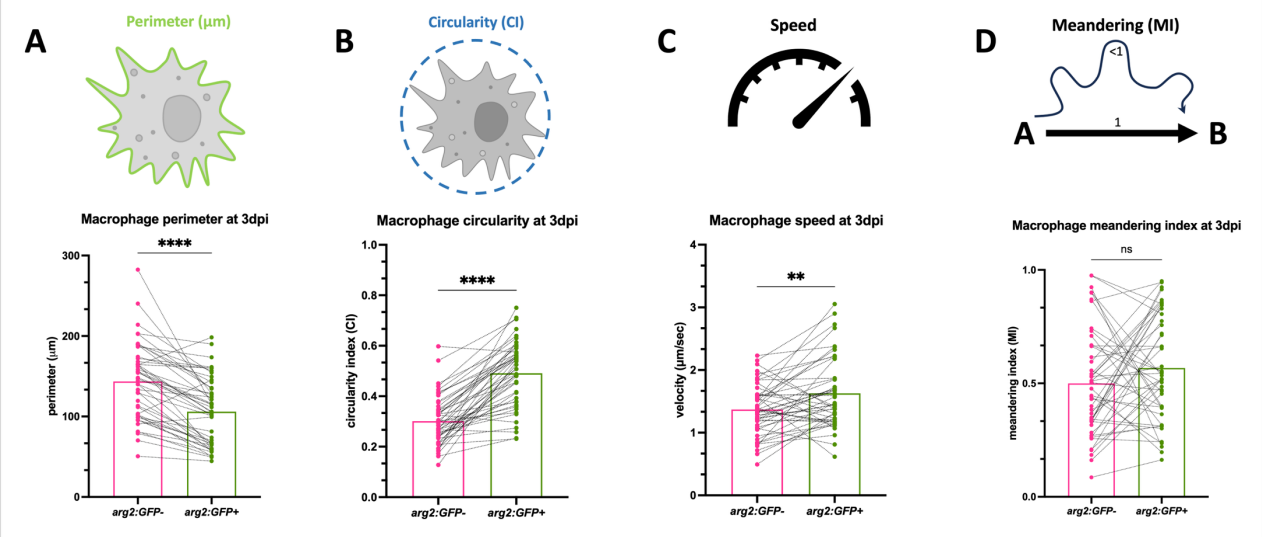


Figure 3.19. *arg2:GFP+* macrophages are smaller, less branched and faster than *arg2:GFP-* macrophages. (**A**) Top: Representation of perimeter analysis obtained in ImageJ. Bottom: Paired comparison of average perimeter (µm) of *arg2:GFP-* macrophages (pink) compared to that of *arg2:GFP+* macrophages (green) across a 1 hour window. (**B**) Top: Representation of circularity index (CI) analysis calculated using ImageJ. Bottom: Paired comparison of average CI of *arg2:GFP-* macrophages (pink) compared to that of *arg2:GFP+* macrophages (green) across a 1-hour window. (**C**) Top: Representation of speed analysis obtained using the ImageJ manual tracking plugin. Bottom: Paired comparison of the average speed (µm/sec) of *arg2:GFP-* macrophages (pink) compared to that of *arg2:GFP+* macrophages (green) across a 1-hour window. (**D**) Top: Representation of how the most direct migratory route equates to a meandering index (MI) of 1. Bottom: Paired comparison of the average MI of *arg2:GFP-* macrophages (pink) and *arg2:GFP+* macrophages (green) across a 1-hour window. N=2 independent experiments, with 47 matched cells (4-5 matched cells per fish, 10 fish total). Statistical significance was calculated using a paired, two-tailed t-test. **P ≤ 0.01; ****P ≤ 0.0001.

Changes to macrophage shape have been directly associated with speed of migration (Travnickova et al., 2021). Extensive macrophage branching (pseudopodia) has been associated with reduced murine macrophage motility *in vitro* (Pixley et al., 2005). Thus, the relationship between macrophage CI and speed was assessed for *arg2:GFP-* and *arg2:GFP+* macrophage populations. Linear regression analysis of the total population showed a statistically significant but weak relationship between CI and speed (p=0.028; R^2=0.051), suggesting that while a global trend exists, CI is a poor predictor of cell velocity (**Fig. 3.20. A**). Notably, the scatter plot reveals that *arg2:GFP-* and *arg2:GFP+* macrophages cluster into two distinct populations. This indicates that the significant p-value is driven by the inherent differences between these two phenotypes – where *arg2:GFP+* cells generally exhibit higher CI and speed – rather than a direct functional coupling between morphology and migration within each group.

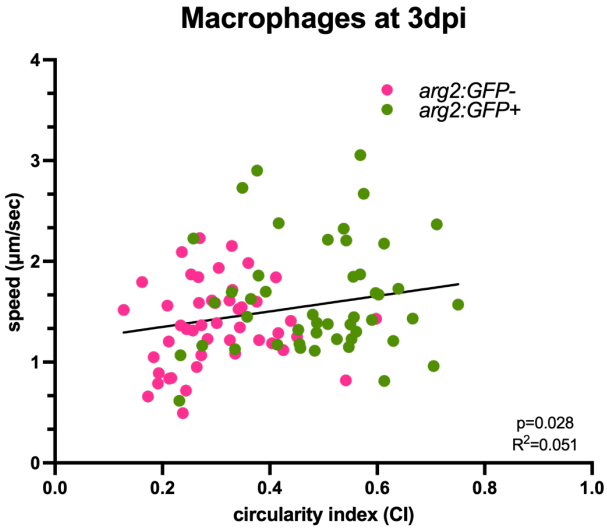


Figure 3.20. Macrophage circularity index does not correlate with speed. (**A**) Scatter plot diagram of circularity index (CI) and speed (µm/sec) of *arg2:GFP-* macrophages (pink dots) and *arg2:GFP+* macrophages (green dots). Statistical significance calculated using a simple linear regression on both groups collated. P value and R^2 value are stated on the graph.

Due to the challenges of FACS purifying *arg2:GFP+* macrophages owed to the faint GFP signal (particularly when compared to neutrophils and ionocytes), single-cell RNAseq (scRNAseq) was performed on whole larvae at 2 dpf following Hif modulation (dominant active *hif-1α* and *hif-2α* - discussed in chapter 5) and *Mm* infection to determine whether *arg2+* macrophages transcriptionally resemble anti-inflammatory macrophages. The first (of two) 10X Genomics chip failed to run, resulting in the experiment being underpowered and therefore identifying few differentially expressed genes (DEGs). As such, the findings presented below are preliminary.

Across all experimental conditions, 71,420 cells were isolated, generating a 25 cluster UMAP (**Fig. 3.21. A**). To identify the macrophage population, *mfap4* and *mpeg1.1* were used as markers (**Fig. 3.21. B**). 888 cells were identified as *mfap4+*, 555 cells as *mpeg1.1+* and 463 cells as *mfap4+ mpeg1.1+*. As *mfap4* is not downregulated by *Mm* and captures the highest number of cells, *mfap4* was used as the dominant marker to identify *arg2+* macrophages (Benard et al., 2015).

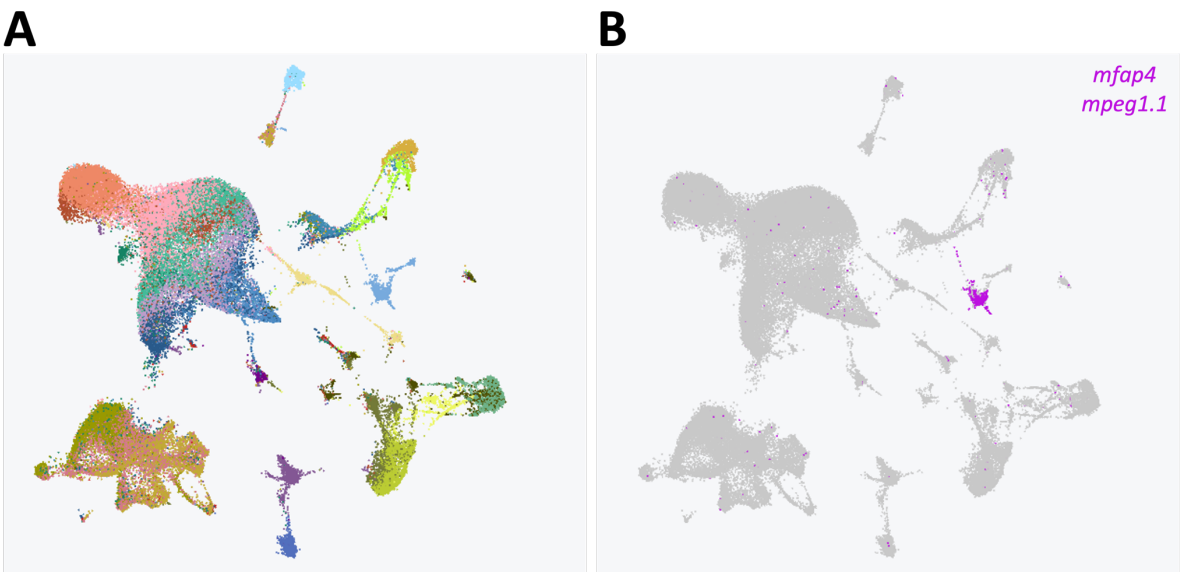


Figure 3.21. Single-cell RNAseq identifies a population of *arg2*+ macrophages. (**A**) UMAP plot generated from whole larvae across all experimental conditions (phenol red, dominant active *hif-1α,* dominant active *hif-2α,* and *Mm*) and biological repeats (2 batches). (**B**) Macrophage cluster (highlighted in purple) identified by *mfap4* and *mpeg1.1* marker gene expression. UMAPs generated in Trailmaker (Parse Biosciences).

To assess the transcriptional profile of *arg2*+ macrophages without DEGs, absolute expression of a custom selection of genes was visualised across each conditions (**Fig. 3.22.**). Pro- and anti-inflammatory-associated genes from published zebrafish and *ex vivo* carp macrophage datasets were evaluated, with *mfap4* and *arg2* expression used as a control to confirm that the *arg2*+ macrophage population was bioinformatically selected (**Fig. 3.22.** – yellow box) (Rougeot et al., 2019; Cronan et al., 2021; Wentzel et al., 2020). Across all conditions, anti-inflammatory-associated genes were more highly expressed, including *nccrp1* and *vegfaa*, with *arg2* being most highly expressed in the *Mm* group (**Fig. 3.22.** – green). Overall, there was lower expression of pro-inflammatory-associated genes, with average expression of *il1b* being highest in the *Mm* group, and increased expression of *il6st* in dominant active *hif-1α* and *hif-2α* groups (**Fig. 3.22** – pink).

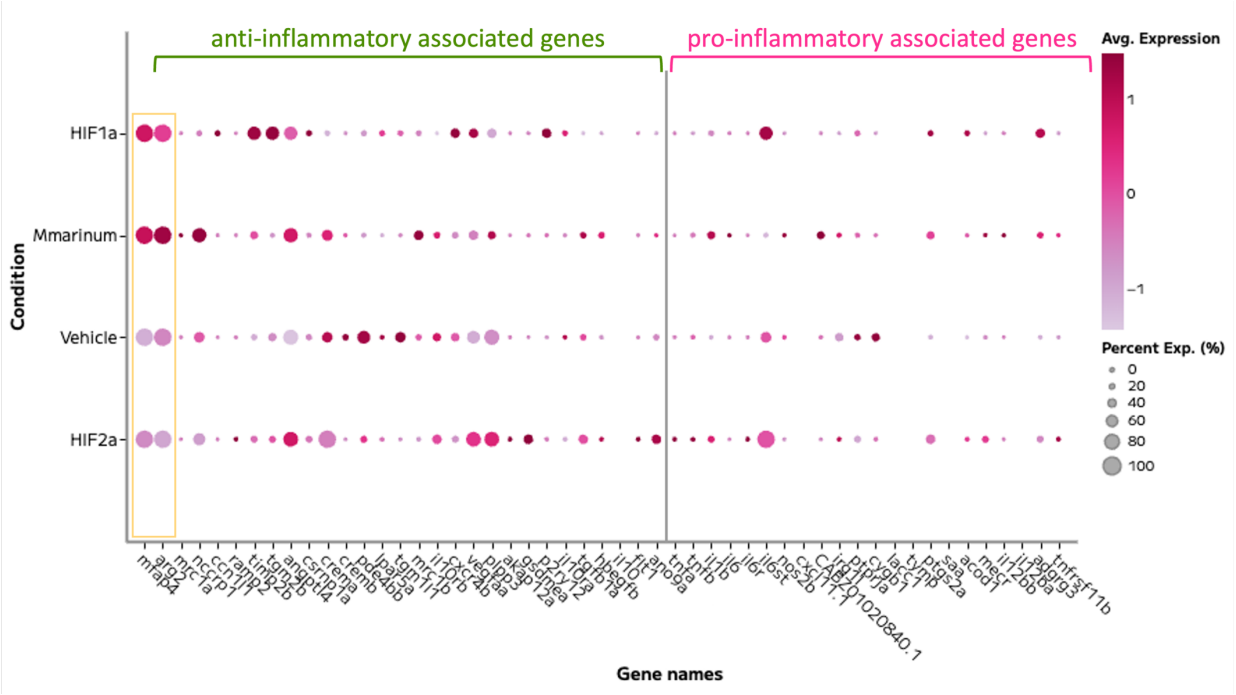


Figure 3.22. *arg2*+ macrophages exhibit an anti-inflammatory transcriptional landscape. Dot plot showing the expression of selected anti-inflammatory-associated (left, green) and pro-inflammatory-associated (right, pink) genes in *arg2+* macrophages across experimental conditions (phenol red/vehicle, dominant active *hif-1α*, Mm and dominant active *hif-2α*). Yellow box indicates expression of *mfap4* (macrophage marker) and *arg2* as a control for bioinformatically identifying *arg2+* macrophages. Dot size represents the percentage of cells expressing each gene, and colour intensity indicates average gene expression. Dot plots generated in Trailmaker (Parse Biosciences).

These morphological (i.e. smaller, more circular) and behavioural characteristics (i.e. faster) of *arg2:GFP+* macrophages resemble *in vitro* M2c polarised murine macrophages (IL-10, TGF-β) and *ex vivo* M2 polarised carp macrophages (Hourani et al., 2023; Wentzel et al., 2020). Additionally, the increased migratory speed observed in *arg2:GFP+* macrophages mirrors that of Arg1+ tumour associated macrophages (TAMs), an M2-like tumour-supporting macrophage phenotype that promotes tumour metastasis (Arlauckas et al., 2018). Moreover, although the scRNAseq findings are preliminary, the transcriptional signature of *arg2*+ macrophages is consistent with an anti-inflammatory macrophage signature. Taken together, these data indicate that *arg2:GFP*+ macrophages exhibit morphological, migratory and transcriptional characteristics that parallel those of anti-inflammatory macrophage populations described in other models.

3.2.4. Determining signalling mechanisms that lead to macrophages *arg2:GFP* expression in *Mm* infection

Infection with HK *Mm* and ΔRD1 *Mm* both induced macrophage *tnfa:GFP* expression, albeit less potently than live *Mm*, indicating that the presence of *Mm* is sufficient to induce a macrophage pro-inflammatory response. Therefore, to determine whether the presence of *Mm* is sufficient to also

induce an anti-inflammatory response, larvae were infected with HK *Mm* and ΔRD1 *Mm*, and macrophage *arg2:GFP* expression examined at several time-points.

In the first instance, macrophage *arg2:GFP* at 3 dpi was examined, as this is the time-point at which the highest proportion of *arg2:GFP*+ macrophages were identified. Mock infection (PVP) did not induce *arg2:GFP* expression in any macrophages within the imaged field of view (**Fig. 3.23. A**), neither through visual observation (**Fig. 3.23. E**) or by measuring *arg2:GFP* fluorescence brightness (**Fig. 3.23. F**). As expected, approximately 25% of macrophages (30 out of 118) were *arg2:GFP+* when infected with live *Mm* (**Fig. 3.23. B, E**). Infection with HK *Mm* (**Fig. 3.23. C**) and ΔRD1 *Mm* (**Fig. 3.23. D**) resulted in upregulation of *arg2:GFP* in a small number of macrophages each (5.8% and 6.2%, respectively; **Fig. 3.23. E**). Whilst HK *Mm* and ΔRD1 *Mm* groups resulted in significantly more *arg2:GFP*+ macrophages visually identified than the PVP group (HK *Mm*: 8 out of 137; ΔRD1 *Mm*: 8 out of 129), only live *Mm* resulted in a significantly elevated macrophage GFP fluorescence brightness (**Fig. 3.23. F**). The discrepancy between visually counted and fluorescence intensity is likely due to brightness/contrast being increased during counts in order to capture any *arg2:GFP+* cells. Thus, the threshold for determining whether a macrophage is *arg2:GFP+* or *arg2:GFP*- is more stringent when measuring fluorescence brightness.

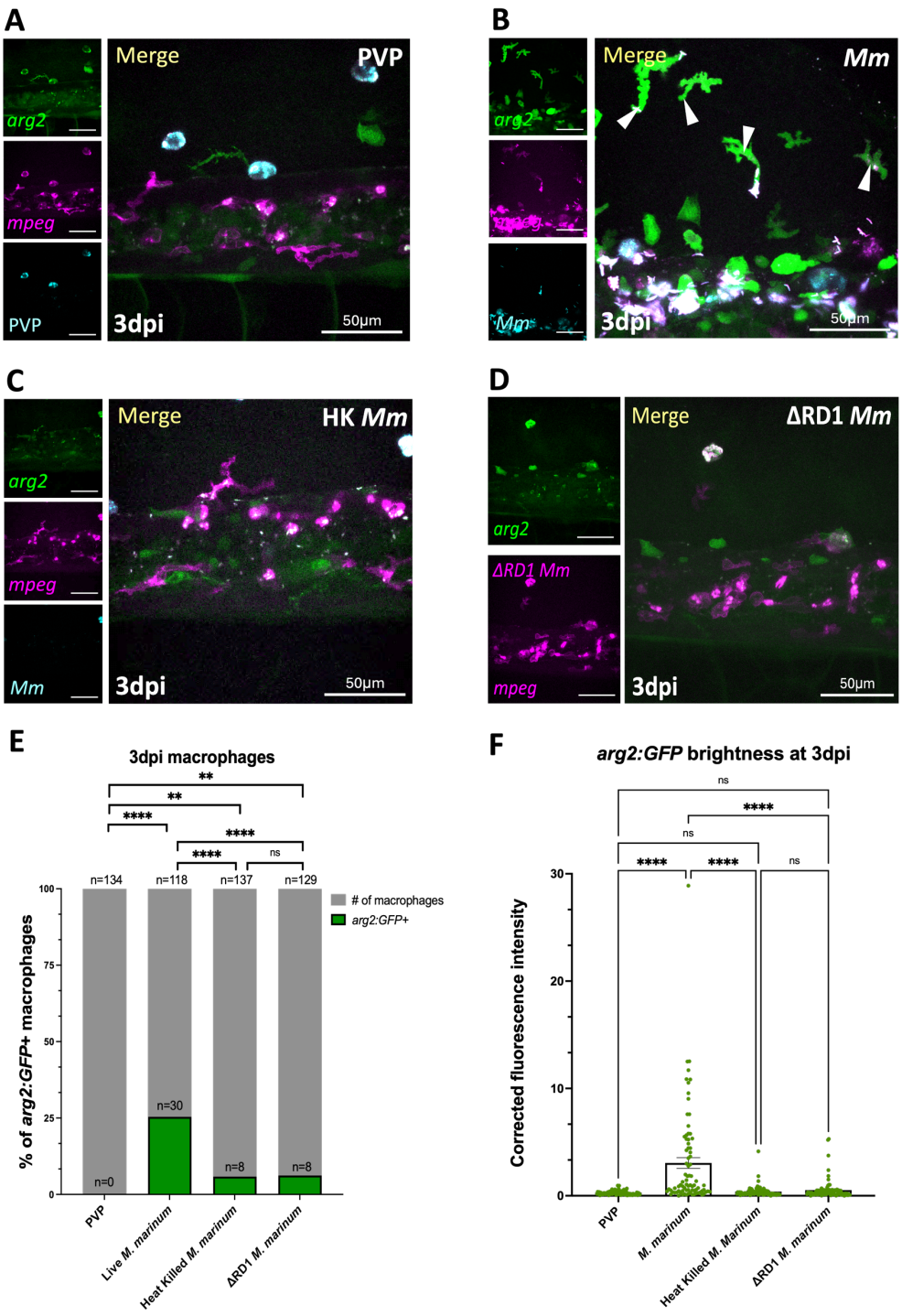


Figure 3.23. Live and virulent *Mm* is required to induce macrophage *arg2:GFP* expression at 3 dpi. (**A-D**) Representative confocal image of 3 dpi *arg2:GFP* crossed to *mpeg:mCherry* infected with (**A**) PVP, (**B**) live *Mm*, (**C**) HK *Mm* or (**D**) ΔRD1 *Mm*. (**E**) Graph illustrating the percentage of *arg2:GFP+* macrophages at 3 dpi. (**F**) moted fluorescence intensity of *mpeg:mCherry+* macrophages in the GFP channel to assess *arg2:GFP* fluorescence brightness. N=3 independent experiments, with 5 larvae per group imaged per experiment. All counts were taken from a 40x field of view near the caudal vein (site of infection) or around clusters of bacteria within the fish. Up to 6 macrophages were measured for fluorescence intensity. Total number of cells are stated on the graph in (**E**). Error bars depict SEM. Statistical significance in (**E**) was calculated using a Chi squared test, followed by Fisher's exact test to determine where significant differences are. Statistical significance in (**F**) was calculated using a one-way ANOVA with Bonferroni's multiple comparisons post hoc test. **P ≤ 0.01, ****P ≤ 0.0001. Scale bars are stated on the images.

As HK *Mm* is cleared faster and ΔRD1 *Mm* fails to form efficient granulomas (Volkman et al., 2004; Davis et al., 2002), macrophage *arg2:GFP* expression was also assessed at the early (1 dpi) and later (4 dpi) stages of infection to determine whether the timings of the inflammatory process are altered.

Similar to at 3 dpi, no macrophages upregulated *arg2:GFP* when injected with PVP at 1 dpi (**Fig. 3.24. A, E, F**). Live *Mm* significantly upregulated macrophages *arg2:GFP*, with 7 out of 131 macrophages upregulating *arg2:GFP* in the field of view (**Fig. 3.24. B, E**). Infection with HK *Mm* resulted in no *arg2:GFP*+ macrophages being identified either visually (**Fig. 3.24. C, E)** or by measuring fluorescence brightness (**Fig. 3.24. F**). However, no significant differences were found between infection with live *Mm* and ΔRD1 *Mm* following visual counts, with 2 out of 157 macrophages being *arg2:GFP*+ (**Fig. 3.24. D, E**). Consistent with the 3 dpi *arg2:GFP* fluorescence measurements, only live *Mm* induced a significant increase in GFP brightness (**Fig. 3.24. F**). These results further demonstrate that fluorescence quantification provides a more reliable and objective means of identifying *arg2:GFP+* macrophages than visual assessment, which can be confounded by image overexposure to reveal any weak GFP signal.

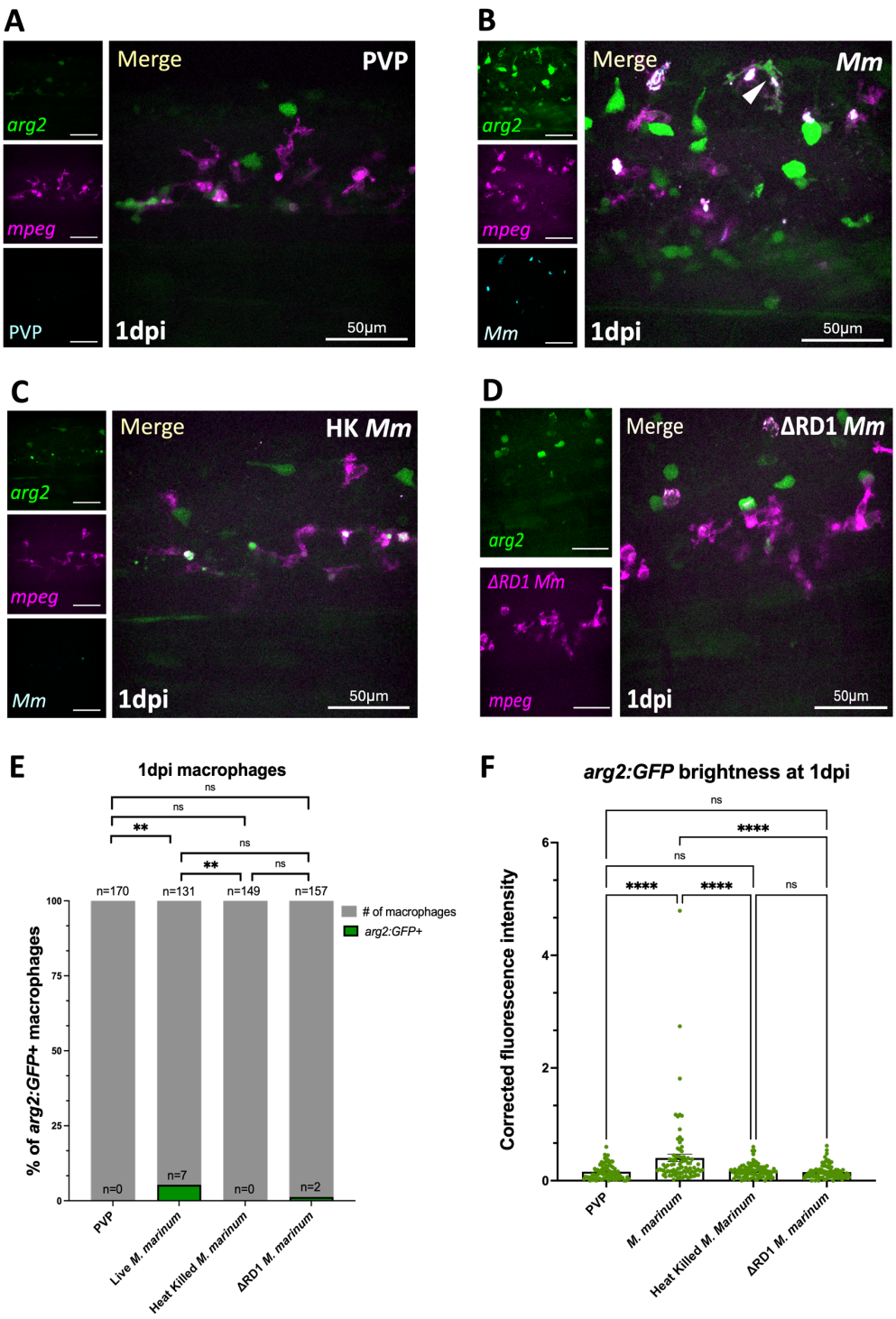


Figure 3.24. Live and virulent *Mm* is required to induce maximal macrophage *arg2:GFP* expression at 1 dpi. (**A-D**) Representative confocal image of 1 dpi *arg2:GFP* crossed to *mpeg:mCherry* infected with (**A**) PVP, (**B**) live *Mm*, (**C**) HK *Mm* or (**D**) ΔRD1 *Mm*. (**E**) Graph illustrating the percentage of *arg2:GFP+* macrophages at 1 dpi. (**F**) Corrected fluorescence intensity of *mpeg:mCherry+* macrophages in the GFP channel to assess *arg2:GFP* fluorescence brightness. N=3 independent experiments, with 5 larvae per group imaged per experiment. All counts were taken from a 40x field of view near the caudal vein (site of infection) or around clusters of bacteria within the fish. Up to 6 macrophages were measured for fluorescence intensity. Error bars depict SEM. Statistical significance in (**E**) was calculated using a Chi squared test, followed by Fisher's exact test to determine where significant differences are. Statistical significance in (**F**) was calculated using a one-way ANOVA with Bonferroni's multiple comparisons post hoc test. **P ≤ 0.01, ****P ≤ 0.0001.

At 4 dpi, mock-infection with PVP did not significantly upregulate macrophage *arg2:GFP* (**Fig. 3.25. A**), either through visual observation (**Fig. 3.25. E**) or by measuring GFP fluorescence brightness (**Fig. X. F**). However, 2 macrophages (out of 96) were visually identified as *arg2:GFP*+ (**Fig. 3.25. E**), which may be due to mild injury to the larvae either during the infection or mounting for imaging process. Following infection with HK *Mm* (**Fig. 3.25. C**), 5 macrophages (out of 100) were identified as *arg2:GFP*+ (**Fig. 3.25. E**). Yet HK *Mm* did not significantly upregulate macrophage *arg2:GFP* expression either visually (**Fig. 3.25. E**) or when measuring fluorescence brightness (**Fig. 3.25. F**) when compared to PVP. No macrophages were identified as being *arg2:GFP*+ following infection with ΔRD1 *Mm* (**Fig. 3.25. D, E, F**). Only infection with live, virulent *Mm* resulted in significant upregulation of macrophage *arg2:GFP* expression both visually (**Fig. 3.25. E**) and in terms of GFP brightness (**Fig. 3.25. F**). A higher proportion of *arg2:GFP*+ macrophages were identified at 4 dpi than expected based on previous observations, with 18.2% macrophages being positive (**Fig. 3.25. E**). This higher proportion can be accounted for the lower number of fish (and macrophages) quantified and two larvae being highly expressing *arg2:GFP* (**Fig. 3.25 B**).

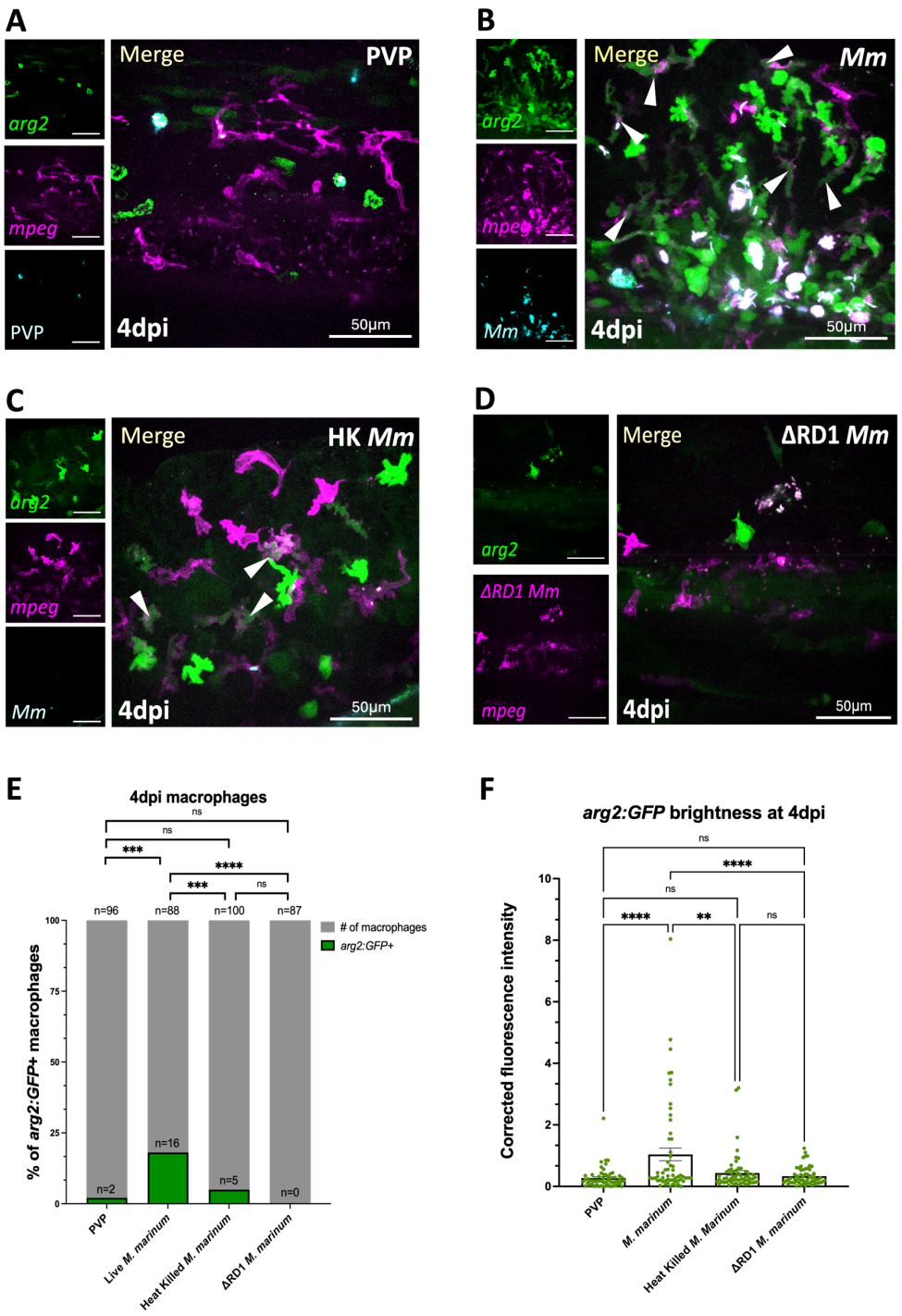


Figure 3.25. Live and virulent *Mm* is required to induce maximal macrophage *arg2:GFP* expression at 4 dpi. (**A-D**) Representative confocal image of 4 dpi *arg2:GFP* crossed to *mpeg:mCherry* infected with (**A**) PVP, (**B**) live *Mm*, (**C**) HK *Mm* or (**D**) ΔRD1 *Mm*. (**E**) Graph illustrating the percentage of *arg2:GFP+* macrophages at 4 dpi. (**F**) Corrected fluorescence intensity of *mpeg:mCherry+* macrophages in the GFP channel to assess *arg2:GFP* fluorescence brightness. N=2 independent experiments, with 5 larvae per group imaged per experiment. All counts were taken from a 40x field of view near the caudal vein (site of infection) or around clusters of bacteria within the fish. Arrowheads indicate *arg2:GFP+* macrophages. Total number of cells counted in (**E**) are stated on the graph. Up to 6 macrophages were measured for fluorescence intensity. Error bars depict SEM. Statistical significance in (**E**) was calculated using a Chi squared test, followed by Fisher's exact test to determine where significant differences are. Statistical significance in (**F**) was calculated using a one-way ANOVA with Bonferroni's multiple comparisons post hoc test. **P ≤ 0.01, ***P ≤ 0.001, ****P ≤ 0.0001.

To confirm that the lack of macrophage *arg2:GFP* expression is not due to macrophages failing to phagocytose the HK *Mm* and ΔRD1 *Mm*, the proportion of *arg2:GFP+* and *arg2:GFP-* macrophages with internalised *Mm* was quantified at 1 and 3 dpi.

The proportion of macrophages that had internalised *Mm* (live and ΔRD1) was similar whether *arg2:GFP+* or *arg2:GFP-* at 1 dpi (**Fig. 3.26. A, C, D**). However, these observations are biased by the very low numbers of *arg2:GFP+* macrophages identified, which is particularly obvious in the ΔRD1 *Mm* group, as although this suggests 50% of *arg2:GFP+* macrophages had internalised *Mm*, this equates to 1 out of 2 macrophages (**Fig. 3.26. D**). Whether *arg2:GFP+* macrophages are able to internalise HK *Mm* at 1 dpi is not clear due to the lack of *arg2:GFP+* macrophages identified (**Fig. 3.26. B, D**).

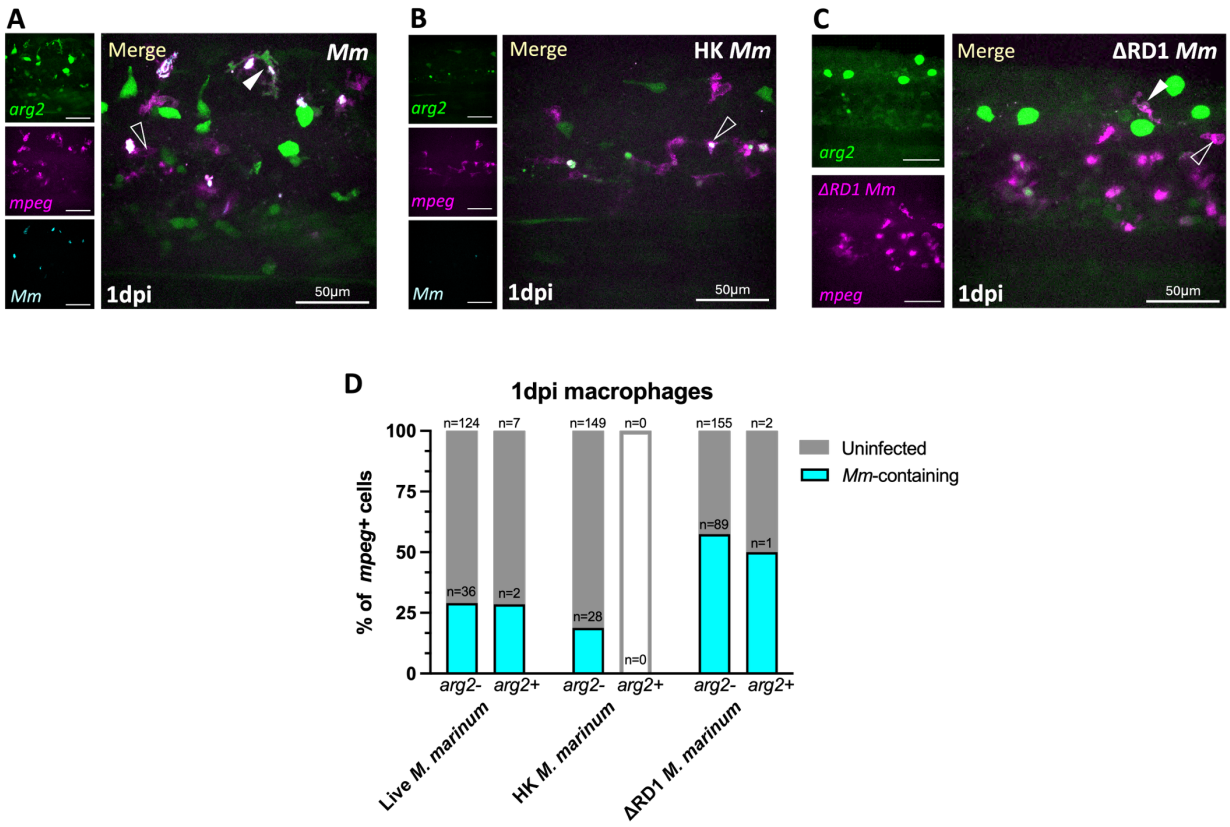


Figure 3.26. The proportion of *arg2:GFP+* and *arg2:GFP-* macrophages with internalised *Mm* is similar whether alive, heat killed or avirulent at 1 dpi. (**A**) Representative confocal image of *arg2:GFP+* macrophage (filled arrowhead) and *arg2:GFP-* macrophage (hollow arrowhead) with internalised live *Mm.* (**B**) Representative confocal image of *arg2:GFP-* macrophage (hollow arrowhead) with internalised HK *Mm.* (**C**) Representative confocal image of *arg2:GFP+* macrophage (filled arrowhead) and *arg2:GFP-* macrophage (hollow arrowhead) with internalised ΔRD1 *Mm.* (**D**) Graph illustrating that the proportion of *arg2:GFP+* and *arg2:GFP-* macrophages with internalised *Mm* at 1 dpi is similar for live and ΔRD1 *Mm*. Counts from N=3 independent experiments. Scale bar stated on the image. Graph legend and total number of cells counted are stated on the graph.

At 3 dpi, examples of *arg2:GFP*- and *arg2:GFP*+ macrophages with internalised *Mm* were identified following infection with live, HK and ΔRD1 *Mm* (**Fig. 3.27**). Approximately 25% of *arg2:GFP*- (27 out of 88) and *arg2:GFP+* (10 out of 30) macrophages had internalised live *Mm* (**Fig. 3.27. A, D**). Following infection with HK *Mm*, 9 out of 129 (6.98%) *arg2:GFP*- macrophages had internalised Mm, with 25% of *arg2:GFP+* macrophages containing *Mm* (2 out of 8) (**Fig. 3.27. B, D**). Infection with ΔRD1 *Mm* resulted in 46.3% *arg2:GFP*- macrophages containing internalised *Mm* (56 out of 121), with 25% of *arg2;GFP*+ macrophages containing *Mm* (2 out of 8) (**Fig. 3.27. C, D**). Similar to at 1 dpi, there is a data bias in these proportions due to the lower number *arg2:GFP*+ macrophages. For example, both HK *Mm* and ΔRD1 *Mm* had 25% of *arg2:GFP+* macrophages with internalised *Mm*, however this proportion accounts for 2 out of 8 macrophages (**Fig. 3.27. D**). Nevertheless, this data demonstrates that the impaired ability for HK *Mm* and ΔRD1 *Mm* to induce macrophage *arg2:GFP* expression is not due to a failure in phagocytosing *Mm*, but rather other mechanism, such as TLR signalling, may be at play.

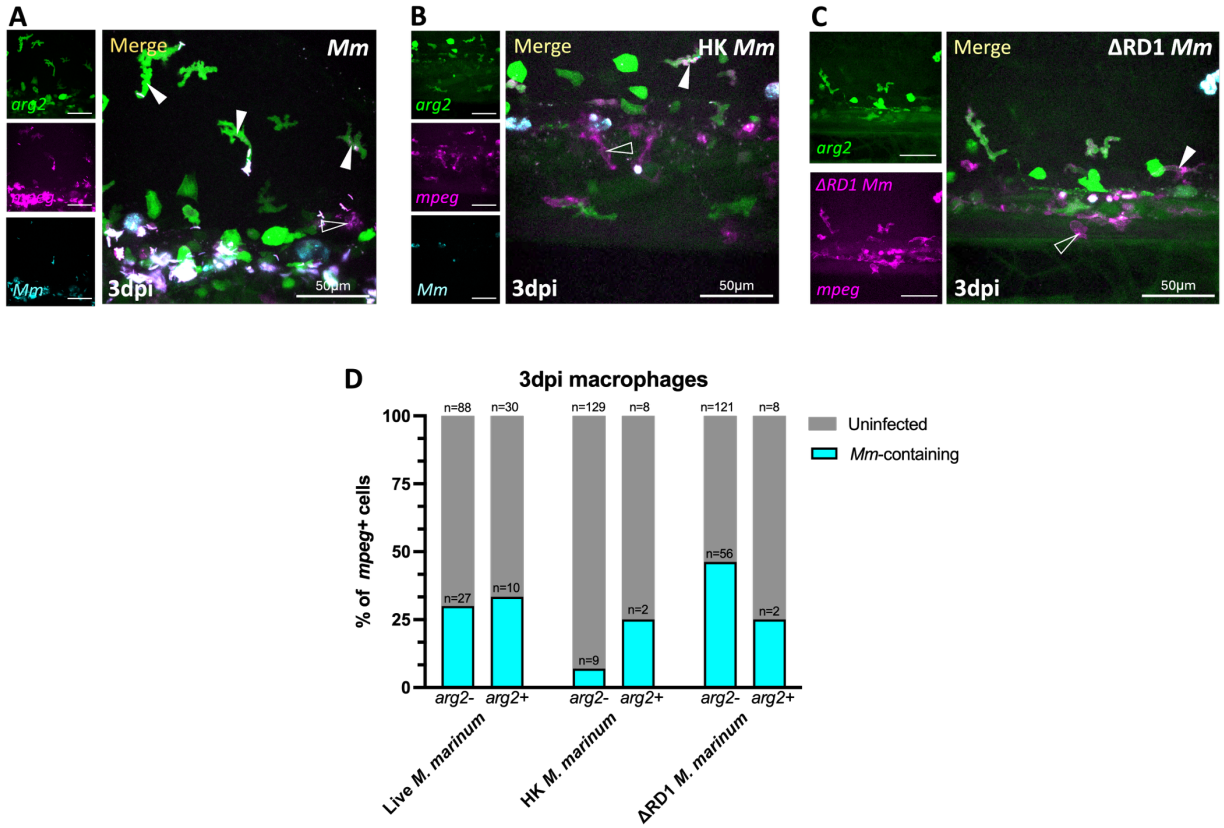


Figure 3.27. Both *arg2:GFP+* and *arg2:GFP*- macrophages contain internalised *Mm* irrespective of whether it is alive, heat killed or avirulent at 3 dpi. (**A**) Representative confocal image of *arg2:GFP+* macrophage (filled arrowhead) and *arg2:GFP*- macrophage (hollow arrowhead) with internalised live *Mm.* (**B**) Representative confocal image of *arg2:GFP*- macrophage (hollow arrowhead) with internalised HK *Mm.* (**C**) Representative confocal image of *arg2:GFP+* macrophage (filled arrowhead) and *arg2:GFP*- macrophage (hollow arrowhead) with internalised ΔRD1 *Mm.* (**D**) Graph illustrating that both *arg2:GFP+* and *arg2:GFP*- macrophages contain internalised *Mm* (live, HK, ΔRD1) at 4 dpi. Counts from N=3 independent experiments. Scale bar stated on the image. Graph legend and total number of cells counted are stated on the graph.

Taken together, this data suggests the presence of *Mm* is not sufficient to induce macrophage *arg2:GFP* expression, despite successful phagocytosis of HK *Mm* and ΔRD1 *Mm*, potentially indicating that macrophage *arg2:GFP* expression is not pathogen-associated molecular patterns (PAMP)-driven. To test this hypothesis, the host toll-like receptor (TLR) signalling adaptor protein MyD88 was knocked down using an e2i2 splice morpholino (MO) to disrupt TLR signalling (with the exception of TLR3, which acts via TRAP-interacting protein) (Meylan et al., 2004).

To validate successful *myd88* knockdown, cDNA from embryos injected with control and *myd88* morpholinos were extracted, amplified and run on an agarose gel. cDNA from control and *myd88* MO injected embryos were both amplified with primers for the housekeeping gene *ef1α* as a control, resulting in strong bands at ~520 bp. As a negative control, a no template control was also run with the *myd88* primers. Embryos injected with the control morpholino resulted in a *myd88* DNA band of approximately 550 bp (**Fig. 3.28**). *myd88* MO injected embryos resulted in the wildtype transcript band (~550 bp) and a morpholino transcript band of approximately 600 bp, as previously described (**Fig. 3.28**) (Bates et al., 2007). Collectively, this demonstrates successful knockdown of host *myd88*.

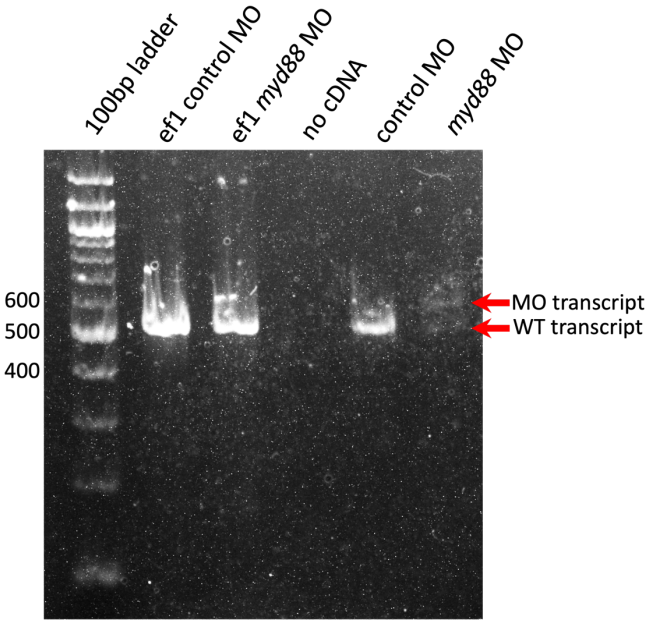


Figure 3.28. Example gel for transcript size of successful MyD88 morpholino knockdown. Total RNA was extracted from control and *myd88* morpholino (MO) injected larvae, and cDNA generated for RT-PCR analysis. First lane: 100 bp ladder. Second and third lane: ef1 primers (housekeeping gene) were used as a control for both control and *myd88* cDNA samples. Fourth lane: a no cDNA control with *myd88* primers was included as a negative control. Fifth lane: *myd88* primers were used in the control injected larvae cDNA, yielding a ~550 bp band. Sixth lane: *myd88* primers were used in *myd88* MO injected larvae cDNA, resulting in the WT transcript band (~550 bp) and the MO transcript band (~600 bp). Red arrows indicate WT and MO transcript bands.

Zebrafish *myd88* morphants are hypersusceptible to uncontrolled *Mm* infection, with significantly higher levels of bacterial burden previously reported (van der Vaart et al., 2013). Higher

levels of bacterial burden make confocal imaging of infected larvae challenging due to the autofluorescence of *Mm*. Therefore, macrophage *arg2:GFP* expression was assessed at 1 dpi, rather than 3 dpi, following systemic infection of 100 CFU of *Mm*-Crimson or PVP.

Embryos injected with the control MO and PVP resulted in 5 out of 208 (2.4%) of macrophages being *arg2:GFP*+ (**Fig. 3.29. A - left, C**). Following infection with Mm, 9.9% of macrophages expressed *arg2:GFP* (19 out of 191) (**Fig. 3.29. A - right, C**). In contrast, *myd88* MO injected embryos resembled control and PVP injected embryos, with only 1 (out of 175; **Fig. 3.29. B - left, C**) macrophages expressing *arg2:GFP* following PVP injection and 4 (out of 204; **Fig. 3.29. B - right, C**) following infection with *Mm*. Fluorescence of GFP was also quantified, identifying that *arg2:GFP* brightness is only significantly elevated in control MO injected embryos following *Mm* infection, with both PVP and *Mm* groups of *myd88* MO injected fish having fluorescence levels akin to embryos injected with control MO and PVP (**Fig. 3.29. D**). Taken together, this suggests that macrophage *arg2:GFP* expression is TLR-dependent.

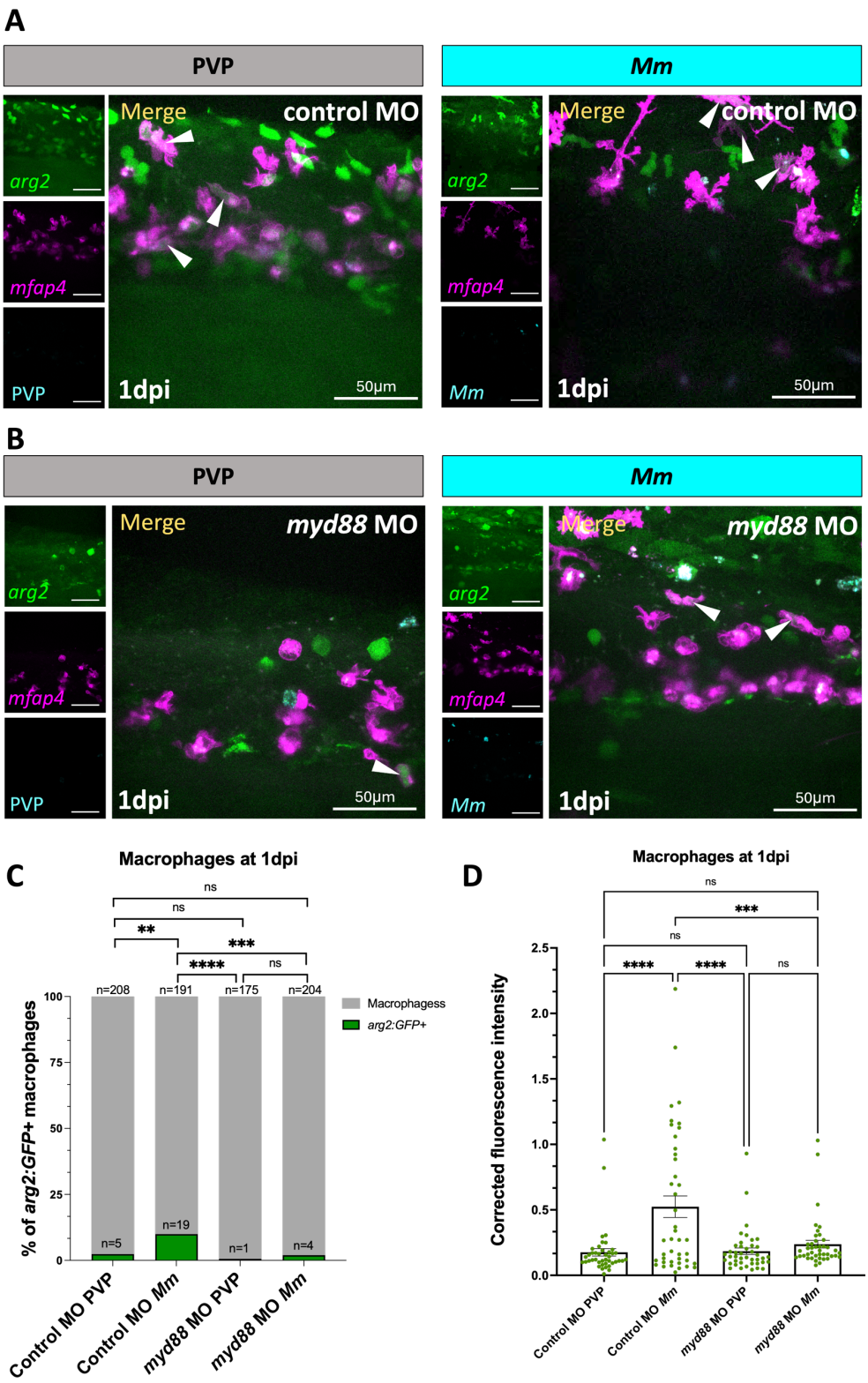


Figure 3.29. Macrophage *arg2:GFP* expression is *myd88*-dependent. (**A**) Representative confocal image of control MO injected *arg2:GFP* crossed with *mfap4:mCherry* embryo following mock infection with PVP (left) or *Mm* (right) at 1 dpi. (**B**) Representative confocal image of *myd88* MO injected *arg2:GFP* crossed with *mfap4:mCherry* embryo following mock infection with PVP (left) or *Mm* (right) at 1 dpi. (**C**) Graph illustrating the percentage of *arg2:GFP+* macrophages at 1 dpi. (**D**) Corrected fluorescence intensity of *mfap4:mCherry+* macrophages in the GFP channel to assess *arg2:GFP* fluorescence brightness. N=3 independent experiments, with 5-7 larvae per group imaged per experiment. All counts were taken from a 40x field of view near the caudal vein (site of infection) or around clusters of bacteria within the fish. Up to 6 macrophages were measured for

fluorescence intensity. Ionocytes are overexposed in the GFP channel to allow for visualisation of *arg2:GFP*+ macrophages. Error bars depict SEM. Statistical significance in (**C**) was calculated using a Chi squared test, followed by Fisher's exact test to determine where significant differences are. Statistical significance in (**D**) was calculated using a one-way ANOVA with Bonferroni's multiple comparisons post hoc test. **P ≤ 0.01, ***P ≤ 0.001, ****P ≤ 0.0001.

To conclude, macrophage *arg2:GFP* expression rises at a point when granulomas begin to form and relies on bacteria being both alive and virulent. Assessment of *arg2:GFP+* macrophage morphology and behaviour over time demonstrates phenotypic similarities to M2c polarised murine macrophages (IL-10/TGF-β), suggesting that the *arg2:GFP* transgenic line may be labelling a population of anti-inflammatory macrophages.

3.3. Discussion

Mycobacterium tuberculosis (*Mtb*) has evolved survival strategies to manipulate macrophage phenotype, with arginase upregulation forming part of a broader strategy to subvert host immunity, disrupt macrophage activation, and facilitating persistence from early infection through to granuloma stages (El Kasmi et al., 2008; Qualls et al., 2010; Pessanha et al., 2012). However, visualising this mycobacteria-mediated modulation of macrophage signalling *in vivo* remains limited. This chapter presents a detailed characterisation of macrophage *tnfa:GFP* and *arg2:GFP* expression, investigates the signalling mechanisms that may drive their upregulation, and explores whether *arg2:GFP+* macrophages represent a putative anti-inflammatory population. Macrophages robustly upregulate *tnfa:GFP* in response to *Mm* infection, with attenuated and heat-killed *Mm* also capable of inducing expression. In contrast, macrophage *arg2:GFP* is upregulated at 3 dpi, coinciding with the initial formation of early granulomas. Phenotypic analysis *of arg2:GFP+* macrophages over time revealed that they are smaller, more circular and faster – characteristics that resemble *in vitro* anti-inflammatory macrophages. Consistent with this phenotype, preliminary single-cell transcriptomic analysis suggests that *arg2+* macrophages preferentially express anti-inflammatory-associated genes. Finally, macrophage *arg2:GFP* expression was found to be TLR-dependent, and required *Mm* to be both alive and virulent.

Zebrafish transgenic reporters for putative pro-inflammatory macrophages, such as the *tnfa:GFP* line, have allowed for *in vivo* visualisation of macrophage signalling following injury infection challenge (Nguyen-Chi et al., 2015; Nguyen-Chi et al., 2017; Lewis and Elks, 2019). To date, in-depth characterisation of macrophage *tnfa:GFP* expression during mycobacterial infection, particularly at higher magnification, remains unexplored. Following *Mm* challenge, there is prominent recruitment of *tnfa:GFP+* macrophages from 1 dpi, with the highest proportion identified at 3 dpi, before numbers of *tnfa:GFP+* macrophages begin to fall at 4 dpi. The robust *tnfa* response seen at 1 dpi is in-line with previous data from our group (Lewis and Elks, 2019). Although the proportion of *tnfa:GFP+* macrophages is highest at 3 dpi, the number of *tnfa+* macrophages between 2 dpi and 3 dpi is very similar. Fewer macrophages were found around the caudal haematopoietic tissue (imaging field of view) at 3 dpi compared to at 2 dpi, suggesting that the difference in proportion of *tnfa+* macrophages identified at 3 dpi is more likely to be due to macrophages migrating elsewhere, rather than increased recruitment of putative pro-inflammatory macrophages. This notion is supported by the finding that macrophage *tnfa:GFP* fluorescence is significantly brighter from 2 dpi (compared to 1 dpi), with no differences identified when compared to 3 dpi, before falling again at 4 dpi. Taken together, this demonstrates that whilst *Mm* induces a robust pro-inflammatory response at all time-points, *tnfa* transcription rises from 2 dpi, before decreasing again at later stages of infection.

The proportion of *tnfa:GFP*-positive macrophages with internalised *Mm*, when compared to *tnfa:GFP*-negative macrophages, was only significantly higher at 2 dpi. This coincides with the time-point at which macrophage *tnfa:GFP* expression and brightness is highest, suggesting that 2 dpi is likely when the macrophage pro-inflammatory phenotype becomes more potent and indicates a time-point prior to increased bacterial killing. The increased prevalence of *tnfa*+ macrophages with internalised bacteria is in line with recent work using primary human monocyte-derived macrophages (MDMs) infected with GFP-tagged *Mtb,* whereby MDMs that were GFP-negative (by-stander macrophages) did not stain for TNF-α via immunofluorescence (Solomon and Bryson, 2023). This data would indicate that the macrophage *tnfa* response does not signal through autocrine-paracrine mechanisms, a finding which contrasts the macrophage arginase response. Indeed, *Mtb*-infected bone marrow-derived macrophages (BMDMs) were found to produce factors which increased *arginase* 1 expression even in by-stander macrophages through autocrine-paracrine signalling (Qualls et al., 2010). However, Solomon and Bryson also found that the elevated levels of TNF-α in *Mtb*-infected MDMs was only driven by a small proportion of TNF-α producers, and that enhancing the TNF-α response did not improve bacterial burden (Solomon and Bryson, 2023). This contrasts with observations made both in this thesis and in the literature, whereby *Mm* results in widespread upregulation of macrophage *tnfa:GFP* expression, particularly from 1-3 dpi. Moreover, upregulation of macrophage *tnfa:GFP* expression through Hif-1α stabilisation in zebrafish larvae also corresponds with a decrease in bacterial burden (Elks et al., 2013; Lewis and Elks, 2019). Whilst only a few *Mtb*-infected MDMs were found to be the cause of elevated TNF-α production, this seems counterproductive for the control of mycobacterial infection and may be highlighting the limitations associated with *in vitro* experiments, especially when compared to whole-organism infection studies (Solomon and Bryson, 2023). Taken together, this data suggests that at whole-organism level, *Mm*-infected macrophages widely upregulate *tnfa* expression at 2 dpi in order to kill phagocytosed bacteria, whilst minimising excessive tissue damage and macrophage necrosis.

Macrophage *tnfa:GFP* expression is upregulated even following infection with heat-killed or RD1-deficient *Mm*, suggesting that the macrophage *tnfa* response to mycobacterial response is PAMP-driven. This finding agreed with my hypothesis, as it supports many reports of heat-killed or attenuated/avirulent mycobacteria inducing TNF-α in TLR-dependent manner, including in zebrafish (Ferreras-Colino et al., 2024; Underhill et al., 1999). Primary peripheral blood macrophages stimulated with heat killed *Mtb* from both lung cancer patients and healthy controls were found to promote a pro-inflammatory phenotype, inducing expression of CD86 (Putri et al., 2022). Bacillus Calmette-Guérin (BCG) is a non-pathogenic strain of *Mycobacterium bovis* that is historically used for TB vaccination, triggers an immune response via TLRs (Marshall et al., 1997; Heldwein et al., 2003). Murine macrophages infected with either live BCG or heat-killed BCG both induced TNF-α production, although the latter to a much lesser degree. Similar trends were observed with different strains of live or heat-killed mycobacteria, with the most potent TNF-α response from a heat-killed strain being from

Mycobacteria vaccae (Marshall et al., 1997). However, TNF-α produced from mononuclear cells isolated from healthy patients only very slightly increased from baseline when stimulated with heat-killed *Mtb* (Selenscig et al., 2009), perhaps highlighting differences between human and murine macrophage responses, or differences between mononuclear cells and macrophages. Whilst macrophages expressed *tnfa:GFP* when infected with heat-killed or ΔRD1 *Mm*, only live *Mm* induced brightest GFP expression. The lack of virulence associated with these two conditions meant that this observation was expected, and this finding agrees with prior research. Murine BMDMs stimulated with heat-killed *Mtb* were found to secrete less IL-1β, another pro-inflammatory cytokine, when compared to live strains. Yet levels of IL-1β were consistently detected via western blot in all heat-killed *Mtb* strains, with none detected in the uninfected group (Krishnan et al., 2013). Furthermore, spleens from adult zebrafish infected with ESX5-deficient *Mm* – one of the type VII secretion systems associated with the secretion of PE and PPE proteins – had increased transcript levels of *tnfa* and *il1b*, highlighting how changes in pathogen virulence still results in robust induction of TNF-α (Ates et al., 2016; Weerdenburg et al., 2012). Collectively, this demonstrates how the macrophage *tnfa* response is both PAMP-driven and largely TLR-independent, with heat-killed and ΔRD1 *Mm* both inducing macrophage *tnfa:GFP* expression, albeit less potently.

Our group recently published a newly generated *arginase 2* transgenic zebrafish line (*arg2:GFP*) to examine expression of this canonical anti-inflammatory marker in leukocytes, thus the *arg2:GFP* line was pursued further to examine macrophage anti-inflammatory signalling in mycobacterial infection (Hammond et al., 2023). Following *Mm* challenge, macrophages upregulate *arg2:GFP* expression at 3 dpi before it falls again. The early (1 dpi) and later (4 dpi) *arg2:GFP* expression in macrophages is in line with our group's previous findings. However, the observed higher proportion of *arg2:GFP*+ macrophages at 3 dpi was a surprising result, as it was hypothesised that the proportion of *arg2:GFP+* macrophages would progressively increase throughout infection, particularly following granuloma formation (4 dpi), due to induction of type 2 signalling (Cronan et al., 2021). Previous work of an *in vitro* model of tuberculous granuloma using human peripheral blood mononuclear cells (PBMCs) found that expression of the M2 marker CD206 increased over time of infection, with its expression being highest on the final day of analysis (9 dpi) (Huang et al., 2015). Similarly, *Arginase 1* mRNA expression increased over time in mice infected with *Mtb* (El Kasmi et al., 2008). Though these observations fail to account for the complex infected tissue that the zebrafish model gives us, both studies show a consistent upwards trend in macrophage anti-inflammatory markers across the infection time-course, which is not in line with my *in vivo* data. However, these studies identified the highest expression of M2 markers at timepoints which may not physiologically match the larval zebrafish infection time-course (9 and 21 dpi, respectively) (Huang et al., 2015; El Kasmi et al., 2008). Alternatively, my data may indicate that the larval zebrafish-*Mm* model may be too early to detect the higher ratio of anti-inflammatory macrophages associated with granuloma structures.

Macrophage *arg2:GFP* fluorescence is only significantly brighter at 3 dpi compared to 1 dpi, suggesting there are also higher levels of *arginase 2* transcription at this timepoint. This presents as an interesting finding, as *Mtb* pathogenic progression is often associated with a steady increase in type 2 signalling and arginase expression. Single cell RNA sequencing (scRNAseq) of adult zebrafish granulomas identified immune cell clusters, including macrophage populations, to be enriched in *arg2* (Cronan et al., 2021). Similarly, expression of both arginase isoforms (Arg1 and Arg2) have been identified in murine, macaque and human granulomas, demonstrating a correlation between arginase expression and disease progression (Mattila et al., 2013; Duque-Correa et al., 2014). For example, in macaques, macrophages associated with type 2 signalling and epithelioid macrophages are found in high *Mtb* burden caseous granulomas, a stage of granuloma formation that histologically correlates with granuloma cavitation and bacterial transmission (Gideon et al., 2022; Kim et al., 2010). However, these studies focus on more advanced stages of TB, whilst the larval zebrafish-*Mm* model specifically examines the early innate immune response to mycobacteria, suggesting that perhaps this gross switch towards alternative macrophage activation is not captured in our model. Collectively, this demonstrates how elevated *arginase 2* transcription seen at 3 dpi may account for modulation of the macrophage pro-inflammatory response to limit tissue damage, rather than capturing this mycobacteria-mediated switch towards an M2-like phenotype.

The proportion of *arg2:GFP*-positive macrophages with internalised *Mm* was similar to *arg2:GFP*-negative macrophages at all time-points, except at 3 dpi, whereby *arg2:GFP*+ macrophages were significantly less likely to have internalised *Mm*, despite this being the time-point with the highest number of *arg2:GFP*+ macrophages. However, whether this difference is caused by *arg2* expressing macrophages being excellent at killing *Mm* or whether they fail to phagocytose the bacteria was initially unclear. Attempting to capture and quantify macrophage phagocytosis of *Mm* in zebrafish larvae is very challenging. Phagocytosis occurs very rapidly (complete within 30 minutes) and involves injecting *Mm* over the yolk sac, followed by fixation and leukocyte staining with L-plastin (Benard et al., 2014). This technique is able to capture approximately 12 phagocytosis events, which is about double the number of events captured when compared to timelapse imaging of *Salmonella typhimurium*-infected larvae (Benard, 2014). Therefore, the chances of capturing a macrophage phagocytosing *Mm* within 30 minutes of infection, that would later become *arg2:GFP*+ at 3 dpi would be extremely unlikely.

To try to address whether a macrophage must have phagocytosed *Mm* in order to become *arg2:GFP*+, I turned to examining the signalling mechanisms that lead to this upregulation. Unlike the macrophage *tnfa* response, *Mm* must be both alive and virulent to induce macrophage *arg2:GFP* expression. While a study suggests that heat-killed BCG upregulates murine peritoneal macrophage arginase based on effects in *Arg1*-deficient macrophages supplemented with L-arginine and L-citrulline,

it does not directly measure arginase expression or activity (Lange et al., 2017). However, heat-killed BCG has also been shown to induce expression of iNOS and NO production in murine macrophages, which similarly take up L-arginine and L-citrulline (Saito and Nakano, 1996), indicating that NO synthesis may be contributing to substrate depletion seen in the study by Lange and colleagues. Without direct quantification of both arginase and iNOS expression/activity, it remains unclear whether arginase or iNOS predominates in modulating mycobacteria-mediated L-arginine depletion during heat-killed BCG stimulation. Therefore, this thesis provides the first quantitative report of heat-killed mycobacteria failing to induce macrophage *arg2* expression at early stages of infection.

The effect of the RD1 virulence locus on macrophage polarisation is better characterised. The ESAT-6 secreted virulence factor (encoded in the RD1 region) has been shown to initially promote polarisation of human monocytes towards an M1 phenotype, with enhanced secretion of pro-inflammatory cytokines, such as TNF-α and IL-12. Yet these cytokines are inhibited in ESAT-6 stimulated terminally activated M1 macrophages, promoting secretion of IL-10, a classically described anti-inflammatory cytokine (Refai et al., 2018). However, the only measure for an M2-like phenotype in this study was the production of IL-10, a cytokine which predominately directs macrophages towards an immunosuppressive phenotype, often acting through restraining M1 activation (Chuang et al., 2016). The conclusions made by Refai *et al*. would be further strengthened by inclusion of a broader panel M2-like phenotypic markers (e.g.: IL-4, IL-13) to fully characterise the impact of ESAT-6 on macrophage activation state (Mantovani et al., 2004). Conversely, there are several published reports that have demonstrated how attenuated strains of *Mtb* result in robust expression of arginase, a finding which contrasts with my observations. Human THP-1 macrophages incubated with H37Ra, an avirulent strain of *Mtb*, resulted in significantly elevated expression of both *ARG1* and *ARG2*, with increased arginase activity also detected (Mahajan et al., 2012; Zhang et al., 1998). Consistent with this, histological staining of lungs from mice identified that intranasal infection with BCG induced expression of Arg1 protein in macrophages (Qualls et al., 2010). These functional differences could be attributed to genome variations between the two mycobacteria species (*Mm* and *Mycobacterium bovis* BCG). For example, ΔRD1 *Mm* still contains an RD4 region, a locus which exerts virulence through biosynthesis of lipooligosaccharides. Yet the RD4 region is absent from all BCG strains (Ru et al., 2017). Thus, ΔRD1 *Mm* may retain other virulence-associated pro-inflammatory responses (e.g. TNF-α and IL-6 production) that does not favour arginase induction (Kurenuma et al., 2009; Qualls et al., 2009). The divergence likely stems not just from the ESX-1, but from broader genetic and immunostimulatory differences between BCG and ΔRD1 *Mm*.

The proportion of *arg2:GFP*+ and *arg2:GFP*- macrophages with internalised bacteria were similar whether infected with live, heat-killed or ΔRD1 *Mm*. As phagocytosis of the bacteria was therefore occurring, this data suggests that other mechanisms, such as the secretion of virulence

factors to escape the phagolysosome, are likely responsible for the upregulation of macrophage *arg2:GFP*. Taken together, this data suggests that macrophage *arg2:GFP* expression relies on secreted virulence factors. Phagocytosis of mycobacteria is known to enhance secretion of virulence factors, especially ESX-1 in order to escape the phagolysosome (Simeone et al., 2012; Lienard et al., 2020). Coupled with the speed at which macrophages phagocytose *Mm* in zebrafish larvae (Benard et al., 2014), it is likely that *arg2:GFP*+ macrophages had previously contained phagocytosed *Mm*. Future studies could use macrophage cells lines, in combination with a library of purified *Mm* proteins, to more rapidly screen for candidate secreted virulence factors which upregulate *arg2* expression. For example, the Rv1987 secreted virulence protein was found to induce M2 polarisation of both RAW264.7 and THP-1 macrophages, with elevated expression of Arg1 identified following incubation with a *Mycobacterium smegmatis* strain overexpressing the virulence protein (Sha et al., 2021). However*, in vitro* experiments such as these lack the complexity of an intact tissue microenvironment, which could be critical for accurately modelling this host-pathogen interaction.

Upregulation of macrophage *arg2:GFP* expression is dependent on toll-like receptor (TLR) signalling. Even in strains of mycobacteria lacking a functional ESX-1 secretion system, such as ΔRD1 *Mm* or BCG, a range of PAMPs (e.g.: cell wall components, such as glycoproteins and lipoarabinomannan) remain, which are recognised by the host immune receptors, including TLRs. It was therefore hypothesised that *Mm*-induced macrophage *arg2:GFP* expression would not be TLR-dependent, as these remaining PAMPs would still interact with TLRs. However, this hypothesis was not supported by the data, with macrophage a*rg2:GFP* expression being largely abolished following morpholino knockdown of the TLR adaptor protein myeloid differentiation factor 88 (MyD88). Similar findings have previously been reported in the literature. Following infection with BCG, mycobacteria-mediated upregulation of Arg1 was abolished in BMDMs isolated from MyD88-deficient mice, both at the mRNA and protein level (El Kasmi et al., 2008). However, this upregulation was only partially reduced in *Tlr2-/-* BMDMs, the primary PRR involved in the detection of mycobacterial cell wall components when in a heterodimer with TLR1 or TLR6 (El Kasmi et al., 2008). These data demonstrates that mycobacteria exert their effects through multiple members of the TLR family, which all signal via the common adaptor MyD88, though not necessarily through direct activation of all TLRs. Instead, mycobacteria may drive arginase expression in an autocrine-paracrine manner. In support of this, MyD88-dependent release of soluble factors – such as IL-6 and IL-10 – from *Mtb*-infected macrophages has been shown to induce Arg1 in uninfected BMDMs from *Myd88-/-* mice (Qualls et al., 2010). To date, there are no reports describing the impact of *myd88* knockdown on arginase expression in zebrafish following *Mm* infection, either in whole larvae or at the macrophage level. However, a recent study demonstrated that *Mm*-infected *myd88* mutant larvae displayed a blunted inflammatory response, with reduced immune cell recruitment and impaired intracellular pathogen control, leading to increased bacterial burden (Hosseini et al., 2021). Given the established role of TLR/MyD88 signalling in

driving macrophage arginase expression, it is plausible to hypothesise that arginase induction would also be impaired in this context (El Kasmi et al., 2008). Taken together, my data demonstrates that macrophage *arg2:GFP* expression is MyD88-dependent. Combined with the observations made following infection with ΔRD1 *Mm*, these findings suggests that full PAMP potency is required to elicit TLR-mediated immune activation – potentially through stimulating MyD88-dependent secretion of soluble factors to upregulate *arg2* in neighbouring cells.

Morphological differences between *arg2:GFP+* and *arg2:GFP-* macrophages were only captured using time-lapse microscopy, not with static confocal imaging. This discrepancy is unsurprising, as static imaging fails to capture the changes in morphology of this highly dynamic and extremely plastic immune cell (Sica and Mantovani, 2012; Schnitzerlein et al., 2025). This limitation was recently highlighted when examining bacterial morphology in response to different antimicrobials. For example, following a 60-minute treatment with different antimicrobials, changes in *Bacillus subtilis* morphology were subtle and failed to distinguish between the antimicrobial classes. The authors hypothesised that the imaging method posed a technical limitation, and therefore adopted time-lapse imaging. Over the course of a 60-minute time-lapse, the effects of different antimicrobials on bacterial morphology and integrity became clearly distinguishable (Ouyang et al., 2022). Similarly, in a zebrafish model of inflammation, individual macrophage morphology was tracked every 2.5 minutes over the course of a 5-hour window (Sipka et al., 2022). Whilst overall differences in morphology were captured as a collective trend over time, there was a large degree of variation between time-points across the 5 hours. Differences between individual macrophages at the same time-point also varied substantially, as evidenced by the large error bars (Sipka et al., 2022). Moreover, this discrepancy between imaging methods highlights the need for time-lapse imaging to determine the morphometric differences between *arg2:GFP-* and *arg2:GFP+* macrophages.

Over the course of a 1-hour window, *arg2:GFP+* macrophages are significantly smaller and more circular, indicating an amoeboid shape with fewer branches, as well as being faster than the nearest *arg2:GFP-* neighbour. Macrophage shape is often associated with activation status, yet there is conflicting evidence within the macrophage biology field as to what morphology corresponds to their polarisation. These contrasting observations can be attributed to differences in culture medium (e.g. RPMI 1640 and DMEM), the cell line (e.g. human, murine, THP-1) and how the macrophages are polarised *in vitro* (Antonsen et al., 2023; Aldo et al., 2013; Schnitzerlein et al., 2025; Hind et al., 2016; Hourani et al., 2023; Rey-Giraud et al., 2012). Despite these challenges, there are various published reports quantifying the phenotype of polarised macrophages that would suggest that *arg2:GFP+* macrophages resemble *in vitro* M2c polarised macrophages. Murine RAW 264.7 cells polarised towards M1 (IFNγ + LPS) were large, with pseudopods creating irregular shapes (Hourani et al., 2023). M2c polarised macrophages (IL-10 + TGF-β) were smaller and more circular (Hourani et al., 2023). Similarly,

M1 polarised human MDMs (IFNγ + LPS) were large and elongated, with M2c MDMs being much smaller and rounder (Rey-Giraud et al., 2012). Whilst IL-10/TGF-β are the most common polarising agents to achieve M2c macrophages, cAMP has also been shown to induce an M2c profile (Negreiros-Lima et al., 2020; Koscsó et al., 2013). This is of note as *ex vivo* carp monocytes polarised with LPS (M1) were also described as being large and irregular in shape, whereas cAMP polarised monocytes were much smaller and rounder (Wentzel et al., 2020). In a larval zebrafish tail fin transection model, the authors observed changes in macrophage morphology that contrast my findings. At wound healing stages, they found an increase in macrophage perimeter and a decrease in circularity index (Sipka et al., 2022). However, macrophage migration in this inflammation model is drastically different to the localised infection model in this thesis, as cell motility to the distal injury site will dictate changes in morphology (Kołodziej et al., 2023). The authors also did not confirm whether this population of macrophages represents an anti-inflammatory population, as this conclusion was extrapolated from their previous qRT-PCR dataset of FACS-purified *tnfa*+ and *tnfa*- macrophages following tail fin amputation (Nguyen-Chi et al., 2015).

Analysis of morphology indicates that *arg2:GFP*+ macrophages may be labelling a population of anti-inflammatory macrophages, and this hypothesis is further supported by the behavioural differences observed, with *arg2:GFP*+ macrophages also being significantly faster. M1 polarised primary human macrophages (IFNγ + LPS) on polyacrylamide gels were found to be significantly less motile and much slower than M2 polarised macrophages (IL-4) (Hind et al., 2016). Similarly, peritumoral macrophages, which are macrophages located around the edges of tumours and are often attributed as being M2-like, were found to have higher migration velocity, as well as having a rounder shape (Gui et al., 2018). Collectively, these morphological and behavioural characteristics suggests that *arg2:GFP+* macrophages most closely resemble M2c polarised macrophage. This observation is particularly interesting given that IL-10, a defining cytokine of the M2c phenotype, is regulated by arginase 2 (Dowling et al., 2021). However, conflicting reports in the literature regarding the relationship between macrophage polarisation and morphology preclude a definitive classification of *arg2:GFP+* macrophages as a discrete anti-inflammatory macrophage populations based solely on phenotypic analyses.

To further assess the identity of *arg2*+ macrophages at the transcriptional level, preliminary scRNAseq was performed. Interpretation of these data is necessarily cautious, as the dataset was underpowered due to a combination of technical and experimental limitations. These included the failure of one sequencing chip and the use of suboptimal developmental timepoints (2 dpf), when macrophage numbers are still relatively low. While 1 dpi is appropriate for capturing infection-associated transcriptional responses, it does not correspond to the peak abundance of *arg2:GFP+* macrophages identified by confocal imaging at 3 dpi. Despite these limitations, the transcriptomic

analysis revealed suggestive trends indicating that *arg2*+ macrophages preferentially express genes associated with anti-inflammatory macrophage phenotypes, alongside lower expression of pro-inflammatory-associated genes. These trends were observed when *arg2*+ macrophage transcriptional profiles were compared with signatures reported for larval *Mm*-infected zebrafish macrophages, *Mm*-induced epithelioid macrophages in adult zebrafish granulomas, and *ex vivo* M2-polarised carp macrophages (Rougeot et al., 2019; Cronan et al., 2021; Wentzel et al., 2020). Although preliminary, these findings are consistent with the phenotypic data and support the hypothesis that *arg2:GFP+* macrophages represent a macrophage population with anti-inflammatory characteristics. Taken together, the combined evidence from morphometric and behavioural analyses, expression of a canonical M2-associated marker (*arg2*), virulence-dependent upregulation of *arg2* during *Mm* infection, and preliminary transcriptomic trends supports the hypothesis that *arg2:GFP+* macrophages – particularly within the larval *Mm* infection model – constitute a population of macrophages with anti-inflammatory functions aimed at modulating host inflammation. This interpretation is further supported by RNA-seq analysis of human wound tissue, which suggests that M2c macrophages play a role during the early stages of wound healing (Lurier et al., 2017).

Despite the insights gained from the experiments within this chapter, several limitations should be acknowledged. Morphological analysis of macrophages in the timelapse data was performed manually on a frame-by-frame basis, which inevitably introduces the potential for user bias and measurement error. Unfortunately, attempts to automate this process using segmentation algorithms, such as Cellpose, were unsuccessful due to the relatively dim fluorescence of *arg2:GFP+* macrophages, particularly when compared to brighter cell types such as neutrophils or ionocytes (Stringer et al., 2021). To attempt to minimise bias, all morphological measurements were completed prior to plotting. This approach appeared effective, as changes in *arg2:GFP*- macrophage morphology were not detected over time, suggesting that observed phenotype shift following *arg2:GFP* expression were biologically genuine.

A significant limitation of the findings presented in this chapter is the scRNAseq dataset, which was underpowered. Although the transcriptional landscape of *arg2*+ macrophages appears to favour an anti-inflammatory programme, only 3.1% of *mfap4*+ macrophages were *arg2*+ across all conditions (27 out of 888 cells). In addition, the analysis was restricted to a custom subset of pro- and anti-inflammatory-associated genes due to time constraints. Consequently, these data are insufficient to conclusively determine whether *arg2*+ macrophages transcriptionally represent a bona fide anti-inflammatory macrophage population. To robustly address this question, the scRNAseq experiment would need to be repeated with increased sequencing depth and appropriate biological replication. This would include sequencing at least two chips to generate robust biological replicates, thereby enabling the identification of DEGs between *arg2+* and *arg2*- macrophages, both within and across

experimental conditions. Furthermore, larval dissociation should be performed at 3 dpi to maximise the capture of *arg2+* macrophages. Collectively, these refinements would allow for a more comprehensive and unbiased assessment of the transcriptional identity of *arg2+* macrophages.

In conclusion, this chapter provides a comprehensive characterisation of macrophage expression of a canonical pro-inflammatory (*tnfa:GFP*) and anti-inflammatory (*arg2:GFP*) markers in *Mm* infection. A high proportion of macrophages upregulate *tnfa:GFP* from 1 dpi, with macrophage *arg2:GFP* expression being low at all time-points except at 3 dpi. Careful quantification of macrophage morphology and behaviour over time found that *arg2:GFP+* macrophages are smaller, more circular and faster than *arg2:GFP-* macrophages – characteristics that phenotypically resemble *in vitro* M2c (IL-10) polarised macrophages. Consistent with these phenotypic observations, preliminary single-cell transcriptomic analysis suggests that *arg2+* macrophages preferentially express anti-inflammatory-associated genes. Together, these analyses add confidence that the *arg2:GFP* transgenic reporter labels a population of anti-inflammatory macrophages. Furthermore, infection with heat-killed and attenuated *Mm* (ΔRD1) demonstrated that the macrophage tnfa response is PAMP-driven and MyD88-independent, whereas the *arg2* response relies on secreted virulence factors and is MyD88-dependent. This chapter provides the first *in vivo* visualisation of mycobacteria-mediated modulation of macrophage phenotype, while also offering insight into some of the mechanisms underlying this modulation.

4. Putative pro-inflammatory macrophages upregulate *arg2:GFP* local to the infection site

Some of the data in this chapter (section 4.2.1.) was published as:

Bastos T.S.B.*, Loynes C.A.*, **Speirs Z.C.***, de Lima J.D., Junior L.W., de Paula A.G.P., Czaikovski A.P., Luz R.B.S., Paredes L.C., Norris M., Tomlinson G.S., de Rocha W.D., Renshaw S.A., Elks P.M., Braga T.T.. Loss of Cathepsin Z enhances pro-inflammatory macrophage responses and promotes tissue regeneration in zebrafish. **In Press, *Disease Models & Mechanisms***. *Authors contributed equally to this work.

4.1. Introduction

4.1.1. Macrophage activation states: beyond the M1/M2 dichotomy

Macrophages exhibit substantial transcriptional plasticity *in vivo*, enabling them to respond dynamically to local microenvironmental cues during infection. While classical *in vitro* polarisation systems impose binary M1 or M2 identities, macrophage activation states are now understood to exist along a continuum, with the capacity for dynamic switching rather than fixed terminal fates. Consistent with this plasticity, *in vitro* studies demonstrate that pro-inflammatory macrophages can adopt anti-inflammatory programmes in response to changing environmental conditions. For example, during skeletal muscle regeneration and within tumour microenvironments, pro-inflammatory macrophages have been shown to transition toward an anti-inflammatory phenotype (Arnold et al., 2007). Genome-wide transcriptional profiling reinforces this plasticity: bulk and single-cell RNA sequencing of a human leukaemia cell line (HL-60) demonstrated that canonical M1/M2 markers are transiently expressed, and that subsets of M2-polarised macrophages can re-polarise towards an M1-like phenotype while retaining M2-specific genes (Carvalho et al., 2021).

Infectious stimuli can also modulate macrophage activation status. For instance, *Thelazia callipaeda*-derived macrophage inhibitory factor (MIF) shifts THP-1 macrophages from an M1- to an M2-like profile, suppressing CD86 and *TNF-*α expression, while increasing CD206 and *Arg1* expression (Yin et al., 2023). Conversely, the *Mtb* virulence factor ESAT-6 induces an early pro-inflammatory programme in human MDMs, followed by suppressed TNF-α and IL-12 production, while increasing IL-10, illustrating pathogen-driven re-polarisation (Refai et al., 2018). However, differences in macrophage ontogeny (human vs. murine), primary vs. immortalised cells, and culture conditions lead to inconsistent findings. This is exemplified by species-specific differences in macrophage responses to *Mtb* infection (Dill-McFarland et al., 2025). Advanced *in vitro* platforms, such as organoids and 3D cultures, attempt to more closely recapitulate TB infection. Recent work developed a lung organoid containing human MDMs, finding that *Mtb* increased expression of IL-6, TNF-α and IL-10, indicative of a mixed M1/M2 phenotype (Kim et al., 2024). Yet these patterns often fail to predict *in vivo* outcomes.

For example, pharmacological arginase inhibition reduced *Mtb* load in RAW 264.7 macrophages, but not in infected mouse lungs (Chauhan et al., 2024).

In vivo, macrophage activation is even more complex. Multiple pathological environments – including chronic inflammation, infection and atherosclerosis – contain macrophages that co-express M1 and M2 markers, challenging the binary model. In human carotid plaques from stroke patients, the dominant macrophage population is CD68+ CD86+ MRC1+, exhibiting simultaneous expression of classical M1 and M2 markers (Kocsy, 2021; Kocsy et al., 2025). Similar mixed phenotypes are detected in bronchoalveolar lavage fluid from patients with lower respiratory infections and *Mycobacterium avium* complex disease (Ikegami et al., 2022). In TB granulomas from humans and macaques, ARG1 and iNOS are frequently co-expressed within CD68+ macrophages, and ARG1 co-localises with HLA-DR – traditionally an M1 marker – in human TB lymph node granulomas (Mattila et al., 2013; Ashenafi et al., 2022).

Crucially, these static *ex vivo* observations cannot determine whether such mixed-marker macrophages represent: (1) macrophages actively transitioning between activation states; (2) stable intermediate or hybrid phenotypes; or (3) distinct macrophage subsets recruited sequentially during infection. The inability to capture temporal dynamics remains a central limitation in the field.

4.1.2. A critical gap: where do polarised macrophages come from?

A fundamental question in TB immunobiology is whether polarised macrophages in granulomas arise through local *in situ* repolarisation or through recruitment of distinct monocyte/macrophage subsets. The general consensus in the TB field is that anti-inflammatory macrophages originate from local reprogramming, most supporting evidence comes from computational trajectory analyses rather than direct temporal observations. In human TB lung granulomas, pseudotime analysis predicts that alveolar macrophages transition into tissue remodelling, M2-like macrophages within the granuloma (Pyle et al., 2025). Similarly, trajectory analysis of granulomas from *Mtb*-infected macaques suggested that these structures are dominated by extravasated monocytes that subsequently polarise towards an M2-like phenotype (Pisu et al., 2025). While this supports monocyte-to-macrophage differentiation, it does not address whether resident macrophages themselves dynamically re-polarise from early pro-inflammatory states to later anti-inflammatory ones.

Additional lines of evidence hint at local reprogramming. Human TB lymph node granulomas show CD68+ macrophages co-expressing E-cadherin, consistent with macrophage-to-epithelioid transitions induced by *Mtb* (Cronan et al., 2016). In mice, spatial multiomics suggests that *Arg1*+ macrophages migrate into necrotising granulomas and differentiate into foamy macrophages (Seto et al., 2022). This is consistent with mouse and human data showing Arg1+ macrophages enriched in

hypoxic, caseating granuloma cores and linked to foamy phenotypes and IL-13/IL-4Rα-driven pathology (Duque-Correa et al., 2014; Pessanha et al., 2012; Heitmann et al., 2014). These studies demonstrate that macrophages can adopt specialised functional states within infected tissues. However, whether analogous transitions occur for classical activation programmes – specifically, whether pro-inflammatory macrophages can repolarise into anti-inflammatory macrophages *in vivo* – remains unresolved. The current data only show that mixed-marker macrophages exist; they do not establish whether these are repolarising cells, stable hybrid states, or independently recruited subsets. Critically, none of these models provide direct temporal resolution, and therefore cannot reveal the real-time trajectories of individual macrophages. Despite advances in imaging and spatial omics, visualising pro- to anti-inflammatory transitions *in situ* has not yet been achieved in mammalian systems. This gap underscores the need for dynamic *in vivo* models capable of following macrophage phenotypic changes over time – an area where zebrafish offers unique advantages.

4.1.3. Leveraging the zebrafish model to resolve macrophage polarisation dynamics

Zebrafish provide a uniquely powerful *in vivo* system for visualising macrophage dynamics with high spatial and temporal resolution. Transcriptional profiling in both larvae and adults demonstrates that zebrafish macrophages, like their mammalian counterparts, occupy a broad activation spectrum. Single-cell RNA sequencing (scRNAseq) of adult *mpeg1.1+* cells identified a pro-inflammatory *lgals3bpb+* macrophages population enriched for genes associated with phagocytosis (e.g.: *cxcl8a*, *mhc22dab*), alongside an anti-inflammatory *ccl34a.4+* subset enriched for tissue repair genes (e.g.: *grn1*, *mrc1b*) (Zhou et al., 2023). The presence of these macrophage clusters enriched for canonical M1- and M2-associated gene modules supports the presence of distinct activation states *in vivo*. In larval *Mm* infection, macrophages initially upregulate classical pro-inflammatory genes, such as *tnfa* and *cxcl11aa*, while downregulating M2-associated genes including *tgfb1a* and *il10*, consistent with an early M1-like response (Rougeot et al., 2019). At later stages of infection, however, zebrafish granulomas exhibit a shift toward type-2 associated transcriptional programmes, including upregulation of M2-associated markers, such as *arg2*, in epithelialized macrophages – mirroring M2-like differentiation described in mammalian TB granulomas (Cronan et al., 2021).

In vivo reporter systems have provided initial insight into these dynamics. The *tnfa:GFP* line robustly labels putative pro-inflammatory macrophages following injury and *Mm* infection (Nguyen-Chi et al., 2015; Lewis and Elks, 2019). Quantitative RT-PCR (qRT-PCR) of sorted *tnfa:GFP+* and *tnfa:GFP-* macrophages revealed enrichment of M1-associated transcripts in *tnfa+* cells (*il1b, il6*) and relative enrichment of some M2-associated transcripts in *tnfa-* cells (*tgfb1, ccr2*), suggesting that these populations broadly reflect opposing inflammatory states (Nguyen-Chi et al., 2015). However, absence of *tnfa:GFP* expression does not equate to a defined anti-inflammatory phenotype. In fact, *tnfa-* macrophages encompass a heterogenous mixture of states. A recent scRNAseq study exemplifies this

complexity. Following neomycin-induced hair cell injury, *mpeg1:GFP+* macrophages displayed modest induction of *il1b* and no *tnfa* expression in early 'effector' states, yet subsequently transitioned into strongly anti-inflammatory and reparative states characterised by upregulation of *il10ra, il4r.1, odc1* and *grn2* (Denans et al., 2022). These findings demonstrate that *tnfa*- macrophages cannot be assumed to be M2-like, and instead may represent multiple transient activation states, including early pro-inflammatory effectors, potential intermediate hybrid states, and later reparative phenotypes. Consequently, while *tnfa:GFP* marks one end of the activation spectrum, it does not resolve the diversity, or temporal transitions, of anti-inflammatory macrophages *in vivo*.

Real-time analysis of macrophage immunometabolism using fluorescence lifetime imaging microscopy (FLIM) further demonstrated that *tnfa:GFP*+ and *tnfa:GFP*- macrophages further demonstrates functional polarisation. Measurements of nicotinamide adenine dinucleotide (phosphate) (NAD(P)H) and flavin adenine dinucleotide (FAD) lifetimes *in vivo* revealed clear metabolic differences between these populations consistent with distinct metabolic programmes (Miskolci et al., 2022). These findings support the interpretation that macrophage subsets *in vivo* exhibit genuine functional polarisation beyond transcriptional differences. Morphological analysis have also been interpreted as evidence of phenotype switching. *tnfa*+ macrophages arriving at tail-fin wounds transition from amoeboid to elongated morphologies and alter migratory behaviour (direct to reverse/circular migration) (Sipka et al., 2022; Nguyen-Chi et al., 2015). While these features have been interpreted as potential transitions toward a reparative phenotype, they may instead reflect movement-associated dynamics, driven by directed migration toward the wound, rather than bona fide acquisition of an anti-inflammatory phenotype. However, direct *in vivo* evidence demonstrating whether *tnfa+* macrophages undergo re-polarisation into anti-inflammatory states remains limited.

In the context of *Mm* infection, *tnfa:GFP* and *il1β:GFP* are strongly induced in macrophages at early stages of infection, demonstrating that these reporters effectively label putative pro-inflammatory macrophages in larvae during mycobacterial infection (Lewis and Elks, 2019; Ogryzko et al., 2019). Yet defining anti-inflammatory macrophages remains challenging. Previous studies inferred the identity of anti-inflammatory macrophages primarily by absence of *tnfa* expression, changes in morphology/migration or limited qRT-PCR panels assessing only a handful of canonical M1/M2 markers (Nguyen-Chi et al., 2015; Sipka et al., 2022). Notably, this panel included *arg1* – an arginase isoform minimally expressed in zebrafish macrophages – but did not examine *arg2*, the physiologically relevant and dominant teleost arginase (Nguyen-Chi et al., 2015; Hammond et al., 2023; Wentzel et al., 2020). As a result, *tnfa*- macrophages cannot be confidently categorised as resting, transitioning, or genuinely anti-inflammatory. More broadly, although zebrafish studies clearly show that macrophages can alter their transcriptional and functional phenotypes in response to microenvironmental cues, the field has lacked tools capable of visualising pro- and anti-inflammatory states simultaneously and in real time.

In Chapter 3, I demonstrated that *arg2:GFP* labels a small but distinct subset of macrophages that phenotypically resemble anti-inflammatory macrophages (smaller, rounder and faster than *arg2:GFP*- macrophages) during *Mm* infection. This now provides an opportunity to directly address a central unresolved question in macrophage biology: are pro- and anti-inflammatory macrophages *in vivo* sequentially recruited as distinct populations, or can individual macrophages dynamically re-polarise within infected tissue?

4.1.4. Hypothesis and aims

Previous studies have suggested that pro-inflammatory macrophages re-polarise towards an anti-inflammatory phenotype during later stages of infection, often inferred from transcriptional profiling of infected *in vitro* macrophages or immunohistochemical characterisation of *ex vivo* granulomas (Mattila et al., 2013; Larenas-Muñoz et al., 2024; Huang et al., 2015; Mizutani et al., 2023). However, direct *in vivo* evidence clarifying whether the accumulation of anti-inflammatory macrophages during mycobacterial infection results from *in situ* re-polarisation of pro-inflammatory macrophages or recruitment of pre-polarised anti-inflammatory macrophages remains limited (**Fig. 4.1.**).

I hypothesise that putative pro-inflammatory macrophages are initially recruited to *Mm* infection sites, and that this same population subsequently upregulates *arg2:GFP* expression and adopts anti-inflammatory characteristics during later stages of pathogenesis, driven by cues within the local tissue microenvironment.

To investigate this hypothesis, I will use zebrafish transgenic reporter lines in combination with live timelapse imaging to address the following aims:

- To generate and validate a stable *tnfa:mCherry-F* transgenic reporter line for use alongside the *arg2:GFP* line.
- To determine whether macrophages upregulate *arg2:GFP* local to the *Mm* infection site or are recruited to infection sites already expressing *arg2:GFP*.
- To visualise and characterise the spatiotemporal dynamics of *tnfa:mCherry-F* and *arg2:GFP* expression in immune cells during *Mm* infection.

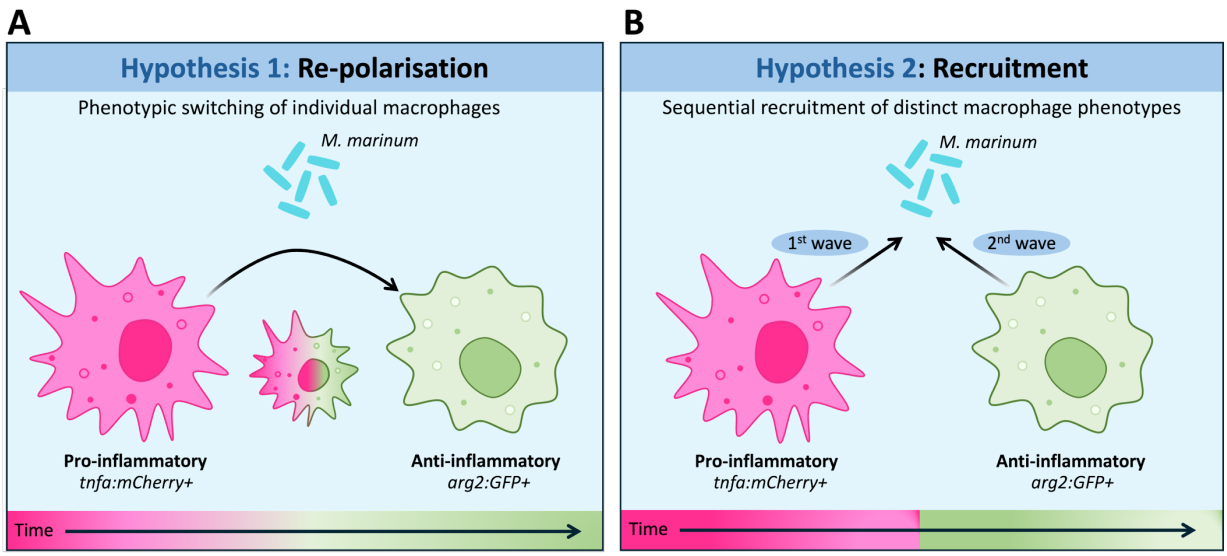


Figure 4.1. Two alternative hypotheses for the mechanisms underlying how macrophage phenotypes transition during mycobacterial infection. (**A**) Re-polarisation hypothesis: individual macrophages undergo a phenotypic switch from a pro-inflammatory to an anti-inflammatory state over time during *Mm* infection. (**B**) Recruitment hypothesis: distinct pro- and anti-inflammatory macrophage subtypes are recruited at different stages of infection. Initially, pro-inflammatory macrophages are recruited (1^{st} wave), followed by recruitment of pre-polarised anti-inflammatory macrophages at later stages (2^{nd} wave), resulting in a temporal shift in the overall macrophage phenotype composition. To test these hypotheses, transgenic reporter lines are used to visualise putative pro-inflammatory (*tnfa:mCherry*) and anti-inflammatory (*arg2:GFP*) macrophages.

4.2. Results

4.2.1. Generating a *tnfa:mCherry* transgenic line to visualise macrophage *tnfa* and *arg2* expression simultaneously

Current zebrafish *tnfa* transgenic reporter lines drive expression of GFP in putative pro-inflammatory macrophages during immune challenge, with the *TgBAC(tnfa:GFP)* line being available at the University of Sheffield (Marjoram et al., 2015). Whilst this transgenic line has provided valuable insight into the macrophage pro-inflammatory response during mycobacterial infection (see section 3.3.1.), the ability to visualise both macrophage pro- and anti-inflammatory dynamics within the same fish is not possible due to both reporters driving expression of GFP. Thus, I aimed to generate a promoter driven *tnfa:mCherry* transgenic reporter line using the *tnfa:eGFP-F* and *mfap4:mCherry-F* plasmids, which were a kind gift from the Nguyen-Chi group (Nguyen-Chi et al., 2015; Nguyen-Chi et al., 2020).

Following subcloning through restriction digest and PCR modification, the full-length *tnfa:mCherry-F* plasmid (hereon in termed *tnfa:mCherry*) was sequenced to validate the construct and identify whether any unintended genetic modifications were present (**Fig. 4.2. A**). Similar to the original *tnfa:GFP* plasmid, the 8380-base pair (bp) plasmid contained the zebrafish *tnfa* promoter of approximately 3.8 kilobases (kb). The *tnfa* promoter was PCR-amplified to exclude the endogenous ATG start codon and intronic sequence, thereby ensuring that the downstream farnesylated mCherry coding sequence was in-frame. The promoter, mCherry and poly(A) tail are flanked by I-SceI meganuclease sites (**Fig. 4.2. A**). Since I-SceI sites are not naturally present in vertebrate genomes, including that of zebrafish, I-SceI-mediated transgenesis eliminates the risk of genome fractionation and DNA linearisation leads to more efficient germline integration of transgenes (Thermes et al., 2002; Soroldoni et al., 2009). The plasmid was co-injected with I-SceI enzyme into the single-cell stage of the fish embryo and a tail fin transection performed to assess *tnfa:mCherry* expression at 20 hours post-amputation (hpA). F0 embryos that specifically expressed *tnfa:mCherry* in cells with macrophage morphology at the wound site were identified, and raised to adulthood (**Fig. 4.2. B**).

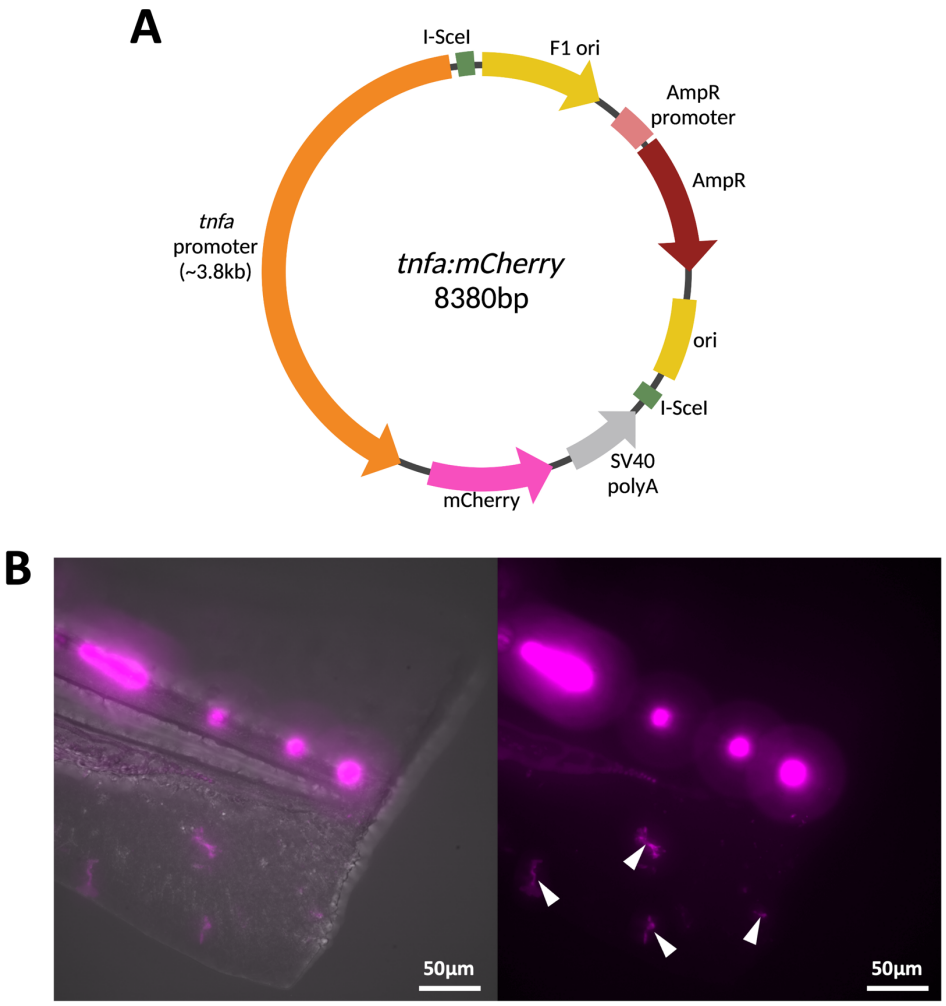


Figure 4.2. *tnfa:mCherry* F0 generation expresses the transgene in cells with macrophage morphology at the wound site following tail fin transection. (**A**) Plasmid map of *tnfa:mCherry*, including the promoter region, farnesylated mCherry, I-SceI sites and antibiotic resistance. Created using BioRender.com (publication licence agreement number CG271K8BA0). (**B**) Representative widefield image (10x magnification) of mCherry+ cells with macrophage morphology at the wound site 20 hours post-amputation (hpA; 4 dpf). Scale bars are stated on the images.

The F0 generation was outcrossed with a wildtype zebrafish (nacre) line and F1 progeny screened for specific expression of mCherry in macrophage-like cells following a tail fin transection in order to identify founder fish. Offspring from founder fish demonstrated robust recruitment of *tnfa:mCherry*+ cells with macrophage morphology to the injury site at 20 hpA (**Fig. 4.3. A**). To confirm that these mCherry+ cells were indeed macrophages, founder fish were outcrossed with *mpeg:nlsClover*, a transgenic line that labels macrophage nuclei. At 20 hpA, all *tnfa:mCherry+* cells also co-localised with subpopulation of *mpeg:nlsClover*+ cells, demonstrating that the *tnfa:mCherry* transgenic line reliable labels putative pro-inflammatory macrophages (**Fig. 4.3. B**).

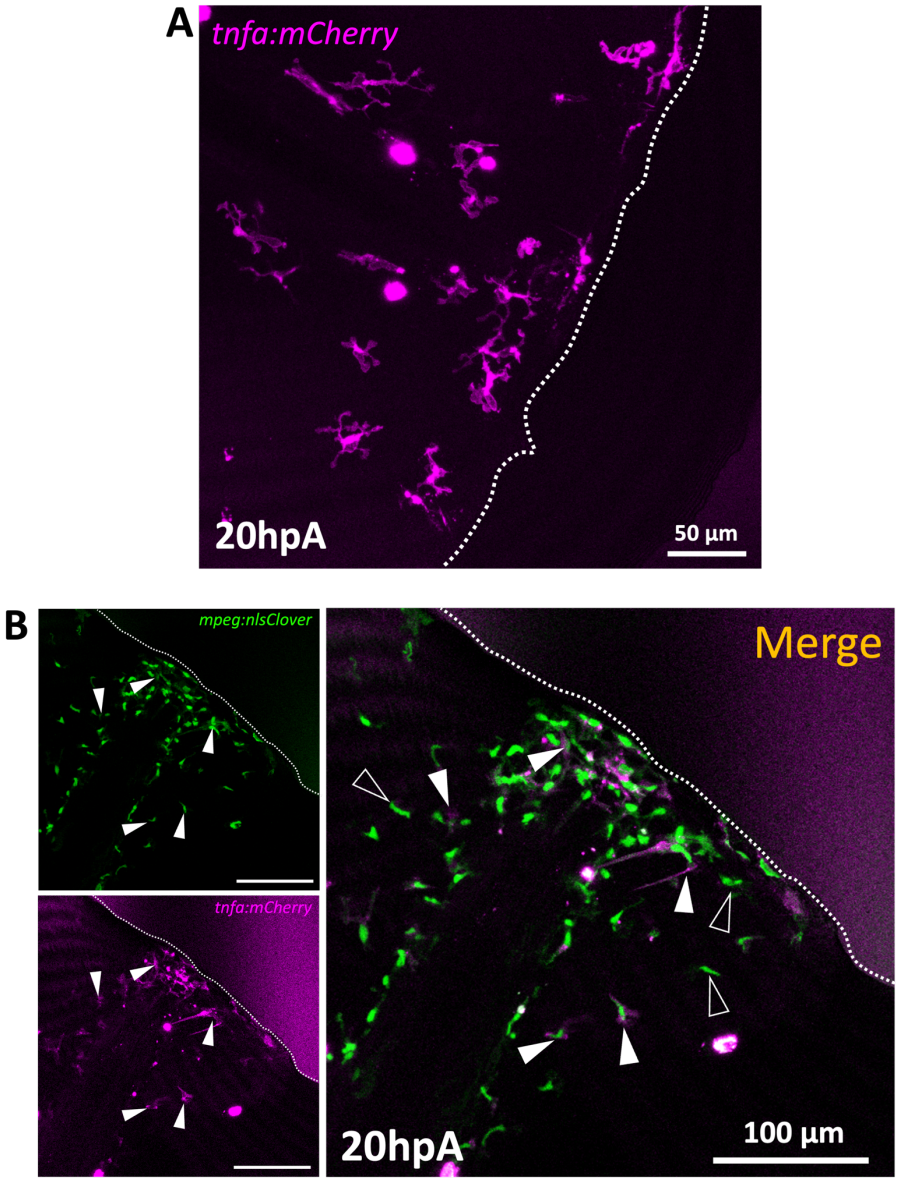


Figure 4.3. A specific subset of macrophages express *tnfa:mCherry* following tail fin transection in F1 progeny. (**A**) Representative confocal image (20x magnification) of mCherry+ cells with macrophage morphology at the injury site at 20 hpA in F1 offspring. (**B**) Representative confocal image (10x magnification) illustrating co-localisation of *tnfa:mCherry+ mpeg:nlsClover+* macrophages at the injury site at 20 hpA. Hollow arrowheads indicate *tnfa:mCherry- mpeg:nlsClover+* cells. Filled arrowheads indicate *tnfa:mCherry+ mpeg:nlsClover+* cells. Scale bars are stated on the images.

The *tnfa:mCherry* transgenic line was further characterised to determine whether its expression was comparable to the *tnfa:GFP* promoter transgenic the plasmid was cloned from. Approximately a 1-hour timelapse of a *tnfa:mCherry+ mpeg:nlsClover* fish was performed to capture the 6 hpA time-point (up to 7 hpA), which is the time-point at which *tnfa:GFP+* cells was found to increase significantly (**Fig. 4.4. A**) (Nguyen-Chi et al., 2015). At 6 hpA, 16.6% of *mpeg:nlsClover+* macrophages were also positive for *tnfa:mCherry* (**Fig. 4.4. B**). This proportion is similar to the approximately 20% of *tnfa:GFP+* macrophages previously identified at 6 hpA (Nguyen-Chi et al., 2015).

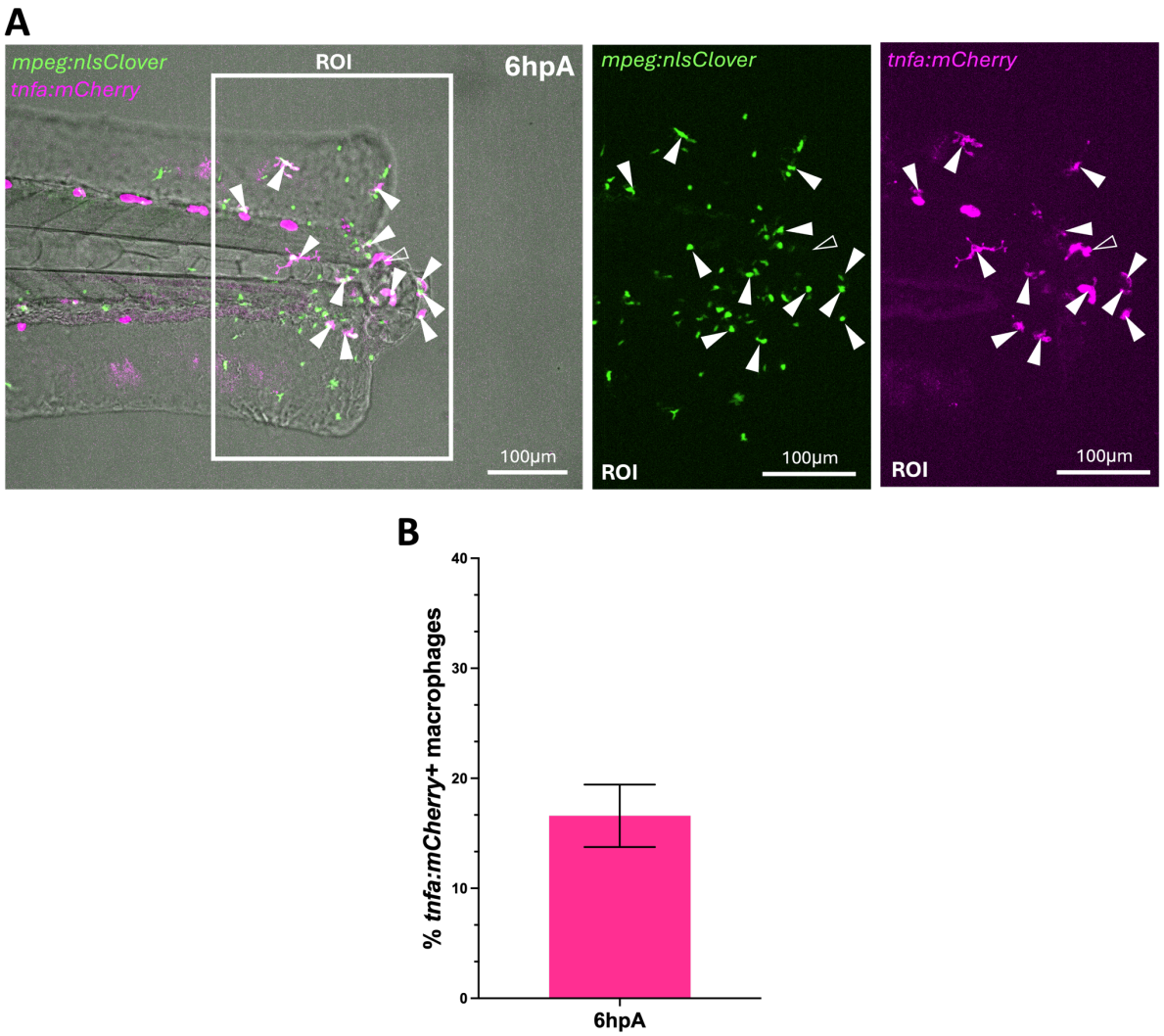


Figure 4.4. Approximately 20% of macrophages upregulate *tnfa:mCherry* at 6 hpA. (**A**) Representative frame (maximum projection) of a timelapse of a *tnfa:mCherry+ mpeg:nlsClover+* larvae at 6 hpA. White ROI box indicates the area of the wound site where macrophages were quantified, with ROI area in the GFP and mCherry channels illustrated to the right. Filled arrowheads indicate *tnfa:mCherry+ mpeg:nlsClover+* macrophages. Hollow arrowhead indicates a *tnfa:mCherry+ mpeg:nlsClover-* cell. (**B**) Graph illustrating the percentage of *tnfa:mCherry+* macrophages identified in the ROI at 6 hpA. Error bars depict SEM. Timelapse time steps were 3 minutes. Scale bar is stated on the image in (**A**). N=6 larvae from 1 independent experiment.

The morphology of *tnfa:mCherry+* macrophages was also assessed, as *tnfa:GFP+* macrophages were previously described as being flattened and lobulated. By zooming in on individual *tnfa:mCherry+* macrophages in the timelapse, morphology could easily be determined due the farnesylated mCherry (**Fig. 4.5. A**). Indeed, *tnfa+* macrophages appeared flattened (**Fig. 4.5. B**; first time-stamp) and there were clear examples of having lobulated morphology (**Fig. 4.5. B**; last timestamp). Together, these data demonstrate that this novel *tnfa:mCherry* transgenic line performs similarly to the *tnfa:GFP* promoter transgenic.

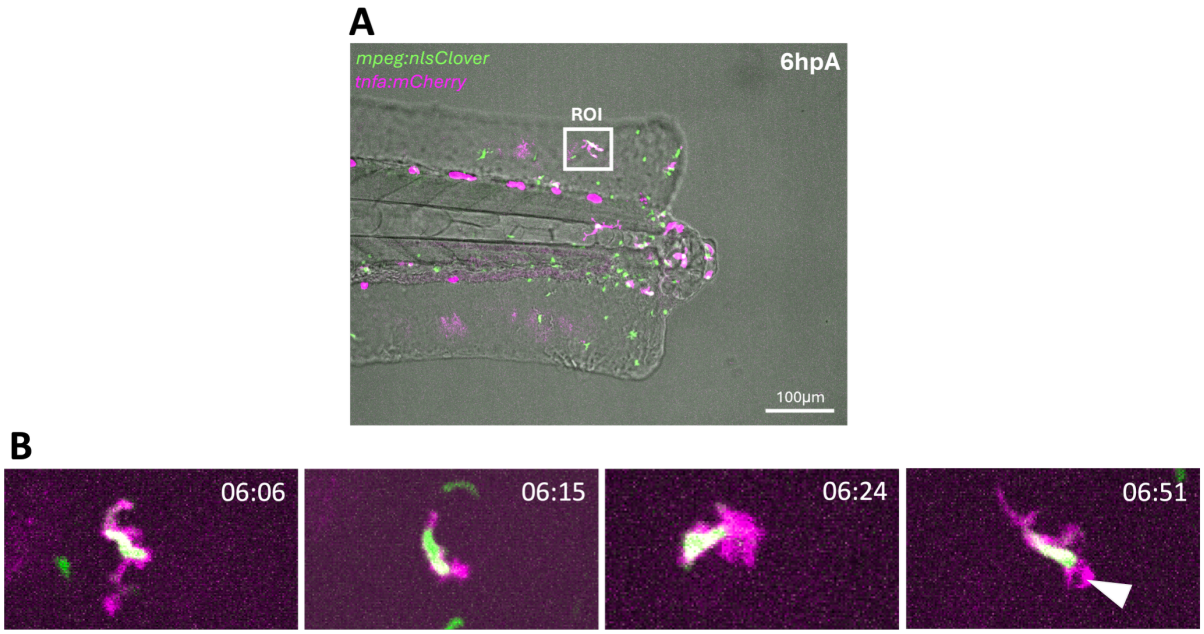


Figure 4.5. *tnfa:mCherry+* macrophages have a flattened and lobulated morphology (**A**). Representative frame (maximum projection) of a timelapse of a *tnfa:mCherry+ mpeg:nlsClover+* larvae at 6 hpA. (**B**) Zoomed area of a *tnfa:mCherry+ mpeg:nlsClover+* macrophage, spanning from 6 minutes (6 hours and 6 minutes post-amputation) up to 51 minutes (6 hours and 51 minutes post-amputation). Timelapse time steps were 3 minutes. White ROI box in (**A**) indicates the zoomed in *tnfa+* macrophage illustrated in (**B**). Scale bar is stated on the still image in (**A**). N=6 larvae from 1 independent experiment.

In order to raise embryos for the next generations without the need for a tail fin transection, expression of the transgene under resting conditions was determined. In the first instance, expression of the transgene was first assessed in the larval gut, as the transgene is expressed in this organ in the *TgBAC(tnfa:GFP)* available at the University of Sheffield under resting conditions (Marjoram et al., 2015). Only autofluorescence was detected in the gut of *tnfa:mCherry+* uninjured larvae at 4 dpf (which corresponds to 20 hpA) (**Fig. 4.6. B**). This was comparable to the gut of nacre embryos imaged using the mCherry laser (**Fig. 4.6. A**). The lack of expression in the gut was expected, due to differences between the *TgBAC(tnfa:GFP)* and *Tg(tnfa:GFP)* promoters.

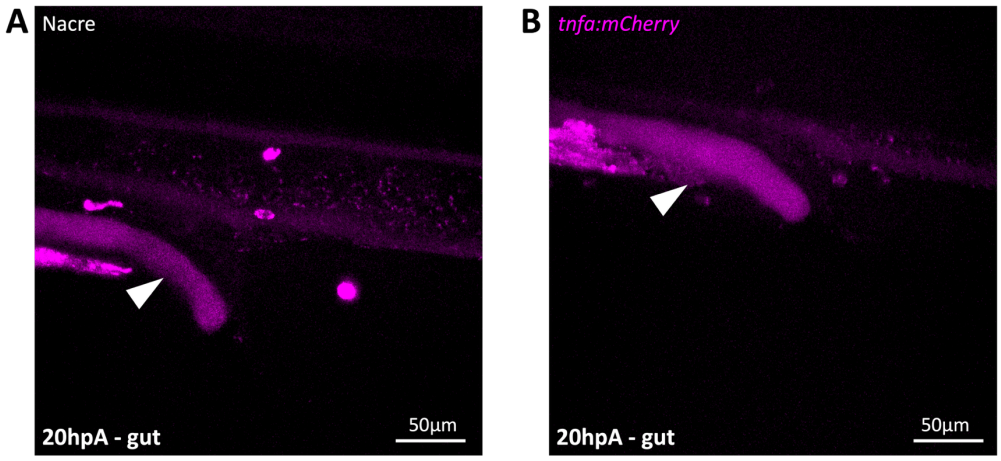


Figure 4.6. *tnfa:mCherry* is not expressed in the gut of F1 progeny under resting conditions. (**A-B**) Representative image of a 4 dpf nacre embryo (**A**) and *tnfa:mCherry+* embryo (**B**) gut imaged under the mCherry laser at the time-point which corresponds with 20 hpA. Filled arrowheads indicate the larval gut. Scale bars are stated on the images. N=6 larvae from 1 independent experiment.

The *Tg(tnfa:GFP)* transgenic line was described as having low levels of GFP expression in the larval pharynx from 3 dpf. Therefore, expression of the mCherry transgene was examined in the pharynx of the F1 offspring under resting conditions. Similar to published observations, the transgene was expressed in the area of the pharyngeal arches (developing gills) of 4 dpf uninjured embryos (**Fig. 4.7. B-C**). However, no mCherry expression was detected in the pharynx of nacre embryos of the same age (**Fig. 4.7. A**). This data indicates that the low level mCherry expression present in the pharynx of unchallenged fish is not due to autofluorescence, as is seen in the gut, and allows for easy screening of progeny.

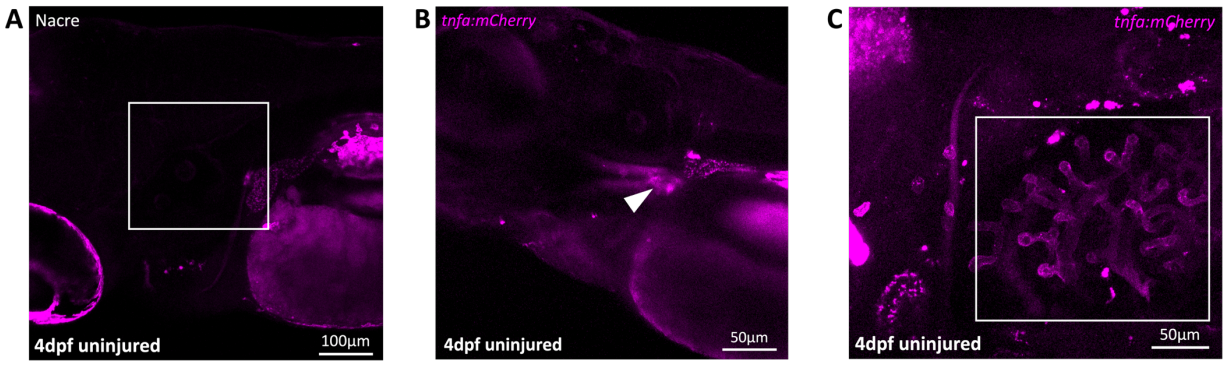


Figure 4.7. Embryos that are *tnfa:mCherry*+ express mCherry in the pharyngeal arches under resting conditions. (**A-B**) Representative confocal images (10x magnification) of the pharynx of nacre (**A**) and *tnfa:mCherry*+ (**B**) embryos at 4 dpf under resting conditions. (**C**) Representative confocal image of the pharynx of *tnfa:mCherry*+ embryo at 20x magnification. White box in (**A**) indicates the location of the pharynx. White arrow in (B) indicates the mCherry+ pharynx. White box in (**C**) highlights the mCherry+ pharyngeal arches (developing gills) at higher magnification. Scale bars are stated on the images. N=6 larvae from 1 independent experiment.

To verify that screening embryos for mCherry expression in the pharynx is a reliable way of selecting *tnfa:mCherry*+ embryos, fish with mCherry- and mCherry+ pharynxes were selected and a tail fin transection performed. As expected, larvae that did not have the transgene present in the pharynx (nacre) did not express mCherry+ cells at the tail fin, both in uninjured and injured conditions (**Fig. 4.8. Ai, Aii**). Meanwhile, larvae screened for mCherry+ pharynx showed recruitment of *tnfa:mCherry*+ cells to the injury site at 20 hpA, while no mCherry expression was detected in the tail fin of uninjured larvae (**Fig. 4.8. Bi, Bii**). Taken together, this data demonstrates that screening embryos for mCherry expression in the pharynx is a reliable means to select for *tnfa:mCherry*+ larvae to raise for subsequent generations.

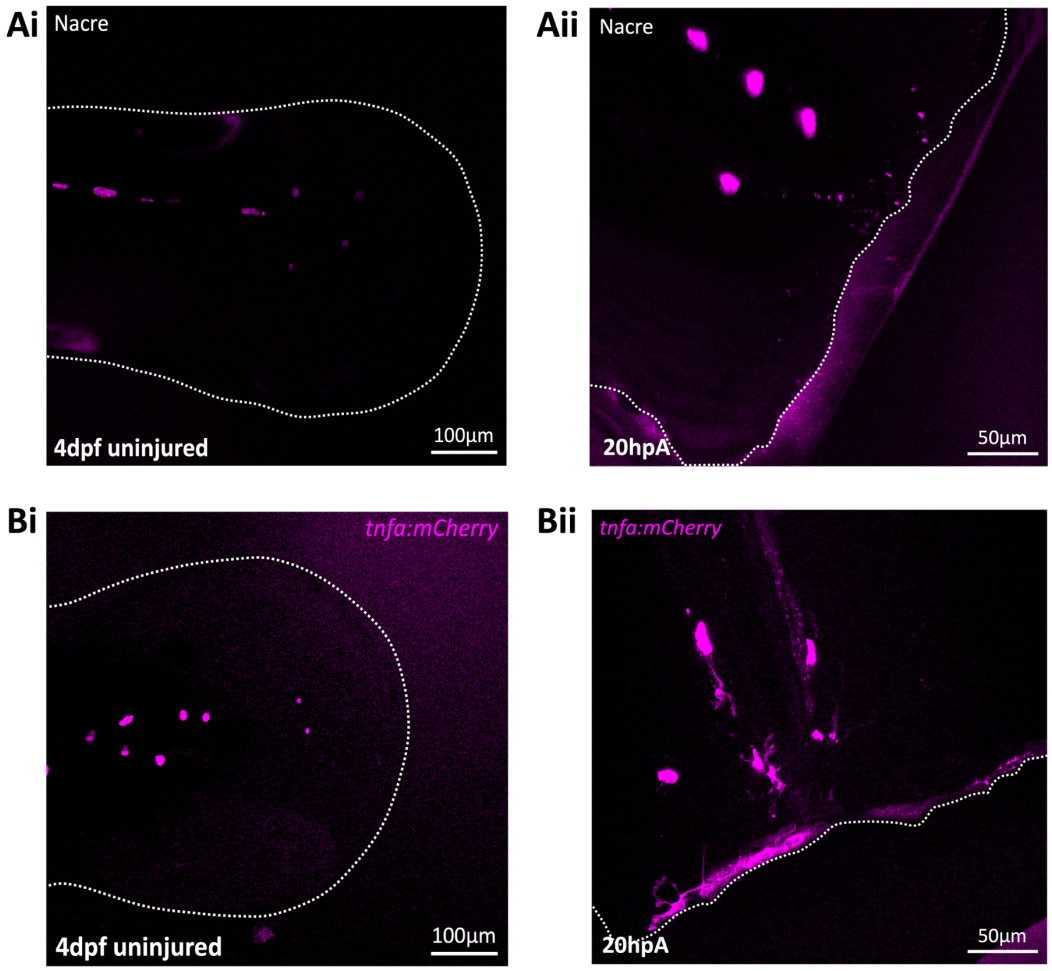


Figure 4.8. Screening embryos for mCherry expression in the pharynx is a reliable way to select *tnfa:mCherry+* larvae. (**A**) Representative confocal images (10x magnification) of a nacre embryo that does not express mCherry in the pharynx, that also does not upregulate *tnfa:mCherry* expression in the tail fin of uninjured (**Ai**) or injured (**Aii**) larvae. (**B**) Representative confocal images (10x magnification) of *tnfa:mCherry*+ embryos that was screened for having an mCherry+ pharynx, with upregulation of *tnfa:mCherry* in macrophage-like cells only detected in injured fish (**Bii**), with no expression identified in uninjured tail fins (**Bi**). Scale bars are stated on the images. N=6 larvae from 1 independent experiment.

As the *TgBAC(tnfa:GFP) and Tg(tnfa:GFP-F*) are different promoters, how similar the *TgBAC(tnfa:GFP)* and *Tg(tnfa:mCherry)* transgenic lines were following tail fin injury was assessed. At 6 hpA, 80% of *tnfa:GFP+* cells were *also tnfa:mCherry+* (**Fig. 4.9. A,B**), with an average of 8 double positive cells identified per larvae (**Fig. 4.9. C**). The BAC promoter is much larger compared to the promoter-driven transgene (50 kb compared to 3.5 kb), meaning that the BAC promoter more closely recapitulates endogenous expression (Marjoram et al., 2015; Nguyen-Chi et al., 2015). It is therefore unsurprising that 15.41% were found to the *tnfa:GFP+ tnfa:mCherry-* (**Fig. 4.9. B**), accounting for approximately 1.5 cells per larvae (**Fig. 4.9. C**). Only 14 cells (4.59%) were *tnfa:GFP- tnfa:mCherry+* (**Fig. 4.9. B**), with less than 1 cell identified in each fish (**Fig. 4.9. C**). While some differences between the *tnfa:GFP* and *tnfa:mCherry* lines are evident, these are likely attributable to the different promoters. Nevertheless, the overall similarity in expression patterns suggests that the findings described in section 3.3.1 characterising the *tnfa:GFP* line in *Mm* infection are also applicable to the *tnfa:mCherry* line.

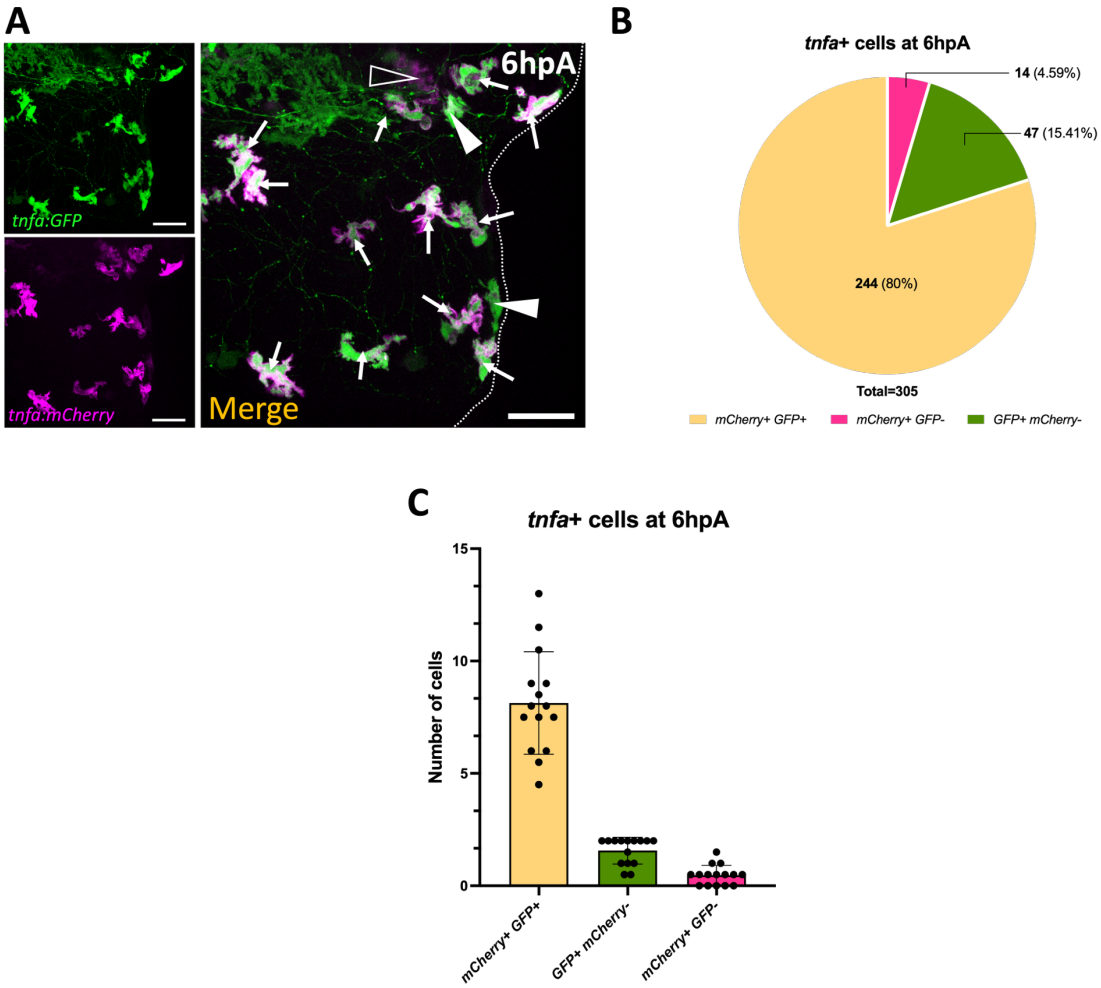


Figure 4.9. The *TgBAC(tnfa:GFP)* and *Tg(tnfa:mCherry-F)* transgenic lines have similar expression patterns following a tail fin injury. (**A**) Representative confocal image (20x magnification) of the tail fin of a *tnfa:GFP+ tnfa:mCherry+* fish at 6 hpA. Arrows indicate double positive cells. Filled arrowhead indicates *tnfa:GFP+ tnfa:mCherry-* cell. Hollow arrowhead indicates *tnfa:GFP- tnfa:mCherry+* cell. The dashed-dotted line indicated the edge of the tail fin wound edge. (**B**) A pie chart illustrating the proportion of the whole population of *tnfa+* cells

that are *tnfa:GFP+ tnfa:mCherry-, tnfa:GFP- tnfa:mCherry+* and double positive. (**C**) A graph illustrating the average number of cells of each category per fish across 2 experiments. Total number of cells in (**B**), both per group and as a whole, are indicated in bold on the graph, with percentages in brackets. Colour keys listed below the pie chart. N=30 fish imaged over 2 independent experiments. Scale bar is 100 μm.

4.2.2. *arg2:GFP* positive macrophages originate from macrophages local to the infection site

Morphological and behavioural analysis of *arg2:GFP+* macrophages during *Mm* infection indicates that *arg2:GFP* expressing macrophages may be labelling an anti-inflammatory macrophage population, as they phenotypically resemble *in vitro* M2c polarised macrophages. Consistent with this phenotypic profile, preliminary scRNAseq suggests that *arg2*+ macrophages exhibit a transcriptional landscape enriched for M2-associated gene expression (see chapter 3, section 3.3.4). There is broad agreement that anti-inflammatory macrophages arise through local polarisation within the infected tissue. Yet, until now, this process has not been directly visualised *in vivo.*

Whilst rare, the timelapses also captured some *arg2:GFP*- macrophages that began expressing *arg2:GFP* at a later time point (**Fig. 4.10.**). These cells could be tracked throughout the time they were in frame, enabling investigation of whether *arg2:GFP*+ macrophages are recruited or arise locally through *in situ* polarisation.

Over the course of the 10-hour timelapse, 12 macrophages that were initially *arg2:GFP*- later expressed *arg2:GFP* (**Fig. 4.10. A**). An example of one of these transitioning macrophages can be seen in **Fig. 4.10. B**. where a macrophage is initially *arg2:GFP*- (**Fig. 4.10. B;** top). It can then be seen upregulating GFP approximately 24 minutes later and is tracked being recruited into the granuloma structure 18 minutes later (**Fig. 4.10. B;** middle and bottom). These transitioning macrophages were then tracked for the duration they were in the field of view to determine whether these phenotypic changes can also be captured.

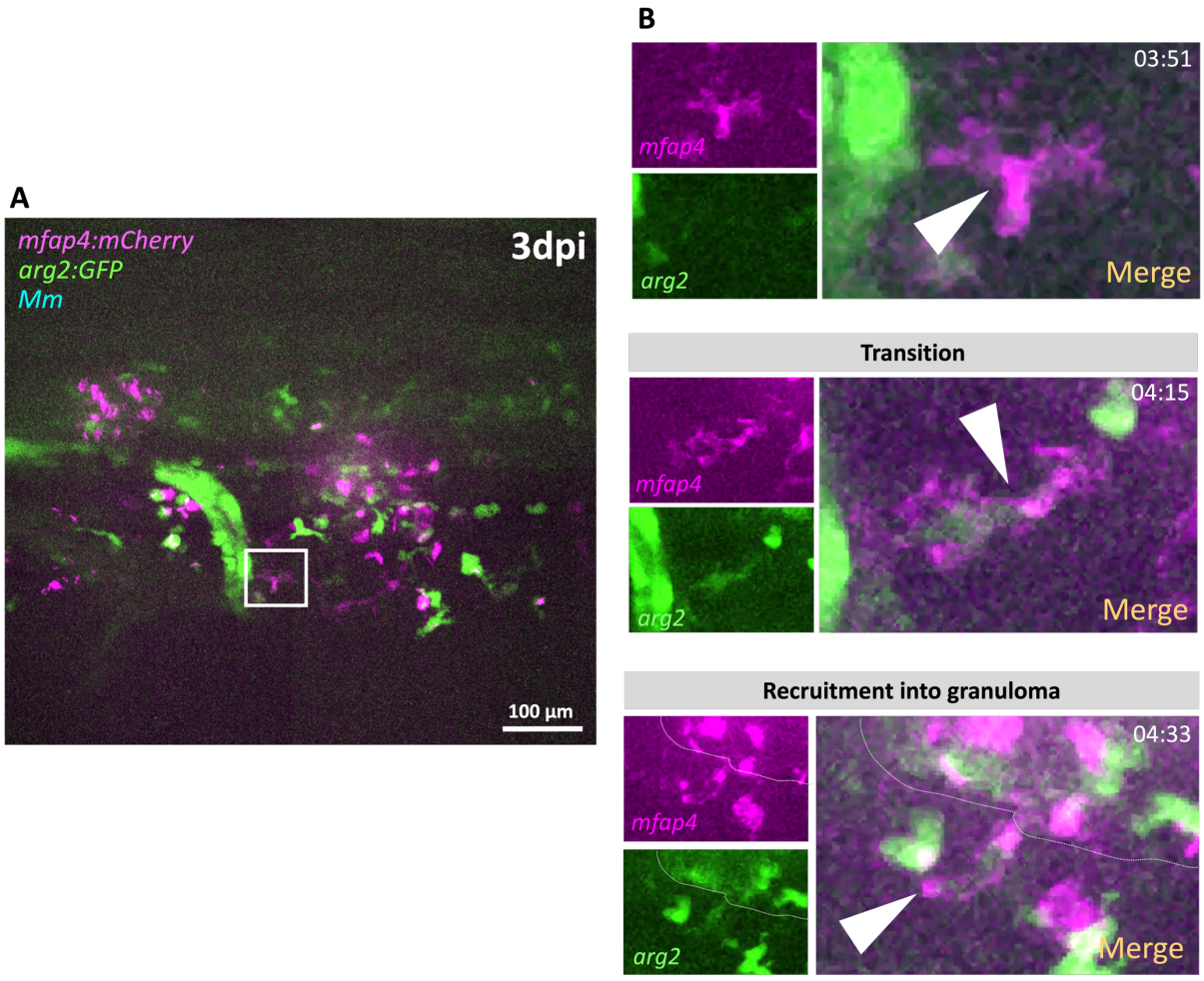


Figure 4.10. Spinning disk timelapse imaging captures *arg2:GFP*- macrophages that later upregulate *arg2:GFP*. (**A**) Representative frame (maximum projection) of a timelapse of 3 dpi *arg2:GFP* larvae crossed with *mfap4:mCherry*. White box indicates *arg2:GFP*- macrophage that expresses *arg2:GFP* at later stages of the timelapse. (**B**) Top: Zoomed area of the *arg2:GFP*- macrophage (white arrowhead) highlighted in the white box in (**A**). Middle: Frame at which point macrophage transitions to expressing *arg2:GFP* (white arrowhead). Bottom: Last frame in which transitioned *arg2:GFP+* macrophage (white arrowhead) is visible as it is recruited into the granuloma (dotted white line). Timelapse time steps were 3 minutes, imaged over 10 hours. Scale bar stated on still image in (**A**).

Manual tracking of macrophage morphology was carried out in each frame as described in section 3.3.4; however, they were tracked for the duration they were in view, not just over the course of a 1-hour window. There is a decreasing trend in macrophage perimeter (**Fig. 4.11. A**) and an increasing trend in circularity index (**Fig. 4.11. B**) from when *arg2:GFP*- macrophages (black lines) begin expressing *arg2:GFP* (green lines). To statistically compare the morphometric descriptors, the average perimeter/CI 1 hour before and 1 hour after *arg2:GFP* was expressed (**Fig. 4.11.**; dotted black line) was calculated for paired analysis. Compared to the hour prior to expressing *arg2:GFP*, macrophages had a significantly smaller average perimeter (155.3 µm vs. 114.7 µm; **Fig. 4.11. C**) and significantly higher CI (0.28 vs. 0.44; **Fig. 4.11. D**).

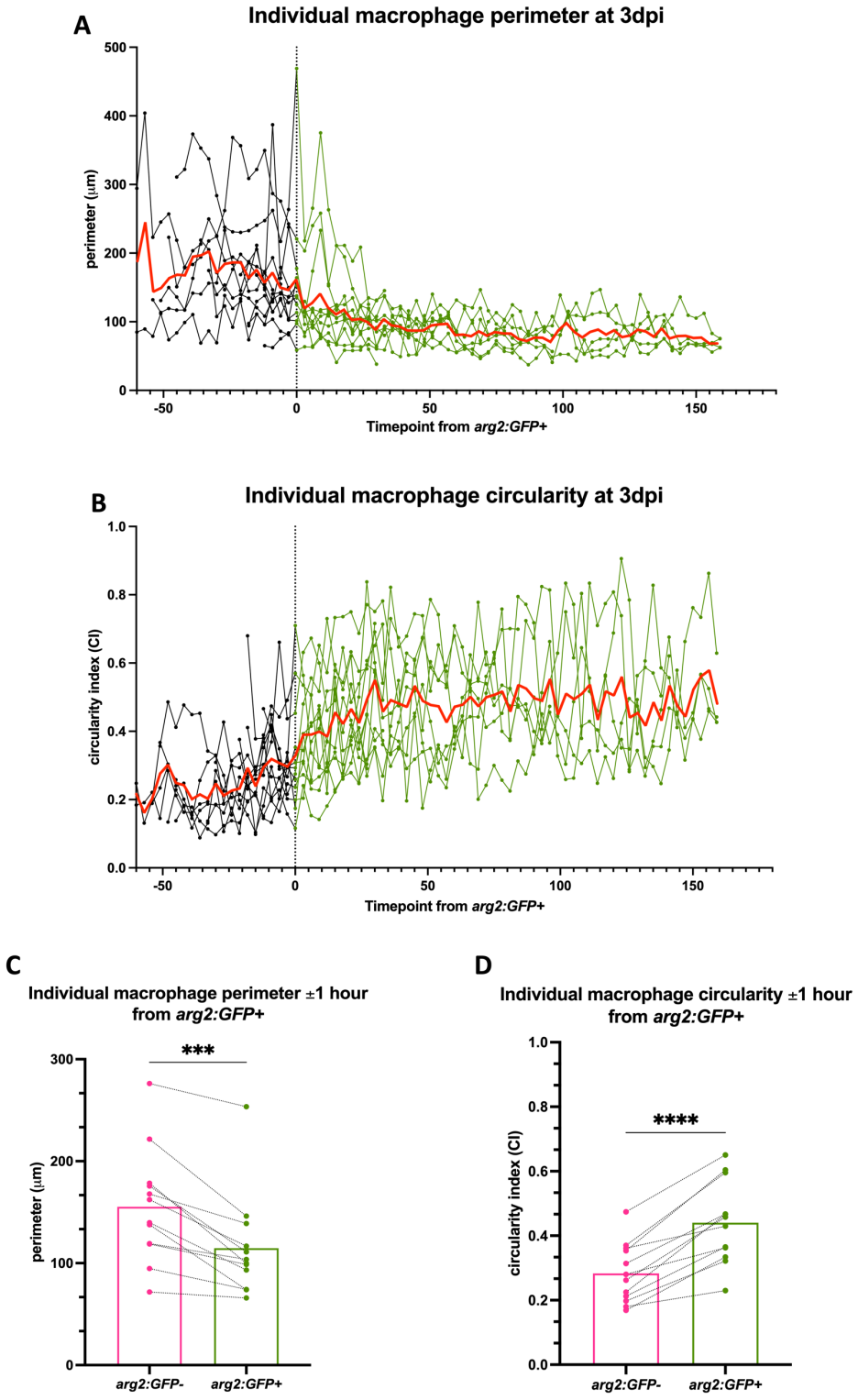


Figure 4.11. *arg2:GFP*- macrophages become smaller and more circular following *arg2:GFP* upregulation. (**A-B**) Line graphs illustrating macrophage perimeter (**A**) and CI (**B**) following *arg2:GFP* expression. Each line depicts a macrophage and 0 on the x-axis (dotted black line) is the point at which *arg2:GFP* is expressed, illustrated in green. Mean line is illustrated in red. (**C**) Paired comparison of the average perimeter (μm) of *arg2:GFP*- macrophages (pink) the hour before *arg2:GFP* expression compared to the hour after *arg2:GFP* expression (green). (**D**) Paired comparison of the average CI of *arg2:GFP*- macrophages (pink) the hour prior to *arg2:GFP* expression compared to the hour after *arg2:GFP* expression (green). N=12 cells identified from 7 larvae over 2 independent experiments. Statistical significance was calculated using a paired, two-tailed t-test. ***P ≤ 0.001; ****P ≤ 0.0001.

To determine whether the behavioural differences (increased speed) identified in *arg2:GFP+* macrophages are also captured in transitioning cells following *arg2:GFP* upregulation, the average speed an hour before and after *arg2:GFP* expression was calculated as with the morphometric descriptors. No significant differences were identified in average speed (1.4 μm/sec vs. 1.7 μm/sec; **Fig. 4.12. A**) or MI (0.49 vs. 0.58; **Fig. 4.12. B**). The difficulty in capturing this behavioural transition is likely due either to the highly dynamic, minute-to-minute nature of macrophage behaviour, or to the delay between the GFP transcription and translation.

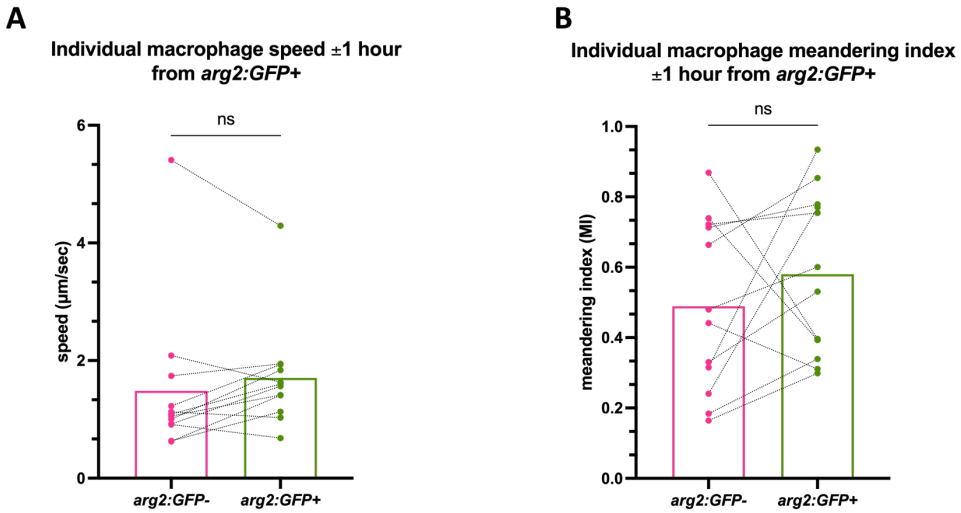


Figure 4.12. Changes in behaviour are not captured when tracking *arg2:GFP*- macrophages that later upregulate *arg2:GFP+*. (**A**) Paired of average speed (μm/sec) of *arg2:GFP*- macrophages (pink) the hour before *arg2:GFP* expression and the hour after *arg2:GFP* expression (green). (**D**) Paired comparison of average MI of *arg2:GFP*- macrophages (pink) the hour prior to *arg2:GFP* expression and the hour after *arg2:GFP* expression (green). N= 12 cells identified from 7 larvae over 2 independent experiments. Statistical significance was calculated using a paired, two-tailed t-test.

Confocal laser phototoxicity may result in changes in cell morphology, such as through triggering apoptosis (Brockway et al., 2019). Thus, macrophages that remain *arg2:GFP*- throughout the course of the timelapse were manually tracked to determine whether this shift in morphology can be attributed to phototoxicity. Both *arg2:GFP*- macrophage perimeter (**Fig. 4.13. A**) and CI (**Fig. 4.13. B**) remained largely even throughout the duration they were in the field of view. The average perimeter/CI was calculated 30 minutes from the start of tracking and 30 minutes before the end in order to statistically compare the morphometric descriptors. No significant differences in *arg2:GFP*- macrophage perimeter (204.1 μm vs. 195.1 μm; **Fig. 4.13. C**) or CI (0.20 vs. 0.22; **Fig. 4.13. D**) were identified between the beginning and end of the timelapse. Although this data confirms that changes in morphology are not due to the mCherry laser, it does not rule out phototoxicity associated with the GFP laser. However, these observations add confidence that changes in macrophage morphology following *arg2:GFP* expression is more likely to be due to changes in phenotype rather than phototoxicity.

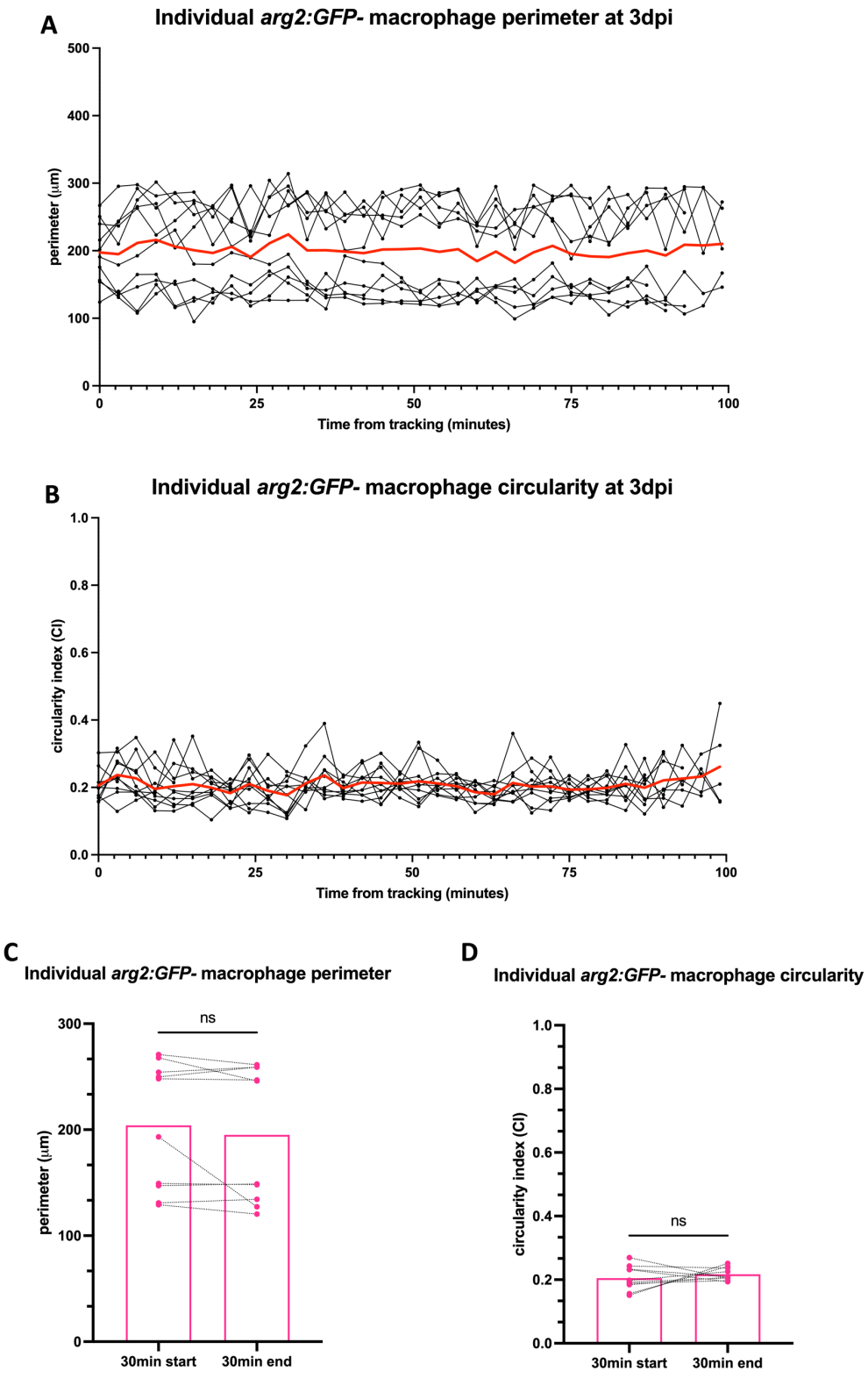


Figure 4.13. *arg2:GFP*- macrophage morphology remains stable throughout timelapse imaging. (**A-B**) Line graphs illustrating *arg2:GFP*- macrophage perimeter (**A**) and CI (**B**) for the duration they are tracked during the timelapses. Each line depicts a macrophage. Mean line is illustrated in red. (**C**) Paired comparison of average perimeter (μm) of *arg2:GFP*- macrophages 30 minutes from the beginning and 30 minutes at the end of the timelapses. (**D**) Paired comparison of average CI of *arg2:GFP*- macrophages 30 minutes from the beginning and 30 minutes at the end of the timelapses. N=5 cells tracked from 10 larvae over 2 independent experiments. Statistical significance was calculated using a paired, two-tailed t-test.

To conclude, by capturing macrophages that subsequently upregulate *arg2:GFP* expression, this data provides the first *in vivo* evidence that anti-inflammatory macrophages polarise locally in response to the infection microenvironment. Furthermore, manual tracking of these transitioning macrophages captured the changes in macrophage morphology (i.e.: smaller, more circular) following upregulation of *arg2:GFP*, but not the increase in speed.

4.2.3. *arg2:GFP* positive macrophages arise from *tnfa:mCherry* positive populations

A key question in the field of macrophage biology is whether macrophages exhibit functional plasticity by re-polarising from pro- to anti-inflammatory states in response to local cues, or whether distinct macrophage subsets are sequentially recruited and retain fixed phenotypes *in vivo*. Indeed, much of our understanding of macrophage plasticity arises from demonstrating that M1/M2 polarisation is reversible depending on cytokine exposure *in vitro* (reviewed by Sica and Mantovani, 2012; Yellanki et al., 2024). Thus, to determine whether putative pro-inflammatory macrophages (*tnfa:mCherry+*) re-polarise towards an anti-inflammatory phenotype (*arg2:GFP+*), or whether they are separate populations of macrophages recruited at different time-points, 3 dpi *Mm*-infected larvae were imaged over a 10-hour timelapse.

An initial striking observation was the abundance of double positive (*tnfa:mCherry+ arg2:GFP+*) cells (**Fig. 4.14. A** - yellow box), with examples of *tnfa:mCherry+ arg2:GFP-* (**Fig. 4.14. A** - pink box) and *tnfa:mCherry- arg2:GFP+* cells (**Fig. 4.14. A** - green box). In the first instance, the number of cells in each of these groups were quantified at the beginning, middle and end of the timelapse. The number of *tnfa:mCherry- arg2:GFP+* cells was highest at all time-points (**Fig. 4.15. A** - beginning: 219 cells; middle: 161 cells; end: 143 cells). However, these fish do not contain a macrophage reporter, and it is therefore likely that most of these *arg2:GFP+* cells are neutrophils (Hammond et al., 2023). Yet most, if not all, *tnfa:mCherry+* cells are likely macrophages, as neutrophils do not upregulate *tnfa:GFP* (Nguyen-Chi et al., 2015; Lewis and Elks, 2019). Thus, the analyses for these timelapse datasets focused on *tnfa:mCherry+ arg2:GFP-* cells (**Fig. 4.14. B** - pink box) and double positive cells (**Fig. 4.14. C** - yellow box), but are referred to hereon in as immune cells due to the lack of a macrophage reporter. At the beginning of the timelapse (0 hours), 54.88% of macrophages were *tnfa:mCherry+ arg2:GFP+*, with 45 cells being double positive and 82 cells only being *tnfa:mCherry+* (**Fig. 4.15.**). A similar proportion of *tnfa:mCherry+ arg2:GFP+* cells were identified at 5 hours, with 55.88% of cells being double positive (68 *tnfa+ arg2*-cells; 38 *tnfa+ arg2+*; **Fig. 4.15.**). At 10 hours, there were more double positive cells than *tnfa:mCherry+ arg2:GFP-* cells, with 83.93% cells being *tnfa:mCherry+ arg2:GFP+* (56 *tnfa+ arg2-* cells; 47 *tnfa+ arg2+*; **Fig. 4.15.**). Interestingly, the number of double positive cells remained relatively similar across the entire 10-hour timelapse (**Fig. 4.15.**).

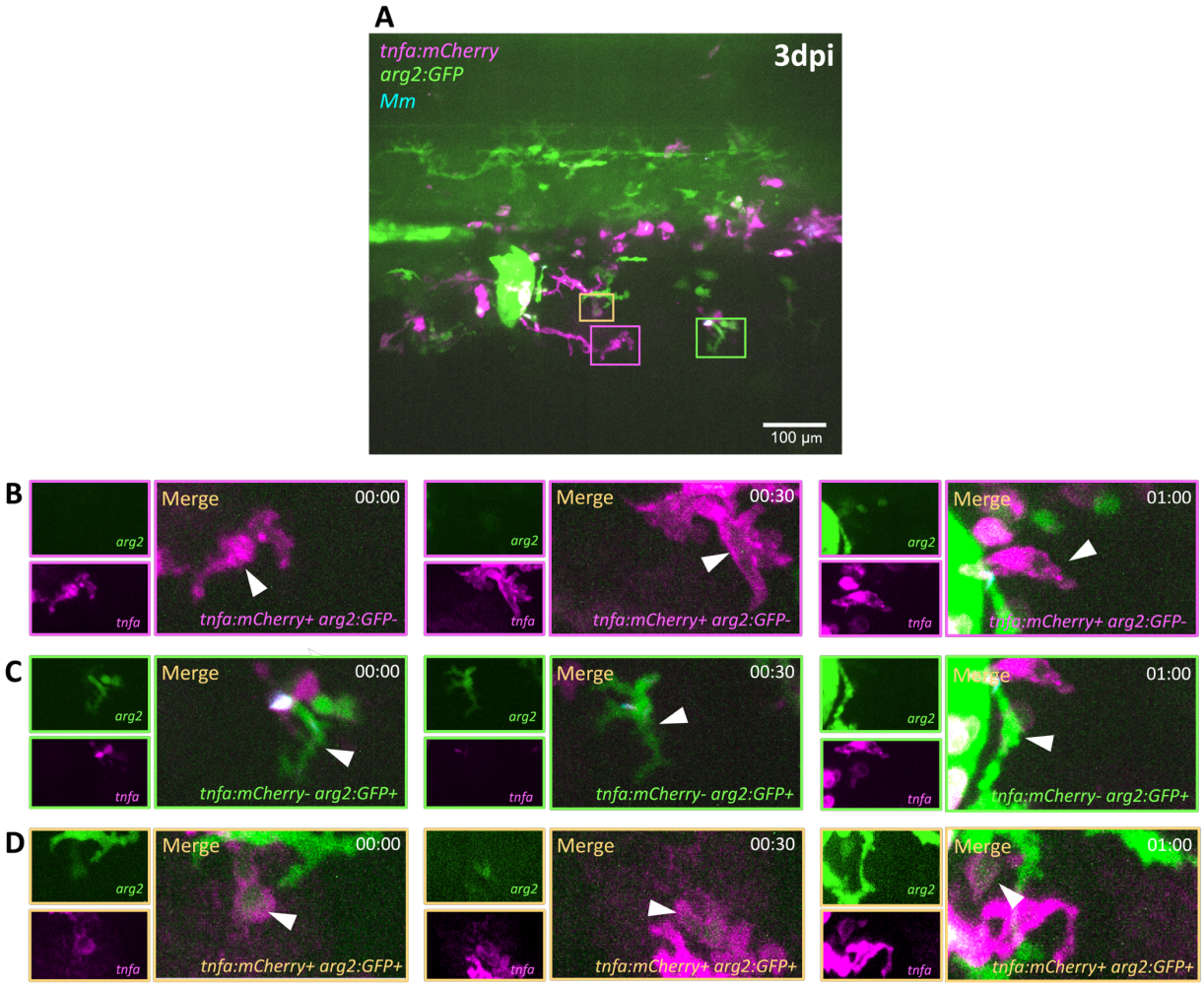


Figure 4.14. Immune cells can express both *tnfa:mCherry* and *arg2:GFP* simultaneously in *Mm* infection at 3 dpi. (**A**) Representative frame (maximum projection) of a spinning disk timelapse of 3 dpi *tnfa:mCherry* larvae crossed with *arg2:GFP*. Pink box highlights *tnfa:mCherry+ arg2:GFP-* cell. Green box highlights *tnfa:mCherry- arg2:GFP+* cell. Yellow box highlights double positive cell. (**B**) Zoomed area of *tnfa:mCherry+ arg2:GFP-* cell (white arrowhead) highlighted in the pink box in (**A**), spanning from the beginning of the timelapse (00:00), 30 minutes and at 1 hour. (**C**) Zoomed area of *tnfa:mCherry- arg2:GFP+* cell (white arrowhead) highlighted in the green box in (**A**), spanning from the beginning of the timelapse (00:00), 30 minutes and at 1 hour. (**D**) Zoomed area of *tnfa:mCherry+ arg2:GFP+* cell (white arrowhead) highlighted in the yellow box in (**A**), spanning from the beginning of the timelapse (00:00), 30 minutes and at 1 hour. Timelapse time steps were 3 minutes, imaged over 10 hours. Scale bar stated on still image in (**A**).

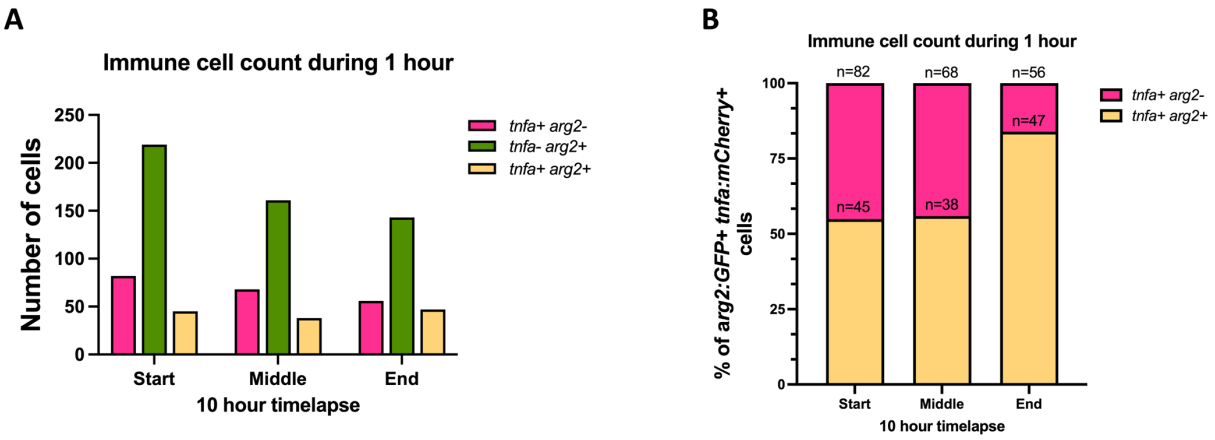


Figure 4.15. Numbers of *tnfa:mCherry+ arg2:GFP+* cells remain similar throughout a 10-hour timelapse of 3 dpi *Mm*-infected larvae. (**A**) Graph illustrating the number *of tnfa:mCherry+ arg2:GFP-, tnfa:mCherry- arg2:GFP+* and double positive cells at the start, middle and end of the timelapse. (**B**) Graph illustrating the percentage of double positive and *tnfa+ arg2-* cells at the start, middle and end of the timelapse. Start: 0 hours; middle: 5 hours; end: 10 hours. N=6 larvae, across 1 independent experiment (pilot).

To assess the phenotype of *tnfa:mCherry+ arg2:GFP-* and double positive cells, the same analysis pipeline described in section 3.3.4 was applied. Briefly, morphometric descriptors (perimeter and circularity index) were obtained by manually drawing around cells over the course of a 1-hour window (double positive cell vs. nearest *tnfa+ arg2-* neighbour). Speed and meandering index (MI) measurements were obtained by using the manual tracking plugin to quantify cell behaviour (see section 3.2.4, **Fig. 3.18.**). Interestingly, the morphology and behaviour of the double positive cells is very similar to the observations made when quantifying *arg2:GFP+* macrophages. Compared to *tnfa+ arg2-* cells, double positive cells had a significantly smaller average perimeter (75.8 μm vs. 108.3 μm; **Fig. 4.16. A**) and a significantly higher circularity index (0.47 vs. 0.34; **Fig. 4.16. B**). In terms of behavioural descriptors, no significant differences between average MI of *tnfa+ arg2-* and double positive cells were identified (0.50 vs. 0.45; **Fig. 4.16. D**). However, double positive cells had a significantly higher average speed when compared their nearest *tnfa+ arg2-* neighbour (1.5 μm/sec vs. 1.16 μm/sec; **Fig. 4.16. C**). These data suggest that the population of double positive cells may be the same population captured when characterising the phenotype of *arg2:GFP+* macrophages.

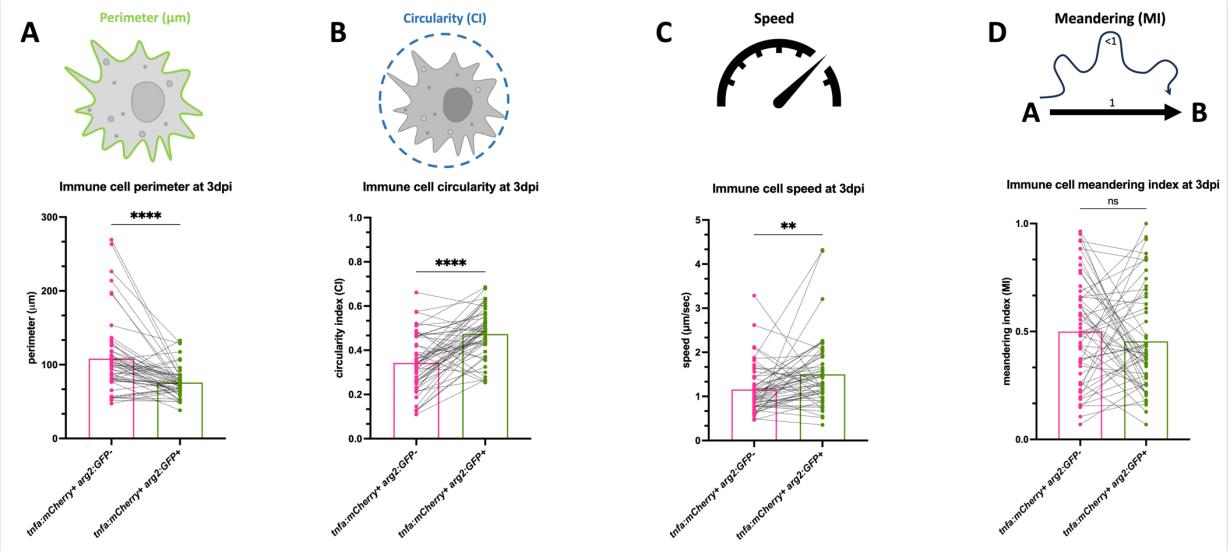


Figure 4.16. *tnfa:mCherry+ arg2:GFP+* immune cells at 3 dpi are smaller, less branched and faster than *tnfa:mCherry+ arg2:GFP-* immune cells. (**A**) Top: Representation of perimeter analysis obtained in ImageJ. Bottom: Paired comparison of the average perimeter (μm) of *tnfa+ arg2-* cells (pink) compared to double positive cells (green) across a 1-hour window. (**B**) Top: Representation of circularity index (CI) analysis calculated using ImageJ. Bottom: Paired comparison of the average CI of *tnfa+ arg2- cells* (pink) compared to double positive cells (green) across a 1-hour window. (**C**) Top: Representation of speed analysis obtained using the ImageJ manual tracking plugin. Bottom: Paired comparison of the average speed (μm/sec) of *tnfa+ arg2-* cells (pink) compared to double positive cells (green) across a 1-hour window. (**D**) Top: Representation of how the most direct migratory route equates to a meandering index (MI) of 1. Bottom: Paired comparison of the average MI of *tnfa+ arg2-* cells (pink) and double positive cells (green) across a 1-hour window. N=53 matched cells (4-5 matched cells per fish, 11 fish total) over 2 independent experiments. Statistical significance was calculated using a paired, two-tailed t-test. **P ≤ 0.01; ****P ≤ 0.0001.

The distance of *tnfa:mCherry+ arg2:GFP+* immune cells from the granuloma centre was quantified to establish whether upregulation of *arg2:GFP* may rely on chemotactic gradients generated by the granuloma. While the mean distance of double positive cells over a 1-hour period was 135.9 μm, though individual cells ranged from 20.8 μm to 390.7 μm from the granuloma (**Fig. 4.17. A**). Notably, there were no significant differences between *tnfa:mCherry+ arg2:GFP-* immune cells and double positive cells when examining the overall migration pattern of these cells over the 1-hour window, with comparable proportions of cells migrating toward or away from the granuloma (**Fig. 4.17. B**).

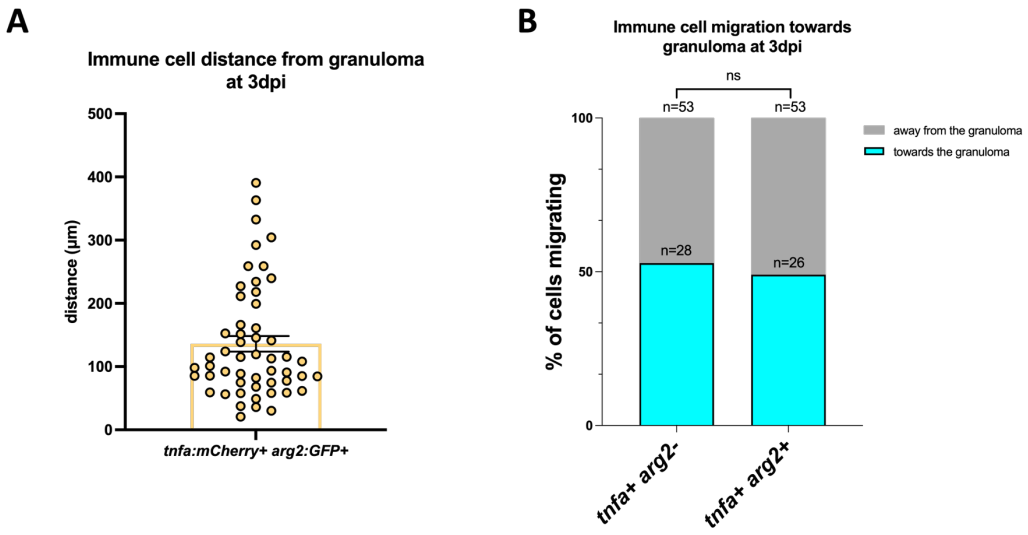


Figure 4.17. *tnfa:mCherry+ arg2:GFP+* immune cells are found at a wide range of distances from the granuloma. (**A**) Graph illustrating the 1-hour average distance of *tnfa+ arg2+* cells from the centre of the granuloma at 3 dpi. Error bars depict SEM. (**B**) Graph illustrating the percentage of *tnfa+ arg2*- and double positive cells migrating along the overall directional pattern, either towards (cyan) or away (grey) from the granuloma at 3 dpi, over a 1-hour window. Total number of cells per group depicted on the graph. Statistical significance in (**B**) was calculated using a Chi squared test. N=53 matched cells (4-5 matched cells per fish, 11 fish total) over 2 independent experiments.

Building on the observation that *tnfa:mCherry+ arg2:GFP+* cells migrate without directional bias and are located at varying distances from the granuloma, I next examined whether the spatial distribution of these double positive cells supports a chemotaxis-independent origin. Specifically, I asked whether these cells arise not by directed migration toward the granuloma in response to chemokine gradients, but rather through local polarisation at the infection sites. A chemotaxis-independent origin would be expected to produce a more dispersed pattern, without spatial enrichment near the granuloma core. First, the XY coordinates of double positive cells were extracted during the manual tracking to quantify cell speed. The coordinates of the centre of the granuloma of each larva were also determined (**Fig. 4.18. A, B**). Because granuloma locations varied between fish, all coordinates were normalised so that the origin point (0,0) represented granuloma centre. The XY locations of double positive cells were then plotted on a scatter graph (**Fig. 4.18. C**). The spatial distribution of double positive cells was highly heterogenous, both within individual fish and across all fish (**Fig. 4.18. C**). For example, the double positive cells represented by fuchsia and grey dots are widely dispersed, along both the X and Y axes (**Fig. 4.18. C**). Over half of the double positive cells clustered around the centre-right of the origin, corresponding to the location of the CHT of many fish (**Fig. 4.18. B**). This is consistent with expectations, as granulomas in this region coincide with the infection site and the region of haematopoiesis.

Collectively, these data support the hypothesis that putative pro-inflammatory macrophages re-polarise, characterised by *arg2:GFP* upregulation, is driven by local cues within the infected tissue, with chemotactic recruitment of *arg2:GFP+* cells to the granuloma unlikely to be the dominant mechanism.

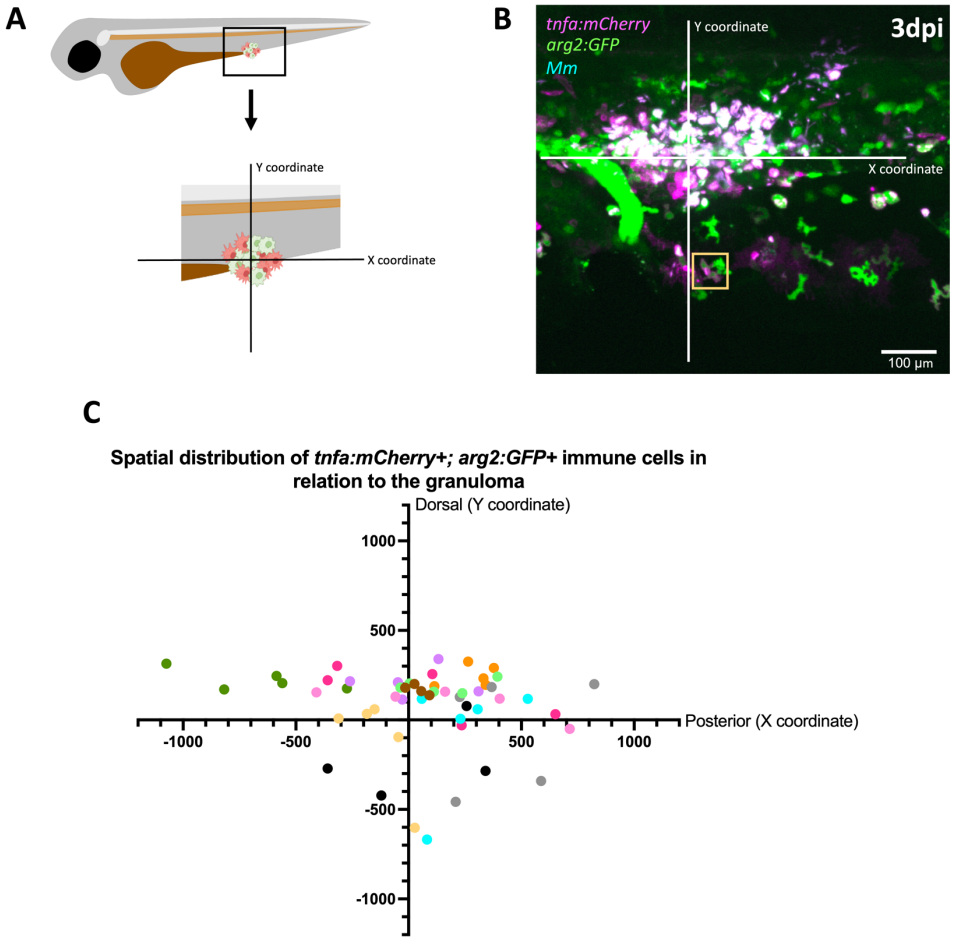


Figure 4.18. The spatial distribution pattern *of tnfa:mCherry+ arg2:GFP+* immune cells relative to the granuloma is heterogenous in 2D maximum intensity projections. (**A**) Schematic illustrating that the origin (0,0) of the coordinate system represents the centre of the granuloma for all double positive cells across all larvae. (**B**) Representative frame (maximum projection) of the spinning disk timelapse of *tnfa:mCherry* larvae crossed with *arg2:GFP* at 3 dpi illustrating how the origin (0,0) is the centre of the granuloma, with the Y and X coordinates labelled. (**C**) Scatter plot illustrating the spatial distribution of *tnfa+ arg2+* cells in relation to the granuloma. Each colour represents a larvae, with dots of the same colour representing individual *tnfa+ arg2+* cell in the same larvae. Fish orientation is labelled on the axis. Yellow box in (**B**) highlights the yellow dot at approximately position -600 on the Y coordinate in (**C**). Scale bar in (**B**) is stated on the image.

To assess whether *arg2:GFP* is upregulated in cells with increased *tnfa* transcription, *tnfa:mCherry* fluorescence intensity of *arg2:GFP+* cells was quantified and compared to that of their nearest *arg2:GFP-* neighbour. No significant differences in mCherry intensity were identified between

the two populations of cells (**Fig. 4.19.**), indicating that double positive cells do not have increased *tnfa* transcription.

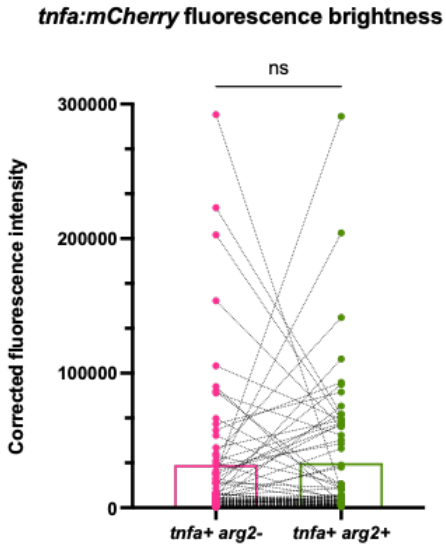


Figure 4.19. *tnfa:mCherry* fluorescence brightness is similar whether *arg2:GFP-* or *arg2:GFP+* at 3 dpi. Corrected fluorescence intensity of *tnfa:mCherry* fluorescence was quantified using ImageJ software at 3 dpi to compare *tnfa:mCherry+ arg2:GFP+* cell brightness (green dots) to its nearest *tnfa:mCherry+ arg2:GFP-* neighbour (pink dots). N=6 paired cells from each fish were quantified (11 larvae in total) over 2 independent experiments. Statistical significance was calculated using a paired, two-tailed t-test.

Similar to the timelapse characterising *arg2:GFP* expressing macrophages, timelapse imaging examining putative pro- and anti-inflammatory macrophages was able to capture *tnfa:mCherry+ arg2:GFP-* cells that later expressed *arg2:GFP* (**Fig. 4.20.**).

Ten *tnfa:mCherry+* cells that were initially *arg2:GFP-* and later became *arg2:GFP* were captured over the 10-hour timelapse (**Fig. 4.20. A**). **Fig. 4.20. B** shows an example of a *tnfa:mCherry+ arg2:GFP-* cell that transitions to being double positive, with GFP upregulation occurring approximately 6 minutes after the cell first appears in the field of view. GFP expression was initially faint, particularly in the frame where the transition begins. However, these transitioning cells could also be tracked from fluorescence negative to positive frame-by-frame in the GFP channel, confirming that they were true double positive cells rather than imaging artefacts (**Fig. 4.20. C**). When focussing on the GFP channel, fluorescence initially detected in the transitioning frame (7 hours and 9 minutes; 07:09) visibly increased over time, peaking around 07:03, before decreasing in the final frame as the cell moved out of focus (**Fig. 4.20. C**). These transitioning cells were tracked for the duration they were in frame to assess whether the phenotypic shift was detectable following the onset of visible GFP expression.

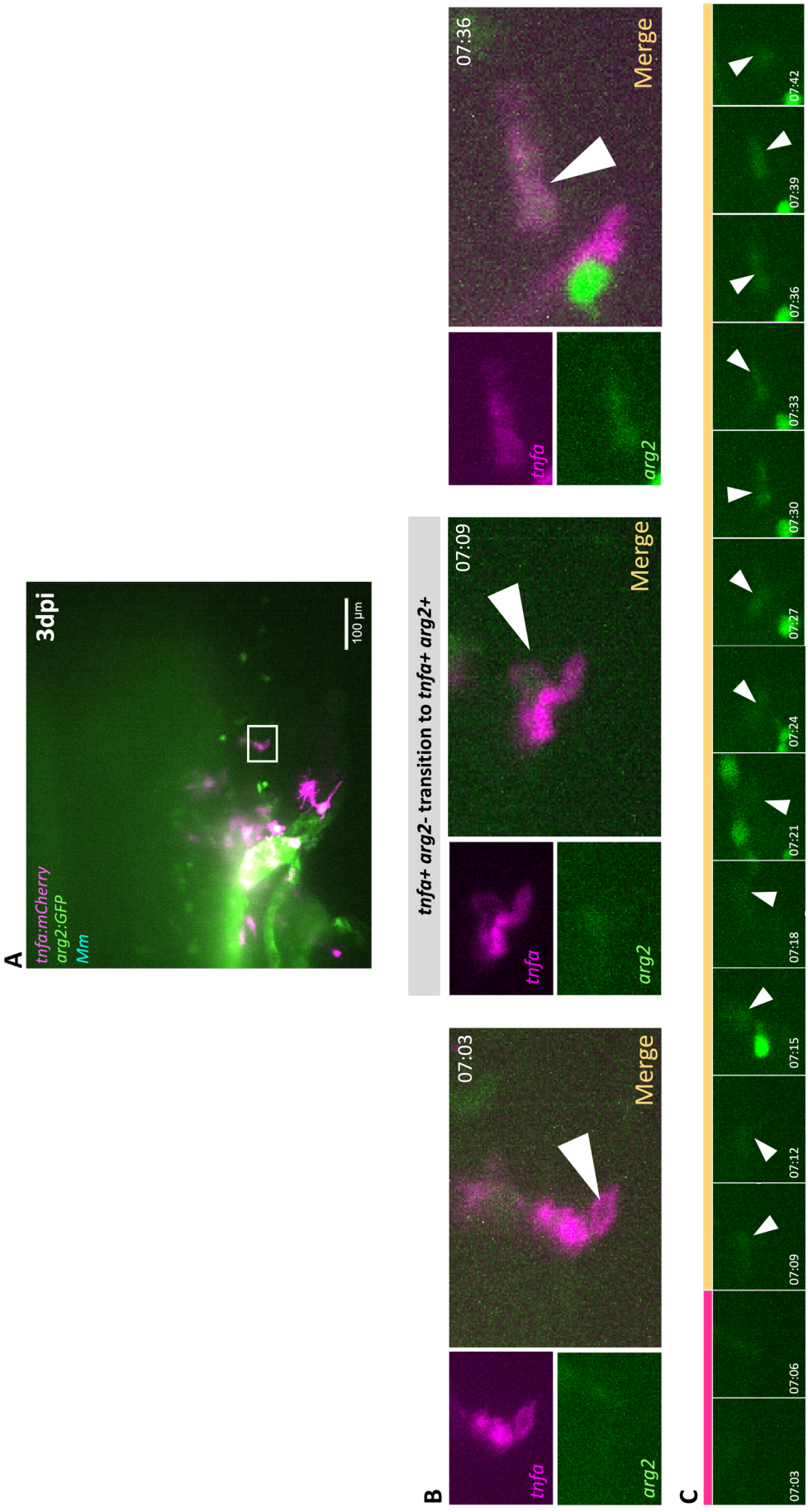


Figure 4.20. Spinning disk timelapse imaging captures *tnfa:mCherry+ arg2:GFP-* immune cells at 3 dpi that later upregulate *arg2:GFP*. (**A**) Representative frame (maximum projection) of a timelapse of 3 dpi *arg2:GFP* larvae crossed with *tnfa:mCherry*. White box indicates *tnfa:mCherry+ arg2:GFP-* cell that expresses *arg2:GFP* at later

stages of the timelapse. (**B**) Left: Zoomed area of the *tnfa:mCherry+ arg2:GFP-* cell (white arrowhead) highlighted in the white box in (**A**). Middle: Frame at which point *tnfa:mCherry+* cell transitions to expressing *arg2:GFP* (white arrowhead). Right: Transitioned *tnfa:mCherry+ arg2:GFP+* macrophage (white arrowhead) is visible at later stages of the timelapse. (**C**) Tracking of transitioning cell in each frame in the GFP channel. First two frames (pink bar) indicate the same *tnfa:mCherry+ arg2:GFP-* cell. At 7 hours 9 minutes (07:09), upregulation of *arg2:GFP* in the same cell becomes visible (white arrowhead). Double positive cell is tracked for the duration it is in frame (yellow bar), demonstrating increased GFP brightness as the timelapse progresses. Timelapse time steps were 3 minutes; timestamps indicate hours:minutes. Scale bar stated on still image in (**A**).

tnfa:mCherry+ arg2:GFP- immune cells that transitioned to being double positive were analysed for the duration they were in the field of view. Manual tracking of cell perimeter (**Fig. 4.21. A**) and circularity index (**Fig. 4.21. B**) showed a decrease and increase in trend for both morphometric descriptors, respectively, from when *arg2:GFP-* cells (black lines) upregulate *arg2:GFP* (green lines). The mean perimeter/CI up to 1 hour before and 1 hour after *arg2:GFP* expression (**Fig. 4.21.**; dotted black line) was calculated to determine whether these morphometric descriptors were statistically different. Paired analysis identified that following *arg2:GFP* expression, double positive cells had a significantly smaller perimeter (78.6 μm vs. 63 μm; **Fig. 4.21. C**) and significantly higher CI (0.42 vs. 0.54; **Fig. 4.21. D**).

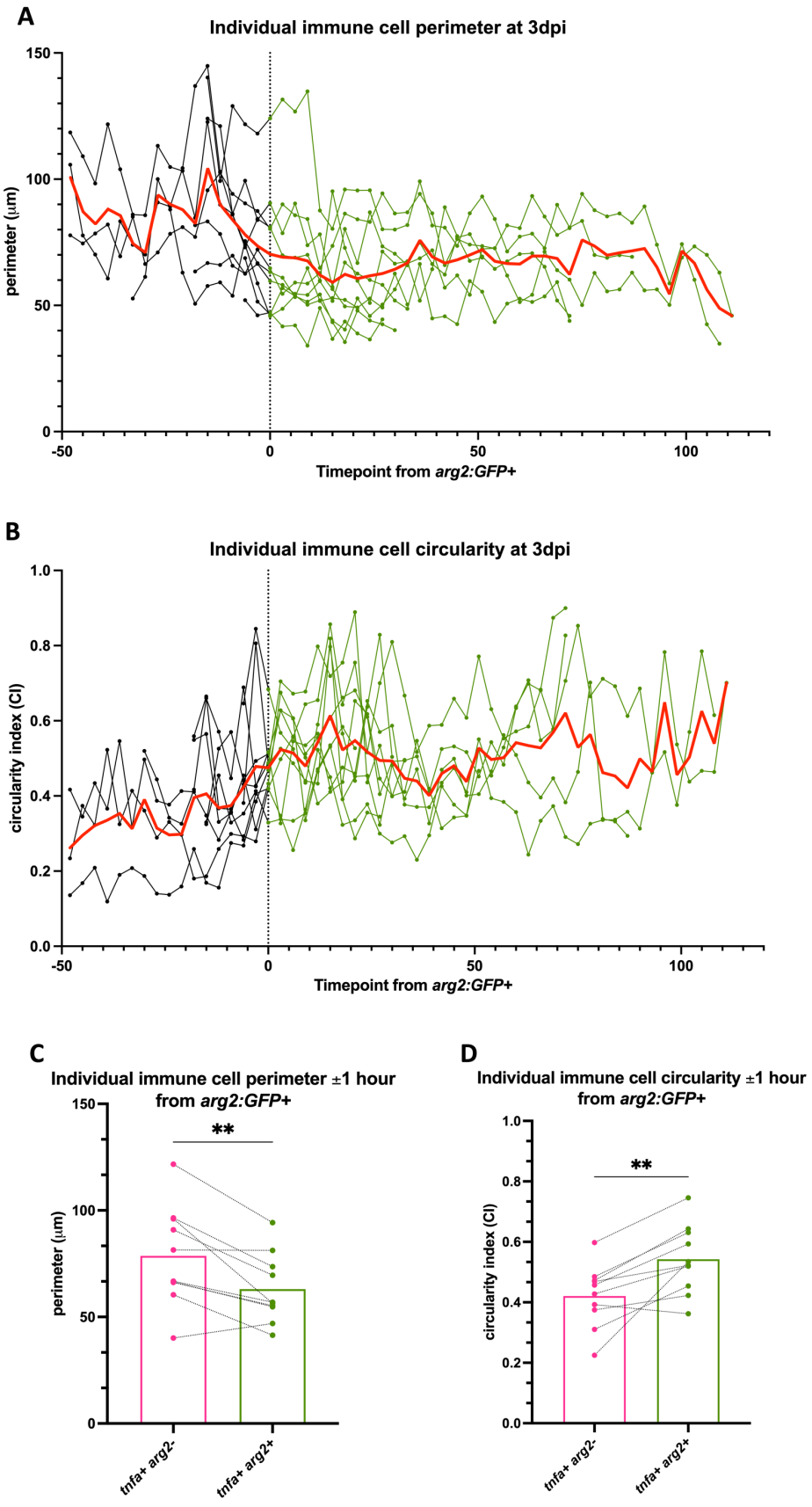


Figure 4.21. *tnfa:mCherry+ arg2:GFP-* immune cells become smaller and more circular following upregulation of *arg2:GFP* at 3 dpi. (**A-B**) Line graphs illustrating *tnfa:mCherry+* cell perimeter (**A**) and CI (**B**) following *arg2:GFP* expression. Each line depicts a macrophage and 0 on the x-axis (dotted black line) is the point at which *arg2:GFP* is expressed, illustrated in green. Mean line is illustrated in red. (**C**) Paired comparison illustrating that the average perimeter (μm) of *tnfa:mCherry+ arg2:GFP-* immune cells (pink) up to an hour before *arg2:GFP* expression is

significantly higher than the hour after *arg2:GFP* expression (green). (**D**) Paired comparison illustrating that the average CI of *tnfa:mCherry+ arg2:GFP-* immune cells (pink) the hour prior to *arg2:GFP* expression is significantly lower than the hour after *arg2:GFP* expression (green). N=10 cells from 6 larvae over 2 independent experiments. Statistical significance was calculated using a paired, two-tailed t-test. **P ≤ 0.01.

The average speed of *tnfa:mCherry+ arg2:GFP-* was calculated for one hour before and after *arg2:GFP* expression to assess whether behavioural changed identified in the nearest neighbour analysis was also detectable in transitioning cells. No significant differences were observed in average speed (1.36 μm/sec vs. 1.7 μm/sec; **Fig. 4.22. A**) or meandering index (0.34 vs. 0.43; **Fig. 4.22. B**). This behavioural shift may occur slightly earlier, due to the delay between *arginase 2* upregulation and subsequent GFP transcription and translation.

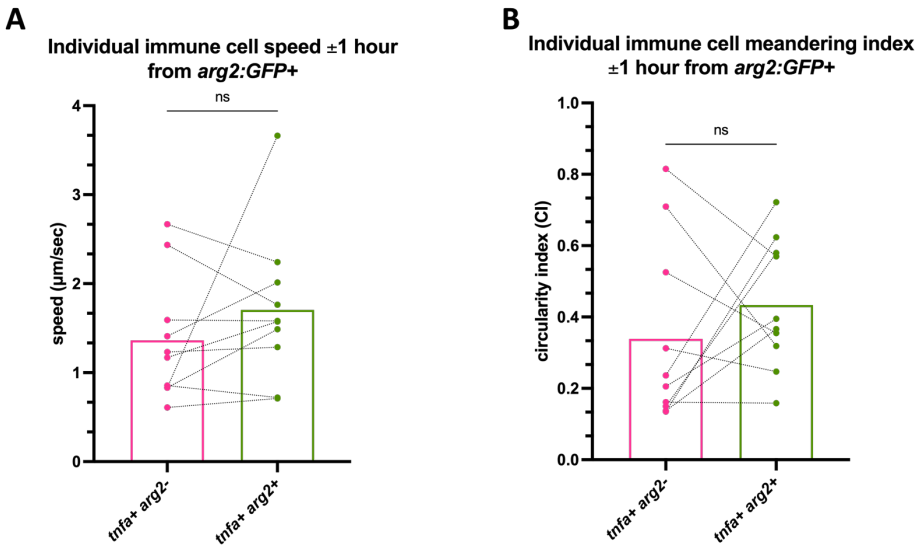


Figure 4.22. Changes in behaviour are not captured when tracking *tnfa:mCherry+ arg2:GFP-* immune cells that transition to being *arg2:GFP+* at 3 dpi. (**A**) Paired comparison of average speed (μm/sec) of *tnfa:mCherry+ arg2:GFP-* immune cells (pink) the hour before *arg2:GFP* expression and the hour after *arg2:GFP* expression (green). (**B**) Paired comparison of average meandering index of *tnfa:mCherry+ arg2:GFP-* immune cells (pink) the hour prior to *arg2:GFP* expression and the hour after *arg2:GFP* expression (green). N=10 cells identified from 6 larvae over 2 independent experiments. Statistical significance was calculated using a paired, two-tailed t-test.

To attempt to account for this delay, the average perimeter, CI and speed of a transitioning cells were calculated up to 30 minutes prior to *arg2:GFP* expression and compared to the nearest neighbouring *tnfa:mCherry+* cell that did not transition. Even at the pre-transition stage, morphological changes were evident, with *tnfa:mCherry+* cells that would later transition displaying a significantly smaller perimeter (190 μm vs. 74.2 μm; **Fig. 4.23. A**) and significantly higher CI (0.24 vs. 0.46; **Fig. 4.23. B**). However, no significant differences in speed were observed (1.23 μm/sec vs. 1.24 μm/sec; **Fig. 4.23. C**). Given that the average speed prior to *arg2:GFP* expression was nearly identical to that of the

nearest non-transitioning cell, this lack of detectable behavioural shift is likely due to the highly dynamic, minute-by-minute nature of macrophage behaviour.

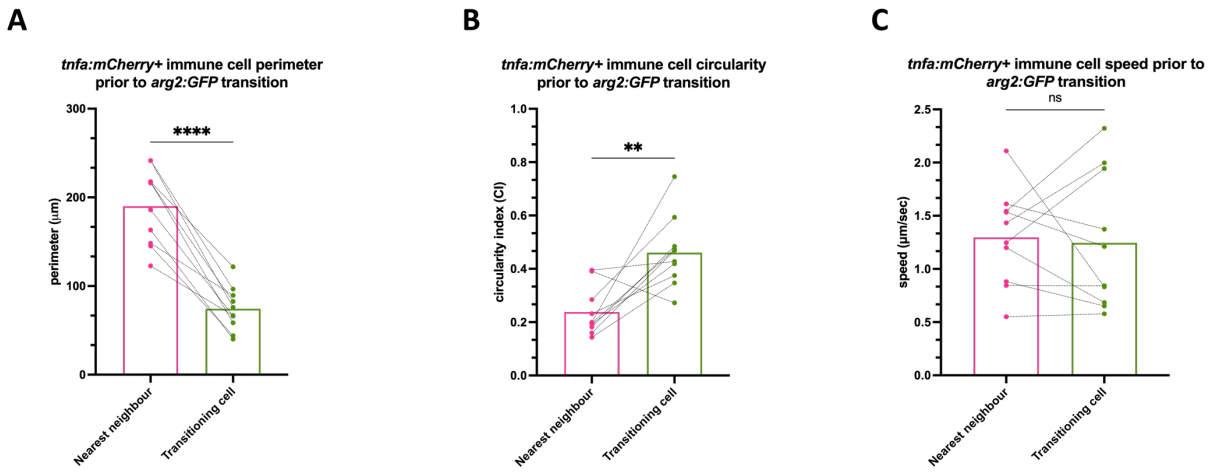


Figure 4.23. Prior *arg2:GFP* upregulation, *tnfa:mCherry+* transitioning cells become smaller and rounder, but the increase in speed is not captured. (**A**) Paired comparison of average perimeter (μm) of a *tnfa:mCherry+ arg2:GFP+* cell up to 30 minutes prior to *arg2:GFP* expression (green) compared to the nearest *tnfa:mCherry+ arg2:GFP-* neighbour (pink). (**B**) Paired comparison of average circularity index (CI) of a *tnfa:mCherry+ arg2:GFP+* cell up to 30 minutes prior to *arg2:GFP* expression (green) compared to the nearest *tnfa:mCherry+ arg2:GFP-* neighbour (pink). (**C**) Paired comparison of average speed (μm/sec) of a *tnfa:mCherry+ arg2:GFP+* cell up to 30 minutes prior to *arg2:GFP* expression (green) and the nearest *tnfa:mCherry+ arg2:GFP-* neighbour (pink). N=10 paired cells identified from 6 larvae over 2 independent experiments. Statistical significance was calculated using a paired, two-tailed t-test. **P ≤ 0.01; *** P ≤ 0.001.

To confirm that the observed changes in immune cell morphology were not due to laser-induced phototoxicity (Brockway et al., 2019), *tnfa:mCherry+ arg2:GFP-* cells were manually tracked for the duration they remained in the field of view. Immune cell perimeter remained stable throughout the timelapse (**Fig. 4.24. A**), and CI also remained largely even consistent (**Fig. 4.24. B**). A slight spike in average CI was observed toward the end of tracking, which may reflect mild phototoxicity, as macrophage rounding has been previously associated with the early stages of cell death (Mostowy et al., 2013). However, when the average perimeter and CI were compared between 30 minutes after the start of tracking and 30 minutes before the end, no significant differences were found in either perimeter (182.5 μm vs. 181.1 μm; **Fig. 4.24. C**) or CI (0.25 vs. 0.27; **Fig. 4.24. D**). Furthermore, while there may be a minor degree of phototoxicity from the mCherry laser, and the effects of GFP excitation remain unclear, these data support the interpretation that the observed shift in *tnfa:mCherry+* immune cell morphology following *arg2:GFP* expression is most likely driven by a change in cell phenotype.

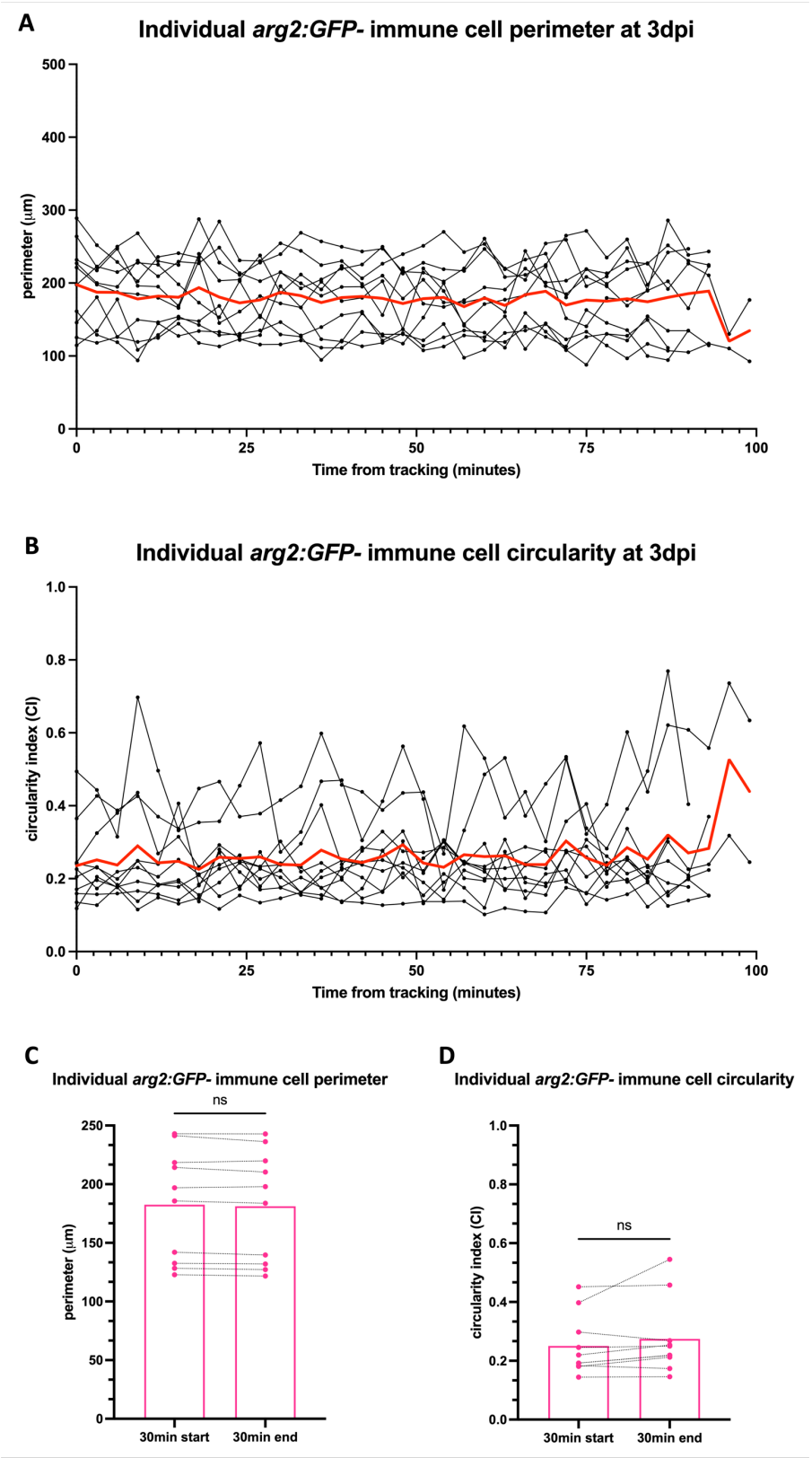


Figure 4.24. *tnfa:mCherry+ arg2:GFP-* immune cell morphology remains stable throughout timelapse imaging. (**A-B**) Line graphs of *tnfa:mCherry+ arg2:GFP-* immune cell perimeter (**A**) and CI (**B**) for the duration they are tracked during the timelapses. Each line depicts a macrophage. Mean line is illustrated in red. (**C**) Paired comparison of average perimeter (µm) of *tnfa:mCherry+ arg2:GFP-* cells 30 minutes from the beginning and 30 minutes at the end of the timelapses. (**D**) Paired comparison of average CI of *tnfa:mCherry+ arg2:GFP-* cells 30 minutes from the beginning and 30 minutes at the end of the timelapses. N=5 cells tracked from 6 larvae over 2 independent experiments. Statistical significance was calculated using a paired, two-tailed t-test.

In conclusion, a population of *arg2:GFP* expressing macrophages appear to originate from resident macrophage populations local to the site of infection. Using a novel *tnfa:mCherry* transgenic line enabled visualisation of putative pro- and anti-inflammatory macrophages for the first time *in vivo*, revealing that *arg2:GFP+* macrophages arise from *tnfa:mCherry+* populations. Furthermore, morphological analysis of *tnfa:mCherry+ arg2:GFP+* cells suggests that these putative pro-inflammatory macrophages change behaviour towards an anti-inflammatory phenotype.

4.3. Discussion

Much of our understanding of macrophage phenotypes, particularly during infection, has been derived from *in vitro* polarisation studies or inference analysis from *in vivo* infection models (Yellanki et al., 2024; Pyle et al., 2025; Pisu et al., 2025). This chapter addresses a key question in macrophage biology: do macrophages that become pro-inflammatory during the infection response then become anti-inflammatory later in infection, or do new macrophage populations move in to alter the polarisation state? By tracking individual macrophages, I found that macrophages upregulated *arg2:GFP* expression *in situ*, rather than migrating into the infection site already expressing this marker. Using a newly generated *tnfa:mCherry* transgenic reporter line, I observed a population of putative pro-inflammatory macrophages that upregulated *arg2:GFP* locally, reinforcing that this re-polarisation is driven by the local infection microenvironment. Morphological and migratory analysis of *tnfa:mCherry+ arg2:GFP+* cells revealed features consistent with murine M2-like macrophages: they were smaller, rounder, and exhibited increased speed. However, no examples of the *tnfa:mCherry* reporter being subsequently downregulated were identified during the timelapse. These findings suggest that *tnfa:mCherry+ arg2:GFP+* cells may represent an immunoregulatory phenotype aimed at controlling the inflammatory response. This represents the first *in vivo* evidence that pro-inflammatory macrophages re-polarise locally in response to mycobacterial infection (**Fig. 4.25.**).

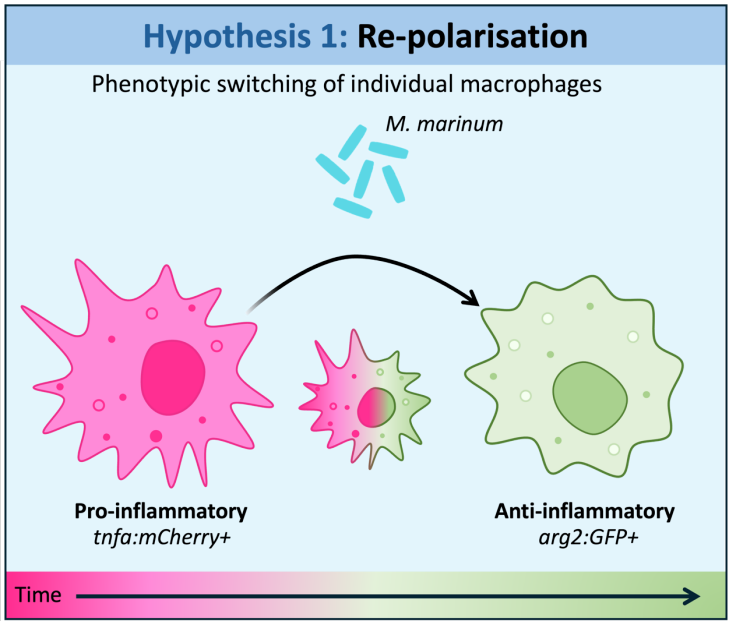


Figure 4.25. Schematic illustrating that putative pro-inflammatory macrophages undergo a phenotypic switch towards an anti-inflammatory state during *in vivo* mycobacterial infection. By using the *tnfa:mCherry* and *arg2:GFP* transgenic reporter lines, I visualised that a population of putative pro-inflammatory macrophages (*tnfa:mCherry+*) can re-polarise towards an anti-inflammatory phenotype over time in *Mm* infection, demonstrated by *arg2:GFP* upregulation and changes in cell morphology and behaviour. This observation supports the first hypothesis (re-polarisation) proposed in Figure 4.1., section 4.1.4, although it does not preclude a contribution from sequential recruitment of pre-polarised macrophages.

The *Tg(tnfa:mCherry-F)* transgenic reporter line generated in this thesis chapter displays a broadly comparable expression pattern to the existing *TgBAC(tnfa:eGFP)* reporter line (Marjoram et al., 2015), particularly in the context of macrophage expression following a tail fin transection. This validates its use as a tool for identifying putative pro-inflammatory macrophages *in vivo*, and crucially, enables real-time visualisation of macrophage polarisation dynamics during infection when used alongside the *arg2:GFP* transgenic reporter. This represents a significant advance, as it provides the first means of dynamically tracking pro- and anti-inflammatory macrophage responses to mycobacterial challenge in a live vertebrate system. The minor differences in expression observed between the *Tg(tnfa:mCherry-F)* and *TgBAC(tnfa:eGFP)* lines, including incomplete co-localisation of reporter signal, likely stems from both construct design and fluorescent protein properties. The BAC reporter includes a 50 kb promoter region to drive GFP expression, closely recapitulating endogenous *tnfa* expression, but BAC transgenesis is technically demanding and time-consuming to generate (Marjoram et al., 2015; Beil et al., 2012). In contrast, the *Tg*(*tnfa:mCherry-F)* line, while having fewer of the gene's natural regulatory elements due to the smaller promoter, it is more experimentally accessibly and still provides a reliable readout of putative pro-inflammatory macrophages (Nguyen-Chi et al., 2015). Additionally, differences in fluorescent protein behaviour may also contribute to variation in expression. mCherry is known to exhibit slower maturation kinetics and greater stability compared to GFP, but it is also much dimmer (Balleza et al., 2018; Zhang et al., 2024; Khmelinskii et al., 2016). Taken together, these factors may influence impact detectable fluorescence, particularly in cells as highly phagocytic and metabolically active as macrophages.

The performance of the *Tg(tnfa:mCherry-F)* and *TgBAC(tnfa:eGFP)* were compared using a tail fin transection model, where the onset of inflammation is well-defined and temporally reproducible (Loynes et al., 2010; Nguyen-Chi et al., 2015; Nguyen-Chi et al., 2017; Sipka et al., 2022). While macrophage responses during infection may differ in magnitude, timing, or polarisation status, infection models lack a clearly defined time 'zero' and introduce greater biological variability (Lewis and Elks, 2019; Ogryzko et al., 2019). The tail fin transection model thus provides a robust system for initial validation. Overall, the *tnfa:mCherry* reporter line offers a practical and validated tool for visualising putative pro-inflammatory macrophages *in vivo*, which, when used alongside the *arg2:GFP* line, enables dynamic imaging of macrophage signalling during infection.

Timelapse imaging captured macrophages that were initially *arg2:GFP-* that transitioned to being *arg2:GFP+* at later stages, indicating that a population of macrophages upregulate *arg2:GFP* locally at the infection site, rather than migrating in already expressing *arg2:GFP*. These transitioning cells, once visibly *arg2:GFP+*, showed a marked morphological shift: their perimeter decreased, and their circularity index increased – changes that are consistent with the conclusion in chapter 3 that *arg2:GFP+* macrophages phenotypically resemble M2c polarised macrophages. However, unlike the

comparison between *arg2:GFP+* macrophages and the nearest *arg2:GFP-* neighbour, there was no clear change in speed which coincided with *arg2:GFP* upregulation. This might reflect how dynamic macrophages are on a minute-by-minute basis. Timesteps of less than 30 seconds were needed to capture the fast changes in macrophage ramification and velocity of *in vivo* human retinal macrophages, highlighting the necessity of high-frequency imaging to accurately resolve dynamic macrophage behaviours (Hammer et al., 2020). Despite tracking of individual macrophages not capturing the change in speed, it is plausible that the morphological changes observed consequently influenced motility. For example, bone-marrow derived macrophages (BMDMs) that were more elongated in shape were found to migrate more slowly, whereas more rounded cells tended to move faster, with velocity further reducing following M1 polarisation with LPS and IFNγ (Hsieh et al., 2019). This phenotype was found to be, at least in part, attributed to changes in integrin expression, with αM integrin being downregulated on rounded macrophages, indicating that integrin interactions with extracellular matrix proteins (such as Laminin) alter macrophage cytoskeleton (Hsieh et al., 2019; Stinson et al., 2024). Furthermore, integrin expression has been directly linked to macrophage polarisation, with integrin β3 expression increasing in IL-4 polarised BMDMs, followed by increased expression of M2 markers such as Arg1 (Shu et al., 2020). Intermediate expression of $\alpha_D\beta_2$ and $\alpha_M\beta_2$ integrins were also identified on M2 polarised murine peritoneal macrophages, which was associated increased migratory capacity (Cui et al., 2018). The lower speed observed in *tnfa:mCherry+ arg2:GFP-* cells may reflect the need for pro-inflammatory macrophages to be more adherent in order to accumulate in the site of infection to exert their antimycobacterial effects. Taken together, it is conceivable that morphological changes in *arg2:GFP+* macrophages alter their adhesive and migratory properties via changes in integrin expression, but that the timelapse imaging in this thesis chapter did not resolve sufficient differences in speed. To confirm whether differences in integrin expression accounts for the different speeds observed between *arg2:GFP+* and non-transitioning cells, zebrafish larvae could be cryosectioned and stained for mCherry (*mfap4:mCherry*), GFP (*arg2:GFP*) and integrins via immunohistochemistry.

Most TB studies support the idea that anti-inflammatory macrophages polarise *in situ*, rather than arrive to infection sites pre-polarised. For example, *in vitro* infection of human monocyte-derived macrophages (MDMs) with *Mtb* showed that macrophages transitioned towards an M2-like phenotype, with increased expression of M2 markers (CD206, CCL17, IL-10) from 3 days to 6 days post-infection (Huang et al., 2015). Anti-inflammatory macrophages have also been found to predominate the centre of granulomas in *Mtb*-infected guinea pigs and human patients with active TB – this spatial enrichment within granulomas implies that macrophages acquire an anti-inflammatory phenotype within the tissue (Mizutani et al., 2023; Huang et al., 1998; Pessanha et al., 2012; Mattila et al., 2013). Immunohistochemical staining of bovine and porcine tuberculous granulomas also revealed a clear trend towards M2 polarisation at later stages, based on the ratio of M1 (iNOS, CD68, CD107a) to M2

markers (Arg1 and CD163) (Larenas-Muñoz et al., 2024). However, some evidence suggests that polarised macrophages may also be recruited. In one study, intratracheal transfer of M2 polarised BMDMs from BALB/c mice into *Mtb*-infected C57BL/6 mice increased lung bacterial burden, suggesting that M2 macrophages migrated to the lungs and impaired the local antimycobacterial response (Bertolini et al., 2016). Despite transfer of pre-polarised M2 macrophages, the authors did not confirm M2 marker expression in the harvested lungs, so the increased susceptibility cannot be definitively attributed to M2 macrophage prevalence. Moreover, this study artificially simulates recruitment of pre-polarised macrophages and likely does not reflect natural migration or polarisation dynamics *in vivo.* Current understanding of whether macrophages polarise *in situ* is largely based on spatial inference from histological staining at fixed timepoints from tissue biopsies and/or *in vitro* studies, which lack the resolution to track macrophage lineage over time during infection. Although the literature broadly supports *in situ* polarisation as the dominant mechanism driving induction of anti-inflammatory macrophages, this thesis chapter demonstrates that macrophages locally upregulate a canonical anti-inflammatory marker (*arg2*), providing the first *in vivo* evidence of *in situ* polarisation.

Timelapse imaging identified a population of *tnfa:mCherry+* cells that co-expressed *arg2:GFP*, which were found to exhibit heterogenous spatial relationships in relation to the granuloma. Forming mycobacterial granuloma structures generate chemotactic and cytokine gradients that establish the spatial organisation of immune cells – a process which has recently been modelled mathematically (Feng, 2024). This theoretical framework has also been supported by experimental observations. For example, spatial gradients have been described in macaque and human TB granulomas, with pro-inflammatory macrophages ($CD163^{dim}$, $iNOS^{+}$, $eNOS^{+}$, $Arg1^{low}$) localised to the core, and anti-inflammatory macrophages ($CD163^{+}$, $iNOS^{+}$, $Arg1^{high}$) predominating at the periphery (Mattila et al., 2013). *In situ* hybridisation of macaque granulomas further supports this, showing high expression of TNF-α and IFN-γ in the central region, with no detectable IL-4+ cells, demonstrating a cytokine gradient capable of driving localised macrophage polarisation (Fuller et al., 2003). These gradients are reinforced by *Mtb* infected immune cells. For instance, human alveolar macrophages exposed to virulent *Mtb* secreted high levels MCP-1 (monocyte chemotactic protein 1), which promotes recruitment of monocytes and T cells (Ferrero et al., 2003). MCP-1 has also been specifically implicated in establishing chemokine gradients recruit these immune cells from the periphery sites of infection/granuloma (Huffnagle et al., 1995; Regev et al., 2012). Taken together, these well-documented gradients that organise granuloma architecture support my finding that macrophages polarisation occurs *in situ*, rather than through recruitment of pre-polarised cells. The heterogenous distribution of *tnfa:mCherry+ arg2:GFP+* cells identified in this chapter suggests that upregulation of these canonical pro- and anti-inflammatory markers is shaped by spatial gradients within the milieu, such as highly localised oxygen and nutrient availability.

Phenotypic quantification of these putative pro-inflammatory macrophages that also expressed *arg2:GFP* revealed that they were smaller, more circular and faster than *tnfa:mCherry+ arg2:GFP-* cells. This analysis mirrors the phenotype of *arg2:GFP+* macrophages identified in the previous results chapter, suggesting that these may represent the same population of cells. There are several reports of macrophages having a mixed M1/M2 expression profile. Flow cytometry of alveolar macrophages from healthy human participants found that over 99% of cells highly expressed surface markers associated with both M1 (CD86) and M2 (CD206) in the steady state (Mitsi et al., 2018). Characterisation of macrophage subtypes in diseased settings has also identified double positive cells. For example, circulating monocytes/macrophages from systemic sclerosis patients have been found to have a mixed M1/M2 profile (Trombetta et al., 2018). Double positive cells were also identified in fibrotic rat renal lesions, and mixed M1/M2 macrophages were found as being the dominant population in human carotid atherosclerotic plaques (Nakagawa et al., 2021; Kocsy, 2021; Kocsy et al., 2025). However, studies such as those above do not identify whether these double positive cells represent a fixed macrophage subtype identity, or whether it captures intermediate macrophages that are in the process of switching from an M1 to an M2 phenotype (Kocsy, 2021). There is evidence that macrophages with an M1/M2 mixed profile are a unique fixed phenotype. In a model of resolving peritonitis, murine macrophages adopted a hybrid M1/M2 phenotype, termed resolving-phase macrophages, which were characterised by elevated IL-10, iNOS and mannose receptor synthesis, but pro-inflammatory cytokine production was minimal (Bystrom et al., 2008). However, the resolution of *ex vivo* analysis of macrophage markers at fixed time points is insufficient to discern whether resolving-phase macrophages constitute a distinct subtype or reflects a transitional state.

The timelapse data in this chapter visualised *tnfa:mCherry+* cells that later upregulated *arg2:GFP*, with changes in morphology (smaller perimeter and increased circularity index) captured following *arg2:GFP* expression. However, there were no examples of these double positive cells subsequently downregulating *tnfa:mCherry* expression. This observation, and the high prevalence of double positive cells identified, may reflect mCherry fluorescence persistence due to the stability of the fluorescent protein, rather than these cells still expressing *tnfa*. However, it is also possible that the timelapse is not capturing re-polarisation of pro-inflammatory macrophages, but rather a phenotypic switch towards an anti-inflammatory state to compensate for excess inflammation. For example, primary human MDMs treated with LPS were found to autoregulate in a paracrine manner, as when the TNF-α response was blocked with soluble TNF receptor, IL-10 secretion also dropped by 70% (Xue et al., 2015). This hyporesponsive phenotype was also observed in LPS-polarised macrophages, whereby p21 regulates this process and limits IFN-β production (Rackov et al., 2016). Additionally, as the proportion of *arg2:GFP+* macrophages was found to decrease again at 4 dpi (see chapter 3; **Fig 3.9**.), this may suggest that these transitioning macrophages are adopting a hyporesponse, anti-inflammatory phenotype by upregulating *arginase 2* in response to *Mm* infection, in order to control their

inflammatory profile and minimise tissue damage. Taken together, my findings could highlight the opportunity to target these early *Mm*-mediated anti-inflammatory macrophages before large scale biasing of macrophages towards an anti-inflammatory phenotype as a potential host-directed therapy (HDT) target.

Similar to the previous results chapter (see section 3.3), *tnfa:mCherry+* cells in the timelapse experiments required manual delineation and frame-by-frame morphological analysis, which was not performed blind. This inevitably introduces the potential for user bias and measurement error. However, as in the preceding chapter, all measurements were completed prior to plotting, and *tnfa:mCherry+ arg2:GFP-* cells did not exhibit the same phenotypic changes observed in those that upregulated *arg2:GFP* expression, suggesting that any potential bias was minimised and that the observed changed in phenotype reflected genuine biological events.

Another limitation of the work presented in this chapter is that most experiments using newly generated lines – particularly those employing the *tnfa:mCherry* line – were not performed using F3 generations of fish due to time constraints. This represents a potential limitation because early-generation transgenic lines may exhibit mosaic or variable transgene expression and incomplete stabilisation of germline transmission, which can introduce variability in labelling efficiency (Felker and Mosimann, 2016). Nevertheless, the *tnfa:mCherry* generations used displayed macrophage-specific labelling and sufficient numbers of fluorescent cells to address the central experimental question: whether *tnfa:mCherry+* macrophages undergo re-polarisation following *arg2:GFP* upregulation, rather than simply quantifying the relative proportions of each cell population. Ideally, with additional time, a *TgBAC(tnfa:mCherry)* transgenic line could have been generated, using the same promoter as the existing *TgBAC(tnfa:GFP)* line available at the University of Sheffield and used in chapter 3. However, BAC transgenesis is an extremely time-consuming and labour-intensive process, particularly when screening for founder fish, and was therefore not feasible within the timeframe of this PhD project.

Finally, a further limitation relates to the relatively low number of transitioning cells (*tnfa:mCherry+ arg2:GFP-* to *tnfa:mCherry+ arg2:GFP+*) captured during the timelapse experiments. This may, at least in part, reflect the use of younger transgenic generations for these imaging experiments. The low number of transitioning macrophages, combined with the variable duration each cell remained within the field of view, made it difficult to accurately track *tnfa:mCherry* fluorescence intensity over time, before and after *arg2:GFP* upregulation. As the onset of visible *arg2:GFP* fluorescence does not correspond to the initial induction of *arginase 2* expression – due to the delay between transcription, translation and fluorophore maturation – a continuous fluorescence trace would have provided a more informative readout for assessing whether re-polarisation predominately

occurs in macrophages with increasing *tnfa:mCherry* expression. This, in turn, could indicate that *arginase 2* induction acts as a regulatory mechanism to modulate inflammatory responses.

To conclude, by generating a *tnfa:mCherry* transgenic line to use alongside the *arg2:GFP* line, I have been able to visualise dynamic expression of these canonical pro- and anti-inflammatory macrophage markers simultaneously *in vivo* during *Mm* infection. Timelapse imaging at 3 dpi found that a substantial proportion of cells were double positive for *tnfa* and *arg2*. These cells were smaller, more circular and faster than *tnfa:mCherry+ arg2:GFP-* cells. Notably, no examples of double positive cells downregulating *tnfa:mCherry* were identified. While this may reflect mCherry persistence despite *tnfa* downregulation, it could also indicate that these double positive cells represent a hyporesponsive phenotype aimed at modulating inflammation. Furthermore, I observed *arg2:GFP-* cells that later upregulated *arg2:GFP* expression, and found the location of these double positive cells to be highly heterogenous. Together, these findings provide direct evidence that macrophage polarisation occurs locally within the infection site, rather than through the recruitment of pre-polarised cells – an important insight that, until now, had only been inferred.

5. Manipulating macrophage phenotype to improve infection outcome

5.1. Introduction

5.1.1. HIF signalling and macrophage polarisation

Hypoxia-inducible factors (HIFs) are central regulators of cellular responses to hypoxia, controlling broad transcriptional programmes that include modulators of innate immunity (Mole et al., 2009). In macrophages, HIF-1α and HIF-2α play distinct and sometimes opposing roles in shaping activation state, metabolism and effector function (Takeda et al., 2010). HIF-1α is strongly associated with classical pro-inflammatory programmes: driving glycolysis, enhancing pro-inflammatory cytokine production and promoting nitric oxide synthesis, thereby supporting antimicrobial macrophage activity (Qiu et al., 2023; Braverman and Stanley, 2017; Takeda et al., 2010). In contrast, HIF-2α has been linked to alternative activation, tissue repair and resolution-phase responses, with several *in vitro* studies reporting that it enhances arginase activity, extracellular matrix-remodelling genes and wound healing pathways (Takeda et al., 2010a; Guerrero et al., 2025; Imtiyaz et al., 2010; Choe et al., 2014; Li et al., 2021).

These HIF-regulated programmes are particularly relevant in chronic infections such as TB, where hypoxia develops within granulomas and inflamed tissues (McCaffrey et al., 2025). Stabilisation of HIFs in this context represents not only an adaptation to reduced oxygen, but a major driver of macrophage functional rewiring. HIF-1α-mediated inflammatory responses in mycobacterial control are well-established across mammalian and zebrafish models (Osada-Oka et al., 2019; Braverman et al., 2016; Elks et al., 2013). By contrast, HIF-2α remains comparatively underexplored, and available data suggests its functions are highly context-dependent (Steinberger and Eubank, 2023). Across different tissue and disease settings, HIF-2α has been reported to exert both pro- and anti-inflammatory effects. For example, in murine cardiac, tumour-associated and recruited hepatic macrophages, Hif-2α was found to promote expression of pro-inflammatory cytokines, such as *Il6*, *Tnf,* and *Il1b* (DeBerge et al., 2021; Imtiyaz et al., 2010; Jeelani et al., 2024). Conversely, in human and murine macrophages, HIF-2α has also been shown to limit inflammation by restraining NLRP3 inflammasome activation and IL-1β secretion (Li et al., 2021). Collectively, these findings underscore that HIF-2α's contribution to macrophage activation *in vivo* is complex, context-specific and far from resolved. Importantly, most mechanistic work has focussed on HIF-2α-dependent regulation of *Arg1* in mammalian macrophages. Whether HIF-2α plays a comparable role in controlling *arg2*, the dominant arginase form in zebrafish, remains unknown.

5.1.2. Modulating macrophage phenotype as a potential HDT

Macrophage-targeted HDTs have gained increasing attention in TB research, driven by the recognition that disease outcome is shaped as much by host inflammatory dynamics as by bacterial burden (Li et al., 2025). Because macrophage populations shift from predominantly pro-inflammatory to predominantly anti-inflammatory states as infection progresses, strategies that modulate when these populations emerge, rather than simply amplifying or suppressing inflammation, represent an attractive therapeutic avenue (Cronan et al., 2021; El Kasmi et al., 2008; Mattila et al., 2013; Luo et al., 2025). Early pro-inflammatory signalling is essential for initial *Mtb* control, yet sustained or excessive inflammatory activity contributes to tissue pathology, cavitation and pathogen dissemination (Huang et al., 2015; Huang et al., 2018; Pisu et al., 2020; Baay-Guzman et al., 2018; Marakalala et al., 2016). Thus, therapeutics that fine-tune the balance and timing of macrophage activation could enhance bacterial clearance while preserving tissue integrity and supporting antibiotic efficacy.

A growing body of evidence suggests that the transition from a pro- to anti-inflammatory macrophage phenotype may be host-protective at later stages of mycobacterial infection. In *Mtb*-infected mice, Arg1+ macrophages were found to limit granuloma-associated immunopathology (Duque-Correa et al., 2014). In zebrafish, depletion of *grna.2+* anti-inflammatory macrophages also had deleterious effects, with increased expression of pro-inflammatory genes (*tnfa*, *il6*) and macrophage death (Luo et al., 2025). Similar protective roles are seen in humans, as TB patients with high *GRN* expression show reduced pulmonary inflammation (Luo et al., 2025). Nevertheless, pro-inflammatory signalling is also important, as treatment with TNF-α antagonists also significantly increase the risk of reactivating latent TB in human patients (Zhang et al., 2017). Conversely, premature induction of anti-inflammatory programmes driven by *Mtb* can impair early bacterial control and create a permissive niche for growth (El Kasmi et al., 2008). These studies highlight that the switch between macrophage states as *Mtb* pathogenesis progresses is a critical determinant of disease outcome. Together, these findings underscore that it is not the presence of either programme per se, but the timely switch between them, that determines disease trajectory.

Importantly, the protective effects of macrophage arginase appear to reflect the actions of its metabolic products, such as polyamines and proline, which regulate lung inflammation by supporting cellular proliferation, extracellular-matrix remodelling and tissue repair (Karadima et al., 2025; Duque-Correa et al., 2014). These processes help maintain granuloma structure and limit immunopathology, thereby enabling pro-inflammatory immune cells to target infection effectively. This implies that understanding the regulatory pathways that induce arginase expression – and therefore the transition toward anti-inflammatory macrophage phenotypes – is crucial for designing HDTs that are both temporally appropriate and functionally balanced.

Despite this therapeutic potential, the precise mechanisms governing macrophage phenotypic switching during infection *in vivo* remain incompletely defined. In mycobacterial infection, the shift from pro-inflammatory to anti-inflammatory phenotypes can be either protective or detrimental depending on timing, yet the upstream regulators controlling this switch, including the relative contributions of HIF signalling and other microenvironmental cues, are not fully resolved (Baay-Guzman et al., 2018; El Kasmi et al., 2008). Because arginase activity (and its downstream metabolic products) actively reshapes tissue environments and macrophage function, delineating the pathways that induce *arg2* expression *in vivo* is essential for designing HDTs that modulate macrophage phenotype appropriately (Karadima et al., 2025). Mechanistic insights into how this pathway is activated will allow HDTs to be precisely tuned: promoting early inflammatory control of bacterial proliferation, while enabling reparative programmes to limit pathology as *Mtb* pathogenesis progresses.

5.1.3. *In vivo* reporters for pharmacological macrophage polarisation

A major barrier to developing macrophage-targeted HDTs is the lack of tools that reveal, in real-time, how pharmacological compounds reshape macrophage activation *in vivo*. Traditional *in vitro* polarisation assays provide valuable mechanistic insight but fail to capture the complex, dynamic cues that drive macrophage behaviour in infected tissues (Chaffey et al., 2024; Shah and Xing, 2025). Likewise, *ex vivo* analyses of granulomas provide only static endpoints, limiting their ability to determine whether drugs alter macrophage recruitment, re-polarisation or functional plasticity over time (Winchell et al., 2020; Rajmani and Surolia, 2024).

Zebrafish larvae overcome many of these limitations. Their optical transparency, conserved innate immune pathways and extensive toolkit of fluorescent reporter lines allow dynamic, whole-organism imaging of macrophage phenotype during infection and following drug treatments (Speirs et al., 2024; Rosowski, 2020; Varela and Meijer, 2022). Existing pro-inflammatory reporters, such as *tnfa:GFP* and *il1β:GFP,* have already been used to visualise of pro-inflammatory macrophage activation following both injury and mycobacterial infection (Nguyen-Chi et al., 2015; Nguyen-Chi et al., 2017; Lewis and Elks, 2019; Ogryzko et al., 2019). Critically, these reporters have also demonstrated their value as *in vivo* readouts for pharmacological screens: sodium butyrate (short-chain fatty acid) and protectin D1 (pro-resolving mediator) reduced *tnfa:GFP+* macrophages at the wound site following a tail-fin transection (Cholan et al., 2020; Nguyen-Chi et al., 2020), while the HIF stabilisers DMOG and FG4592 upregulated macrophage *tnfa:GFP* and *il1β:GFP* expression, revealing that hypoxia-mimetic drugs can bias macrophages towards a pro-inflammatory phenotype (Lewis and Elks, 2019; Ogryzko et al., 2019). Large-scale chemical screens using *il1β:GFP* larvae also identified compounds such as cimetidine (H2 receptor antagonist) that reduced macrophage inflammation and improve tissue repair in both zebrafish and mice following spinal cord injury, highlighting the translational utility of zebrafish reporter-based drug screens (Oprişoreanu et al., 2023).

However, until recently, an equivalent anti-inflammatory macrophage reporter was not available. As a result, drug effects could only be quantified by reductions in pro-inflammatory markers, without determining whether compounds promote anti-inflammatory programmes, alter macrophage population balance, or simply suppress activation globally. This gap has restricted the ability to assess whether candidate HDTs genuinely enhance anti-inflammatory macrophage functions – an essential requirement for therapeutically modulating macrophage phenotypes in TB.

The development of the *arg2:GFP* transgenic line attempts to address this gap by providing the first *in vivo* reporter of a canonical anti-inflammatory macrophage population in zebrafish (Hammond et al., 2023). In chapters 3 and 4, I showed that *arg2:GFP* labels a distinct subpopulation of macrophages with morphological, behavioural and transcriptional features consistent with *in vitro* anti-inflammatory macrophages. This reporter could therefore represent a crucial tool for directly visualising anti-inflammatory macrophage responses and for assessing whether pharmacological compounds drive shifts in macrophage activation toward anti-inflammatory programmes. Together with *tnfa*- and *il1b*-based reporters, *arg2:GFP* enables simultaneous tracking of pro- and anti-inflammatory macrophage states, providing a platform for high-resolution screening of macrophage-modulating HDTs *in vivo*.

5.1.4. Hypothesis and aims

Targeting macrophages to alter their activation status represents a promising host-directed therapy (HDT) strategy to counter the growing threat of antibiotic-resistant strains of *Mycobacterium tuberculosis* (Kilinç et al., 2021). HIF-α isoforms exert opposing effects on macrophage nitric oxide homeostasis *in vitro*, with Hif-1α upregulating iNOS and Hif-2α promoting arginase expression (Takeda et al., 2010a). Consistent with this, genetic stabilisation of Hif-1α and reduction of Hif-2α enhances resistance to *Mm* infection in zebrafish through an iNOS-dependent mechanism, largely mediated by neutrophils – the principal innate immune source of reactive nitrogen species in zebrafish and humans (Elks et al., 2013). In contrast, the contribution of Hif-2α to arginase regulation in leukocytes (both macrophages and neutrophils) *in vivo* remains poorly understood.

A second outstanding question concerns whether newly developed pro- and anti-inflammatory macrophage reporter lines can be used as *in vivo* readouts for pharmacological modulation of macrophage phenotype. Such tools would provide a foundation for screening HDTs that shift macrophage activation balance during infection.

I hypothesise that *arg2:GFP* expression is regulated by Hif-2α signalling, and that the transgenic reporter can be used as a functional *in vivo* readout for anti-inflammatory macrophages induced by known M2-polarising mediators.

To investigate these hypotheses, I will use genetic manipulation of Hif-α signalling pathways and pharmacological treatments to address the following aims:

- To determine whether Hif-2α stabilisation upregulates *arg2:GFP* expression in neutrophils and macrophages.
- To assess whether putative pro-inflammatory macrophages (*tnfa:mCherry+)* require Hif-2α signalling to transition toward an anti-inflammatory (*arg2:GFP+*) phenotype.
- To evaluate whether macrophage *arg2:GFP* expression is induced following pharmacological modulation of Hif-α signalling and treatment with anti-inflammatory compounds under resting conditions.

5.2. Results

5.2.1. Stabilisation of Hif-2α signalling upregulated leukocyte *arg2:GFP* expression both under resting conditions and in immune challenge

HIF-α isoforms have been shown to exert opposing effects on nitric oxide homeostasis in murine macrophage *in vitro* (Takeda et al., 2010). M1 polarisation (IFNγ, LPS) rapidly induced HIF-1α expression, in turn upregulating *iNOS*. M2 polarisation (IL-4, IL-13) gradually induced HIF-2α, leading to increased *arginase 1* expression. Importantly, genetic stabilisation of Hif-1α in zebrafish larvae, which is known to be host-protective in *Mm* infection, upregulated macrophage *tnfa:GFP* expression both at rest and during immune challenge (Elks et al., 2013; Lewis and Elks, 2019). Given that, similar to murine macrophages, Hif-1α stabilisation *in vivo* promotes a putative pro-inflammatory macrophage phenotype, I aimed to explore the effect of Hif-2α stabilisation on leukocyte *arg2:GFP* expression.

Single cell injection of dominant active *hif-α* variants has previously been shown to stabilise Hif-α in zebrafish embryos (Elks et al., 2013). To validate RNA quality and its ability to genetically stabilise Hif-α signalling, dominant active *hif-1α* (DA1), dominant active *hif-1α* (DA2), dominant negative *hif-1α* (DN1) and dominant negative *hif-2α* (DN2) RNAs were injected into *Tg(phd3:GFP)i114,* which serve as a reporter for Hif-1α activity. As *phd3* is a downstream target of Hif-α signalling, successful stabilisation of Hif-α should result in GFP expression (Santhakumar et al., 2012; Elks et al., 2013). Indeed, injection with DA *hif-1α* and DA *hif-2α* led to robust *phd3:GFP* expression at 1 dpf, indicating effective upregulation of this Hif-α target (**Fig. 5.1**). In contrast, embryos injected with dominant negative *hif-α* variants or the phenol red (PR) vehicle control did not show *phd3:GFP* induction. Together, these results confirm successful genetic stabilisation of Hif-α and validate the RNA quality for future experiments.

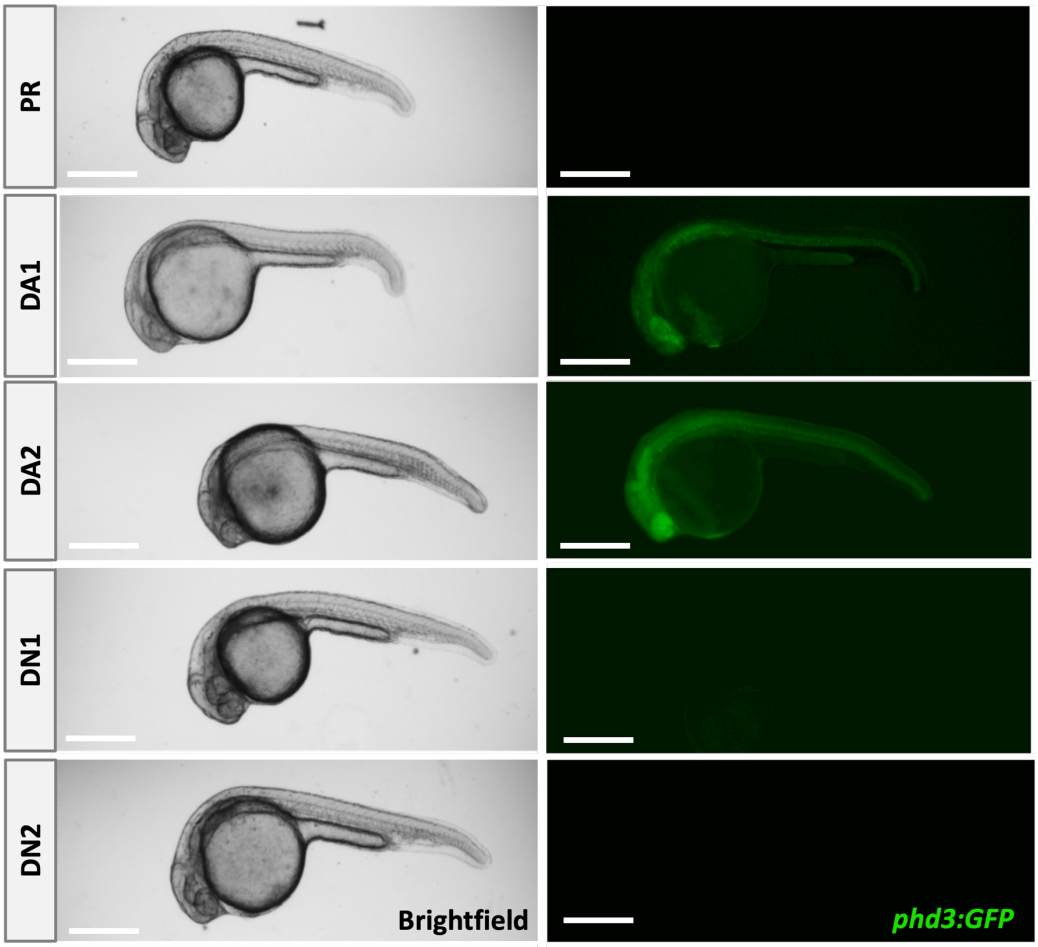


Figure 5.1. Dominant active *hif-1α* and *hif-2α* RNA induced *phd3:GFP* expression. At the single cell stage, *phd3:GFP* zebrafish embryos were injected with either phenol red (PR), dominant active *hif-1α* (DA1), dominant active *hif-2α* (DA2), dominant negative *hif-1α* (DN1) or dominant negative *hif-2α* (DN2). Zebrafish embryos were screened for GFP expression at 1 dpf to validate the quality of the RNA, with GFP upregulation in fish injected with dominant active Hif-α variants demonstrating successful HIF-α stabilisation. Scale bar is 1 mm.

As neutrophils are the predominant leukocyte to upregulate *arg2:GFP* during immune challenge, I first aimed to assess neutrophil *arg2:GFP* expression following Hif-2α stabilisation (Hammond et al., 2023). Embryos from the *arg2:GFP* line were crossed with the *Tg(lyz:mCherry)* neutrophil reporter line and injected at the single cell stage with either PR or DA *hif-2α*. At 1 dpf, embryos were injected with PVP, a commonly used mock-infection control (Hammond et al., 2023). In the PR-injected controls, a small proportion of neutrophils upregulated *arg2:GFP* expression, with 33 out of 442 neutrophils (8.1%) identified GFP+ by visual inspection (**Fig. 5.2. A, C**). Leukocytes do not upregulate *arg2:GFP* following PVP-mock infection, thus this upregulation is most likely caused a mild injury caused during the mounting process for imaging, with *arg2:GFP*+ neutrophils only identified in 4 fish (out of 17) (Hammond et al., 2023). In contrast, significantly more neutrophils expressed *arg2:GFP* following DA2 injection, with 177 out of 668 neutrophils (38%) showing visible *arg2:GFP* expression (**Fig. 5.2. A, C**). In chapter 3, quantification of *arg2:GFP* fluorescence intensity was identified as a more stringent method for distinguishing between *arg2:GFP-* and *arg2:GFP+* macrophages (see section 3.3.4).

Based on this, neutrophil *arg2:GFP* fluorescence intensity was quantified. Neutrophil *arg2:GFP* fluorescence was significantly higher in DA *hif-2α* injected embryos compared to PR injected controls (**Fig. 5.2. D**).

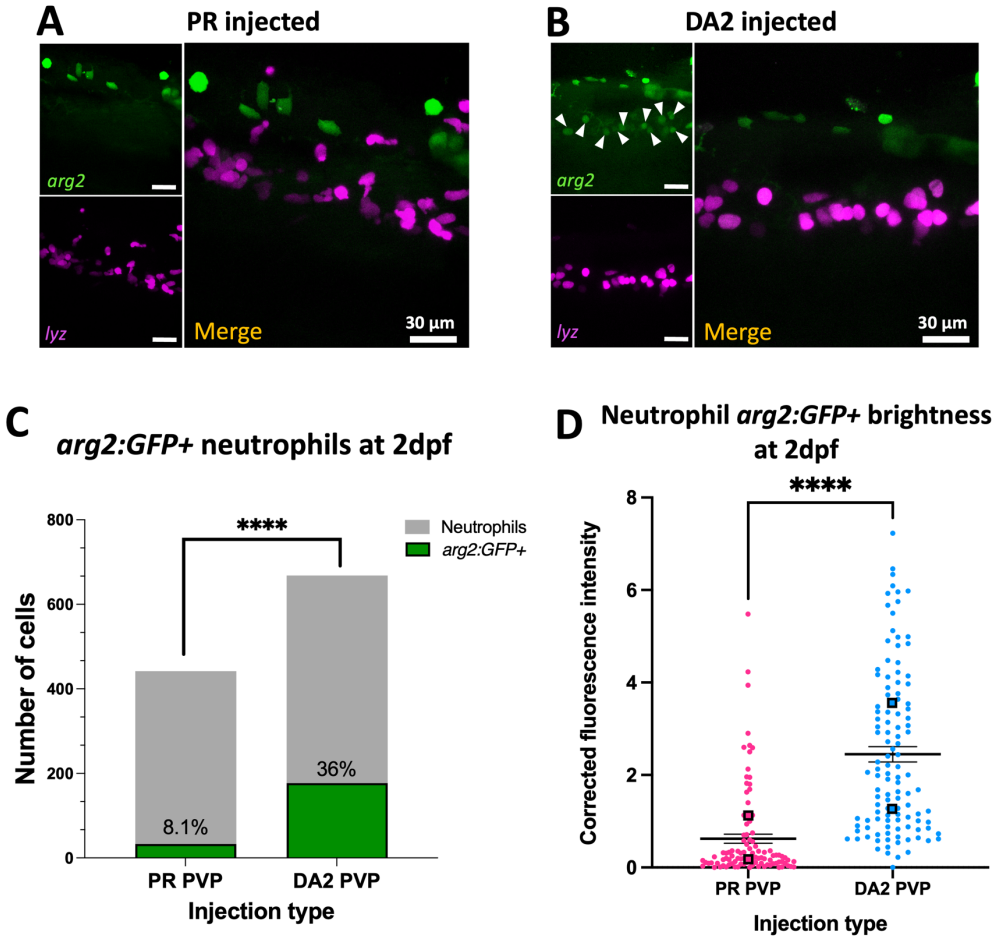


Figure 5.2. Neutrophils upregulate *arg2:GFP* following genetic stabilisation of Hif-2α under resting conditions. (**A**) Representative confocal image of 2 dpf *arg2:GFP* crossed with *lyz:mCherry* larvae injected with PR at the single cell stage and injection of PVP in the caudal vein at 1 dpf. (**B**) Representative confocal image of 2 dpf *arg2:GFP* crossed with *lyz:mCherry* larvae injected with DA *hif-2α* at the single cell stage and infection of PVP in the caudal vein at 1 dpf. (**C**) Graph illustrating that there is a higher proportion of *arg2:GFP+ lyz:mCherry+* cells at 2 dpf when injected with DA2 compared to PR. (**D**) Corrected fluorescence intensity of individual neutrophils in the GFP channels was measured to assess upregulation of *arg2:GFP*. Quantification from N=102-114 cells from 17-19 fish, over 2 independent experiments. Error bars indicate SEM. Statistical significance in (**C**) was calculated using a Fisher's exact test. Statistical significance in (**D**) was calculates using an unpaired *t*-test. ****P ≤ 0.0001. All counts were taken from a 40x field of view near the caudal vein. White arrowheads indicate *arg2:GFP+* neutrophils. Scale bars are stated on the images.

Following the observation that Hif-2α stabilisation upregulates neutrophil *arg2:GFP* expression, I next investigated whether *arg2:GFP* is also upregulated in macrophages under resting conditions. *arg2:GFP* expression in macrophages was observed only in embryos injected with DA *hif-2α*, with no positive cells detected in PR-injected controls (**Fig. 5.3. A-B**) – neither by visual inspection (**Fig. 5.3. C**)

nor by quantification of GFP fluorescence intensity (**Fig. 5.3. D**). In contrast, 9.4% of macrophages (20 out of 213; from 12 out of 28 fish) in DA *hif-2α* injected embryos were *arg2:GFP+* (**Fig. 5.3. B**) and their GFP fluorescence intensity was significantly higher than that of PR injected controls (**Fig. 5.3. D**). The number of *arg2:GFP+* cells with immune cell morphology was also quantified. Only 20 *arg2:GFP+* cells were also *mpeg:mCherry+,* while 176 *arg2:GFP+* cells were *mpeg:mCherry-* (**Fig. 5.3. E**). This suggests that Hif-2α-mediated *arg2:GFP* predominantly occurs in neutrophils. Taken together, these findings demonstrate that, consistent with *in vitro* data from murine macrophages, Hif-2α stabilisation upregulates *arginase* expression in leukocytes *in vivo*.

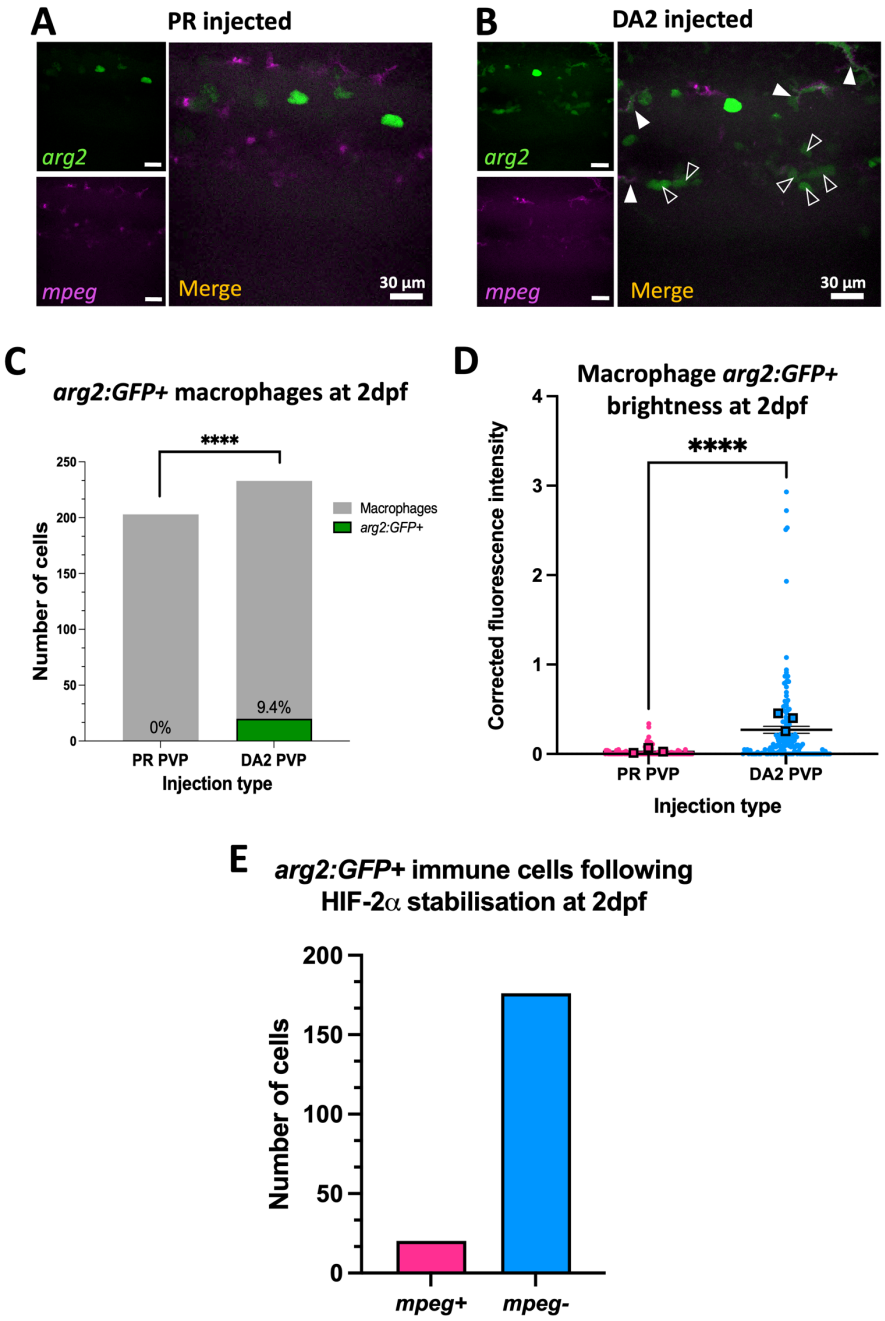


Figure 5.3. Macrophages upregulate *arg2:GFP* following genetic stabilisation of Hif-2α under resting conditions. (**A**) Representative confocal image of 2 dpf *arg2:GFP* crossed with *mpeg:mCherry* larvae injected with PR at the single cell stage and injection of PVP in the caudal vein at 1 dpf. (**B**) Representative confocal image of 2 dpf *arg2:GFP* crossed with *mpeg:mCherry* larvae injected with DA *hif*-2α at the single cell stage and infection of PVP in the caudal vein at 1 dpf. (**C**) Graph illustrating the proportion of *arg2:GFP+ mpeg:mCherry+* cells at 2 dpf when injected with DA2 compared to PR. (**D**) Corrected fluorescence intensity of individual macrophages in the GFP channels was measured to assess upregulation of *arg2:GFP*. (**E**) Graph illustrating the number of *arg2:GFP+* cells with immune cell morphology that were *mpeg:mCherry+* or *mpeg:mCherry-*. Quantification from N=138-155 cells from 27-29 fish, over 3 independent experiments. Error bars indicate SEM. Statistical significance in (**C**) was calculated using a Fisher's exact test. Statistical significance in (**D**) was calculates using an unpaired *t*-test. ****P ≤ 0.0001. All counts were taken from a 40x field of view near the caudal vein. White arrowheads indicate *arg2:GFP+* macrophages. Hollow arrowheads indicate *arg2:GFP+* cells with neutrophil morphology. Scale bars are stated on the images.

Hif-1α stabilisation has previously been shown to upregulate iNOS in neutrophils at 1 dpi, leading to increased nitrosylation levels and reduced *Mm* burden (Elks et al., 2013). This iNOS-dependent, host protective mechanism was also observed following Hif-2α inhibition using DN *hif-2α* Therefore, the effect of Hif-α isoform manipulation on neutrophil *arg2:GFP* expression was investigated to determine whether enhanced Hif-1α signalling (via DA *hif-1α* or DN *hif-2α*) results in reduced *arginase 2* expression as a consequence of iNOS upregulation.

At 1 dpi, PR injected, mock-infected (PVP) controls did not induce neutrophil *arg2:GFP* expression, with only 4 examples of *arg2:GFP+ lyz:mCherry+* cells identified (**Fig. 5.4. A**). Neutrophils upregulated *arg2:GFP* expression in PR injected embryos following *Mm* infection, with *arg2:GFP* fluorescence intensity significantly increasing as previously reported (**Fig. 5.4. Bi, C**) (Hammond et al., 2023). DA *hif-2α* significantly increased neutrophil *arg2:GFP* expression compared to controls (**Fig. 5.4. Biv, C**). As hypothesised, DN *hif-2α* significantly downregulated neutrophil *arg2:GFP* (**Fig. 5.4. Bv, C**), but DA1 did not significantly impact GFP expression compared to PR controls (**Fig. 5.4. Bii, C**). Interestingly, inhibition of Hif-1α signalling with DN *hif-1α* resulted in a modest but statistically significant decrease in neutrophil *arg2:GFP* (**Fig. 5.4. Biii, C**). These results demonstrate that the host protective effect of DN *hif-2α* arises from the coordinated upregulation of neutrophil iNOS and downregulation of *arginase 2*, rather than from either mechanism alone. Coupled with the finding that DA *hif-1α* did not affect *arg2:GFP* expression, these data demonstrate that Hif-2α signalling specifically modulates neutrophil *arginase 2* at the 1 dpi stage of pathogenesis.

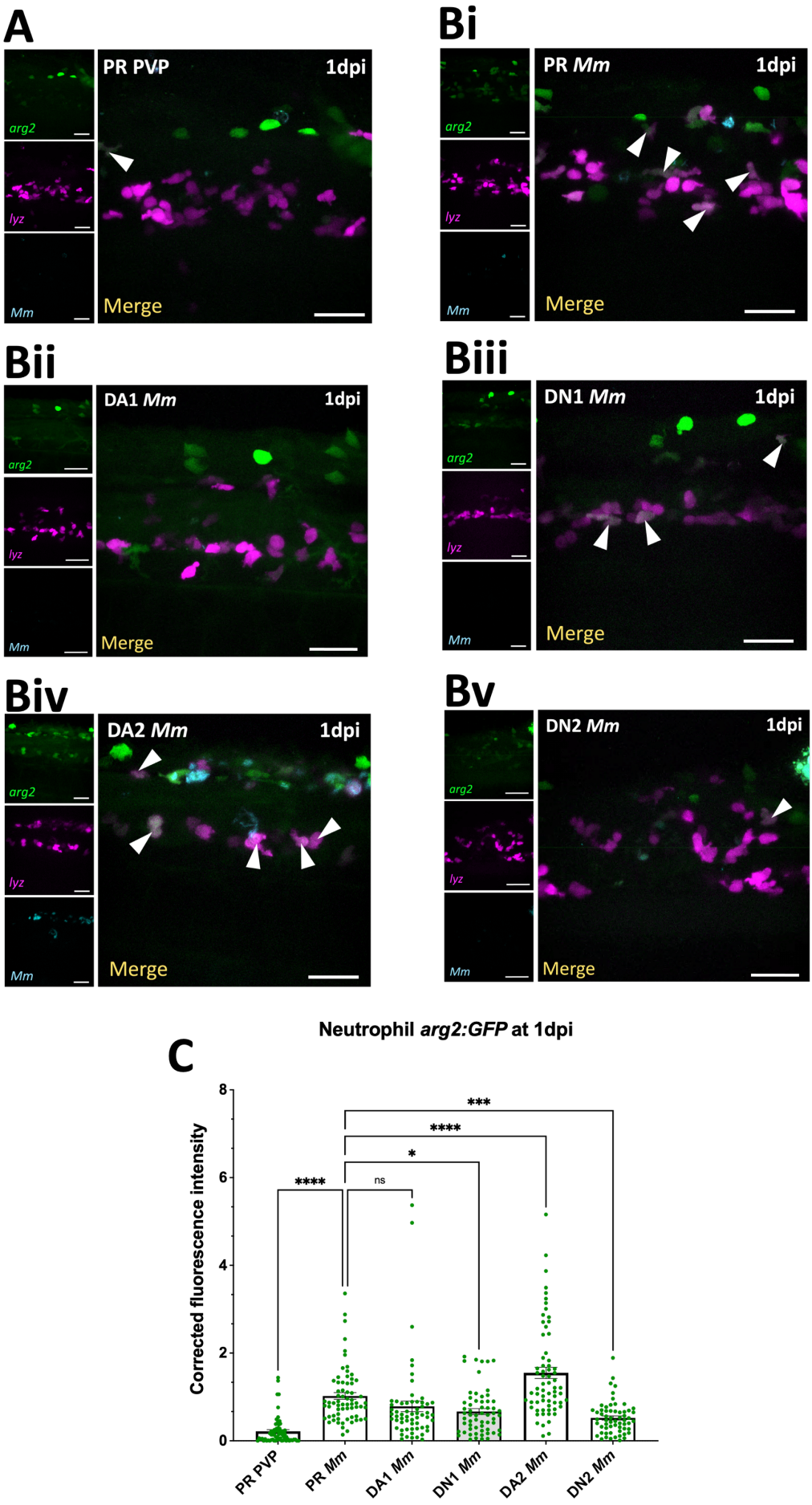


Figure 5.4. Only genetic stabilisation of Hif-2α, not Hif-1α, increases neutrophil *arg2:GFP* expression in *Mm* infection at 1 dpi. (**A**) Representative confocal image of 1 dpi *arg2:GFP* crossed to *lyz:mCherry* injected with PR at

the single cell stage and mock-infected with PVP. (**B**) Representative confocal image of 1 dpi *arg2:GFP* crossed to *lyz:mCherry* injected with (**Bi**) PR, (**Bii**) DA *hif*-1α, (**Biii**) DN *hif*-1α, (**Biv**) DA *hif*-2α or (**Bv**) DN *hif*-2α at the single cell stage and infected with *Mm*. (**C**) Corrected fluorescence intensity of *lyz:mCherry+* neutrophils in the GFP channel to assess *arg2:GFP* fluorescence brightness. N=3 independent experiments, with 2-5 larvae per group imaged per experiment. All counts were taken from a 40x field of view near the caudal vein (site of infection) or around clusters of bacteria within the fish. Up to 6 of the brightest *lyz:mCherry+* neutrophils were measured for fluorescence intensity. Arrowheads indicate *arg2:GFP+ lyz:mCherry+* cells. Error bars depict SEM. Statistical significance was calculated using a one-way ANOVA with Bonferroni's multiple comparisons post hoc test. Scale bar = 30 μm.

The host protective effects of DA *hif-1*α and DN *hif-2*α on bacterial burden were previously determined at 4 dpi (Elks et al., 2013). Thus, neutrophil *arg2:GFP* expression following Hif-α modulation was also assessed at 4 dpi. A similar pattern to what was observed at 1 dpi was seen at this later timepoint. No examples of *arg2:GFP+* neutrophils were identified in PR embryos following a mock infection, an observation that is supported by the lack of GFP fluorescence detected (**Fig. 5.5. A, C**). Compared to mock-infected fish, PR injected embryos significantly upregulated *arg2:GFP* in neutrophils (**Fig. 5.5. Bi, C**). As expected, DA *hif-2*α significantly increased neutrophil *arg2:GFP* expression compared to PR controls (**Fig. 5.5. Biv, C**). Similar to the 1 dpi measurement, DA *hif-1*α did not significantly affect neutrophil *arg2:GFP* (**Fig. 5.5. Bii, C**), whilst the significant decrease in *arg2:GFP* fluorescence intensity was also significantly downregulated in DN *hif-2*α injected larvae (**Fig. 5.5. Bv, C**). Notably, DN *hif-1*α significantly decreased neutrophil *arg2:GFP* expression to levels similar to that of DN *hif-2a* injected fish at this later stage of infection (**Fig. 5.5 Biii, C**).

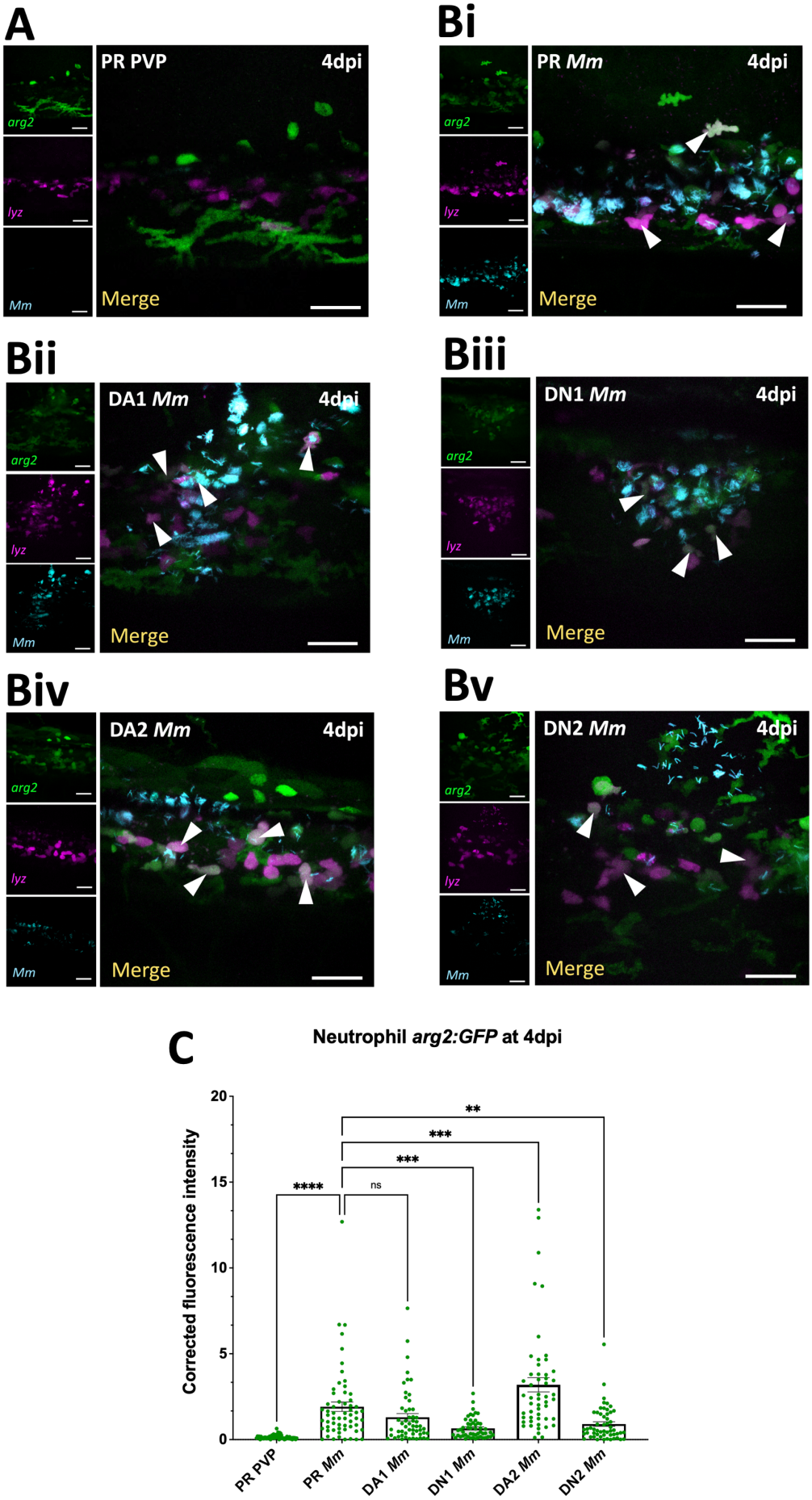


Figure 5.5. Only genetic stabilisation of Hif-2α, not Hif-1α, increases neutrophil *arg2:GFP* expression in *Mm* infection at 4 dpi. (**A**) Representative confocal image of 4 dpi *arg2:GFP* crossed to *lyz:mCherry* injected with PR at

the single cell stage and mock-infected with PVP. (**B**) Representative confocal image of 4 dpi *arg2:GFP* crossed to *lyz:mCherry* injected with (**Bi**) PR, (**Bii**) DA *hif*-1α, (**Biii**) DN *hif*-1α, (**Biv**) DA *hif*-2α or (**Bv**) DN *hif*-2α at the single cell stage and infected with *Mm*. (**C**) Corrected fluorescence intensity of *lyz:mCherry+* neutrophils in the GFP channel to assess *arg2:GFP* fluorescence brightness. N=3 independent experiments, with 3-4 larvae per group imaged per experiment. All counts were taken from a 40x field of view near the caudal vein (site of infection) or around clusters of bacteria within the fish. Up to 6 of the brightest *lyz:mCherry+* neutrophils were measured for fluorescence intensity. Arrowheads indicate *arg2:GFP+ lyz:mCherry+* cells. Error bars depict SEM. Statistical significance was calculated using a one-way ANOVA with Bonferroni's multiple comparisons post hoc test. Scale bar = 30 μm.

Dr Piotr Szkuta (previous PhD student in the Elks lab) found that neutrophils inside granulomas had lower anti-nitrotyrosine levels (indirect measure of nitric oxide production) compared to those outside the granuloma (Szkuta, 2020). However, DA *hif-1*α rescued this downregulation, with no significant differences found between neutrophils inside and outside the granuloma. The lower levels of anti-nitrotyrosine is thought to be caused by mycobacteria-mediated downregulation of iNOS and subsequent reduced nitric oxide production (Espinosa-Cueto et al., 2015). Another mycobacterial strategy to evade immune killing is through arginase upregulation, competing with iNOS for L-arginine to reduce nitric oxide production (El Kasmi et al., 2008). Therefore, *arg2:GFP* fluorescence intensity of neutrophils inside and outside granulomas was quantified to determine whether *arginase 2* levels differ following Hif-α modulation.

In line with the previous observation that neutrophils within granulomas have lower levels of anti-nitrotyrosine staining, *arg2:GFP+* neutrophils inside granulomas were significantly brighter than those outside the granuloma in control PR-injected fish (**Fig. 5.6. A**). This difference was abrogated following DA *hif-1*α injection, with neutrophils inside and outside granulomas displaying similar *arg2:GFP* fluorescence intensity, with those outside the granuloma appearing brighter (**Fig. 5.6. B**). Notably, *Mm* granulomas appeared to have an additive effect on DA *hif-2*α-mediated *arg2:GFP* upregulation, with *arg2:GFP+* neutrophils within granulomas exhibiting significantly greater fluorescence than those outside (**Fig. 5.6. C**). In DN *hif-2*α injected fish, *arg2:GFP* fluorescence of neutrophils inside the granuloma were significantly brighter than those outside (**Fig. 5.6. D**). Taken together, these findings support that Hif-1α stabilisation mitigates mycobacteria-mediated suppression of nitric oxide production in neutrophils, by preventing *arginase 2* upregulation, in addition to upregulating iNOS.

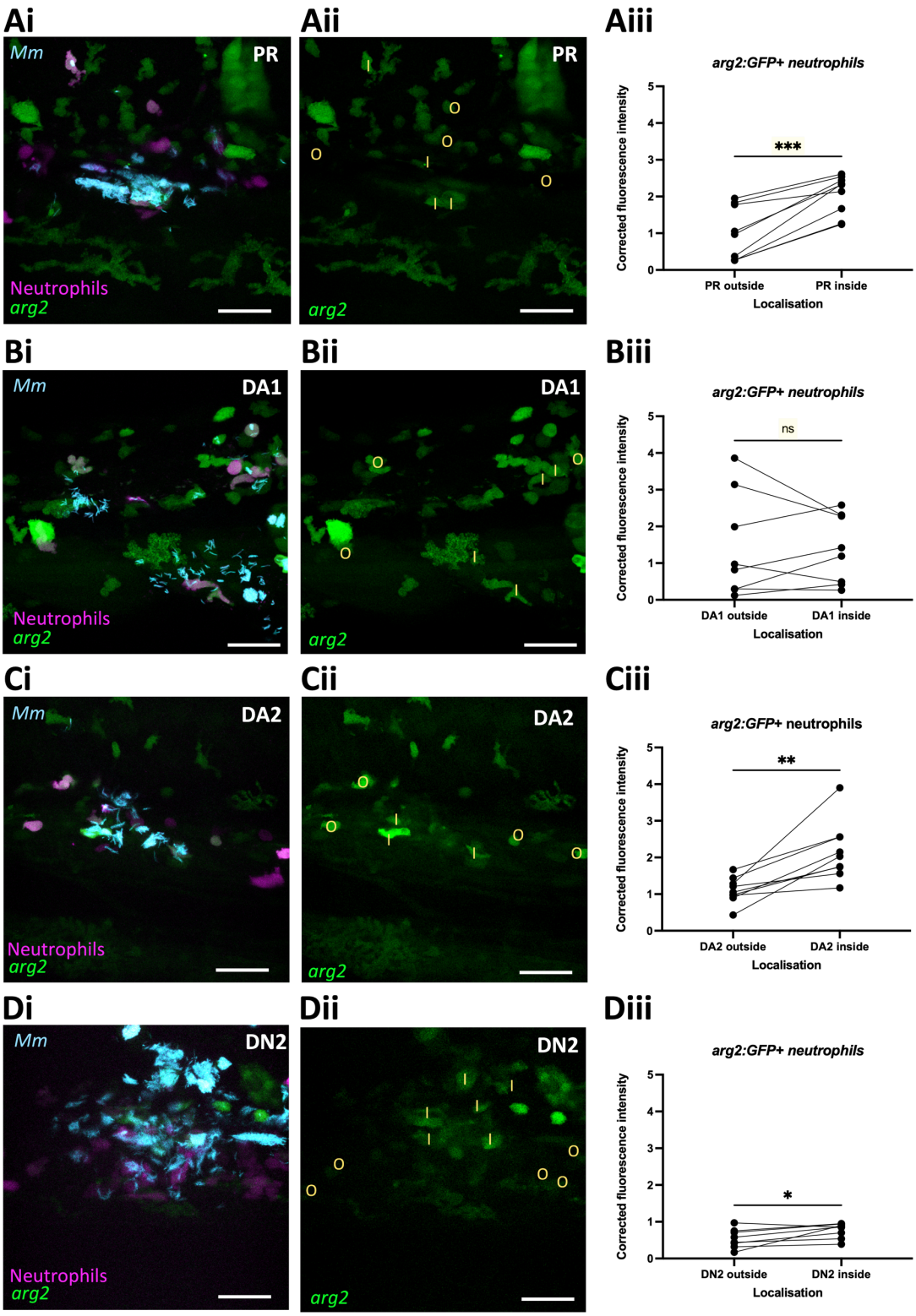


Figure 5.6. Neutrophils outside granuloma structures upregulate *arg2:GFP* expression following Hif-1α stabilisation, while neutrophils inside granulomas upregulate *arg2:GFP* following genetic downregulation of Hif-2α. (**Ai-Di**) Representative confocal images of an *Mm* granulomas at 4 dpi of *arg2:GFP* crossed to *lyz:mCherry* injected with (**Ai**) PR, (**Bi**) DA *hif*-1α, (**Ci**) DA *hif*-2α or (**Di**) DN *hif*-2α. (**Aii-Dii**) Representative confocal images from (**Ai-Di**) of only the GFP channel, illustrating the *arg2:GFP+* neutrophils that were quantified. (Aiii-Diii) Graph illustrating *arg2:GFP* fluorescence intensity of neutrophils outside (O) and inside (I) the granuloma. N=3 independent experiments, with 8-9 paired cells (2-3 paired cells per fish, 8-9 fish total per condition). Statistical significance was calculated using a paired, two-tailed t-test. *P ≤ 0.05; **P ≤ 0.01 ***P ≤ 0.001.

To conclude, Hif-2α stabilisation upregulates *arg2:GFP* expression in both neutrophils and macrophages under resting conditions, with the effect being most prominent in neutrophils, the primary leukocyte population to upregulate *arg2:GFP* during immune challenge. Consistent with data from *in vitro* murine macrophages, these findings confirm that *arginase 2* is a Hif-2α target *in vivo*. Genetic stabilisation of Hif-1α abrogated mycobacteria-mediated downregulation of neutrophil *arg2:GFP* expression within granulomas, adding to our understanding the host-protective role of DA *hif-1a*. Furthermore, DN *hif-1α* significantly reduced neutrophil *arg2:GFP* expression, suggesting that Hif-1α inhibition may inhibit *arginase 2* expression through non-canonical downstream effects.

5.2.2. Hif-2α is partially required for *tnfa:mCherry+ arg2:GFP-* cells to become *arg2:GFP+*

Hif-2α stabilisation upregulated leukocyte *arg2:GFP* expression in resting conditions, with modulation of Hif-2α signalling found to alter neutrophil *arg2:GFP* during *Mm* infection (see section 5.2.1; **Fig 5.2-5.6**). Although arginase has been identified as a HIF-2α target in murine macrophages *in vitro* (Takeda et al., 2010), whether HIF-2α is required for arginase expression *in vivo* remains poorly defined. Furthermore, while HIF-2α is classically associated with anti-inflammatory states (Takeda et al., 2010a), its role in facilitating the transition from a pro-inflammatory to an anti-inflammatory phenotype during infection is currently unknown. I therefore used DN *hif-2α* to determine whether Hif-2α signalling is required for putative pro-inflammatory macrophages to upregulate *arg2:GFP* during *Mm* infection. Additionally, whether the host protective effects of modulating leukocyte arginase (e.g. via DN *hif-2α*) are neutrophil- or macrophage-dependent was also investigated.

Initial observations at 3 dpi showed that approximately 50% of immune cells were *tnfa:mCherry+ arg2:GFP+* with the proportion of double positive cells increasing towards the end of the timelapse (see section 4.2.3, **Fig. 4.15. B**). This high proportion of double positive cells led me to ask at what time point in *Mm* pathogenesis do *tnfa:mCherry+* cells upregulate *arg2:GFP*. To address this, *tnfa:mCherry; arg2:GFP* larvae were imaged on the confocal microscope in the at 45 hours post-infection (hpi; 2 dpi), 50 hpi (2 dpi), 68 hpi (3 dpi) and 73 hpi (3 dpi) as a pilot experiment. At 45 hpi (hpi; 2 dpi), 12.7% of cells (8 out of 71) were double positive (**Fig. 5.7. Ai, Aii**). Slightly fewer cells were identified as double positive at 50 hpi (2 dpi), with 7.85% of cells (4 out of 55) being *tnfa+ arg2+* (**Fig. 5.7. Bi, Bii**). Significantly more *tnfa:mCherry+* cells were identified at 3 dpi, with 124 and 129 cells at 68 hpi and 73 hpi, respectively (**Fig. 5.7. C-D**). Over a quarter of cells (26.53%; 26 out of 124) were *tnfa+ arg2+* at 68 hpi (**Fig. 5.7. Ci, Cii**), rising to 30.3% (30 out of 129) at 73 hpi (**Fig. 5.7. Di, Dii**). This demonstrated that *tnfa:mCherry+* cells primarily transitioned to being *tnfa:mCherry+ arg2:GFP+* between 2 dpi and 3 dpi. Therefore, infected larvae were imaged in an overnight timelapse at 2 dpi to determine whether more of these transitioning cells could be captured.

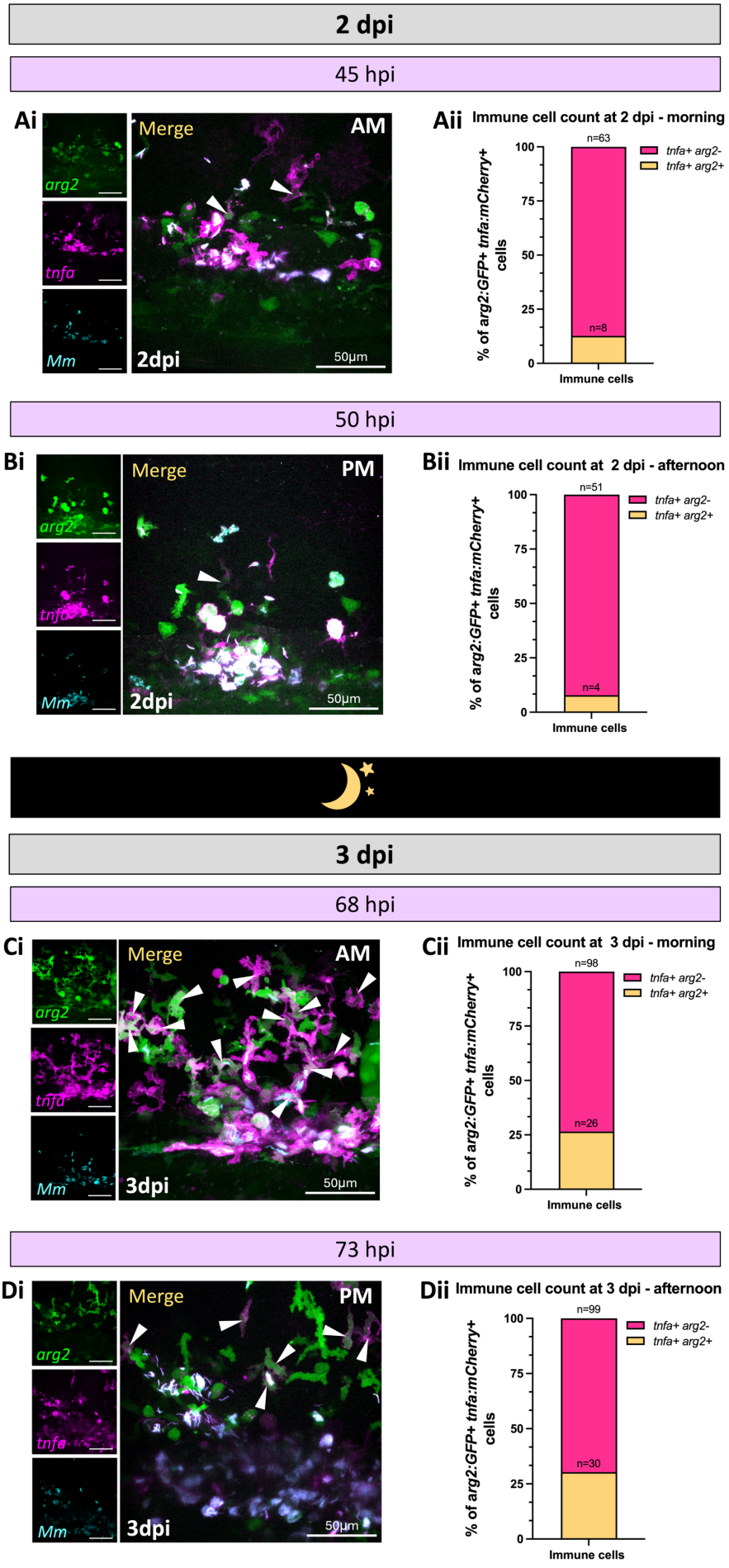


Figure 5.7. Confocal imaging at two timepoints at 2 dpi and 3 dpi suggests most *tnfa:mCherry+* cells transition to also being *arg2:GFP+* overnight. (**Ai**) Representative confocal image of *arg2:GFP* crossed with *tnfa:mCherry* at

45 hpi (2 dpi). (**Aii**) Graph illustrating the percentage of *arg2:GFP+ tnfa:mCherry+* cells at 45 hpi (2 dpi). (**Bi**) Representative confocal image of *arg2:GFP* crossed with *tnfa:mCherry* at 50 hpi (2 dpi). (**Bii**) Graph illustrating the percentage of *arg2:GFP+ tnfa:mCherry+* cells at 50 hpi (2 dpi). (**Ci**) Representative confocal image of *arg2:GFP* crossed with *tnfa:mCherry* at 68 hpi (3 dpi). (**Cii**) Graph illustrating the percentage of *arg2:GFP+ tnfa:mCherry+* cells at 68 hpi (3 dpi). (**Di**) Representative confocal image of *arg2:GFP* crossed with *tnfa:mCherry* 73 hpi (3 dpi). (**Dii**) Graph illustrating the percentage of *arg2:GFP+ tnfa:mCherry+* cells at 73 hpi (3 dpi). Total number of cells are indicated on the graphs. N=1 independent pilot experiment. Arrowheads indicate *tnfa:mCherry+ arg2:GFP+* cells. Black rectangle and moon/stars indicates overnight incubation of *Mm*-infected larvae. Scale bars are stated on the images. AM, morning; PM, afternoon.

In the first instance, I aimed to verify that *tnfa:mCherry+ arg2:GFP+* previously observed at 3 dpi were also present at 2 dpi, as well as the cells being phenotypically similar. Over the course of a 10-hour timelapse, examples of *tnfa:mCherry+ arg2:GFP-* (**Fig. 5.8. A, B** - pink box) and *tnfa:mCherry+ arg2:GFP+* cells (**Fig. 5.8. A, C** - yellow box) were identified in overnight timelapses at 2 dpi.

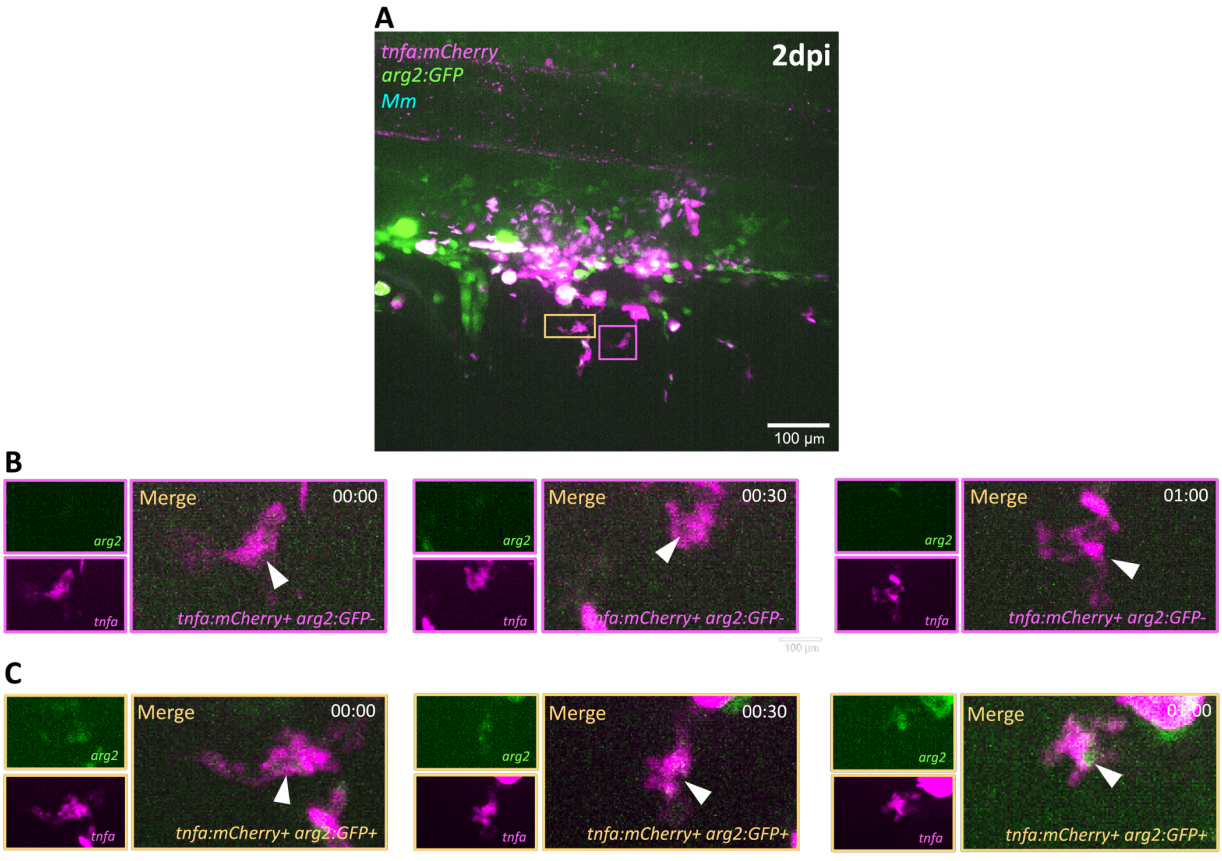


Figure 5.8. *tnfa:mCherry+ arg2:GFP+* immune cells are captured in timelapses at 2 dpi. (**A**) Representative frame (maximum projection) of a spinning disk timelapse of 2 dpi *tnfa:mCherry* larvae crossed with *arg2:GFP*. Pink box highlights *tnfa:mCherry+ arg2:GFP-* cell. Yellow box highlights double positive cell. (**B**) Zoomed area of *tnfa:mCherry+ arg2:GFP-* cell (white arrowhead) highlighted in the pink box in (**A**), spanning from the beginning of the timelapse (00:00), 30 minutes and at 1 hour. (**C**) Zoomed area of *tnfa:mCherry+ arg2:GFP+* cell (white arrowhead) highlighted in the yellow box in (**A**), spanning from the beginning of the timelapse (00:00), 30 minutes and at 1 hour. Timelapse time steps were 3 minutes, imaged over 10 hours. Scale bar stated on still image in (**A**).

To confirm that the *tnfa:mCherry+ arg2:GFP+* cells identified at 2 dpi phenotypically resemble those at 3 dpi, cell morphology (perimeter and circularity index) and behaviour (speed and meandering index) was assessed over a 1-hour window (double positive cell vs. nearest *tnfa+ arg2+* neighbour). Compared to *tnfa:mCherry+ arg2:GFP-* cells, double positive cells had a significantly smaller average perimeter (72.5 μm vs. 109 μm; **Fig. 5.9. A**) and a significantly higher average circularity index (0.51 vs. 0.31; **Fig. 5.9. B**). No significant differences in meandering index were identified between the two populations of cells (0.51 vs. 0.55; **Fig. 5.9. D**). Yet double positive cells had a significantly higher average speed when compared to their nearest *tnfa+ arg2-* neighbour (1.79 μm/sec vs. 1.47 μm/sec; **Fig. 5.9. C**). Taken together, these data demonstrate that *tnfa:mCherry+ arg2:GFP+* cells at 2 dpi phenotypically resemble those characterised at 3 dpi.

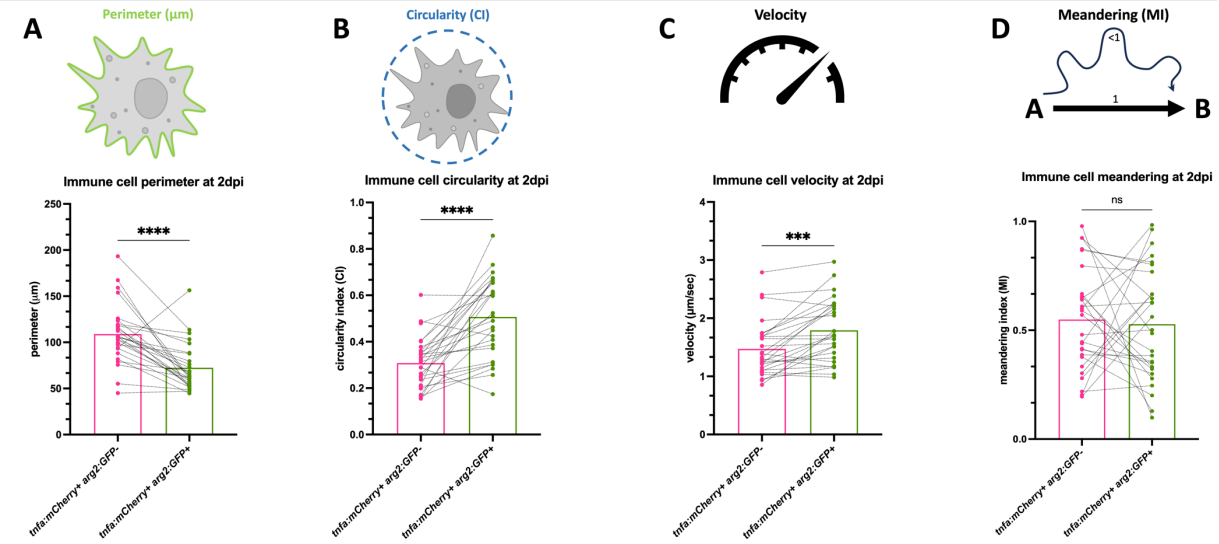


Figure 5.9. *tnfa:mCherry+ arg2:GFP-* immune cells at 2 dpi are larger, more branched and faster than *tnfa:mCherry+ arg2:GFP+* immune cells. (**A**) Top: Representation of perimeter analysis obtained in ImageJ. Bottom: Paired comparison illustrating that the average perimeter (μm) of *tnfa+ arg2-* cells (pink) is significantly higher than that of double positive cells (green) across a 1-hour window. (**B**) Top: Representation of circularity index (CI) analysis calculated using ImageJ. Bottom: Paired comparison illustrating that the average CI of *tnfa+ arg2- cells* (pink) is significantly lower than that of double positive cells (green) across a 1-hour window. (**C**) Top: Representation of speed analysis obtained using the ImageJ manual tracking plugin. Bottom: Paired comparison illustrating that the average speed (μm/sec) of *tnfa+ arg2-* cells (pink) is significantly lower than that of double positive cells (green) across a 1-hour window. (**D**) Top: Representation of how the most direct migratory route equates to a meandering index (MI) of 1. Bottom: Paired comparison illustrating that there is no significant difference between the average MI of *tnfa+ arg2-* cells (pink) and double positive cells (green) across a 1-hour window. N=27 matched cells (3 matched cells per fish, 9 fish total), over 2 independent experiments. Statistical significance was calculated using a paired, two-tailed t-test. ***P ≤ 0.001; ****P ≤ 0.0001.

Based on the confocal imaging data, most *tnfa:mCherry+ arg2:GFP-* cells transition to being double positive overnight between 2 dpi and 3 dpi. Thus, as expected, an overnight timelapse at 2 dpi captured more of these transitioning cells (**Fig. 5.10. A**). More transitioning cells were identified at 2 dpi compared to 3 dpi (16 cells vs. 10 cells), with one fish having 5 examples of *tnfa:mCherry+* cells upregulating *arg2:GFP* within the timelapse window. An example of *a tnfa:mCherry+ arg2:GFP-* cell that transitions to being double positive can be seen in **Fig. 5.10. Bi**, with GFP being faintly visible 27 minutes after the cell is first in the field of view. This same cell was in the field of view for an hour following the transition, with GFP fluorescence being more prominent at this time-point (**Fig. 5.10. Bi**). To confirm that these transitioning cells were indeed double positive, cells were tracked frame-by-frame in the GFP(**Fig. 5.10. Bii**), with an example of this process illustrated for the cell in **Fig. 5.10. Bi**. Faint *arg2:GFP* fluorescence was initially detected 2 hours and 6 minutes (02:06) after the *tnfa:mCherry+* cell was in the field of view, and could be tracked in each frame until the cell moved out of focus an hour later (**Fig. 5.10. Bii** - yellow bar). These transitioning cells were tracked until they were no longer in frame to confirm whether the phenotypic switch observed in transitioning cells at 3 dpi is also seen at 2 dpi.

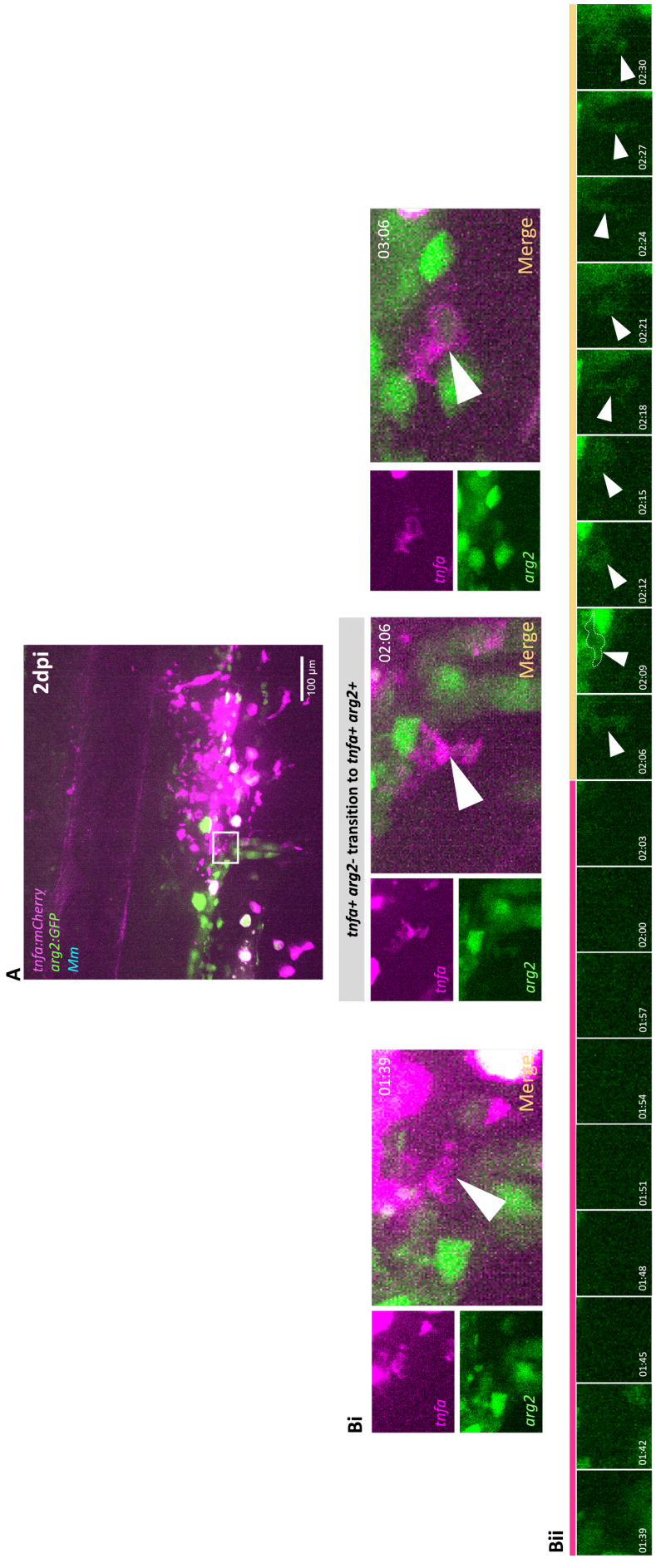


Figure 5.10. Spinning disk timelapse imaging at 2 dpi captures *tnfa:mCherry+ arg2:GFP-* cells that later also express *arg2:GFP.* (**A**) Representative frame (maximum projection) of a timelapse of 2 dpi *arg2:GFP* larvae

crossed with *tnfa:mCherry*. White box indicates *tnfa:mCherry+ arg2:GFP-* cell that expresses *arg2:GFP* at later stages of the timelapse. (**Bi**) Left: Zoomed area of the *tnfa:mCherry+ arg2:GFP-* cell (white arrowhead) highlighted in the white box in (**A**). Middle: Frame at which point *tnfa:mCherry+* cell transitions to expressing *arg2:GFP* (white arrowhead). Right: Transitioned *tnfa:mCherry+ arg2:GFP+* macrophage (white arrowhead) is visible at later stages of the timelapse. (**Bii**) Tracking of transitioning cell in each frame in the GFP channel. First half of the frames (9 frames; pink bar) indicate the same *tnfa:mCherry+ arg2:GFP-* cell. At 2 hours 6 minutes (02:06), upregulation of *arg2:GFP* in the same cell becomes visible (white arrowhead). Double positive cell is tracked for the duration it is in frame (yellow bar). Timelapse time steps were 3 minutes; timestamps indicate hours:minutes. White dotted line in (Bii) at frame 02:09 highlights the *arg2:GFP+* cell surrounded by *arg2:GFP* signal that is not of interest. Scale bar stated on still image in (**A**).

Manual tracking of transitioning cells identified a decrease in cell perimeter (**Fig. 5.11. A**) and increase in circularity index (**Fig. 5.11 B**) following *arg2:GFP* upregulation (green lines). To determine whether there was a statistical difference between these morphometric descriptors, the average perimeter/CI up to 1 hour before and 1 hour after *arg2:GFP* expression (**Fig. 5.11.**; dotted black line) was calculated. Following *arg2:GFP* expression, *tnfa:mCherry+ arg2:GFP+* cells had a significantly smaller perimeter (85.3 μm vs. 64.7 μm; **Fig. 5.11. C**) and significantly higher CI (0.35 vs. 48; **Fig. 5.11. D**).

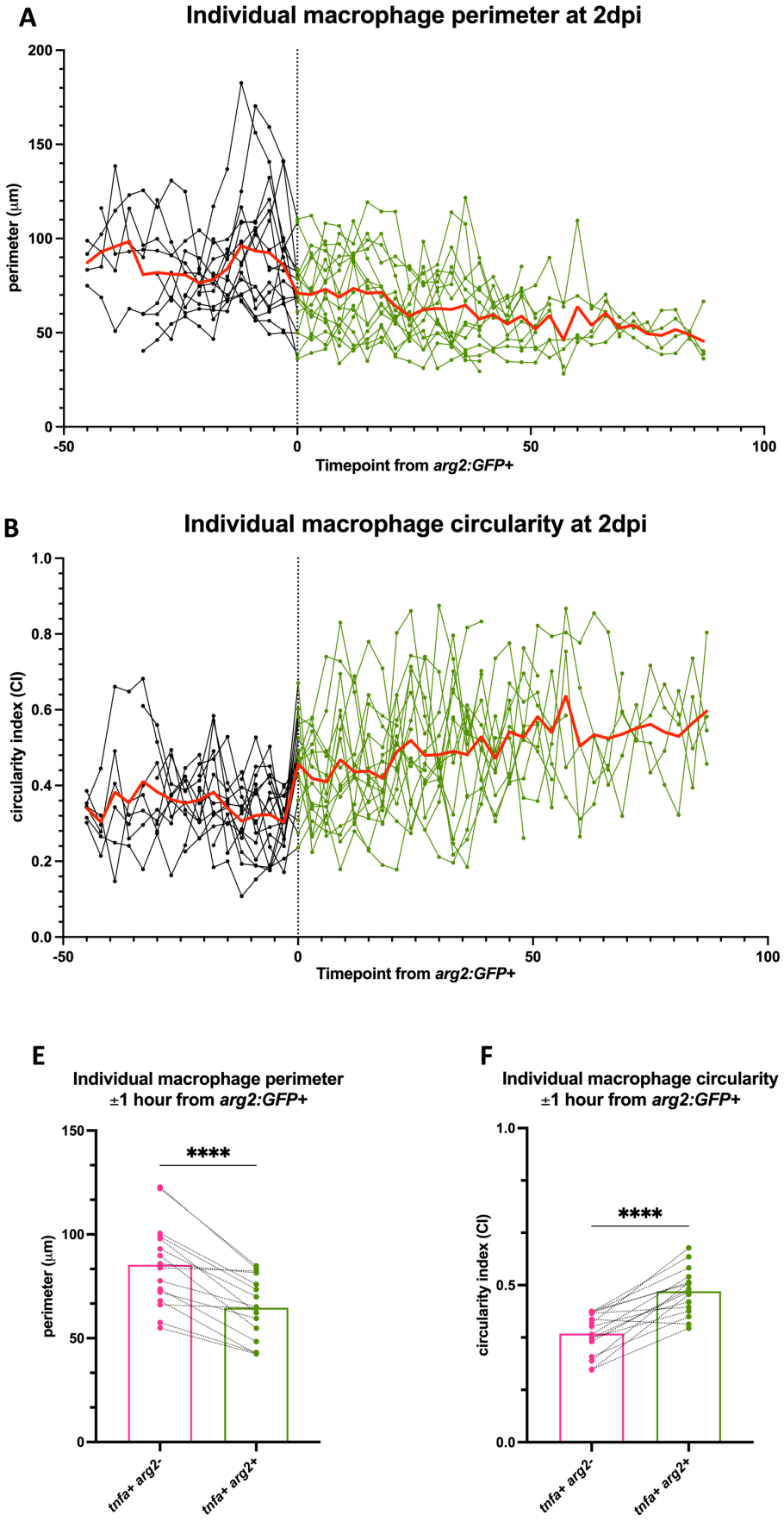


Figure 5.11. Changes in morphology are captured when tracking *tnfa:mCherry+ arg2:GFP+* immune cells that transition to being *arg2:GFP+*. (**A-B**) Line graphs illustrating decreasing trend in *tnfa:mCherry+* cell perimeter (**A**) and CI (**B**) following *arg2:GFP* expression. Each line depicts a macrophage and 0 on the x-axis (dotted black line) is the point at which *arg2:GFP* is expressed, illustrated in green. Mean line is illustrated in red. (**C**) Paired

comparison illustrating that the average perimeter (μm) of *tnfa:mCherry+ arg2:GFP-* immune cells (pink) up an hour before *arg2:GFP* expression is significantly higher than the hour after *arg2:GFP* expression (green). (**D**) Paired comparison illustrating that the average CI of *tnfa:mCherry+ arg2:GFP-* immune cells (pink) the hour prior to *arg2:GFP* expression is significantly lower than the hour after *arg2:GFP* expression (green). N=16 cells identified from 7 larvae, over 2 independent experiments. Statistical significance was calculated using a paired, two-tailed t-test. ****P ≤ 0.0001.

To assess whether transitioning cells exhibit behavioural changes such as those observed when comparing *tnfa:mCherry+ arg2:GFP+* cells to their nearest neighbour, the average speed of double positive cells was calculated up to one hour before and after *arg2:GFP* upregulation. No significant differences in average speed (1.63 μm/sec vs. 1.9 μm/sec; **Fig. 5.12. A**) or meandering index (0.57 vs. 0.62; **Fig. 5.12. B**) were observed.

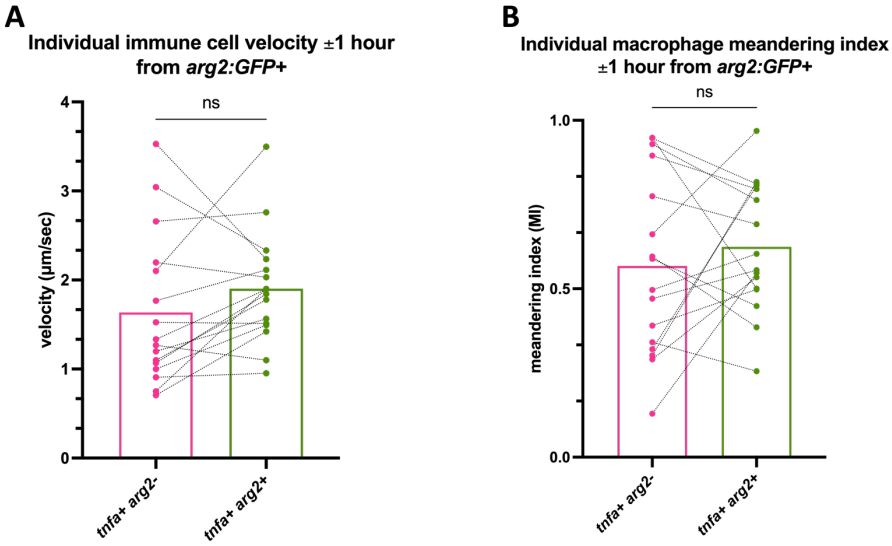


Figure 5.12. Changes in behaviour are not captured when tracking *tnfa:mCherry+ arg2:GFP-* immune cells that transition to being *arg2:GFP+* at 2 dpi (**A**) Paired comparison illustrating that there is no significant difference between the average speed (μm/sec) of *tnfa:mCherry+ arg2:GFP-* immune cells (pink) the hour before *arg2:GFP* expression and the hour after *arg2:GFP* expression (green). (**D**) Paired comparison illustrating that there is no significant difference between the average meandering index of *tnfa:mCherry+ arg2:GFP-* immune cells (pink) the hour prior to *arg2:GFP* expression and the hour after *arg2:GFP* expression (green). N=16 cells identified from 7 larvae, over 2 independent. Statistical significance was calculated using a paired, two-tailed t-test.

Taken together, these data confirm that *tnfa:mCherry+ arg2:GFP+* cells at 2 dpi are phenotypically similar to those previously identified and characterised at 3 dpi.

As putative pro-inflammatory macrophages upregulated *arg2:GFP* overnight at 2 dpi (**Fig. 5.7**), embryos were injected with DN *hif-2a* at the single cell stage and a 10-hour overnight timelapse at 2 dpi

was performed to determine whether Hif-2α signalling plays a mechanistic role in driving macrophage *arg2:GFP* expression during *Mm* infection.

In PR-control injected embryos, 36.67% (22 out of 60) of *tnfa:mCherry+* cells upregulated *arg2:GFP* expression over the course of the overnight spinning disk timelapse (**Fig. 5.13. C**), including 12 examples where *tnfa:mCherry+ arg2:GFP-* cells (**Fig. 5.13. Ai**) transitioned to being double positive across 4 fish (**Fig. 5.13. Aii**). The proportion of double positive cells in PR-injected larvae was comparable to that observed in 3 dpi fish imaged using the confocal microscope in the morning (26.53%; **Fig. 5.7.Ci**). In contrast, the percentage of *tnfa:mCherry+ arg2:GFP+* cells was significantly reduced following DN *hif-2α* injection, with only 5.63% (4 out of 71) identified as double positive (**Fig. 5.13. C**). Notably, no examples of *tnfa:mCherry+ arg2:GFP-* cells (**Fig. 5.13. Bi**) upregulating *arg2:GFP* (**Fig. 5.13. Bii**) were identified over the 10-hour timelapse across 6 fish. This data demonstrates that Hif-2α is partially required for *tnfa:mCherry+* cells to upregulate *arg2:GFP* expression in *Mm* infection.

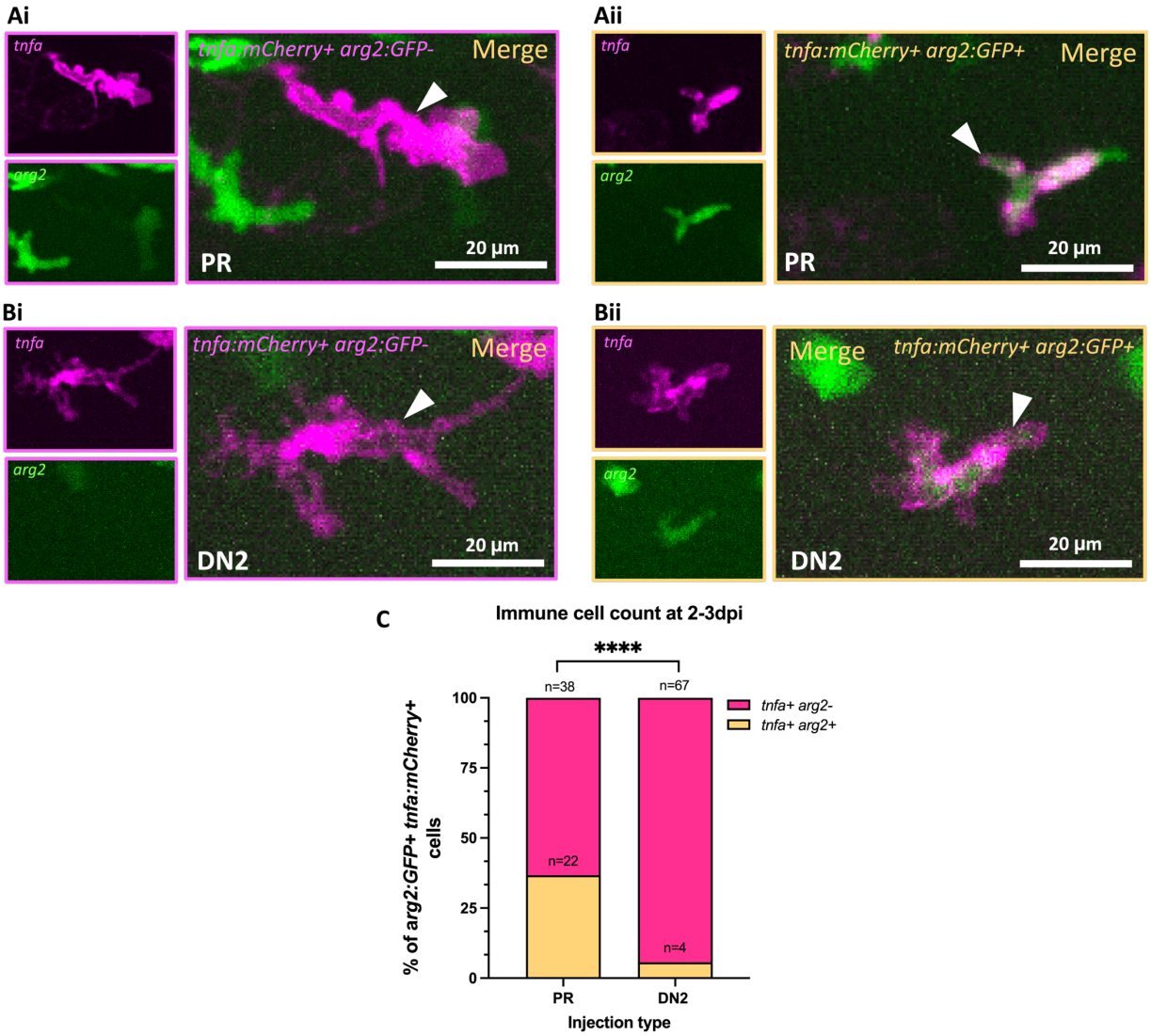


Figure 5.13. Hif-2α is partially required for *tnfa:mCherry+ arg2:GFP-* cells to transition to double positive. (**A**) Zoomed area of *tnfa:mCherry+ arg2:GFP-* cell (**Ai**) and *tnfa:mCherry+ arg2:GFP+* cell (**Aii**) identified in the overnight timelapse in a PR-injected control larvae. (**B)** Zoomed area of *tnfa:mCherry+ arg2:GFP-* cell (**Bi**) and

tnfa:mCherry+ arg2:GFP+ cell (**Bii**) identified in the overnight timelapse in a DN *hif-2a*-injected control larvae. (**C**) Graph illustrating the percentage of double positive and *tnfa+ arg2-* cells identified throughout the timelapse. N=2 independent experiments, with 2 PR-injected and 3 DN *hif-2a*-injected larvae per experiment. Total number of cells counted are stated on the graph. Arrowheads in (**A-B**) indicate cell of interest. Statistical significance was calculated using a Fisher's exact test. ****P ≤ 0.0001.

Given that DN *hif-2α* prevents putative pro-inflammatory macrophages from upregulating *arg2:GFP* expression, I next asked investigated whether its host protective effects are mediated by the suppression of arginase upregulation in either neutrophils or macrophages, in addition to its known role in promoting iNOS expression in neutrophils (Elks et al., 2013).

To address this question, I first depleted neutrophils by injecting 500 μM *csf3r* morpholino (MO) at the single cell stage of *Tg(mpx:GFP)* neutrophil reporter zebrafish (Ellett et al., 2011; Liongue et al., 2009). *Mm*-infected MO injected larvae were treated with an arginase inhibitor (nor-NOHA) and bacterial burden assessed to determine the macrophage contribution to the protective effect of inhibiting arginase activity (Gobert et al., 2000; Szkuta et al., paper in preparation). To validate whether neutrophil numbers remain significantly depleted at 5 dpf, neutrophils were counted from the caudal vein to the posterior of larvae. At 2 dpf, *csf3r* MO-injected fish exhibited a 63.62% reduction in neutrophils, with an average of 21.13 cells compared to 66.33 in control MO-injected fish (**Fig. 5.14. C**). This depletion was similar at 3 dpf, with morphants averaging 33.47 neutrophils versus 93 in control controls (64.01% reduction) (**Fig. 5.14. C**). By 4 dpf, the neutrophil population began to recover, coinciding with the development of the pronephric kidney marrow (Speirs et al., 2024), although numbers remained reduced – *csf3r* morphants had an average of 51.47 neutrophils compared to 115.67 in controls, representing a 55.5% reduction in neutrophils (**Fig. 5.14. C**). At 5 dpf, a 45.58% reduction persisted, with morphants averaging 70.13 neutrophils compared to 128.87 in controls (**Fig. 5.14. C**). Despite partial recovery from 4 dpf onwards, neutrophil numbers remained significantly depleted from 2 dpf to 5 dpf (**Fig. 5.14. A-B**). These findings confirm that at 5 dpf, *csf3r*-mediated neutrophil depletion remains sufficiently pronounced to allow for investigation of neutrophil/macrophage arginase contributions to bacterial burden.

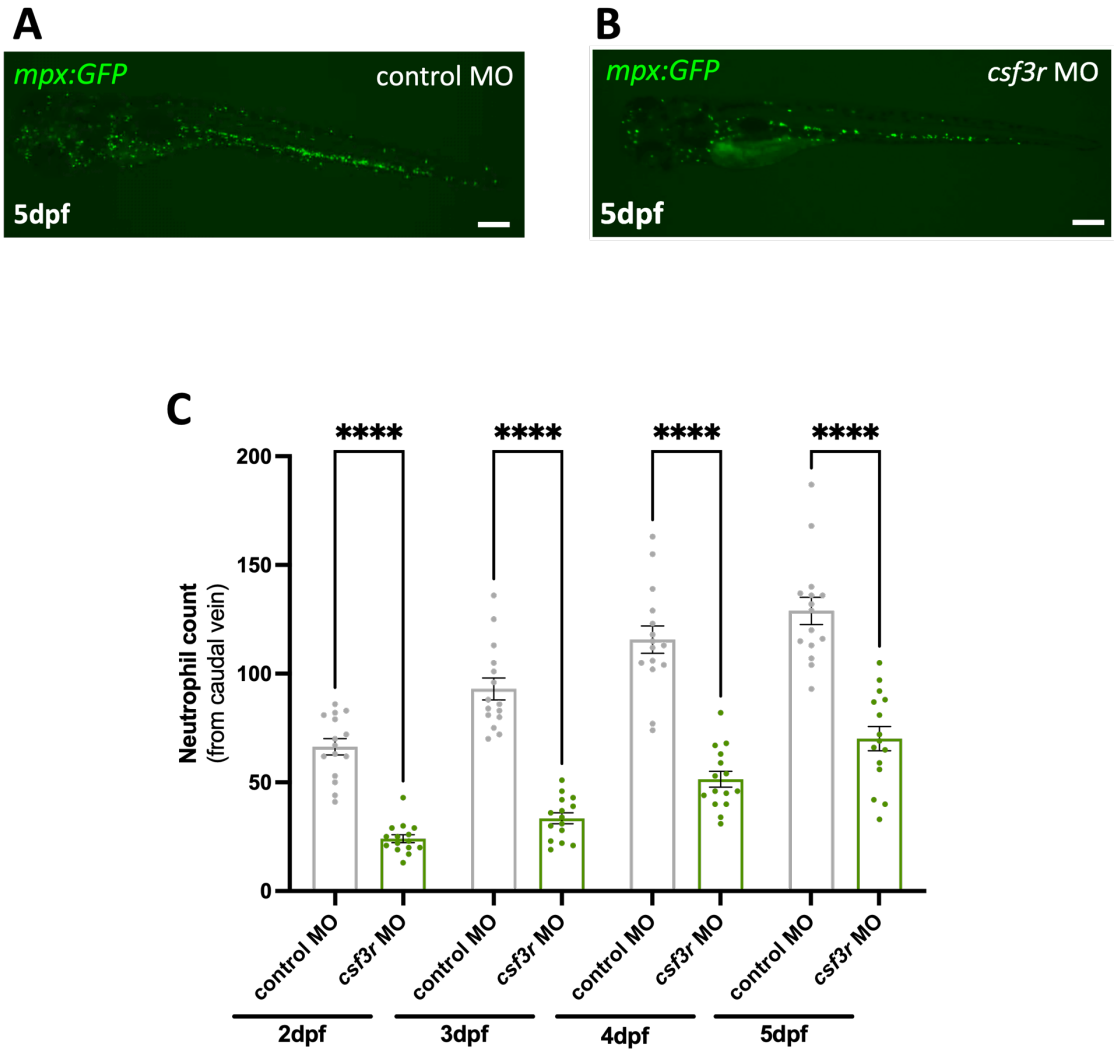


Figure 5.14. *csf3r* morpholino-mediated neutrophil depletion persists for up to 5 dpf. (**A-B**) Representative widefield images of 5 dpf Tg*(mpx:GFP)*i114 zebrafish larvae following single cell injection with (**A**) control morpholino or (**B**) *csf3r* morpholino. (**C**) Neutrophil counts were determined from the caudal vein to the posterior of control or *csf3r* morpholino injected larvae from 2 dpf to 5 dpf. N=1 independent experiment (pilot), with neutrophils quantified from 15 fish of each group for each time-point. Statistical significance was calculated using a one-way ANOVA with Bonferroni's post hoc test to compare the means of each time-point. ****P ≤ 0.0001. Scale bars in (**A-B**) are 1 mm.

To pharmacologically inhibit arginase, nor-NOHA was used to immersion-treat *csf3r* morphants and control MO-injected larvae prior to assessment of *Mm* burden at 4 dpi (5 dpf) using widefield imaging (**Fig. 5.15. A-B**). In DMSO-treated controls (solvent control), no significant differences in bacterial burden were observed between control MO and *csfr3* MO-injected larvae (412.55 pixels vs. 561.062 pixels respectively; **Fig. 5.15. A, C**). In contrast, nor-NOHA treatment significantly reduced bacterial burden in control MO-injected larvae (74.07 pixels), compared to both DMSO-treated control (412.55 pixels) and *csf3r* MO-injected groups (561.062 pixels; **Fig. 5.15. A-C**). However, this protective effect was lost in *csf3r* morphants: nor-NOHA-treated morphants exhibited significantly higher bacterial burden than all other groups, with bacterial pixels nearly doubling relative to their DMSO-treated

(1102.17 pixels vs. 561.062 pixels; **Fig. 5.15. A-C**). These findings demonstrate that a full neutrophil population is required for nor-NOHA-mediated protection against *Mm* infection, and suggests that the macrophage transition from a pro-inflammatory (*tnfa:mCherry+*) to anti-inflammatory phenotype (*arg2:GFP+*) is host-protective. Moreover, these data demonstrates that the host protective effect of DN2-mediated arginase downregulation is primarily due to increased neutrophil NO production (Elks et al., 2013).

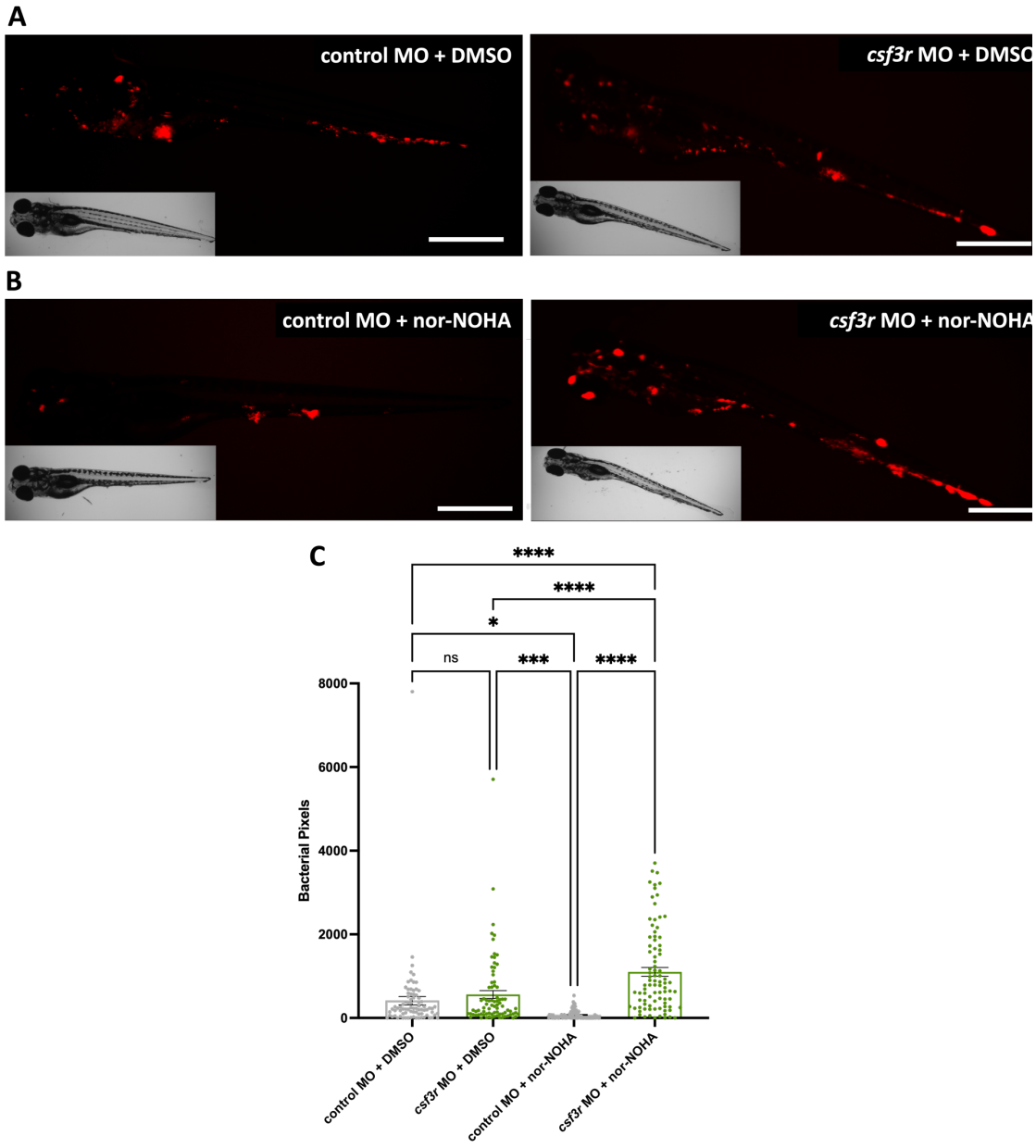


Figure 5.15. Pharmacological inhibition of arginase in neutrophil-depleted larvae leads to an increase in bacterial burden. (**A**) Representative widefield images of *Mm* burden in DMSO-treated control larvae injected with either control morpholino (left) or *csf3r* morpholino (right) at 5 dpf. (**B**) Representative widefield images of *Mm* burden in nor-NOHA-treated larvae injected with either control morpholino (left) or *csf3r* morpholino (right) at 5 dpf. (**C**) Fluorescent images of *Mm* burden from (**A**) were analysed using ZF4 software to calculate bacterial pixels. N=3 independent experiments, with 27-29 larvae imaged per group. Statistical significance was calculated using a one-way ANOVA with Bonferroni's multiple comparisons post hoc test. *P ≤ 0.05; ***P ≤ 0.001; ****P ≤ 0.0001. Scale bars in (**A-B**) are 1 mm.

As bacterial burden was increased in nor-NOHA-treated *csf3r* morphants, I next assessed whether the host-protective role of macrophage arginase contributes to granuloma formation and architecture. Widefield images were re-analysed using QuantiFish to quantify the number of fluorescent foci (granulomas), the number of large granulomas (minimum area considered a focus adjusted to a value of 20) and the bacterial dissemination (**Fig. 5.16**). In control larvae, despite bacterial burden being lower in nor-NOHA treated fish (**Fig. 5.15. C**), there were no significant differences in the total number of foci between DMSO- and nor-NOHA-treated fish (8.81 vs. 7.15; **Fig. 5.16. A, D, E**). However, the number of large foci was significantly reduced following nor-NOHA treatment (6 vs. 2.6; **Fig. 5.16. B, D, E**). Spatial distribution analysis revealed no significant differences between DMSO- or nor-NOHA-treated control larvae (7.4 vs. 6.4; **Fig. 5.16. C, D, E**), indicating that arginase inhibition alone does not affect bacterial dissemination in the presence of a full neutrophil population. As expected, comparison between control larvae and *csf3r* morphants treated with DMSO revealed a significant increase in the total number of foci (8.81 vs. 15.75; **Fig. 5.16. A, D, E**), the number of large foci (6 vs. 10.35; **Fig. 5.16. B, D, E**) and bacterial spatial distribution (7.4 vs. 13.16; **Fig. 5.16. C, D, E**), illustrating the host-protective contribution of neutrophils to *Mm* control. In contrast to control larvae, nor-NOHA treatment of *csf3r* morphants resulted in a marked increase in granuloma number and size, in addition to increased bacterial burden. Nor-NOHA-treated *csf3r* morphants exhibited a significantly higher number of foci compared to DMSO-treated morphants (25.54 vs. 15.74; **Fig. 5.16. A, D, E**), as well as significantly increased number of large granulomas (17.1 vs. 10.35; **Fig. 5.16. B, D, E**). Furthermore, bacterial dissemination was significantly elevated in nor-NOHA-treated *csf3r* morphants relative to DMSO-treated morphants (19.41 vs. 13.16; **Fig. 5.16. C, D, E**). Taken together, these findings indicate that macrophage arginase contributes to limiting granuloma number and size, as well as restricting bacterial dissemination, particularly in the absence of neutrophil-mediated control.

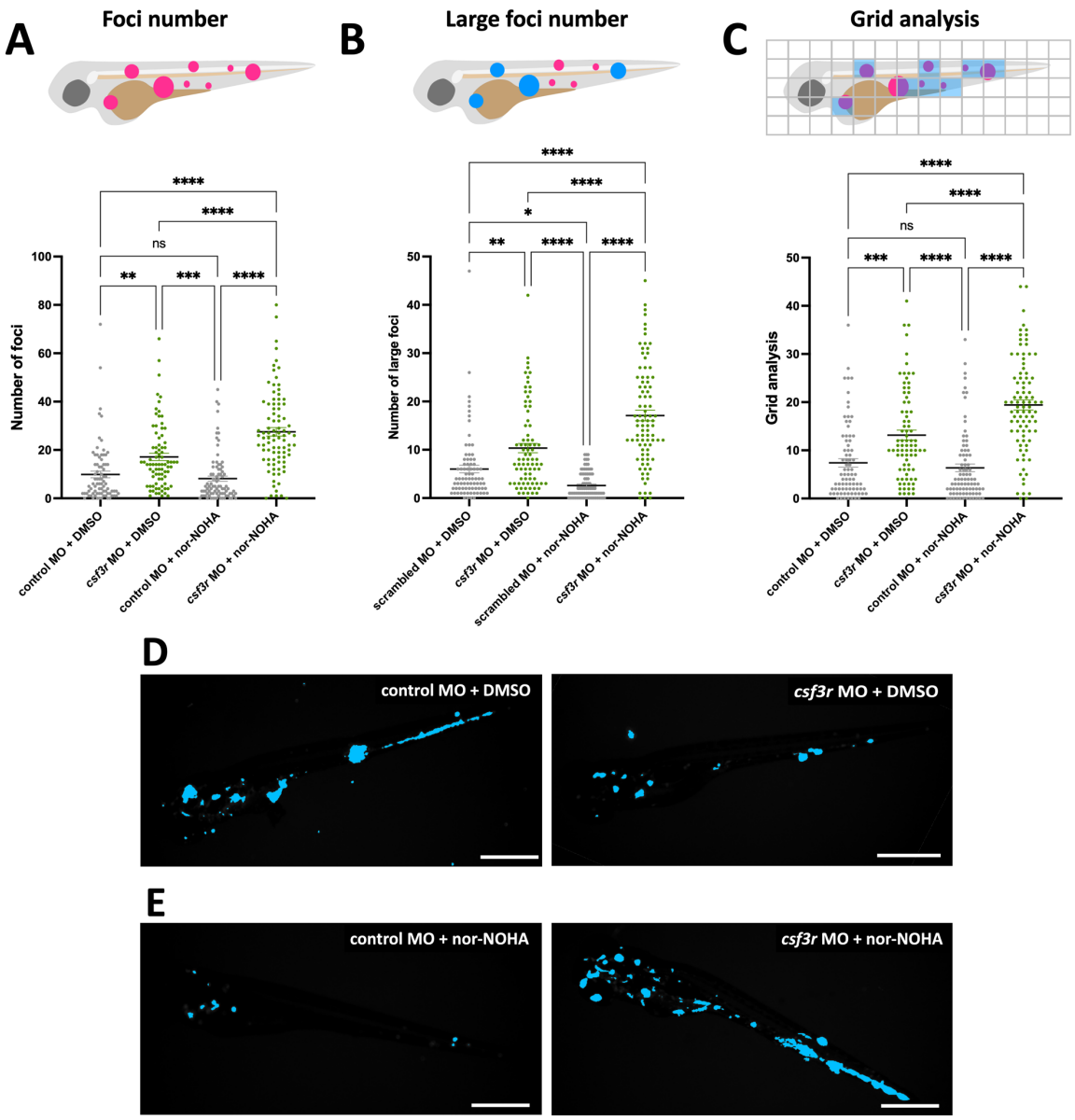


Figure 5.16. Pharmacological inhibition of arginase in neutrophil-depleted larvae leads to increased granuloma number, size and bacterial dissemination. (A-C) Top: Representation of parameters (granuloma number, **A**; large granuloma number, **B**; and spatial distribution, **C**) obtained using QuantiFish software to analyse fluorescent images of bacterial pixels. Down: Graphs illustrating that the arginase inhibition using nor-NOHA in *csf3r* MO-mediated neutrophil depleted fish, granulomas numbers (**A**), size (**B**), and dissemination (**C**) are increased. Nor-NOHA treatment does not affect granuloma number (**A**) or dissemination (**C**), but reduces granuloma size (**B**) in control MO fish treated. (**D**) Representative image of positive pixels detected using QuantiFish of *Mm* burden in DMSO-treated control larvae injected with either control morpholino (left) or *csf3r* morpholino (right) at 5 dpf. (**B**) Representative image of positive pixels detected using QuantiFish of *Mm* burden in DMSO-treated control larvae injected with either control morpholino (left) or *csf3r* morpholino (right) at 5 dpf. N=3 independent experiments, with 27-29 larvae imaged per group. Statistical significance was calculated using a one-way ANOVA with Bonferroni's multiple comparisons post hoc test. *P ≤ 0.05; ***P ≤ 0.001; ****P ≤ 0.0001. Scale bars in (**D-E**) are 1 mm.

In summary, Hif-2α is required for *tnfa*-expressing, putative pro-inflammatory macrophages to upregulate *arg2:GFP* and transition to a more anti-inflammatory phenotype. In parallel, pharmacological inhibition of arginase in neutrophil-depleted zebrafish larvae resulted in a significantly higher bacterial burden, but also led to exacerbated granuloma formation and increased bacterial burden. Together, these findings demonstrate that the macrophage switch from a pro-inflammatory (*tnfa:mCherry+*) to an anti-inflammatory (*arg2:GFP+*) state, and arginase activity within macrophages, are host-protective during *Mm* infection. Moreover, these data suggests that the host-protective effects observed following genetic reduction of Hif-2α signalling are likely due to increased iNOS-mediated antimicrobial activity in neutrophils and altered arginase levels in macrophages.

5.2.3. Therapeutic manipulation of macrophage phenotype

Manipulating macrophage phenotype represents a promising HDT strategy for mycobacterial infection, aiming to enhance bacterial clearance while minimising tissue damage and inflammation. Pharmacological Hif-1α stabilisation has previously been shown to upregulate *TgBAC(tnfa:GFP)* expression in the absence of immune challenge (Lewis. and Elks, 2019), illustrating how transgenic reporter lines can be used to assess the effects of compounds on macrophage phenotype *in vivo*. Building on this, larvae were treated with published M2-polarising mediators to investigate whether the *arg2:GFP* transgenic line can serve as a readout for pharmacological modulation of macrophages towards an anti-inflammatory phenotype.

A recent study demonstrated that systemic injection of protectin D1 (PD1), a pro-resolving lipid mediator, accelerated changes in macrophage behaviour in a zebrafish larval model of tail-wounding (Sipka et al., 2022). These behavioural changes correlated with expression of M2-associated markers (e.g. *tgfb1, ccr2*) in *tnfa:GFP*-negative macrophages during the resolution phase of inflammation (Nguyen-Chi et al., 2015; Sipka et al., 2022). As these data suggest that PD1 promotes an anti-inflammatory macrophage phenotype, I hypothesised that PD1 treatment would increase the proportion of *arg2:GFP+* macrophages at 2 dpi, indicating accelerated upregulation of this canonical M2 marker.

Larvae were injected with PD1 or 50% ethanol (EtOH; solvent control) into the caudal vein one hour after systemic *Mm* infection, and macrophage *arg2:GFP* expression was assessed. At 2 dpi, 2.59% of macrophages were *arg2:GFP+* (3 out of 116) in EtOH-injected control fish (**Fig. 5.17. A, C**), which is comparable to the percentage observed at 2 dpi in chapter 3 (2.77%; see section 3.32). However, PD1 treatment did not significantly increase the proportion of *arg2:GFP+* macrophages at this earlier time-point, with 2.5% of macrophages (2 out of 80) identified as *arg2:GFP+* (**Fig. 5.17. B, C**).

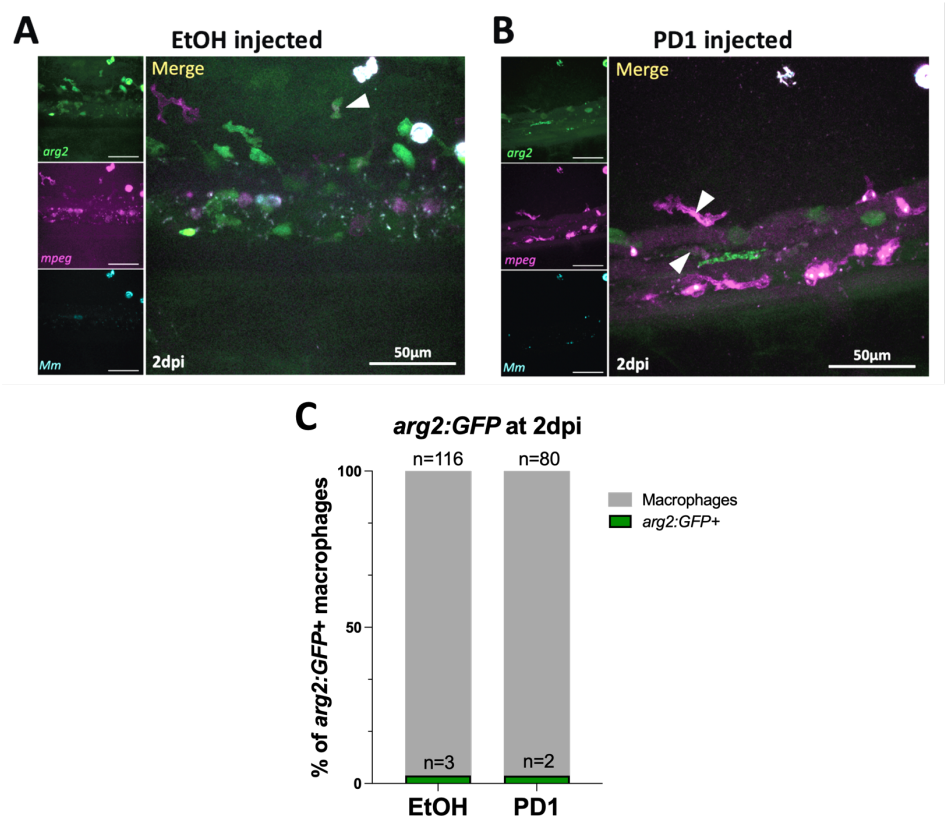


Figure 5.17. Protectin D1 does not upregulate macrophage *arg2:GFP* expression at 2 dpi. (**A**) Representative confocal image of 2 dpi *arg2:GFP* crossed to *mpeg:mCherry* injected with 1 nL of 50% ethanol (EtOH; solvent control) into the caudal vein 1 hour after *Mm* infection. (**B**) Representative confocal image of 2 dpi *arg2:GFP* crossed to *mpeg:mCherry* injected with 1 nL (200 pg) of protectin D1 (PD1) into the caudal vein 1 hour after *Mm* infection. (**C**) Graph illustrating the percentage of *arg2:GFP+* macrophages at 2 dpi. N=2 independent experiments, with 5-6 fish imaged per group per experiment. Total number of cells counted are stated on the graph. Statistical significance was calculated using a Fisher's exact test (no statistical significances identified). Arrowheads in (**A-B**) indicate *arg2:GFP+* macrophages. Scale bars are stated on the images.

Flow cytometry analysis of *mpeg:mCherry+* cells found that immersion-based PD1 treatment did not increase total macrophage numbers (Nguyen-Chi et al., 2020). However, while intravenous PD1 injection was shown to increase cell proliferation (as indicated by PH3+ staining), macrophage numbers were not quantified following this alternative treatment route (Nguyen-Chi et al., 2020). Thus, macrophage in uninjected, EtOH and PD1-injected larvae were quantified in the absence of immune challenge.

EtOH-injected fish had similar macrophage counts compared to uninjected controls (mean of 64.4 compared to 67 respectively; **Fig. 5.18. A**). However, PD1-injected fish had significantly more macrophages at 2 dpf compared to both uninjected and EtOH-injected fish (average of 80.33 macrophages; **Fig. 5.18. A**). Taken together, intravenous PD1 treatment expands the macrophage

population, but it does not upregulate macrophage *arg2:GFP* expression at earlier stages of *Mm* pathogenesis.

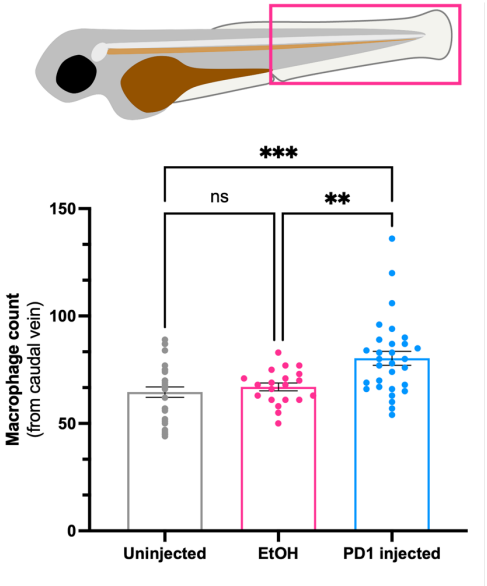


Figure 5.18. Systemic injection of PD1 expands the macrophage population in unchallenged larvae. (A) Top: Schematic illustrating the region from the caudal vein to the posterior of the fish (pink box), representing where macrophage numbers were counted. Bottom: Graph illustrating that number of macrophages counted in the region of interest of PD1-injected larvae (blue) is significantly higher than that in uninjected (grey) and EtOH-injected (pink) fish at 2 dpf. N=3 independent experiments. Statistical significance was calculated using a one-way ANOVA with Bonferroni's multiple comparisons post hoc test. **P ≤ 0.01; ***P ≤ 0.001.

There are many compounds known to promote anti-inflammatory leukocyte phenotypes; however, conducting a comprehensive *in vivo* drug screen to examine macrophage *arg2:GFP* expression was beyond the scope of this PhD. Instead, four categories of compounds were selected for investigation. These compounds include the pro-inflammatory macrophage-promoting pan-hydroxylase inhibitors dimethyloxaloylglycine (DMOG) and FG4592 (Roxadustat), both of which have been shown to upregulate *TgBAC(tnfa:GFP)* expression via Hif-1α (Lewis and Elks, 2019). However, as these compounds are nonspecific inhibitors of prolyl hydroxylases, they are also capable of stabilising Hif-2α (Jaśkiewicz et al., 2022; Jaakkola et al., 2001). The second category includes the lipid mediators prostaglandin E_2 (PGE_2) and dimethyl-PGE_2 (a more stable PGE_2 analogue), which have been shown to exert both pro- and anti-inflammatory effects on leukocytes (Loynes et al., 2018; Feng et al., 2012; Evans et al., 2019; Scher and Pillinger, 2009). Sodium butyrate, a short-chain fatty acid and histone deacetylase (HDAC) inhibitor, represents the third category; recent evidence suggests its anti-inflammatory effects are conserved in zebrafish (Cholan et al., 2020; Li et al., 2025). Finally, dexamethasone, a potent glucocorticoid, has previously been shown to inhibit macrophage *tnfa* expression in several zebrafish wounding models (Cavone et al., 2021; Xie et al., 2019).

As a pilot experiment to identify which of the above compounds warranted further investigation, unchallenged zebrafish larvae were immersion-treated for 24 hours with these potential M2-polarising mediators and macrophage *arg2:GFP* expression was assessed the following day (2 dpf). No *arg2:GFP+* macrophages were identified in larvae treated with FG4592 or dimethyl-PGE_2 (**Fig. 5.19. A**). In contrast, a single *arg2:GFP+* macrophage was observed in both PGE_2- and sodium butyrate-treated embryos, accounting for 2.13% (1 out of 47) and 2.44% (1 out of 41) of macrophages, respectively, within the imaged field of view (**Fig. 5.19. A**). Notably, in addition to the elevated background GFP fluorescence, the solvent control for sodium butyrate (MilliQ) also had an example of an *arg2:GFP+* macrophages (**Fig. 5.19. A, C**), potentially resulting from mild mechanical injury during mounting for imaging.

Dexamethasone-treated larvae exhibited 7.69% *arg2:GFP+* macrophages (2 out of 26), although this increase was not statistically significant compared to DMSO (solvent control) treated fish (**Fig. 5.19. A**). In contrast, DMOG treatment led to a statistically significantly increase in the proportion of *arg2:GFP+* macrophages, with 11.11% (5 out of 45) identified (**Fig. 5.19. A, D**). However, quantification of macrophage *arg2:GFP* fluorescence did not reveal any significant differences between compound-treated groups and their respective vehicle controls (**Fig. 5.19. B**).

Despite macrophage *arg2:GFP* brightness not being affected, DMOG treatment resulted in a significantly greater number of *arg2:GFP+* macrophages compared to the DMSO control, with examples of *arg2:GFP+ mpeg:mCherry*- cells that had neutrophil-like morphology (**Fig. 5.19. D;** asterisk). Given this finding, and previous evidence that genetic stabilisation of Hif-2α upregulates macrophage *arg2:GFP* expression, the pan-hydroxylase inhibitors (DMOG and FG4592) were selected for further investigation.

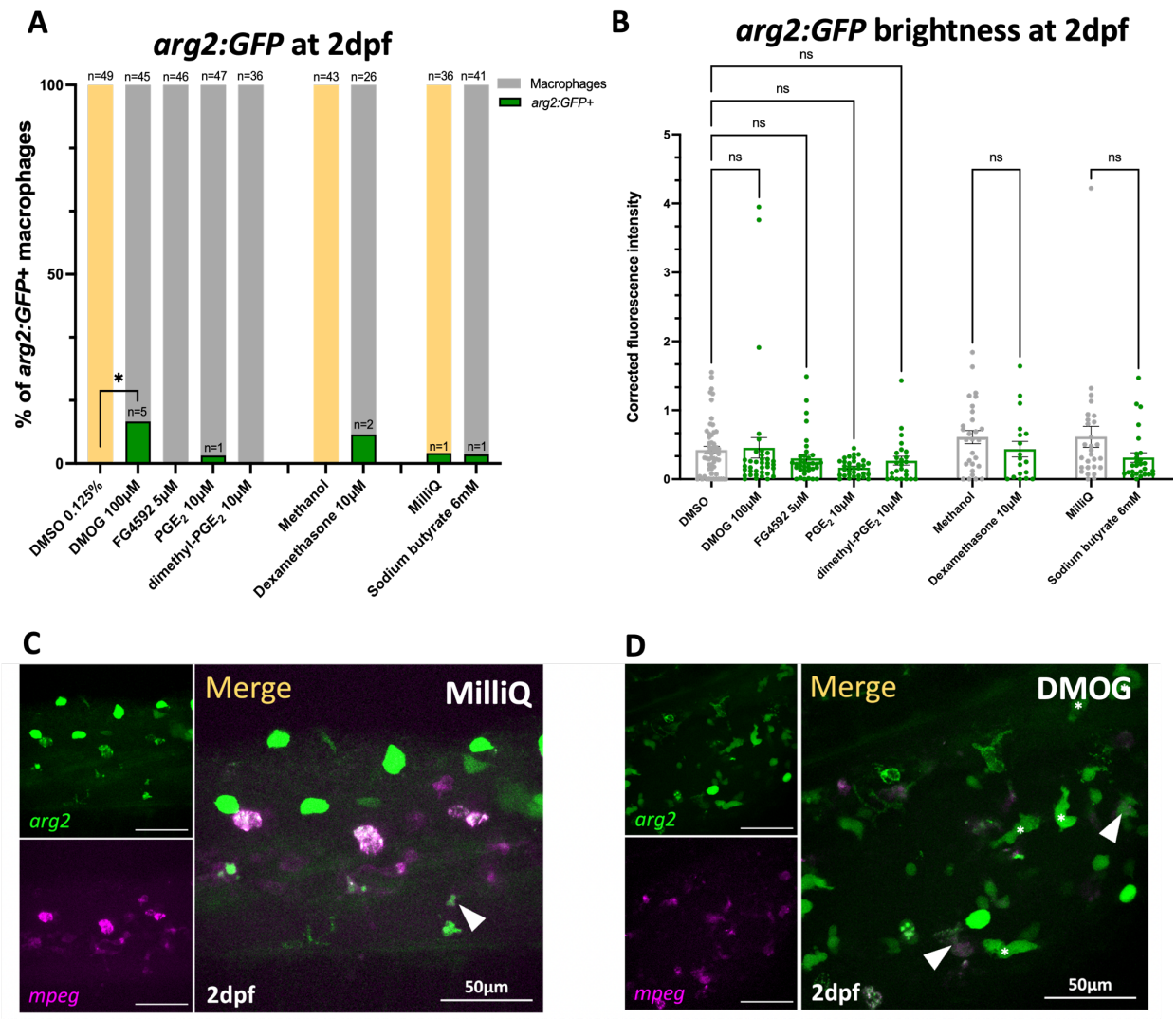


Figure 5.19. Immersion treatment with M2-associated mediators does not significantly upregulate macrophage *arg2:GFP* expression under resting conditions. (**A**) Graph illustrating the percentage of *arg2:GFP+* macrophages (green bars) identified from a 40x field of view near the caudal vein in 2 dpf larvae immersion treated with various M2 mediators (grey bars) and solvent controls (yellow bars). Total number of cells counted are stated on the graph. (**B**) Corrected fluorescence intensity of *arg2:GFP* fluorescence of *mpeg:mCherry+* cells was quantified using ImageJ software at 2 dpf, comparing individual compounds (green) to their respective solvent control (grey). (**C**) Confocal image of 2 dpf *arg2:GFP* crossed with *mpeg:mCherry* incubated with MilliQ (solvent control), highlighting the only *arg2:GFP+* macrophage identified. (**D**) Representative confocal image of 2 dpf *arg2:GFP* crossed with *mpeg:mCherry* incubated with 100 µM DMOG. N=1 independent experiment (pilot). Arrowheads in (**A-B**) indicate *arg2:GFP+ mpeg:mCherry+* cells. White asterisks in (**B**) highlight *arg2:GFP+ mpeg:mCherry-* cells with neutrophil-like morphology. Statistical significance in (**A**) was calculated using a Chi squared test, followed by Fisher's exact test to determine where the significant differences are. Statistical significance in (**B**) was calculated using a one-way ANOVA with Bonferroni's multiple comparisons post hoc test. Error bars depict SEM. *P ≤ 0.05. Scale bars are stated on the images.

Although DMOG appeared to be the most promising compound for upregulating macrophage *arg2:GFP* expression under resting conditions, only two faint *arg2:GFP+* macrophages were observed among 82 cells (2.44%; **Fig. 5.20. A, D**). No *arg2:GFP+* macrophages were identified in DMSO control or

FG4592-treated larvae (**Fig. 5.20. A, C, E**). To account for potential background GFP fluorescence, such as that seen in MilliQ-treated fish in the previous figure (**Fig. 5.19. C**), *mpeg:mCherry* single-transgenic larvae were also treated with pan-hydroxylase inhibitors and macrophage fluorescence in the GFP channel was quantified. No significant differences in macrophage *arg2:GFP* fluorescence were detected in any of the compound-treated conditions compared to controls (**Fig. 5.20. B**). These data indicate that pharmacological Hif-α stabilisation does not upregulate macrophage *arg2:GFP* expression under resting conditions.

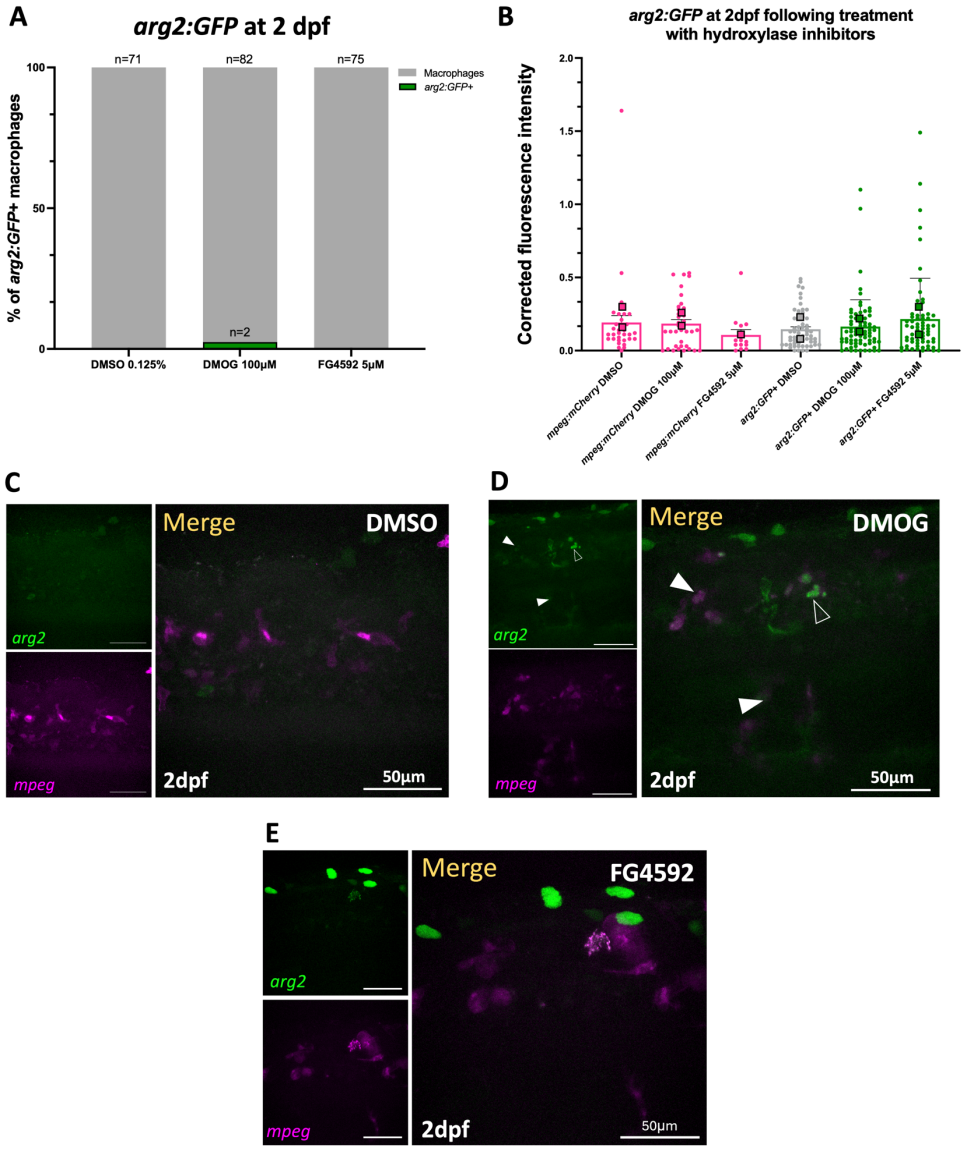


Figure 5.20. Immersion treatment with pan hydroxylase inhibitors does not upregulate macrophage *arg2:GFP* expression under resting conditions. (**A**) Graph illustrating the percentage of *arg2:GFP+* macrophages identified from a 40x field of view near the caudal vein in 2 dpf larvae immersion treated with DMSO 0.125% (solvent control), DMOG 100 μM or FG4592 5 μM. Total number of cells counted are stated on the graph. (**B**) Corrected fluorescence intensity of GFP fluorescence of *mpeg:mCherry+* cells was quantified using ImageJ software at 2 dpf. Pink bars are control *mpeg:mCherry+* single transgenic fish treated with DMSO (solvent control), DMOG or FG4592. Grey bar indicates DMSO-treated *arg2:GFP* larvae crossed with *mpeg:mCherry*. Green bar indicates *arg2:GFP* crossed with *mpeg:mCherry* treated with DMOG or FG4592. (**C-D**) Representative confocal images of

arg2:GFP crossed to mpeg:mCherry treated with DMSO (**C**), DMOG (**D**) or FG4592 (**E**). N=2 independent experiments. Statistical significance in (**A**) was calculated using a Chi squared test. Statistical significance in (**B**) was calculated using a one-way ANOVA with Bonferroni's multiple comparisons post hoc test (no statistical significances identified). Error bars depict SEM. Scale bars are stated on the images.

When imaging FG4592-treated larvae, an interesting observation I made was that macrophage appeared more circular. Therefore, morphometric descriptors (area, perimeter and circularity index) were obtained by manually drawing around macrophages in DMSO, DMOG and FG4592 treated fish. No significant differences in between the average area of macrophages were identified between groups (202.74 μm^2, 211.97 μm^2 and 214.28 μm^2, respectively; **Fig. 5.21. A**). Whilst no significant differences in perimeter were identified between DMOG and DMSO controls (71.58 μm vs. 70.32 μm, respectively), macrophages in FG4592 treated larvae were slightly smaller, albeit not significantly (65.98 μm; **Fig. 5.21. B**). Most strikingly, macrophages from FG4592 treated fish were significantly more circular compared to both DMSO (0.64 vs. 0.54; **Fig. 5.21. D**) and DMOG (0.64 vs. 053; **Fig. 5.21. A, E**). Whilst it is possible that this macrophage phenotype may be caused by the stock of FG4592 being mildly toxic, these morphometric descriptors resemble characteristics associated with *in vitro* murine anti-inflammatory macrophages. Together, these observations may indicate that FG4592 promotes an arginase-independent anti-inflammatory macrophage profile (e.g. *in vitro* M2b polarised murine macrophages), although potential toxic effects cannot be excluded (Van den Bossche et al., 2012; Wang et al., 2019).

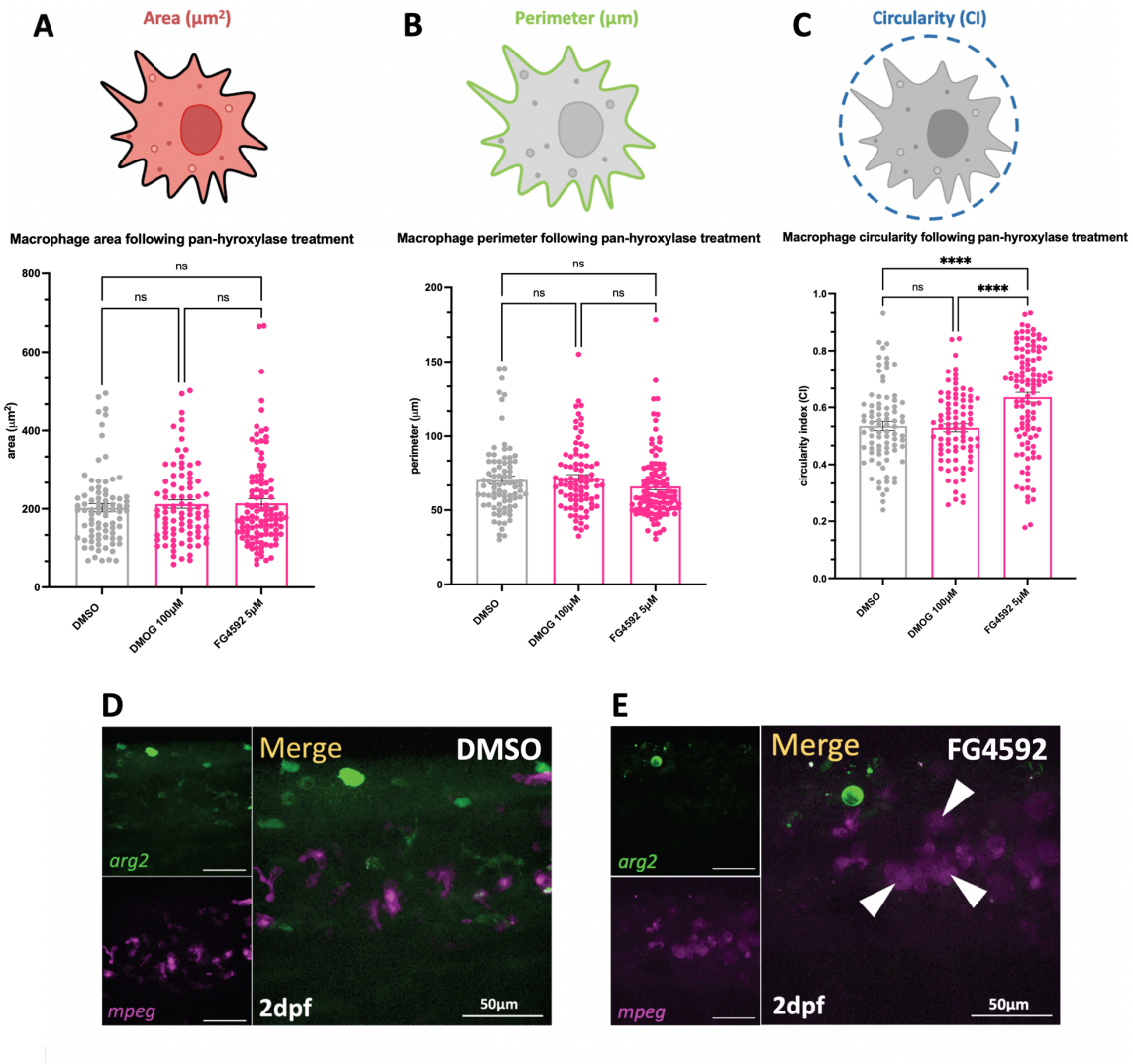


Figure 5.21. Macrophages become more circular following treatment with the pan-hydroxylase inhibitor FG4592 without an immune challenge. (**A-C**) Up: Representation of morphometric descriptors (area, perimeter, circularity index) determined in ImageJ to analyse macrophage shape. Down: Graphs illustrating the area (**A**), perimeter (**B**) and circularity index (**C**) of *mpeg:mCherry+* macrophages following treatment with DMSO (solvent control), DMOG 100 µM or FG4592 5 µM. (**D-E**) Representative confocal images of *arg2:GFP* crossed with *mpeg:mCherry* at 2 dpf treated with DMSO (**D**) or FG4592 (**E**). N=2 independent experiments. Error bars indicate SEM. Statistical significances in (**A-C**) were calculated using a one-way ANOVA with Bonferroni's multiple comparisons post hoc test. Scale bars are stated on the images. Arrowheads in (**E**) indicate circular macrophages. ****P ≤ 0.0001.

In conclusion, although attempts to assess anti-inflammatory effects of selected compounds using macrophage *arg2:GFP* expression as a readout were unsuccessful, this thesis chapter demonstrates that, consistent with findings in murine macrophages *in vitro*, *arginase* is a Hif-2α target *in vivo*.

5.3. Discussion

The rise of antimicrobial-resistant strains of *Mycobacterium tuberculosis* (*Mtb*) underscores the urgent need to develop alternative therapeutic strategies (Kilinç et al., 2021; World Health Organization, 2025). Manipulating macrophage activation status represents a promising HDT approach against mycobacterial infection, as promoting a pro-inflammatory macrophage phenotype has been shown to enhance bacterial clearance, but may also result in excessive inflammation and tissue pathology (Shen et al., 2023; Mehta et al., 2023; Lewis and Elks, 2019; Ogryzko et al., 2019; Redente et al., 2010). Although our understanding of how modulating the anti-inflammatory programme may be beneficial in mycobacterial infection remains limited, this may represent an HDT strategy capable of mitigating such detrimental inflammatory responses. This chapter demonstrated that genetic stabilisation of Hif-2α upregulated *arg2:GF*P expression in both neutrophils and macrophages. Timelapse imaging revealed that putative pro-inflammatory macrophages require Hif-2α signalling to transition towards an anti-inflammatory phenotype during infection. Importantly, pharmacological inhibition of arginase in neutrophil-depleted zebrafish not only resulted in increased bacterial burden, but also led to increased granuloma number and size, as well as enhanced bacterial dissemination. Together, these findings indicate that macrophage arginase activity – and the associated switch from a pro-inflammatory to an anti-inflammatory macrophage state – is host-protective during *Mm* infection. Finally, pharmacological treatment with canonical M2-polarising mediators did not induce macrophage *arg2:GFP* expression in the absence of immune challenge, highlighting the requirement for inflammatory context to engage anti-inflammatory macrophage programmes *in vivo.*

Stabilisation of Hif-2α using dominant active *hif-1α* upregulated leukocyte *arg2:GFP* expression in unchallenged larvae. Genetic upregulation of Hif-2α induced *arg2:GFP* expression predominantly occurred in neutrophils, which is consistent with this being the primary immune cell to upregulate *arg2:GFP* during immune challenge (Hammond et al., 2023). Previous work found that Hif-1α stabilisation upregulated iNOS in neutrophils, whereas DA *hif-2α* resulted in reduced neutrophil nitric oxide levels (Elks et al., 2013). Together, these findings are in line with *in vitro* mammalian macrophages demonstrating that HIF-α isoforms have opposing roles on nitric oxide homeostasis (Takeda et al., 2010a). The iNOS/arginase axis is widely regarded as a key mechanism regulating macrophage polarisation and function; however, this paradigm largely derives from studies in the murine immune system (El Kasmi et al., 2008). In contrast, human neutrophils are the primary leukocyte expressing this axis. Neutrophils upregulate iNOS and produce high levels of nitric oxide in immune challenge (Jablonska et al., 2008; Chacón et al., 2024; Munder et al., 2005). Although human monocyte-derived macrophages generate detectable nitric oxide following *in vitro* infection with *Mtb*, these levels were found to be insufficient to exert bactericidal activity (Jung et al., 2013). Moreover, whereas murine macrophages robustly induce Arginase 1 expression, human macrophages show little to no induction at either the transcript or protein level, while polymorphonuclear neutrophils display

strong Arginase 1 upregulation and high enzymatic activity (Munder et al., 2005). It is possible that the apparent discrepancy between human and murine macrophages arises from artefacts introduced by *in vitro* culture systems, as human monocytes have been shown to induce iNOS expression following M1 stimulation (Weinberg et al., 1995). Indeed, human alveolar macrophages isolated from TB patient lungs and lung transplant recipients produce high levels of nitric oxide, with pronounced anti-nitrotyrosine staining co-localising with iNOS+ macrophages in post-mortem human myocardial infarction hearts (Hickman-Davis et al., 2002; Steiner et al., 1996; Wilmes et al., 2023). Nevertheless, the prominence of neutrophils as the major source of nitric oxide and arginase activity in both humans and zebrafish suggests that this may not simply represent an artefact. Instead, it indicates that zebrafish may more accurately recapitulate the human innate immune system than murine models, providing a particularly relevant system for examining the regulation and functional consequences of the iNOS/arginase axis.

At both early (1 dpi) and later (4 dpi) stages of *Mm* pathogenesis, genetic stabilisation and inhibition of Hif-1α each downregulated neutrophil *arg2:GFP* expression. Previous work showed that genetic downregulation of Hif-1α produced bacterial burdens comparable to control fish, an effect attributed to reduced neutrophil nitric oxide production (Elks et al., 2013). Given that Hif-1α primarily promotes pro-inflammatory and glycolytic programs – including *iNOS* expression – whereas Hif-2α supports oxidative and anti-inflammatory pathways such as *arginase* expression, it was anticipated that Hif-1α stabilisation might indirectly suppress *arg2:GFP* via transcriptional and metabolic competition between iNOS and arginase pathways (Takeda et al., 2010a; Steinberger and Eubank, 2023; Li et al., 2018). Conversely, because *arg2* is not a known Hif-1α target, dominant-negative Hif-1α was expected to have little effect on neutrophil arginase levels, with *arg2:GFP* expression predicted to remain similar to control fish. The data only partially supported the hypothesis: Hif-1α stabilisation reduced neutrophil *arg2:GFP*, consistent with transcriptional and metabolic competition between iNOS and arginase pathways, but dominant-negative *hif-1α* also reduced neutrophil *arg2*, contrary to the expectation that *arginase* levels be unchanged. These findings indicate that *arg2* expression in neutrophils is primarily driven by Hif-2α, but that perturbation of Hif-1α can also indirectly suppress *arg2* expression. A potential explanation is that the truncated dominant-negative Hif-1α protein interferes with Hif-2α activity by competing for shared cofactors such as Hif-β or transcriptional co-activators (e.g.: p300/CBP), thereby disturbing the transcriptional balance required for Hif-2α function. Supporting this, several studies have linked HIF-1α perturbation to altered arginase expression, despite HIF-1α not being a canonical regulator of arginase. In human endothelial cells, HIF-1α silencing prevented the hypoxia- or PHD inhibitor-induced upregulation of Arg2 protein (Liang et al., 2019). Similarly, endothelial-specific deletion of Hif-1α in mice modestly reduced whole-lung *Arg1* and *Arg2* expression under chronic hypoxia (Cowburn et al., 2016). Thus, while Hif-1α is unlikely to directly regulate *arg2* transcription in neutrophils, dominant-negative *hif-1α* may downregulate *arg2:GFP* indirectly. These results support a

model in which HIF-2α acts as the principal regulator of neutrophil *arg2*, while dominant-negative *hif-1α* modulates its expression indirectly through competition for shared cofactors or interference within overlapping HIF transcriptional pathways.

Genetic Hif-1α stabilisation prevents *arg2:GFP* upregulation in early granuloma-associated neutrophils, which may account, at least in part, for the host-protective effects of downregulating Hif-1α on bacterial burden. When comparing across experimental groups (control, Hif-2α stabilisation and Hif-2α downregulation), *arg2:GFP* intensity appeared brighter in neutrophils located outside of granulomas, rather than Hif-1α stabilisation directly abrogating *arg2:GFP* upregulation within granulomas. This observation should, however, be interpreted with caution, as corrected fluorescent intensity measurements are expressed in arbitrary units, limiting the reliability of comparisons between different fish and treatment conditions. The most robust internal comparison is therefore within individual fish – specifically, between neutrophils inside versus outside granulomas – to minimise inter-sample variability.

This offers a complementary perspective to work by Dr Piotr Szkuta (previous PhD student in the Elks lab), who demonstrated that genetic downregulation of Hif-1α was able to counteract *Mm*-mediated depletion of neutrophil nitric oxide production within granulomas (Szkuta, 2020; Elks et al., 2014). Together, these findings reinforce the concept of an iNOS/arginase regulatory balance in nitric oxide homeostasis, whereby Hif-1α stabilisation enhances nitric oxide production through iNOS upregulation while simultaneously suppressing arginase expression – collectively contributing to improved host control of bacterial burden. However, targeting leukocyte activation states within granulomas must be approached cautiously, as timing throughout mycobacterial pathogenesis is critical. For instance, Hif-1α-mediated pro-inflammatory macrophage polarisation was found to be host-protective at early stages of mycobacterial infection (Lewis and Elks, 2019). Yet, during established granulomas formation, excessive Hif-1α signalling, particularly in pro-inflammatory macrophages, can exacerbate *Mtb* infection in murine models (Baay-Guzman et al., 2018; Domingo-Gonzalez et al., 2017). Indeed, Hif-1α inhibition at more advanced stages of *Mtb* pathogenesis reduced both bacterial burden and tissue damage in mice (Baay-Guzman et al., 2018; Domingo-Gonzalez et al., 2017). Rather than shifting macrophages towards a terminally anti-inflammatory phenotype, the host-protective effects of Hif-1α inhibition at advanced stages of infection may indicate a dampening of excessive pro-inflammatory activation. This hypothesis is supported by findings in LPS-stimulated BMDMs, where expression of *il1b*, but not *tnfa*, was significantly reduced following treatment with a HIF-1α inhibitor (Kong et al., 2023).

Achieving the bactericidal capacity associated with pro-inflammatory macrophages while retaining anti-inflammatory macrophage properties represents an exciting HDT strategy. Systemic

administration of an M2 polarising cytokine (IL-33), or adoptive transfer of M2-polarised BMDMs into *Mtb*-infected mice, ameliorated advanced mycobacterial infection, despite reduced *iNOS* expression (Piñeros et al., 2017). Similarly, IL-4/IL-13 pre-treatment of murine BMDMs and human MDMs shifted macrophages towards an M1-like profile (elevated TNF-α, increased *NOS2* and decreased *Arg1* expression) and enhanced bacterial killing, while retaining an M2-associated OXPHOS metabolism (Lundahl et al., 2022). Taken together, these studies highlight the therapeutic potential of temporally targeting the HIF pathway to modulate macrophage phenotype according to the stage of mycobacterial pathogenesis – enhancing bactericidal capacity while preserving anti-inflammatory functions that limit host tissue damage.

As leukocyte *arg2:GFP* expression was upregulated following Hif-2α stabilisation under resting conditions, I hypothesised that *tnfa:mCherry+* cells would require Hif-2α signalling to upregulate *arg2:GFP* and transition to an anti-inflammatory phenotype during *Mm* infection. This hypothesis was supported by my data, as downregulation of Hif-2α abrogated *arg2:GFP* upregulation, demonstrating that putative pro-inflammatory macrophages partially require Hif-2α signalling to re-polarise towards an anti-inflammatory phenotype. Overexpression of Hif-2α has been shown to dampen the pro-inflammatory status of murine adipose tissue macrophages in arginase-dependent manner, since pharmacological inhibition of arginase restored TNF-α and IL-1β secretion (Choe et al., 2014). These results corroborate earlier work that Hif-α isoforms differentially regulate macrophage polarisation status, though Hif-2α likely acts through multiple downstream mechanisms beyond direct transcriptional control of iNOS/arginase (Takeda et al., 2010a). For example, myeloid-specific deletion of murine HIF-2α exacerbated NLRP3 inflammasome activation (increased IL-1β and IL-18 secretion), a multiprotein complex pathway that mediates M1 macrophage polarisation (Li et al., 2021; Zhang et al., 2020). Yet the authors identified that Hif-2α was exerting these anti-inflammatory effects by directly downregulating *CPT1A*, an enzyme involved in mitochondrial fatty acid oxidation, rather than solely through modulating arginase activity (Li et al., 2021). This contrasts my data, where cells still upregulated *tnfa:mCherry* expression following Hif-2α downregulation during *Mm* infection. The discrepancy likely arises from cytokine clearance prior to ELISA detection rather than a genuine difference in cytokine production. For instance, Faes et al., (2021) reported that serum TNF-α and IL-1β were low in patients with abdominal sepsis, whereas levels were markedly higher in peritoneal fluid, illustrating the clearance pattern of these cytokines. Taken together, my data provides mechanistic evidence that Hif-2α signalling is partially responsible for putative pro-inflammatory macrophages to transition into an *arg2:GFP+* anti-inflammatory phenotype during *Mm* infection.

The host-protective effects of pharmacological arginase inhibition during mycobacterial infection is neutrophil-dependent, as this protection is lost following *csf3r* morpholino-mediated neutrophil depletion. This demonstrates that, as in humans, the iNOS/arginase axis is most prominent

in zebrafish neutrophil (Hammond et al., 2023; Jablonska et al., 2008; Chacón et al., 2024; Munder et al., 2005). Consequently, the reduction in bacterial burden observed with Hif-2α downregulation likely arises predominantly through upregulation of neutrophil iNOS and increased NO production, and, to a lesser extent, suppression of neutrophil *arginase 2* expression (Elks et al., 2013). The *csf3r* morpholino significantly depleted neutrophil numbers by approximately 50% at all developmental time-points (2-5 dpf) but did not completely eliminate the population. This partial depletion suggests that despite inhibition of some neutrophil arginase, the protective effect of arginase inhibition requires the presence of a full neutrophil population. However, assessing the role of macrophage arginase in mycobacterial infection would have been a more challenging approach. *irf8* morpholino-mediated macrophage depletion results in hypersusceptibility to *Mm*, heightened systemic pro-inflammatory signalling (e.g.: increased *tnfa* expression), and compensatory neutrophil expansion (Szkuta, 2020; Espín-Palazón et al., 2014; Li et al., 2011). Similar complications arise with liposomal clodronate-mediated macrophage depletion, which induces transient inflammation due to apoptotic macrophages, leads to uncontrolled infection, and allows approximately a 75% recovery of the macrophage population by 5 dpf (Yang et al., 2021; Szkuta, 2020). Given the current zebrafish genetic toolkit, *csf3r*-mediated neutrophil depletion remains the most appropriate strategy for dissecting the relative contributions of neutrophil and macrophage arginase to mycobacterial infection – short of generating stable mutant zebrafish lines.

Among pharmacological inhibitors, nor-NOHA has been most extensively studied in infectious contexts, though findings remain similarly inconsistent. In M1-polarised human MDMs, *Candida albicans*-mediated suppression of NO production was reversed by nor-NOHA treatment, resulting in improved fungal killing (Wagener et al., 2017). Likewise, nor-NOHA reduced *Salmonella* burden in macrophages *in vitro*, and oral administration decreased bacterial loads across multiple organs in infected mice (Lahiri et al., 2008). In BALB/c mice infected with *Leishmania tropica* or *Leishmania major*, nor-NOHA reduced parasite proliferation as detected by RT-PCR (Nahidi et al., 2020). Yet the protective effects of nor-NOHA on *Leishmania* species *in vivo* are inconsistent, with parasite density at the site of infection reportedly unchanged (Nahidi et al., 2020; Schleicher et al., 2016).

Recent work in *Mtb* infection has revealed similar discrepancies. Nor-NOHA reduced bacterial burden in murine macrophages *in vitro* by promoting an M1-like phenotype (Chauhan et al., 2024). *In vivo*, nor-NOHA increased pulmonary expression of pro-inflammatory cytokines (e.g. IL-1β, TNF-α, IL-6), consistent with an M1-skewed immune response, but did not significantly alter bacterial burden (Chauhan et al., 2024). In contrast, our group has shown that nor-NOHA is host-protective in zebrafish models of mycobacterial infection, demonstrated in this chapter by a significant decrease in bacterial burden in control morpholino-injected fish (Szkuta et al., paper in preparation). This protection likely reflects enhanced early neutrophil-mediated antimicrobial activity following arginase inhibition.

However, the increased bacterial burden seen in neutrophil-depleted fish treated with nor-NOHA treatment highlights the host-beneficial role of arginase activity during *Mm* infection (**Fig. 5.22.**). Importantly, arginase inhibition did not simply affect bacterial load, but was also associated with increased granuloma number, an increased proportion of large granulomas, and enhanced bacterial dissemination, indicating a failure to properly organise and contain infection. Together, these findings suggest that arginase activity – and the associated macrophage transition from a pro-inflammatory (*tnfa*+) to an anti-inflammatory (*arg2*+) state – contributes not only to bacterial control but also to effective granuloma formation and architecture. This interpretation is strongly supported by work in mammalian and zebrafish systems. In *Mtb*-infected mice, deletion of macrophage *Arg1* in a *Nos2*-deficient background resulted in an increased number of granulomas, which were enlarged and more necrotic, demonstrating that arginase-expressing macrophages are required to constrain granulomatous pathology and maintain granuloma integrity (Duque-Correa et al., 2014). Similarly, in adult *Mm*-infected zebrafish, disruption of type 2 signalling through *stat6* or *il4r* impairs macrophage-to-epithelioid transition and leads to defective granuloma architecture (Cronan et al., 2021). Although *arg2* was not directly targeted in that study, scRNAseq analysis revealed enrichment of *arg2* expression within epithelioid macrophages in granulomas, linking arginase expression to granuloma organisation. Together, these data support a conserved role for arginase-expressing anti-inflammatory macrophages in shaping granuloma architecture across species and disease contexts. In this light, the increased granuloma burden, enlargement, and dissemination observed following nor-NOHA treatment in neutrophil-depleted larvae likely reflects disruption of macrophage arginase-dependent programmes required for granuloma organisation and containment. Rather than simply dampening inflammation, arginase activity appears to support a controlled phenotypic transition that is necessary for stabilising granulomatous structures and limiting bacterial spread.

To directly confirm whether arginase activity during the *tnfa:mCherry+ to arg2:GFP+* transition is itself host-protective, future experiments could combine overnight timelapse imaging from 2 dpi with acute nor-NOHA treatment prior to imaging. This approach would allow real-time visualisation of whether inhibiting arginase activity during this critical window disrupts macrophage morphological transitions, impairs granuloma organisation, or promotes bacterial dissemination, thereby providing causal evidence that the phenotypic switch itself contributes to host protection. Together, these findings underscore the context-dependent and often unpredictable outcomes of pharmacological inhibition during infection. The dual inhibition of arginase 1 and arginase 2 by compounds such as nor-NOHA likely contributes to this variability, as isoform- and tissue-specific functions of arginase are simultaneously disrupted. Consequently, the limited efficacy and translatability of current arginase inhibitors highlight the need for more selective, macrophage-targeted approaches to dissect arginase function and improve the therapeutic potential of host-directed strategies in tuberculosis.

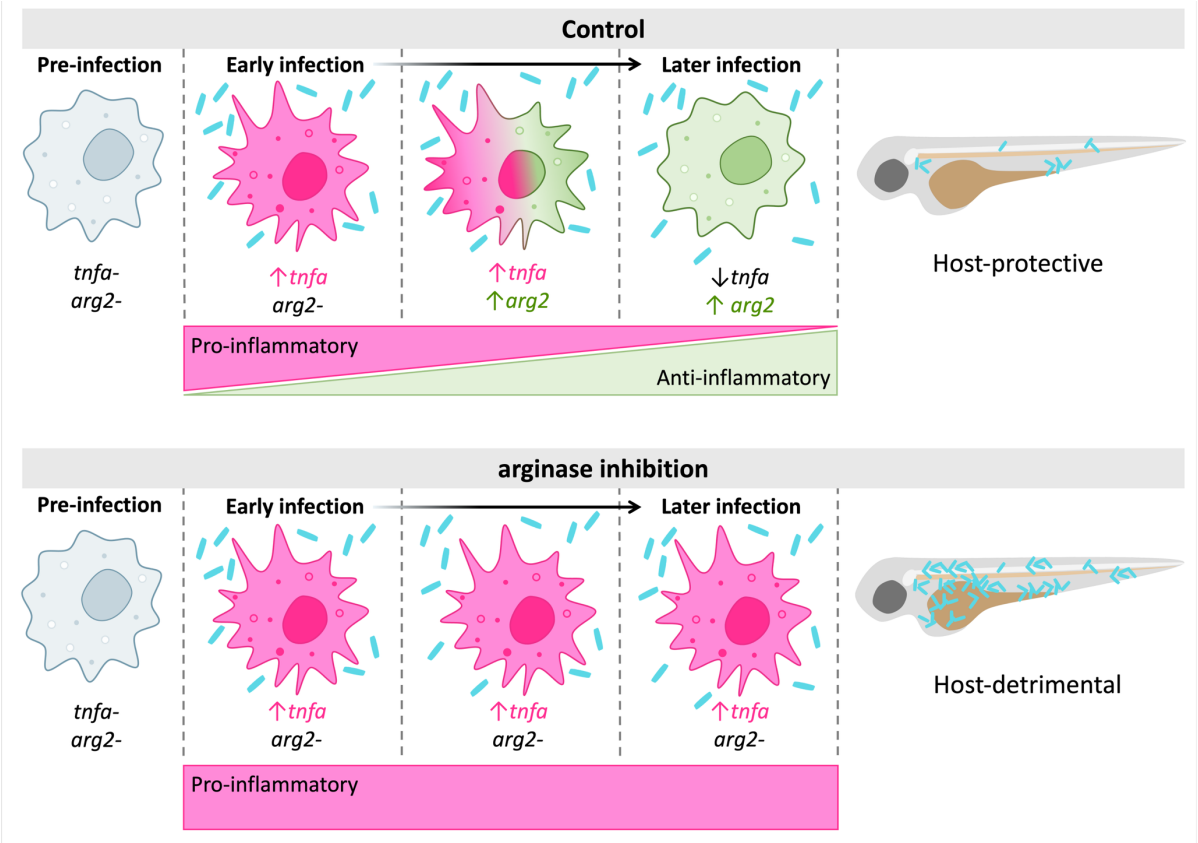


Figure 5.22. Inhibition of arginase activity in pro-inflammatory macrophages and preventing the phenotypic switch is host-detrimental. Under resting conditions, macrophages do not express *tnfa:mCherry/tnfa:GFP* or *arg2:GFP*. Following *Mm* infection, macrophages upregulate *tnfa* expression, adopting a pro-inflammatory phenotype at early stages of infection. At 2-3 dpi, macrophages upregulate *arg2:GFP*, switching to an anti-inflammatory phenotype. At later stages of larval infection, macrophages begin downregulating *tnfa*. This results in variable clearance of *Mm*, but is overall host-protective. When Hif-2α signalling is downregulated using dominant negative Hif-2α, pro-inflammatory *tnfa:mCherry+* macrophages fail to upregulate *arg2:GFP* and switch to an anti-inflammatory phenotype at later stages of infection. Pharmacological inhibition of macrophage arginase results in uncontrolled infection, suggesting that inhibiting macrophage arginase activity – and the associated pro- to anti-inflammatory phenotypic switch – is critical for effective granuloma organisation and host-protection during mycobacterial infection. Inspired by Ogryzko et al., (2019)

The *arg2:GFP* transgenic line did not provide a readout for assessing the anti-inflammatory activity of selected M2 mediators on macrophage phenotype under resting conditions. However, the absence of macrophage *arg2:GFP* upregulation in unchallenged larvae does not necessarily indicate a lack of anti-inflammatory activity. Rather, it suggests that *arg2* expression may require a primed or inflammatory context (e.g.: infection or injury) to be inducible. Accordingly, the *arg2:GFP* line may prove more useful for screening anti-inflammatory macrophage compounds in immune-challenged assays, where *arg2:GFP* expression is already activated.

DMOG and FG4592 are pan-prolyl hydroxylase domain (PHD) inhibitors that stabilise Hif-1α, leading to upregulation of macrophage *tnfa:GFP* under resting conditions in zebrafish, consistent with a

shift toward a pro-inflammatory phenotype (Lewis and Elks, 2019). In contrast, DMOG reduces TNF-α production and inhibits differentiation into CD68+/CD80+ M1 macrophages in LPS-stimulated mouse peritoneal macrophages (Hirai et al., 2018). These divergent responses likely reflect species- and context-dependent differences in NF-κB/TNF-α feedback loops and Hif signalling. In mice, DMOG-mediated PHD inhibition attenuates IL-1β-driven NF-κB activity and downstream TNF-α in a HIF-1α-independent manner (Scholz et al., 2013; Takeda et al., 2009; Guha and Mackman, 2001). By contrast, in zebrafish, pharmacological inhibition of NF-κB paradoxically increases macrophage *tnfa:GFP* expression after tail fin transection, indicating that the core feedback circuitry is conserved but may be less effective at suppressing *tnfa* transcription in zebrafish than in mice (Arkoudi et al., 2025; Nguyen-Chi et al., 2015; Lewis and Elks, 2019). Despite this apparent attenuation of negative feedback, *arg2:GFP* is not upregulated in resting macrophages following PHD inhibition, consistent with a Hif-1α-dominated pro-inflammatory responses. However, this does not exclude Hif-2α-mediated, arginase-independent anti-inflammatory programmes. For instance, in murine BMDMs, FG4592 increased HIF-2α expression and decreased IL-1β secretion following NLRP3 inflammasome activation, demonstrating an anti-inflammatory effect that does not rely on arginase induction (Li et al., 2021). Furthermore, the morphological shift towards more circular macrophages observed after FG4592 treatment in this chapter is reminiscent of M2b-like phenotypes described *in vitro*, although potential toxicity cannot be excluded as a contributing factor (Van den Bossche et al., 2012; Wang et al., 2019). Overall, the pleiotropic and partially HIF-independent effects of pan-PHD inhibitors complicate mechanistic interpretation. A clearer understanding of isoform-specific Hif signalling and its modulation – through targeted delivery systems and selective stabilisation, such as direct Hif-2α agonists or myeloid-specific micelle delivery of FG4592 – will be essential for the rational design of HDTs that fine-tune macrophage function to promote *Mtb* clearance (Wu et al., 2019; DeBerge et al., 2024).

Beyond Hif stabilisation, other immunomodulatory compounds with well-characterised anti-inflammatory activity also failed to induce macrophage *arg2:GFP* expression under resting conditions. Treatments with sodium butyrate, PGE_2, dimethyl-PGE_2 and dexamethasone did not upregulate *arg2:GFP* despite their established capacity to attenuate inflammatory signalling, including in zebrafish models. Exogenous PGE_2 treatment enhanced inflammation resolution in a tail fin transection model, characterised by accelerated neutrophil reverse migration (Loynes et al., 2018). In line with this, pharmacological inhibition of PGE_2 production in zebrafish larvae increased the prevalence of inflammatory macrophages during cancer initiation (Feng et al., 2012). However, cyclooxygenase inhibition was found to reduce Hif-1α-mediated macrophage *tnfa:GFP* expression, emphasising the dual role of PGE_2 in modulating leukocyte pro- and anti-inflammatory properties (Lewis and Elks, 2019). Dimethyl-PGE_2 treatment modestly increased fungal burden in zebrafish infected with eicosanoid-deficient *Cryptococcus neoformans* (Evans et al., 2019). As *Cryptococcus neoformans* preferentially infects host macrophages to promote its survival and proliferation, these findings suggest that

dimethyl-PGE_2 promotes a pathogen-permissive, anti-inflammatory macrophage phenotype (Evans et al., 2019). In a tail fin injury model, sodium butyrate treatment reduced the number of *TgBAC(tnfa:GFP)*-positive macrophages and overall GFP fluorescence intensity at the wound site (Cholan et al., 2020). Similarly, dexamethasone treatment decreased *tnfa*+ macrophages numbers and *tnfa* mRNA expression following spinal cord and tail fin transection (Cholan et al., 2020; Cavone et al., 2021). Taken together, these findings highlight the limitation of the *arg2:GFP* transgenic line as a reporter for pharmacological anti-inflammatory macrophage activation under resting conditions. Thus, without an immune challenge, changes in *tnfa* reporter intensity likely remains the most sensitive measure of macrophage modulation, although this approach is restricted to these compounds acting upstream of TNF-α signalling.

In conclusion, this chapter establishes that, similar to murine macrophages, Hif-α isoforms differentially regulate *iNOS* and *arginase 2* expression, confirming *arginase 2* as a Hif-2α target in zebrafish leukocytes. Hif-2α signalling is also required for the re-polarisation of putative pro-inflammatory macrophages during *Mm* infection, as evidenced by *arg2:GFP* upregulation and corresponding changes in morphology. Notably, pharmacological inhibition of macrophage arginase during mycobacterial infection was host-detrimental, resulting not only in increased bacterial burden but also in increased granuloma number and size, as well as enhanced bacterial dissemination. These findings indicate that macrophage arginase activity, and the associated transition from a *tnfa*+ pro-inflammatory state to an *arg2*+ anti-inflammatory state, contributes to effective granuloma organisation and is host-protective during infection. Finally, the pilot compound screen also revealed that the unchallenged larval assay was not suitable for assessing the effects of anti-inflammatory mediators on macrophage *arg2:GFP* expression, as *arg2* was not induced under resting conditions. This suggests that *arg2:GFP* expression may need to be first activated by an immune challenge before testing whether candidate M2-polarising compounds can enhance its expression or increase the proportion of *arg2:GFP*+ macrophages. Under such infection-relevant conditions, the *arg2:GFP* line may still serve as a valuable platform for screening compounds that promote protective anti-inflammatory macrophage responses.

6. Identification of alternative anti-inflammatory macrophage marker genes

Some of the introduction (1; section 6.1.3) and data (2; section 6.2.1) in this chapter were published as:

(1) **Speirs, Z.C.**, Loynes, C.A., Mathiessen, H., Elks, P.M., Renshaw, S.A. and Jørgensen, L.v.G. What can we learn about fish neutrophil and macrophage response to immune challenge from studies in zebrafish. *Fish & Shellfish Immunology.* 2024 May; 148:109490. doi.org/10.1016/j.fsi.2024.109490

(2) Bastos T.S.B.*, Loynes C.A.*, **Speirs Z.C.***, de Lima J.D., Junior L.W., de Paula A.G.P., Czaikovski A.P., Luz R.B.S., Paredes L.C., Norris M., Tomlinson G.S., de Rocha W.D., Renshaw S.A., Elks P.M., Braga T.T.. Loss of Cathepsin Z enhances pro-inflammatory macrophage responses and promotes tissue regeneration in zebrafish. **In Press, *Disease Models & Mechanisms***. *Authors contributed equally to this work.

6.1. Introduction

6.1.1. Macrophages polarise on a wide spectrum *in vivo*

Macrophages display substantial phenotypic plasticity *in vivo*, integrating diverse environmental cues to adopt context-specific activation states. Classical *in vitro* systems typically polarise resting macrophages (M0) using specific stimuli, such as LPS or IL-4, to induce M1- or M2-polarised macrophages as a means to examine pro- and anti-inflammatory phenotypes (Atri et al., 2018; Xia et al., 2023; Baidžajevas et al., 2020). Additional subdivisions of M2 macrophages (M2a-d) have been proposed to reflect stimulus-specific transcriptional programmes (Mills et al., 2000; Shapouri-Moghaddam et al., 2018). However, these categories capture only a fraction of the diversity observed *in vivo*, where macrophages exhibit overlapping and hybrid transcriptional states (Mills and Ley, 2014; Xue et al., 2014; Martinez and Gordon, 2014; Bosco, 2019). Indeed, in human disease tissue, macrophages frequently co-express markers associated with both M1 and M2 activation – for example, CD40+ CD163+ double-positive macrophages in multiple sclerosis lesions and CD68+ CD86+ MRC1+ macrophages in carotid plaques (Vogel et al., 2013; Kocsy et al., 2025). Furthermore, transcriptomic comparisons between *in vitro* M1/M2 polarised BMDMs and *ex vivo* murine peritoneal macrophages reveal limited overlap in differentially expressed genes between M1/M2 signatures and substantial marker intermixing (Orecchioni et al., 2019). Taken together, these findings emphasise that macrophage activation states *in vivo* represent a continuum rather than discrete M1/M2 identities.

In zebrafish, transgenic lines such as *tnfa:eGFP* have enabled visualisation of pro-inflammatory macrophage activation during injury and infection (McWhorter et al., 2013; Lewis and Elks, 2019; Ogryzko et al., 2019; Bojarczuk et al., 2016; Nguyen-Chi et al., 2017). Examples of how the *tnfa:GFP* line can be used to perform an in-depth characterisation of putative pro-inflammatory macrophage responses in *Mm* are detailed in chapter 3 of this thesis. In contrast, tools to visualise ant-inflammatory

or wound-repair-associated macrophages have been limited, and such cells are often inferred indirectly (e.g.: *tnfa*-negative cells or morphology-based assessments) rather than identified through dedicated markers (Xie et al., 2019; Sipka et al., 2022).

The recently developed *arg2:GFP* line has begun to fill this gap by reporting expression of *arginase 2*, a canonical M2-marker upregulated in *ex vivo* carp macrophages (Hammond et al., 2023; Wentzel et al., 2020). My previous results chapters further characterised *arg2:GFP*-expressing macrophages, showing that they share features with *in vitro* anti-inflammatory macrophages. However, as only a minority of macrophages upregulate *arg2:GFP* during early infection, additional markers are likely required to capture the spectrum of anti-inflammatory programmes *in vivo*.

In M2-polarised carp monocytes, *ccn1l1* (previously known as *cyr61l1*) was the most highly upregulated gene, whereas *arg2* ranked sixth (Wentzel et al., 2020). *ccn1l1* encodes an extracellular matrix-associated matricellular protein whose mammalian orthologue (*CCN1*) has known roles in tissue repair, angiogenesis and wound healing (Chen et al., 2001; Kim et al., 2022; Jun et al., 2015). This suggests potential relevance to anti-inflammatory macrophage functions, and motivates the examination of a *ccn1l1* promoter zebrafish transgenic reporter line as a possible complementary tool.

6.1.2. Conserved cross-species anti-inflammatory macrophage markers

Given the breadth of macrophage heterogeneity, multiple markers are often required to define macrophage activation states (Wei et al., 2023; Jablonski et al., 2015; Jiang et al., 2024). This highlights a key potential limitation of zebrafish transgenic lines: is a single reporter enough? Zebrafish studies frequently rely on transcriptional profiling (qPCR, RNA-seq) rather than single transgenic markers to classify macrophages (Morales and Allende, 2019; Denans et al., 2022). For example, *tnfa:GFP*+ macrophages were validated as pro-inflammatory only after demonstrating co-expression of additional M1-associated genes such as *il1b* and *il6* (Nguyen-Chi et al., 2015). Furthermore, whilst genes such as *arg2* and *ccn1l1* may be reliable anti-inflammatory macrophage markers in zebrafish, they were identified following M2 polarisation of carp monocytes, another teleost fish species (Wentzel et al., 2020). This raises the question of how well they translate to mammalian systems. Identifying additional anti-inflammatory macrophage markers that are conserved across zebrafish and humans would therefore enhance the translational relevance of zebrafish immunology and help bridge findings across species.

6.1.3. The resting state of larval zebrafish macrophages

Interpreting macrophage behaviour during infection or injury requires understanding their baseline phenotype. Although zebrafish transgenic lines have provided valuable insight into macrophage function, they do not conclusively differentiate between macrophages and monocytes, nor

tissue-resident and monocyte-derived macrophage populations (Speirs et al., 2024). Despite these challenges, there is evidence that supports the presence of both monocytes and monocyte-derived macrophages in zebrafish (Bojarczuk et al., 2016; Walton et al., 2015; Bohaud et al., 2021; Silva et al., 2021). Using transgenic lines such as *mpeg1:mCherry*, Moyse and Richardson identified a small population of cells hypothesised to be monocytes in an adult zebrafish heart injury model (Moyse and Richardson, 2020). In larvae, Ccr2+ putative monocytes, but not tissue-resident macrophages, are recruited during mycobacterial infection (Cambier et al., 2014b; Cambier et al., 2017). However, further work is needed to characterise whether cells that differentially express Ccr2 are true populations of monocytes and macrophages (Cambier et al., 2014b; Cambier et al., 2017; Sommer et al., 2021). Whilst the current literature likely focuses on the role of tissue-resident macrophages in zebrafish as a consequence of this limitation, there is a growing body of evidence revealing the heterogeneity of these populations both in adults and larvae (Morales and Allende, 2019). Furthermore, defining the transcriptional profile of zebrafish macrophages at steady state – and determining whether this aligns more closely with mammalian tissue-resident or monocyte-derived macrophages – would provide essential context for interpreting their subsequent activation dynamics during infection or injury.

6.1.3. Hypothesis and aims

Given the evolutionary conservation of many macrophage-associated signalling pathways, and the genetic similarity between zebrafish and humans, I hypothesised that zebrafish possess additional anti-inflammatory macrophage markers beyond *arg2* that are conserved across vertebrates and detectable during infection (Howe et al., 2013).

To investigate leukocyte anti-inflammatory signalling *in vivo*, Amy Lewis (previous Research Assistant in the Elks group) used BAC transgenesis to drive eGFP expression under the control of *ccn1l1* promoter. To address my hypothesis, I combined *in silico* analyses with experimental validation using a novel transgenic line during immune challenge to focus on three research aims:

- To define the resting state of larval zebrafish macrophages by comparing their transcriptional signatures to mammalian tissue-resident and monocyte-derived macrophage profiles.
- To identify candidate anti-inflammatory macrophage marker genes with translational relevance, based on conserved expression in zebrafish and human datasets.
- To generate a stable *ccn1l1:eGFP* transgenic line and characterise its expression both in resting conditions and in macrophages during immune challenge.

6.2. Results

6.2.1. Data mining zebrafish infection RNAseq data for anti-inflammatory macrophage candidate genes

The availability of pan-macrophage transgenic lines and pro-inflammatory cytokines, such as *mpeg1:mCherry* and *tnfa:GFP*, respectively, have enabled detailed *in vivo* visualisation of macrophage behaviour and provided evidence for pro-inflammatory macrophage polarisation in a range of immune challenges (Nguyen-Chi et al., 2015; Rougeot et al., 2019; Guilliams et al., 2022; Mazzolini et al., 2020; Lewis and Elks, 2019). Comparison of larval zebrafish macrophage RNAseq with homologs of polarised human monocyte-derived macrophages suggested that zebrafish macrophages had a pro- and anti-inflammatory genetic signature, including expression of *tnfa* (pro-inflammatory) and *il10* (anti-inflammatory). Despite this comparison, the resting state of zebrafish macrophages, particularly in the larvae, is poorly understood, with this dataset being the only genetic profiling of larval zebrafish macrophages (Rougeot et al., 2019). Furthermore, whilst analysis of deferentially expressed genes can provide some insight into the potential phenotype of these leukocytes, it fails to take into account how expression of several genes may work in conjunction to contribute to specific biological processes and pathways (Stanford et al., 2020). Thus, KEGG analyses of polarised human PBMC RNAseq datasets were used to identify common KEGG pathways in the zebrafish macrophage dataset to understand how these networks of upregulated genes may work together as a system.

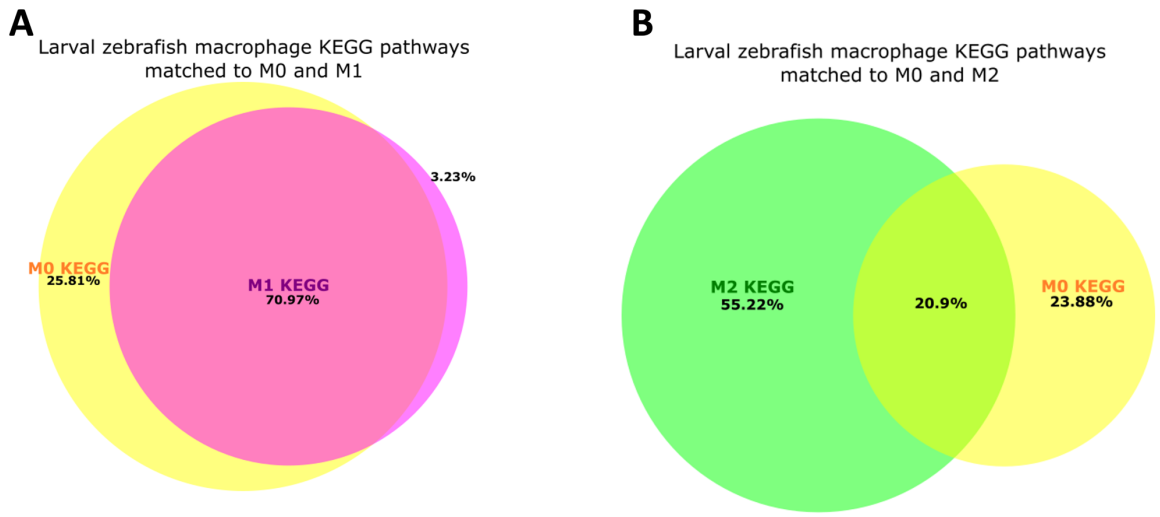


Figure 6.1. **Zebrafish macrophage KEGG pathways are most similar to human macrophages polarised towards M2a.** (**A**) Overlap of larval zebrafish macrophage KEGG pathways matched to KEGG pathways identified from human M0 and M1 polarised PBMCs. (**B**) Overlap of larval zebrafish macrophage M0-matched and M2-matched KEGG pathways. Up to 100 pathways compared in both PBMC and zebrafish macrophage KEGG analyses. Proportional Venn diagrams created using DeepVenn (Hulsen, 2022).

KEGG analysis identified from the upregulated genes in the larval zebrafish macrophage dataset were compared to those identified from a published RNAseq data set of human PBMCs polarised

towards M1 (with IFNγ and LPS) or M2a (with IL-4) (Rougeot et al., 2019; He et al., 2021). Zebrafish KEGG pathways were categorised on whether they were present in the KEGG analysis of human M0, M1 or M2 polarised macrophages. When comparing M0-associated and M1-associated KEGG pathways, 70.97% were found in both analyses. Core M0-associated pathways accounted for 25.81%, with only 3.23% found in M1-associated pathway (**Fig. 6.1.A**). However, M2a-associated KEGG pathways resulted in a much more discreet group when compared to M0-associated, with 55. 22% being present only in M2a-associated KEGG pathways and only 20.9% of M0- and M2a-associated pathways overlapping (**Fig. 6.1.B**). Together, this suggests that the genetic network of upregulated genes in resting larval zebrafish macrophages resemble human macrophages polarised towards M2a.

Current zebrafish transgenic lines do not differentiate between monocytes, tissue-resident macrophages and monocyte-derived macrophages (MDMs), particularly in larvae. In adult zebrafish, different macrophage transgenic lines (e.g. *mpeg:mCherry, csf1ra:GFP*) were used in tandem to examine co-expression of these transgenes in a heart injury model. A small population of *csf1ra*+ *mpeg*- cells were identified and hypothesised to be a population of monocytes (Moyse and Richardson, 2020). *ccr2* morpholino knockdown and Hoechst dye (monocyte stain) identified that Ccr2+ cells were recruited in mycobacterial infection. However, whether these putative peripheral monocytes are true populations of monocytes remains to be seen (Cambier et al., 2014b; Cambier et al., 2017). Thus, to assess whether matched larval zebrafish KEGG pathways most resemble monocytes or tissue-resident macrophages, pathways were compared to polarised human PBMCs (monocytes) and MDMs (tissue-resident macrophages) (Baidžajevas et al., 2020; He et al., 2021; Rougeot et al., 2019). When compared to KEGG pathways identified from PBMCs, M2a-associated pathways remained the largest and most discreet group (36.27% exclusively M2a-associated), with the second biggest group accounting for the pathways that were not associated with any macrophage polarisation KEGG pathways (33.33%; unmatched KEGG). Meanwhile, M0-associated and M1-associated pathways have a large number of overlapping pathways (14.71%), with few pathways overlapping all three polarisation statuses (6.86%) (**Fig. 6.2.A**). However, when comparing KEGG pathways associated to those identified from polarised MDMs, the functional differences the pathways identified were not clear. Pathways that were not able to be matched to any of the analyses accounted for over half of the pathways identified (55.77%), with those associated to M0, M1 (IFNγ+LPS), M2a (IL-4) and M2c (IL-10) polarised MDMs overlapping substantially (**Fig. 6.2.B**). Despite the large number of overlapping pathways, M2a-associated pathways remained the second largest group (12.5%), adding confidence to the hypothesis that the transcriptional profile of resting larval macrophages most closely aligns to M2a polarised human macrophages (**Fig. 6.2.B**). Taken together, comparison of KEGG pathways from upregulated genes in larval zebrafish macrophages suggests that they are transcriptionally more similar to M2a polarised circulating monocytes than tissue-resident macrophages.

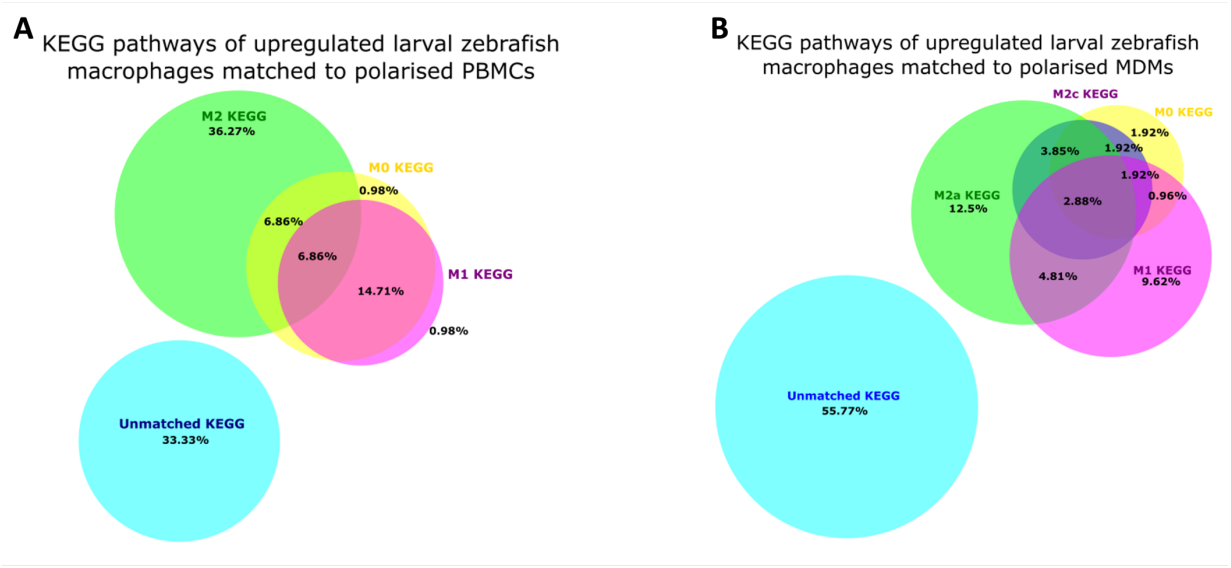


Figure 6.2. Zebrafish macrophage KEGG pathways are more similar to circulating monocytes than tissue-resident macrophages. (**A**) Overlap of larval zebrafish macrophage KEGG pathways matched to KEGG pathways identified from human M0, M1 (IFNγ and LPS) and M2a polarised PBMCs. Pathways that were not found in any of the human KEGG analyses are categorised as unmatched. (**B**) Overlap of larval zebrafish macrophage KEGG pathways matched to KEGG pathways identified from human M0, M1 (IFNγ and LPS) M2a (IL-4) and M2c (IL-10) polarised MDMs. Pathways that were not found in any of the human KEGG analyses are categorised as unmatched. Proportional Venn diagrams created using DeepVenn (Hulsen, 2022).

To further understand what pathways may be involved in the resting polarisation state of larval zebrafish macrophages based on the KEGG analyses, upregulated genes known to be involved in macrophage polarisation at the molecular level (e.g. IRF/STAT signalling) were examined (Sica and Mantovani, 2012). When examining genes in *mpeg:mCherry*+ cells compared to *mpeg:mCherry*- cells, 4 genes associated with the induction of M1 macrophages were upregulated, including *il12a* (5.24 log_2FC) and *ifng1-2* (24.17 log_2FC) (**Fig. 6.3.A**). 8 genes associated with molecularly determining M2 polarisation were upregulated, including *il10* (34.43 log_2FC) (**Fig. 6.3.A**). Interestingly, both isoforms of the zebrafish ortholog of *MRC1*, a key canonical marker of M2 polarisation were upregulated (*mrc1a*: 5.29 log_2FC and *mrc1b* 5.278 log_2FC) (**Fig. 6.3.A**). Upregulation of other key genes associated with M2 macrophage polarisation include *il4* (0.8 log_2FC) and *stat6* (0.1 log_2FC) (**Fig. 6.3.A**). Coupled with the upregulation of *mrc1a*/*mrc1b*, it suggests that the IL-4/STAT6 molecular pathway may be responsible for the M2a transcriptional signature identified in the KEGG analysis.

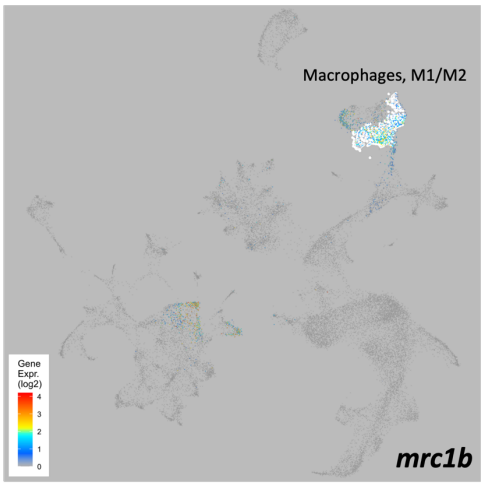
To determine whether increased expression of this canonical M2 marker is the result of larvae being a developing system, macrophage expression of *mrc1a/mrcb1* across different stages of development was assessed using Daniocell, a published single-cell gene expression resource (Sur et al., 2023). Expression of *mrc1a* was low across all developmental stages up to 5 dpf (data not shown), but UMAP of the haematopoietic system illustrated clear expression of *mrc1b* in macrophages (**Fig. 6.3.B**). Larval zebrafish macrophage RNAseq dataset obtained from Rougeot and colleagues used 6 dpf

zebrafish (Rougeot et al., 2019), yet expression of *mrc1b* was highest at 72-94 hpf (3-4 dpf), before falling again (**Fig. 6.3.C**). This demonstrates that increased expression of this canonical M2 marker is not due to the larvae being a developing system, but rather a true reflection of unchallenged zebrafish macrophages. Taken together, this data suggests that larval zebrafish macrophages may have the machinery to activate an M1-like response, but in their resting state exhibit an M2a phenotype.

A

Gene	TPM *mpeg:mCherry-*	TPM *mpeg:mCherry+*	log_2FC
ifng1-2	**0**	**1.89357153**	**24.1746066**
il12bb	**4.579584959**	**497.491349**	**6.76331077**
il12a	**0.86439896**	**32.650817**	**5.23927795**
irf3	1.402498618	5.83386586	2.05645287
irf4a	0	0.66733395	29.3138337
stat6	24.81764717	26.6612864	0.10338004
mrc1b	**1.248573301**	**48.4294708**	**5.27753281**
irf4b	0.501593698	2.28249091	2.18601799
mrc1a	**0.073701669**	**2.87497244**	**5.28570702**
il4	14.04836115	25.8365611	0.87901222
il10	**0**	**23.0993499**	**34.4271332**
klf4	11.79652549	15.0837579	0.35463391

B



C

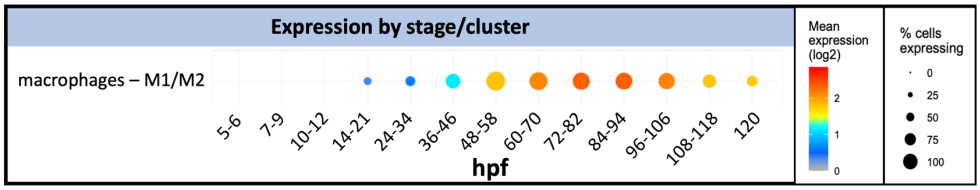


Figure 6.3. IL-4/STAT6 molecular pathway genes are upregulated in zebrafish macrophages under resting conditions. (**A**) Expression of genes associated with the molecular pathways that determine macrophage polarisation in *mpeg:mCherry*- cells and *mpeg:mCherry*+ cells. Orange cells indicate M1 associated genes. Green cells indicate M2 associated genes. (**B**) UMAP of the larval haematopoietic system illustrating expression of *mrc1b* in the macrophage cluster. (**C**) Expression of *mrc1b* in macrophages across zebrafish development up to 5 dpf. Expression data was obtained from Daniocell (Sur et al., 2023). Abbreviations: TPM, transcripts per million; FC, fold change; hpf, hours post-fertilisation.

Zebrafish transgenic lines such as *tnfa:GFP* and *il1β:GFP* are incredibly useful tools for visualising macrophage pro-inflammatory signalling *in vivo* (Ogryzko et al., 2019; Nguyen-Chi et al., 2015; Lewis and Elks, 2019). However, most studies examining macrophage signalling in zebrafish *in vivo* have had to rely on macrophages being negative for these pro-inflammatory reporters as a proxy for the macrophage anti-inflammatory response. Thus, publicly available RNAseq datasets were interrogated to identify candidate anti-inflammatory macrophage genes that could be used to generate zebrafish transgenic reporter lines which may aid in the visualisation of macrophage heterogeneity *in vivo*, particularly during immune challenge. To identify genes that could be translated to human models, an

RNAseq dataset from zebrafish *Mm* infected macrophages was compared to the polarised MDM dataset used in the KEGG analyses (Rougeot et al., 2019; Baidžajevas et al., 2020). Genes upregulated in MDMs polarised towards an anti-inflammatory phenotype (IL-4 or IL-10 stimulated) and zebrafish *Mm* infected macrophages were isolated, and three candidate genes were identified: *ocstamp*, *ctsz* and *nccrp1* (**Fig. 6.4.**). In addition to downregulation in MDMs polarised towards a pro-inflammatory phenotype (IFNγ and LPS stimulated; -0.65 log_2FC) *OCSTAMP* (osteoclast stimulatory transmembrane protein) is significantly upregulated in MDMs polarised with IL-4 (1.48 log_2FC, **Fig. 6.4. Ai**), as well as significantly elevated transcript levels being identified in zebrafish *Mm* infected macrophages compared to uninfected macrophages (960.3 TPM compared to 2 TPM, **Fig. 6.4. C**). This was the only mutual gene that was significantly elevated in both datasets. Similarly, *CTSZ* (cathepsin Z) is downregulated in M1 polarised MDMs (-0.38 log_2FC) and significantly elevated when stimulated with IL-4 (0.54 log_2FC, **Fig. 6.4. Aii**). Although *ctsz* transcript levels are high in uninfected macrophages, they are elevated in zebrafish infected macrophages (2586 TPM compared to 1587.3 TPM, **Fig. 6.4. C**). Finally, *NCCRP1* (P1, F-box associated domain containing) is significantly upregulated in MDMs stimulated with IL-4 and IL-10 (6.01 log_2FC and 1.08 log_2FC, respectively), however it is also significantly upregulated in MDMs stimulated with IFNγ and LPS (5.62 log_2FC; **Fig. 6.4. Aiii**). This gene has been included as a candidate anti-inflammatory marker as it is upregulated in zebrafish infected macrophages (1770 TPM compared to 367.7 TPM; **Fig. 6.4. C**).

Interestingly, there is low expression of *ocstamp* and *ctsz* in adult zebrafish leukocyte populations (**Fig. 6.4. Bi, Bii**), suggesting that these genes could be likely candidates for anti-inflammatory macrophages as low expression levels in unchallenged fish would be expected. Following an immune challenge, expression of *ocstamp* and *ctsz* would then be expected to rise following recruitment of anti-inflammatory macrophages. However, *nccrp1* is more widely expressed, particularly in both neutrophil and monocyte adult zebrafish leukocyte populations (**Fig. 6.4. Biii**), suggesting that this gene may not be specific enough to label anti-inflammatory macrophages.

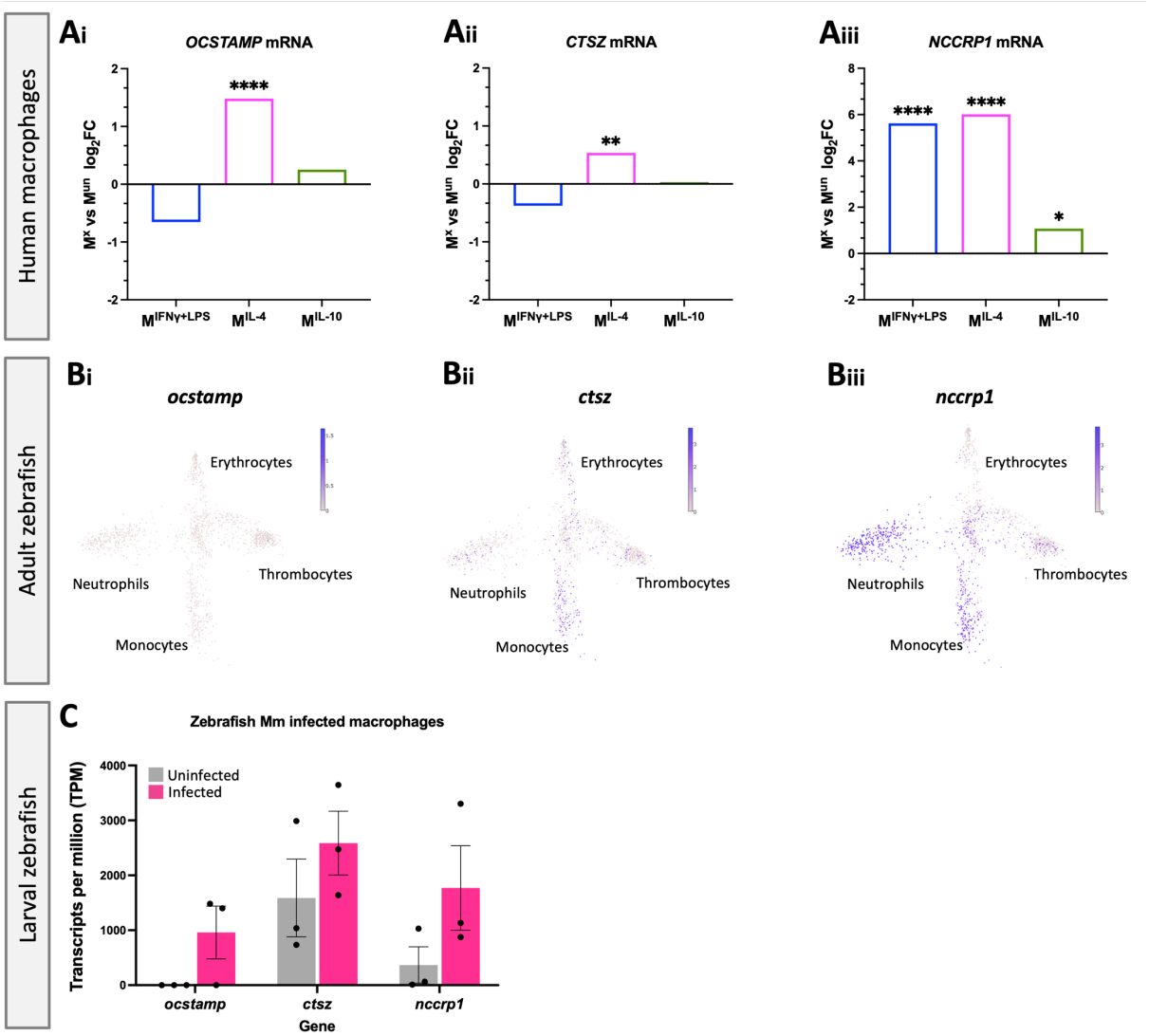


Figure 6.4. Comparison between zebrafish *Mm* infected macrophage and human polarised macrophage RNAseq datasets identified 3 candidate genes. (**A**) RNAseq of human macrophages polarised *in vitro* from 8 donors (Baidžajevas et al., 2020). M1 macrophages were polarised with IFNγ+LPS ($M^{IFN+LPS}$); M2 macrophages were polarised with either IL-4 (M^{IL-4}) or IL-10 (M^{IL-10}). M^{x} were compared to unpolarised macrophages (M^{un}). (**B**) Gene expression of adult zebrafish leukocytes was determined using the Blood Atlas of Single Cells in zebrafish (Athanasiadis et al., 2017). Each arm of the diagram indicates a haematopoietic cell population, and each dot represents separate scRNAseq repeats performed. Populations are labelled on the image. Deeper colour indicates higher gene expression in that population. (**C**) RNAseq of 5 dpi isolated zebrafish macrophages following *Mm* infection (Rougeot et al., 2019). Data is average from 3 replicates comparing *Mm* infected and uninfected macrophages. Error bars depict SEM. Statistical significance shown are: *FDR < 0.05; **FDR < 0.01; ***FDR < 0.001; ****FDR < 0.0001.

To further determine expression levels of macrophage candidate genes in zebrafish larvae, haematopoietic expression of the genes were assessed using Daniocell and ISH data available from ZFIN.org (Thisse and Thisse, 2004; Thisse and Thisse, 2005; Sur et al., 2023). Expression of *ocstamp* was not detected in the haematopoietic system, thus no UMAP specifically of the haematopoietic system and macrophage cluster could be seen (**Fig. 6.5. Ai**). This adds confidence to the potential use of

ocstamp as a specific anti-inflammatory macrophage marker, with immune challenge further polarising macrophages towards an M2-like phenotype at healing stages. Both *cstz* and *nccrp1* are expressed in the macrophage clusters of the haematopoietic UMAP (**Fig. 6.5. Aii, Aiii**). Expression of *ctsz* from 3 hours post-fertilisation (hpf; ~1,000 cells) up to 5 dpf suggests highest expression at approximately 4.5 dpf (108-118 hpf), before starting to fall again (**Fig. 6.5. Aii**). Given that *ctsz* expression in adult zebrafish leukocyte populations is low, the higher expression identified at 4.5 dpf in unchallenged larval macrophages may be due to the larvae being a developing system (**Fig. 6.4. Bii**). Nevertheless, *cstz* remains an interesting candidate due to *ISH* data highlighting *cstz* expression in a population of blood cells within the caudal haematopoietic tissue in unchallenged larvae (Thisse and Thisse, 2004) (**Fig. 6.5. B**). Macrophage expression of *nccrp1* across development (0.5 – 5 dpf) remains low by comparison, suggesting that it is not part of a developmental wave of gene expression changes (**Fig. 6.5. Aiii**). Coupled with the *nccrp1* ISH data which indicated labelling of a small blood cell population and that larval macrophages most closely match the transcriptional profile of M2a polarised macrophages, the expression patter of this gene suggests that it may be specific enough to label anti-inflammatory macrophages *in vivo* (Thisse and Thisse, 2005) (**Fig. 6.5. C**).

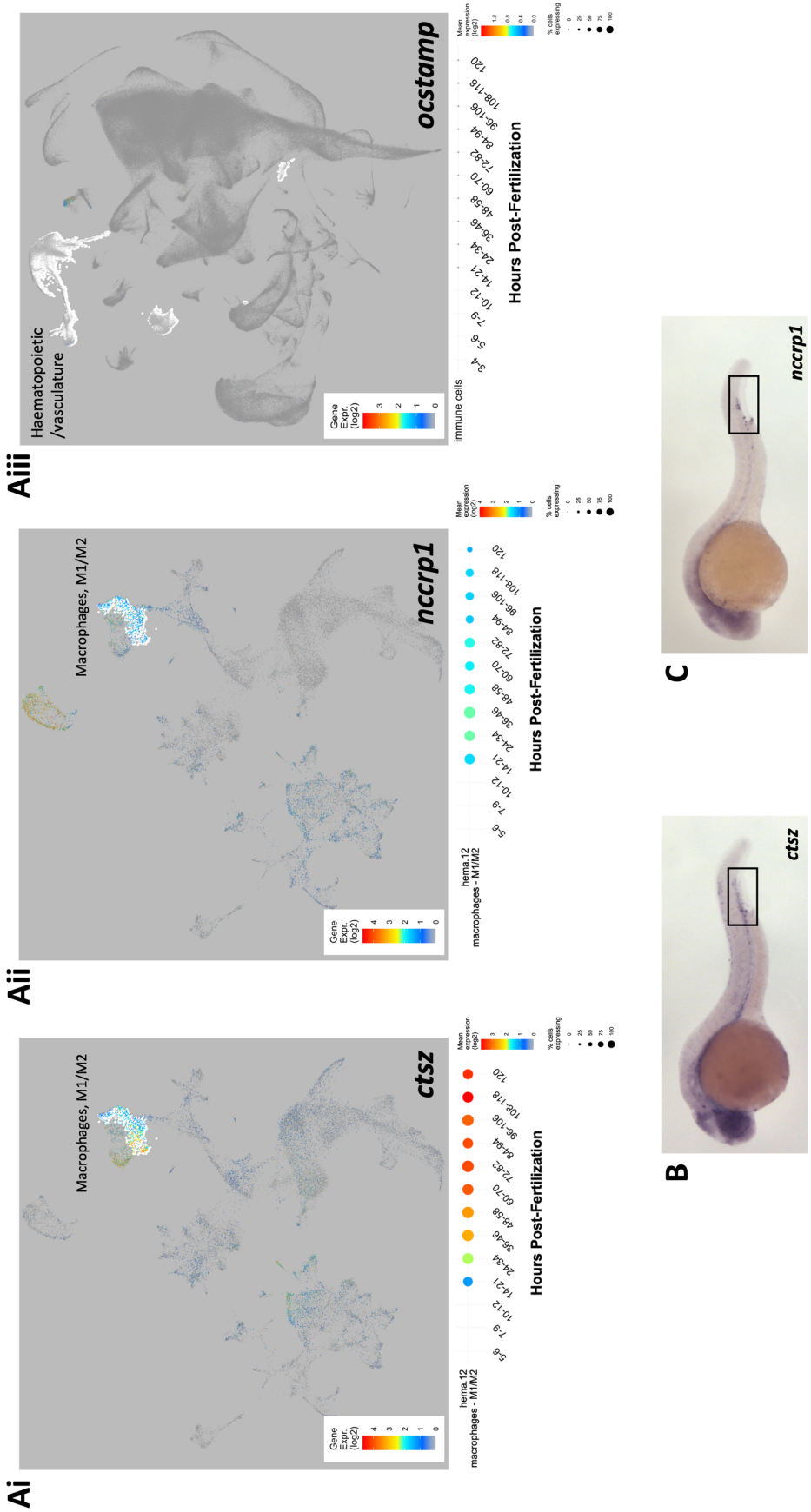


Figure 6.5. Under resting conditions, *ctsz* and *nccrp1* are expressed in larval zebrafish macrophages, with very low expression levels of *ocstamp* in haematopoietic populations. (**Ai-iii**) UMAPs of the larval haematopoietic/vasculature cluster (**Ai,** *ocstamp*) and the macrophage cluster within the haematopoietic system (**Aii**, *ctsz*; **Aiii**, *nccrp1*) expression of the candidate genes. Timeline below UMAPs indicates gene expression across larval development up to 5 dpf. (**B**) *In situ* hybridisation (ISH) data of *ctsz* obtained from ZFIN.org highlights some

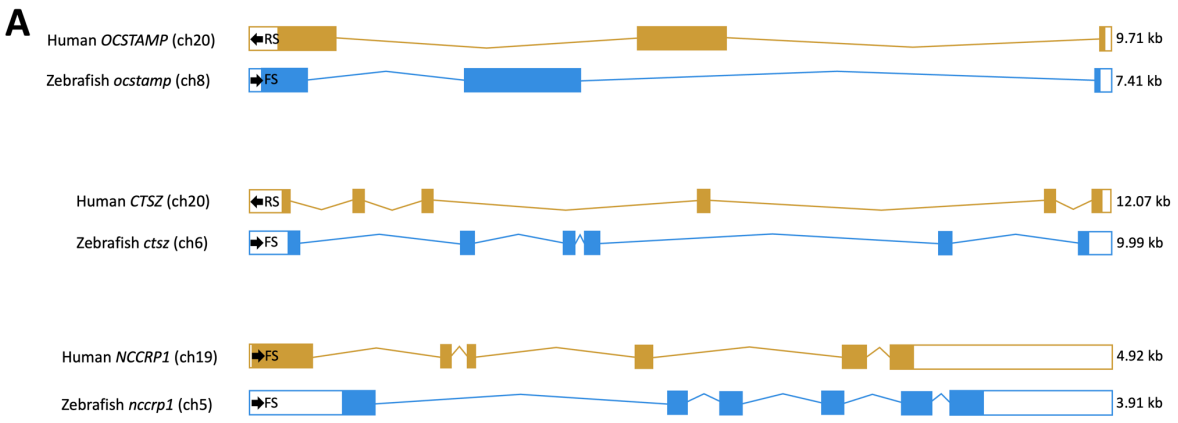
blood cell labelling in unchallenged larvae (Thisse and Thisse, 2004). (**C**) ISH data of *nccrp1* obtained from ZFIN.org highlights a small subpopulation of blood cells in unchallenged larvae (Thisse and Thisse, 2005). UMAPs were obtained from Daniocell (Sur et al., 2023).

Zebrafish genes often have multiple isoforms of genes due to a genome duplication event approximately 350 million years ago (Hoegg et al., 2004); however, these three candidate genes (*ocstamp*, *ctsz* and *nccrp1*) have only a single isoform annotated in the genome in the Ensembl database. Comparison of gene organisation of zebrafish *ocstamp* (ENSDARG00000022139), *ctsz* (ENSDARG00000043081) and *nccrp1* (ENSDARG00000035326) to human orthologues found high homology, with all three genes having the same number of exons as human counterparts. Zebrafish *ocstamp*, like human *OCSTAMP*, has 3 exons, with small non-coding regions at the beginning of exon 1 and the end of exon 3. Zebrafish *ocstamp* is smaller than the human orthologue (7.41 kb compared to 9.71 kb), and whilst human *OCSTAMP* is found on the reverse strand of chromosome 20, zebrafish *ocstamp* is located on the forward strand of chromosome 8 (**Fig. 6.6. A**). Human and zebrafish *CTSZ* both share 6 exons. Whilst both have a small non-coding region at the start of exon 1, zebrafish *cstz* has a larger non-coding region at the end of exon 6 compared to the human orthologue. Human *CTSZ* is larger than zebrafish *ctsz* (12.07 kb compared to 9.99 kb) and it is located on the reverse strand of chromosome 20, whereas zebrafish *ctsz* is located on the forward strand of chromosome 6 (**Fig. 6.6. A**). Similarly, human and zebrafish *NCCRP1* also have 6 exons, with both genes having a larger non-coding region at the end of exon 6. However, zebrafish *nccrp1* has a larger non-coding region at the start of exon 1. As with the other candidate genes, human *NCCRP1* is slightly larger than the zebrafish orthologue (4.92 kb compared to 3.91 kb), but both zebrafish and human *NCCRP1* are located on forward chromosome strands (chromosome 5 and 19, respectively) (**Fig. 6.6. A**). Interestingly, all three zebrafish genes share synteny with human orthologues (identified from the ZFIN database).

The size of the proteins encoded by these candidate genes was assessed next. Looking at the overall protein size of *OCSTAMP* (in amino acids, aa), zebrafish *ocstamp* is smaller than the human counterpart (473 aa compared to 566 aa) (**Fig. 6.6. B**). By using the NCBI Blast Global Align tool to compare human sequences to zebrafish orthologues, zebrafish *ocstamp* was found to share the highest identities match (46%) of the three candidate genes, indicating high amino acid homology (**Fig. 6.6. C**). Zebrafish and human *CTSZ* and *NCCRP1* encode proteins of very similar sizes (*CTSZ*: 301 aa (zebrafish) and 303 aa (human); *NCCRP1*: 237 aa (zebrafish) and 275 aa (human), with zebrafish *ctsz* and *nccrp1* also having high identity matches for human orthologues (34% and 45%, respectively) (**Fig. 6.6. B-C**).

Together, these data identify additional candidate genes for polarised macrophages, which, following validation, could be used as markers for anti-inflammatory macrophages in zebrafish. Due to the heterogeneity of the macrophage phenotype, this could allow us to further elucidate macrophage

signalling, by expanding on the tools available to aid in addressing my hypotheses. Additionally, the similarities in gene organisation also suggests a potentially conserved role of these genes between human and zebrafish as the high degree of synteny results in minimal chromosomal rearrangement and indicates species (Hu et al., 2019), suggesting that these candidate genes could translate to human systems.



B

Protein size (aa)	Human	Zebrafish
OCSTAMP	566	473
CTSZ	303	301
NCCRP1	275	237

C

Amino acid homology	Percent identities (%)
OCSTAMP	46
CTSZ	34
NCCRP1	45

Figure 6.6. Zebrafish gene organisation of candidate genes share high homology with human orthologues. (**A**) Gene organisation of human genes (yellow) and zebrafish gene (blue) orthologues share very similar exon numbers and coding exons. (**B**) Human and zebrafish protein sizes (amino acids, aa) of all three candidate genes are very similar. (**C**) NCBI Blast Global Align comparing zebrafish sequences to human sequences identified high amino acid homology, depicted as percent identities. Exon maps in (**A**) generated from the Ensembl database. Filled sections indicate coding exons, empty sections indicate non-coding exons. Chromosome number (ch), strand direction (forward strand, FS; reverse strand, RS) and gene size in kilobases (kb) stated on exon maps. Protein size in (**B**) was determined using the Ensembl database.

6.2.2. *ccn1l1:eGFP* as an alternative anti-inflammatory macrophage reporter

The pro-inflammatory *tnfa* transgenic reporter robustly labels pro-inflammatory macrophages (Nguyen-Chi et al., 2015; Lewis and Elks, 2019). However, the anti-inflammatory macrophage phenotype *in vitro* appears to be more heterogenous, and various markers to develop an anti-inflammatory macrophage reporter line have been proposed (Wiegertjes et al., 2016). RNAseq of *ex vivo* M2 polarised carp macrophages identified significant upregulation of various genes, including *ccn1l1* (cellular communication network factor 1, like 1 – previously known as *cyr61l1*; 0.2 RPKM compared to 103.8 RPKM) (Wentzel et al., 2020). Many human genes have at least one zebrafish orthologue, with sequence and function frequently being homologous (Vilella et al., 2009). As *ccn1l1*

only has orthologues in other fish species, such as Atlantic salmon (*Salmo salar;* identified from the Ensemble database), zebrafish *ccn1l1* (ENSDARG00000035422) and *ccn1* (ENSDARG00000023062) genes were compared for similarities with human *CCN1* (ENSG00000142871) at the gene and protein level.

The human CCN1 protein structure was overlayed with a predicted Alphafold model of zebrafish ccn1l1 and ccn1 proteins (**Fig. 6.7**). Predicted protein structure of zebrafish ccn1l1 highlighted a high degree of structural similarities, both in alpha helix and gross fold, when compared to human CCN1 (**Fig. 6.7. A**). However, the zebrafish ccn1 predicted protein structure was less well conserved, highlighting that the zebrafish ccn1l1 protein is likely most similar to the human CCN1 protein (**Fig. 6.7. B**).

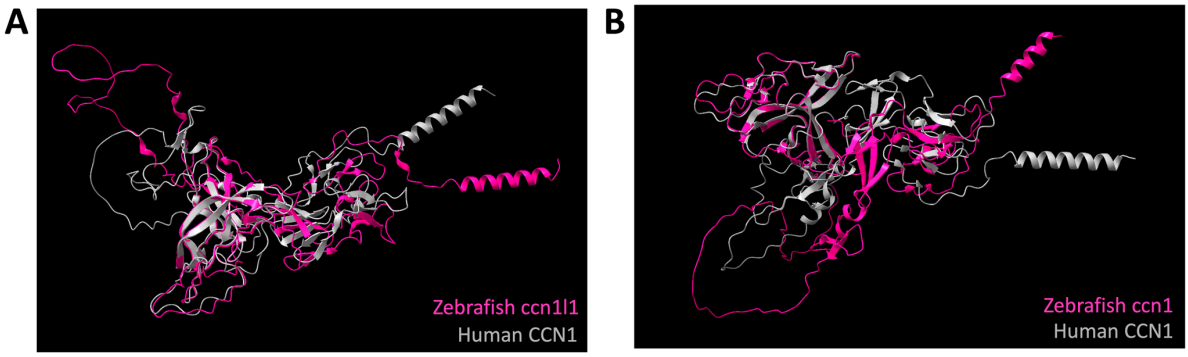


Figure 6.7. Human CCN1 protein structure is similar to zebrafish ccn1l1. (**A**) Overlay of ccn1l1 predicted protein structure of zebrafish (pink) and human CCN1 (grey). (**B**) Overlay of ccn1 predicted protein structure of zebrafish (pink) and human CCN1 (grey). Predicated protein structures were sourced from AlphaFold DB (Jumper et al., 2021; Varadi et al., 2024). Overlays of predicted protein structures were produced using UCSF ChimeraX, developed by the Resource for Biocomputing, Visualization, and Informatics at the University of California, San Francisco, USA (Pettersen et al., 2021) .

Human CCN1 is a matricellular protein that plays a role in a diverse range of biological functions (Schober et al., 2002; Juric et al., 2012; Yang et al., 2018). The CCN1 protein contains a secretory signal peptide (SP), followed by four distinct modules (**Fig. 6.8**). These include insulin-like growth factor binding protein (IGFBP) domain, von Willebrand type C domain (vWC), thrombospondin-1 domain (TSR, also known as TSP1) and a cystine knot domain (CT). The vWC domain contains a V2 integrin binding site and the CT domain has both integrin heparin sulphate proteoglycan (HSPG) binding sites. The domains are linked by a hinge region between vWC and TSR (Yang et al., 2018; Juric et al., 2012; Marinkovic et al., 2022; Chen et al., 2004). The CCN1 protein has been shown to play a role in promoting cellular proliferation during wound healing and myofibroblast senescence *in vitro* in human and rodent models (Schober et al., 2002; Borkham-Kamphorst et al., 2014). Importantly, CCN1 has been found to play a role in innate immunity, with infections resulting in increased expression in several *in vitro* models (Johannes et al., 1999; Kim et al., 2004; Kurozumi et al., 2008; Wiedmaier et al., 2008).

Although the CCN1 protein has been shown to promote a pro-inflammatory macrophage phenotype in macrophage and fibroblast cell lines, recent work found *ccn1l1* to be significantly upregulated (10.48 log_2FC) at the time of macrophage recruitment (2 dpi) in a zebrafish ablation-regeneration model of retinal pigment epithelium (Lu et al., 2022; Bai et al., 2010; Juric et al., 2012). Thus, *ccn1l1* remained an interesting candidate to investigate macrophage-specific anti-inflammatory signalling in zebrafish.

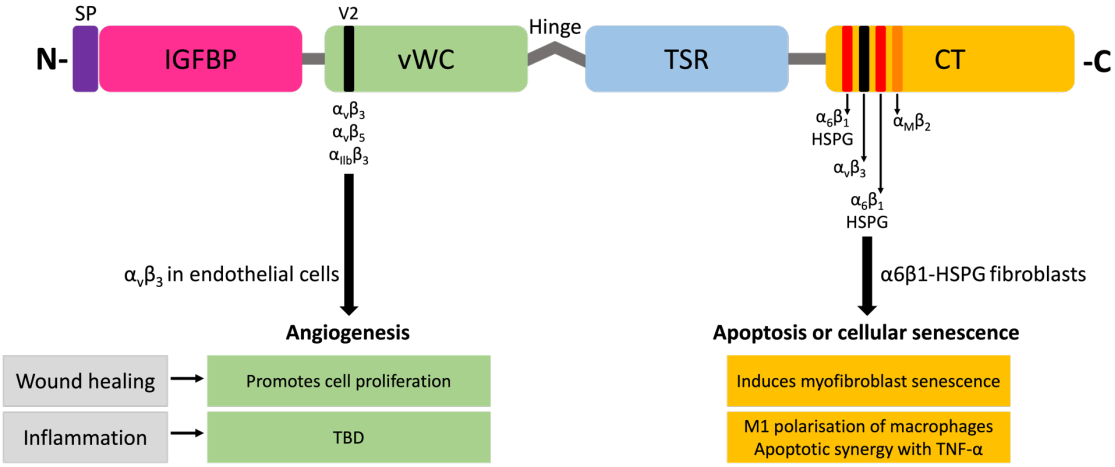
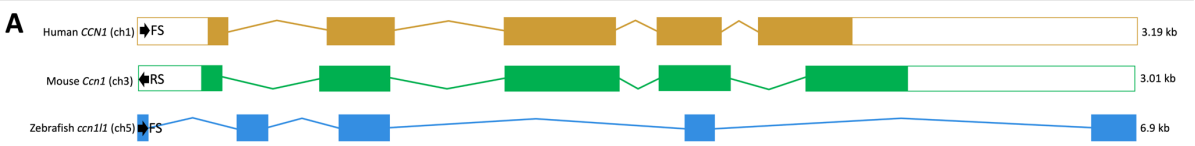


Figure 6.8. Human CCN1 protein has been shown to play a role in tissue repair and macrophage polarisation. The human CCN1 protein has a secretory signal peptide (SP) at the N-terminus. The protein has four modular domains, consisting of insulin-like growth factor binding protein (IGFBP), von Willebrand type C (vWC), thrombospondin-1 (TSR) and cystine knot (CT). The vWC and TSR domains are linked via a hinge region. The vWC domain contains a V2 integrin binding sites, resulting in downstream mechanisms associated with angiogenesis. The CT domains contains several integrin and heparan sulphate proteoglycan (HSPG) binding sites, with downstream mechanisms associated with apoptosis and senescence in macrophages and fibroblasts. Adapted from Yang et al., (2018; Juric et al., (2012).

Zebrafish only have a single isoform of the *ccn1l1* gene, identified from the Ensembl database. The gene organisation of human *CCN1* (ENSG00000142871) and mouse *Ccn1* (ENSMUSG00000028195) demonstrate a high degree of conserved synteny as previously described (Hu et al., 2019), with gene organisation homology to zebrafish *ccn1l1* also identified (**Fig. 6.9. A**). All three genes have 5 exons, but human and mouse genes also have small non-coding regions the beginning of exon 1 and larger non-coding regions at the end of exon 5, with none found on the zebrafish *ccn1l1* gene. Human and mouse *CCN1/Ccn1* are similar in size (3.19 kb and 3.01 kb, respectively), with zebrafish *ccn1l1* being over twice the size (6.9 kb). Human *CCN1* and zebrafish *ccn1l1* can both be found on forward strand (chromosome 1 and 5, respectively), whilst mouse *Ccn1* is found on the reverse strand of chromosome 3. The NCBI Blast Global Align tool was used to align human and mouse sequences to zebrafish *ccn1l1*, identifying that both *CCN1* and *Ccn1* had a 45.1% alignment (**Fig. 6.9. B**). This lower percentage of alignment is unsurprising given that *ccn1l1* is substantially larger than its mammalian counterparts, meaning over 50% of the zebrafish sequence would not have an alignment. Despite this discrepancy in size, all three genes encode proteins of a similar size (*CCN1*: 381 aa; *Ccn1*: 379 aa; *ccn1l1*: 383; **Fig. 6.9. C**), and

zebrafish *ccn1l1* also having high identity matches to human and mouse orthologues (45% and 43%, respectively) (**Fig. 6.9. D**). Importantly, almost no expression of *ccn1l1* is found in adult or larval leukocyte populations (**Fig. 6.9. E-F**), with expression only found in the larval vasculature system (**Fig. 6.9. F**).



B

Species	Gene	% alignment (to zebrafish)
Human	*CCN1*	45.1
Mouse	*Ccn1*	45.1
Zebrafish	*ccn1l1*	100

C

Species	Protein size (aa)
Human	381
Mouse	379
Zebrafish	383

D

Species	Percent identities (%)
Human	45
Mouse	43

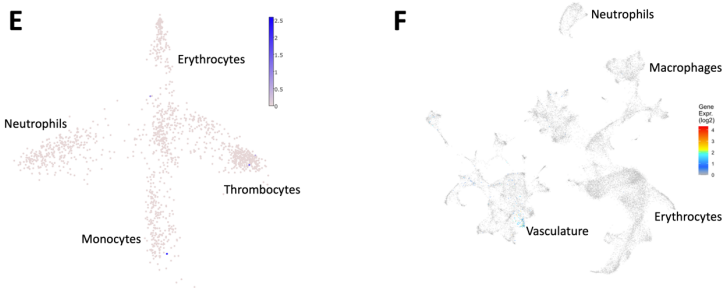


Figure 6.9. Zebrafish *ccn1l1* shares homology with human and mouse *CCN1/Ccn1.* (**A**) Gene organisation of human *CCN1* (yellow), mouse *Ccn1* (green) and zebrafish *ccn1l1* (blue) share very similar exon numbers and coding regions. (**B**) Human and mouse sequences have a low alignment percentage, likely due to differences in gene size. (**C**) Human, mouse and zebrafish protein size (amino acids, aa) are very similar. (**D**) NCBI Blast Global Align comparing zebrafish sequences to human *CCN1* and mouse *Ccn1* sequences identified high amino acid homology, depicted as percent identities. (**E**) *ccn1l1* gene expression in adult zebrafish leukocyte populations was determined using the Blood Atlas of Single Cells in zebrafish (Athanasiadis et al., 2017). Each arm of the diagram indicates a haematopoietic cell population and each dot represents separate scRNAseq repeats performed. Populations are labelled on the image. Deeper colour indicates higher gene expression in that population. (**F**) UMAP of *ccn1l1* expression in the larval haematopoietic system. Leukocyte populations and cells associated with the vasculature are labelled. Grey indicates no expression and red indicates higher expression. Exon maps in (**A**) generated from the Ensembl database. Filled sections indicate coding exons, empty sections indicate non-coding exons. Chromosome number (ch), strand direction (forward strand, FS; reverse strand, RS) and gene size in kilobases (kb) stated on exon maps. Protein size in (**C**) was determined using the Ensembl database. UMAP in (**F**) was obtained from Daniocell (Sur et al., 2023).

The carp genome underwent an additional whole-genome duplication compared to zebrafish, thus the zebrafish *ccn1l1* sequence was aligned to the carp orthologue encoded on chromosome 8 (ENSCCRG00000035740) and chromosome 16 (ENSCCRG00000024280). Comparative genomics using the Ensembl database identified a high target percent identity that was similar for both chromosomes 16 and 8 (83.03% and 82.34% respectively) (**Fig. 6.10. A**). The GenomeNet database was used to align

the zebrafish ccn1l1 protein sequence to each of the carp proteins using ClustalW. Comparable to the sequence alignment, both carp cc1l1 proteins had a similar high pairwise alignment score (chromosome 16: 83.0287%; chromosome 8: 82.7676% (**Fig. 6.10. B-C**). This high degree of conservation suggests that, irrespective from which carp chromosome *ccn1l1* was transcribed following M2 polarisation, this gene may also be upregulated in zebrafish anti-inflammatory macrophages.



Figure 6.10. Carp and zebrafish *ccn1l1* sequence and protein alignment indicates gene conservation. (**A**) Zebrafish *ccn1l1* sequence had a high target percent identity (Target%id) when compared to carp orthologues on both chromosomes 16 and 8. (**B-C**) Zebrafish ccn1l1 protein was aligned to carp ccn1l1 encoded on chromosome 16 (**B**) and chromosome 8 (**C**), with both resulting in high pairwise alignment scores. Table in (**A**) was obtained from Ensembl. Protein alignments in (**B-C**) were obtained from the GenomeNet database (www.genome.jp) following ClustalW sequence alignment.

Given the homology to human CCN1 and that ccn1l1 is highly conserved to its carp orthologue, *ccn1l1* presented as an interesting candidate to pursue in zebrafish. To examine macrophage *ccn1l1* expression in zebrafish larvae *in vivo*, Amy Lewis (previous Research Assistant in the Elks group) generated a *ccn1l1* BAC, driving expression of eGFP under the control of the *ccn1l1* promoter (*TgBAC(ccn1l1:eGFP)*, hereon in termed *ccn1l1:eGFP*). Following generation of a stable transgenic line, it was characterised using confocal microscopy under resting conditions and in immune challenge.

In situ hybridisation data submitted to ZFIN.org (Thisse and Thisse, 2004) shows strong expression of *ccn1l1* in the otic vesicle and midline of unchallenged zebrafish (**Fig. 6.11. A**), thus F0

injected larvae were screened for specific GFP expression in these areas to raise. The F0 generation was outcrossed with a wildtype zebrafish (LWT) line and the F1 offspring were screened for specific expression of GFP within the otic vesicle and midline, identifying two F0 founder fish. Positive F1 embryos were raised to adulthood and outcrossed again with a wildtype nacre line. Positive F2 embryos were then raised to adulthood to ensure a stable transgenic line which were used for experiments. GFP is brightly and specifically expressed in the otic vesicle of F2 progeny, which can easily be screened under a stereo fluorescent microscope (**Fig. 6.11. B**). Confocal imaging was used to further examine GFP expression of the otic vesicles, as *ccn1l1* has recently been found to be a key regulator for proper canal formation (Mori et al., 2025).The *ccn1l1:eGFP* line appears to be labelling three developing semicircular canals and the epithelial pillars, which presents as a potential useful tool for researchers examining the zebrafish developing inner ear as current transgenic lines only label the ventral projection (Baxendale and Whitfield, 2016; Whitfield et al., 2002). At lower and higher magnification, the three canals are clearly visible in the developing inner ear of 2 dpf larvae (**Fig. 6.11. Ci-Cii**). At later stages of development (4 dpf), the three canals can be seen to have curved round to form the structure of the larval zebrafish ear (**Fig. 6.11. Ciii**).

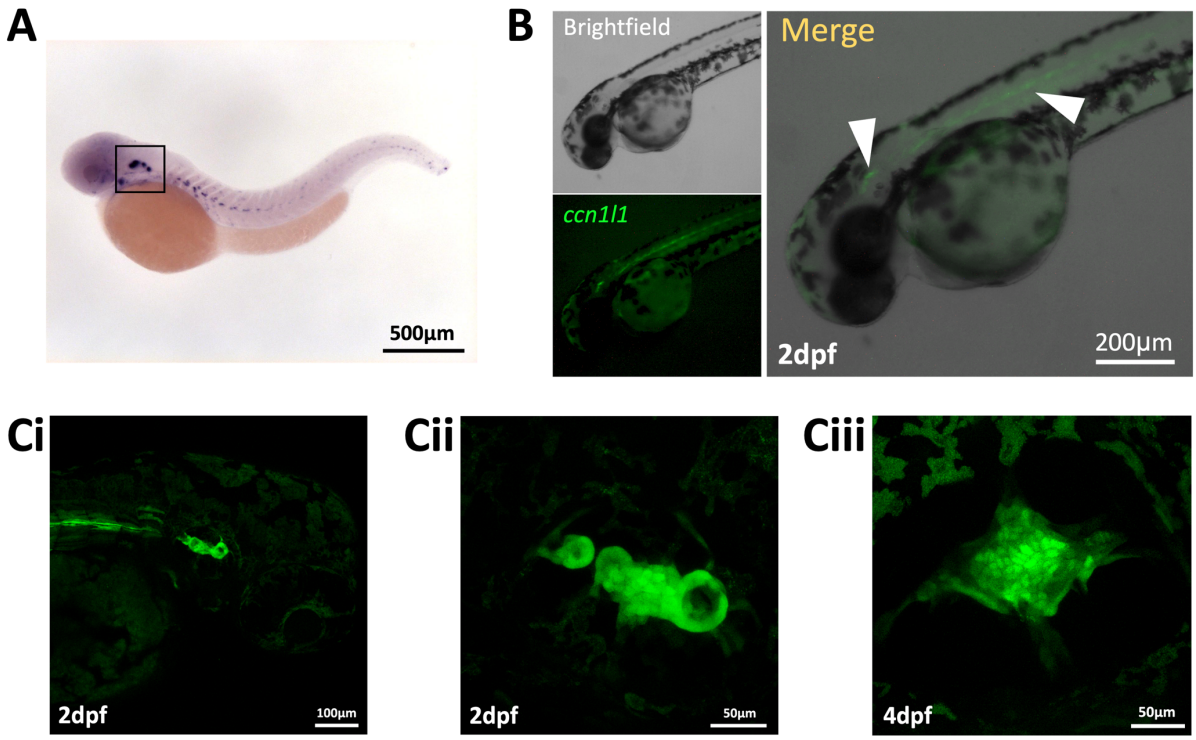


Figure 6.11. The *Tg(ccn1l1:eGFP)* transgenic line shows expression of GFP in the otic vesicle and midline under resting conditions, recapitulating *ccn1l1 in situ* hybridisation expression pattern. (**A**) *In situ* hybridisation data obtained from ZFIN.org shows strong expression of *ccn1l1* in the ear (Thisse and Thisse, 2004). (**B**) Representative stereo fluorescence image of F2 generation *ccn1l1:eGFP*, with strong expression in otic vesicle (left-hand arrow) and the midline (right-hand arrow). (**Ci-ii**) Representative confocal image of the otic vesicle of 2 dpf *ccn1l1:eGFP* embryo at 20x magnification (**Ci**) and 40x magnification (**Cii**). (**Ciii**) Representative confocal image of the otic vesicle of 4 dpf *ccn1l1:eGFP* embryo at 40x magnification. Scale bars are stated on the images.

With a stable transgenic line generated, I aimed to determine if macrophages upregulate *ccn1l1:eGFP* throughout *Mm* infection pathogenesis in the larvae (1-4 dpi) to determine whether this transgenic line could be used as an *in vivo* reporter for anti-inflammatory macrophages during infection. Adult *ccn1l1:eGFP* transgenic fish were crossed with the macrophage reporter *mpeg:mCherry* and larvae were systemically infected via the caudal vein with 100 CFU of *Mm* at 1 dpf. Using confocal microscopy, infected larvae were imaged at 1-4 dpi in the region of the caudal vein or around clusters of bacteria within the fish, checking for *ccn1l1:eGFP* otic vesicle expression to screen for GFP+ larvae.

Out of a total of 53 larvae imaged from 1 to 4 dpi, only 3 *ccn1l1:eGFP+ mpeg:mCherry+* cells were identified at 1 dpi, 3 dpi and 4 dpi (**Fig. 6.12. A, C, D**). Whilst identification of these potential double positive cells was initially encouraging, no further examples were identified at any of the infection timepoints (**Fig. 6.12**). Furthermore, confocal imaging at a higher magnification (40x) highlighted the high levels of background fluorescence present in the *ccn1l1:eGFP* transgenic line (**Fig. 6.12. B**).

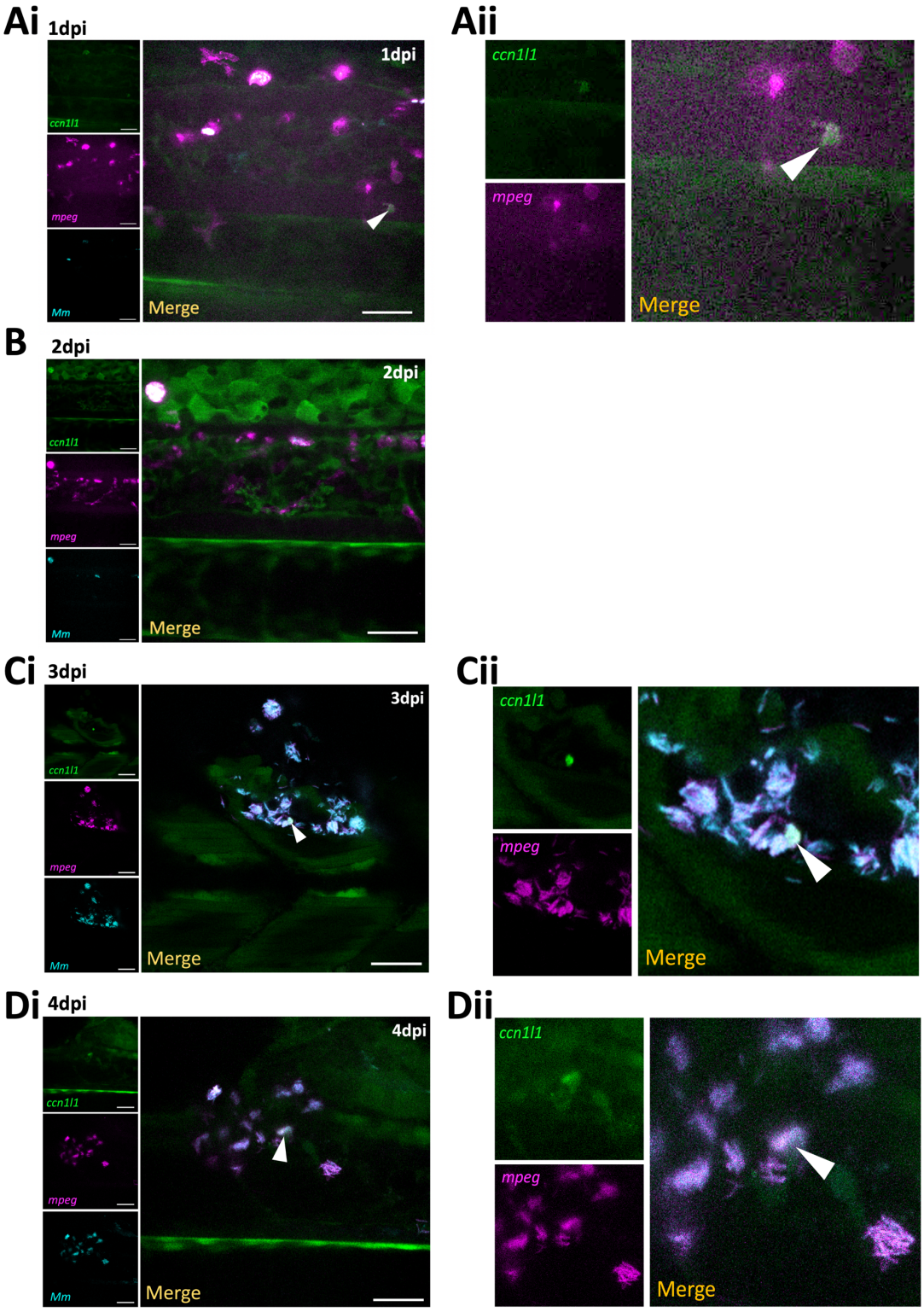


Figure 6.12. Macrophages do not express *ccn1l1:eGFP* following *Mm* infection. (**Ai-Di**) Representative confocal images of *mpeg:mCherry+ ccn1l1:eGFP+* larvae at 1-4 dpi. (**Aii, Cii, Dii**) Close-up of individual *mpeg:mCherry+ ccn1l1:eGFP+* cells. All images were taken from a 40x field of view near the caudal vein (site of infection) or within clusters of bacteria within the fish. White arrowheads indicate *mpeg:mCherry+* cells that express cytoplasmic GFP. Data for 1 and 4 dpi is from N=2 independent experiments; n=19 and n=13 larvae imaged, respectively. Data from 2 and 3 dpi is from N=1 independent experiment; n=12 and n=9 larvae imaged, respectively. All images are maximum projections, with the exception of 3dpi (C), which is a single z-stack in order to identify the potential double positive cell amongst the somite background fluorescence. Scale bar = 50 μm.

The macrophage anti-inflammatory phenotype is very heterogeneous, with different stimulus (e.g. IL-4, TGF-β) resulting in different M2 polarised phenotypes (e.g. M2a-d) (Ferrante and Leibovich, 2012). Therefore, I next asked whether a different stimulus was required to induce macrophage *ccn1l1:eGFP* expression. *Ex vivo* carp monocytes upregulated *ccn1l1* following M2 polarisation with cAMP, thus *mpeg:mCherry+ ccn1l1:eGFP+* larvae were pre-treated for 4 hours with cAMP (or sterile water as a vehicle control) prior to a sterile tail fin transection at 2 dpf and imaged at 1 to 3 days post-amputation (dpA). Treatment with cAMP did not upregulate *ccn1l1:eGFP* expression in *mpeg:mCherry+* cells at the tail fin wound at any of the timepoints, including at the regeneration stages (up to 3 dpA; **Fig. 6.13. A-C**).

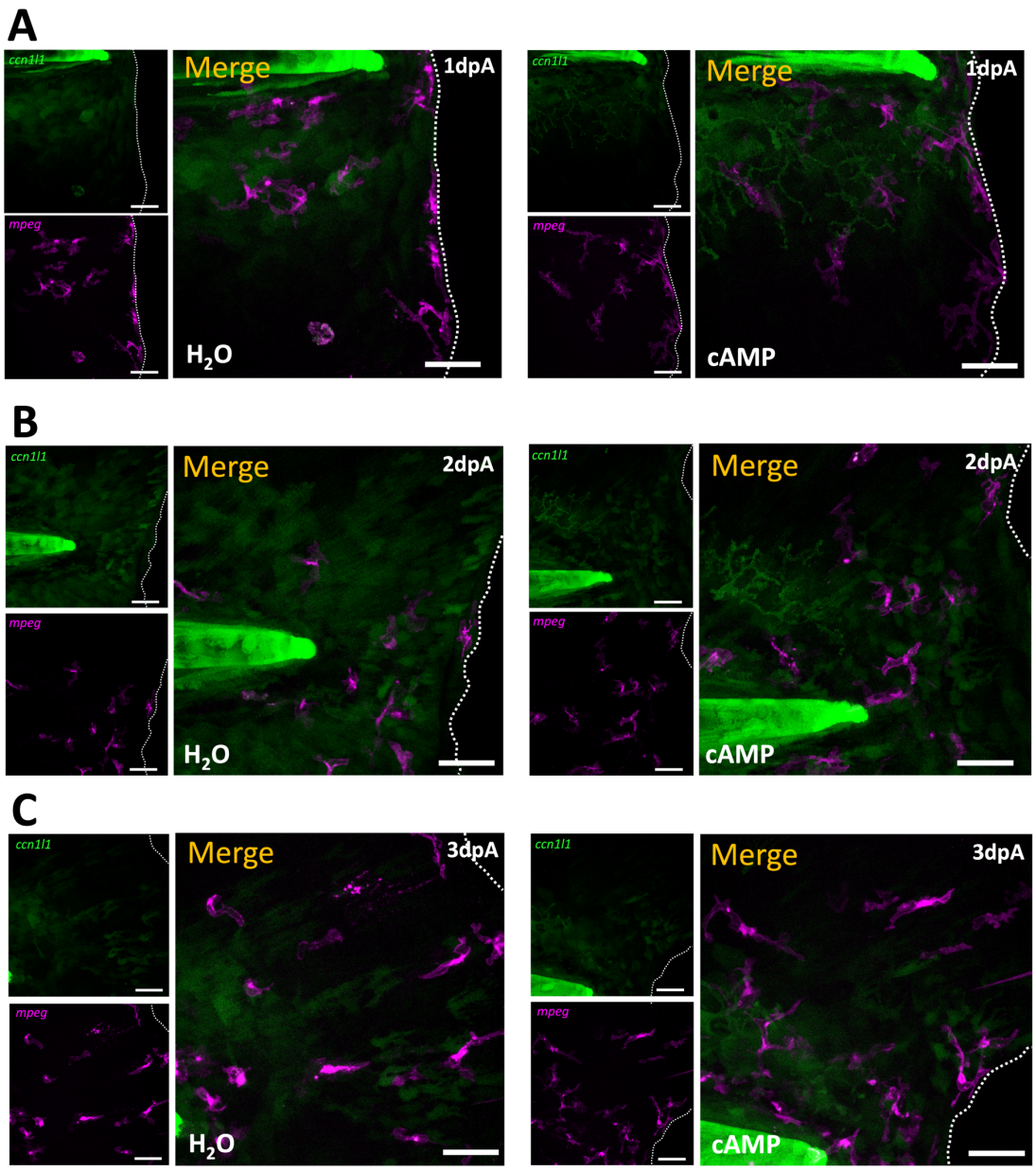


Figure 6.13. Macrophages do not express *ccn1l1:eGFP* following pre-treatment with cAMP and tail fin transection. (**A-C**) Representative confocal images of *mpeg:mCherry+ ccn1l1:eGFP+* larvae at 1-3 dpA following pre-treatment with cAMP or sterile water as a vehicle control. All images were taken from a 40x field of view at the tail fin wound. The dashed-dotted line indicated the edge of the tail fin wound edge. Embryos in (**A**) and (**B**)

were injured at 3 dpf. Embryos in (**C**) were injured at 2 dpf. N=1 independent experiment; n=4-5 larvae imaged per experimental condition. All images are maximum projections. Scale bar = 50 μm.

Together this data suggests that the *ccn1l1:eGFP* transgenic line is not a reliable reporter for anti-inflammatory macrophages during infection and inflammation challenge, at least not during the larval stages. Nevertheless, the *ccn1l1:eGFP* line remains a useful tool for other researchers examining larval development of the inner ear.

To conclude, the novel *arg2:GFP* transgenic line developed by our group remains the most promising *in vivo* for anti-inflammatory macrophages in zebrafish larvae. Whilst the *ccn1l1:eGFP* transgenic line did not result in macrophage expression during immune challenge, if validated (e.g. through the generation of new transgenic lines), the candidate genes identified from human MDMs, particularly *ctsz*, may robustly label anti-inflammatory macrophages in the larval zebrafish model.

6.3. Discussion

Mtb is characterised by its ability to exploit macrophages to evade pathogen clearance, reprogramming this innate immune cell towards a more anti-inflammatory, and consequently less antimicrobial, phenotype (Asrat et al., 2014; El Kasmi et al., 2008; Gao et al., 2004; Levitte et al., 2016). However, until recently there have been limited tools and no transgenic line to directly study anti-inflammatory immune signalling *in vivo*, with most previous work relying on analysis of cell morphology and dynamics of *tnfa:GFP*- macrophages (Sipka et al., 2022; Nguyen-Chi et al., 2015). This chapter explores the potential of several candidate genes that could be used to develop zebrafish transgenic reporter lines for anti-inflammatory macrophages, which, alongside pro-inflammatory macrophage reporters (e.g. *tnfa:GFP*), would be an invaluable tool to investigate macrophage phenotype *in vivo* (Wiegertjes et al., 2016; Nguyen-Chi et al., 2015; Marjoram et al., 2015). Furthermore, generation of successful transgenic lines to visualise leukocyte anti-inflammatory signalling enables interrogation of how mycobacteria is able to interact with host macrophages in *in vivo* microenvironments (Nguyen-Chi et al., 2017; Ogryzko et al., 2019).

Through comparison of up to 100 KEGG pathways formed from upregulated genes in resting larval zebrafish and human macrophage RNAseq datasets, this thesis identified that they transcriptionally most closely resemble human monocytes. The current dogma is that immune challenge, such as infection, causes mass recruitment of circulating monocytes to infected tissues, where they differentiate into macrophages and polarise according to local signals (e.g. cytokines) (Boulakirba et al., 2018; Iijima et al., 2011; Alexander et al., 2019; Chaintreuil et al., 2023). However, it is unclear whether infiltrating monocytes/monocyte-derived macrophages arrive at infection sites in their naïve (M0) state *in vivo*, polarising towards either phenotype (M1- or M2-like) locally, or whether they arrive polarised at the tissue (Alhamdi et al., 2019; Arnold et al., 2007). Thus, understanding the resting state of larval zebrafish macrophages could aid in our understanding of macrophage phenotypes and their recruitment during infection.

Evidence of Ccr2+ putative monocytes have been described in zebrafish larvae, yet the transgenic tools we currently have available (e.g. *mpeg:mCherry*) fail to definitively differentiate between monocytes, monocyte-derived macrophages and tissue-resident macrophages (Speirs et al., 2024; Mathias et al., 2009; Nguyen-Chi et al., 2015; Deng et al., 2022; Cambier et al., 2014b; Cambier et al., 2017). However, although the enriched KEGG pathways suggest that zebrafish macrophages are more similar to human monocytes, this assumes that human and zebrafish mononuclear phagocyte populations (MNPs) are entirely functionally comparable. How human MNPs function may not translate to zebrafish systems, with several studies attempting to define these MNPs with the tools available. Morales and Allende identified that tissue-resident *mpeg*+ cells located in peripheral tissues, not in the caudal haematopoietic tissue (CHT) migrated faster both during homeostasis and to the site of injury

following tailfin amputation (Morales and Allende, 2019). Tissue-resident macrophages (*csf1ra*+) were also found to proliferate rapidly in an adult zebrafish heart injury model, with only low levels of *ccr2* detected via RT-PCR (Moyse et al., 2024). However, the rapid expansion of the macrophage population cannot solely account for the proliferation of *csf1ra*+ macrophages, perhaps suggesting recruitment of a population of cells hypothesised to be monocytes (Moyse and Richardson, 2020; Moyse et al., 2024). These observations contrast with mammalian systems, which usually sees vast recruitment of circulating monocytes to injured tissues that differentiate into responding macrophages (Villar et al., 2023; Weinberger et al., 2024; Liao et al., 2018). Therefore, whilst the similarities between the biological networks associated with human monocytes and larval macrophages upregulated genes provides insight into how we must interpret published and future studies, current literature also emphasises how much is yet needed to delineate zebrafish monocytes/macrophages.

Larval zebrafish macrophages were identified as being transcriptionally most similar to M2a polarised PBMCs when comparing KEGG pathways, with IL-4/STAT6 pathway genes being upregulated. Mammalian macrophage morphology has often been associated with their activation status *in vitro*, but whether these map to adult and larval zebrafish macrophages remains unclear. M2a polarised mouse macrophages (with IL-4/IL-13) are often described as being narrow and elongated (Hourani et al., 2023; McWhorter et al., 2013). Yet electron microscopy on sections of adult zebrafish head kidney and spleen, demonstrated that zebrafish macrophages were large, and although heterogenous in shape, appeared more rounded than elongated (Lieschke et al., 2001). A population of *cd45:DsRed+; mhc2dab:GFP+* cells isolated from adult transgenic zebrafish were also described as having macrophage characteristics, including predominantly having a rounded morphology (Wittamer et al., 2011). Similarly, cytological staining of larval zebrafish blood cells isolated from the posterior blood island were also identified as being large and rounded (Bertrand et al., 2007). However, although macrophage morphology changes depending on the polarising agents they are exposed to *in vitro*, descriptions of these morphologies varies substantially in the literature. It is widely accepted that M0 macrophages exhibit a mix of circular and fusiform shapes, but despite many reports of M2a (IL-4) polarised macrophages having elongated morphologies, there are also reports of M2a macrophages being circular (Vogel et al., 2014; Mondadori et al., 2023; Smith et al., 2025; Hourani et al., 2023). Macrophage morphology following exposure to polarising agents has been demonstrated to vary depending on the cell culture used, with differences observed between immortalised BMDMs (iBMDMs) and two murine tumour cells lines (RAW264.7 and LLC), as well as differences reported depending on which culture media was used to mature macrophages (NHS vs. M-CSF vs. GM-CSF) (Xie et al., 2024; Vogel et al., 2014). Collectively, this highlights the variability of observations between research groups and emphasises the challenge of mapping resting zebrafish macrophage morphology to the morphology of *in vitro* polarised macrophages.

The development of zebrafish transgenic reporters such as *tnfa:GFP* has enabled characterisation of the molecular signature of *tnfa*+ macrophages, providing convincing evidence for the presence of pro-inflammatory macrophage populations, but whether larval macrophages polarise on a spectrum from M0 (resting) to M2 (anti-inflammatory) akin to *in vitro* mammalian studies is poorly understood (Speirs et al., 2024; Nguyen-Chi et al., 2015; Rougeot et al., 2019). Gene set enrichment analysis of larval zebrafish macrophage RNAseq showed a preference for M2-enriched genes when compared to polarised PBMCs, although this enrichment was not significant (Rougeot et al., 2019). Interestingly, mammalian tissue-resident macrophages, including alveolar macrophages and airspace macrophages, are enriched in M2-associated genes (e.g. *Tgfb1, Mrc1*), supporting the view that resting larval macrophages are more likely to be M2-like than M0 (Misharin et al., 2017; Mould et al., 2019). Genes associated with the IL-4/STAT6 molecular pathway were also found to be upregulated alongside other M2-associated genes (e.g. *il10 mrc1a/b*), providing some insight into the potential molecular mechanism governing this M2a genetic network. Macrophages also had elevated transcripts of M1-associated genes (e.g. *ifng1-2, il12bb*, *il12a*) suggesting that they have the machinery to respond with a pro-inflammatory phenotype during immune challenge, but that during resting states there may be a transcriptional block, for example STAT6-mediated STAT1 suppression (Ohmori and Hamilton, 2000). Presence of both M1-like and M2-like markers have also been identified simultaneously in carotid plaques from stroke patients, with the largest population of macrophages being double-positive (CD86+ MRC1+) following immunofluorescence stain (Kocsy et al., 2024). This finding supports the hypothesis that macrophages may have the machinery to polarise towards M1 or M2 under the correct stimulus, rather than separate populations being primed to be either M1- or M2-like. Additionally, qPCR analysis of pro-inflammatory cytokines in an *il10* zebrafish mutant resulted in a significant increase in macrophage *tnfa* mRNA in response to poly I:C treatment following a tailfin amputation (Bottiglione, 2020). This study supports the hypothesis that steady state zebrafish macrophages are M2-like, as IL-10-mediated transcriptional repression of pro-inflammatory genes, such as *tnfa,* are lost in the *il10-/-* mutant (Bottiglione, 2020; Castellucci et al., 2015). Furthermore, IL4R/STAT6 signalling was found to be pivotal for the development of M2-like epithelioid macrophages during necrotic granuloma formation in the zebrafish-*Mm* model, highlighting how immune challenge amplifies this signalling axis (Cronan et al., 2021). Taken together, this points at resting larval macrophages having the transcriptional machinery to respond to stimuli, whilst their resting state transcriptionally resembling human M2a polarised macrophages. However, our understanding of their resting state is still in its infancy, thus as new tools become available to characterise MNPs/macrophages and interrogate their steady state phenotype, a clearer picture may emerge.

Here, I have identified three candidate anti-inflammatory macrophage marker genes (*OCSTAMP, CTSZ* and *NCCRP1*) from M2 polarised human monocyte-derived macrophages (MDMs) that have zebrafish orthologues that share a high degree of homology. If these genes are validated as being

specific for anti-inflammatory macrophages in zebrafish, they have the potential to demonstrate translational impact. Generation of transgenic zebrafish lines to visualise these anti-inflammatory macrophages *in vivo* during immune challenge and following genetic manipulation (e.g. CRISRP-Cas9 mutagenesis) may result in findings that could directly translate to human systems, by-passing the need for murine experiments. Under resting conditions, *osteoclast stimulatory transmembrane protein* (*ocstamp*) expression is undetected in haematopoietic populations, including macrophages, in zebrafish larvae. Yet this gene was pursued further due to the elevated transcript levels only identified in *Mm*-infected larval macrophages, suggesting the potential for it to be a specific marker for anti-inflammatory macrophages in zebrafish. Overexpression of *OCSTAMP* has been found to suppress M1 polarisation in RAW264.7 cell culture, and whilst osteoclasts are a bone marrow-resident cells with phagocytic activity, they are derived from the macrophage lineage (Yuan et al., 2017; Lee et al., 2021). Upregulation of *Ocstamp* was also identified in isolated alveolar macrophages from BALB/c mice following infection with *Cryptococcus neoformans*, a fungal pathogen well known to modulate macrophages towards and M2-like phenotype to promote its survival (Hansakon et al., 2022; Hansakon et al., 2021). In contrast, a recent study using a mouse model of silicosis found that siRNA inhibition of *Ocstamp* resulted in increased M2 markers in alveolar macrophages (CD86, MHCII), suggesting that *Ocstamp* enhances M1 polarisation (Wu et al., 2025). Whilst the pro-inflammatory macrophage response to silica is well documented, silicosis is also associated with reduced bone density, in some cases resulting in osteoporosis (Tsugita et al., 2017; Liu et al., 2021; Hui et al., 2018). Thus, it is likely the presence M1-like macrophages that contribute to lung tissue fibrosis and elevated levels of a gene that promotes osteoclast differentiation for bone reabsorption occurs in tandem within the respiratory microenvironment, rather than as a consequence of each other, resulting in the pathological hallmarks of silicosis. Mature osteoclasts are only identified in juvenile zebrafish (approximately 20 dpf) and, like in humans, play a vital role in bone remodelling (Witten et al., 2001; Witten and Huysseune, 2010). Cells expressing osteoclast-associated genes (e.g. *mm9, ctsk*) have been identified in zebrafish larvae, but expression of a *ctsk* transgenic reporter was only induced following treatment with osteoclastogenic compounds (Sharif et al., 2014). Thus, as *ocstamp*, a key gene upregulated during osteoclast differentiation is not expressed in larvae and mature osteoclasts are not found, this gene has the potential to be a macrophage specific anti-inflammatory marker in our zebrafish larval model (Sharif et al., 2014; Witten and Huysseune, 2010; Yang et al., 2008).

Larval zebrafish expressed *cathepsin Z* (*ctsz*) in several haematopoietic populations, including macrophages, with elevated transcripts identified following *Mm* infection. Expression of *ctsz* was recently confirmed as being most highly expressed in inflammatory macrophages, with strong *in situ* hybridisation signal detected at the injury site of zebrafish larvae at 24 hours post-tail fin amputation – a time-point by macrophages persist but neutrophils have migrated away (Bastos et al., In Press; Loynes et al., 2010). Cathepsin Z is cysteine proteases that plays a role in regulating immune responses,

including immune cell migration and adhesion (Szulc-Dąbrowska et al., 2020; Zavašnik-Bergant and Turk, 2007). *Ctsz* mRNA levels have been found to be elevated in murine M2-like tumour-associated macrophages (TAMs) and elevated expression levels were recently identified specifically in macrophages via immunofluorescence and single-cell analysis in human clear cell renal cell carcinoma tissue sections (Zhang et al., 2022; Cui et al., 2021). scRNAseq analysis of granulomas from *Mm*-infected zebrafish and *Mtb*-infected macaques also identified *CTSZ* to be most highly expressed in macrophages (Meade et al., 2025). Importantly, CTSZ protein was also found to co-localise with CD68+ macrophages in biopsied granulomas from TB patients, demonstrating that cathepsin Z expression is conserved across species following mycobacterial infection (Meade et al., 2025). Thais Bastos, a visiting PhD student, progressed Cathepsin Z to CRISPR-Cas9 studies in zebrafish. Following caudal fin amputation, *ctsz* crispant zebrafish larvae had increased numbers of pro-inflammatory macrophages (*tnfa:GFP+* macrophages) at the injury site at 24 hpA, a timepoint by which most *tnfa*+ macrophages dissipate for the later stages of the regeneration process in wild-type fish (Bastos et al., In Press). Interestingly, cathepsin transcript levels, including *CTSZ*, were found to be elevated in human *Mtb*-infected M1 polarised macrophages (Khan et al., 2022). This differs from the transcriptional profile of murine-derived *Mtb*-infected macrophages polarised towards M2 (IL-4/IL-13) (Khan et al., 2022; Roy et al., 2018). This may suggest differential control of *Mtb* between species, however a recent study using *Mtb*-infected *Ctsz*$^{-/-}$ mice found elevated levels of TNF-α and IL1-β, which correlated with increased bacterial burden (Meade et al., 2025). Furthermore, human *CTSZ* single nucleotide polymorphisms that were found to be associated with reduced TB severity also resulted in increased *CTSZ* expression following *in vitro Mtb* infection (Meade et al., 2025). Taken together, this points towards *ctsz* playing a role in regulating pro-inflammatory macrophages by promoting an anti-inflammatory phenotype to manage excess inflammation and promote survival. This suggests that not only may this gene be a useful candidate in our larval zebrafish model, but may also be translated to mammalian systems, including humans.

Macrophage transcript levels of *P1, F-box associated domain containing* (*nccrp1*) increased nearly 5-fold following *Mm* infection in larval zebrafish, presenting as an interesting candidate to identify anti-inflammatory macrophages. There are currently no studies which have examined the potential role of *NCCRP1* on macrophage phenotype, with human *NCCRP1* being associated with squamous epithelium containing tissues (Kallio et al., 2011). However, its orthologue in several fish species (e.g. zebrafish, Atlantic salmon, Nile tilapia, northern snakehead, yellow croaker) has been associated with non-specific cytotoxic cells (NCCs), particularly during infection challenge (Sun et al., 2024; Hu et al., 2024a; Jaso-Friedmann et al., 1997; Niu et al., 2020; Wu et al., 2021; Yao et al., 2024; Teng et al., 2023). However, Niu et al., (2020) found *nccrp1* to not be solely expressed in NCCs, with single-cell RNAseq (scRNAseq) identifying expression in macrophage populations of isolated poly I:C-treated head kidney-derived leukocytes from Nile tilapia (Niu et al., 2020). Despite the lack of

mammalian data on the function of *NCCRP1* in macrophage polarisation, the elevated transcript levels of *NCCRP1* in polarised human monocyte-derived macrophages suggests a potentially conserved role in modulating macrophage phenotype between human and fish species (Rougeot et al., 2019; Beyer et al., 2012). However, *NCCRP1* mRNA levels were also found to be elevated in human macrophages polarised with IFNγ+LPS, suggesting that perhaps *nccrp1* may be contributing towards a balanced immune response, rather than being a specific marker for anti-inflammatory macrophages (Baidžajevas et al., 2020).

A stable generation of the BAC *ccn1l1:GFP* was successfully generated, with bright and specific GFP expression in the otic vesicle, consistent with the publish ISH data available on ZFIN.org (Thisse and Thisse, 2004). However, macrophages did not upregulate *ccn1l1:GFP* expression following injury or infection challenge. A total of 53 embryos were imaged from 1 to 4 dpi, but only three examples of *ccn1l1*+ macrophages were identified. As *ccn1l1* was identified as a candidate gene due to being significantly upregulated in *ex vivo* carp macrophages polarised towards M2 with cAMP, it was explored whether cAMP treatment was the stimulus required to induce macrophage *ccn1l1:GFP* in zebrafish larvae (Wentzel et al., 2020). Despite treatment with cAMP and a tail fin amputation, no examples of *ccn1l1*+ macrophages were identified at three different timepoints following amputation. As carp underwent an extra round of genome duplication compared to zebrafish, with zebrafish having 25 chromosome pairs and carp having 50 pairs, it was hypothesised that perhaps the carp *ccn1l1* duplicates are differentially expressed (Xu et al., 2014; Howe et al., 2013). For example, zebrafish *sonic hedgehog* (*shh*) has duplicated copies, with *shha* being widely expressed in the visual system, musculature and somites, whilst *shhb* is more concentrated to the nervous system (Vauti et al., 2020; Wang et al., 2007). Thus, zebrafish *ccn1l1* was aligned to the carp orthologue encoded on chromosome 8 and chromosome 16, as if it only aligns with the sequence on the chromosome from which carp *ccn1l1* was not transcribed following polarisation, it may explain why there was minimal macrophage expression of *ccn1l1:GFP* in immune challenge. However, zebrafish *ccn1l1* sequence and protein alignments scores were high for each carp *ccn1l1* gene on both chromosomes, suggesting the lack of macrophage *ccn1l1:GFP* expression is not due to differential expression of carp *ccn1l1*. It is possible that the three macrophages identified as being *ccn1l1*+ were artifacts. Macrophages have been found to closely associat with zebrafish pigment cells such as xanthoblasts, as well as being efficient phagocytes that clear debris (Eom and Parichy, 2017). Thus, it is conceivable that what was actually captured were macrophages having phagocytosed, or being closed associated with, light-reflecting iridophores pigment cells (Kelsh et al., 1996).

Zebrafish *ccn1l1* shares a high degree of homology with human and murine orthologues, yet mammalian *CCN1/Ccn1* is associated with pro-inflammatory macrophage responses. The role of *CCN1* in during in immune challenge is well described, with immune challenge upregulating its expression in

many tissues, including fibroblasts (Chen et al., 2001). Treatment of splenic macrophage cells lines with soluble CCN1 resulted in upregulation of many genes associated with the inflammatory responses, including TNF-α, IL-1β and IL-6 (Bai et al., 2010). Using both murine and human cell culture models, CCN1 was identified at being critical for host defence against infection, having a vital role in phagocytosis, bacterial killing and toll-like receptor activation (Jun and Lau, 2020). However, whilst macrophage CCN1 is associated with an inflammatory response, it also has an emerging role in inflammation resolution. Macrophage *Ccn1* was found to be vital for efferocytosis of apoptotic neutrophils, upregulation of *Tgfb1* expression following phagocytosis and play a critical role in wound healing (Kim et al., 2022; Jun et al., 2015). Additionally, recent work has found *ccn1l1* to be significantly upregulated (10.48 $\log_2$FC) at the time of macrophage recruitment (2 days post-injury) in a zebrafish ablation-regeneration model of retinal pigment epithelium (Lu et al., 2022). Taken together, it suggests that *ccn1l1* does not act as a marker for anti-inflammatory macrophages, but rather modulates the surrounding inflammatory response in order to promote inflammation resolution.

A key limitation of this chapter is that the three candidate genes identified through data mining (*ocstamp, nccrp1*, and *ctsz*) were not explored further to confirm their roles in macrophage biology due to time constraints. Ideally, follow-up experiments would include generating transgenic reporter lines to visualise their endogenous expression, for example by using novel knock-in reporter technologies, to assess their expression in leukocytes following immune challenge (Zhang et al., 2023). A visiting PhD student, Thais Bastos, investigated these genes using CRISPR/Cas9-mediated knockdown and assessed macrophage *tnfa:GFP* expression in the resulting crispants (Bastos et al., In Press). Only loss of *ctsz* resulted in an increased prevalence of putative pro-inflammatory macrophages at the wound site following tail fin transection. While these findings provide some convincing evidence that *ctsz* contributed to the modulation of anti-inflammatory macrophage populations – and may represent a useful marker for these cells – it is important to recognise that these genes are not macrophage-specific and likely perform functions in other cell types. For example, *ocstamp* is essential for pre-osteoclast fusion, and its manipulation would therefore be expected to impact bone remodelling processes (Witwicka et al., 2015).

The use of crispants also introduces additional caveats, as these animals are systemic mosaic mutants in which the extent and distribution of mutagenesis vary between cells and individual fish. A recent study using next-generation sequencing demonstrated that crispants can mimic stable knockout lines due to the high insertion/deletion efficiency achieved (Debaenst et al., 2025). However, although generating a stable knockout would eliminate mosaicism, such mutants may still exhibit genetic compensation for the loss of these proteins, complicating interpretation of phenotypic outcomes. For example, while *slc25a46* crispants display robust motoneuron defects in zebrafish, these disease-associated phenotypes are lost in stable mutants due to the upregulation of compensatory genes

(Buglo et al., 2020). Ideally, macrophage-specific deletion of these candidate genes would enable a more definitive assessment of their cell-autonomous roles in macrophage polarisation. However, achieving cell-type specific knockout in zebrafish remains considerably more challenging than in mammalian systems. In principle, several conditional knockout strategies have shown promise, but issues such as Cas9 promoter silencing and Cas9-associated toxicity currently limits their long-term effectiveness, demonstrating that the technology for targeted, cell-type specific gene disruption in zebrafish is still in its infancy (Ablain et al., 2015; Singh Angom et al., 2023; Shin et al., 2023; Ferreira et al., 2021).

To conclude, this chapter discusses several candidate anti-inflammatory macrophage marker genes that could be used as zebrafish reporter lines to examine macrophage phenotypes *in vivo*. Data mining from human and zebrafish RNAseq datasets identified three genes which could be pursued further. Although beyond the scope of this thesis, characterising macrophage expression of these genes following *Mm* infection may identify a potentially conserved role of these genes in anti-inflammatory macrophage signalling between zebrafish and humans. Despite *ccn1l1* being the most upregulated gene in *ex vivo* polarised carp macrophages, using a novel *ccn1l1:GFP* transgenic line (Wentzel et al., 2020), I showed that zebrafish macrophages did not upregulate *ccn1l1* following immune challenge. Furthermore, the *arg2:GFP* transgenic line remains the most promising existing reporter for labelling a population of anti-inflammatory macrophages *in vivo*.

7. General discussion

Macrophages are among the most plastic cells of the immune system, capable of adopting diverse activation states in response to changing microenvironmental conditions. Classical *in vitro* systems have often reduced this heterogeneity to an M1/M2 dichotomy, yet evidence from mammalian tissues, human pathology and omics datasets shows that macrophage activation is far more dynamic and context-dependent than this binary model suggests (Xue et al., 2014; Strizova et al., 2023; Takiguchi et al., 2021; Mackaness, 1962; Nathan et al., 1983). A major unresolved question in the field is pro-inflammatory macrophages can dynamically change their activation state to become anti-inflammatory, or whether the observed heterogeneity reflects the sequential recruitment of distinct macrophage subsets at different stages of immune challenge. Addressing this question requires temporal resolution that has been difficult to achieve in mammalian systems. In this thesis, I used the zebrafish larval model to provide real-time, *in vivo* evidence that pro-inflammatory macrophages can transition towards an anti-inflammatory state during mycobacterial infection (summarised in **Fig. 7.1**). Using the *tnfa:mCherry* reporter, I identified putative pro-inflammatory macrophages and tracked their behaviour relative to *arg2:GFP* expression, a reporter driven by an *arg2* promoter, a canonical anti-inflammatory macrophage marker *in vitro* (Hammond et al., 2023). During *Mm* infection, a subset of *tnfa:mCherry+* putative pro-inflammatory macrophages subsequently upregulated *arg2:GFP* and exhibited altered morphology and behaviour, consistent with a shift toward an anti-inflammatory phenotype. Supporting this phenotypic evidence, single-cell RNA sequencing (scRNAseq) of whole larvae indicates that *arg2+* macrophages show transcriptional features characteristic of M2-like states, with enrichment of anti-inflammatory genes. Through genetic manipulation of Hif signalling, I found that Hif-2α is partially required for pro-inflammatory macrophages to upregulate *arg2:GFP in vivo*. Furthermore, both genetic inhibition of arginase expression and pharmacological inhibition of arginase activity resulted in uncontrolled bacterial proliferation. Notably, pharmacological arginase inhibition was also associated with increased granuloma number, a higher proportion of large granulomas and enhanced bacterial dissemination, suggesting that macrophage arginase activity is required not only for limiting bacterial growth but also for shaping granuloma architecture and containment. These findings indicate that the transition toward an arginase-expressing macrophage state is likely host-protective. Collectively, this work directly addresses a central question in the field by demonstrating that individual macrophages can undergo a phenotypic switch *in vivo* and highlights macrophage polarisation pathways as promising targets for host-directed therapies (HDTs) for TB.

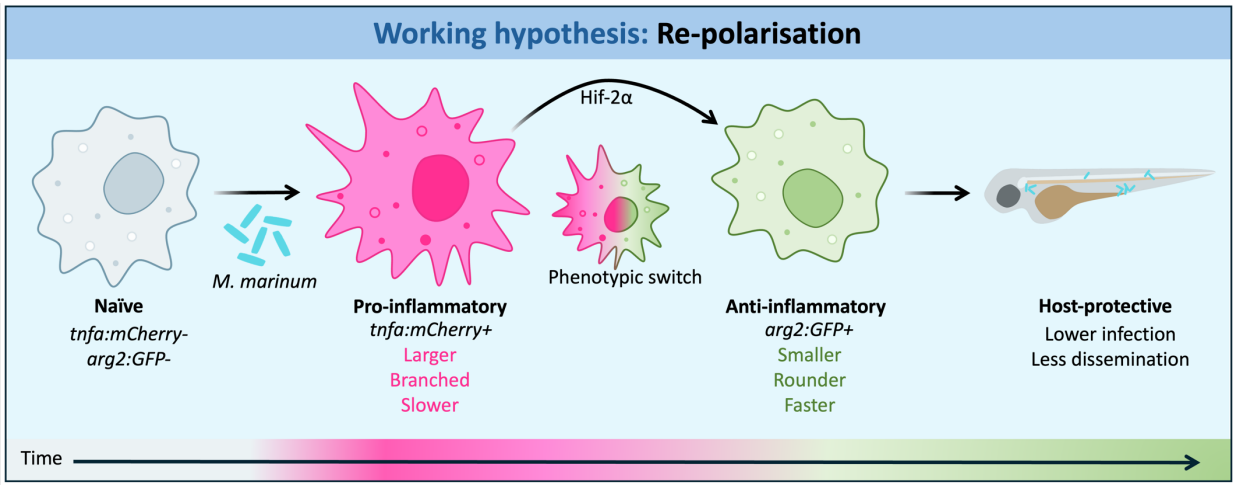


Figure 7.1. Pro-inflammatory macrophages undergo a phenotypic switch *in vivo*, and this change in phenotype is host-protective. Prior to infection, naïve macrophages do not express canonical pro- to anti-inflammatory macrophage reporters (*tnfa:mCherry* and *arg2:GFP,* respectively*). Mm* infection robustly induces expression of putative pro-inflammatory macrophages (*tnfa:mCherry+*). As *Mm* pathogenesis progresses, a subpopulation of *tnfa:mCherry+* cells undergo a phenotypic switch following upregulation of *arg2:GFP*, which is partially dependent on Hif-2α. These transitioned cells have a smaller perimeter, are more circular and have a higher speed than *arg2:GFP-* macrophages. Pharmacological and genetic disruption of host arginase leads to uncontrolled infection, characterised by increased bacterial burden, more granulomas, and greater dissemination, suggesting that this phenotypic switch is host-protective.

In the first instance, I found that a subset of macrophages upregulated *arg2:GFP* coinciding with the early formation of innate granuloma structures. These *arg2:GFP+* macrophages differed markedly from their *arg2:GFP-* counterparts: they were smaller, more circular, and moved with greater speed. Several studies, particularly those employing machine-learning approaches, have reported these consistent morphological differences between *in vitro* polarised macrophage subsets. For example, naïve human macrophages were described as large and irregular, M1 macrophages (IFNγ-stimulated) as smaller and elongated, and M2 macrophages (IL-4-stimulated) as much larger and flattened (Rostam et al., 2017). Using membrane-labelled RAW 264.7 macrophages, (Hourani et al., 2023) further subdivided these characteristics: M2a and M2d macrophages were elongated (with M2a being much narrower), M2b macrophages were flattened and granular, while M2c macrophages were smaller and rounded – a morphology strikingly similar to the *arg2:GFP+* phenotype observed in this thesis. However, the striking variability between studies likely reflects differences in cell lines, polarising stimuli, cell culture media, and imaging conditions, highlighting the limitations of extrapolating *in vitro* morphology to *in vivo* biology. Here, I demonstrate that putative pro-inflammatory macrophages can upregulate a canonical anti-inflammatory marker (*arg2*) while simultaneously undergoing co-ordinated morphological and behavioural changes. Supporting this phenotypic evidence, scRNAseq indicates that *arg2:GFP+* macrophages also exhibit a transcriptional landscape consistent with an anti-inflammatory state.

Together, these findings provide direct *in vivo* evidence of a pro- to anti-inflammatory transition within individual macrophages in living tissue.

My observations that *arg2:GFP+* macrophages emerge as innate granulomas begin to form – and that they display distinct morphological and behavioural features – raise the possibility that these cells are not only phenotypically anti-inflammatory but also transcriptionally skewed toward an anti-inflammatory state, as supported by the preliminary scRNAseq analyses showing enrichment of anti-inflammatory-associated gene expression, potentially contributing directly to early granuloma formation rather than functioning solely at later tissue-repair stages. While some *in vitro* models have suggested that only pro-inflammatory or M1-polarised macrophages form granuloma-like aggregates (Huang et al., 2015), these reductionist systems lack the cellular diversity and spatial cues present *in vivo*. Evidence from other granulomatous diseases supports a more nuanced interpretation: in murine sarcoidosis models, IL-13–driven M2 polarisation promotes macrophage aggregation through Mac-1–dependent mechanisms (Podolnikova et al., 2016; Cao et al., 2015) and work in the zebrafish-*Mm* system demonstrates that IL-4-dependent M2-like signalling is required for epithelialisation and organisation of early granuloma structures (Cronan et al., 2021). Consistent with these findings, the appearance of *arg2:GFP+* macrophages at the onset of innate granuloma formation in this thesis suggests that early transitions toward anti-inflammatory or epithelializing macrophage states may be integral to establishing granuloma architecture. If time and resources had permitted, this hypothesis could be tested by selectively ablating *arg2* in macrophages using novel CRISPR-based vector systems for zebrafish that are being trialled in Sheffield (e.g.: *mfap4:Cas9* and ubiquitous expression of guide RNAs targeting *arg2*) (Wang et al., 2021). Such an approach would enable assessment of whether loss of arginase specifically within macrophages disrupts granuloma initiation, epithelialisation or early structural organisation (Cronan et al., 2016; Cronan et al., 2021). Complementary staining for epithelial markers, such as E-cadherin, would further determine whether these early *arg2:GFP+* macrophages act as precursors to epithelioid macrophages during granuloma formation (Cronan et al., 2016; Cronan et al., 2021). Thus, rather than being restricted to later reparative phases, anti-inflammatory macrophage programmes may contribute to the initial structuring of granulomas *in vivo*; however, demonstrating this conclusively will require macrophage-specific perturbation of *arg2*, potentially in a conditional manner using heat-shock-inducible systems, to assess whether *arg2*-expressing macrophages are functionally required for stabilising early cellular networks that facilitate initial containment of mycobacterial growth (Singh et al., 2023).

In this thesis, macrophage morphology was quantified in 2D using maximum intensity projections of z-stacks, following established approaches for dynamics *in vivo* analysis (Sipka et al., 2022). While this method allows consistent comparison across time-lapse datasets, it inevitably collapses 3D cell shape into a 2D plane. As such, macrophages that appear small and round in

projection may possess greater volume or complex protrusions in 3D that are lost during projection. This limitation is further compounded by the fact that imaging was performed in relatively thick tissues (whole larvae), where macrophages are not polarised in a single orientation or constrained to a defined imaging plane; across the number of cells analysed, these differences in orientation likely averaged out fine-scale shape features that would otherwise distinguish activation states. This becomes particularly relevant in light of recent work demonstrating that manipulating macrophage volume itself can influence activation state: reducing the volume of resting and M1-polarised murine macrophages using polyethylene glycol promoted a shift toward an anti-inflammatory transcriptional programme (Yang et al., 2024). These observations suggests that cell size and 3D morphology are not merely descriptive features but may actively contribute to macrophage functional states. Consequently, the current analysis may underestimate the structural diversity of *arg2:GFP+* macrophages. Importantly, the timelapse imaging datasets generated in this thesis provide a foundation for future re-analysis using higher-end computational pipelines capable of full 3D volumetric segmentation and shape quantification. Such approaches could reveal volumetric, surface or spatial features that further define anti-inflammatory programming *in vivo*.

As a consequence of these complexities in morphological analysis, most *in vivo* or *ex vivo* assessment of macrophage phenotype depend on marker expression rather than morphology, using immunostaining or cytometry to assign macrophages to canonical M1- or M2-like states (Jameson et al., 2022; McKinnon, 2018). Even where morphology has been quantified, interpretations are complicated. For example, CD163+ tumour associated-macrophages (TAMs) in colorectal liver metastasis were larger and more highly branched than macrophages in healthy tissue (Donadon et al., 2020). Yet despite TAMs traditionally being associated with M2-like phenotypes, they encompass both M1- and M2-like programmes and represent a distinct pathological macrophage population (Pan et al., 2020; Franklin et al., 2014). In an *ex vivo* mouse spinal cord injury model, IL-10 treatment increased Arg1+ macrophages, which displayed a significantly rounder morphology, consistent with the *arg2:GFP+* morphological profile in this work (Margul et al., 2016). The degree to which such *ex vivo* murine studies can be generalised to human macrophage biology remains uncertain. Recent label-free imaging platforms attempt to predict macrophage activation states directly within intact tissues, yet this field remains in its infancy. For example, two-photon excited fluorescence lifetime imaging (FLIM) distinguished M1 and M2 macrophages in human dermis, but classification relied on signatures derived from *in vitro* polarised murine PBMCs, again raising questions of translational fidelity (Kröger et al., 2022). Taken together, the existing literature underscores the difficulty of defining macrophage subtypes *in vivo* using morphology alone. Despite this uncertainty, the findings presented in this thesis add *in vivo* evidence that upregulation of a canonical anti-inflammatory macrophage marker (*arg2*) correlates with co-ordinated changes in cell shape and behaviour, and is accompanied by a transcriptional landscape that appears skewed towards an anti-inflammatory profile. Together, these

observations represent an important step towards understanding how anti-inflammatory programmes manifest at the functional and morphological level within living tissues – something that has been inferred primarily from *in vitro* systems but seldom demonstrated *in vivo*.

Having identified that *arg2:GFP+* macrophages morphologically, behaviourally and transcriptionally resemble *in vitro* and *ex vivo* murine anti-inflammatory macrophages, I investigated whether these cells are distinct from pro-inflammatory macrophages, or whether they arise from *tnfa:mCherry*+ macrophages. Much of our understanding of macrophage polarisation dynamics is derived from fixed tissues, transcriptomic analyses, or blood samples – typically from humans, non-human primates (NHP) or mice – which offer only static snapshots of highly dynamic processes. In a wide range of human pathologies, including atherosclerotic plaques, rheumatoid synovium, and chronic liver disease, macrophages frequently co-express canonical M1 and M2 markers, suggesting either stable hybrid states or cells caught mid-transition (Kocsy et al., 2025; Ramachandran et al., 2019; Tardito et al., 2019; Fernández-Regueras et al., 2023). Similar patterns emerge in non-infectious injury models: after myocardial infarction or spinal cord injury, murine macrophages often exhibit mixed transcriptional profiles consistent with broad activation continuums rather than discrete states (Dick et al., 2019; Stapenhorst França and Gensel, 2025). In infectious settings, including NHP and human TB granulomas, co-localisation of iNOS and Arg1, or HLA-DR and Arg1, is frequently interpreted as evidence of macrophage reprogramming, yet these observations cannot distinguish true sequential repolarisation from the coexistence of multiple recruited subsets (Mattila et al., 2013; Ashenafi et al., 2022). The absence of temporal resolution has therefore forced the field to rely heavily on inference. Computational models of macrophage behaviour – ranging from continuum-based descriptions of phenotype space to agent-based simulations – consistently predict that successful immune responses require continuous transitions between activation states rather than fixed, mutually exclusive phenotypes (Cilfone et al., 2013; Almansour et al., 2024). Similarly, murine *in vivo* studies have demonstrated that macrophages can adopt M1- or M2-like programmes when exposed to phenotype-shifting cues during injury or infection. For example, mesenchymal stem cell-derived and M2 macrophage-derived exosomes have been shown to promote an anti-inflammatory macrophage phenotype in rodents, ameliorating acute pancreatitis and improving cutaneous wound closure (Li et al., 2024; Kim et al., 2019; Kallemeijn et al., 2023). However, confirming that the same individual cell undergoes this transition, rather than shifts in population composition arising from recruitment of M1- or M2-like macrophages, still requires euthanasia and end-point tissue analysis. Consequently, although macrophage ‘re-polarisation’ is widely proposed, direct visualisation of this process has remained elusive across mammalian systems. This broader context highlights the significance of the findings in this thesis: using real-time *in vivo* imaging in zebrafish, I show that individual *tnfa:mCherry+* macrophages can subsequently upregulate *arg2:GFP* and acquire morphological and behavioural features consistent with anti-inflammatory macrophages within the infected tissue microenvironment.

These data provide direct, cell-resolved evidence that macrophage phenotype switching occurs *in vivo*, complementing and extending observations from human, NHP, and murine studies where such transitions have largely been inferred rather than observed.

Blocking the pro- to anti-inflammatory transition – either by preventing macrophage *arg2:GFP* induction through Hif-2α genetic inhibition or by pharmacologically inhibiting macrophage arginase activity – is host-detrimental in the zebrafish-*Mm* model. Importantly, pharmacological disruption of macrophage arginase activity not only impaired bacterial control but was also associated with increased numbers of granulomas, enlargement of granulomatous lesions and enhanced bacterial dissemination, indicating a failure to properly organise and contain infection. This raises an important question: is arginase induction fundamentally host-protective, or is it solely a pathway that mycobacteria exploit to subvert macrophage microbicidal function? Arginase converts L-arginine into ornithine, which feeds polyamine and proline biosynthesis; these metabolites support cell proliferation, extracellular-matrix remodelling and collagen deposition, and thereby promote repair of damaged tissue (Caldwell et al., 2015; Novak and Koh, 2013). Arginase-dependent polyamine generation has also been linked directly to *arg2* induction in zebrafish, with increased polyamine levels accompanying arginase upregulation (Banerjee et al., 2021). Experimental work in a murine *Pseudomonas aeruginosa*-induced lung inflammation model has shown that myeloid Arg1 limits excessive immunopathology rather than directly reducing pathogen load, highlighting a model in which arginase-expressing macrophages act as 'damage controllers' that allow inflammatory effector cells, such as pro-inflammatory macrophages and lymphocytes, to function without destroying the surrounding tissue (Haydar et al., 2021; Schleicher et al., 2016). Consistent with this model, macrophage-specific deletion of Arg1 *Mtb*-infected mice results in increased granuloma number, enlarged and more necrotic granulomas, and worsened disease outcomes, demonstrating that macrophage arginase activity is required for proper granuloma organisation and tissue protection (Duque-Correa et al., 2014). Downstream arginase products can also feedback on macrophage phenotype: IL-4–induced polyamine production via the Arg1–ornithine decarboxylase axis enhances E-cadherin expression and homotypic interactions in alternatively activated macrophages, providing a mechanistic link between arginase activity, cell-cell interactions, and maintenance of an M2-like programme (Van den Bossche et al., 2009). Within this framework, the finding that disrupting arginase-dependent switching in zebrafish leads to uncontrolled mycobacterial proliferation is consistent with arginase functioning as an active regulator of inflammatory tone and tissue protection, rather than simply a passive marker of anti-inflammatory macrophage polarisation. However, this does not exclude the possibility that *Mtb* exploits arginase induction to suppress macrophage microbicidal activity, particularly because arginase is widely thought to compete with iNOS, thereby limiting NO production (Rath et al., 2014). Disentangling host-protective from pathogen-driven arginase functions will require experiments that selectively disrupt specific branches of the arginase pathway – for example, by blocking downstream polyamine synthesis (e.g.: spermidine)

without removing arginase itself (Robertson et al., 2020; Frohnhöfer et al., 2016; Jeong et al., 2018). Such experiments would aid in elucidating whether arginase solely supports bacterial survival by suppressing macrophage killing or whether its primary role is to maintain a tissue environment compatible with sustained host control.

Evidence from diverse injury and infection models supports this view across species – that arginase is not merely a marker of anti-inflammatory macrophages, but an active regulator of macrophage function, repair and inflammatory tone. In helminth infection, arginase activity contributes directly to host defence. For example, during *Nippostrongylus brasiliensis* infection, Arg1 expression is markedly elevated in macrophages and epithelial cells, and this rise in arginase activity is host-protective: depletion of L-arginine limits nematode survival, revealing a mechanism in which arginase-dependent substrate consumption restricts parasite growth (Chen et al., 2022). Complementary work in other helminth models demonstrates that Arg1+ macrophages help modulate Th2-mediated inflammation and regulate tissue remodelling, whereas disruption of arginase activity leads to prolonged inflammation, impaired repair and worsened tissue architecture (e.g.: *Schistosoma mansoni*, *Heligmosomoides polygyrus*) – supporting a conserved role for arginase in orchestrating both parasite control and tissue protection (Pesce et al., 2009; Esser-von Bieren et al., 2013). Across sterile injury settings, arginase-driven polyamine and proline pathways further regulate leukocyte recruitment, matrix remodelling and resolution, placing arginase-expressing macrophages in a distinct pro-healing niche rather than simply representing absence of M1 signalling (Haydar et al., 2021). Conversely, several pathogens exploit aspects of this transition: *Salmonella enterica* and *Brucella abortus* induce macrophage states characterised by immunoregulatory and metabolic rewiring even when arginase is not the primary pathway analysed (Pham et al., 2020; Wang et al., 2022). Taken together, these examples support a model in which shifts from pro- to anti-inflammatory macrophage states, and the accompanying arginase-dependent metabolic reprogramming, can be either host-protective or pathogen-exploited depending on timing and context.

In the context of mycobacterial infection, optimal outcomes likely require a temporally coordinated sequence. Early in infection, an iNOS–TNF–HIF-1α–dominated programme is essential for restricting mycobacterial growth (Li et al., 2024). Nitric oxide (NO) itself, however, functions not only as a bactericidal molecule but also as a metabolic and transcriptional signal. In macrophages, NO stabilises HIF-1α, modulates glycolytic flux, and shapes central TCA-cycle metabolites – including succinate, citrate, and the immunoregulatory metabolite itaconate – which collectively reinforce pro-inflammatory activation (Bailey et al., 2019; Braverman and Stanley, 2017; Baseler et al., 2016). These observations from murine and human macrophages emphasise that M1 activation is a metabolically integrated state, not merely the presence of NOS2. As infection progresses, however, a sustained NO-high inflammatory state becomes damaging: excessive nitrosative stress contributes to necrosis,

cavitation and bacterial dissemination (Krueger et al., 2025). At this stage, anti-inflammatory and tissue-protective pathways, including arginase upregulation, become increasingly important. In mycobacterial infection, arginase-expressing macrophages have been shown across systems to mediate immunomodulatory and pro-repair functions. For example, in *Mtb*-infected mice, *Arg1*+ macrophages were required to limit neutrophil and T-cell-driven lung pathology (Nandi and Behar, 2011; Duque-Correa et al., 2014). In human macrophage models, arginase-dependent metabolic rewiring (polyamines, proline) has been shown to dampen inflammatory signalling and promote cytoskeletal remodelling and resolution-phase behaviour (Zhang et al., 2020; Fitzsimons et al., 2023). These findings align closely with the zebrafish data presented in this thesis: inhibiting macrophage arginase activity or preventing *arg2* induction resulted in uncontrolled *Mm* expansion, with increased granuloma burden, larger granulomatous structures, and enhanced dissemination, supporting a model in which arginase-dependent macrophage programmes are required for both bacterial containment and granuloma organisation. Together, this suggests that the pro- to anti-inflammatory macrophage transition observed *in vivo* is not merely a phenotypic marker of resolution, but likely reflects an arginase-dependent state that is host-protective within the complex tissue microenvironment of mycobacterial infection.

Although this thesis identified an *arg2*-expressing macrophage population that clearly emerges during early infection and contributes to host defence, an important limitation is that *arg2* likely marks only a subset of anti-inflammatory macrophage states rather than the full spectrum of anti-inflammatory programmes. Evidence from mammalian systems show that M2 phenotypes are highly heterogenous, with distinct transcriptional, metabolic and functional modules that do not uniformly require arginase activity (Rőszer, 2015). For example, in murine allergic and Th2-driven lung inflammation models, conditional deletion of Arg1 in myeloid cells failed to alter lung inflammation, airway hyperresponsiveness, or lung mechanics, suggesting that Arg1 is not strictly necessary for resolution of certain inflammatory processes (Barron et al., 2013). Likewise, stable overexpression of human *ARG1* in THP-1 macrophages did not suppress inflammatory activation or inhibit M1-polarisation, indicating that arginase activity alone is not sufficient to impose an anti-inflammatory programme in all macrophage lineages (Walvekar et al., 2025). Together, these findings highlight that arginase upregulation represents only one module within a broader landscape of M2-associated pathways, many of which operate independently of arginase. In this context, the *arg2:GFP* reporter used here likely captures only one 'flavour' of anti-inflammatory macrophages, while missing others with alternative regulatory or metabolic specialisations. This limitation affects how my data should be interpreted: although I demonstrate that a putative pro- to anti-inflammatory transition coinciding with *arg2:GFP* upregulation, I cannot conclude that all anti-inflammatory macrophages follow this trajectory, nor that arginase defines the predominant regulatory programme *in vivo*. Addressing this will require moving beyond the larval stages used here. Adult zebrafish, which develop fully mature granulomas

and show strong evidence of type 2 signalling, provide an opportunity to test how *arg2*-expressing macrophages behave during chronic infection (Cronan et al., 2021). Specifically, examining whether the *arg2*+ population expands within mature granulomas would help determine whether *arg2:GFP+* cells represent a stable anti-inflammatory macrophage subset, whereas spatial restriction or loss of *arg2* expression at later stages would suggest that *arg2* marks only an early, transitional state. Parallel development of new transgenic reporters, such as those marking *grna.2+* macrophages identified in adult *Mm* granulomas, may allow simultaneous visualisation of multiple regulatory macrophage states *in vivo* (Luo et al., 2025). Integrating these reporters with high-resolution imaging and immunostaining of adult granulomas would provide a more comprehensive mapping of anti-inflammatory macrophage heterogeneity and help define how *arg2* fits within the wider regulatory landscape of macrophage polarisation during mycobacterial infection.

From a translational standpoint, the complexity described above – namely the heterogeneity of anti-inflammatory macrophages, that arginase likely marks only one subset of these states and the evidence that M2-associated functions can occur independently of arginase – has important implications. Therapies aimed solely at boosting arginase activity may be ineffective and, in some contexts, may even be harmful, because macrophage phenotype switching is not driven by arginase alone but by co-ordinated metabolic, transcriptional and signalling networks. Effective HDTs will therefore need to target macrophage re-programming as a whole, guiding cells toward functional states that integrate anti-inflammatory, matrix-remodelling and immunoregulatory roles while preserving enough antimicrobial capacity to contain pathogens. This broader perspective is consistent with the heterogeneity observed across human, NHP and rodent tissues, where macrophages rarely exist as distinct M1 or M2 subsets but instead distribute across mixed, transitional, or hybrid phenotypes. Within this framework, the findings of this thesis – that Hif-2α signalling promotes *arg2* upregulation *in vivo*, and that disruption of this pathway is host-detrimental – should be viewed as part of a wider network of macrophage functional programming. Importantly, HIF-2α is already a clinically druggable pathway: selective HIF-2 inhibitors (e.g.: belzutifan) are licenced for renal cell carcinoma and have demonstrated acceptable safety profiles in humans (Fallah et al., 2024). This establishes HIF-2 as a tractable therapeutic axis and raises the possibility that carefully tuned modulation of HIF-2 activity could be repurposed for immunomodulation in TB. However, given the multi-dimensional nature of macrophage phenotype switching, HIF-2-directed interventions will need to be evaluated not in isolation, but in the context of broader transcriptional and metabolic programmes that shape macrophage state *in vivo*.

At the same time, these results highlight the limitations of relying on a single reporter line, such as *arg2:GFP*, to define anti-inflammatory macrophages *in vivo*. While *arg2* marks an important subset, other anti-inflammatory programmes, such as granulin-expressing macrophages required for

inflammatory control in zebrafish *Mm* granulomas or the conserved cathepsin z (*ctsz*) signature identified in chapter 6 (Bastos et al., In Press), may operate independently of arginase (Luo et al., 2025). Developing additional *in vivo* reporters for these potentially anti-inflammatory pathways will be essential for dissecting macrophage state dynamics and for screening pharmacological compounds that modulate them. In this context, future HDT discovery will benefit from multiparameter macrophage reporter systems capable of capturing the diverse molecular routes through which macrophages adopt healing or immunoregulatory identities. Integrating such tools with real-time imaging approaches, such as those used in this thesis, will be a critical step towards manipulating macrophage plasticity in disease.

There are some important limitations associated with the findings in this thesis. First, the characterisation of *arg2:GFP+* macrophages was based primarily on behavioural and morphological analysis. Although these phenotypic features are consistent with *in vitro* and *ex vivo* descriptions of anti-inflammatory macrophages, I cannot yet conclusively define *arg2:GFP+* macrophages as M2-like *in vivo*, nor define where they sit along the broader activation spectrum. A key technical bottleneck is that FACS purifying *arg2:GFP+* macrophages is challenging: in larvae, macrophage *arg2:GFP* signal is much dimmer than that of ionocytes and neutrophils, making it very difficult to sort. To address this limitation, we used scRNAseq on whole larvae under defined experimental conditions (e.g.: HIF pathway modulation and *Mm* infection), to bioinformatically isolate *arg2*-expressing macrophages. While this approach represents a necessary shift towards an omics-level characterisation, the resulting dataset is currently underpowered and remains preliminary. These data offer suggestive trends, with enrichment of anti-inflammatory-associated genes, but they do not yet provide the resolution to define specific metabolic or immunoregulatory modules. Consequently, it remains unclear whether *arg2+* macrophages represent a single anti-inflammatory program or a heterogeneous mixture of distinct sub-states, and would allow identification of additional functional modules beyond the limited gene sets examined in the preliminary dataset. Looking forward, achieving robust statistical power will be essential to enable rigorous differential gene expression analyses between *arg2+* and *arg2-* populations. This would allow for a deeper comparison across experimental conditions and a more nuanced mapping against known M2a-d subtypes (Peng et al., 2025; Smyth et al., 2024). Finally, translational validation will be essential: extending existing arg2 immunostaining of human tuberculin skin test samples and conducting human MDM studies would bridge the gap between the zebrafish *arg2:GFP* reporter and human macrophage biology.

A second key limitation is that all dynamic imaging in this thesis was performed in the larval zebrafish model. On the one hand, this is a major strength, as larvae <5.2 dpf are not protected under A(SP)A, making them highly valuable for ethically favourable, medium- to high-throughput compound screening and for non-invasive, real-time imaging of innate immune responses (Oprişoreanu et al.,

2023; Elks et al., 2013). This also provides a substantial 3Rs benefit. Replicating these experiments in mice would require large numbers of protected animals: for example, a priori power calculation (effect size 0.7, 80% power) indicates that at least 11 mice per condition would be needed to detect differences in macrophage phenotype transitions – and this does not include additional animals needed to generate BMDMs for *in vitro* experiments (**Fig. 7.2**) (Faul et al., 2009). By enabling longitudinal tracking of individual macrophages within a single organism, the zebrafish model both replaces and reduces mammalian use, preventing significant numbers of protected animals from being used. The absence of a mature adaptive immune system at these stages also simplifies interpretation, allowing direct interrogation of innate macrophage-*Mm* interactions without confounding lymphocyte contributions. On the other hand, this same feature is a biological limitation. In TB and other chronic infections, T cells clearly shape macrophage activation, but it remains incompletely resolved whether T helper 1 and T helper 2 cells (T_H1/T_H2) shape macrophage polarisation *de novo* or primarily amplify and stabilise macrophage states that are already instructed by local cues (Song et al., 2025; Khan et al., 2022; Hoerter et al., 2025; Krishna Prasad et al., 2025). By working with larvae, this thesis cannot address how adaptive immunity might further modulate or stabilise the observed pro- to anti-inflammatory switch.

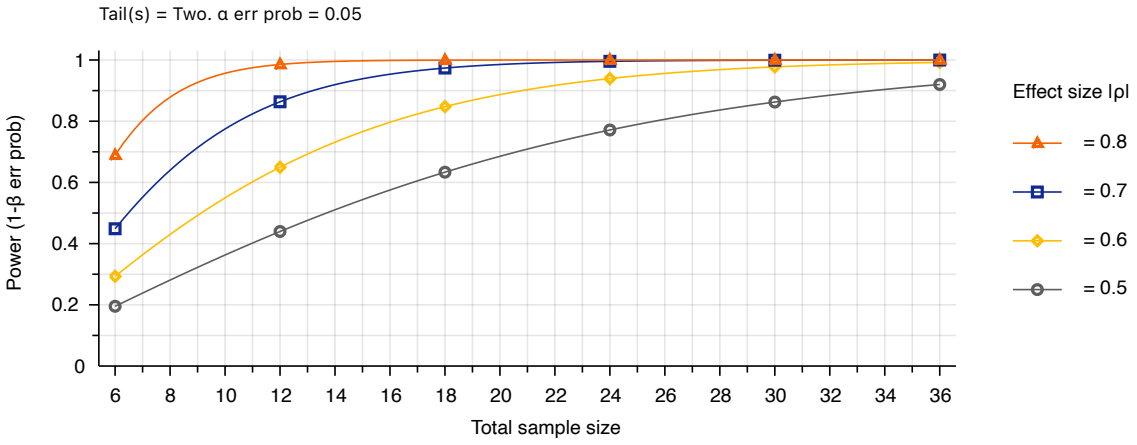


Figure 7.2. Power analysis to estimate how many mice would be required to examine macrophage polarisation dynamics. A priori analysis to determine sample size needed estimates that 11 mice would be required to achieve a statistical power of 0.8, where the calculated effect size was 0.7 (blue line). This calculation includes *in vivo* mice required to address the research question, but does not include any mice that may have been used to extract BMDMs. Calculations and graphs generated using G*Power 3.1 (Faul et al., 2009).

There are also temporal and technical constraints. The timelapse imaging windows did not capture *tnfa:mCherry+ arg2:GFP+* cells that subsequently downregulated *tnfa:mCherry* expression, a pattern hypothesised to occur in the later stages of adult *Mm* pathogenesis, when type 2 immune signalling and macrophage epithelisation occurs in granuloma formation (Cronan et al., 2021). Extending imaging beyond 5.2 dpf and into protected stages, where both adaptive immunity and more mature granulomas are established, could reveal clearer patterns of macrophage *tnfa:mCherry*

downregulation and progressive *arg2:GFP* upregulation over time. In addition, this work relied on reporters with relatively stable fluorescent proteins, which lacks ability to detect rapid, transient changes in gene expression (Mateus and Avery, 2000). Generating versions of *tnfa:mCherry* and *arg2:GFP* with destabilised fluorescent proteins (shorter half-lives) would improve temporal resolution of switching events and help determine whether *tnfa:mCherry+ arg2:GFP+* intermediates exist or whether they are macrophages in the process of transitioning from pro- to anti-inflammatory states (Molina et al., 2007).

7.1. Future prospects: targeting macrophage phenotype as a HDT

With the rise of antimicrobial-resistant TB, a major future direction emerging from this thesis is the potential to use zebrafish for the development of macrophage-targeted HDTs – an area of growing interest but limited clinical progress (Li et al., 2025). Although macrophages are central to TB pathogenesis, most HDTs aimed at modulating macrophage activation remain in pre-clinical stages, highlighting the need for experimental platforms that can bridge mechanistic discovery and therapeutic testing more rapidly. The tools developed in this thesis – particularly the ability to visualise putative pro- and anti-inflammatory macrophages (*tnfa:mCherry* and *arg2:GFP*, respectively) in real time – provide an avenue to accelerate this pipeline by enabling direct, dynamic readouts of drug effects on macrophage phenotype and bacterial burden *in vivo*.

A key limitation of the work in this thesis is that select M2-mediators were tested only under resting conditions, where leukocyte *arg2* expression is absent. Future studies will need to evaluate candidate HDTs in the context of active inflammation or infection, where *arg2* is already induced, to determine whether compounds genuinely enhance anti-inflammatory macrophage programmes. Furthermore, reliance on the *arg2:GFP* reporter alone means that compounds influencing macrophage phenotype via arginase-independent pathways may be overlooked, highlighting the need for additional anti-inflammatory macrophage reporters (e.g.: *grna.2* and *ctsz*) (Luo et al., 2025; Bastos et al., In Press). Nevertheless, using dual reporters (*tnfa:mCherry* and *arg2:GFP* simultaneously) offers a more powerful strategy for HDT screening, distinguishing compounds that suppress inflammation from those that reprogramme macrophages across the inflammatory spectrum while monitoring bacterial burden in parallel. The zebrafish system is well suited for this role: it already underpins high-throughput identification of pro-inflammatory modulators (e.g., *tnfa:GFP* screens; (Lewis and Elks, 2019)) and anti-inflammatory compounds (e.g.: *il1β:GFP* screens; (Oprişoreanu et al., 2023). Incorporating macrophage phenotype reporters extends this capacity toward precision immunomodulation, enabling discovery of drugs that shape macrophage behaviour at specific infection and inflammation resolution stages. This is especially relevant for TB, where effective immunity requires a temporal balance: a strong early pro-inflammatory response, followed by a dampening of this pro-inflammatory response to limit immunopathology and tissue damage at later stages of *Mtb* pathogenesis (Baay-Guzman et al., 2018).

However, excessive dampening of the pro-inflammatory signalling is also host-detrimental, with TNF-α inhibitors shown to interfere with granuloma organisation and promoting reactivation of latent TB (Arbués et al., 2020; Mezouar et al., 2019). HDTs must therefore fine-tune, rather than blunt, macrophage responses.

Among the macrophage pathways highlighted in this thesis, HIF-2α emerges as a particularly promising HDT target. HIF-2α modulation represents a particularly promising avenue, as I found it to partially regulate macrophage arginase expression, and because HIF-2α inhibitors (e.g.: belzutifan) are already licenced and safe in oncology (Fallah et al., 2024). From a pre-clinical perspective, rational development of HIF-2-targeted HDTs will require control of timing, dosing and TB disease stage. This could be approached experimentally by combining selective HIF-2α inhibition or activation with standard antibiotic therapy at defined points during infection and systematically comparing outcomes. Crucially, evaluation must extend beyond bacterial burden to include granuloma architecture, fibrosis, cavitation, and high-resolution macrophage state mapping using scRNAseq or spatial transcriptomics. These approaches will help determine whether HIF-2 manipulation truly reprogrammes macrophages into beneficial functional states rather than merely alleviating inflammation (Li et al., 2021; Zou et al., 2024). Zebrafish and murine mycobacterial models are well suited for such staged analyses: zebrafish allow longitudinal imaging to identify when HIF-2α modulation preserves containment versus precipitates granuloma breakdown, while mice or NHPs permit assessment of lung physiology, pathology, and relapse.

From a clinical standpoint, any future HIF-2α–modulating HDT is likely to be adjunctive to antibiotic therapy, rather than stand-alone. The most plausible indication is active pulmonary TB, where excessive inflammation predicts cavitation, fibrosis or long-term pulmonary impairment (Tiwari and Martineau, 2023). In this context, cell-type and stage-specific modulation of macrophage HIF-2α becomes critical. At early stages of infection, selective inhibition of macrophage Hif-2α might enhance Hif-1α-driven antimycobacterial activity, allowing macrophages to sustain pro-inflammatory responses that are essential for early bacterial control (Elks et al., 2013; Lewis and Elks, 2019; Ogryzko et al., 2019; Thompson et al., 2014). Evidence suggests this strategy must be macrophage-specific. Inhibiting Hif-2α in macrophages early in infection could potentiate Hif-1α-mediated antimycobacterial programmes, but systemic inhibition would risk affecting other leukocytes differently (Elks et al., 2013). For example, Hif-2α enhances pro-inflammatory programmes in neutrophils, meaning that systemic inhibition could unintentionally dampen neutrophil-mediated tissue damage, while systemic stabilisation risks amplifying it (Thompson et al., 2014). These opposing cell-specific consequences highlight the need for targeted delivery strategies (e.g.: macrophage-directed nanoparticles) to safely exploit temporal windows in which HIF-2α modulation is beneficial rather than harmful (Pi et al., 2024; Swami et al., 2025). However, at later disease stages – when tissue damage arises from uncontrolled inflammation –

macrophages-specific stabilisation of HIF-2α may instead be beneficial, promoting an anti-inflammatory macrophage phenotype that limit immunopathology while maintaining sufficient antimicrobial capacity within granulomas (Luo et al., 2025; Baay-Guzman et al., 2018). These opposing temporal roles imply that the effects of HIF-2α modulation depends on both when and in which cell type it is modulated. Consequently, translation of HIF-2α-modulating HDTs into the clinic will require: (1) rigorous screening for latent TB, as inappropriate suppression or activation of regulatory macrophage states during granuloma maintenance may destabilise containment (Alıravcı et al., 2025); (2) careful patient selection, restricted to individuals with confirmed active TB; and (3) longitudinal monitoring of radiological and microbiological endpoints to ensure that fine-tuning macrophage HIF-2α does not impair host defence or exacerbate tissue damage. Taken together, these constraints on timing, cell-type specificity and disease stage mean that precise modulation of macrophage HIF-2α will be essential for safe clinical translation. These considerations become even more critical in drug-resistant TB, where macrophage phenotypes within MDR/XDR lesions differ markedly from drug-sensitive disease and may require tailored HDT strategies

Clinical data suggest that M2-biased macrophage landscapes are enriched in MDR-TB/XDR-TB lesions, raising the possibility macrophage-targeted HDTs may need to be tailored to the *Mtb* strain, lesion microenvironment, or stage of disease progression (Cho et al., 2020). Importantly, the beneficial effects of promoting a transition toward an M2-like state are unlikely to stem from M2 identity alone, but from the effector functions and metabolic products generated by these cells, such as polyamines derived from arginase activity, proline-driven collagen synthesis, and other tissue-repair pathways induced by the M2 transcriptional programme (Szondi et al., 2021; Yurdagul et al., 2020; Wang et al., 2025). These metabolites and functions can limit excessive inflammation and create conditions in which antimicrobial effector cells can operate more effectively. However, the therapeutic implications differ markedly between sterile injury and infection. In multiple rodent injury models, driving an M1 to M2 transition typically improves outcomes in sterile inflammation, including pancreatitis, cutaneous wound healing and autoimmune hepatitis, reflecting the fact that wound healing primarily benefits from enhanced resolution and matrix remodelling (Li et al., 2024; Kim et al., 2019; Lin et al., 2024). In contrast, during infection, particularly with pathogens such as *Mtb*, promoting M2-like programmes too early can compromise bacterial control, whereas delaying the M2 transition can exacerbate tissue pathology (Baay-Guzman et al., 2018). Thus, timing and context are critical: macrophage phenotype switching must be modulated with far greater precision during infection than in wound healing, where amplifying M2-associated repair pathways is generally advantageous. This distinction underscores the need for HDTs that fine-tune macrophage polarisation dynamics, but supports the broader relevance of macrophage phenotype modulation across disease contexts.

Technological advances further expand the translational potential of this work. AI-based drug discovery is rapidly identifying novel *Mtb* drug targets and virtual screening of new and repurposed immunomodulatory compounds (Memon et al., 2025). These compounds could then be funnelled through the zebrafish reporter platform for rapid *in vivo* validation, before advancing to mammalian systems. In parallel, nanoparticle-based HDT delivery systems now allow targeting of therapeutics specifically to macrophages, enabling delivery of HDTs and HDT-antibiotic conjugates directly into infected macrophages, potentially overcoming limitations of systemic immunomodulation (Chen et al., 2022; Ma et al., 2021; Shen et al., 2023). Importantly, limited efficacy of arginase-targeted inhibitors like nor-NOHA to improve TB outcomes in mice reinforces that HDTs must go beyond single pathways, such as arginase, and instead target the broader phenotypic switch (Chauhan et al., 2024).

Finally, this framework aligns with growing interest in repurposed drugs as HDTs, particularly in treatment of TB. Several macrophage-targeted interventions have recently demonstrated that re-shaping host responses, rather than directly killing bacteria, can meaningfully improve disease outcomes (Li et al., 2025). Importantly, emerging clinical and pre-clinical data indicate that promoting anti-inflammatory and tissue-protective macrophage programmes can be as critical as enhancing bactericidal activity. For example, adjunctive use of macrophage-modulating agents such as PDE4 inhibitors (e.g. CC-11050) or mTOR modulators (everolimus) in TB clinical trials has been associated with reduced inflammatory pathology and improved lung outcomes without compromising bacterial clearance, supporting a role for macrophage-centred HDTs alongside antibiotics (Tukvadze et al., 2025). This therapeutic concept is increasingly reflected in intellectual property activity, with several patents claiming macrophage-targeted HDTs designed to modulate macrophages rather than directly target *Mtb*. Notably, ceased patent WO2014039011A1 covered formulations of calcitriol (vitamin D_3) and related compounds as adjunct therapies to enhance host immunity – a strategy that has been investigated in TB to boost macrophage antimicrobial responses and mitigate immunopathology (Singhal and De Libero, 2014). Additionally, the active patent US10806736 claims small molecules that activate host transcriptional programmes (such as p53) to enhance macrophage antimicrobial function, conceptually aligning with approaches that reshape macrophage phenotype to support pathogen control while limiting tissue damage (Song, 2020). Collectively, these patents frame macrophage modulation as a means to synergise with or enhance the efficacy of standard antimicrobials rather than replace them, underscoring recognition that controlling immunopathology and directing macrophage function is a therapeutically valuable endpoint in its own right. Crucially, experimental studies now provide *in vivo* proof-of-principle for these patent-driven concepts. For example, targeted delivery of calcitriol using poly(lactide) nanoparticles selectively to macrophages improved *Mtb* control in mice not only through modest bacteriostatic activity, but by markedly reducing lung pathology, highlight how limiting tissue damage is itself a major determinant of host survival (Reddy et al., 2024). Likewise, the repurposed drug benztropine, originally used for Parkinson's disease, was recently shown to reduce

Mtb and *Salmonella* burden in THP-1 macrophages and in mouse infection models by modulating macrophage histamine receptor-1 signalling, demonstrating how altering macrophage activation – rather than directly targeting bacteria – can restore host-protective immune function (Sahile et al., 2025). In combination, these clinical, experimental, and patent-driven advances point toward a future in which precise, context-dependent reprogramming of macrophage phenotypes can be harnessed to improve TB outcomes while minimising collateral tissue injury.

Collectively, the tools and findings of this thesis help position the zebrafish macrophage reporter system as a powerful platform to accelerate the HDT pipeline. By enabling rapid, real-time assessment of macrophage phenotype switching and bacterial control within a living host, this model offers a tractable pre-clinical step between *in vitro* screening and mammalian validation. Crucially, the simultaneous use of *tnfa:mCherry* and *arg2:GFP* reporters may allow for HDT candidate to be evaluated not only for antimicrobial efficacy (bacterial burden), but also for their ability to fine-tune macrophage activation states at different stages of mycobacterial pathogenesis. In this way, the zebrafish system provides a versatile and ethically accessible platform to identify, assess and refine macrophage-targeted HDTs that re-programme host innate immunity to improve outcomes in mycobacterial infection.

7.2. Concluding remarks

In conclusion, this thesis establishes *arg2:GFP* as an *in vivo* reporter of a macrophage population that phenotypically resembles anti-inflammatory macrophages described *in vitro*, and provides the first real-time evidence that individual *tnfa:mCherry+* pro-inflammatory macrophages can switch phenotype during mycobacterial infection. These *tnfa*+ to *arg2*+ transitions were accompanied by co-ordinated changes in macrophage morphology and behaviour following *arg2:GFP* upregulation, revealing dynamics plasticity long inferred from *in vitro* and *ex vivo* mammalian studies but not previously observed directly *in vivo*. Consistent with this phenotypic profile, preliminary scRNAseq suggests that *arg2+* macrophages transcriptionally appear M2-like, preferentially expressing anti-inflammatory-associated genes. Mechanistically, this work demonstrates that *Mm* virulence-TLR interactions contribute to macrophage *arg2:GFP* induction. Consistent with mammalian systems, Hif-2α was found to upregulate leukocyte *arg2:GFP* during resting conditions, and Hif-2α signalling was partially required for *tnfa:mCherry*+ to transition to an *arg2:GFP+* state. Importantly, genetic and pharmacological disruption of macrophage arginase activity resulted in loss of bacterial control and was associated with larger granulomas and enhanced bacterial dissemination, indicating that this phenotypic switch – and the associated increase in macrophage arginase activity – is host-protective, likely through modulation of inflammatory tone and preserving tissue integrity. Although widely used M2-polarising mediators did not induce macrophage *arg2:GFP* under resting conditions, this highlights the need for inflammatory context to activate reparative programmes *in vivo*. Given the breadth of the

anti-inflammatory macrophage spectrum, additional candidate genes were identified via datamining that may provide more nuanced markers with translational relevance. Together, these findings demonstrate that individual *tnfa:mCherry*+ pro-inflammatory macrophages can repolarise during mycobacterial infection, highlighting dynamic macrophage plasticity *in vivo*. When combined with pro-inflammatory reporters, the *arg2:GFP* zebrafish reporter line provides a versatile platform for simultaneous assessment of macrophage phenotype and bacterial burden, offering a valuable early-stage tool to accelerate macrophage-targeted HDT discovery prior to validation in mammalian models.

8. Bibliography

Ablain, J., Durand, E.M., Yang, S., Zhou, Y. and Zon, L.I. 2015. A CRISPR/Cas9 vector system for tissue-specific gene disruption in zebrafish. *Dev Cell.* **32**(6), pp.756-764.

Adams, D.O. 1974. The structure of mononuclear phagocytes differentiating *in vivo*. I. Sequential fine and histologic studies of the effect of Bacillus Calmette-Guerin (BCG). *Am J Pathol.* **76**(1), pp.17-48.

Agarwal, P., Combes, T.W., Shojaee-Moradie, F., Fielding, B., Gordon, S., Mizrahi, V. and Martinez, F.O. 2020. Foam Cells Control Mycobacterium tuberculosis Infection. *Frontiers in Microbiology.* **Volume 11 - 2020**.

Ahmad, F., Rani, A., Alam, A., Zarin, S., Pandey, S., Singh, H., Hasnain, S.E. and Ehtesham, N.Z. 2022. Macrophage: A Cell With Many Faces and Functions in Tuberculosis. *Front Immunol.* **13**, p747799.

Ajoolabady, A., Pratico, D., Lin, L., Mantzoros, C.S., Bahijri, S., Tuomilehto, J. and Ren, J. 2024. Inflammation in atherosclerosis: pathophysiology and mechanisms. *Cell Death & Disease.* **15**(11), p817.

Aldo, P.B., Craveiro, V., Guller, S. and Mor, G. 2013. Effect of culture conditions on the phenotype of THP-1 monocyte cell line. *Am J Reprod Immunol.* **70**(1), pp.80-86.

Alexander, N.O., Varvara, A.O., Nikita, G.N., Veronika, A.M., Andrey, V.G., Elena, B.R., Dongwei, Z. and Dimitry, A.C. 2019. Monocyte differentiation and macrophage polarization. *Vessel Plus.* **3**, p10.

Alexander, R.K., Liou, Y.H., Knudsen, N.H., Starost, K.A., Xu, C., Hyde, A.L., Liu, S., Jacobi, D., Liao, N.S. and Lee, C.H. 2020. Bmal1 integrates mitochondrial metabolism and macrophage activation. *Elife.* **9**.

Alhamdi, J.R., Peng, T., Al-Naggar, I.M., Hawley, K.L., Spiller, K.L. and Kuhn, L.T. 2019. Controlled M1-to-M2 transition of aged macrophages by calcium phosphate coatings. *Biomaterials.* **196**, pp.90-99.

Alıravcı, I.D., Mutlu, P., Oymak, S., Guney, U.I. and Keskin, O. 2025. Risk of Latent Tuberculosis Infection Reactivation in Patients Treated with Tumor Necrosis Factor Antagonists: A Five-Year Retrospective Study. *Tropical Medicine and Infectious Disease.* [Online]. **10**(7), p190.

Almansour, S., Dunster, J.L., Crofts, J.J. and Nelson, M.R. 2024. Modelling the continuum of macrophage phenotypes and their role in inflammation. *Mathematical Biosciences.* **377**, p109289.

Alsayed, S.S.R. and Gunosewoyo, H. 2023. Tuberculosis: Pathogenesis, Current Treatment Regimens and New Drug Targets. *Int J Mol Sci.* **24**(6).

Anders, H.-J. and Ryu, M. 2011. Renal microenvironments and macrophage phenotypes determine progression or resolution of renal inflammation and fibrosis. *Kidney International.* **80**(9), pp.915-925.

Andersson, M. and Kettunen, P. 2021. Effects of Holding Density on the Welfare of Zebrafish: A Systematic Review. *Zebrafish.* **18**(5), pp.297-306.

Andrews, J.T., Zhang, Z., Prasad, G.V.R.K., Huey, F., Nazarova, E.V., Wang, J., Ranaraja, A., Weinkopff, T., Li, L.-X., Mu, S., Birrer, M.J., Huang, S.C.-C., Zhang, N., Argüello, R.J., Philips, J.A., Mattila, J.T. and Huang, L. 2024. Metabolically active neutrophils represent a permissive niche for Mycobacterium tuberculosis. *Mucosal Immunology.* **17**(5), pp.825-842.

Animals (Scientific Procedures) Act 1986. ([Online]).

Antonelli, L.R., Gigliotti Rothfuchs, A., Gonçalves, R., Roffê, E., Cheever, A.W., Bafica, A., Salazar, A.M., Feng, C.G. and Sher, A. 2010. Intranasal Poly-IC treatment exacerbates tuberculosis in mice through the pulmonary recruitment of a pathogen-permissive monocyte/macrophage population. *J Clin Invest.* **120**(5), pp.1674-1682.

Antonsen, K.W., Friis, H.N., Sorensen, B.S., Etzerodt, A., Moestrup, S.K. and Møller, H.J. 2023. Comparison of culture media reveals that non-essential amino acids strongly affect the phenotype of human monocyte-derived macrophages. *Immunology.* **170**(3), pp.344-358.

Antonsen, K.W., Jensen, A.G., Carstensen, M., Nejsum, L.N., Sorensen, B.S., Etzerodt, A., Moestrup, S.K. and Møller, H.J. 2024. Proinflammatory polarization strongly reduces human macrophage *in vitro* phagocytosis of tumor cells in response to CD47 blockade. *European Journal of Immunology.* **54**(7), p2350824.

Arbués, A., Brees, D., Chibout, S.-D., Fox, T., Kammüller, M. and Portevin, D. 2020. TNF-α antagonists differentially induce TGF-β1-dependent resuscitation of dormant-like Mycobacterium tuberculosis. *PLOS Pathogens.* **16**(2), pe1008312.

Arkoudi, K., Yuan, Y., Cumine, A.P., Dyer, C., Busch-Nentwich, E., Bravo, I., Feng, Y. and Knight, R.D. 2025. An NF-kB/TNF-alpha signalling feedback loop acts to coordinate tissue regeneration and macrophage behaviour in zebrafish. *npj Regenerative Medicine.* **10**(1), p27.

Arlauckas, S.P., Garren, S.B., Garris, C.S., Kohler, R.H., Oh, J., Pittet, M.J. and Weissleder, R. 2018. Arg1 expression defines immunosuppressive subsets of tumor-associated macrophages. *Theranostics.* **8**(21), pp.5842-5854.

Arnaiz, E., Miar, A., Bridges, E., Prasad, N., Hatch, S.B., Ebner, D., Lawrie, C.H. and Harris, A.L. 2021. Differential effects of HIF2α antagonist and HIF2α silencing in renal cancer and sensitivity to repurposed drugs. *BMC Cancer.* **21**(1), p896.

Arnold, L., Henry, A., Poron, F., Baba-Amer, Y., van Rooijen, N., Plonquet, A., Gherardi, R.K. and Chazaud, B. 2007. Inflammatory monocytes recruited after skeletal muscle injury switch into antiinflammatory macrophages to support myogenesis. *J Exp Med.* **204**(5), pp.1057-1069.

Arredouani, M.S., Palecanda, A., Koziel, H., Huang, Y.C., Imrich, A., Sulahian, T.H., Ning, Y.Y., Yang, Z., Pikkarainen, T., Sankala, M., Vargas, S.O., Takeya, M., Tryggvason, K. and Kobzik, L. 2005. MARCO is the major binding receptor for unopsonized particles and bacteria on human alveolar macrophages. *J Immunol.* **175**(9), pp.6058-6064.

Ashenafi, S., Muvva, J.R., Mily, A., Snäll, J., Zewdie, M., Chanyalew, M., Rehn, A., Rahman, S., Aseffa, G., Bekele, A., Aderaye, G., Lema, B., Svensson, M. and Brighenti, S. 2022. Immunosuppressive Features of the Microenvironment in Lymph Nodes Granulomas from Tuberculosis and HIV-Co-Infected Patients. *Am J Pathol.* **192**(4), pp.653-670.

Ashley, J.W., Hancock, W.D., Nelson, A.J., Bone, R.N., Tse, H.M., Wohltmann, M., Turk, J. and Ramanadham, S. 2016. Polarization of Macrophages toward M2 Phenotype Is Favored by Reduction in iPLA2β (Group VIA Phospholipase A2). *J Biol Chem.* **291**(44), pp.23268-23281.

Ashokcoomar, S., Naidoo, T.J., Cumming, B.M., Baig, Z., Truebody, B., Mackenzie, J.S., Steyn, A.J.C. and Pillay, M. 2025. Mycobacterium tuberculosis curli pili reduces oxygen consumption rate of THP-1 macrophages during early infection. *The International Journal of Biochemistry & Cell Biology.* **185**, p106802.

Asrat, S., de Jesús, D.A., Hempstead, A.D., Ramabhadran, V. and Isberg, R.R. 2014. Bacterial pathogen manipulation of host membrane trafficking. *Annu Rev Cell Dev Biol.* **30**, pp.79-109.

Ates, L.S., van der Woude, A.D., Bestebroer, J., van Stempvoort, G., Musters, R.J., Garcia-Vallejo, J.J., Picavet, D.I., Weerd, R., Maletta, M., Kuijl, C.P., van der Wel, N.N. and Bitter, W. 2016. The ESX-5 System of Pathogenic Mycobacteria Is Involved In Capsule Integrity and Virulence through Its Substrate PPE10. *PLoS Pathog.* **12**(6), pe1005696.

Athanasiadis, E.I., Botthof, J.G., Andres, H., Ferreira, L., Lio, P. and Cvejic, A. 2017. Single-cell RNA-sequencing uncovers transcriptional states and fate decisions in haematopoiesis. *Nature Communications.* **8**(1), p2045.

Atri, C., Guerfali, F.Z. and Laouini, D. 2018. Role of Human Macrophage Polarization in Inflammation during Infectious Diseases. *Int J Mol Sci.* **19**(6).

Avdic, S., Cao, J.Z., McSharry, B.P., Clancy, L.E., Brown, R., Steain, M., Gottlieb, D.J., Abendroth, A. and Slobedman, B. 2013. Human cytomegalovirus interleukin-10 polarizes monocytes toward a deactivated M2c phenotype to repress host immune responses. *J Virol.* **87**(18), pp.10273-10282.

Baay-Guzman, G.J., Duran-Padilla, M.A., Rangel-Santiago, J., Tirado-Rodriguez, B., Antonio-Andres, G., Barrios-Payan, J., Mata-Espinosa, D., Klunder-Klunder, M., Vega, M.I., Hernandez-Pando, R. and Huerta-Yepez, S. 2018. Dual role of hypoxia-inducible factor 1 α in experimental pulmonary tuberculosis: its implication as a new therapeutic target. *Future Microbiology.* **13**(7), pp.785-798.

Bai, T., Chen, C.C. and Lau, L.F. 2010. Matricellular protein CCN1 activates a proinflammatory genetic program in murine macrophages. *J Immunol.* **184**(6), pp.3223-3232.

Baidžajevas, K., Hadadi, É., Lee, B., Lum, J., Shihui, F., Sudbery, I., Kiss-Tóth, E., Wong, S.C. and Wilson, H.L. 2020. Macrophage polarisation associated with atherosclerosis differentially affects their capacity to handle lipids. *Atherosclerosis.* **305**, pp.10-18.

Bailey, J.D., Diotallevi, M., Nicol, T., McNeill, E., Shaw, A., Chuaiphichai, S., Hale, A., Starr, A., Nandi, M., Stylianou, E., McShane, H., Davis, S., Fischer, R., Kessler, B.M., McCullagh, J., Channon, K.M. and Crabtree, M.J. 2019. Nitric Oxide Modulates Metabolic Remodeling in Inflammatory Macrophages through TCA Cycle Regulation and Itaconate Accumulation. *Cell Reports.* **28**(1), pp.218-230.e217.

Bailey, J.D., Shaw, A., McNeill, E., Nicol, T., Diotallevi, M., Chuaiphichai, S., Patel, J., Hale, A., Channon, K.M. and Crabtree, M.J. 2020. Isolation and culture of murine bone marrow-derived macrophages for nitric oxide and redox biology. *Nitric Oxide.* **100-101**, pp.17-29.

Balleza, E., Kim, J.M. and Cluzel, P. 2018. Systematic characterization of maturation time of fluorescent proteins in living cells. *Nature Methods.* **15**(1), pp.47-51.

Bandarra, D., Biddlestone, J., Mudie, S., Müller, H.A. and Rocha, S. 2015. HIF-1α restricts NF-κB-dependent gene expression to control innate immunity signals. *Dis Model Mech.* **8**(2), pp.169-181.

Banerjee, B., Khrystoforova, I., Polis, B., Zvi, I.B. and Karasik, D. 2021. Acute hypoxia elevates arginase 2 and induces polyamine stress response in zebrafish via evolutionarily conserved mechanism. *Cellular and Molecular Life Sciences.* **79**(1), p41.

Barisch, C. and Soldati, T. 2017. Mycobacterium marinum Degrades Both Triacylglycerols and Phospholipids from Its Dictyostelium Host to Synthesise Its Own Triacylglycerols and Generate Lipid Inclusions. *PLOS Pathogens.* **13**(1), pe1006095.

Barron, L., Smith, A.M., El Kasmi, K.C., Qualls, J.E., Huang, X., Cheever, A., Borthwick, L.A., Wilson, M.S., Murray, P.J. and Wynn, T.A. 2013. Role of arginase 1 from myeloid cells in th2-dominated lung inflammation. *PLoS One.* **8**(4), pe61961.

Baseler, W.A., Davies, L.C., Quigley, L., Ridnour, L.A., Weiss, J.M., Hussain, S.P., Wink, D.A. and McVicar, D.W. 2016. Autocrine IL-10 functions as a rheostat for M1 macrophage glycolytic commitment by tuning nitric oxide production. *Redox Biol.* **10**, pp.12-23.

Bates, J.M., Akerlund, J., Mittge, E. and Guillemin, K. 2007. Intestinal Alkaline Phosphatase Detoxifies Lipopolysaccharide and Prevents Inflammation in Zebrafish in Response to the Gut Microbiota. *Cell Host & Microbe.* **2**(6), pp.371-382.

Batte, C., Namusobya, M.S., Kirabo, R., Mukisa, J., Adakun, S. and Katamba, A. 2021. Prevalence and factors associated with non-adherence to multi-drug resistant tuberculosis (MDR-TB) treatment at Mulago National Referral Hospital, Kampala, Uganda. *Afr Health Sci.* **21**(1), pp.238-247.

Baxendale, S. and Whitfield, T.T. 2016. Chapter 6 - Methods to study the development, anatomy, and function of the zebrafish inner ear across the life course. In: Detrich, H.W., et al. eds. *Methods in Cell Biology.* Academic Press, pp.165-209.

Beil, J., Fairbairn, L., Pelczar, P. and Buch, T. 2012. Is BAC Transgenesis Obsolete? State of the Art in the Era of Designer Nucleases. *BioMed Research International.* **2012**(1), p308414.

Benard, E., Racz, P.I., Rougeot, J., Nezhinsky, A.E., Verbeek, F.J., Spaink, H.P. and Meijer, A.H. 2015. Macrophage-expressed perforins mpeg1 and mpeg1.2 have an anti-bacterial function in zebrafish. *J Innate Immun.* **7**(2), pp.136-152.

Benard, E.L. 2014. *Key innate immune components controlling intracellular infection*. PhD thesis, Leiden University.

Benard, E.L., Racz, P.I., Rougeot, J., Nezhinsky, A.E., Verbeek, F.J., Spaink, H.P. and Meijer, A.H. 2015. Macrophage-expressed perforins mpeg1 and mpeg1.2 have an anti-bacterial function in zebrafish. *J Innate Immun.* **7**(2), pp.136-152.

Benard, E.L., Roobol, S.J., Spaink, H.P. and Meijer, A.H. 2014. Phagocytosis of mycobacteria by zebrafish macrophages is dependent on the scavenger receptor Marco, a key control factor of pro-inflammatory signalling. *Developmental & Comparative Immunology.* **47**(2), pp.223-233.

Benoit, M., Desnues, B. and Mege, J.-L. 2008. Macrophage Polarization in Bacterial Infections. *The Journal of Immunology.* **181**(6), pp.3733-3739.

Bernardo, M.E. and Fibbe, W.E. 2013. Mesenchymal stromal cells: sensors and switchers of inflammation. *Cell Stem Cell.* **13**(4), pp.392-402.

Bernut, A., Dupont, C., Ogryzko, N.V., Neyret, A., Herrmann, J.-L., Floto, R.A., Renshaw, S.A. and Kremer, L. 2019. CFTR Protects against Mycobacterium abscessus Infection by Fine-Tuning Host Oxidative Defenses. *Cell Reports.* **26**(7), pp.1828-1840.e1824.

Bernut, A., Herrmann, J.L., Kissa, K., Dubremetz, J.F., Gaillard, J.L., Lutfalla, G. and Kremer, L. 2014. Mycobacterium abscessus cording prevents phagocytosis and promotes abscess formation. *Proc Natl Acad Sci U S A.* **111**(10), pp.E943-952.

Bertolini, T.B., de Souza, A.I., Gembre, A.F., Piñeros, A.R., Prado Rde, Q., Silva, J.S., Ramalho, L.N. and Bonato, V.L. 2016. Genetic background affects the expansion of macrophage subsets in the lungs of Mycobacterium tuberculosis-infected hosts. *Immunology.* **148**(1), pp.102-113.

Bertrand, J.Y., Kim, A.D., Violette, E.P., Stachura, D.L., Cisson, J.L. and Traver, D. 2007. Definitive hematopoiesis initiates through a committed erythromyeloid progenitor in the zebrafish embryo. *Development.* **134**(23), pp.4147-4156.

Bertrand, J.Y., Kim, A.D., Violette, E.P., Stachura, D.L., Cisson, J.L. and Traver, D. 2007. Definitive hematopoiesis initiates through a committed erythromyeloid progenitor in the zebrafish embryo. *Development.* **134**(23), pp.4147-4156.

Beyer, M., Mallmann, M.R., Xue, J., Staratschek-Jox, A., Vorholt, D., Krebs, W., Sommer, D., Sander, J., Mertens, C., Nino-Castro, A., Schmidt, S.V. and Schultze, J.L. 2012. High-resolution transcriptome of human macrophages. *PLoS One.* **7**(9), pe45466.

Bi, W., Zhu, L., Wang, C., Liang, Y., Liu, J., Shi, Q. and Tao, E. 2011. Rifampicin inhibits microglial inflammation and improves neuron survival against inflammation. *Brain Research.* **1395**, pp.12-20.

Bianchini, R., Roth-Walter, F., Ohradanova-Repic, A., Flicker, S., Hufnagl, K., Fischer, M.B., Stockinger, H. and Jensen-Jarolim, E. 2019. IgG4 drives M2a macrophages to a regulatory M2b-like phenotype: potential implication in immune tolerance. *Allergy.* **74**(3), pp.483-494.

Bo, H., Moure, U.A.E., Yang, Y., Pan, J., Li, L., Wang, M., Ke, X. and Cui, H. 2023. Mycobacterium tuberculosis-macrophage interaction: Molecular updates. *Front Cell Infect Microbiol.* **13**, p1062963.

Bohaud, C., Johansen, M.D., Jorgensen, C., Ipseiz, N., Kremer, L. and Djouad, F. 2021. The Role of Macrophages During Zebrafish Injury and Tissue Regeneration Under Infectious and Non-Infectious Conditions. *Front Immunol.* **12**, p707824.

Bojarczuk, A., Miller, K.A., Hotham, R., Lewis, A., Ogryzko, N.V., Kamuyango, A.A., Frost, H., Gibson, R.H., Stillman, E., May, R.C., Renshaw, S.A. and Johnston, S.A. 2016. Cryptococcus neoformans Intracellular Proliferation and Capsule Size Determines Early Macrophage Control of Infection. *Sci Rep.* **6**, p21489.

Borkham-Kamphorst, E., Schaffrath, C., Van de Leur, E., Haas, U., Tihaa, L., Meurer, S.K., Nevzorova, Y.A., Liedtke, C. and Weiskirchen, R. 2014. The anti-fibrotic effects of CCN1/CYR61 in primary portal myofibroblasts are mediated through induction of reactive oxygen species resulting in cellular senescence, apoptosis and attenuated TGF-β signaling. *Biochimica et Biophysica Acta (BBA) - Molecular Cell Research.* **1843**(5), pp.902-914.

Bosco, M.C. 2019. Macrophage polarization: Reaching across the aisle? *Journal of Allergy and Clinical Immunology.* **143**(4), pp.1348-1350.

Botella, H., Peyron, P., Levillain, F., Poincloux, R., Poquet, Y., Brandli, I., Wang, C., Tailleux, L., Tilleul, S., Charrière, G.M., Waddell, S.J., Foti, M., Lugo-Villarino, G., Gao, Q., Maridonneau-Parini, I., Butcher, P.D., Castagnoli, P.R., Gicquel, B., de Chastellier, C. and Neyrolles, O. 2011. Mycobacterial p(1)-type ATPases mediate resistance to zinc poisoning in human macrophages. *Cell Host Microbe.* **10**(3), pp.248-259.

Bottiglione, F. 2020. *Investigating the role of il-4, il-13 and il-10 cytokines in zebrafish immune responses*. thesis, The University of Manchester.

Boulakirba, S., Pfeifer, A., Mhaidly, R., Obba, S., Goulard, M., Schmitt, T., Chaintreuil, P., Calleja, A., Furstoss, N., Orange, F., Lacas-Gervais, S., Boyer, L., Marchetti, S., Verhoeyen, E., Luciano, F., Robert, G., Auberger, P. and Jacquel, A. 2018. IL-34 and CSF-1 display an equivalent macrophage differentiation ability but a different polarization potential. *Sci Rep.* **8**(1), p256.

Bozzaro, S. and Eichinger, L. 2011. The professional phagocyte Dictyostelium discoideum as a model host for bacterial pathogens. *Curr Drug Targets.* **12**(7), pp.942-954.

Brace, P.T., Tezera, L.B., Bielecka, M.K., Mellows, T., Garay, D., Tian, S., Rand, L., Green, J., Jogai, S., Steele, A.J., Millar, T.M., Sanchez-Elsner, T., Friedland, J.S., Proud, C.G. and Elkington, P.T. 2017.

Mycobacterium tuberculosis subverts negative regulatory pathways in human macrophages to drive immunopathology. *PLoS Pathog.* **13**(6), pe1006367.

Braga, S., Vieira, M., Barbosa, P., Ramos, J.P. and Duarte, R. 2024. Tuberculosis screening in the European migrant population: a scoping review of current practices. *Breathe (Sheff).* **20**(1), p230357.

Braian, C., Hogea, V. and Stendahl, O. 2013. Mycobacterium tuberculosis- induced neutrophil extracellular traps activate human macrophages. *J Innate Immun.* **5**(6), pp.591-602.

Braverman, J., Sogi, K.M., Benjamin, D., Nomura, D.K. and Stanley, S.A. 2016. HIF-1α Is an Essential Mediator of IFN-γ-Dependent Immunity to Mycobacterium tuberculosis. *J Immunol.* **197**(4), pp.1287-1297.

Braverman, J. and Stanley, S.A. 2017. Nitric Oxide Modulates Macrophage Responses to Mycobacterium tuberculosis Infection through Activation of HIF-1α and Repression of NF-κB. *J Immunol.* **199**(5), pp.1805-1816.

Brigo, N., Pfeifhofer-Obermair, C., Tymoszuk, P., Demetz, E., Engl, S., Barros-Pinkelnig, M., Dichtl, S., Fischer, C., Valente De Souza, L., Petzer, V., von Raffay, L., Hilbe, R., Berger, S., Seifert, M., Schleicher, U., Bogdan, C. and Weiss, G. 2021. Cytokine-Mediated Regulation of ARG1 in Macrophages and Its Impact on the Control of Salmonella enterica Serovar Typhimurium Infection. *Cells.* [Online]. **10**(7).

Brockway, N.L., Cook, Z.T., O'Gallagher, M.J., Tobias, Z.J.C., Gedi, M., Carey, K.M., Unni, V.K., Pan, Y.A., Metz, M.R. and Weissman, T.A. 2019. Multicolor lineage tracing using *in vivo* time-lapse imaging reveals coordinated death of clonally related cells in the developing vertebrate brain. *Developmental Biology.* **453**(2), pp.130-140.

Buchan, K.D., Prajsnar, T.K., Ogryzko, N.V., de Jong, N.W.M., van Gent, M., Kolata, J., Foster, S.J., van Strijp, J.A.G. and Renshaw, S.A. 2019. A transgenic zebrafish line for *in vivo* visualisation of neutrophil myeloperoxidase. *PLOS ONE.* **14**(4), pe0215592.

Buglo, E., Sarmiento, E., Martuscelli, N.B., Sant, D.W., Danzi, M.C., Abrams, A.J., Dallman, J.E. and Züchner, S. 2020. Genetic compensation in a stable slc25a46 mutant zebrafish: A case for using F0 CRISPR mutagenesis to study phenotypes caused by inherited disease. *PLOS ONE.* **15**(3), pe0230566.

Burgess A, Vigneron S, Brioudes E, Labbé JC, Lorca T, Castro A. Loss of human Greatwall results in G2 arrest and multiple mitotic defects due to deregulation of the cyclin B-Cdc2/PP2A balance. Proc Natl Acad Sci U S A. 2010 Jul 13;**107**(28):12564-9.

Bystrom, J., Evans, I., Newson, J., Stables, M., Toor, I., van Rooijen, N., Crawford, M., Colville-Nash, P., Farrow, S. and Gilroy, D.W. 2008. Resolution-phase macrophages possess a unique inflammatory phenotype that is controlled by cAMP. *Blood.* **112**(10), pp.4117-4127.

Caldwell, R.B., Toque, H.A., Narayanan, S.P. and Caldwell, R.W. 2015. Arginase: an old enzyme with new tricks. *Trends Pharmacol Sci.* **36**(6), pp.395-405.

Caldwell, R.W., Rodriguez, P.C., Toque, H.A., Narayanan, S.P. and Caldwell, R.B. 2018. Arginase: A Multifaceted Enzyme Important in Health and Disease. *Physiol Rev.* **98**(2), pp.641-665.

Calmette, A., Bocquet, A. and Negre, L. 1921. Contribution à l'étude du bacille tuberculeux bilié. *Ann Inst Pasteur.* **9**, pp.561-570.

Cambier, C.J., Falkow, S. and Ramakrishnan, L. 2014a. Host Evasion and Exploitation Schemes of Mycobacterium tuberculosis. *Cell.* **159**(7), pp.1497-1509.

Cambier, C.J., O'Leary, S.M., O'Sullivan, M.P., Keane, J. and Ramakrishnan, L. 2017. Phenolic Glycolipid Facilitates Mycobacterial Escape from Microbicidal Tissue-Resident Macrophages. *Immunity.* **47**(3), pp.552-565.e554.

Cambier, C.J., Takaki, K.K., Larson, R.P., Hernandez, R.E., Tobin, D.M., Urdahl, K.B., Cosma, C.L. and Ramakrishnan, L. 2014b. Mycobacteria manipulate macrophage recruitment through coordinated use of membrane lipids. *Nature.* **505**(7482), pp.218-222.

Campbell, L., Saville, C.R., Murray, P.J., Cruickshank, S.M. and Hardman, M.J. 2013. Local arginase 1 activity is required for cutaneous wound healing. *J Invest Dermatol.* **133**(10), pp.2461-2470.

Cao, C., Zhao, J., Doughty, E.K., Migliorini, M., Strickland, D.K., Kann, M.G. and Zhang, L. 2015. Mac-1 Regulates IL-13 Activity in Macrophages by Directly Interacting with IL-13Rα1 *. *Journal of Biological Chemistry.* **290**(35), pp.21642-21651.

Cardenal-Muñoz, E., Arafah, S., López-Jiménez, A.T., Kicka, S., Falaise, A., Bach, F., Schaad, O., King, J.S., Hagedorn, M. and Soldati, T. 2017. Mycobacterium marinum antagonistically induces an autophagic response while repressing the autophagic flux in a TORC1- and ESX-1-dependent manner. *PLoS Pathog.* **13**(4), pe1006344.

Carranza, C., Pedraza-Sanchez, S., de Oyarzabal-Mendez, E. and Torres, M. 2020. Diagnosis for Latent Tuberculosis Infection: New Alternatives. *Frontiers in Immunology.* **Volume 11 - 2020**.

Carvalho, K., Rebboah, E., Jansen, C., Williams, K., Dowey, A., McGill, C. and Mortazavi, A. 2021. Uncovering the Gene Regulatory Networks Underlying Macrophage Polarization Through Comparative Analysis of Bulk and Single-Cell Data. *bioRxiv.* p2021.2001.2020.427499.

Castellucci, M., Rossato, M., Calzetti, F., Tamassia, N., Zeminian, S., Cassatella, M.A. and Bazzoni, F. 2015. IL-10 disrupts the Brd4-docking sites to inhibit LPS-induced CXCL8 and TNF-α expression in monocytes: Implications for chronic obstructive pulmonary disease. *J Allergy Clin Immunol.* **136**(3), pp.781-791.e789.

Cavone, L., McCann, T., Drake, L.K., Aguzzi, E.A., Oprişoreanu, A.M., Pedersen, E., Sandi, S., Selvarajah, J., Tsarouchas, T.M., Wehner, D., Keatinge, M., Mysiak, K.S., Henderson, B.E.P., Dobie, R., Henderson, N.C., Becker, T. and Becker, C.G. 2021. A unique macrophage subpopulation signals directly to progenitor cells to promote regenerative neurogenesis in the zebrafish spinal cord. *Dev Cell.* **56**(11), pp.1617-1630.e1616.

Celada, A., Gray, P.W., Rinderknecht, E. and Schreiber, R.D. 1984. Evidence for a gamma-interferon receptor that regulates macrophage tumoricidal activity. *J Exp Med.* **160**(1), pp.55-74.

Chacón, P., Vega-Rioja, A., Doukkali, B., del Valle Rodriguez, A., Fernández-Delgado, L., Domínguez-Cereijo, L., Segura, C., Pérez-Machuca, B.M., Perkins, J.R., El Bekay, R., Cornejo-García, J.A., Hajji, N., Monteseirín, J. and Rivas-Pérez, D. 2024. Human Neutrophils Couple Nitric Oxide Production and Extracellular Trap Formation in Allergic Asthma. *American Journal of Respiratory and Critical Care Medicine.* **210**(5), pp.593-606.

Chacón-Salinas, R., Serafín-López, J., Ramos-Payán, R., Méndez-Aragón, P., Hernández-Pando, R., Van Soolingen, D., Flores-Romo, L., Estrada-Parra, S. and Estrada-García, I. 2005. Differential pattern of cytokine expression by macrophages infected *in vitro* with different Mycobacterium tuberculosis genotypes. *Clin Exp Immunol.* **140**(3), pp.443-449.

Chaffey, L.E., Roberti, A., Bowman, A., O'Brien, C.J.O., Som, L., Purvis, G.S.D. and Greaves, D.R. 2024. Drug repurposing screen identifies novel anti-inflammatory activity of sunitinib in macrophages. *European Journal of Pharmacology.* **969**, p176437.

Chaintreuil, P., Kerreneur, E., Bourgoin, M., Savy, C., Favreau, C., Robert, G., Jacquel, A. and Auberger, P. 2023. The generation, activation, and polarization of monocyte-derived macrophages in human malignancies. *Frontiers in Immunology.* **Volume 14 - 2023**.

Chan, J., Tanaka, K., Carroll, D., Flynn, J. and Bloom, B.R. 1995. Effects of nitric oxide synthase inhibitors on murine infection with Mycobacterium tuberculosis. *Infect Immun.* **63**(2), pp.736-740.

Chauhan, S., Nusbaum, R.J., Huante, M.B., Holloway, A.J., Endsley, M.A., Gelman, B.B., Lisinicchia, J.G. and Endsley, J.J. 2024. Therapeutic Modulation of Arginase with nor-NOHA Alters Immune Responses in Experimental Mouse Models of Pulmonary Tuberculosis including in the Setting of Human Immunodeficiency Virus (HIV) Co-Infection. *Tropical Medicine and Infectious Disease.* [Online]. **9**(6).

Chen, C.C., Mo, F.E. and Lau, L.F. 2001. The angiogenic factor Cyr61 activates a genetic program for wound healing in human skin fibroblasts. *J Biol Chem.* **276**(50), pp.47329-47337.

Chen, F., El-Naccache, D.W., Ponessa, J.J., Lemenze, A., Espinosa, V., Wu, W., Lothstein, K., Jin, L., Antao, O., Weinstein, J.S., Damani-Yokota, P., Khanna, K., Murray, P.J., Rivera, A., Siracusa, M.C. and Gause, W.C. 2022. Helminth resistance is mediated by differential activation of recruited monocyte-derived alveolar macrophages and arginine depletion. *Cell Rep.* **38**(2), p110215.

Chen, N., Leu, S.-J., Todorović, V., Lam, S.C.T. and Lau, L.F. 2004. Identification of a Novel Integrin αvβ3 Binding Site in CCN1 (CYR61) Critical for Pro-angiogenic Activities in Vascular Endothelial Cells*. *Journal of Biological Chemistry.* **279**(42), pp.44166-44176.

Chen, P.S., Chiu, W.T., Hsu, P.L., Lin, S.C., Peng, I.C., Wang, C.Y. and Tsai, S.J. 2020. Pathophysiological implications of hypoxia in human diseases. *J Biomed Sci.* **27**(1), p63.

Chen, R., Zou, J., Chen, J., Zhong, X., Kang, R. and Tang, D. 2025. Pattern recognition receptors: function, regulation and therapeutic potential. *Signal Transduction and Targeted Therapy.* **10**(1), p216.

Chen, S., Li, R., Cheng, C., Xu, J.-Y., Jin, C., Gao, F., Wang, J., Zhang, J., Zhang, J., Wang, H., Lu, L., Xu, G.-T. and Tian, H. 2018. Pseudomonas aeruginosa infection alters the macrophage phenotype switching process during wound healing in diabetic mice. *Cell Biology International.* **42**(7), pp.877-889.

Chen, S., Saeed, A.F.U.H., Liu, Q., Jiang, Q., Xu, H., Xiao, G.G., Rao, L. and Duo, Y. 2023. Macrophages in immunoregulation and therapeutics. *Signal Transduction and Targeted Therapy.* **8**(1), p207.

Chen, S., Wang, J., Tang, K., Liao, H., Xu, Y., Wang, L. and Niu, C. 2022. Multi-Modal Imaging Monitored M2 Macrophage Targeting Sono-Responsive Nanoparticles to Combat MRSA Deep Infections. *Int J Nanomedicine.* **17**, pp.4525-4546.

Chen, Y.-Y., Yang, F.-L., Wu, S.-H., Lin, T.-L. and Wang, J.-T. 2016. Mycobacterium marinum mmar_2318 and mmar_2319 are Responsible for Lipooligosaccharide Biosynthesis and Virulence Toward Dictyostelium. *Frontiers in Microbiology.* **Volume 6 - 2015**.

Cheng, Y., Chaturvedi, R., Asim, M., Bussière, F.I., Xu, H., Casero, R.A. and Wilson, K.T. 2005. Helicobacter pylori-induced Macrophage Apoptosis Requires Activation of Ornithine Decarboxylase by c-Myc*. *Journal of Biological Chemistry.* **280**(23), pp.22492-22496.

Cho, H.J., Lim, Y.-J., Kim, J., Koh, W.-J., Song, C.-H. and Kang, M.-W. 2020. Different macrophage polarization between drug-susceptible and multidrug-resistant pulmonary tuberculosis. *BMC Infectious Diseases.* **20**(1), p81.

Choe, S.S., Shin, K.C., Ka, S., Lee, Y.K., Chun, J.-S. and Kim, J.B. 2014. Macrophage HIF-2α Ameliorates Adipose Tissue Inflammation and Insulin Resistance in Obesity. *Diabetes.* **63**(10), pp.3359-3371.

Choi, S.-W., Im, J.-J., Yoon, S.-E., Kim, S.-H., Cho, J.-H., Jeong, S.-J., Park, K.-A. and Moon, Y.-S. 2023. Lower socioeconomic status associated with higher tuberculosis rate in South Korea. *BMC Pulmonary Medicine.* **23**(1), p418.

Choi, T.-Y., Choi, T.-I., Lee, Y.-R., Choe, S.-K. and Kim, C.-H. 2021. Zebrafish as an animal model for biomedical research. *Experimental & Molecular Medicine.* **53**(3), pp.310-317.

Cholan, P.M., Han, A., Woodie, B.R., Watchon, M., Kurz, A.R., Laird, A.S., Britton, W.J., Ye, L., Holmes, Z.C., McCann, J.R., David, L.A., Rawls, J.F. and Oehlers, S.H. 2020. Conserved anti-inflammatory effects and sensing of butyrate in zebrafish. *Gut Microbes.* **12**(1), pp.1-11.

Choudhury, R. 2018. Hypoxia and hyperbaric oxygen therapy: a review. *Int J Gen Med.* **11**, pp.431-442.

Chuang, Y., Hung, M.E., Cangelose, B.K. and Leonard, J.N. 2016. Regulation of the IL-10-driven macrophage phenotype under incoherent stimuli. *Innate Immun.* **22**(8), pp.647-657.

Chung, C., Jeong, D., Sohn, H., Choi, H. and Kang, Y.A. 2024. Low household income increases the risk of tuberculosis recurrence: a retrospective nationwide cohort study in South Korea. *Public Health.* **226**, pp.228-236.

Cilfone, N.A., Perry, C.R., Kirschner, D.E. and Linderman, J.J. 2013. Multi-scale modeling predicts a balance of tumor necrosis factor-α and interleukin-10 controls the granuloma environment during Mycobacterium tuberculosis infection. *PLoS One.* **8**(7), pe68680.

Clay, H., Volkman, H.E. and Ramakrishnan, L. 2008. Tumor necrosis factor signaling mediates resistance to mycobacteria by inhibiting bacterial growth and macrophage death. *Immunity.* **29**(2), pp.283-294.

Clemens, D.L. and Horwitz, M.A. 1995. Characterization of the Mycobacterium tuberculosis phagosome and evidence that phagosomal maturation is inhibited. *J Exp Med.* **181**(1), pp.257-270.

Cohen, S.B., Gern, B.H., Delahaye, J.L., Adams, K.N., Plumlee, C.R., Winkler, J.K., Sherman, D.R., Gerner, M.Y. and Urdahl, K.B. 2018. Alveolar Macrophages Provide an Early Mycobacterium tuberculosis Niche and Initiate Dissemination. *Cell Host Microbe.* **24**(3), pp.439-446.e434.

Corrado, C. and Fontana, S. 2020. Hypoxia and HIF Signaling: One Axis with Divergent Effects. *Int J Mol Sci.* **21**(16).

Cosma Christine, L., Klein, K., Kim, R., Beery, D. and Ramakrishnan, L. 2006. Mycobacterium marinum Erp Is a Virulence Determinant Required for Cell Wall Integrity and Intracellular Survival. *Infection and Immunity.* **74**(6), pp.3125-3133.

Courtney, K.D., Infante, J.R., Lam, E.T., Figlin, R.A., Rini, B.I., Brugarolas, J., Zojwalla, N.J., Lowe, A.M., Wang, K., Wallace, E.M., Josey, J.A. and Choueiri, T.K. 2018. Phase I Dose-Escalation Trial of PT2385, a First-in-Class Hypoxia-Inducible Factor-2α Antagonist in Patients With Previously Treated Advanced Clear Cell Renal Cell Carcinoma. *J Clin Oncol.* **36**(9), pp.867-874.

Cowburn, A.S., Crosby, A., Macias, D., Branco, C., Colaço, R.D., Southwood, M., Toshner, M., Crotty Alexander, L.E., Morrell, N.W., Chilvers, E.R. and Johnson, R.S. 2016. HIF2α-arginase axis is essential for the development of pulmonary hypertension. *Proc Natl Acad Sci U S A.* **113**(31), pp.8801-8806.

Cox, H.S., Morrow, M. and Deutschmann, P.W. 2008. Long term efficacy of DOTS regimens for tuberculosis: systematic review. *Bmj.* **336**(7642), pp.484-487.

Coşkun, S., Chao, H., Vasavada, H., Heydari, K., Gonzales, N., Zhou, X., de Crombrugghe, B. and Hirschi, K.K. 2014. Development of the fetal bone marrow niche and regulation of HSC quiescence and homing ability by emerging osteolineage cells. *Cell Rep.* **9**(2), pp.581-590.

Cronan, M.R., Beerman, R.W., Rosenberg, A.F., Saelens, J.W., Johnson, M.G., Oehlers, S.H., Sisk, D.M., Jurcic Smith, K.L., Medvitz, N.A., Miller, S.E., Trinh, L.A., Fraser, S.E., Madden, J.F., Turner, J., Stout, J.E., Lee, S. and Tobin, D.M. 2016. Macrophage Epithelial Reprogramming Underlies Mycobacterial Granuloma Formation and Promotes Infection. *Immunity.* **45**(4), pp.861-876.

Cronan, M.R., Hughes, E.J., Brewer, W.J., Viswanathan, G., Hunt, E.G., Singh, B., Mehra, S., Oehlers, S.H., Gregory, S.G., Kaushal, D. and Tobin, D.M. 2021. A non-canonical type 2 immune response coordinates tuberculous granuloma formation and epithelialization. *Cell.* **184**(7), pp.1757-1774 e1714.

Cui, C., Chakraborty, K., Tang, X.A., Schoenfelt, K.Q., Hoffman, A., Blank, A., McBeth, B., Pulliam, N., Reardon, C.A., Kulkarni, S.A., Vaisar, T., Ballabio, A., Krishnan, Y. and Becker, L. 2021. A lysosome-targeted DNA nanodevice selectively targets macrophages to attenuate tumours. *Nature Nanotechnology.* **16**(12), pp.1394-1402.

Cui, K., Ardell, C.L., Podolnikova, N.P. and Yakubenko, V.P. 2018. Distinct Migratory Properties of M1, M2, and Resident Macrophages Are Regulated by αDβ2 and αMβ2 Integrin-Mediated Adhesion. *Frontiers in Immunology.* **Volume 9 - 2018**.

Cumming, B.M., Addicott, K.W., Adamson, J.H. and Steyn, A.J. 2018. Mycobacterium tuberculosis induces decelerated bioenergetic metabolism in human macrophages. *Elife.* **7**.

Cyktor, J.C., Carruthers, B., Kominsky, R.A., Beamer, G.L., Stromberg, P. and Turner, J. 2013. IL-10 inhibits mature fibrotic granuloma formation during Mycobacterium tuberculosis infection. *J Immunol.* **190**(6), pp.2778-2790.

Dall'Asta, M., Derlindati, E., Ardigò, D., Zavaroni, I., Brighenti, F. and Del Rio, D. 2012. Macrophage polarization: the answer to the diet/inflammation conundrum? *Nutr Metab Cardiovasc Dis.* **22**(5), pp.387-392.

Dang, B., Gao, Q., Zhang, L., Zhang, J., Cai, H., Zhu, Y., Zhong, Q., Liu, J., Niu, Y., Mao, K., Xiao, N., Liu, W.H., Lin, S.H., Huang, J., Huang, S.C., Ho, P.C. and Cheng, S.C. 2023. The glycolysis/HIF-1α axis defines the inflammatory role of IL-4-primed macrophages. *Cell Rep.* **42**(5), p112471.

Dang, E.V., Lei, S., Radkov, A., Volk, R.F., Zaro, B.W. and Madhani, H.D. 2022. Secreted fungal virulence effector triggers allergic inflammation via TLR4. *Nature.* **608**(7921), pp.161-167.

Daniel, J., Maamar, H., Deb, C., Sirakova, T.D. and Kolattukudy, P.E. 2011. Mycobacterium tuberculosis Uses Host Triacylglycerol to Accumulate Lipid Droplets and Acquires a Dormancy-Like Phenotype in Lipid-Loaded Macrophages. *PLOS Pathogens.* **7**(6), pe1002093.

Dartois, V.A. and Rubin, E.J. 2022. Anti-tuberculosis treatment strategies and drug development: challenges and priorities. *Nat Rev Microbiol.* **20**(11), pp.685-701.

Davis, A.S., Vergne, I., Master, S.S., Kyei, G.B., Chua, J. and Deretic, V. 2007. Mechanism of inducible nitric oxide synthase exclusion from mycobacterial phagosomes. *PLoS Pathog.* **3**(12), pe186.

Davis, J.M., Clay, H., Lewis, J.L., Ghori, N., Herbomel, P. and Ramakrishnan, L. 2002. Real-time visualization of mycobacterium-macrophage interactions leading to initiation of granuloma formation in zebrafish embryos. *Immunity.* **17**(6), pp.693-702.

Davis, J.M. and Ramakrishnan, L. 2009. The role of the granuloma in expansion and dissemination of early tuberculous infection. *Cell.* **136**(1), pp.37-49.

Davison, J.M., Akitake, C.M., Goll, M.G., Rhee, J.M., Gosse, N., Baier, H., Halpern, M.E., Leach, S.D. and Parsons, M.J. 2007. Transactivation from Gal4-VP16 transgenic insertions for tissue-specific cell labeling and ablation in zebrafish. *Dev Biol.* **304**(2), pp.811-824.

de Oliveira Rezende, A., Sabóia, R.S., da Costa, A.C., da Silva Monteiro, D.M., Zagmignan, A., Santiago, L.Â., Carvalho, R.C., Pereira, P.V., Junqueira-Kipnis, A.P. and de Sousa, E.M. 2022. Restricted

Activation of the NF-κB Pathway in Individuals with Latent Tuberculosis Infection after HIF-1α Blockade. *Biomedicines.* [Online]. **10**(4).

de Sena-Tomás, C., Rebola Lameira, L., Rebocho da Costa, M., Naique Taborda, P., Laborde, A., Orger, M., de Oliveira, S. and Saúde, L. 2024. Neutrophil immune profile guides spinal cord regeneration in zebrafish. *Brain, Behavior, and Immunity.* **120**, pp.514-531.

Debaenst, S., Jarayseh, T., De Saffel, H., Bek, J.W., Boone, M., Josipovic, I., Kibleur, P., Kwon, R.Y., Coucke, P.J. and Willaert, A. 2025. Crispant analysis in zebrafish as a tool for rapid functional screening of disease-causing genes for bone fragility. *eLife.* **13**, pRP100060.

DeBerge, M., Lantz, C., Dehn, S., Sullivan, D.P., van der Laan, A.M., Niessen, H.W.M., Flanagan, M.E., Brat, D.J., Feinstein, M.J., Kaushal, S., Wilsbacher, L.D. and Thorp, E.B. 2021. Hypoxia-inducible factors individually facilitate inflammatory myeloid metabolism and inefficient cardiac repair. *Journal of Experimental Medicine.* **218**(9), pe20200667.

DeBerge, M., Schroth, S., Du, F., Yeap, X.Y., Wang, J.-J., Zhang, Z.J., Ansari, M.J., Scott, E.A. and Thorp, E.B. 2024. Hypoxia inducible factor 2α promotes tolerogenic macrophage development during cardiac transplantation through transcriptional regulation of colony stimulating factor 1 receptor. *Proceedings of the National Academy of Sciences.* **121**(26), pe2319623121.

Deghmane, A.E., Soualhine, H., Bach, H., Sendide, K., Itoh, S., Tam, A., Noubir, S., Talal, A., Lo, R., Toyoshima, S., Av-Gay, Y. and Hmama, Z. 2007. Lipoamide dehydrogenase mediates retention of coronin-1 on BCG vacuoles, leading to arrest in phagosome maturation. *J Cell Sci.* **120**(Pt 16), pp.2796-2806.

Dehn, S., DeBerge, M., Yeap, X.Y., Yvan-Charvet, L., Fang, D., Eltzschig, H.K., Miller, S.D. and Thorp, E.B. 2016. HIF-2α in Resting Macrophages Tempers Mitochondrial Reactive Oxygen Species To Selectively Repress MARCO-Dependent Phagocytosis. *J Immunol.* **197**(9), pp.3639-3649.

Dekkers, B.G.J., Kerstjens, H.A.M., Breisnes, H.W., Leeming, D.J., Anthony, R.M., Frijlink, H.W., van der Werf, T.S., Kosterink, J.G.W., Alffenaar, J.-W.C. and Akkerman, O.W. 2025. Azithromycin as Host-Directed Therapy for Pulmonary Tuberculosis: A Randomized Pilot Trial. *The Journal of Infectious Diseases.* **231**(5), pp.e891-e900.

Denans, N., Tran, N.T.T., Swall, M.E., Diaz, D.C., Blanck, J. and Piotrowski, T. 2022. An anti-inflammatory activation sequence governs macrophage transcriptional dynamics during tissue injury in zebrafish. *Nature Communications.* **13**(1), p5356.

Deng, B., Wehling-Henricks, M., Villalta, S.A., Wang, Y. and Tidball, J.G. 2012. IL-10 triggers changes in macrophage phenotype that promote muscle growth and regeneration. *J Immunol.* **189**(7), pp.3669-3680.

Deng, Y., Wang, H., Liu, X., Yuan, H., Xu, J., de Thé, H., Zhou, J. and Zhu, J. 2022. Zbtb14 regulates monocyte and macrophage development through inhibiting pu.1 expression in zebrafish. *eLife.* **11**, pe80760.

Depierre, M., Mularski, A., Ruppel, A., Le Clainche, C., Balland, M. and Niedergang, F. 2025. A crosstalk between adhesion and phagocytosis integrates macrophage functions into their microenvironment. *iScience.* **28**(4), p112067.

Depping, R., Steinhoff, A., Schindler, S.G., Friedrich, B., Fagerlund, R., Metzen, E., Hartmann, E. and Köhler, M. 2008. Nuclear translocation of hypoxia-inducible factors (HIFs): Involvement of the classical importin α/β pathway. *Biochimica et Biophysica Acta (BBA) - Molecular Cell Research.* **1783**(3), pp.394-404.

Deretic, V. and Fratti, R.A. 1999. Mycobacterium tuberculosis phagosome. *Molecular Microbiology.* **31**(6), pp.1603-1609.

Dharmadhikari, A.S. and Nardell, E.A. 2008. What animal models teach humans about tuberculosis. *Am J Respir Cell Mol Biol.* **39**(5), pp.503-508.

Di Giovannantonio, M., Hartley, F., Elshenawy, B., Barberis, A., Hudson, D., Shafique, H.S., Allott, V.E.S., Harris, D.A., Lord, S.R., Haider, S., Harris, A.L., Buffa, F.M. and Harris, B.H.L. 2025. Defining hypoxia in cancer: A landmark evaluation of hypoxia gene expression signatures. *Cell Genom.* **5**(2), p100764.

Dick, S.A., Macklin, J.A., Nejat, S., Momen, A., Clemente-Casares, X., Althagafi, M.G., Chen, J., Kantores, C., Hosseinzadeh, S., Aronoff, L., Wong, A., Zaman, R., Barbu, I., Besla, R., Lavine, K.J., Razani, B., Ginhoux, F., Husain, M., Cybulsky, M.I., ... and Epelman, S. 2019. Self-renewing resident cardiac macrophages limit adverse remodeling following myocardial infarction. *Nature Immunology.* **20**(1), pp.29-39.

Dill-McFarland, K.A., Peterson, G., Lim, P.N., Skerrett, S., Hawn, T.R., Rothchild, A.C. and Campo, M. 2025. Shared and distinct responses of human and murine alveolar macrophages and monocyte-derived macrophages to Mycobacterium tuberculosis. *bioRxiv.* p2025.2002.2028.640814.

Ding, Y.E., Wong, M.T.J., Norazmi, M.N., Balakrishnan, V. and Tye, G.J. 2025. Advancement in diagnostic approaches for latent tuberculosis: distinguishing recent from remote infections. *One Health Outlook.* **7**(1), p19.

Diriba, G., Alemu, A., Yenew, B., Tola, H.H., Gamtesa, D.F., Mollalign, H., Eshetu, K., Moga, S., Abdella, S., Tollera, G., Kebede, A. and Dangisso, M.H. 2023. Epidemiology of extensively drug-resistant tuberculosis among patients with multidrug-resistant tuberculosis: A systematic review and meta-analysis. *Int J Infect Dis.* **132**, pp.50-63.

Dirks, R.P., Ordas, A., Jong-Raadsen, S., Brittijn, S.A., Haks, M.C., Henkel, C.V., Oravcova, K., Racz, P.I., Tuinhof-Koelma, N., Korzeniowska Nee Wiweger, M.I., Gillespie, S.H., Meijer, A.H., Ottenhoff, T.H.M., Jansen, H.J. and Spaink, H.P. 2024. The Human Pathogen Mycobacterium tuberculosis and the Fish Pathogen Mycobacterium marinum Trigger a Core Set of Late Innate Immune Response Genes in Zebrafish Larvae. *Biology (Basel).* **13**(9).

Dodd, P.J., Osman, M., Cresswell, F.V., Stadelman, A.M., Lan, N.H., Thuong, N.T.T., Muzyamba, M., Glaser, L., Dlamini, S.S. and Seddon, J.A. 2021. The global burden of tuberculous meningitis in adults: A modelling study. *PLOS Glob Public Health.* **1**(12), pe0000069.

Doedens, A.L., Stockmann, C., Rubinstein, M.P., Liao, D., Zhang, N., DeNardo, D.G., Coussens, L.M., Karin, M., Goldrath, A.W. and Johnson, R.S. 2010. Macrophage expression of hypoxia-inducible factor-1 alpha suppresses T-cell function and promotes tumor progression. *Cancer Res.* **70**(19), pp.7465-7475.

Domingo-Gonzalez, R., Das, S., Griffiths, K.L., Ahmed, M., Bambouskova, M., Gopal, R., Gondi, S., Muñoz-Torrico, M., Salazar-Lezama, M.A., Cruz-Lagunas, A., Jiménez-Álvarez, L., Ramirez-Martinez, G., Espinosa-Soto, R., Sultana, T., Lyons-Weiler, J., Reinhart, T.A., Arcos, J., de la Luz Garcia-Hernandez, M., Mastrangelo, M.A., ... and Khader, S.A. 2017. Interleukin-17 limits hypoxia-inducible factor 1α and development of hypoxic granulomas during tuberculosis. *JCI Insight.* **2**(19).

Donadon, M., Torzilli, G., Cortese, N., Soldani, C., Di Tommaso, L., Franceschini, B., Carriero, R., Barbagallo, M., Rigamonti, A., Anselmo, A., Colombo, F.S., Maggi, G., Lleo, A., Cibella, J., Peano, C., Kunderfranco, P., Roncalli, M., Mantovani, A. and Marchesi, F. 2020. Macrophage morphology correlates with single-cell diversity and prognosis in colorectal liver metastasis. *Journal of Experimental Medicine.* **217**(11), pe20191847.

Dorman Susan, E., Nahid, P., Kurbatova Ekaterina, V., Phillips Patrick, P.J., Bryant, K., Dooley Kelly, E., Engle, M., Goldberg Stefan, V., Phan Ha, T.T., Hakim, J., Johnson John, L., Lourens, M., Martinson Neil, A., Muzanyi, G., Narunsky, K., Nerette, S., Nguyen Nhung, V., Pham Thuong, H.,

Pierre, S., ... and Chaisson Richard, E. 2021. Four-Month Rifapentine Regimens with or without Moxifloxacin for Tuberculosis. *New England Journal of Medicine.* **384**(18), pp.1705-1718.

Dowling, J.K., Afzal, R., Gearing, L.J., Cervantes-Silva, M.P., Annett, S., Davis, G.M., De Santi, C., Assmann, N., Dettmer, K., Gough, D.J., Bantug, G.R., Hamid, F.I., Nally, F.K., Duffy, C.P., Gorman, A.L., Liddicoat, A.M., Lavelle, E.C., Hess, C., Oefner, P.J., ... and McCoy, C.E. 2021. Mitochondrial arginase-2 is essential for IL-10 metabolic reprogramming of inflammatory macrophages. *Nature Communications.* **12**(1), p1460.

Doyle, A.G., Herbein, G., Montaner, L.J., Minty, A.J., Caput, D., Ferrara, P. and Gordon, S. 1994. Interleukin-13 alters the activation state of murine macrophages *in vitro*: comparison with interleukin-4 and interferon-gamma. *Eur J Immunol.* **24**(6), pp.1441-1445.

Duque-Correa, M.A., Kühl, A.A., Rodriguez, P.C., Zedler, U., Schommer-Leitner, S., Rao, M., Weiner, J., Hurwitz, R., Qualls, J.E., Kosmiadi, G.A., Murray, P.J., Kaufmann, S.H.E. and Reece, S.T. 2014. Macrophage arginase-1 controls bacterial growth and pathology in hypoxic tuberculosis granulomas. *Proceedings of the National Academy of Sciences.* **111**(38), pp.E4024-E4032.

Dutta, N.K., Bruiners, N., Zimmerman, M.D., Tan, S., Dartois, V., Gennaro, M.L. and Karakousis, P.C. 2020. Adjunctive Host-Directed Therapy With Statins Improves Tuberculosis-Related Outcomes in Mice. *J Infect Dis.* **221**(7), pp.1079-1087.

Dzik, J.M. 2014. Evolutionary Roots of Arginase Expression and Regulation. *Frontiers in Immunology.* **5**.

Ehrt, S., Schnappinger, D., Bekiranov, S., Drenkow, J., Shi, S., Gingeras, T.R., Gaasterland, T., Schoolnik, G. and Nathan, C. 2001. Reprogramming of the macrophage transcriptome in response to interferon-gamma and Mycobacterium tuberculosis: signaling roles of nitric oxide synthase-2 and phagocyte oxidase. *J Exp Med.* **194**(8), pp.1123-1140.

El Kasmi, K.C., Qualls, J.E., Pesce, J.T., Smith, A.M., Thompson, R.W., Henao-Tamayo, M., Basaraba, R.J., König, T., Schleicher, U., Koo, M.S., Kaplan, G., Fitzgerald, K.A., Tuomanen, E.I., Orme, I.M., Kanneganti, T.D., Bogdan, C., Wynn, T.A. and Murray, P.J. 2008. Toll-like receptor-induced arginase 1 in macrophages thwarts effective immunity against intracellular pathogens. *Nat Immunol.* **9**(12), pp.1399-1406.

Elkington, P., Shiomi, T., Breen, R., Nuttall, R.K., Ugarte-Gil, C.A., Walker, N.F., Saraiva, L., Pedersen, B., Mauri, F., Lipman, M., Edwards, D.R., Robertson, B.D., D'Armiento, J. and Friedland, J.S. 2011. MMP-1 drives immunopathology in human tuberculosis and transgenic mice. *The Journal of Clinical Investigation.* **121**(5), pp.1827-1833.

Elks, P.M., Brizee, S., van der Vaart, M., Walmsley, S.R., van Eeden, F.J., Renshaw, S.A. and Meijer, A.H. 2013. Hypoxia inducible factor signaling modulates susceptibility to mycobacterial infection via a nitric oxide dependent mechanism. *PLoS Pathog.* **9**(12), pe1003789.

Elks, P.M., Renshaw, S.A., Meijer, A.H., Walmsley, S.R. and van Eeden, F.J. 2015. Exploring the HIFs, buts and maybes of hypoxia signalling in disease: lessons from zebrafish models. *Dis Model Mech.* **8**(11), pp.1349-1360.

Elks, P.M., van der Vaart, M., van Hensbergen, V., Schutz, E., Redd, M.J., Murayama, E., Spaink, H.P. and Meijer, A.H. 2014. Mycobacteria counteract a TLR-mediated nitrosative defense mechanism in a zebrafish infection model. *PLoS One.* **9**(6), pe100928.

Elks, P.M., van Eeden, F.J., Dixon, G., Wang, X., Reyes-Aldasoro, C.C., Ingham, P.W., Whyte, M.K.B., Walmsley, S.R. and Renshaw, S.A. 2011. Activation of hypoxia-inducible factor-1α (Hif-1α) delays inflammation resolution by reducing neutrophil apoptosis and reverse migration in a zebrafish inflammation model. *Blood.* **118**(3), pp.712-722.

Ellett, F., Elks, P.M., Robertson, A.L., Ogryzko, N.V. and Renshaw, S.A. 2015. Defining the phenotype of neutrophils following reverse migration in zebrafish. *J Leukoc Biol.* **98**(6), pp.975-981.

Ellett, F., Pase, L., Hayman, J.W., Andrianopoulos, A. and Lieschke, G.J. 2011. mpeg1 promoter transgenes direct macrophage-lineage expression in zebrafish. *Blood.* **117**(4), pp.e49-56.

Ellett, F., Pase, L., Hayman, J.W., Andrianopoulos, A. and Lieschke, G.J. 2011. mpeg1 promoter transgenes direct macrophage-lineage expression in zebrafish. *Blood.* **117**(4), pp.e49-e56.

Elliot, A.M., Ribeiro Bravo, I., Zhao, Y., Wang, Z., Astorga Johansson, J., Hutton, E., Cunningham, R., Myllymäki, H., Chang, K.Y., Cholewa-Waclaw, J., Kelly, L., Beltran, M., Lewis, A., Elks, P.M., Hansen, C.G., Henderson, N.C. and Feng, Y. 2025. Oncogenic Ras activation in permissive somatic cells triggers rapid-onset phenotypic plasticity and elicits a tumor-promoting neutrophil response. *Cell Rep.* **44**(11), p116478.

Elo, B., Villano, C.M., Govorko, D. and White, L.A. 2007. Larval zebrafish as a model for glucose metabolism: expression of phosphoenolpyruvate carboxykinase as a marker for exposure to anti-diabetic compounds. *Journal of Molecular Endocrinology.* **38**(4), pp.433-440.

Emery, J.C., Richards, A.S., Dale, K.D., McQuaid, C.F., White, R.G., Denholm, J.T. and Houben, R. 2021. Self-clearance of Mycobacterium tuberculosis infection: implications for lifetime risk and population at-risk of tuberculosis disease. *Proc Biol Sci.* **288**(1943), p20201635.

Eom, D.S. and Parichy, D.M. 2017. A macrophage relay for long-distance signaling during postembryonic tissue remodeling. *Science.* **355**(6331), pp.1317-1320.

Epelman, S., Lavine, K.J., Beaudin, A.E., Sojka, D.K., Carrero, J.A., Calderon, B., Brija, T., Gautier, E.L., Ivanov, S., Satpathy, A.T., Schilling, J.D., Schwendener, R., Sergin, I., Razani, B., Forsberg, E.C., Yokoyama, W.M., Unanue, E.R., Colonna, M., Randolph, G.J. and Mann, D.L. 2014. Embryonic and adult-derived resident cardiac macrophages are maintained through distinct mechanisms at steady state and during inflammation. *Immunity.* **40**(1), pp.91-104.

Espinosa-Cueto, P., Escalera-Zamudio, M., Magallanes-Puebla, A., López-Marín, L.M., Segura-Salinas, E. and Mancilla, R. 2015. Mycobacterial glycolipids di-O-acylated trehalose and tri-O-acylated trehalose downregulate inducible nitric oxide synthase and nitric oxide production in macrophages. *BMC Immunol.* **16**, p38.

Espín-Palazón, R., Stachura, D.L., Campbell, C.A., García-Moreno, D., Del Cid, N., Kim, A.D., Candel, S., Meseguer, J., Mulero, V. and Traver, D. 2014. Proinflammatory signaling regulates hematopoietic stem cell emergence. *Cell.* **159**(5), pp.1070-1085.

Esser-von Bieren, J., Mosconi, I., Guiet, R., Piersgilli, A., Volpe, B., Chen, F., Gause, W.C., Seitz, A., Verbeek, J.S. and Harris, N.L. 2013. Antibodies Trap Tissue Migrating Helminth Larvae and Prevent Tissue Damage by Driving IL-4Rα-Independent Alternative Differentiation of Macrophages. *PLOS Pathogens.* **9**(11), pe1003771.

Evans, R.J., Pline, K., Loynes, C.A., Needs, S., Aldrovandi, M., Tiefenbach, J., Bielska, E., Rubino, R.E., Nicol, C.J., May, R.C., Krause, H.M., O'Donnell, V.B., Renshaw, S.A. and Johnston, S.A. 2019. 15-keto-prostaglandin E2 activates host peroxisome proliferator-activated receptor gamma (PPAR-γ) to promote Cryptococcus neoformans growth during infection. *PLOS Pathogens.* **15**(3), pe1007597.

Evans, S., Butler, J.R., Mattila, J.T. and Kirschner, D.E. 2020. Systems biology predicts that fibrosis in tuberculous granulomas may arise through macrophage-to-myofibroblast transformation. *PLoS Comput Biol.* **16**(12), pe1008520.

Faes, S., Hübner, M., Demartines, N. and Hahnloser, D. 2021. Cytokine clearance in serum and peritoneal fluid of patients undergoing damage control surgery with abdominal negative pressure therapy for abdominal sepsis. *Pleura Peritoneum.* © 2020 Seraina Faes et al., published by De Gruyter, Berlin/Boston., pp.31-38.

Faivre, A. and de Seigneux, S. 2024. The role of hypoxia in chronic kidney disease: a nuanced perspective. *Curr Opin Nephrol Hypertens.* **33**(4), pp.414-419.

Fallah, J., Heiss, B.L., Joeng, H.K., Weinstock, C., Gao, X., Pierce, W.F., Chukwurah, B., Bhatnagar, V., Fiero, M.H., Amiri-Kordestani, L., Pazdur, R., Kluetz, P.G. and Suzman, D.L. 2024. FDA Approval Summary: Belzutifan for Patients with Advanced Renal Cell Carcinoma. *Clin Cancer Res.* **30**(22), pp.5003-5008.

Faul, F., Erdfelder, E., Buchner, A. and Lang, A.-G. 2009. Statistical power analyses using G*Power 3.1: Tests for correlation and regression analyses. *Behavior Research Methods.* **41**(4), pp.1149-1160.

Felker, A. and Mosimann, C. 2016. Contemporary zebrafish transgenesis with Tol2 and application for Cre/lox recombination experiments. *Methods Cell Biol.* **135**, pp.219-244.

Feng, P. 2024. A spatial model to understand tuberculosis granuloma formation and its impact on disease progression. **25**(1), pp.19-35.

Feng, Y., Renshaw, S. and Martin, P. 2012. Live imaging of tumor initiation in zebrafish larvae reveals a trophic role for leukocyte-derived PGE_2. *Curr Biol.* **22**(13), pp.1253-1259.

Fernández-Regueras, M., Carbonell, C., Salete-Granado, D., García, J.L., Gragera, M., Pérez-Nieto, M., Morán-Plata, F.J., Mayado, A., Torres, J.L., Corchete, L.A., Usategui-Martín, R., Bueno-Martínez, E., Rojas-Pirela, M., Sabio, G., González-Sarmiento, R., Orfao, A., Laso, F.J., Almeida, J. and Marcos, M. 2023. Predominantly Pro-Inflammatory Phenotype with Mixed M1/M2 Polarization of Peripheral Blood Classical Monocytes and Monocyte-Derived Macrophages among Patients with Excessive Ethanol Intake. *Antioxidants (Basel).* **12**(9).

Ferrante, C.J. and Leibovich, S.J. 2012. Regulation of Macrophage Polarization and Wound Healing. *Adv Wound Care (New Rochelle).* United States, pp.10-16.

Ferreira, F.J., Carvalho, L., Logarinho, E. and Bessa, J. 2021. foxm1 Modulates Cell Non-Autonomous Response in Zebrafish Skeletal Muscle Homeostasis. *Cells.* **10**(5).

Ferreras-Colino, E., Contreras, M., Risalde, M.A., Sevilla, I.A., Delgado, E., Domínguez, L., Gortazar, C. and de la Fuente, J. 2024. Heat-inactivated mycobacteria activate the toll-like receptor 2 and 4 pathways in the zebrafish model of tuberculosis. *Vaccine.* **42**(3), pp.403-409.

Ferrero, E., Biswas, P., Vettoretto, K., Ferrarini, M., Uguccioni, M., Piali, L., Leone, B.E., Moser, B., Rugarli, C. and Pardi, R. 2003. Macrophages exposed to Mycobacterium tuberculosis release chemokines able to recruit selected leucocyte subpopulations: focus on gammadelta cells. *Immunology.* **108**(3), pp.365-374.

Ferrero, G., Mahony, C.B., Dupuis, E., Yvernogeau, L., Di Ruggiero, E., Miserocchi, M., Caron, M., Robin, C., Traver, D., Bertrand, J.Y. and Wittamer, V. 2018. Embryonic Microglia Derive from Primitive

Macrophages and Are Replaced by cmyb-Dependent Definitive Microglia in Zebrafish. *Cell Reports.* **24**(1), pp.130-141.

Fine, P.E. 1995. Variation in protection by BCG: implications of and for heterologous immunity. *Lancet.* **346**(8986), pp.1339-1345.

Finotto, S., Neurath, M.F., Glickman, J.N., Qin, S., Lehr, H.A., Green, F.H., Ackerman, K., Haley, K., Galle, P.R., Szabo, S.J., Drazen, J.M., De Sanctis, G.T. and Glimcher, L.H. 2002. Development of spontaneous airway changes consistent with human asthma in mice lacking T-bet. *Science.* **295**(5553), pp.336-338.

Fitzsimons, S., Muñoz-San Martín, M., Nally, F., Dillon, E., Fashina, I.A., Strowitzki, M.J., Ramió-Torrentà, L., Dowling, J.K., De Santi, C. and McCoy, C.E. 2023. Inhibition of pro-inflammatory signaling in human primary macrophages by enhancing arginase-2 via target site blockers. *Molecular Therapy Nucleic Acids.* **33**, pp.941-959.

Flannagan, R.S., Cosío, G. and Grinstein, S. 2009. Antimicrobial mechanisms of phagocytes and bacterial evasion strategies. *Nat Rev Microbiol.* **7**(5), pp.355-366.

Flynn, J.L., Gideon, H.P., Mattila, J.T. and Lin, P.L. 2015. Immunology studies in non-human primate models of tuberculosis. *Immunol Rev.* **264**(1), pp.60-73.

Forlenza, M., Fink, I.R., Raes, G. and Wiegertjes, G.F. 2011. Heterogeneity of macrophage activation in fish. *Dev Comp Immunol.* **35**(12), pp.1246-1255.

Foster, S.L., Hargreaves, D.C. and Medzhitov, R. 2007. Gene-specific control of inflammation by TLR-induced chromatin modifications. *Nature.* **447**(7147), pp.972-978.

Franklin, R.A., Liao, W., Sarkar, A., Kim, M.V., Bivona, M.R., Liu, K., Pamer, E.G. and Li, M.O. 2014. The cellular and molecular origin of tumor-associated macrophages. *Science.* **344**(6186), pp.921-925.

Fratti, R.A., Chua, J., Vergne, I. and Deretic, V. 2003. Mycobacterium tuberculosis glycosylated phosphatidylinositol causes phagosome maturation arrest. *Proc Natl Acad Sci U S A.* **100**(9), pp.5437-5442.

Frohnhöfer, H.G., Geiger-Rudolph, S., Pattky, M., Meixner, M., Huhn, C., Maischein, H.M., Geisler, R., Gehring, I., Maderspacher, F., Nüsslein-Volhard, C. and Irion, U. 2016. Spermidine, but not spermine, is essential for pigment pattern formation in zebrafish. *Biol Open.* **5**(6), pp.736-744.

Fuller Craig, L., Flynn JoAnne, L. and Reinhart Todd, A. 2003. *In situ* Studyof Abundant Expression of Proinflammatory Chemokines and Cytokines inPulmonary Granulomas That Develop in

Cynomolgus MacaquesExperimentally Infected with Mycobacteriumtuberculosis. *Infection and Immunity.* **71**(12), pp.7023-7034.

Gaines, S.W. 2022. *Tails of twists and turns: Using zebrafish to unravel neutrophil chromatin remodelling*. PhD thesis, University of Sheffield.

Galli, S.J., Borregaard, N. and Wynn, T.A. 2011. Phenotypic and functional plasticity of cells of innate immunity: macrophages, mast cells and neutrophils. *Nature Immunology.* **12**(11), pp.1035-1044.

Galloway, J.L., Wingert, R.A., Thisse, C., Thisse, B. and Zon, L.I. 2005. Loss of Gata1 but Not Gata2 Converts Erythropoiesis to Myelopoiesis in Zebrafish Embryos. *Developmental Cell.* **8**(1), pp.109-116.

Galván-Peña, S. and O'Neill, L.A. 2014. Metabolic reprograming in macrophage polarization. *Front Immunol.* **5**, p420.

Gao, L.Y., Guo, S., McLaughlin, B., Morisaki, H., Engel, J.N. and Brown, E.J. 2004. A mycobacterial virulence gene cluster extending RD1 is required for cytolysis, bacterial spreading and ESAT-6 secretion. *Mol Microbiol.* **53**(6), pp.1677-1693.

Gao, R.Y., Wang, M., Liu, Q., Feng, D., Wen, Y., Xia, Y., Colgan, S.P., Eltzschig, H.K. and Ju, C. 2020. Hypoxia-Inducible Factor-2α Reprograms Liver Macrophages to Protect Against Acute Liver Injury Through the Production of Interleukin-6. *Hepatology.* **71**(6), pp.2105-2117.

Ge, S.X., Jung, D. and Yao, R. 2020. ShinyGO: a graphical gene-set enrichment tool for animals and plants. *Bioinformatics.* **36**(8), pp.2628-2629.

Gharavi, A.T., Hanjani, N.A., Movahed, E. and Doroudian, M. 2022. The role of macrophage subtypes and exosomes in immunomodulation. *Cellular & Molecular Biology Letters.* **27**(1), p83.

Gibson, J.F., Bojarczuk, A., Evans, R.J., Kamuyango, A.A., Hotham, R., Lagendijk, A.K., Hogan, B.M., Ingham, P.W., Renshaw, S.A. and Johnston, S.A. 2022. Blood vessel occlusion by Cryptococcus neoformans is a mechanism for haemorrhagic dissemination of infection. *PLOS Pathogens.* **18**(4), pe1010389.

Gideon, H.P., Hughes, T.K., Tzouanas, C.N., Wadsworth, M.H., Tu, A.A., Gierahn, T.M., Peters, J.M., Hopkins, F.F., Wei, J.-R., Kummerlowe, C., Grant, N.L., Nargan, K., Phuah, J.Y., Borish, H.J., Maiello, P., White, A.G., Winchell, C.G., Nyquist, S.K., Ganchua, S.K.C., ... and Shalek, A.K. 2022. Multimodal profiling of lung granulomas in macaques reveals cellular correlates of tuberculosis control. *Immunity.* **55**(5), pp.827-846.e810.

Gilliland, H.N., Soverina, S., Conner, K.N., Vielma, T.E. and Olive, A.J. 2025. Differential activation of NF-κB and HIF-1α between alveolar-like macrophages and myeloid-derived macrophages drive inflammatory differences following Mycobacterium abscessus infection. *bioRxiv.* p2025.2004.2003.647026.

Glynn, J.R., Fielding, K., Mzembe, T., Sichali, L., Banda, L., McLean, E., Kanjala, C., Crampin, A.C., Ponnighaus, J.M., Warndorff, D.K. and Fine, P.E.M. 2021. BCG re-vaccination in Malawi: 30-year follow-up of a large, randomised, double-blind, placebo-controlled trial. *Lancet Glob Health.* **9**(10), pp.e1451-e1459.

Gobert, A.P., Cheng, Y., Wang, J.Y., Boucher, J.L., Iyer, R.K., Cederbaum, S.D., Casero, R.A., Jr., Newton, J.C. and Wilson, K.T. 2002. Helicobacter pylori induces macrophage apoptosis by activation of arginase II. *J Immunol.* **168**(9), pp.4692-4700.

Gobert, A.P., Daulouede, S., Lepoivre, M., Boucher, J.L., Bouteille, B., Buguet, A., Cespuglio, R., Veyret, B. and Vincendeau, P. 2000. L-Arginine availability modulates local nitric oxide production and parasite killing in experimental trypanosomiasis. *Infect Immun.* **68**(8), pp.4653-4657.

Gobert, A.P., McGee, D.J., Akhtar, M., Mendz, G.L., Newton, J.C., Cheng, Y., Mobley, H.L. and Wilson, K.T. 2001. Helicobacter pylori arginase inhibits nitric oxide production by eukaryotic cells: a strategy for bacterial survival. *Proc Natl Acad Sci U S A.* **98**(24), pp.13844-13849.

Gondin, J., Théret, M., Duhamel, G., Pegan, K., Mathieu, J.R.R., Peyssonnaux, C., Cuvellier, S., Latroche, C., Chazaud, B., Bendahan, D. and Mounier, R. 2015. Myeloid HIFs Are Dispensable for Resolution of Inflammation during Skeletal Muscle Regeneration. *The Journal of Immunology.* **194**(7), pp.3389-3399.

Gopal, A.A., Rappaz, B., Rouger, V., Martyn, I.B., Dahlberg, P.D., Meland, R.J., Beamish, I.V., Kennedy, T.E. and Wiseman, P.W. 2016. Netrin-1-Regulated Distribution of UNC5B and DCC in Live Cells Revealed by TICCS. *Biophys J.* **110**(3), pp.623-634.

Gordon, S. 2008. Elie Metchnikoff: father of natural immunity. *European journal of immunology.* **38**(12), pp.3257-3264.

Gordon, S. 2016. Phagocytosis: An Immunobiologic Process. *Immunity.* **44**(3), pp.463-475.

Gross, T.J., Kremens, K., Powers, L.S., Brink, B., Knutson, T., Domann, F.E., Philibert, R.A., Milhem, M.M. and Monick, M.M. 2014. Epigenetic silencing of the human NOS2 gene: rethinking the role of nitric oxide in human macrophage inflammatory responses. *J Immunol.* **192**(5), pp.2326-2338.

Grosset, J. 2003. Mycobacterium tuberculosis in the extracellular compartment: an underestimated adversary. *Antimicrob Agents Chemother.* **47**(3), pp.833-836.

Guerrero Quiles, C., Julia Gonzalez, A., Foussat, A.S., Olympitis, A., Lodhi, T., Smith, V., Reardon, M., Shabbir, R., Lunj, S., Reeves, K., Baker, A., Eyers, M., Marshall, G., Smith, T.A.D., Hoskin, P., James, N.D., Hall, E., Huddart, R.A., Porta, N., ... and West, C.M. 2025. Hypoxia-induced extracellular matrix changes are conserved in cancer and directly impact radiotherapy benefit. *bioRxiv.* p2025.2004.2004.647191.

Guha, M. and Mackman, N. 2001. LPS induction of gene expression in human monocytes. *Cellular Signalling.* **13**(2), pp.85-94.

Gui, P., Ben-Neji, M., Belozertseva, E., Dalenc, F., Franchet, C., Gilhodes, J., Labrousse, A., Bellard, E., Golzio, M., Poincloux, R., Maridonneau-Parini, I. and Le Cabec, V. 2018. The Protease-Dependent Mesenchymal Migration of Tumor-Associated Macrophages as a Target in Cancer Immunotherapy. *Cancer Immunology Research.* **6**(11), pp.1337-1351.

Guilliams, M., Bonnardel, J., Haest, B., Vanderborght, B., Wagner, C., Remmerie, A., Bujko, A., Martens, L., Thoné, T., Browaeys, R., De Ponti, F.F., Vanneste, B., Zwicker, C., Svedberg, F.R., Vanhalewyn, T., Gonçalves, A., Lippens, S., Devriendt, B., Cox, E., ... and Scott, C.L. 2022. Spatial proteogenomics reveals distinct and evolutionarily conserved hepatic macrophage niches. *Cell.* **185**(2), pp.379-396.e338.

Guilliams, M. and van de Laar, L. 2015. A Hitchhiker's Guide to Myeloid Cell Subsets: Practical Implementation of a Novel Mononuclear Phagocyte Classification System. *Frontiers in Immunology.* **Volume 6 - 2015**.

Guo, Y., Deng, Y., Huang, Z., Luo, Q., Peng, Y., Chen, J., Jiang, H., Ye, J. and Li, J. 2016. EBP50 induces apoptosis in macrophages by upregulating nitric oxide production to eliminate intracellular Mycobacterium tuberculosis. *Sci Rep.* **6**, p18961.

Hackett, E.E., Charles-Messance, H., O'Leary, S.M., Gleeson, L.E., Muñoz-Wolf, N., Case, S., Wedderburn, A., Johnston, D.G.W., Williams, M.A., Smyth, A., Ouimet, M., Moore, K.J., Lavelle, E.C., Corr, S.C., Gordon, S.V., Keane, J. and Sheedy, F.J. 2020. Mycobacterium tuberculosis Limits Host Glycolysis and IL-1β by Restriction of PFK-M via MicroRNA-21. *Cell Rep.* **30**(1), pp.124-136.e124.

Hamilton, N., Rutherford, H.A., Petts, J.J., Isles, H.M., Weber, T., Henneke, M., Gärtner, J., Dunning, M.J. and Renshaw, S.A. 2020. The failure of microglia to digest developmental apoptotic cells contributes to the pathology of RNASET2-deficient leukoencephalopathy. *Glia.* **68**(7), pp.1531-1545.

Hammer, D.X., Agrawal, A., Villanueva, R., Saeedi, O. and Liu, Z. 2020. Label-free adaptive optics imaging of human retinal macrophage distribution and dynamics. *Proceedings of the National Academy of Sciences.* **117**(48), pp.30661-30669.

Hammond, F. 2022. *Targeting host-derived signalling to activate leukocytes and improve infection outcomes in zebrafish models*. PhD thesis, University of Sheffield.

Hammond, F.R., Lewis, A. and Elks, P.M. 2020. If it's not one thing, HIF's another: immunoregulation by hypoxia inducible factors in disease. *The FEBS Journal.* **287**(18), pp.3907-3916.

Hammond, F.R., Lewis, A., Speirs, Z.C., Anderson, H.E., Sipka, T., Williams, L.G., Nguyen-Chi, M., Meijer, A.H., Wiegertjes, G.F. and Elks, P.M. 2023. An arginase 2 promoter transgenic illuminates immune cell polarisation in zebrafish. *Disease Models & Mechanisms.* pdmm.049966.

Hanna, N., Koliwer-Brandl, H., Lefrançois Louise, H., Kalinina, V., Cardenal-Muñoz, E., Appiah, J., Leuba, F., Gueho, A., Hilbi, H., Soldati, T. and Barisch, C. 2021. Zn2+ Intoxication of Mycobacterium marinum during Dictyostelium discoideum Infection Is Counteracted by Induction of the Pathogen Zn2+ Exporter CtpC. *mBio.* **12**(1), pp.10.1128/mbio.01313-01320.

Hansakon, A., Ngamphiw, C., Tongsima, S. and Angkasekwinai, P. 2022. Arginase 1 Expression by Macrophages Promotes Cryptococcus neoformans Proliferation and Invasion into Brain Microvascular Endothelial Cells. *The Journal of Immunology.* **210**(4), pp.408-419.

Hansakon, A., Png, C.W., Zhang, Y. and Angkasekwinai, P. 2021. Macrophage-Derived Osteopontin Influences the Amplification of Cryptococcus neoformans-Promoting Type 2 Immune Response. *J Immunol.* **207**(8), pp.2107-2117.

Hargreaves, S., Nellums, L.B., Johnson, C., Goldberg, J., Pantelidis, P., Rahman, A. and Friedland, F.J.S. 2020. Delivering multi-disease screening to migrants for latent TB and blood-borne viruses in an emergency department setting: A feasibility study. *Travel Med Infect Dis.* **36**, p101611.

Harjula, S.-K.E., Ojanen, M.J.T., Taavitsainen, S., Nykter, M. and Rämet, M. 2018. Interleukin 10 mutant zebrafish have an enhanced interferon gamma response and improved survival against a Mycobacterium marinum infection. *Scientific Reports.* **8**(1), p10360.

Hashimoto, D., Chow, A., Noizat, C., Teo, P., Beasley, M.B., Leboeuf, M., Becker, C.D., See, P., Price, J., Lucas, D., Greter, M., Mortha, A., Boyer, S.W., Forsberg, E.C., Tanaka, M., van Rooijen, N., García-Sastre, A., Stanley, E.R., Ginhoux, F., ... and Merad, M. 2013. Tissue-resident macrophages self-maintain locally throughout adult life with minimal contribution from circulating monocytes. *Immunity.* **38**(4), pp.792-804.

Hatherill, M. and Cobelens, F. 2022. Infant BCG vaccination is beneficial, but not sufficient. *The Lancet Global Health.* **10**(9), pp.e1220-e1221.

Haydar, D., Gonzalez, R., Garvy, B.A., Garneau-Tsodikova, S., Thamban Chandrika, N., Bocklage, T.J. and Feola, D.J. 2021. Myeloid arginase-1 controls excessive inflammation and modulates T cell responses in Pseudomonas aeruginosa pneumonia. *Immunobiology.* **226**(1), p152034.

Haynes, A.M., Ovadiuc, C., Peterson, G.J., Worodria, W., Nalukwago, S., Muwanguzi, T., Nsereko, M., Stein, C.M., Dill-McFarland, K.A., Mayanja-Kizza, H., Boom, W.H., Segnitz, R.M. and Hawn, T.R. 2025. Alveolar macrophage transcriptional signatures associated with resistance to TST/IGRA conversion following Mycobacterium tuberculosis exposure. *BMC Genomics.* **26**(1), p983.

He, L., Jhong, J.H., Chen, Q., Huang, K.Y., Strittmatter, K., Kreuzer, J., DeRan, M., Wu, X., Lee, T.Y., Slavov, N., Haas, W. and Marneros, A.G. 2021. Global characterization of macrophage polarization mechanisms and identification of M2-type polarization inhibitors. *Cell Rep.* **37**(5), p109955.

Heaster, T.M., Heaton, A.R., Sondel, P.M. and Skala, M.C. 2021. Intravital Metabolic Autofluorescence Imaging Captures Macrophage Heterogeneity Across Normal and Cancerous Tissue. *Front Bioeng Biotechnol.* **9**, p644648.

Heitmann, L., Abad Dar, M., Schreiber, T., Erdmann, H., Behrends, J., McKenzie, A.N.J., Brombacher, F., Ehlers, S. and Hölscher, C. 2014. The IL-13/IL-4Rα axis is involved in tuberculosis-associated pathology. *The Journal of Pathology.* **234**(3), pp.338-350.

Heldwein, K.A., Liang, M.D., Andresen, T.K., Thomas, K.E., Marty, A.M., Cuesta, N., Vogel, S.N. and Fenton, M.J. 2003. TLR2 and TLR4 serve distinct roles in the host immune response against Mycobacterium bovis BCG. *Journal of Leukocyte Biology.* **74**(2), pp.277-286.

Herbomel, P., Thisse, B. and Thisse, C. 1999. Ontogeny and behaviour of early macrophages in the zebrafish embryo. *Development.* **126**(17), pp.3735-3745.

Herbomel, P., Thisse, B. and Thisse, C. 2001. Zebrafish early macrophages colonize cephalic mesenchyme and developing brain, retina, and epidermis through a M-CSF receptor-dependent invasive process. *Dev Biol.* **238**(2), pp.274-288.

Hickman-Davis, J.M., O'Reilly, P., Davis, I.C., Peti-Peterdi, J., Davis, G., Young, K.R., Devlin, R.B. and Matalon, S. 2002. Killing of Klebsiella pneumoniae by human alveolar macrophages. *American Journal of Physiology-Lung Cellular and Molecular Physiology.* **282**(5), pp.L944-L956.

Hind, L.E., Lurier, E.B., Dembo, M., Spiller, K.L. and Hammer, D.A. 2016. Effect of M1-M2 Polarization on the Motility and Traction Stresses of Primary Human Macrophages. *Cell Mol Bioeng.* **9**(3), pp.455-465.

Hirai, K., Furusho, H., Hirota, K. and Sasaki, H. 2018. Activation of hypoxia-inducible factor 1 attenuates periapical inflammation and bone loss. *Int J Oral Sci.* **10**(2), p12.

Hirayama, D., Iida, T. and Nakase, H. 2017. The Phagocytic Function of Macrophage-Enforcing Innate Immunity and Tissue Homeostasis. *Int J Mol Sci.* **19**(1).

Hoegg, S., Brinkmann, H., Taylor, J.S. and Meyer, A. 2004. Phylogenetic timing of the fish-specific genome duplication correlates with the diversification of teleost fish. *J Mol Evol.* **59**(2), pp.190-203.

Hoerter, A., Petrucciani, A., Bonifacio, J., Arnett, E., Schlesinger, L.S. and Pienaar, E. 2025. Timing matters in macrophage/CD4+ T cell interactions: an agent-based model comparing Mycobacterium tuberculosis host-pathogen interactions between latently infected and naïve individuals. *mSystems.* **10**(3), pe0129024.

Hoffmann-Młodzianowska, M., Maksym, R.B., Pucia, K., Kuciak, M., Mackiewicz, A. and Kieda, C. 2024. Endometriosis development in relation to hypoxia: a murine model study. *Mol Med.* **30**(1), p195.

Hortle, E., Johnson, K.E., Johansen, M.D., Nguyen, T., Shavit, J.A., Britton, W.J., Tobin, D.M. and Oehlers, S.H. 2019. Thrombocyte Inhibition Restores Protective Immunity to Mycobacterial Infection in Zebrafish. *J Infect Dis.* **220**(3), pp.524-534.

Hosseini, R., Lamers, G.E.M., Bos, E., Hogendoorn, P.C.W., Koster, A.J., Meijer, A.H., Spaink, H.P. and Schaaf, M.J.M. 2021. The adapter protein Myd88 plays an important role in limiting mycobacterial growth in a zebrafish model for tuberculosis. *Virchows Arch.* **479**(2), pp.265-275.

Houben, D., Demangel, C., van Ingen, J., Perez, J., Baldeón, L., Abdallah, A.M., Caleechurn, L., Bottai, D., van Zon, M., de Punder, K., van der Laan, T., Kant, A., Bossers-de Vries, R., Willemsen, P., Bitter, W., van Soolingen, D., Brosch, R., van der Wel, N. and Peters, P.J. 2012. ESX-1-mediated translocation to the cytosol controls virulence of mycobacteria. *Cellular Microbiology.* **14**(8), pp.1287-1298.

Hourani, T., Perez-Gonzalez, A., Khoshmanesh, K., Luwor, R., Achuthan, A.A., Baratchi, S., O'Brien-Simpson, N.M. and Al-Hourani, A. 2023. Label-free macrophage phenotype classification using machine learning methods. *Sci Rep.* **13**(1), p5202.

Howe, K., Clark, M.D., Torroja, C.F., Torrance, J., Berthelot, C., Muffato, M., Collins, J.E., Humphray, S., McLaren, K., Matthews, L., McLaren, S., Sealy, I., Caccamo, M., Churcher, C., Scott, C., Barrett, J.C., Koch, R., Rauch, G.-J., White, S., ... and Stemple, D.L. 2013. The zebrafish reference genome sequence and its relationship to the human genome. *Nature.* **496**(7446), pp.498-503.

Hsieh, J.Y., Keating, M.T., Smith, T.D., Meli, V.S., Botvinick, E.L. and Liu, W.F. 2019. Matrix crosslinking enhances macrophage adhesion, migration, and inflammatory activation. *APL Bioengineering.* **3**(1), p016103.

Hsu, K., Traver, D., Kutok, J.L., Hagen, A., Liu, T.X., Paw, B.H., Rhodes, J., Berman, J.N., Zon, L.I., Kanki, J.P. and Look, A.T. 2004. The pu.1 promoter drives myeloid gene expression in zebrafish. *Blood.* **104**(5), pp.1291-1297.

Hu, C., Zhang, N., Hong, Y., Tie, R., Fan, D., Lin, A., Chen, Y., Xiang, L. and Shao, J. 2024a. *Single-cell RNA sequencing unveils the hidden powers of zebrafish kidney for generating both hematopoiesis and adaptive antiviral immunity*. eLife Sciences Publications, Ltd. 2024/03/05. Available from: http://dx.doi.org/10.7554/eLife.92424.2

Hu, C., Zhang, N., Hong, Y., Tie, R., Fan, D., Lin, A., Chen, Y., Xiang, L.-x. and Shao, J.-z. 2024b. Single-cell RNA sequencing unveils the hidden powers of zebrafish kidney for generating both hematopoiesis and adaptive antiviral immunity. *eLife.* **13**, pRP92424.

Hu, K., Tao, Y., Li, J., Liu, Z., Zhu, X. and Wang, Z. 2019. A Comparative Genomic and Phylogenetic Analysis of the Origin and Evolution of the CCN Gene Family. *Biomed Res Int.* **2019**, p8620878.

Hu, Y., Wei, X., Liao, Z., Gao, Y., Liu, X., Su, J. and Yuan, G. 2018. Transcriptome Analysis Provides Insights into the Markers of Resting and LPS-Activated Macrophages in Grass Carp (Ctenopharyngodon idella). *Int J Mol Sci.* **19**(11).

Huaman, M.A. and Sterling, T.R. 2019. Treatment of Latent Tuberculosis Infection-An Update. *Clin Chest Med.* **40**(4), pp.839-848.

Huang, L., Nazarova, E.V., Tan, S., Liu, Y. and Russell, D.G. 2018. Growth of Mycobacterium tuberculosis *in vivo* segregates with host macrophage metabolism and ontogeny. *Journal of Experimental Medicine.* **215**(4), pp.1135-1152.

Huang, L.E., Gu, J., Schau, M. and Bunn, H.F. 1998. Regulation of hypoxia-inducible factor 1alpha is mediated by an O2-dependent degradation domain via the ubiquitin-proteasome pathway. *Proc Natl Acad Sci U S A.* **95**(14), pp.7987-7992.

Huang, X., Wu, J., Xu, J., Wang, H., Chen, Z., Fan, X.-Y. and Hu, Z. 2025. Mycobacterium tuberculosis Antigen Rv1471 Induces Innate Immune Memory and Adaptive Immunity Against Infection. *The Journal of Infectious Diseases.* **231**(5), pp.1127-1140.

Huang, Z., Luo, Q., Guo, Y., Chen, J., Xiong, G., Peng, Y., Ye, J. and Li, J. 2015. Mycobacterium tuberculosis-Induced Polarization of Human Macrophage Orchestrates the Formation and Development of Tuberculous Granulomas *In vitro*. *PLOS ONE.* **10**(6), pe0129744.

Huante, M.B., Gupta, S., Calderon, V.C., Koo, S.J., Sinha, M., Luxon, B.A., Garg, N.J. and Endsley, J.J. 2016. Differential inflammasome activation signatures following intracellular infection of human macrophages with Mycobacterium bovis BCG or Trypanosoma cruzi. *Tuberculosis (Edinb).* **101s**, pp.S35-s44.

Huber, B. and Joshi, S. 2023. CNS tuberculoma in an immunocompetent patient: A case report of multi-drug hypersensitivity to RIPE therapy. *IDCases.* **33**, pe01886.

Huffnagle, G.B., Strieter, R.M., Standiford, T.J., McDonald, R.A., Burdick, M.D., Kunkel, S.L. and Toews, G.B. 1995. The role of monocyte chemotactic protein-1 (MCP-1) in the recruitment of monocytes and CD4+ T cells during a pulmonary Cryptococcus neoformans infection. *J Immunol.* **155**(10), pp.4790-4797.

Hui, Z., Dingjie, X., Yuan, Y., Zhongqiu, W., Na, M., Mingjian, B., Yu, G., Guangyuan, L., Xuemin, G., Shifeng, L., Yucong, G., Fang, Y., Summer, R. and Hong, X. 2018. Silicosis decreases bone mineral density in rats. *Toxicology and Applied Pharmacology.* **348**, pp.117-122.

Hulsen, T. 2022. DeepVenn--a web application for the creation of area-proportional Venn diagrams using the deep learning framework Tensorflow. js. *arXiv preprint arXiv:2210.04597.*

Hutchins, A.P., Diez, D. and Miranda-Saavedra, D. 2013. The IL-10/STAT3-mediated anti-inflammatory response: recent developments and future challenges. *Briefings in Functional Genomics.* **12**(6), pp.489-498.

Iijima, N., Mattei, L.M. and Iwasaki, A. 2011. Recruited inflammatory monocytes stimulate antiviral Th1 immunity in infected tissue. *Proceedings of the National Academy of Sciences.* **108**(1), pp.284-289.

Ikegami, H., Yamasaki, K., Ogawa, M., Nemoto, K., Akata, K., Noguchi, S., Fukuda, K., Kawanami, T., Mukae, H. and Yatera, K. 2022. Reduced phagocytic activity of human alveolar macrophages infected with Mycobacterium avium complex. *Journal of Infection and Chemotherapy.* **28**(11), pp.1506-1512.

Imtiyaz, H.Z., Williams, E.P., Hickey, M.M., Patel, S.A., Durham, A.C., Yuan, L.J., Hammond, R., Gimotty, P.A., Keith, B. and Simon, M.C. 2010. Hypoxia-inducible factor 2alpha regulates macrophage function in mouse models of acute and tumor inflammation. *J Clin Invest.* **120**(8), pp.2699-2714.

Iniesta, V., Carcelén, J., Molano, I., Peixoto Pablo, M.V., Redondo, E., Parra, P., Mangas, M., Monroy, I., Campo Maria, L., Nieto Carlos, G. and Corraliza, I. 2005. Arginase I Induction during Leishmania major Infection Mediates the Development of Disease. *Infection and Immunity.* **73**(9), pp.6085-6090.

Isles, H.M., Loynes, C.A., Alasmari, S., Kon, F.C., Henry, K.M., Kadochnikova, A., Hales, J., Muir, C.F., Keightley, M.-C., Kadirkamanathan, V., Hamilton, N., Lieschke, G.J., Renshaw, S.A. and Elks, P.M. 2021. Pioneer neutrophils release chromatin within *in vivo* swarms. *eLife.* **10**, pe68755.

Jaakkola, P., Mole, D.R., Tian, Y.M., Wilson, M.I., Gielbert, J., Gaskell, S.J., von Kriegsheim, A., Hebestreit, H.F., Mukherji, M., Schofield, C.J., Maxwell, P.H., Pugh, C.W. and Ratcliffe, P.J. 2001. Targeting of HIF-alpha to the von Hippel-Lindau ubiquitylation complex by O2-regulated prolyl hydroxylation. *Science.* **292**(5516), pp.468-472.

Jablonska, E., Ratajczak, W. and Jablonski, J. 2008. Role of the p38 MAPK pathway in induction of iNOS expression in human leukocytes. *Folia Biol (Krakow).* **56**(1-2), pp.83-89.

Jablonski, K.A., Amici, S.A., Webb, L.M., Ruiz-Rosado Jde, D., Popovich, P.G., Partida-Sanchez, S. and Guerau-de-Arellano, M. 2015. Novel Markers to Delineate Murine M1 and M2 Macrophages. *PLoS One.* **10**(12), pe0145342.

Jaeckel, G. 2014. *Immunopathogenesis of chronic Mycobacterium marinum infection in adult zebrafish (Danio rerio)*. PhD thesis, University of Stirling.

Jagannathan-Bogdan, M. and Zon, L.I. 2013. Hematopoiesis. *Development.* **140**(12), pp.2463-2467.

Jaggi, U., Yang, M., Matundan, H.H., Hirose, S., Shah, P.K., Sharifi, B.G. and Ghiasi, H. 2020. Increased phagocytosis in the presence of enhanced M2-like macrophage responses correlates with increased primary and latent HSV-1 infection. *PLoS Pathog.* **16**(10), pe1008971.

Jameson, V.J., Luke, T., Yan, Y., Hind, A., Evrard, M., Man, K., Mackay, L.K., Kallies, A., Villadangos, J.A., McWilliam, H.E.G. and Perez-Gonzalez, A. 2022. Unlocking autofluorescence in the era of full spectrum analysis: Implications for immunophenotype discovery projects. *Cytometry Part A.* **101**(11), pp.922-941.

Jamwal, S.V., Mehrotra, P., Singh, A., Siddiqui, Z., Basu, A. and Rao, K.V.S. 2016. Mycobacterial escape from macrophage phagosomes to the cytoplasm represents an alternate adaptation mechanism. *Scientific Reports.* **6**(1), p23089.

Jaso-Friedmann, L., Leary, J.H., 3rd and Evans, D.L. 1997. NCCRP-1: a novel receptor protein sequenced from teleost nonspecific cytotoxic cells. *Mol Immunol.* **34**(12-13), pp.955-965.

Jaśkiewicz, M., Moszyńska, A., Króliczewski, J., Cabaj, A., Bartoszewska, S., Charzyńska, A., Gebert, M., Dąbrowski, M., Collawn, J.F. and Bartoszewski, R. 2022. The transition from HIF-1 to HIF-2 during prolonged hypoxia results from reactivation of PHDs and HIF1A mRNA instability. *Cell Mol Biol Lett.* **27**(1), p109.

Jeelani, I., Moon, J.-S., da Cunha, F.F., Nasamran, C.A., Jeon, S., Zhang, X., Bandyopadhyay, G.K., Dobaczewska, K., Mikulski, Z., Hosseini, M., Liu, X., Kisseleva, T., Brenner, D.A., Singh, S., Loomba, R., Kim, M. and Lee, Y.S. 2024. HIF-2α drives hepatic Kupffer cell death and proinflammatory recruited macrophage activation in nonalcoholic steatohepatitis. *Science Translational Medicine.* **16**(764), peadi0284.

Jeong, J.W., Cha, H.J., Han, M.H., Hwang, S.J., Lee, D.S., Yoo, J.S., Choi, I.W., Kim, S., Kim, H.S., Kim, G.Y., Hong, S.H., Park, C., Lee, H.J. and Choi, Y.H. 2018. Spermidine Protects against Oxidative Stress in Inflammation Models Using Macrophages and Zebrafish. *Biomol Ther (Seoul).* **26**(2), pp.146-156.

Jiang, J., Hiron, T.K., Agbaedeng, T.A., Malhotra, Y., Drydale, E., Bancroft, J., Ng, E., Reschen, M.E., Davison, L.J. and O'Callaghan, C.A. 2024. A Novel Macrophage Subpopulation Conveys Increased Genetic Risk of Coronary Artery Disease. *Circulation Research.* **135**(1), pp.6-25.

Jiang, Q., Kumar, R., Zhao, Y., Subbian, S. and Shi, L. 2025. Arginine as host directed therapy in tuberculosis: insights from modulating arginine metabolism by supplementation and arginase inhibition. *One Health Advances.* **3**(1), p5.

Jiang, Z., Zhen, J., Abulikena, Y., Gao, C., Huang, L., Huang, T. and Xie, J. 2024. Mycobacterium tuberculosis VII secretion system effector molecule Rv2347c blocks the maturation of phagosomes and activates the STING/TBK1 signaling pathway to inhibit cell autophagy. *Microbiology Spectrum.* **12**(11), pp.e01188-01124.

Jindani, A., Harrison, T.S., Nunn, A.J., Phillips, P.P., Churchyard, G.J., Charalambous, S., Hatherill, M., Geldenhuys, H., McIlleron, H.M., Zvada, S.P., Mungofa, S., Shah, N.A., Zizhou, S., Magweta, L., Shepherd, J., Nyirenda, S., van Dijk, J.H., Clouting, H.E., Coleman, D., ... and Mitchison, D.A. 2014. High-dose rifapentine with moxifloxacin for pulmonary tuberculosis. *N Engl J Med.* **371**(17), pp.1599-1608.

Jo, K.W., Yoon, Y.S., Kim, H.W., Kim, J.Y. and Kang, Y.A. 2025. Diagnosis and Treatment of Latent Tuberculosis Infection in Adults in South Korea. *Tuberc Respir Dis (Seoul).* **88**(1), pp.56-68.

Jobe, T., Stephan, J., Wells, C.K., De Silva, M., Lorkiewicz, P.K., Hill, B.G. and Wysoczynski, M. 2025. Phase partitioning of the neutrophil oxidative burst is coordinated by accessory pathways of glucose metabolism and mitochondrial activity. *Journal of Biological Chemistry.* **301**(1), p108091.

Johannes, G., Carter, M.S., Eisen, M.B., Brown, P.O. and Sarnow, P. 1999. Identification of eukaryotic mRNAs that are translated at reduced cap binding complex eIF4F concentrations using a cDNA microarray. *Proc Natl Acad Sci U S A.* **96**(23), pp.13118-13123.

Johansen, M.D., Kasparian, J.A., Hortle, E., Britton, W.J., Purdie, A.C. and Oehlers, S.H. 2018. Mycobacterium marinum infection drives foam cell differentiation in zebrafish infection models. *Developmental & Comparative Immunology.* **88**, pp.169-172.

Jonasch, E., Donskov, F., Iliopoulos, O., Rathmell, W.K., Narayan Vivek, K., Maughan Benjamin , L., Oudard, S., Else, T., Maranchie Jodi, K., Welsh Sarah, J., Thamake, S., Park Eric, K., Perini Rodolfo, F., Linehan, W.M. and Srinivasan, R. 2021. Belzutifan for Renal Cell Carcinoma in von Hippel–Lindau Disease. *New England Journal of Medicine.* **385**(22), pp.2036-2046.

Jumper, J., Evans, R., Pritzel, A., Green, T., Figurnov, M., Ronneberger, O., Tunyasuvunakool, K., Bates, R., Žídek, A., Potapenko, A., Bridgland, A., Meyer, C., Kohl, S.A.A., Ballard, A.J., Cowie, A., Romera-Paredes, B., Nikolov, S., Jain, R., Adler, J., ... and Hassabis, D. 2021. Highly accurate protein structure prediction with AlphaFold. *Nature.* **596**(7873), pp.583-589.

Jun, J.-I. and Lau, L.F. 2020. CCN1 is an opsonin for bacterial clearance and a direct activator of Toll-like receptor signaling. *Nature Communications.* **11**(1), p1242.

Jun, J.I., Kim, K.H. and Lau, L.F. 2015. The matricellular protein CCN1 mediates neutrophil efferocytosis in cutaneous wound healing. *Nat Commun.* **6**, p7386.

Jung, J.Y., Madan-Lala, R., Georgieva, M., Rengarajan, J., Sohaskey, C.D., Bange, F.C. and Robinson, C.M. 2013. The intracellular environment of human macrophages that produce nitric oxide promotes growth of mycobacteria. *Infect Immun.* **81**(9), pp.3198-3209.

Juric, V., Chen, C.C. and Lau, L.F. 2012. TNFα-induced apoptosis enabled by CCN1/CYR61: pathways of reactive oxygen species generation and cytochrome c release. *PLoS One.* **7**(2), pe31303.

Kajimura, Y., Taguchi, A., Nagao, Y., Yamamoto, K., Masuda, K., Shibata, K., Asaoka, Y., Furutani-Seiki, M., Tanizawa, Y. and Ohta, Y. 2024. E4BP4 in macrophages induces an anti-inflammatory phenotype that ameliorates the severity of colitis. *Communications Biology.* **7**(1), p527.

Kalish, S.V., Lyamina, S.V., Usanova, E.A., Manukhina, E.B., Larionov, N.P. and Malyshev, I.Y. 2015. Macrophages Reprogrammed *In vitro* Towards the M1 Phenotype and Activated with LPS Extend Lifespan of Mice with Ehrlich Ascites Carcinoma. *Med Sci Monit Basic Res.* **21**, pp.226-234.

Kallemeijn, W.W., Spear, S., Walton, J., Bussi, C., Soudy, C., Flynn, H.R., Skehel, M., Carling, D., Solari, R., McNeish, I.A. and Tate, E.W. 2023. Abstract 439: From foe to friend: *In vivo* reprogramming of tumor-associated macrophages to an anti-cancer phenotype by modulating N-myristoyltransferase activity. *Cancer Research.* **83**(7_Supplement), pp.439-439.

Kallio, H., Tolvanen, M., Jänis, J., Pan, P.-w., Laurila, E., Kallioniemi, A., Kilpinen, S., Tuominen, V.J., Isola, J., Valjakka, J., Pastorekova, S., Pastorek, J. and Parkkila, S. 2011. Characterization of Non-Specific Cytotoxic Cell Receptor Protein 1: A New Member of the Lectin-Type Subfamily of F-Box Proteins. *PLOS ONE.* **6**(11), pe27152.

Kallio, P.J., Wilson, W.J., O'Brien, S., Makino, Y. and Poellinger, L. 1999. Regulation of the hypoxia-inducible transcription factor 1alpha by the ubiquitin-proteasome pathway. *J Biol Chem.* **274**(10), pp.6519-6525.

Kanehisa, M., Furumichi, M., Sato, Y., Ishiguro-Watanabe, M. and Tanabe, M. 2021. KEGG: integrating viruses and cellular organisms. *Nucleic Acids Research.* **49**(D1), pp.D545-D551.

Kangongwe, M.H., Mwanza, W., Mwamba, M., Mwenya, J., Muzyamba, J., Mzyece, J., Hamukale, A., Tembo, E., Nsama, D., Chimzizi, R., Mubanga, A., Tambatamba, B., Mudenda, S. and Lishimpi, K. 2024. Drug resistance profiles of Mycobacterium tuberculosis clinical isolates by genotype *MTB*DRplus line probe assay in Zambia: findings and implications. *JAC Antimicrob Resist.* **6**(4), pdlae122.

Karadima, E., Chavakis, T. and Alexaki, V.I. 2025. Arginine metabolism in myeloid cells in health and disease. *Seminars in Immunopathology.* **47**(1), p11.

Karnan, A., Jadhav, U., Ghewade, B., Ledwani, A. and Shivashankar, P. 2024. A Comprehensive Review on Long vs. Short Regimens in Multidrug-Resistant Tuberculosis (MDR-TB) Under Programmatic Management of Drug-Resistant Tuberculosis (PMDT). *Cureus.* **16**(1), pe52706.

Kavalukas, S.L., Uzgare, A.R., Bivalacqua, T.J. and Barbul, A. 2012. Arginase inhibition promotes wound healing in mice. *Surgery.* **151**(2), pp.287-295.

Keane, J., Gershon, S., Wise, R.P., Mirabile-Levens, E., Kasznica, J., Schwieterman, W.D., Siegel, J.N. and Braun, M.M. 2001. Tuberculosis associated with infliximab, a tumor necrosis factor alpha-neutralizing agent. *N Engl J Med.* **345**(15), pp.1098-1104.

Kelsh, R.N., Brand, M., Jiang, Y.-J., Heisenberg, C.-P., Lin, S., Haffter, P., Odenthal, J., Mullins, M.C., Eeden, F.J.M.v., Furutani-Seiki, M., Granato, M., Hammerschmidt, M., Kane, D.A., Warga, R.M., Beuchle, D., Vogelsang, L. and Nüsslein-Volhard, C. 1996. Zebrafish pigmentation mutations and the processes of neural crest development. *Development.* **123**(1), pp.369-389.

Kemmler, C.L., Moran, H.R., Murray, B.F., Scoresby, A., Klem, J.R., Eckert, R.L., Lepovsky, E., Bertho, S., Nieuwenhuize, S., Burger, S., D'Agati, G., Betz, C., Puller, A.C., Felker, A., Ditrychova, K., Bötschi, S., Affolter, M., Rohner, N., Lovely, C.B., ... and Mosimann, C. 2023. Next-generation plasmids for transgenesis in zebrafish and beyond. *Development.* **150**(8).

Kerber, E.L., Padberg, C., Koll, N., Schuetzhold, V., Fandrey, J. and Winning, S. 2020. The Importance of Hypoxia-Inducible Factors (HIF-1 and HIF-2) for the Pathophysiology of Inflammatory Bowel Disease. *International Journal of Molecular Sciences.* [Online]. **21**(22).

Khan, A., Singh, V.K., Hunter, R.L. and Jagannath, C. 2019. Macrophage heterogeneity and plasticity in tuberculosis. *Journal of Leukocyte Biology.* **106**(2), pp.275-282.

Khan, A., Zhang, K., Singh, V.K., Mishra, A., Kachroo, P., Bing, T., Won, J.H., Mani, A., Papanna, R., Mann, L.K., Ledezma-Campos, E., Aguillon-Duran, G., Canaday, D.H., David, S.A., Restrepo, B.I., Viet, N.N., Phan, H., Graviss, E.A., Musser, J.M., ... and Jagannath, C. 2022. Human M1 macrophages express unique innate immune response genes after mycobacterial infection to defend against tuberculosis. *Communications Biology.* **5**(1), p480.

Khmelinskii, A., Meurer, M., Ho, C.T., Besenbeck, B., Füller, J., Lemberg, M.K., Bukau, B., Mogk, A. and Knop, M. 2016. Incomplete proteasomal degradation of green fluorescent proteins in the context of tandem fluorescent protein timers. *Mol Biol Cell.* **27**(2), pp.360-370.

Kiazyk, S. and Ball, T.B. 2017. Latent tuberculosis infection: An overview. *Can Commun Dis Rep.* **43**(3-4), pp.62-66.

Kienle, K., Glaser, K.M., Eickhoff, S., Mihlan, M., Knöpper, K., Reátegui, E., Epple, M.W., Gunzer, M., Baumeister, R., Tarrant, T.K., Germain, R.N., Irimia, D., Kastenmüller, W. and Lämmermann, T. 2021. Neutrophils self-limit swarming to contain bacterial growth *in vivo*. *Science.* **372**(6548).

Kilinç, G., Saris, A., Ottenhoff, T.H.M. and Haks, M.C. 2021. Host-directed therapy to combat mycobacterial infections. *Immunol Rev.* **301**(1), pp.62-83.

Kim, B.H. and Zhang, G. 2020. Generating Stable Knockout Zebrafish Lines by Deleting Large Chromosomal Fragments Using Multiple gRNAs. *G3 (Bethesda).* **10**(3), pp.1029-1037.

Kim, H., Wang, S.Y., Kwak, G., Yang, Y., Kwon, I.C. and Kim, S.H. 2019. Exosome-Guided Phenotypic Switch of M1 to M2 Macrophages for Cutaneous Wound Healing. *Advanced Science.* **6**(20), p1900513.

Kim, K.H., Cheng, N. and Lau, L.F. 2022. Cellular communication network factor 1-stimulated liver macrophage efferocytosis drives hepatic stellate cell activation and liver fibrosis. *Hepatology Communications.* **6**(10).

Kim, M.J., Wainwright, H.C., Locketz, M., Bekker, L.G., Walther, G.B., Dittrich, C., Visser, A., Wang, W., Hsu, F.F., Wiehart, U., Tsenova, L., Kaplan, G. and Russell, D.G. 2010. Caseation of human tuberculosis granulomas correlates with elevated host lipid metabolism. *EMBO Mol Med.* **2**(7), pp.258-274.

Kim, S.-Y., Choi, J.-A., Choi, S., Kim, K.K., Song, C.-H. and Kim, E.-M. 2024. Advances in an *In vitro* Tuberculosis Infection Model Using Human Lung Organoids for Host-Directed Therapies. *PLOS Pathogens.* **20**(7), pe1012295.

Kim, S.H., Lee, K.M., Lee, G.S., Seong, J.W. and Kang, T.J. 2017. Rifampicin Alleviates Atopic Dermatitis-Like Response *in vivo* and *in vitro*. *Biomol Ther (Seoul).* **25**(6), pp.634-640.

Kim, S.M., Park, J.H., Chung, S.K., Kim, J.Y., Hwang, H.Y., Chung, K.C., Jo, I., Park, S.I. and Nam, J.H. 2004. Coxsackievirus B3 infection induces cyr61 activation via JNK to mediate cell death. *J Virol.* **78**(24), pp.13479-13488.

Kimura, Y., Hisano, Y., Kawahara, A. and Higashijima, S.-i. 2014. Efficient generation of knock-in transgenic zebrafish carrying reporter/driver genes by CRISPR/Cas9-mediated genome engineering. *Scientific Reports.* **4**(1), p6545.

Kirchhoff, R., Chromik, M.A. and Schebb, N.H. 2025. Phagocytosis is differentially regulated by LPS in M1- and M2-like macrophages via PGE2 formation and EP4 signaling. *Prostaglandins & Other Lipid Mediators.* **178**, p106998.

Knudsen-Clark, A.M., Mwangi, D., Cazarin, J., Morris, K., Baker, C., Hablitz, L.M., McCall, M.N., Kim, M. and Altman, B.J. 2024. Circadian rhythms of macrophages are altered by the acidic tumor microenvironment. *EMBO reports.* **25**(11), pp.5080-5112-5112.

Kocsy, K. 2021. *Role and Function of Macrophages in Symptomatic Carotid Stenosis*. PhD thesis, University of Sheffield.

Kocsy, K., Deshmukh, S., Nawaz, S., Ali, A.N., Baig, S., Balami, J.S., Majid, A., Kiss-Toth, E., Francis, S. and Redgrave, J. 2024. Reprogramming Human Inflammatory Macrophages in Symptomatic Carotid Stenosis: Potential Mechanisms for Stabilisation of Atherosclerotic Carotid Plaques. *bioRxiv.* p2024.2006.2011.598440.

Kocsy, K., Deshmukh, S., Nawaz, S., Ali, A.N., Baig, S., Balami, J.S., Majid, A., Kiss-Toth, E., Francis, S. and Redgrave, J. 2025. Reprogramming human macrophages in symptomatic carotid stenosis: Stabilization of atherosclerotic carotid plaques. *Atherosclerosis.* **404**, p119180.

Kong, X., Liu, W., Zhang, X., Zhou, C., Sun, X., Cheng, L., Lin, J., Xie, Z. and Li, J. 2023. HIF-1α inhibition in macrophages preserves acute liver failure by reducing IL-1β production. *The FASEB Journal.* **37**(9), pe23140.

Koscsó, B., Csóka, B., Kókai, E., Németh, Z.H., Pacher, P., Virág, L., Leibovich, S.J. and Haskó, G. 2013. Adenosine augments IL-10-induced STAT3 signaling in M2c macrophages. *J Leukoc Biol.* **94**(6), pp.1309-1315.

Kołodziej, T., Mielnicka, A., Dziob, D., Chojnacka, A.K., Rawski, M., Mazurkiewicz, J. and Rajfur, Z. 2023. Morphomigrational description as a new approach connecting cell's migration with its morphology. *Scientific Reports.* **13**(1), p11006.

Krishna Prasad, G.V.R., Grigsby, S.J., Erkenswick, G.A., Portal-Celhay, C., Mittal, E., Yang, G., Fallon, S.M., Chen, F., Klevorn, T., Jain, N., Li, Y., Mitreva, M., Martinot, A.J., Ernst, J.D. and Philips, J.A. 2025. Macrophage-T cell interactions promote SLAMF1 expression for enhanced TB defense. *Nature Communications.* **16**(1), p6794.

Krishnan, N., Robertson, B.D. and Thwaites, G. 2013. Pathways of IL-1β secretion by macrophages infected with clinical Mycobacterium tuberculosis strains. *Tuberculosis.* **93**(5), pp.538-547.

Kroner, A., Greenhalgh, Andrew D., Zarruk, Juan G., Passos dos Santos, R., Gaestel, M. and David, S. 2014. TNF and Increased Intracellular Iron Alter Macrophage Polarization to a Detrimental M1 Phenotype in the Injured Spinal Cord. *Neuron.* **83**(5), pp.1098-1116.

Kroon, E.E., Coussens, A.K., Kinnear, C., Orlova, M., Möller, M., Seeger, A., Wilkinson, R.J., Hoal, E.G. and Schurr, E. 2018. Neutrophils: Innate Effectors of TB Resistance? *Front Immunol.* **9**, p2637.

Krueger, G., Faisal, S. and Dorhoi, A. 2025. Microenvironments of tuberculous granuloma: advances and opportunities for therapy. *Frontiers in Immunology.* **Volume 16 - 2025**.

Krzywinska, E. and Stockmann, C. 2018. Hypoxia, Metabolism and Immune Cell Function. *Biomedicines.* **6**(2).

Kröger, M., Scheffel, J., Shirshin, E.A., Schleusener, J., Meinke, M.C., Lademann, J., Maurer, M. and Darvin, M.E. 2022. Label-free imaging of M1 and M2 macrophage phenotypes in the human dermis *in vivo* using two-photon excited FLIM. *eLife.* **11**, pe72819.

Kumar Jha, P., Aikawa, M. and Aikawa, E. 2024. Macrophage Heterogeneity and Efferocytosis: Beyond the M1/M2 Dichotomy. *Circulation Research.* **134**(2), pp.186-188.

Kumar, P., Cameron, J., Saviola, B. and Venketaraman, V. 2025. Mycobacterium marinum Immune Evasion in Zebrafish. *Pathogens.* [Online]. **14**(9), p908.

Kumar, R., Kolloli, A., Bhargavi, G., Husain, S., Ghanny, S., Soteropoulos, P. and Subbian, S. 2025. Inflammasome activation differences underpin different Mycobacterium tuberculosis infection outcomes. *bioRxiv.* p2025.2006.2006.658135.

Kumari, A., Pahuja, I., Negi, K., Ghoshal, A., Mukopadhyay, S., Agarwal, M., Mathew, B., Maras, J.S., Chaturvedi, S., Bhaskar, A. and Dwivedi, V.P. 2023. Withaferin A Protects against Primary and Recurrent Tuberculosis by Modulating Mycobacterium-Specific Host Immune Responses. *Microbiol Spectr.* **11**(2), pe0058323.

Kurenuma, T., Kawamura, I., Hara, H., Uchiyama, R., Daim, S., Dewamitta, S.R., Sakai, S., Tsuchiya, K., Nomura, T. and Mitsuyama, M. 2009. The RD1 locus in the Mycobacterium tuberculosis genome contributes to activation of caspase-1 via induction of potassium ion efflux in infected macrophages. *Infect Immun.* **77**(9), pp.3992-4001.

Kurozumi, K., Hardcastle, J., Thakur, R., Shroll, J., Nowicki, M., Otsuki, A., Chiocca, E.A. and Kaur, B. 2008. Oncolytic HSV-1 infection of tumors induces angiogenesis and upregulates CYR61. *Mol Ther.* **16**(8), pp.1382-1391.

Lahiri, A., Das, P. and Chakravortty, D. 2008. Arginase modulates Salmonella induced nitric oxide production in RAW264.7 macrophages and is required for Salmonella pathogenesis in mice model of infection. *Microbes and Infection.* **10**(10), pp.1166-1174.

Lange, S.M., McKell, M.C., Schmidt, S.M., Hossfeld, A.P., Chaturvedi, V., Kinder, J.M., McAlees, J.W., Lewkowich, I.P., Way, S.S., Turner, J. and Qualls, J.E. 2017. l-Citrulline Metabolism in Mice Augments CD4(+) T Cell Proliferation and Cytokine Production *In vitro*, and Accumulation in the Mycobacteria-Infected Lung. *Front Immunol.* **8**, p1561.

Larenas-Muñoz, F., Hamed, M.G., Ruedas-Torres, I., María Sánchez-Carvajal, J., Domínguez, J., José Pallarés, F., Carrasco, L., Rodríguez-Gómez, I.M. and Gómez-Laguna, J. 2024. Macrophage polarization in lymph node granulomas from cattle and pigs naturally infected with Mycobacterium tuberculosis complex. *Veterinary Pathology.* **61**(5), pp.792-802.

Latour, Y.L., Gobert, A.P. and Wilson, K.T. 2020. The role of polyamines in the regulation of macrophage polarization and function. *Amino Acids.* **52**(2), pp.151-160.

Lauterbach, M.A., Hanke, J.E., Serefidou, M., Mangan, M.S.J., Kolbe, C.-C., Hess, T., Rothe, M., Kaiser, R., Hoss, F., Gehlen, J., Engels, G., Kreutzenbeck, M., Schmidt, S.V., Christ, A., Imhof, A., Hiller, K. and Latz, E. 2019. Toll-like Receptor Signaling Rewires Macrophage Metabolism and Promotes Histone Acetylation via ATP-Citrate Lyase. *Immunity.* **51**(6), pp.997-1011.e1017.

Le, Y., Cao, W., Zhou, L., Fan, X., Liu, Q., Liu, F., Gai, X., Chang, C., Xiong, J., Rao, Y., Li, A., Xu, W., Liu, B., Wang, T., Wang, B. and Sun, Y. 2020. Infection of Mycobacterium tuberculosis Promotes Both M1/M2 Polarization and MMP Production in Cigarette Smoke-Exposed Macrophages. *Front Immunol.* **11**, p1902.

Lee, C.J., Paull, G.C. and Tyler, C.R. 2022. Improving zebrafish laboratory welfare and scientific research through understanding their natural history. *Biological Reviews.* **97**(3), pp.1038-1056.

Lee, H.C., Lin, C.Y. and Tsai, H.J. 2021. Zebrafish, an *In vivo* Platform to Screen Drugs and Proteins for Biomedical Use. *Pharmaceuticals (Basel).* **14**(6).

Lee, J.-W., Bae, S.-H., Jeong, J.-W., Kim, S.-H. and Kim, K.-W. 2004. Hypoxia-inducible factor (HIF-1)α: its protein stability and biological functions. *Experimental & Molecular Medicine.* **36**(1), pp.1-12.

Lee, J.-W., Lee, I.-H., Iimura, T. and Kong, S.W. 2021. Two macrophages, osteoclasts and microglia: from development to pleiotropy. *Bone Research.* **9**(1), p11.

Leiba, J., Sipka, T., Begon-Pescia, C., Bernardello, M., Tairi, S., Bossi, L., Gonzalez, A.-A., Mialhe, X., J. Gualda, E., Loza-Alvarez, P., Blanc-Potard, A., Lutfalla, G. and Nguyen-Chi, M. 2023. Dynamics of macrophage polarization support Salmonella persistence in a whole living organism. *bioRxiv.* p2023.2005.2009.539693.

Lerner, T.R., Borel, S., Greenwood, D.J., Repnik, U., Russell, M.R., Herbst, S., Jones, M.L., Collinson, L.M., Griffiths, G. and Gutierrez, M.G. 2017. Mycobacterium tuberculosis replicates within necrotic human macrophages. *J Cell Biol.* **216**(3), pp.583-594.

Levitte, S., Adams, Kristin N., Berg, Russell D., Cosma, Christine L., Urdahl, Kevin B. and Ramakrishnan, L. 2016. Mycobacterial Acid Tolerance Enables Phagolysosomal Survival and Establishment of Tuberculous Infection *In vivo*. *Cell Host & Microbe.* **20**(2), pp.250-258.

Lewis, A. and Elks, P.M. 2019. Hypoxia Induces Macrophage tnfa Expression via Cyclooxygenase and Prostaglandin E2 *in vivo*. *Front Immunol.* **10**, p2321.

Lewis, N.D., Asim, M., Barry, D.P., Singh, K., de Sablet, T., Boucher, J.L., Gobert, A.P., Chaturvedi, R. and Wilson, K.T. 2010. Arginase II restricts host defense to Helicobacter pylori by attenuating inducible nitric oxide synthase translation in macrophages. *J Immunol.* **184**(5), pp.2572-2582.

Li, C., Wang, J., Xu, J.-F., Pi, J. and Zheng, B. 2024. Roles of HIF-1α signaling in Mycobacterium tuberculosis infection: New targets for anti-TB therapeutics? *Biochemical and Biophysical Research Communications.* **711**, p149920.

Li, C., Wang, Y., Li, Y., Yu, Q., Jin, X., Wang, X., Jia, A., Hu, Y., Han, L., Wang, J., Yang, H., Yan, D., Bi, Y. and Liu, G. 2018. HIF1α-dependent glycolysis promotes macrophage functional activities in protecting against bacterial and fungal infection. *Scientific Reports.* **8**(1), p3603.

Li, C.-X., Zhang, Y., Dong, X., Zhang, L., Liu, M.-D., Li, B., Zhang, M.-K., Feng, J. and Zhang, X.-Z. 2019. Artificially Reprogrammed Macrophages as Tumor-Tropic Immunosuppression-Resistant Biologics to Realize Therapeutics Production and Immune Activation. *Advanced Materials.* **31**(15), p1807211.

Li, H., Chee, C.B.E., Geng, T., Pan, A. and Koh, W.P. 2022. Joint Associations of Multiple Lifestyle Factors With Risk of Active Tuberculosis in the Population: The Singapore Chinese Health Study. *Clin Infect Dis.* **75**(2), pp.213-220.

Li, H., Du, R., Xiang, A., Liu, Y., Guan, M. and He, H. 2024. Bone marrow mesenchymal stem cell-derived exosomal miR-181a-5p promotes M2 macrophage polarization to alleviate acute pancreatitis through ZEB2-mediated RACK1 ubiquitination. *The FASEB Journal.* **38**(23), pe70042.

Li, J., Wang, Y., He, L., Yang, L., Tao, T., Bai, L. and Luo, Y. 2025. Host-directed therapeutic targets in macrophages and their ligands against mycobacteria tuberculosis. *Infection and Immunity.* **93**(10), pp.e00063-00025.

Li, L., Jin, H., Xu, J., Shi, Y. and Wen, Z. 2011. Irf8 regulates macrophage versus neutrophil fate during zebrafish primitive myelopoiesis. *Blood.* **117**(4), pp.1359-1369.

Li, L., Yan, B., Shi, Y.Q., Zhang, W.Q. and Wen, Z.L. 2012. Live imaging reveals differing roles of macrophages and neutrophils during zebrafish tail fin regeneration. *J Biol Chem.* **287**(30), pp.25353-25360.

Li, P., Ma, C., Li, J., You, S., Dang, L., Wu, J., Hao, Z., Zhi, Y., Chen, L. and Sun, S. 2022. Proteomic characterization of four subtypes of M2 macrophages derived from human THP-1 cells. *J Zhejiang Univ Sci B.* **23**(5), pp.407-422.

Li, X., Zhang, X., Xia, J., Zhang, L., Chen, B., Lian, G., Yun, C., Yang, J., Yan, Y., Wang, P., Wang, X., Liu, B., Liu, H., Liang, H., Pang, Y., Wang, X. and Jiang, C. 2021. Macrophage HIF-2α suppresses NLRP3 inflammasome activation and alleviates insulin resistance. *Cell Reports.* **36**(8), p109607.

Li, Y., He, Y., Miao, K., Zheng, Y., Deng, C. and Liu, T.M. 2020. Imaging of macrophage mitochondria dynamics *in vivo* reveals cellular activation phenotype for diagnosis. *Theranostics.* **10**(7), pp.2897-2917.

Li, Y.-Q., Shi, R.-Z., Pan, Y.-Q., Shah, P.T. and Xing, L. 2025. Impact of sodium butyrate on lipopolysaccharide-induced inflammatory response in zebrafish. *International Immunopharmacology.* **165**, p115501.

Liang, J., Ran, Y., Hu, C., Zhou, J., Ye, L., Su, W., Liu, Z. and Xi, J. 2025. Inhibition of HIF-1α ameliorates pulmonary fibrosis by suppressing M2 macrophage polarization through PRMT1/STAT6 signals. *International Immunopharmacology.* **146**, p113931.

Liang, X., Arullampalam, P., Yang, Z. and Ming, X.-F. 2019. Hypoxia Enhances Endothelial Intercellular Adhesion Molecule 1 Protein Level Through Upregulation of Arginase Type II and Mitochondrial Oxidative Stress. *Frontiers in Physiology.* **Volume 10 - 2019**.

Liao, X., Shen, Y., Zhang, R., Sugi, K., Vasudevan, N.T., Alaiti, M.A., Sweet, D.R., Zhou, L., Qing, Y., Gerson, S.L., Fu, C., Wynshaw-Boris, A., Hu, R., Schwartz, M.A., Fujioka, H., Richardson, B., Cameron, M.J., Hayashi, H., Stamler, J.S. and Jain, M.K. 2018. Distinct roles of resident and nonresident macrophages in nonischemic cardiomyopathy. *Proceedings of the National Academy of Sciences.* **115**(20), pp.E4661-E4669.

Liebold, I., Al Jawazneh, A., Casar, C., Lanzloth, C., Leyk, S., Hamley, M., Wong, M.N., Kylies, D., Gräfe, S.K., Edenhofer, I., Aranda-Pardos, I., Kriwet, M., Haas, H., Krause, J., Hadjilaou, A., Schromm, A.B., Richardt, U., Eggert, P., Tappe, D., ... and Bosurgi, L. 2024. Apoptotic cell identity induces distinct functional responses to IL-4 in efferocytic macrophages. *Science.* **384**(6691), peabo7027.

Lienard, J., Nobs, E., Lovins, V., Movert, E., Valfridsson, C. and Carlsson, F. 2020. The Mycobacterium marinum ESX-1 system mediates phagosomal permeabilization and type I interferon production via separable mechanisms. *Proc Natl Acad Sci U S A.* **117**(2), pp.1160-1166.

Lieschke, G.J., Oates, A.C., Crowhurst, M.O., Ward, A.C. and Layton, J.E. 2001. Morphologic and functional characterization of granulocytes and macrophages in embryonic and adult zebrafish. *Blood.* **98**(10), pp.3087-3096.

Lin, J., Lin, H.-w., Wang, Y.-x., Fang, Y., Jiang, H.-m., Li, T., Huang, J., Zhang, H.-d., Chen, D.-z. and Chen, Y.-p. 2024. FGF4 ameliorates the liver inflammation by reducing M1 macrophage polarization in experimental autoimmune hepatitis. *Journal of Translational Medicine.* **22**(1), p717.

Lin, P.L., Ford, C.B., Coleman, M.T., Myers, A.J., Gawande, R., Ioerger, T., Sacchettini, J., Fortune, S.M. and Flynn, J.L. 2014. Sterilization of granulomas is common in active and latent tuberculosis despite within-host variability in bacterial killing. *Nat Med.* **20**(1), pp.75-79.

Liongue, C., Hall, C.J., O'Connell, B.A., Crosier, P. and Ward, A.C. 2009. Zebrafish granulocyte colony-stimulating factor receptor signaling promotes myelopoiesis and myeloid cell migration. *Blood.* **113**(11), pp.2535-2546.

Lister, J.A., Robertson, C.P., Lepage, T., Johnson, S.L. and Raible, D.W. 1999. nacre encodes a zebrafish microphthalmia-related protein that regulates neural-crest-derived pigment cell fate. *Development.* **126**(17), pp.3757-3767.

Liu, J., Guan, L., Wang, E., Schuchman, E.H., He, X. and Zeng, M. 2021. SiO(2) stimulates macrophage stress to induce the transformation of lung fibroblasts into myofibroblasts and its relationship with the sphingomyelin metabolic pathway. *J Appl Toxicol.* **41**(10), pp.1584-1597.

Liu, J., Yuan, X., Fan, C. and Ma, G. 2024. Application of the zebrafish model in human viral research. *Virus Research.* **341**, p199327.

Liu, L., Lu, Y., Martinez, J., Bi, Y., Lian, G., Wang, T., Milasta, S., Wang, J., Yang, M., Liu, G., Green, D.R. and Wang, R. 2016. Proinflammatory signal suppresses proliferation and shifts macrophage metabolism from Myc-dependent to HIF1α-dependent. *Proceedings of the National Academy of Sciences.* **113**(6), pp.1564-1569.

Liu, R., Muliadi, V., Mou, W., Li, H., Yuan, J., Holmberg, J., Chambers, B.J., Ullah, N., Wurth, J., Alzrigat, M., Schlisio, S., Carow, B., Larsson, L.G. and Rottenberg, M.E. 2022. HIF-1 stabilization in T cells hampers the control of Mycobacterium tuberculosis infection. *Nature Communications.* **13**(1), p5093.

Lodge, K.M., Cowburn, A.S., Li, W. and Condliffe, A.M. 2020. The Impact of Hypoxia on Neutrophil Degranulation and Consequences for the Host. *Int J Mol Sci.* **21**(4).

Lombardi, O., Li, R., Halim, S., Choudhry, H., Ratcliffe, P.J. and Mole, D.R. 2022. Pan-cancer analysis of tissue and single-cell HIF-pathway activation using a conserved gene signature. *Cell Rep.* **41**(7), p111652.

Loynes, C.A., Lee, J.A., Robertson, A.L., Steel, M.J., Ellett, F., Feng, Y., Levy, B.D., Whyte, M.K.B. and Renshaw, S.A. 2018. PGE(2) production at sites of tissue injury promotes an anti-inflammatory neutrophil phenotype and determines the outcome of inflammation resolution *in vivo*. *Sci Adv.* **4**(9), peaar8320.

Loynes, C.A., Martin, J.S., Robertson, A., Trushell, D.M., Ingham, P.W., Whyte, M.K. and Renshaw, S.A. 2010. Pivotal Advance: Pharmacological manipulation of inflammation resolution during spontaneously resolving tissue neutrophilia in the zebrafish. *J Leukoc Biol.* **87**(2), pp.203-212.

Lu, F., Leach, L.L. and Gross, J.M. 2022. mTOR activity is essential for retinal pigment epithelium regeneration in zebrafish. *PLOS Genetics.* **18**(3), pe1009628.

Lu, X.J., Chen, Q., Rong, Y.J., Chen, F. and Chen, J. 2017. CXCR3.1 and CXCR3.2 Differentially Contribute to Macrophage Polarization in Teleost Fish. *J Immunol.* **198**(12), pp.4692-4706.

Lundahl, M.L.E., Mitermite, M., Ryan, D.G., Case, S., Williams, N.C., Yang, M., Lynch, R.I., Lagan, E., Lebre, F.M., Gorman, A.L., Stojkovic, B., Bracken, A.P., Frezza, C., Sheedy, F.J., Scanlan, E.M., O'Neill, L.A.J., Gordon, S.V. and Lavelle, E.C. 2022. Macrophage innate training induced by IL-4 and IL-13 activation enhances OXPHOS driven anti-mycobacterial responses. *eLife.* **11**, pe74690.

Luo, G., Wen, Y., Wang, M., Wang, H., Li, D., Liao, M., Zeng, D., Luo, S., Niu, L., Sun, T., Sun, P., Qin, L., Li, W., Song, S., Takiff, H.E., Zhang, S., Gao, Q., Zhang, Z. and Yan, B. 2025. A granulin-positive macrophage subtype in mycobacterial granulomas alleviates tissue damage by limiting excessive inflammation. *Proceedings of the National Academy of Sciences.* **122**(31), pe2413946122.

Luo, G., Zeng, D., Liu, J., Li, D., Takiff, H.E., Song, S., Gao, Q. and Yan, B. 2024. Temporal and cellular analysis of granuloma development in mycobacterial infected adult zebrafish. *Journal of Leukocyte Biology.* **115**(3), pp.525-535.

Lurier, E.B., Dalton, D., Dampier, W., Raman, P., Nassiri, S., Ferraro, N.M., Rajagopalan, R., Sarmady, M. and Spiller, K.L. 2017. Transcriptome analysis of IL-10-stimulated (M2c) macrophages by next-generation sequencing. *Immunobiology.* **222**(7), pp.847-856.

Ly, L.H., Russell, M.I. and McMurray, D.N. 2008. Cytokine Profiles in Primary and Secondary Pulmonary Granulomas of Guinea Pigs with Tuberculosis. *American Journal of Respiratory Cell and Molecular Biology.* **38**(4), pp.455-462.

Ma, C., Wu, M., Ye, W., Huang, Z., Ma, X., Wang, W., Wang, W., Huang, Y., Pan, X. and Wu, C. 2021. Inhalable solid lipid nanoparticles for intracellular tuberculosis infection therapy: macrophage-

targeting and pH-sensitive properties. *Drug Delivery and Translational Research.* **11**(3), pp.1218-1235.

Mackaness, G.B. 1962. Cellular resistance to infection. *J Exp Med.* **116**(3), pp.381-406.

Madigan, C.A., Cambier, C.J., Kelly-Scumpia, K.M., Scumpia, P.O., Cheng, T.Y., Zailaa, J., Bloom, B.R., Moody, D.B., Smale, S.T., Sagasti, A., Modlin, R.L. and Ramakrishnan, L. 2017. A Macrophage Response to Mycobacterium leprae Phenolic Glycolipid Initiates Nerve Damage in Leprosy. *Cell.* **170**(5), pp.973-985.e910.

Magez, S., Radwanska, M., Drennan, M., Fick, L., Baral, T.N., Allie, N., Jacobs, M., Nedospasov, S., Brombacher, F., Ryffel, B. and De Baetselier, P. 2007. Tumor necrosis factor (TNF) receptor-1 (TNFp55) signal transduction and macrophage-derived soluble TNF are crucial for nitric oxide-mediated Trypanosoma congolense parasite killing. *J Infect Dis.* **196**(6), pp.954-962.

Mahajan, S., Dkhar, H.K., Chandra, V., Dave, S., Nanduri, R., Janmeja, A.K., Agrewala, J.N. and Gupta, P. 2012. Mycobacterium tuberculosis Modulates Macrophage Lipid-Sensing Nuclear Receptors PPARγ and TR4 for Survival. *The Journal of Immunology.* **188**(11), pp.5593-5603.

Mai, D., Jahn, A., Murray, T., Morikubo, M., Lim, P.N., Cervantes, M.M., Pham, L.K., Nemeth, J., Urdahl, K., Diercks, A.H., Aderem, A. and Rothchild, A.C. 2024. Exposure to Mycobacterium remodels alveolar macrophages and the early innate response to Mycobacterium tuberculosis infection. *PLOS Pathogens.* **20**(1), pe1011871.

Mancino, G., Placido, R., Bach, S., Mariani, F., Montesano, C., Ercoli, L., Zembala, M. and Colizzi, V. 1997. Infection of Human Monocytes with Mycobacterium tuberculosis Enhances Human Immunodeficiency Virus Type 1 Replication and Transmission to T Cells. *The Journal of Infectious Diseases.* **175**(6), pp.1531-1535.

Mangtani, P., Abubakar, I., Ariti, C., Beynon, R., Pimpin, L., Fine, P.E., Rodrigues, L.C., Smith, P.G., Lipman, M., Whiting, P.F. and Sterne, J.A. 2014. Protection by BCG vaccine against tuberculosis: a systematic review of randomized controlled trials. *Clin Infect Dis.* **58**(4), pp.470-480.

Mantovani, A., Sica, A., Sozzani, S., Allavena, P., Vecchi, A. and Locati, M. 2004. The chemokine system in diverse forms of macrophage activation and polarization. *Trends Immunol.* England, pp.677-686.

Marakalala, M.J., Raju, R.M., Sharma, K., Zhang, Y.J., Eugenin, E.A., Prideaux, B., Daudelin, I.B., Chen, P.Y., Booty, M.G., Kim, J.H., Eum, S.Y., Via, L.E., Behar, S.M., Barry, C.E., 3rd, Mann, M., Dartois, V. and Rubin, E.J. 2016. Inflammatory signaling in human tuberculosis granulomas is spatially organized. *Nat Med.* **22**(5), pp.531-538.

Marelli-Berg, F.M. and Jangani, M. 2018. Metabolic regulation of leukocyte motility and migration. *J Leukoc Biol.* **104**(2), pp.285-293.

Margul, D.J., Park, J., Boehler, R.M., Smith, D.R., Johnson, M.A., McCreedy, D.A., He, T., Ataliwala, A., Kukushliev, T.V., Liang, J., Sohrabi, A., Goodman, A.G., Walthers, C.M., Shea, L.D. and Seidlits, S.K. 2016. Reducing neuroinflammation by delivery of IL-10 encoding lentivirus from multiple-channel bridges. *Bioeng Transl Med.* **1**(2), pp.136-148.

Marinkovic, M., Dai, Q., Gonzalez, A.O., Tran, O.N., Block, T.J., Harris, S.E., Salmon, A.B., Yeh, C.-K., Dean, D.D. and Chen, X.-D. 2022. Matrix-bound Cyr61/CCN1 is required to retain the properties of the bone marrow mesenchymal stem cell niche but is depleted with aging. *Matrix Biology.* **111**, pp.108-132.

Marino, S., Cilfone, N.A., Mattila, J.T., Linderman, J.J., Flynn, J.L. and Kirschner, D.E. 2015. Macrophage polarization drives granuloma outcome during Mycobacterium tuberculosis infection. *Infect Immun.* **83**(1), pp.324-338.

Marjoram, L., Alvers, A., Deerhake, M.E., Bagwell, J., Mankiewicz, J., Cocchiaro, J.L., Beerman, R.W., Willer, J., Sumigray, K.D., Katsanis, N., Tobin, D.M., Rawls, J.F., Goll, M.G. and Bagnat, M. 2015. Epigenetic control of intestinal barrier function and inflammation in zebrafish. *Proc Natl Acad Sci U S A.* **112**(9), pp.2770-2775.

Marshall, B.G., Chambers, M.A., Wangoo, A., Shaw, R.J. and Young, D.B. 1997. Production of tumor necrosis factor and nitric oxide by macrophages infected with live and dead mycobacteria and their suppression by an interleukin-10-secreting recombinant. *Infect Immun.* **65**(5), pp.1931-1935.

Marshall, J.S., Warrington, R., Watson, W. and Kim, H.L. 2018. An introduction to immunology and immunopathology. *Allergy, Asthma & Clinical Immunology.* **14**(2), p49.

Martinez, F. and Gordon, S. 2014. The M1 and M2 paradigm of macrophage activation: time for reassessment. *F1000Prime Rep.* **6**, p13.

Martinez, F., Helming, L. and Gordon, S. 2009. Alternative Activation of Macrophages: An Immunologic Functional Perspective. *Annual Review of Immunology.* **27**(1), pp.451-483.

Martinez, F.O., Gordon, S., Locati, M. and Mantovani, A. 2006. Transcriptional profiling of the human monocyte-to-macrophage differentiation and polarization: new molecules and patterns of gene expression. *J Immunol.* **177**(10), pp.7303-7311.

Martinez, F.O., Helming, L., Milde, R., Varin, A., Melgert, B.N., Draijer, C., Thomas, B., Fabbri, M., Crawshaw, A., Ho, L.P., Ten Hacken, N.H., Cobos Jiménez, V., Kootstra, N.A., Hamann, J., Greaves, D.R., Locati, M., Mantovani, A. and Gordon, S. 2013. Genetic programs expressed in resting and IL-4 alternatively activated mouse and human macrophages: similarities and differences. *Blood.* **121**(9), pp.e57-69.

Martinez, F.O., Sica, A., Mantovani, A. and Locati, M. 2008. Macrophage activation and polarization. *FBL.* **13**(2), pp.453-461.

Martín-González, J., Montero-Bullón, J.F. and Lacal, J. 2021. Dictyostelium discoideum as a non-mammalian biomedical model. *Microb Biotechnol.* **14**(1), pp.111-125.

Martínez-Colón, G.J. and Moore, B.B. 2018. Prostaglandin E(2) as a Regulator of Immunity to Pathogens. *Pharmacol Ther.* **185**, pp.135-146.

Marín Franco, J.L., Genoula, M., Corral, D., Duette, G., Ferreyra, M., Maio, M., Dolotowicz, M.B., Aparicio-Trejo, O.E., Patiño-Martínez, E., Charton, A., Métais, A., Fuentes, F., Soldan, V., Moraña, E.J., Palmero, D., Ostrowski, M., Schierloh, P., Sánchez-Torres, C., Hernández-Pando, R., ... and Balboa, L. 2020. Host-Derived Lipids from Tuberculous Pleurisy Impair Macrophage Microbicidal-Associated Metabolic Activity. *Cell Reports.* **33**(13).

Mase, S.R. and Chorba, T. 2019. Treatment of Drug-Resistant Tuberculosis. *Clin Chest Med.* **40**(4), pp.775-795.

Mastrogiovanni, M., Martínez-Navarro, F.J., Bowman, T.V. and Cayuela, M.L. 2024. Inflammation in Development and Aging: Insights from the Zebrafish Model. *Int J Mol Sci.* **25**(4).

Mateus, C. and Avery, S.V. 2000. Destabilized green fluorescent protein for monitoring dynamic changes in yeast gene expression with flow cytometry. *Yeast.* **16**(14), pp.1313-1323.

Mathias, J.R., Dodd, M.E., Walters, K.B., Yoo, S.K., Ranheim, E.A. and Huttenlocher, A. 2009. Characterization of zebrafish larval inflammatory macrophages. *Developmental & Comparative Immunology.* **33**(11), pp.1212-1217.

Matta, S.K. and Kumar, D. 2016. Hypoxia and classical activation limits Mycobacterium tuberculosis survival by Akt-dependent glycolytic shift in macrophages. *Cell Death Discovery.* **2**(1), p16022.

Mattila, J.T., Ojo, O.O., Kepka-Lenhart, D., Marino, S., Kim, J.H., Eum, S.Y., Via, L.E., Barry, C.E., 3rd, Klein, E., Kirschner, D.E., Morris, S.M., Jr., Lin, P.L. and Flynn, J.L. 2013. Microenvironments in tuberculous granulomas are delineated by distinct populations of macrophage subsets and expression of nitric oxide synthase and arginase isoforms. *J Immunol.* **191**(2), pp.773-784.

Mayadas, T.N., Cullere, X. and Lowell, C.A. 2014. The multifaceted functions of neutrophils. *Annu Rev Pathol.* **9**, pp.181-218.

Mazzolini, J., Le Clerc, S., Morisse, G., Coulonges, C., Kuil, L.E., van Ham, T.J., Zagury, J.-F. and Sieger, D. 2020. Gene expression profiling reveals a conserved microglia signature in larval zebrafish. *Glia.* **68**(2), pp.298-315.

McCaffrey, E.F., Delmastro, A.C., Fitzhugh, I., Ranek, J.S., Douglas, S., Peters, J.M., Fullaway, C.C., Bosse, M., Liu, C.C., Gillen, C., Greenwald, N.F., Anzick, S., Martens, C., Winfree, S., Bai, Y., Sowers, C., Goldston, M., Kong, A., Boonrat, P., ... and Angelo, M. 2025. The immunometabolic topography of tuberculosis granulomas governs cellular organization and bacterial control. *bioRxiv.*

McKinnon, K.M. 2018. Flow Cytometry: An Overview. *Current Protocols in Immunology.* **120**(1), pp.5.1.1-5.1.11.

McWhorter, F.Y., Wang, T., Nguyen, P., Chung, T. and Liu, W.F. 2013. Modulation of macrophage phenotype by cell shape. *Proc Natl Acad Sci U S A.* **110**(43), pp.17253-17258.

Meade, R.K., Adefisayo, O.O., Gontijo, M.T.P., Harris, S.J., Pyle, C.J., Wilburn, K.M., Ecker, A.M.V., Hughes, E.J., Garcia, P.D., Ivie, J., McHenry, M.L., Benchek, P.H., Mayanja-Kizza, H., Neff, J.L., Ko, D.C., Stout, J.E., Stein, C.M., Hawn, T.R., Tobin, D.M. and Smith, C.M. 2025. Cathepsin Z is a conserved susceptibility factor underlying tuberculosis severity. *PLOS Biology.* **23**(9), pe3003377.

Mehta, P., Datta, D., Dahiya, P. and Mazumder, S. 2023. miR-155-Induced Activation of Pro-Inflammatory Stat1/TBX21 Pathway and M1-Signature Genes Incite Macrophage Apoptosis and Clearance of Mycobacterium fortuitum in Zebrafish. *Microbiology Research.* [Online]. **14**(2), pp.559-579.

Meira, L., Chaves, C., Araújo, D., Almeida, L., Boaventura, R., Ramos, A., Carvalho, T., Osório, N.S., Castro, A.G., Rodrigues, F., Guimarães, J.T., Saraiva, M. and Bastos, H.N. 2019. Predictors and outcomes of disseminated tuberculosis in an intermediate burden setting. *Pulmonology.* **25**(6), pp.320-327.

Memon, S., Bibi, S. and He, G. 2025. Integration of AI and ML in Tuberculosis (TB) Management: From Diagnosis to Drug Discovery. *Diseases.* **13**(6).

Mendoza-Coronel, E. and Ortega, E. 2017. Macrophage Polarization Modulates FcγR- and CD13-Mediated Phagocytosis and Reactive Oxygen Species Production, Independently of Receptor Membrane Expression. *Frontiers in Immunology.* **Volume 8 - 2017**.

Meng, B., Zhao, N., Mlcochova, P., Ferreira, I.A.T.M., Ortmann, B.M., Davis, T., Wit, N., Rehwinkel, J., Cook, S., Maxwell, P.H., Nathan, J.A. and Gupta, R.K. 2024. Hypoxia drives HIF2-dependent reversible macrophage cell cycle entry. *Cell Reports.* **43**(7), p114471.

Menon Aruna, R., Prest Rebecca, J., Tobin David, M. and Champion Patricia, A. 2025. Mycobacterium marinum as a model for understanding principles of mycobacterial pathogenesis. *Journal of Bacteriology.* **207**(5), pp.e00047-00025.

Menozzi, F.D., Reddy, V.M., Cayet, D., Raze, D., Debrie, A.-S., Dehouck, M.-P., Cecchelli, R. and Locht, C. 2006. Mycobacterium tuberculosis heparin-binding haemagglutinin adhesin (HBHA) triggers receptor-mediated transcytosis without altering the integrity of tight junctions. *Microbes and Infection.* **8**(1), pp.1-9.

Meylan, E., Burns, K., Hofmann, K., Blancheteau, V., Martinon, F., Kelliher, M. and Tschopp, J. 2004. RIP1 is an essential mediator of Toll-like receptor 3–induced NF-κB activation. *Nature Immunology.* **5**(5), pp.503-507.

Mezouar, S., Diarra, I., Roudier, J., Desnues, B. and Mege, J.L. 2019. Tumor Necrosis Factor-Alpha Antagonist Interferes With the Formation of Granulomatous Multinucleated Giant Cells: New Insights Into Mycobacterium tuberculosis Infection. *Front Immunol.* **10**, p1947.

Miller, B.H., Fratti, R.A., Poschet, J.F., Timmins, G.S., Master, S.S., Burgos, M., Marletta, M.A. and Deretic, V. 2004. Mycobacteria inhibit nitric oxide synthase recruitment to phagosomes during macrophage infection. *Infect Immun.* **72**(5), pp.2872-2878.

Mills, C.D., Kincaid, K., Alt, J.M., Heilman, M.J. and Hill, A.M. 2000. M-1/M-2 macrophages and the Th1/Th2 paradigm. *J Immunol.* **164**(12), pp.6166-6173.

Mills, C.D. and Ley, K. 2014. M1 and M2 Macrophages: The Chicken and the Egg of Immunity. *Journal of Innate Immunity.* **6**(6), pp.716-726.

Misharin, A.V., Morales-Nebreda, L., Reyfman, P.A., Cuda, C.M., Walter, J.M., McQuattie-Pimentel, A.C., Chen, C.I., Anekalla, K.R., Joshi, N., Williams, K.J.N., Abdala-Valencia, H., Yacoub, T.J., Chi, M., Chiu, S., Gonzalez-Gonzalez, F.J., Gates, K., Lam, A.P., Nicholson, T.T., Homan, P.J., ... and Perlman, H. 2017. Monocyte-derived alveolar macrophages drive lung fibrosis and persist in the lung over the life span. *J Exp Med.* **214**(8), pp.2387-2404.

Mishra, B.B., Moura-Alves, P., Sonawane, A., Hacohen, N., Griffiths, G., Moita, L.F. and Anes, E. 2010. Mycobacterium tuberculosis protein ESAT-6 is a potent activator of the NLRP3/ASC inflammasome. *Cellular Microbiology.* **12**(8), pp.1046-1063.

Miskolci, V., Tweed, K.E., Lasarev, M.R., Britt, E.C., Walsh, A.J., Zimmerman, L.J., McDougal, C.E., Cronan, M.R., Fan, J., Sauer, J.-D., Skala, M.C. and Huttenlocher, A. 2022. *In vivo* fluorescence lifetime imaging of macrophage intracellular metabolism during wound responses in zebrafish. *eLife.* **11**, pe66080.

Mitsi, E., Kamng'ona, R., Rylance, J., Solórzano, C., Jesus Reiné, J., Mwandumba, H.C., Ferreira, D.M. and Jambo, K.C. 2018. Human alveolar macrophages predominately express combined classical M1 and M2 surface markers in steady state. *Respiratory Research.* **19**(1), p66.

Mizutani, T., Ano, T., Yoshioka, Y., Mizuta, S., Takemoto, K., Ouchi, Y., Morita, D., Kitano, S., Miyachi, H., Tsuruyama, T., Fujiwara, N. and Sugita, M. 2023. Neutrophil S100A9 supports M2 macrophage niche formation in granulomas. *iScience.* **26**(3), p106081.

Mohapatra, A., Howard, Z. and Ernst, J.D. 2025. CCR2 recruits monocytes to the lung, while CX3CR1 modulates positioning of monocyte-derived CD11c (pos) cells in the lymph node during pulmonary tuberculosis. *bioRxiv.*

Mole, D.R., Blancher, C., Copley, R.R., Pollard, P.J., Gleadle, J.M., Ragoussis, J. and Ratcliffe, P.J. 2009. Genome-wide Association of Hypoxia-inducible Factor (HIF)-1α and HIF-2α DNA Binding with Expression Profiling of Hypoxia-inducible Transcripts*. *Journal of Biological Chemistry.* **284**(25), pp.16767-16775.

Molina, G.A., Watkins, S.C. and Tsang, M. 2007. Generation of FGF reporter transgenic zebrafish and their utility in chemical screens. *BMC Dev Biol.* **7**, p62.

Momma, T.Y. and Ottaviani, J.I. 2022. There is no direct competition between arginase and nitric oxide synthase for the common substrate l-arginine. *Nitric Oxide.* **129**, pp.16-24.

Mondadori, C., Chandrakar, A., Lopa, S., Wieringa, P., Talò, G., Perego, S., Lombardi, G., Colombini, A., Moretti, M. and Moroni, L. 2023. Assessing the response of human primary macrophages to defined fibrous architectures fabricated by melt electrowriting. *Bioactive Materials.* **21**, pp.209-222.

Morales, R.A. and Allende, M.L. 2019. Peripheral Macrophages Promote Tissue Regeneration in Zebrafish by Fine-Tuning the Inflammatory Response. *Front Immunol.* **10**, p253.

Morelli, M.P., Martin, C., Pellegrini, J.M., Blanco, F., Bigi, F., Ciallella, L., Musella, R., Rodriguez Mieres, A., de Casado, G.C., Palmero, D.J. and García, V.E. 2025. Neutrophils from tuberculosis patients are polarized toward pro-inflammatory and anti-inflammatory phenotypes according to the disease severity. *The Journal of Immunology.* **214**(6), pp.1173-1186.

Mori, Y., Robin, P., Briggs, A.B., Levic, D.S., Wang, J., Heikes, K.L., Bagnat, M., Hannezo, E. and Munjal, A. 2025. A self-limiting mechanotransduction feedback loop ensures robust organ formation. *bioRxiv.*

Moss, C.E., Johnston, S.A., Kimble, J.V., Clements, M., Codd, V., Hamby, S., Goodall, A.H., Deshmukh, S., Sudbery, I., Coca, D., Wilson, H.L. and Kiss-Toth, E. 2024. Aging-related defects in macrophage function are driven by MYC and USF1 transcriptional programs. *Cell Reports.* **43**(4).

Mostowy, S., Boucontet, L., Mazon Moya, M.J., Sirianni, A., Boudinot, P., Hollinshead, M., Cossart, P., Herbomel, P., Levraud, J.P. and Colucci-Guyon, E. 2013. The zebrafish as a new model for the *in vivo* study of Shigella flexneri interaction with phagocytes and bacterial autophagy. *PLoS Pathog.* **9**(9), pe1003588.

Mould, K.J., Jackson, N.D., Henson, P.M., Seibold, M. and Janssen, W.J. 2019. Single cell RNA sequencing identifies unique inflammatory airspace macrophage subsets. *JCI Insight.* **4**(5).

Moyse, B., Moss, J., Bevan, L., Scott, A., Wittamer, V. and Richardson, R.J. 2024. *Defining mononuclear phagocyte distribution and behaviour in the zebrafish heart*. eLife Sciences Publications, Ltd. 2024/07/24. Available from: http://dx.doi.org/10.7554/eLife.98849.1

Moyse, B.R. and Richardson, R.J. 2020. A Population of Injury-Responsive Lymphoid Cells Expresses mpeg1.1 in the Adult Zebrafish Heart. *ImmunoHorizons.* **4**(8), pp.464-474.

Muijsers, R.B., ten Hacken, N.H., Van Ark, I., Folkerts, G., Nijkamp, F.P. and Postma, D.S. 2001. L-Arginine is not the limiting factor for nitric oxide synthesis by human alveolar macrophages *in vitro*. *Eur Respir J.* **18**(4), pp.667-671.

Muir, C.F., Reyes-Aldasoro, C.C., Prajsnar, T.K., Michno, B.J., Cholewa-Waclaw, J., Ho, Y.X., Bernut, A., Loynes, C.A., Elworthy, S., Bowden, K.A., Cadby, A.J., Prince, L.R., King, J.S., Ellett, F., Condliffe, A.M. and Renshaw, S.A. 2025. A subset of neutrophil phagosomes is characterised by pulses of Class I PI3K activity. *Dis Model Mech.* **18**(9).

Munder, M., Mollinedo, F., Calafat, J., Canchado, J., Gil-Lamaignere, C., Fuentes, J.M., Luckner, C., Doschko, G., Soler, G., Eichmann, K., Müller, F.-M., Ho, A.D., Goerner, M. and Modolell, M. 2005. Arginase I is constitutively expressed in human granulocytes and participates in fungicidal activity. *Blood.* **105**(6), pp.2549-2556.

Murayama, E., Kissa, K., Zapata, A., Mordelet, E., Briolat, V., Lin, H.-F., Handin, R.I. and Herbomel, P. 2006. Tracing Hematopoietic Precursor Migration to Successive Hematopoietic Organs during Zebrafish Development. *Immunity.* **25**(6), pp.963-975.

Murphy, D.M., Walsh, A., Stein, L., Petrasca, A., Cox, D.J., Brown, K., Duffin, E., Jameson, G., Connolly, S.A., O'Connell, F., O'Sullivan, J., Basdeo, S.A., Keane, J. and Phelan, J.J. 2024. Human Macrophages Activate Bystander Neutrophils' Metabolism and Effector Functions When Challenged with Mycobacterium tuberculosis. *Int J Mol Sci.* **25**(5).

Myllymäki, H., Bäuerlein, C.A. and Rämet, M. 2016. The Zebrafish Breathes New Life into the Study of Tuberculosis. *Frontiers in Immunology.* **Volume 7 - 2016**.

Mössner, J., Hammermann, R. and Racké, K. 2001. Concomitant down-regulation of L-arginine transport and nitric oxide (NO) synthesis in rat alveolar macrophages by the polyamine spermine. *Pulm Pharmacol Ther.* **14**(4), pp.297-305.

Nahidi, S., Gholami, E., Taslimi, Y., Habibzadeh, S., Seyed, N., Davarpanah, E., Ghanadan, A., Rafati, S. and Taheri, T. 2020. The outcome of arginase activity inhibition in BALB/c mice hosting Leishmania tropica. *Parasite Immunology.* **42**(3), pe12691.

Naicker, N., Rodel, H., Perumal, R., Ganga, Y., Bernstein, M., Benede, N., Abdool Karim, S., Padayacthi, N., Sigal, A. and Naidoo, K. 2023. Metformin Increases Cell Viability and Regulates Pro-Inflammatory Response to *Mtb*. *Infect Drug Resist.* **16**, pp.3629-3638.

Nakagawa, M., Karim, M.R., Izawa, T., Kuwamura, M. and Yamate, J. 2021. Immunophenotypical Characterization of M1/M2 Macrophages and Lymphocytes in Cisplatin-Induced Rat Progressive Renal Fibrosis. *Cells.* **10**(2).

Nakanishi, M. and Rosenberg, D.W. 2013. Multifaceted roles of PGE2 in inflammation and cancer. *Semin Immunopathol.* **35**(2), pp.123-137.

Nandi, B. and Behar, S.M. 2011. Regulation of neutrophils by interferon-γ limits lung inflammation during tuberculosis infection. *J Exp Med.* **208**(11), pp.2251-2262.

Nathan, C.F. and Hibbs, J.B. 1991. Role of nitric oxide synthesis in macrophage antimicrobial activity. *Current Opinion in Immunology.* **3**(1), pp.65-70.

Nathan, C.F., Murray, H.W., Wiebe, M.E. and Rubin, B.Y. 1983. Identification of interferon-gamma as the lymphokine that activates human macrophage oxidative metabolism and antimicrobial activity. *J Exp Med.* **158**(3), pp.670-689.

Negreiros-Lima, G.L., Lima, K.M., Moreira, I.Z., Jardim, B.L.O., Vago, J.P., Galvão, I., Teixeira, L.C.R., Pinho, V., Teixeira, M.M., Sugimoto, M.A. and Sousa, L.P. 2020. Cyclic AMP Regulates Key Features of Macrophages via PKA: Recruitment, Reprogramming and Efferocytosis. *Cells.* **9**(1).

Neupane, A.S., Willson, M., Chojnacki, A.K., Vargas E Silva Castanheira, F., Morehouse, C., Carestia, A., Keller, A.E., Peiseler, M., DiGiandomenico, A., Kelly, M.M., Amrein, M., Jenne, C., Thanabalasuriar, A. and Kubes, P. 2020. Patrolling Alveolar Macrophages Conceal Bacteria from the Immune System to Maintain Homeostasis. *Cell.* **183**(1), pp.110-125.e111.

Nguyen-Chi, M., Laplace-Builhe, B., Travnickova, J., Luz-Crawford, P., Tejedor, G., Phan, Q.T., Duroux-Richard, I., Levraud, J.-P., Kissa, K., Lutfalla, G., Jorgensen, C. and Djouad, F. 2015. Identification of polarized macrophage subsets in zebrafish. *eLife.* **4**, pe07288.

Nguyen-Chi, M., Laplace-Builhé, B., Travnickova, J., Luz-Crawford, P., Tejedor, G., Lutfalla, G., Kissa, K., Jorgensen, C. and Djouad, F. 2017. TNF signaling and macrophages govern fin regeneration in zebrafish larvae. *Cell Death Dis.* **8**(8), pe2979.

Nguyen-Chi, M., Luz-Crawford, P., Balas, L., Sipka, T., Contreras-López, R., Barthelaix, A., Lutfalla, G., Durand, T., Jorgensen, C. and Djouad, F. 2020. Pro-resolving mediator protectin D1 promotes epimorphic regeneration by controlling immune cell function in vertebrates. *Br J Pharmacol.* **177**(17), pp.4055-4073.

Niu, J., Huang, Y., Liu, X., Zhang, Z., Tang, J., Wang, B., Lu, Y., Cai, J. and Jian, J. 2020. Single-cell RNA-seq reveals different subsets of non-specific cytotoxic cells in teleost. *Genomics.* **112**(6), pp.5170-5179.

Novak, M.L. and Koh, T.J. 2013. Macrophage phenotypes during tissue repair. *Journal of Leukocyte Biology.* **93**(6), pp.875-881.

Noël, W., Raes, G., Hassanzadeh Ghassabeh, G., De Baetselier, P. and Beschin, A. 2004. Alternatively activated macrophages during parasite infections. *Trends in Parasitology.* **20**(3), pp.126-133.

Ogryzko, N.V., Lewis, A., Wilson, H.L., Meijer, A.H., Renshaw, S.A. and Elks, P.M. 2019. Hif-1α-Induced Expression of Il-1β Protects against Mycobacterial Infection in Zebrafish. *J Immunol.* **202**(2), pp.494-502.

Ohmori, Y. and Hamilton, T.A. 2000. Interleukin-4/STAT6 represses STAT1 and NF-kappa B-dependent transcription through distinct mechanisms. *J Biol Chem.* **275**(48), pp.38095-38103.

Oprişoreanu, A.M., Ryan, F., Richmond, C., Dzekhtsiarova, Y., Carragher, N.O., Becker, T., David, S. and Becker, C.G. 2023. Drug screening in zebrafish larvae reveals inflammation-related modulators of secondary damage after spinal cord injury in mice. *Theranostics.* **13**(8), pp.2531-2551.

Ordway, D., Henao-Tamayo, M., Orme, I.M. and Gonzalez-Juarrero, M. 2005. Foamy macrophages within lung granulomas of mice infected with Mycobacterium tuberculosis express molecules

characteristic of dendritic cells and antiapoptotic markers of the TNF receptor-associated factor family. *J Immunol.* **175**(6), pp.3873-3881.

Orecchioni, M., Ghosheh, Y., Pramod, A.B. and Ley, K. 2019. Macrophage Polarization: Different Gene Signatures in M1(LPS+) vs. Classically and M2(LPS–) vs. Alternatively Activated Macrophages. *Frontiers in Immunology.* **Volume 10 - 2019**.

Osada-Oka, M., Goda, N., Saiga, H., Yamamoto, M., Takeda, K., Ozeki, Y., Yamaguchi, T., Soga, T., Tateishi, Y., Miura, K., Okuzaki, D., Kobayashi, K. and Matsumoto, S. 2019. Metabolic adaptation to glycolysis is a basic defense mechanism of macrophages for Mycobacterium tuberculosis infection. *Int Immunol.* **31**(12), pp.781-793.

Oskam, J.J.M. 2024. *Investigation of Neutrophil Swarming to Mycobacterium marinum Infection in Zebrafish*. PhD thesis, University of Sheffield.

Ouyang, X., Hoeksma, J., Lubbers, R.J.M., Siersma, T.K., Hamoen, L.W. and den Hertog, J. 2022. Classification of antimicrobial mechanism of action using dynamic bacterial morphology imaging. *Scientific Reports.* **12**(1), p11162.

Pace, J.L., Russell, S.W., Schreiber, R.D., Altman, A. and Katz, D.H. 1983. Macrophage activation: priming activity from a T-cell hybridoma is attributable to interferon-gamma. *Proc Natl Acad Sci U S A.* **80**(12), pp.3782-3786.

Padmapriydarsini, C., Mamulwar, M., Mohan, A., Shanmugam, P., Gomathy, N.S., Mane, A., Singh, U.B., Pavankumar, N., Kadam, A., Kumar, H., Suresh, C., Reddy, D., Devi, P., Ramesh, P.M., Sekar, L., Jawahar, S., Shandil, R.K., Singh, M., Menon, J. and Guleria, R. 2022. Randomized Trial of Metformin With Anti-Tuberculosis Drugs for Early Sputum Conversion in Adults With Pulmonary Tuberculosis. *Clin Infect Dis.* **75**(3), pp.425-434.

Pahuja, I., Verma, A., Ghoshal, A., Mukhopadhyay, S., Kumari, A., Shaji, A., Chaturvedi, S., Dwivedi, V.P. and Bhaskar, A. 2023. Biapenem, a Carbapenem Antibiotic, Elicits Mycobacteria Specific Immune Responses and Reduces the Recurrence of Tuberculosis. *Microbiol Spectr.* **11**(4), pe0085823.

Pan, Y., Yu, Y., Wang, X. and Zhang, T. 2020. Tumor-Associated Macrophages in Tumor Immunity. *Frontiers in Immunology.* **Volume 11 - 2020**.

Pandey, S., Kant, S., Khawary, M. and Tripathi, D. 2022. Macrophages in Microbial Pathogenesis: Commonalities of Defense Evasion Mechanisms. *Infect Immun.* **90**(5), pe0029121.

Park, M., Kim, Y.S. and Song, H. 2025. Macrophages: a double-edged sword in female reproduction and disorders. *Experimental & Molecular Medicine.* **57**(2), pp.285-297.

Pellegrini, J.M., Martin, C., Morelli, M.P., Schander, J.A., Tateosian, N.L., Amiano, N.O., Rolandelli, A., Palmero, D.J., Levi, A., Ciallella, L., Colombo, M.I. and García, V.E. 2021. PGE2 displays immunosuppressive effects during human active tuberculosis. *Scientific Reports.* **11**(1), p13559.

Peng, Y., Zhu, X., Gao, L., Wang, J., Liu, H., Zhu, T., Zhu, Y., Tang, X., Hu, C., Chen, X., Chen, H., Chen, Y. and Guo, A. 2022. Mycobacterium tuberculosis Rv0309 Dampens the Inflammatory Response and Enhances Mycobacterial Survival. *Frontiers in Immunology.* **Volume 13 - 2022**.

Pesce, J.T., Ramalingam, T.R., Mentink-Kane, M.M., Wilson, M.S., El Kasmi, K.C., Smith, A.M., Thompson, R.W., Cheever, A.W., Murray, P.J. and Wynn, T.A. 2009. Arginase-1-expressing macrophages suppress Th2 cytokine-driven inflammation and fibrosis. *PLoS Pathog.* **5**(4), pe1000371.

Pessanha, A.P., Martins, R.A.P., Mattos-Guaraldi, A.L., Vianna, A. and Moreira, L.O. 2012. Arginase-1 expression in granulomas of tuberculosis patients. *FEMS Immunology & Medical Microbiology.* **66**(2), pp.265-268.

Pettersen, E.F., Goddard, T.D., Huang, C.C., Meng, E.C., Couch, G.S., Croll, T.I., Morris, J.H. and Ferrin, T.E. 2021. UCSF ChimeraX: Structure visualization for researchers, educators, and developers. *Protein Science.* **30**(1), pp.70-82.

Pham, T.H.M., Brewer, S.M., Thurston, T., Massis, L.M., Honeycutt, J., Lugo, K., Jacobson, A.R., Vilches-Moure, J.G., Hamblin, M., Helaine, S. and Monack, D.M. 2020. Salmonella-Driven Polarization of Granuloma Macrophages Antagonizes TNF-Mediated Pathogen Restriction during Persistent Infection. *Cell Host & Microbe.* **27**(1), pp.54-67.e55.

Phan, Q.T., Sipka, T., Gonzalez, C., Levraud, J.P., Lutfalla, G. and Nguyen-Chi, M. 2018. Neutrophils use superoxide to control bacterial infection at a distance. *PLoS Pathog.* **14**(7), pe1007157.

Phan, T.H., van Leeuwen, L.M., Kuijl, C., Ummels, R., van Stempvoort, G., Rubio-Canalejas, A., Piersma, S.R., Jiménez, C.R., van der Sar, A.M., Houben, E.N.G. and Bitter, W. 2018. EspH is a hypervirulence factor for Mycobacterium marinum and essential for the secretion of the ESX-1 substrates EspE and EspF. *PLOS Pathogens.* **14**(8), pe1007247.

Pi, J., Chen, D., Wang, J., Yang, E., Yang, J., Liu, Y., Yu, J., Xia, J., Huang, X., Chen, L., Ruan, Y., Xu, J.F., Yang, F. and Shen, L. 2024. Macrophage targeted graphene oxide nanosystem synergize antibiotic killing and host immune defense for Tuberculosis Therapy. *Pharmacol Res.* **208**, p107379.

Pimton, P., Lecht, S., Stabler, C.T., Johannes, G., Schulman, E.S. and Lelkes, P.I. 2015. Hypoxia enhances differentiation of mouse embryonic stem cells into definitive endoderm and distal lung cells. *Stem Cells Dev.* **24**(5), pp.663-676.

Pisu, D., Huang, L., Grenier, J.K. and Russell, D.G. 2020. Dual RNA-Seq of *Mtb*-Infected Macrophages *In vivo* Reveals Ontologically Distinct Host-Pathogen Interactions. *Cell Rep.* **30**(2), pp.335-350.e334.

Pisu, D., Johnston, L., Mattila, J.T. and Russell, D.G. 2024. The frequency of CD38(+) alveolar macrophages correlates with early control of M. tuberculosis in the murine lung. *Nat Commun.* **15**(1), p8522.

Pisu, D., Sunny, P.S., Nelson, M.L., Junecko, B.F., Venugopalan, R., Rodgers, M.A., Borish, H.J., Maiello, P., Scanga, C.A., Lin, P.L., Flynn, J.L., Russell, D.G. and Mattila, J.T. 2025. Spatially-distinct programming of macrophage diversity within the granulomas of Mycobacterium tuberculosis infected nonhuman primates. *bioRxiv.* p2025.2006.2012.659348.

Pixley, F.J., Xiong, Y., Yu, R.Y.-L., Sahai, E.A., Stanley, E.R. and Ye, B.H. 2005. BCL6 suppresses RhoA activity to alter macrophage morphology and motility. *Journal of Cell Science.* **118**(9), pp.1873-1883.

Piñeros, A.R., Campos, L.W., Fonseca, D.M., Bertolini, T.B., Gembre, A.F., Prado, R.Q., Alves-Filho, J.C., Ramos, S.G., Russo, M. and Bonato, V.L. 2017. M2 macrophages or IL-33 treatment attenuate ongoing Mycobacterium tuberculosis infection. *Sci Rep.* **7**, p41240.

Podolnikova, N.P., Kushchayeva, Y.S., Wu, Y., Faust, J. and Ugarova, T.P. 2016. The Role of Integrins αMβ2 (Mac-1, CD11b/CD18) and αDβ2 (CD11d/CD18) in Macrophage Fusion. *The American Journal of Pathology.* **186**(8), pp.2105-2116.

Portevin, D., Via, L.E., Eum, S. and Young, D. 2012. Natural killer cells are recruited during pulmonary tuberculosis and their *ex vivo* responses to mycobacteria vary between healthy human donors in association with KIR haplotype. *Cell Microbiol.* **14**(11), pp.1734-1744.

Prame Kumar, K., Nicholls, A.J. and Wong, C.H.Y. 2018. Partners in crime: neutrophils and monocytes/macrophages in inflammation and disease. *Cell Tissue Res.* **371**(3), pp.551-565.

Prasanna, P., Herrera, B., Schlesinger, L.S., Paiardini, M. and Sharan, R. 2025. Advances in host-directed therapy for tuberculosis and HIV coinfection: enhancing immune responses. *Trends in Microbiology.* **33**(9), pp.961-975.

Puissegur, M.P., Lay, G., Gilleron, M., Botella, L., Nigou, J., Marrakchi, H., Mari, B., Duteyrat, J.L., Guerardel, Y., Kremer, L., Barbry, P., Puzo, G. and Altare, F. 2007. Mycobacterial lipomannan induces granuloma macrophage fusion via a TLR2-dependent, ADAM9- and beta1 integrin-mediated pathway. *J Immunol.* **178**(5), pp.3161-3169.

Putri, D.U., Feng, P.-H., Lin, C.-F., Haryana, S.M., Soesatyo, M.H.N.E., Lee, K.-Y. and Han, C.-L. 2022. Proteomic networks associated with tumor-educated macrophage polarization and cytotoxicity potentiated by heat-killed tuberculosis. *Scientific Reports.* **12**(1), p6881.

Pyle Charlie, J., Wang, L., Beerman Rebecca, W., Jain, V., Ohman Henry, K.E., Thompson Brandon, A., Abramson Karen, R., Ko Dennis, C., Gregory Simon, G., Smith Clare, M., Neff Jadee, L., Richardson Rebecca, J., Stout Jason, E. and Tobin David, M. 2025. Paired single-cell and spatial transcriptional profiling reveals a central osteopontin macrophage response mediating tuberculous granuloma formation. *mBio.* **0**(0), pp.e01559-01525.

Qian, B.Z., Li, J., Zhang, H., Kitamura, T., Zhang, J., Campion, L.R., Kaiser, E.A., Snyder, L.A. and Pollard, J.W. 2011. CCL2 recruits inflammatory monocytes to facilitate breast-tumour metastasis. *Nature.* **475**(7355), pp.222-225.

Qiu, B., Yuan, P., Du, X., Jin, H., Du, J. and Huang, Y. 2023. Hypoxia inducible factor-1α is an important regulator of macrophage biology. *Heliyon.* **9**(6), pe17167.

Qualls, J.E., DeFreitas, A., Smith, A.M., Watowich, S.S. and Murray, P.J. 2009. Direct and indirect type-1 arginase (Arg1) induction following Mycobacterium bovis (BCG) infection (43.1). *The Journal of Immunology.* **182**(Supplement_1), pp.43.41-43.41.

Qualls, J.E. and Murray, P.J. 2016. Immunometabolism within the tuberculosis granuloma: amino acids, hypoxia, and cellular respiration. *Semin Immunopathol.* **38**(2), pp.139-152.

Qualls, J.E., Neale, G., Smith, A.M., Koo, M.S., DeFreitas, A.A., Zhang, H., Kaplan, G., Watowich, S.S. and Murray, P.J. 2010. Arginine usage in mycobacteria-infected macrophages depends on autocrine-paracrine cytokine signaling. *Sci Signal.* **3**(135), pra62.

Rackov, G., Hernández-Jiménez, E., Shokri, R., Carmona-Rodríguez, L., Mañes, S., Álvarez-Mon, M., López-Collazo, E., Martínez-A, C. and Balomenos, D. 2016. p21 mediates macrophage reprogramming through regulation of p50-p50 NF-κB and IFN-β. *The Journal of Clinical Investigation.* **126**(8), pp.3089-3103.

Raes, G., De Baetselier, P., Noël, W., Beschin, A., Brombacher, F. and Hassanzadeh Gh, G. 2002. Differential expression of FIZZ1 and Ym1 in alternatively versus classically activated macrophages. *J Leukoc Biol.* **71**(4), pp.597-602.

Rajmani, R.S. and Surolia, A. 2024. Antimycobacterial and healing effects of Pranlukast against *MTB* infection and pathogenesis in a preclinical mouse model of tuberculosis. *Front Immunol.* **15**, p1347045.

Ramachandran, P., Dobie, R., Wilson-Kanamori, J.R., Dora, E.F., Henderson, B.E.P., Luu, N.T., Portman, J.R., Matchett, K.P., Brice, M., Marwick, J.A., Taylor, R.S., Efremova, M., Vento-Tormo, R., Carragher, N.O., Kendall, T.J., Fallowfield, J.A., Harrison, E.M., Mole, D.J., Wigmore, S.J., ... and Henderson, N.C. 2019. Resolving the fibrotic niche of human liver cirrhosis at single-cell level. *Nature.* **575**(7783), pp.512-518.

Ramakrishnan, L. 2012. Revisiting the role of the granuloma in tuberculosis. *Nat Rev Immunol.* **12**(5), pp.352-366.

Ramkhelawon, B., Yang, Y., van Gils, J.M., Hewing, B., Rayner, K.J., Parathath, S., Guo, L., Oldebeken, S., Feig, J.L., Fisher, E.A. and Moore, K.J. 2013. Hypoxia induces netrin-1 and Unc5b in atherosclerotic plaques: mechanism for macrophage retention and survival. *Arterioscler Thromb Vasc Biol.* **33**(6), pp.1180-1188.

Ranawat, N. and Masai, I. 2021. Mechanisms underlying microglial colonization of developing neural retina in zebrafish. *eLife.* **10**, pe70550.

Rath, M., Müller, I., Kropf, P., Closs, E.I. and Munder, M. 2014. Metabolism via Arginase or Nitric Oxide Synthase: Two Competing Arginine Pathways in Macrophages. *Front Immunol.* **5**, p532.

Reddy, D.V.S., Sofi, H.S., Roy, T., Verma, S., Washimkar, K.R., Raman, S.K., Singh, S., Azmi, L., Ray, L., Singh, J., Mugale, M.N., Singh, A.K. and Misra, A. 2024. Macrophage-targeted versus free calcitriol as host-directed adjunct therapy against Mycobacterium tuberculosis infection in mice is bacteriostatic and mitigates tissue pathology. *Tuberculosis.* **148**, p102536.

Redente, E.F., Higgins, D.M., Dwyer-Nield, L.D., Orme, I.M., Gonzalez-Juarrero, M. and Malkinson, A.M. 2010. Differential polarization of alveolar macrophages and bone marrow-derived monocytes following chemically and pathogen-induced chronic lung inflammation. *Journal of Leukocyte Biology.* **88**(1), pp.159-168.

Refai, A., Gritli, S., Barbouche, M.R. and Essafi, M. 2018. Mycobacterium tuberculosis Virulent Factor ESAT-6 Drives Macrophage Differentiation Toward the Pro-inflammatory M1 Phenotype and Subsequently Switches It to the Anti-inflammatory M2 Phenotype. *Front Cell Infect Microbiol.* **8**, p327.

Regev, D., Surolia, R., Karki, S., Zolak, J., Montes- Worboys, A., Oliva, O., Guroji, P., Saini, V., Steyn, A.J.C., Agarwal, A. and Antony, V.B. 2012. Heme oxygenase-1 promotes granuloma

development and protects against dissemination of mycobacteria. *Laboratory Investigation.* **92**(11), pp.1541-1552.

Renna, M., Schaffner, C., Brown, K., Shang, S., Tamayo, M.H., Hegyi, K., Grimsey, N.J., Cusens, D., Coulter, S., Cooper, J., Bowden, A.R., Newton, S.M., Kampmann, B., Helm, J., Jones, A., Haworth, C.S., Basaraba, R.J., DeGroote, M.A., Ordway, D.J., ... and Floto, R.A. 2011. Azithromycin blocks autophagy and may predispose cystic fibrosis patients to mycobacterial infection. *The Journal of Clinical Investigation.* **121**(9), pp.3554-3563.

Renshaw, S.A., Loynes, C.A., Trushell, D.M.I., Elworthy, S., Ingham, P.W. and Whyte, M.K.B. 2006. A transgenic zebrafish model of neutrophilic inflammation. *Blood.* **108**(13), pp.3976-3978.

Renson, P., Rose, N., Le Dimna, M., Mahé, S., Keranflec'h, A., Paboeuf, F., Belloc, C., Le Potier, M.-F. and Bourry, O. 2017. Dynamic changes in bronchoalveolar macrophages and cytokines during infection of pigs with a highly or low pathogenic genotype 1 PRRSV strain. *Veterinary Research.* **48**(1), p15.

Resende, M., Ferreira, C.M., Barbosa, A.M., Cardoso, M.S., Sousa, J., Saraiva, M., Castro, A.G., Appelberg, R. and Torrado, E. 2020. Myeloid HIF-1α regulates pulmonary inflammation during experimental Mycobacterium tuberculosis infection. *Immunology.* **159**(1), pp.121-129.

Rey-Giraud, F., Hafner, M. and Ries, C.H. 2012. *In vitro* Generation of Monocyte-Derived Macrophages under Serum-Free Conditions Improves Their Tumor Promoting Functions. *PLOS ONE.* **7**(8), pe42656.

Rhoades, E.R., Frank, A.A. and Orme, I.M. 1997. Progression of chronic pulmonary tuberculosis in mice aerogenically infected with virulent Mycobacterium tuberculosis. *Tubercle and Lung Disease.* **78**(1), pp.57-66.

Rhoades, E.R., Geisel, R.E., Butcher, B.A., McDonough, S. and Russell, D.G. 2005. Cell wall lipids from Mycobacterium bovis BCG are inflammatory when inoculated within a gel matrix: Characterization of a new model of the granulomatous response to mycobacterial components. *Tuberculosis.* **85**(3), pp.159-176.

Richard, D.E., Berra, E. and Pouyssegur, J. 2000. Nonhypoxic pathway mediates the induction of hypoxia-inducible factor 1alpha in vascular smooth muscle cells. *J Biol Chem.* **275**(35), pp.26765-26771.

Robertson, M.A., Padgett, L.R., Fine, J.A., Chopra, G. and Mastracci, T.L. 2020. Targeting polyamine biosynthesis to stimulate beta cell regeneration in zebrafish. *Islets.* **12**(5), pp.99-107.

Roca, F.J. and Ramakrishnan, L. 2013. TNF dually mediates resistance and susceptibility to mycobacteria via mitochondrial reactive oxygen species. *Cell.* **153**(3), pp.521-534.

Roca, F.J., Whitworth, L.J., Redmond, S., Jones, A.A. and Ramakrishnan, L. 2019. TNF Induces Pathogenic Programmed Macrophage Necrosis in Tuberculosis through a Mitochondrial-Lysosomal-Endoplasmic Reticulum Circuit. *Cell.* **178**(6), pp.1344-1361.e1311.

Romagnoli, A., Etna, M.P., Giacomini, E., Pardini, M., Remoli, M.E., Corazzari, M., Falasca, L., Goletti, D., Gafa, V., Simeone, R., Delogu, G., Piacentini, M., Brosch, R., Fimia, G.M. and Coccia, E.M. 2012. ESX-1 dependent impairment of autophagic flux by Mycobacterium tuberculosis in human dendritic cells. *Autophagy.* **8**(9), pp.1357-1370.

Rosales, C. 2018. Neutrophil: A Cell with Many Roles in Inflammation or Several Cell Types? *Front Physiol.* **9**, p113.

Rosenthal, A.H., Rothfield, L.D. and Dauer, L.C. 2019. Disseminated tuberculosis in a healthy adolescent female. *Cureus.* **11**(6).

Rosowski, E.E. 2020. Determining macrophage versus neutrophil contributions to innate immunity using larval zebrafish. *Dis Model Mech.* **13**(1).

Rostam, H.M., Reynolds, P.M., Alexander, M.R., Gadegaard, N. and Ghaemmaghami, A.M. 2017. Image based Machine Learning for identification of macrophage subsets. *Sci Rep.* **7**(1), p3521.

Rougeot, J., Torraca, V., Zakrzewska, A., Kanwal, Z., Jansen, H.J., Sommer, F., Spaink, H.P. and Meijer, A.H. 2019. RNAseq Profiling of Leukocyte Populations in Zebrafish Larvae Reveals a cxcl11 Chemokine Gene as a Marker of Macrophage Polarization During Mycobacterial Infection. *Frontiers in Immunology.* **10**.

Roy, S., Schmeier, S., Kaczkowski, B., Arner, E., Alam, T., Ozturk, M., Tamgue, O., Parihar, S.P., Kawaji, H., Itoh, M., Lassmann, T., Carninci, P., Hayashizaki, Y., Forrest, A.R.R., Guler, R., Bajic, V.B., Brombacher, F. and Suzuki, H. 2018. Transcriptional landscape of Mycobacterium tuberculosis infection in macrophages. *Sci Rep.* **8**(1), p6758.

Roy, T., Seth, A., Shafi, H., Reddy, D.V.S., Raman, S.K., Chakradhar, J.V.U.S., Verma, S., Bharti, R., Azmi, L., Ray, L. and Misra, A. 2024. Transcriptional regulation of suppressors of cytokine signaling during infection with Mycobacterium tuberculosis in human THP-1-derived macrophages and in mice. *Microbes and Infection.* **26**(3), p105282.

Ru, H., Liu, X., Lin, C., Yang, J., Chen, F., Sun, R., Zhang, L. and Liu, J. 2017. The Impact of Genome Region of Difference 4 (RD4) on Mycobacterial Virulence and BCG Efficacy. *Front Cell Infect Microbiol.* **7**, p239.

Ruley, K.M., Ansede, J.H., Pritchett, C.L., Talaat, A.M., Reimschuessel, R. and Trucksis, M. 2004. Identification of Mycobacterium marinum virulence genes using signature-tagged mutagenesis and the goldfish model of mycobacterial pathogenesis. *FEMS Microbiology Letters.* **232**(1), pp.75-81.

Rückerl, D., Campbell, S.M., Duncan, S., Sutherland, T.E., Jenkins, S.J., Hewitson, J.P., Barr, T.A., Jackson-Jones, L.H., Maizels, R.M. and Allen, J.E. 2017. Macrophage origin limits functional plasticity in helminth-bacterial co-infection. *PLoS Pathog.* **13**(3), pe1006233.

Rőszer, T. 2015. Understanding the Mysterious M2 Macrophage through Activation Markers and Effector Mechanisms. *Mediators of Inflammation.* **2015**, p816460.

Sabrautzki, S., Miller, M., Kague, E. and Brielmeier, M. 2021. Welfare Assessment of Adult Laboratory Zebrafish: A Practical Guide. *Zebrafish.* **18**(4), pp.282-292.

Sahile, H.A., Christofferson, M., Alford, M.A., Rens, C., Haghdadi, H., Chao, J.D., Langdon, G., Hancock, R.E.W., Chen, J. and Av-Gay, Y. 2025. The Parkinson's drug benztropine possesses histamine receptor 1-dependent host-directed antimicrobial activity against Mycobacterium tuberculosis. *npj Antimicrobials and Resistance.* **3**(1), p70.

Saito, S. and Nakano, M. 1996. Nitric oxide production by peritoneal macrophages of Mycobacterium bovis BCG-infected or non-infected mice: regulatory roles of T lymphocytes and cytokines. *Journal of Leukocyte Biology.* **59**(6), pp.908-915.

Samstein, M., Schreiber, H.A., Leiner, I.M., Susac, B., Glickman, M.S. and Pamer, E.G. 2013. Essential yet limited role for $CCR2^{+}$ inflammatory monocytes during Mycobacterium tuberculosis-specific T cell priming. *Elife.* **2**, pe01086.

Sanderson, L.E., Chien, A.T., Astin, J.W., Crosier, K.E., Crosier, P.S. and Hall, C.J. 2015. An inducible transgene reports activation of macrophages in live zebrafish larvae. *Dev Comp Immunol.* **53**(1), pp.63-69.

Santhakumar, K., Judson, E.C., Elks, P.M., McKee, S., Elworthy, S., van Rooijen, E., Walmsley, S.S., Renshaw, S.A., Cross, S.S. and van Eeden, F.J. 2012. A zebrafish model to study and therapeutically manipulate hypoxia signaling in tumorigenesis. *Cancer Res.* **72**(16), pp.4017-4027.

Santucci, P., Aylan, B., Botella, L., Bernard Elliott, M., Bussi, C., Pellegrino, E., Athanasiadi, N. and Gutierrez Maximiliano, G. 2022. Visualizing Pyrazinamide Action by Live Single-Cell Imaging of Phagosome Acidification and Mycobacterium tuberculosis pH Homeostasis. *mBio.* **13**(2), pp.e00117-00122.

Sarathy, J.P. and Dartois, V. 2020. Caseum: a Niche for Mycobacterium tuberculosis Drug-Tolerant Persisters. *Clin Microbiol Rev.* **33**(3).

Scher, J.U. and Pillinger, M.H. 2009. The Anti-Inflammatory Effects of Prostaglandins. *Journal of Investigative Medicine.* **57**(6), pp.703-708.

Schild, Y., Mohamed, A., Wootton, E.J., Lewis, A. and Elks, P.M. 2020. Hif-1alpha stabilisation is protective against infection in zebrafish comorbid models. *The FEBS Journal.* **287**(18), pp.3925-3943.

Schilperoort, M., Ngai, D., Sukka, S.R., Avrampou, K., Shi, H. and Tabas, I. 2023. The role of efferocytosis-fueled macrophage metabolism in the resolution of inflammation. *Immunol Rev.* **319**(1), pp.65-80.

Schioppa, T., Uranchimeg, B., Saccani, A., Biswas, S.K., Doni, A., Rapisarda, A., Bernasconi, S., Saccani, S., Nebuloni, M., Vago, L., Mantovani, A., Melillo, G. and Sica, A. 2003. Regulation of the chemokine receptor CXCR4 by hypoxia. *J Exp Med.* **198**(9), pp.1391-1402.

Schleicher, U., Paduch, K., Debus, A., Obermeyer, S., König, T., Kling, J.C., Ribechini, E., Dudziak, D., Mougiakakos, D., Murray, P.J., Ostuni, R., Körner, H. and Bogdan, C. 2016. TNF-Mediated Restriction of Arginase 1 Expression in Myeloid Cells Triggers Type 2 NO Synthase Activity at the Site of Infection. *Cell Rep.* **15**(5), pp.1062-1075.

Schnitzerlein, M., Greto, E., Wegner, A., Möller, A., Aust, O., Ben Brahim, O., Blumenthal, D.B., Zaburdaev, V. and Uderhardt, S. 2025. Cellular morphodynamics as quantifiers for functional states of resident tissue macrophages *in vivo*. *PLOS Computational Biology.* **21**(5), pe1011859.

Schober, J.M., Chen, N., Grzeszkiewicz, T.M., Jovanovic, I., Emeson, E.E., Ugarova, T.P., Ye, R.D., Lau, L.F. and Lam, S.C.T. 2002. Identification of integrin αMβ2 as an adhesion receptor on peripheral blood monocytes for Cyr61 (CCN1) and connective tissue growth factor (CCN2): immediate-early gene products expressed in atherosclerotic lesions. *Blood.* **99**(12), pp.4457-4465.

Scholz, C.C., Cavadas, M.A., Tambuwala, M.M., Hams, E., Rodríguez, J., von Kriegsheim, A., Cotter, P., Bruning, U., Fallon, P.G., Cheong, A., Cummins, E.P. and Taylor, C.T. 2013. Regulation of IL-1β-induced NF-κB by hydroxylases links key hypoxic and inflammatory signaling pathways. *Proc Natl Acad Sci U S A.* **110**(46), pp.18490-18495.

Schulz, C., Perdiguero, E.G., Chorro, L., Szabo-Rogers, H., Cagnard, N., Kierdorf, K., Prinz, M., Wu, B., Jacobsen, S.E.W., Pollard, J.W., Frampton, J., Liu, K.J. and Geissmann, F. 2012. A Lineage of Myeloid Cells Independent of Myb and Hematopoietic Stem Cells. *Science.* **336**(6077), pp.86-90.

Scotton, C.J., Martinez, F.O., Smelt, M.J., Sironi, M., Locati, M., Mantovani, A. and Sozzani, S. 2005. Transcriptional profiling reveals complex regulation of the monocyte IL-1 beta system by IL-13. *J Immunol.* **174**(2), pp.834-845.

Selenscig, D.A., Martinel-Lamas, D.J., Fiorenza, G.L., Farroni, M.A., Bogué, C.R. and Dlugovitzky, D.G. 2009. Studies on the activating capacity of heat killed M. tuberculosis and its culture filtrate proteins on polymorphonuclear neutrophils and peripheral mononuclear cells from tuberculosis patients. *Inmunología.* **28**(4), pp.161-172.

Seto, S., Nakamura, H., Guo, T.C., Hikichi, H., Wakabayashi, K., Miyabayashi, A., Nagata, T., Hijikata, M. and Keicho, N. 2022. Spatial multiomic profiling reveals the novel polarization of foamy macrophages within necrotic granulomatous lesions developed in lungs of C3HeB/FeJ mice infected with Mycobacterium tuberculosis. *Front Cell Infect Microbiol.* **12**, p968543.

Sha, S., Shi, Y., Tang, Y., Jia, L., Han, X., Liu, Y., Li, X. and Ma, Y. 2021. Mycobacterium tuberculosis Rv1987 protein induces M2 polarization of macrophages through activating the PI3K/Akt1/mTOR signaling pathway. *Immunology & Cell Biology.* **99**(6), pp.570-585.

Shah, P.T. and Xing, L. 2025. The anti-mycobacterial potential of ibuprofen. *Tuberculosis.* **152**, p102638.

Shamaei, M., Mortaz, E., Pourabdollah, M., Garssen, J., Tabarsi, P., Velayati, A. and Adcock, I.M. 2018. Evidence for M2 macrophages in granulomas from pulmonary sarcoidosis: A new aspect of macrophage heterogeneity. *Human Immunology.* **79**(1), pp.63-69.

Shapouri-Moghaddam, A., Mohammadian, S., Vazini, H., Taghadosi, M., Esmaeili, S.-A., Mardani, F., Seifi, B., Mohammadi, A., Afshari, J.T. and Sahebkar, A. 2018. Macrophage plasticity, polarization, and function in health and disease. *Journal of Cellular Physiology.* **233**(9), pp.6425-6440.

Sharif, F., de Bakker, M.A. and Richardson, M.K. 2014. Osteoclast-like Cells in Early Zebrafish Embryos. *Cell J.* **16**(2), pp.211-224.

Shen, L., Liao, K., Yang, E., Yang, F., Lin, W., Wang, J., Fan, S., Huang, X., Chen, L., Shen, H., Jin, H., Ruan, Y., Liu, X., Zeng, G., Xu, J.-F. and Pi, J. 2023. Macrophage targeted iron oxide nanodecoys augment innate immunological and drug killings for more effective Mycobacterium Tuberculosis clearance. *Journal of Nanobiotechnology.* **21**(1), p369.

Shi, L.Z., Wang, R., Huang, G., Vogel, P., Neale, G., Green, D.R. and Chi, H. 2011. HIF1alpha-dependent glycolytic pathway orchestrates a metabolic checkpoint for the differentiation of TH17 and Treg cells. *J Exp Med.* **208**(7), pp.1367-1376.

Shiau, C.E., Kaufman, Z., Meireles, A.M. and Talbot, W.S. 2015. Differential Requirement for irf8 in Formation of Embryonic and Adult Macrophages in Zebrafish. *PLOS ONE.* **10**(1), pe0117513.

Shin, M., Yin, H.M., Shih, Y.H., Nozaki, T., Portman, D., Toles, B., Kolb, A., Luk, K., Isogai, S., Ishida, K., Hanasaka, T., Parsons, M.J., Wolfe, S.A., Burns, C.E., Burns, C.G. and Lawson, N.D. 2023. Generation and application of endogenously floxed alleles for cell-specific knockout in zebrafish. *Dev Cell.* **58**(22), pp.2614-2626.e2617.

Shosha, E., Shahror, R.A., Morris, C.A., Xu, Z., Lucas, R., McGee-Lawrence, M.E., Rusch, N.J., Caldwell, R.B. and Fouda, A.Y. 2023. The arginase 1/ornithine decarboxylase pathway suppresses HDAC3 to ameliorate the myeloid cell inflammatory response: implications for retinal ischemic injury. *Cell Death & Disease.* **14**(9), p621.

Shu, Y., Qin, M., Song, Y., Tang, Q., Huang, Y., Shen, P. and Lu, Y. 2020. M2 polarization of tumor-associated macrophages is dependent on integrin β3 via peroxisome proliferator-activated receptor-γ up-regulation in breast cancer. *Immunology.* **160**(4), pp.345-356.

Sica, A. and Mantovani, A. 2012. Macrophage plasticity and polarization: *in vivo* veritas. *J Clin Invest.* **122**(3), pp.787-795.

Sierro, F., Evrard, M., Rizzetto, S., Melino, M., Mitchell, A.J., Florido, M., Beattie, L., Walters, S.B., Tay, S.S., Lu, B., Holz, L.E., Roediger, B., Wong, Y.C., Warren, A., Ritchie, W., McGuffog, C., Weninger, W., Le Couteur, D.G., Ginhoux, F., ... and Bertolino, P. 2017. A Liver Capsular Network of Monocyte-Derived Macrophages Restricts Hepatic Dissemination of Intraperitoneal Bacteria by Neutrophil Recruitment. *Immunity.* **47**(2), pp.374-388.e376.

Silva, D., Silva, M.V.D., Barros, C.C.O., Alexandre, P.B.D., Timóteo, R.P., Catarino, J.S., Sales-Campos, H., Machado, J.R., Rodrigues, D.B.R., Oliveira, C.J. and Rodrigues, V. 2018. TNF-α blockade impairs *in vitro* tuberculous granuloma formation and down modulate Th1, Th17 and Treg cytokines. *PLoS One.* **13**(3), pe0194430.

Silva Miranda, M., Breiman, A., Allain, S., Deknuydt, F. and Altare, F. 2012. The tuberculous granuloma: an unsuccessful host defence mechanism providing a safety shelter for the bacteria? *Clin Dev Immunol.* **2012**, p139127.

Silva, N.J., Dorman, L.C., Vainchtein, I.D., Horneck, N.C. and Molofsky, A.V. 2021. *In situ* and transcriptomic identification of microglia in synapse-rich regions of the developing zebrafish brain. *Nature Communications.* **12**(1), p5916.

Simeone, R., Bobard, A., Lippmann, J., Bitter, W., Majlessi, L., Brosch, R. and Enninga, J. 2012. Phagosomal Rupture by Mycobacterium tuberculosis Results in Toxicity and Host Cell Death. *PLOS Pathogens.* **8**(2), pe1002507.

Singh Angom, R., Wang, Y., Wang, E., Dutta, S.K. and Mukhopadhyay, D. 2023. Conditional, Tissue-Specific CRISPR/Cas9 Vector System in Zebrafish Reveals the Role of Nrp1b in Heart Regeneration. *Arteriosclerosis, Thrombosis, and Vascular Biology.* **43**(10), pp.1921-1934.

Singhal, A. and De Libero, G. 2014. *Methods to inhibit intracellular growth of bacteria and to treat bacteria-mediated disease*.

Singhal, A., Jie, L., Kumar, P., Hong, G.S., Leow, M.K., Paleja, B., Tsenova, L., Kurepina, N., Chen, J., Zolezzi, F., Kreiswirth, B., Poidinger, M., Chee, C., Kaplan, G., Wang, Y.T. and De Libero, G. 2014. Metformin as adjunct antituberculosis therapy. *Sci Transl Med.* **6**(263), p263ra159.

Singhal, R., Mitta, S.R., Das, N.K., Kerk, S.A., Sajjakulnukit, P., Solanki, S., Andren, A., Kumar, R., Olive, K.P., Banerjee, R., Lyssiotis, C.A. and Shah, Y.M. 2021. HIF-2α activation potentiates oxidative cell death in colorectal cancers by increasing cellular iron. *J Clin Invest.* **131**(12).

Sipka, T., Park, S.A., Ozbilgic, R., Balas, L., Durand, T., Mikula, K., Lutfalla, G. and Nguyen-Chi, M. 2022. Macrophages undergo a behavioural switch during wound healing in zebrafish. *Free Radical Biology and Medicine.* **192**, pp.200-212.

Skugor, S., Glover, K.A., Nilsen, F. and Krasnov, A. 2008. Local and systemic gene expression responses of Atlantic salmon (Salmo salar L.) to infection with the salmon louse (Lepeophtheirus salmonis). *BMC Genomics.* **9**, p498.

Smith, H.L., Foxall, R.B., Duriez, P.J., Teal, E.L., Hoppe, A.D., Kanczler, J.M., Gray, J.C. and Beers, S.A. 2025. Comparison of human macrophages derived from peripheral blood and bone marrow. *The Journal of Immunology.* pvkae032.

Solomon, J.M., Leung, G.S. and Isberg, R.R. 2003. Intracellular replication of Mycobacterium marinum within Dictyostelium discoideum: efficient replication in the absence of host coronin. *Infect Immun.* **71**(6), pp.3578-3586.

Solomon, S.L. and Bryson, B.D. 2023. Single-cell analysis reveals a weak macrophage subpopulation response to Mycobacterium tuberculosis infection. *Cell Reports.* **42**(11), p113418.

Sommer, F., Ortiz Zacarías, N.V., Heitman, L.H. and Meijer, A.H. 2021. Inhibition of macrophage migration in zebrafish larvae demonstrates *in vivo* efficacy of human CCR2 inhibitors. *Developmental & Comparative Immunology.* **116**, p103932.

Song, C.-H. 2020. *Method for preventing or treating tuberculosis by a P53 expression regulating composition for M. tuberculosis control in cells and the use thereof*. US10806736B2.

Song, Q., Chaudagar, K., Zhang, X. and Waller, E.K. 2025. T cell-macrophage crosstalk in GVHD and cancer immunotherapy. *Cell Investigation.* **1**(4), p100035.

Soroldoni, D., Hogan, B.M. and Oates, A.C. 2009. Simple and Efficient Transgenesis with Meganuclease Constructs in Zebrafish. In: Lieschke, G.J., et al. eds. *Zebrafish: Methods and Protocols.* Totowa, NJ: Humana Press, pp.117-130.

Speirs, Z.C., Loynes, C.A., Mathiessen, H., Elks, P.M., Renshaw, S.A. and Jørgensen, L.v.G. 2024. What can we learn about fish neutrophil and macrophage response to immune challenge from studies in zebrafish. *Fish & Shellfish Immunology.* **148**, p109490.

Stachura, D.L., Svoboda, O., Campbell, C.A., Espín-Palazón, R., Lau, R.P., Zon, L.I., Bartunek, P. and Traver, D. 2013. The zebrafish granulocyte colony-stimulating factors (Gcsfs): 2 paralogous cytokines and their roles in hematopoietic development and maintenance. *Blood.* **122**(24), pp.3918-3928.

Stachura, D.L. and Traver, D. 2011. Cellular dissection of zebrafish hematopoiesis. *Methods Cell Biol.* **101**, pp.75-110.

Stanford, B.C.M., Clake, D.J., Morris, M.R.J. and Rogers, S.M. 2020. The power and limitations of gene expression pathway analyses toward predicting population response to environmental stressors. *Evol Appl.* **13**(6), pp.1166-1182.

Stapenhorst França, F. and Gensel, J.C. 2025. Redefining macrophage phenotypes after spinal cord injury: An open data approach. *Experimental Neurology.* **388**, p115222.

Statin Adjunctive Therapy for TB (StAT- TB). 2018. [Online database].

Stein, C.M., Nsereko, M., Malone, L.L., Okware, B., Kisingo, H., Nalukwago, S., Chervenak, K., Mayanja-Kizza, H., Hawn, T.R. and Boom, W.H. 2019. Long-term Stability of Resistance to Latent Mycobacterium tuberculosis Infection in Highly Exposed Tuberculosis Household Contacts in Kampala, Uganda. *Clin Infect Dis.* **68**(10), pp.1705-1712.

Stein, M., Keshav, S., Harris, N. and Gordon, S. 1992. Interleukin 4 potently enhances murine macrophage mannose receptor activity: a marker of alternative immunologic macrophage activation. *J Exp Med.* **176**(1), pp.287-292.

Steinberger, K.J. and Eubank, T.D. 2023. The Underexplored Landscape of Hypoxia-Inducible Factor 2 Alpha and Potential Roles in Tumor Macrophages: A Review. *Oxygen.* [Online]. **3**(1), pp.45-76.

Steiner, P., Efferent, L., Durkin, H.G., Joseph, G.K. and Nowakowskf, M. 1996. Nitric Oxide Production by Human Alveolar Macrophages in Pulmonary Disease. *Annals of the New York Academy of Sciences.* **797**(1), pp.246-249.

Stetsenko, V., Gail, D.P., Reba, S.M., Suzart, V.G., Schauner, R., Sandhu, A.K., Sette, A., Haj Dezfulian, M., Lindestam Arlehamn, C.S. and Carpenter, S.M. 2025. Human CD4+ T cells recognize Mycobacterium tuberculosis–infected macrophages amid broader responses. *Journal of Experimental Medicine.* **222**(12), pe20250460.

Stewart, P., Patel, S., Comer, A., Muneer, S., Nawaz, U., Quann, V., Bansal, M. and Venketaraman, V. 2023. Role of B Cells in Mycobacterium Tuberculosis Infection. *Vaccines (Basel).* **11**(5).

Stinson, M.W., Liu, S., Laurenson, A.J. and Rotty, J.D. 2024. Macrophage migration is differentially regulated by fibronectin and laminin through altered adhesion and myosin II localization. *Mol Biol Cell.* **35**(2), par22.

Stirling, D.R., Suleyman, O., Gil, E., Elks, P.M., Torraca, V., Noursadeghi, M. and Tomlinson, G.S. 2020. Analysis tools to quantify dissemination of pathology in zebrafish larvae. *Scientific Reports.* **10**(1), p3149.

Stoop, E.J., Schipper, T., Rosendahl Huber, S.K., Nezhinsky, A.E., Verbeek, F.J., Gurcha, S.S., Besra, G.S., Vandenbroucke-Grauls, C.M., Bitter, W. and van der Sar, A.M. 2011. Zebrafish embryo screen for mycobacterial genes involved in the initiation of granuloma formation reveals a newly identified ESX-1 component. *Dis Model Mech.* **4**(4), pp.526-536.

Stringer, C., Wang, T., Michaelos, M. and Pachitariu, M. 2021. Cellpose: a generalist algorithm for cellular segmentation. *Nature Methods.* **18**(1), pp.100-106.

Strizova, Z., Benesova, I., Bartolini, R., Novysedlak, R., Cecrdlova, E., Foley, Lily K. and Striz, I. 2023. M1/M2 macrophages and their overlaps – myth or reality? *Clinical Science.* **137**(15), pp.1067-1093.

Stumpo, R., Kauer, M., Martin, S. and Kolb, H. 1999. Alternative activation of macrophage by IL-10. *Pathobiology.* **67**(5-6), pp.245-248.

Subbian, S., Koo, M.S., Tsenova, L., Khetani, V., Zeldis, J.B., Fallows, D. and Kaplan, G. 2016. Pharmacologic Inhibition of Host Phosphodiesterase-4 Improves Isoniazid-Mediated Clearance of Mycobacterium tuberculosis. *Front Immunol.* **7**, p238.

Subbian, S., Tsenova, L., Holloway, J., Peixoto, B., O'Brien, P., Dartois, V., Khetani, V., Zeldis, J.B. and Kaplan, G. 2016. Adjunctive Phosphodiesterase-4 Inhibitor Therapy Improves Antibiotic Response to Pulmonary Tuberculosis in a Rabbit Model. *EBioMedicine.* **4**, pp.104-114.

Subbian, S., Tsenova, L., Kim, M.-J., Wainwright, H.C., Visser, A., Bandyopadhyay, N., Bader, J.S., Karakousis, P.C., Murrmann, G.B., Bekker, L.-G., Russell, D.G. and Kaplan, G. 2015. Lesion-Specific Immune Response in Granulomas of Patients with Pulmonary Tuberculosis: A Pilot Study. *PLOS ONE.* **10**(7), pe0132249.

Sun, J., Ruiz Daniels, R., Balic, A., Andresen, A.M.S., Bjørgen, H., Dobie, R., Henderson, N.C., Koppang, E.O., Martin, S.A.M., Fosse, J.H., Taylor, R.S. and Macqueen, D.J. 2024. Cell atlas of the Atlantic salmon spleen reveals immune cell heterogeneity and cell-specific responses to bacterial infection. *Fish & Shellfish Immunology.* **145**, p109358.

Sun, Q., Huang, J., Gu, Y., Liu, S. and Zhu, X. 2022. Dynamic changes of macrophage activation in mice infected with Trichinella spiralis. *International Immunopharmacology.* **108**, p108716.

Sur, A., Wang, Y., Capar, P., Margolin, G. and Farrell, J.A. 2023. Single-cell analysis of shared signatures and transcriptional diversity during zebrafish development. *bioRxiv.*

Susen, R.M., Bauer, R., Olesch, C., Fuhrmann, D.C., Fink, A.F., Dehne, N., Jain, A., Ebersberger, I., Schmid, T. and Brüne, B. 2019. Macrophage HIF-2α regulates tumor-suppressive Spint1 in the tumor microenvironment. *Mol Carcinog.* **58**(11), pp.2127-2138.

Swaim, L.E., Connolly, L.E., Volkman, H.E., Humbert, O., Born, D.E. and Ramakrishnan, L. 2006. Mycobacterium marinum infection of adult zebrafish causes caseating granulomatous tuberculosis and is moderated by adaptive immunity. *Infect Immun.* **74**(11), pp.6108-6117.

Swami, R., Popli, P., Sal, K., Challa, R.R., Vallamkonda, B., Garg, M. and Dora, C.P. 2025. A review on biomacromolecular ligand-directed nanoparticles: New era in macrophage targeting. *Int J Biol Macromol.* **306**(Pt 4), p141740.

Swaminathan, S. and Rekha, B. 2010. Pediatric tuberculosis: global overview and challenges. *Clin Infect Dis.* **50 Suppl 3**, pp.S184-194.

Szkuta, P.T. 2020. *The role of neutrophils in mycobacterial infection in zebrafish*. PhD thesis, University of Sheffield.

Szondi, D.C., Wong, J.K., Vardy, L.A. and Cruickshank, S.M. 2021. Arginase Signalling as a Key Player in Chronic Wound Pathophysiology and Healing. *Front Mol Biosci.* **8**, p773866.

Szulc-Dąbrowska, L., Bossowska-Nowicka, M., Struzik, J. and Toka, F.N. 2020. Cathepsins in Bacteria-Macrophage Interaction: Defenders or Victims of Circumstance? *Frontiers in Cellular and Infection Microbiology.* **10**.

Takeda, K., Ichiki, T., Narabayashi, E., Inanaga, K., Miyazaki, R., Hashimoto, T., Matsuura, H., Ikeda, J., Miyata, T. and Sunagawa, K. 2009. Inhibition of Prolyl Hydroxylase Domain-Containing Protein Suppressed Lipopolysaccharide-Induced TNF-α Expression. *Arteriosclerosis, Thrombosis, and Vascular Biology.* **29**(12), pp.2132-2137.

Takeda, N., O'Dea, E.L., Doedens, A., Kim, J.W., Weidemann, A., Stockmann, C., Asagiri, M., Simon, M.C., Hoffmann, A. and Johnson, R.S. 2010a. Differential activation and antagonistic function of HIF-a isoforms in macrophages are essential for NO homeostasis. *Genes Dev.* **24**(5), pp.491-501.

Takeda, N., O'Dea, E.L., Doedens, A., Kim, J.W., Weidemann, A., Stockmann, C., Asagiri, M., Simon, M.C., Hoffmann, A. and Johnson, R.S. 2010b. Differential activation and antagonistic function of HIF-{alpha} isoforms in macrophages are essential for NO homeostasis. *Genes Dev.* **24**(5), pp.491-501.

Takeuchi, O. and Akira, S. 2010. Pattern recognition receptors and inflammation. *Cell.* **140**(6), pp.805-820.

Takiguchi, H., Yang, C.X., Yang, C.W.T., Sahin, B., Whalen, B.A., Milne, S., Akata, K., Yamasaki, K., Yang, J.S.W., Cheung, C.Y., Vander Werff, R., McNagny, K.M., Leitao Filho, F.S., Shaipanich, T., van Eeden, S.F., Obeidat, M.e., Leung, J.M. and Sin, D.D. 2021. Macrophages with reduced expressions of classical M1 and M2 surface markers in human bronchoalveolar lavage fluid exhibit pro-inflammatory gene signatures. *Scientific Reports.* **11**(1), p8282.

Tan, E.L., Qin, Y., Yang, J., Li, X.J., Liu, T.Q., Yang, G.B., Li, Y.J., Zhang, Z.Z., Lu, Z.H., Wang, J.C., Zheng, J.X. and Zhang, S.X. 2025. Global burden of MDR-TB and XDR-TB: trends, inequities, and future implications for public health planning. *BMC Infect Dis.* **25**(1), p1225.

Tan, S. and Russell, D.G. 2015. Trans-species communication in the Mycobacterium tuberculosis-infected macrophage. *Immunol Rev.* **264**(1), pp.233-248.

Tardito, S., Martinelli, G., Soldano, S., Paolino, S., Pacini, G., Patane, M., Alessandri, E., Smith, V. and Cutolo, M. 2019. Macrophage M1/M2 polarization and rheumatoid arthritis: A systematic review. *Autoimmunity Reviews.* **18**(11), p102397.

Tarique, A.A., Logan, J., Thomas, E., Holt, P.G., Sly, P.D. and Fantino, E. 2015. Phenotypic, functional, and plasticity features of classical and alternatively activated human macrophages. *Am J Respir Cell Mol Biol.* **53**(5), pp.676-688.

Taylor, C.T. and Colgan, S.P. 2017. Regulation of immunity and inflammation by hypoxia in immunological niches. *Nat Rev Immunol.* **17**(12), pp.774-785.

Teng, J., Cui, M.Y., Zhao, Y., Chen, H.J., Du, W.J., Xue, L.Y. and Ji, X.S. 2023. Expression changes of non-specific cytotoxic cell receptor (NCCRP1) and proliferation and migration of NCCs post-Nocardia seriolae infection in Northern Snakehead. *Developmental & Comparative Immunology.* **139**, p104576.

Thermes, V., Grabher, C., Ristoratore, F., Bourrat, F., Choulika, A., Wittbrodt, J. and Joly, J.S. 2002. I-SceI meganuclease mediates highly efficient transgenesis in fish. *Mech Dev.* **118**(1-2), pp.91-98.

Thisse, B. and Thisse, C. 2004. *Fast Release Clones: a high throughput expression analysis.* ZFIN Direct Data Submission. Available from: http://zfin.org

Thisse, C. and Thisse, B. 2005. *High Throughput Expression Analysis of ZF-Models Consortium Clones.* ZFIN Direct Data Submission Available from: zfin.org

Thompson, A.A., Elks, P.M., Marriott, H.M., Eamsamarng, S., Higgins, K.R., Lewis, A., Williams, L., Parmar, S., Shaw, G., McGrath, E.E., Formenti, F., Van Eeden, F.J., Kinnula, V.L., Pugh, C.W., Sabroe, I., Dockrell, D.H., Chilvers, E.R., Robbins, P.A., Percy, M.J., ... and Walmsley, S.R. 2014. Hypoxia-inducible factor 2α regulates key neutrophil functions in humans, mice, and zebrafish. *Blood.* **123**(3), pp.366-376.

Thong, L., Sandby Thomas, O., Ó Gallchobhair, O., Duffin, E., Yennemadi, A.S., Leisching, G., Murphy, D.M., Nadarajan, P., O'Connell, F., O'Sullivan, M.P., Basdeo, S.A., Cox, D.J. and Keane, J. 2025. Dexamethasone inhibits Mycobacterium tuberculosis-induced glycolysis but preserves antimicrobial function in primary human macrophages. *Scientific Reports.* **15**(1), p34310.

Thwaites, G.E., Nguyen, D.B., Nguyen, H.D., Hoang, T.Q., Do, T.T., Nguyen, T.C., Nguyen, Q.H., Nguyen, T.T., Nguyen, N.H., Nguyen, T.N., Nguyen, N.L., Vu, N.T., Cao, H.H., Tran, T.H., Pham, P.M., Nguyen, T.D., Stepniewska, K., White, N.J. and Farrar, J.J. 2004. Dexamethasone for the treatment of tuberculous meningitis in adolescents and adults. *N Engl J Med.* **351**(17), pp.1741-1751.

Tian, N., Chu, H., Li, Q., Sun, H., Zhang, J., Chu, N. and Sun, Z. 2025. Host-directed therapy for tuberculosis. *European Journal of Medical Research.* **30**(1), p267.

Tiwari, D. and Martineau, A.R. 2023. Inflammation-mediated tissue damage in pulmonary tuberculosis and host-directed therapeutic strategies. *Semin Immunol.* **65**, p101672.

Tobin, D.M. and Ramakrishnan, L. 2008. Comparative pathogenesis of Mycobacterium marinum and Mycobacterium tuberculosis. *Cellular Microbiology.* **10**(5), pp.1027-1039.

Torraca, V., Masud, S., Spaink, H.P. and Meijer, A.H. 2014. Macrophage-pathogen interactions in infectious diseases: new therapeutic insights from the zebrafish host model. *Disease Models & Mechanisms.* **7**(7), pp.785-797.

Travnickova, J., Nhim, S., Abdellaoui, N., Djouad, F., Nguyen-Chi, M., Parmeggiani, A. and Kissa, K. 2021. Macrophage morphological plasticity and migration is Rac signalling and MMP9 dependant. *Scientific Reports.* **11**(1), p10123.

Trede, N.S., Langenau, D.M., Traver, D., Look, A.T. and Zon, L.I. 2004. The Use of Zebrafish to Understand Immunity. *Immunity.* **20**(4), pp.367-379.

Trombetta, A.C., Soldano, S., Contini, P., Tomatis, V., Ruaro, B., Paolino, S., Brizzolara, R., Montagna, P., Sulli, A., Pizzorni, C., Smith, V. and Cutolo, M. 2018. A circulating cell population showing both M1 and M2 monocyte/macrophage surface markers characterizes systemic sclerosis patients with lung involvement. *Respir Res.* **19**(1), p186.

Tsai, M.C., Chakravarty, S., Zhu, G., Xu, J., Tanaka, K., Koch, C., Tufariello, J., Flynn, J. and Chan, J. 2006. Characterization of the tuberculous granuloma in murine and human lungs: cellular composition and relative tissue oxygen tension. *Cellular Microbiology.* **8**(2), pp.218-232.

Tsarouchas, T.M., Wehner, D., Cavone, L., Munir, T., Keatinge, M., Lambertus, M., Underhill, A., Barrett, T., Kassapis, E., Ogryzko, N., Feng, Y., van Ham, T.J., Becker, T. and Becker, C.G. 2018. Dynamic control of proinflammatory cytokines Il-1β and Tnf-α by macrophages in zebrafish spinal cord regeneration. *Nature Communications.* **9**(1), p4670.

Tsugita, M., Morimoto, N. and Nakayama, M. 2017. SiO2 and TiO2 nanoparticles synergistically trigger macrophage inflammatory responses. *Particle and Fibre Toxicology.* **14**(1), p11.

Tukvadze, N., Mashatole, S., Jacobs, A., Ngwanto, T., Heinrich, N., Van Rie, A., Crudu, V., Tudor, E., Goginashvili, L., Ibraim, E., Khosa, C., Howell, P., Rajaram, S., Naidoo, K., Niemann, S., Reither, K. and Wallis, R.S. 2025. DRTB-HDT: a randomized controlled trial of two adjunctive host-directed therapies in rifampin-resistant tuberculosis. *BMC Infectious Diseases.* **25**(1), p768.

Turner, R.D. and Bothamley, G.H. 2015. Cough and the Transmission of Tuberculosis. *The Journal of Infectious Diseases.* **211**(9), pp.1367-1372.

Turvey, S.E. and Broide, D.H. 2010. Innate immunity. *J Allergy Clin Immunol.* **125**(2 Suppl 2), pp.S24-32.

UKHSA. 2014. *Tuberculosis (TB): migrant health guide.* [Online]. [Accessed 9 December]. Available from: https://www.gov.uk/guidance/tuberculosis-tb-migrant-health-guide?utm_source=chatgpt.com

Underhill, D.M., Ozinsky, A., Smith, K.D. and Aderem, A. 1999. Toll-like receptor-2 mediates mycobacteria-induced proinflammatory signaling in macrophages. *Proc Natl Acad Sci U S A.* **96**(25), pp.14459-14463.

van den Berg, M.P.M., Kurhade, S.H., Maarsingh, H., Erceg, S., Hulsbeek, I.R., Boekema, P.H., Kistemaker, L.E.M., van Faassen, M., Kema, I.P., Elsinga, P.H., Dömling, A., Meurs, H. and Gosens, R. 2020. Pharmacological Screening Identifies SHK242 and SHK277 as Novel Arginase Inhibitors with Efficacy against Allergen-Induced Airway Narrowing *In vitro* and *In vivo*. *The Journal of Pharmacology and Experimental Therapeutics.* **374**(1), pp.62-73.

Van den Bossche, J., Bogaert, P., van Hengel, J., Guérin, C.J., Berx, G., Movahedi, K., Van den Bergh, R., Pereira-Fernandes, A., Geuns, J.M.C., Pircher, H., Dorny, P., Grooten, J., De Baetselier, P. and Van Ginderachter, J.A. 2009. Alternatively activated macrophages engage in homotypic and heterotypic interactions through IL-4 and polyamine-induced E-cadherin/catenin complexes. *Blood.* **114**(21), pp.4664-4674.

Van den Bossche, J., Lamers, W.H., Koehler, E.S., Geuns, J.M., Alhonen, L., Uimari, A., Pirnes-Karhu, S., Van Overmeire, E., Morias, Y., Brys, L., Vereecke, L., De Baetselier, P. and Van Ginderachter, J.A. 2012. Pivotal Advance: Arginase-1-independent polyamine production stimulates the expression of IL-4-induced alternatively activated macrophage markers while inhibiting LPS-induced expression of inflammatory genes. *J Leukoc Biol.* **91**(5), pp.685-699.

van der Sar, A.M., Abdallah, A.M., Sparrius, M., Reinders, E., Vandenbroucke-Grauls, C.M. and Bitter, W. 2004. Mycobacterium marinum strains can be divided into two distinct types based on genetic diversity and virulence. *Infect Immun.* **72**(11), pp.6306-6312.

van der Sar, A.M., Spaink, H.P., Zakrzewska, A., Bitter, W. and Meijer, A.H. 2009. Specificity of the zebrafish host transcriptome response to acute and chronic mycobacterial infection and the role of innate and adaptive immune components. *Molecular Immunology.* **46**(11), pp.2317-2332.

van der Vaart, M., van Soest, J.J., Spaink, H.P. and Meijer, A.H. 2013. Functional analysis of a zebrafish myd88 mutant identifies key transcriptional components of the innate immune system. *Dis Model Mech.* **6**(3), pp.841-854.

van Dijk, K.S.E., Begon-Pescia, C., de Bruin, B.A., Özbilgiç, R., Elks, P.M., Nguyen-Chi, M.E. and Forlenza, M. 2025. During an inflammatory response, zebrafish tnfa and tnfb are expressed by different cell types and have distinct expression kinetics. *bioRxiv.* p2025.2011.2004.686030.

van Furth, R., Cohn, Z.A., Hirsch, J.G., Humphrey, J.H., Spector, W.G. and Langevoort, H.L. 1972. The mononuclear phagocyte system: a new classification of macrophages, monocytes, and their precursor cells. *Bull World Health Organ.* **46**(6), pp.845-852.

Varadi, M., Bertoni, D., Magana, P., Paramval, U., Pidruchna, I., Radhakrishnan, M., Tsenkov, M., Nair, S., Mirdita, M., Yeo, J., Kovalevskiy, O., Tunyasuvunakool, K., Laydon, A., Žídek, A., Tomlinson, H., Hariharan, D., Abrahamson, J., Green, T., Jumper, J., ... and Velankar, S. 2024. AlphaFold Protein Structure Database in 2024: providing structure coverage for over 214 million protein sequences. *Nucleic Acids Research.* **52**(D1), pp.D368-D375.

Varela, M. and Meijer, A.H. 2022. A fresh look at mycobacterial pathogenicity with the zebrafish host model. *Mol Microbiol.* **117**(3), pp.661-669.

Varin, A., Mukhopadhyay, S., Herbein, G. and Gordon, S. 2010. Alternative activation of macrophages by IL-4 impairs phagocytosis of pathogens but potentiates microbial-induced signalling and cytokine secretion. *Blood.* **115**(2), pp.353-362.

Vauti, F., Stegemann, L.A., Vögele, V. and Köster, R.W. 2020. All-age whole mount *in situ* hybridization to reveal larval and juvenile expression patterns in zebrafish. *PLoS One.* **15**(8), pe0237167.

Verrall, A.J., Netea, M.G., Alisjahbana, B., Hill, P.C. and van Crevel, R. 2014. Early clearance of Mycobacterium tuberculosis: a new frontier in prevention. *Immunology.* **141**(4), pp.506-513.

Via, L.E., Fratti, R.A., McFalone, M., Pagán-Ramos, E., Deretic, D. and Deretic, V. 1998. Effects of cytokines on mycobacterial phagosome maturation. *Journal of Cell Science.* **111**(7), pp.897-905.

Via, L.E., Lin, P.L., Ray, S.M., Carrillo, J., Allen, S.S., Eum, S.Y., Taylor, K., Klein, E., Manjunatha, U., Gonzales, J., Lee, E.G., Park, S.K., Raleigh, J.A., Cho, S.N., McMurray, D.N., Flynn, J.L. and Barry, C.E., 3rd. 2008. Tuberculous granulomas are hypoxic in guinea pigs, rabbits, and nonhuman primates. *Infect Immun.* **76**(6), pp.2333-2340.

Vidyarthi, A., Khan, N., Agnihotri, T., Negi, S., Das, D.K., Aqdas, M., Chatterjee, D., Colegio, O.R., Tewari, M.K. and Agrewala, J.N. 2018. TLR-3 Stimulation Skews M2 Macrophages to M1 Through IFN-αβ Signaling and Restricts Tumor Progression. *Frontiers in Immunology.* **Volume 9 - 2018**.

Vieira, S.M., Lemos, H.P., Grespan, R., Napimoga, M.H., Dal-Secco, D., Freitas, A., Cunha, T.M., Verri, W.A., Jr., Souza-Junior, D.A., Jamur, M.C., Fernandes, K.S., Oliver, C., Silva, J.S., Teixeira, M.M. and Cunha, F.Q. 2009. A crucial role for TNF-alpha in mediating neutrophil influx induced by endogenously generated or exogenous chemokines, KC/CXCL1 and LIX/CXCL5. *Br J Pharmacol.* **158**(3), pp.779-789.

VijayKumar, S., Borja, M., Neff, N., Royer, L.A. and Lange, M. 2024. Maximizing single cell dissociation protocol for individual zebrafish embryo. *MethodsX.* **13**, p102958.

Vilella, A.J., Severin, J., Ureta-Vidal, A., Heng, L., Durbin, R. and Birney, E. 2009. EnsemblCompara GeneTrees: Complete, duplication-aware phylogenetic trees in vertebrates. *Genome Res.* **19**(2), pp.327-335.

Villar, J., Ouaknin, L., Cros, A. and Segura, E. 2023. Monocytes differentiate along two alternative pathways during sterile inflammation. *EMBO reports.* **24**(7), pe56308.

Vogel, D.Y.S., Glim, J.E., Stavenuiter, A.W.D., Breur, M., Heijnen, P., Amor, S., Dijkstra, C.D. and Beelen, R.H.J. 2014. Human macrophage polarization *in vitro*: Maturation and activation methods compared. *Immunobiology.* **219**(9), pp.695-703.

Vogel, D.Y.S., Vereyken, E.J.F., Glim, J.E., Heijnen, P.D.A.M., Moeton, M., van der Valk, P., Amor, S., Teunissen, C.E., van Horssen, J. and Dijkstra, C.D. 2013. Macrophages in inflammatory multiple sclerosis lesions have an intermediate activation status. *Journal of Neuroinflammation.* **10**(1), p809.

Volkman, H.E., Clay, H., Beery, D., Chang, J.C., Sherman, D.R. and Ramakrishnan, L. 2004. Tuberculous granuloma formation is enhanced by a mycobacterium virulence determinant. *PLoS Biol.* **2**(11), pe367.

Wagener, J., MacCallum Donna, M., Brown Gordon, D. and Gow Neil, A.R. 2017. Candida albicans Chitin Increases Arginase-1 Activity in Human Macrophages, with an Impact on Macrophage Antimicrobial Functions. *mBio.* **8**(1), pp.e01820-01816.

Wallace, E.M., Rizzi, J.P., Han, G., Wehn, P.M., Cao, Z., Du, X., Cheng, T., Czerwinski, R.M., Dixon, D.D., Goggin, B.S., Grina, J.A., Halfmann, M.M., Maddie, M.A., Olive, S.R., Schlachter, S.T., Tan, H., Wang, B., Wang, K., Xie, S., ... and Josey, J.A. 2016. A Small-Molecule Antagonist of HIF2α Is Efficacious in Preclinical Models of Renal Cell Carcinoma. *Cancer Res.* **76**(18), pp.5491-5500.

Wallis, R.S., Ginindza, S., Beattie, T., Arjun, N., Likoti, M., Edward, V.A., Rassool, M., Ahmed, K., Fielding, K., Ahidjo, B.A., Vangu, M.D.T. and Churchyard, G. 2021. Adjunctive host-directed therapies for

pulmonary tuberculosis: a prospective, open-label, phase 2, randomised controlled trial. *Lancet Respir Med.* **9**(8), pp.897-908.

Walton, E.M., Cronan, M.R., Beerman, R.W. and Tobin, D.M. 2015. The Macrophage-Specific Promoter mfap4 Allows Live, Long-Term Analysis of Macrophage Behavior during Mycobacterial Infection in Zebrafish. *PLOS ONE.* **10**(10), pe0138949.

Walvekar, K.P., Vangapally, S., Andugulapati, S.B. and Chilaka, S. 2025. Stable expression of human arginase 1 does not suppress inflammation or M1 macrophage polarization in THP-1 monocytes. *Next Research.* **2**(3), p100656.

Wang, G.L. and Semenza, G.L. 1995. Purification and characterization of hypoxia-inducible factor 1. *J Biol Chem.* **270**(3), pp.1230-1237.

Wang, H., Maeda, Y., Fukutomi, Y. and Makino, M. 2013. An *in vitro* model of Mycobacterium lepraeinduced granuloma formation. *BMC Infectious Diseases.* **13**(1), p279.

Wang, J.-Y., Hsueh, P.-R., Wang, S.-K., Jan, I.S., Lee, L.-N., Liaw, Y.-S., Yang, P.-C. and Luh, K.-T. 2007. Disseminated tuberculosis: a 10-year experience in a medical center. *Medicine.* **86**(1), pp.39-46.

Wang, L., Shang, X., Qi, X., Ba, D., Lv, J., Zhou, X., Wang, H., Shaxika, N., Wang, J. and Ma, X. 2020. Clinical Significance of M1/M2 Macrophages and Related Cytokines in Patients with Spinal Tuberculosis. *Dis Markers.* **2020**, p2509454.

Wang, L., Yang, K., Xie, X., Wang, S., Gan, H., Wang, X. and Wei, H. 2025. Macrophages as Multifaceted Orchestrators of Tissue Repair: Bridging Inflammation, Regeneration, and Therapeutic Innovation. *J Inflamm Res.* **18**, pp.8945-8959.

Wang, L.-x., Zhang, S.-x., Wu, H.-j., Rong, X.-l. and Guo, J. 2019. M2b macrophage polarization and its roles in diseases. *Journal of Leukocyte Biology.* **106**(2), pp.345-358.

Wang, N., Sun, Y.-H., Liu, J., Wang, Y.-P. and Zhu, Z.-Y. 2007. Molecular characterization of common carp (Cyprinus carpio) Sonic Hedgehog and discovery of its maternal expression. *Development Genes and Evolution.* **217**(4), pp.299-305.

Wang, R., Lan, C., Benlagha, K., Camara, N.O.S., Miller, H., Kubo, M., Heegaard, S., Lee, P., Yang, L., Forsman, H., Li, X., Zhai, Z. and Liu, C. 2024. The interaction of innate immune and adaptive immune system. *MedComm.* **5**(10), pe714.

Wang, S., Wang, J., Chen, Z., Luo, J., Guo, W., Sun, L. and Lin, L. 2024. Targeting M2-like tumor-associated macrophages is a potential therapeutic approach to overcome antitumor drug resistance. *npj Precision Oncology.* **8**(1), p31.

Wang, T., Liu, H., Lian, G., Zhang, S.-Y., Wang, X. and Jiang, C. 2017. HIF1α-induced glycolysis metabolism is essential to the activation of inflammatory macrophages. *Mediators of inflammation.* **2017**(1), p9029327.

Wang, Y., Hsu, A.Y., Walton, E.M., Park, S.J., Syahirah, R., Wang, T., Zhou, W., Ding, C., Lemke, A.P., Zhang, G., Tobin, D.M. and Deng, Q. 2021. A robust and flexible CRISPR/Cas9-based system for neutrophil-specific gene inactivation in zebrafish. *Journal of Cell Science.* **134**(8), pjcs258574.

Wang, Y., Xi, J., Yi, J., Meng, C., Zhao, X., Sun, Z., Zhang, H., Deng, X., Ma, Z., Li, H., Wang, Y. and Chen, C. 2022. Brucella induces M1 to M2 polarization of macrophages through STAT6 signaling pathway to promote bacterial intracellular survival. *Research in Veterinary Science.* **145**, pp.91-101.

Watkins, B.Y., Joshi, S.A., Ball, D.A., Leggett, H., Park, S., Kim, J., Austin, C.D., Paler-Martinez, A., Xu, M., Downing, K.H. and Brown, E.J. 2012. Mycobacterium marinum SecA2 promotes stable granulomas and induces tumor necrosis factor alpha *in vivo*. *Infect Immun.* **80**(10), pp.3512-3520.

Weerdenburg, E.M., Abdallah, A.M., Mitra, S., de Punder, K., van der Wel, N.N., Bird, S., Appelmelk, B.J., Bitter, W. and van der Sar, A.M. 2012. ESX-5-deficient Mycobacterium marinum is hypervirulent in adult zebrafish. *Cell Microbiol.* **14**(5), pp.728-739.

Wehrli, W., Knüsel, F., Schmid, K. and Staehelin, M. 1968. Interaction of rifamycin with bacterial RNA polymerase. *Proceedings of the National Academy of Sciences.* **61**(2), pp.667-673.

Wei, Q., Deng, Y., Yang, Q., Zhan, A. and Wang, L. 2023. The markers to delineate different phenotypes of macrophages related to metabolic disorders. *Front Immunol.* **14**, p1084636.

Weinberg, J.B., Misukonis, M.A., Shami, P.J., Mason, S.N., Sauls, D.L., Dittman, W.A., Wood, E.R., Smith, G.K., McDonald, B., Bachus, K.E. and et al. 1995. Human mononuclear phagocyte inducible nitric oxide synthase (iNOS): analysis of iNOS mRNA, iNOS protein, biopterin, and nitric oxide production by blood monocytes and peritoneal macrophages. *Blood.* **86**(3), pp.1184-1195.

Weinberger, T., Messerer, D., Joppich, M., Fischer, M., Garcia, C., Kumaraswami, K., Wimmler, V., Ablinger, S., Räuber, S., Fang, J., Liu, L., Liu, W.H., Winterhalter, J., Lichti, J., Tomas, L., Esfandyari, D., Percin, G., Salamanca, S.M., Hidalgo, A., ... and Schulz, C. 2024. *Resident and recruited macrophages differentially contribute to cardiac healing after myocardial ischemia*. eLife Sciences Publications, Ltd. 2024/03/04. Available from: http://dx.doi.org/10.7554/eLife.89377.3

Wentzel, A.S., Petit, J., van Veen, W.G., Fink, I.R., Scheer, M.H., Piazzon, M.C., Forlenza, M., Spaink, H.P. and Wiegertjes, G.F. 2020. Transcriptome sequencing supports a conservation of macrophage polarization in fish. *Sci Rep.* **10**(1), p13470.

Wesemann, D.R. and Benveniste, E.N. 2003. STAT-1 alpha and IFN-gamma as modulators of TNF-alpha signaling in macrophages: regulation and functional implications of the TNF receptor 1:STAT-1 alpha complex. *J Immunol.* **171**(10), pp.5313-5319.

Westerfield, M. 2000. *The Zebrafish Book: A Guide for the Laboratory Use of Zebrafish (Danio Rerio).* University of Oregon Press.

White, R.M., Sessa, A., Burke, C., Bowman, T., LeBlanc, J., Ceol, C., Bourque, C., Dovey, M., Goessling, W., Burns, C.E. and Zon, L.I. 2008. Transparent adult zebrafish as a tool for *in vivo* transplantation analysis. *Cell Stem Cell.* **2**(2), pp.183-189.

Whitfield, T.T., Riley, B.B., Chiang, M.-Y. and Phillips, B. 2002. Development of the zebrafish inner ear. *Developmental Dynamics.* **223**(4), pp.427-458.

Whittington, A.M., Turner, F.S., Baark, F., Templeman, S., Kirwan, D.E., Roufosse, C., Krishnan, N., Robertson, B.D., Chong, D.L.W., Porter, J.C., Gilman, R.H. and Friedland, J.S. 2023. An acidic microenvironment in Tuberculosis increases extracellular matrix degradation by regulating macrophage inflammatory responses. *PLoS Pathog.* **19**(7), pe1011495.

Wiedmaier, N., Müller, S., Köberle, M., Manncke, B., Krejci, J., Autenrieth, I.B. and Bohn, E. 2008. Bacteria induce CTGF and CYR61 expression in epithelial cells in a lysophosphatidic acid receptor-dependent manner. *International Journal of Medical Microbiology.* **298**(3), pp.231-243.

Wiegertjes, G.F., Wentzel, A.S., Spaink, H.P., Elks, P.M. and Fink, I.R. 2016. Polarization of immune responses in fish: The 'macrophages first' point of view. *Molecular Immunology.* **69**, pp.146-156.

Wilkins-Rodríguez, A.A., Salazar-Schettino, P.M., Manning-Cela, R.G. and Gutiérrez-Kobeh, L. 2024. Differential Regulation of L-Arginine Metabolism through NOS2 and Arginases during Infection with Trypanosoma cruzi. *Pathogens.* [Online]. **13**(10), p878.

Wilmes, V., Kur, I.M., Weigert, A., Verhoff, M.A., Gradhand, E. and Kauferstein, S. 2023. iNOS expressing macrophages co-localize with nitrotyrosine staining after myocardial infarction in humans. *Frontiers in Cardiovascular Medicine.* **Volume 10 - 2023**.

Winchell, C.G., Mishra, B.B., Phuah, J.Y., Saqib, M., Nelson, S.J., Maiello, P., Causgrove, C.M., Ameel, C.L., Stein, B., Borish, H.J., White, A.G., Klein, E.C., Zimmerman, M.D., Dartois, V., Lin, P.L., Sassetti, C.M. and Flynn, J.L. 2020. Evaluation of IL-1 Blockade as an Adjunct to Linezolid Therapy for Tuberculosis in Mice and Macaques. *Frontiers in Immunology.* **Volume 11 - 2020**.

Wittamer, V., Bertrand, J.Y., Gutschow, P.W. and Traver, D. 2011. Characterization of the mononuclear phagocyte system in zebrafish. *Blood.* **117**(26), pp.7126-7135.

Witten, P.E., Hansen, A. and Hall, B.K. 2001. Features of mono- and multinucleated bone resorbing cells of the zebrafish Danio rerio and their contribution to skeletal development, remodeling, and growth. *J Morphol.* **250**(3), pp.197-207.

Witten, P.E. and Huysseune, A. 2010. The unobtrusive majority: mononucleated bone resorbing cells in teleost fish and mammals. *Journal of Applied Ichthyology.* **26**(2), pp.225-229.

Witwicka, H., Hwang, S.-Y., Reyes-Gutierrez, P., Jia, H., Odgren, P.E., Donahue, L.R., Birnbaum, M.J. and Odgren, P.R. 2015. Studies of OC-STAMP in Osteoclast Fusion: A New Knockout Mouse Model, Rescue of Cell Fusion, and Transmembrane Topology. *PLOS ONE.* **10**(6), pe0128275.

Wolf, A.J., Desvignes, L., Linas, B., Banaiee, N., Tamura, T., Takatsu, K. and Ernst, J.D. 2008. Initiation of the adaptive immune response to Mycobacterium tuberculosis depends on antigen production in the local lymph node, not the lungs. *J Exp Med.* **205**(1), pp.105-115.

World Health Organization. 2025. *Global Tuberculosis Report.* [Online]. [Accessed 27 February]. Available from: https://www.who.int/publications/i/item/9789240116924

Wu, D., Su, X., Lu, J., Li, S., Hood, B.L., Vasile, S., Potluri, N., Diao, X., Kim, Y., Khorasanizadeh, S. and Rastinejad, F. 2019. Bidirectional modulation of HIF-2 activity through chemical ligands. *Nature Chemical Biology.* **15**(4), pp.367-376.

Wu, J., Zhang, B., Du, W., Shi, Y., Xie, C., Ke, Y. and Yi, X. 2025. OC-STAMP is a potential biomarker and therapeutic target for Silicosis: an exploratory investigation. *Journal of Translational Medicine.* **23**(1), p214.

Wu, L., Gao, A., Li, L., Chen, J., Li, J. and Ye, J. 2021. A Single-Cell Transcriptome Profiling of Anterior Kidney Leukocytes From Nile Tilapia (Oreochromis niloticus). *Front Immunol.* **12**, p783196.

Wumaier, R., Zhang, K., Zhou, J., Wen, Z., Chen, Z., Luo, G., Wang, H., Qin, J., Du, B., Ren, H., Song, Y., Gao, Q. and Yan, B. 2025. Mycobacteria Exploit Host GPR84 to Dampen Pro-Inflammatory Responses and Promote Infection in Macrophages. *Microorganisms.* **13**(1).

Wynn, T.A., Chawla, A. and Pollard, J.W. 2013. Macrophage biology in development, homeostasis and disease. *Nature.* **496**(7446), pp.445-455.

Xia, T., Fu, S., Yang, R., Yang, K., Lei, W., Yang, Y., Zhang, Q., Zhao, Y., Yu, J., Yu, L. and Zhang, T. 2023. Advances in the study of macrophage polarization in inflammatory immune skin diseases. *Journal of Inflammation.* **20**(1), p33.

Xiang, T., Zou, Y., Jiang, X., Xu, L., Zhang, L., Zhou, C., Hu, Y., Ye, X., Yang, X.-D., Jiang, X. and Zheng, Y. 2024. Irisflorentin promotes bacterial phagocytosis and inhibits inflammatory responses in macrophages during bacterial infection. *Heliyon.* **10**(1), pe23225.

Xie, D.-k., Yao, J., Li, P.-h., Zhu, Y.-w., Chen, J.-n., Cao, X.-l., Cheng, S.-l., Chen, Y.-m., Huang, Y.-f., Wang, L., Wang, Z.-h., Qiao, R., Ge, J.-m., Yue, H., Wei, L., Liu, Z.-y., Han, H., Qin, H.-y. and Zhao, J.-l. 2024. Phenotypic comparison and the potential antitumor function of immortalized bone marrow-derived macrophages (iBMDMs). *Frontiers in Immunology.* **Volume 15 - 2024**.

Xie, Y., Tolmeijer, S., Oskam, J.M., Tonkens, T., Meijer, A.H. and Schaaf, M.J.M. 2019. Glucocorticoids inhibit macrophage differentiation towards a pro-inflammatory phenotype upon wounding without affecting their migration. *Dis Model Mech.* **12**(5).

Xu, P., Zhang, X., Wang, X., Li, J., Liu, G., Kuang, Y., Xu, J., Zheng, X., Ren, L., Wang, G., Zhang, Y., Huo, L., Zhao, Z., Cao, D., Lu, C., Li, C., Zhou, Y., Liu, Z., Fan, Z., ... and Sun, X. 2014. Genome sequence and genetic diversity of the common carp, Cyprinus carpio. *Nature Genetics.* **46**(11), pp.1212-1219.

Xue, J., Schmidt, S.V., Sander, J., Draffehn, A., Krebs, W., Quester, I., De Nardo, D., Gohel, T.D., Emde, M., Schmidleithner, L., Ganesan, H., Nino-Castro, A., Mallmann, M.R., Labzin, L., Theis, H., Kraut, M., Beyer, M., Latz, E., Freeman, T.C., ... and Schultze, J.L. 2014. Transcriptome-based network analysis reveals a spectrum model of human macrophage activation. *Immunity.* **40**(2), pp.274-288.

Xue, J., Schmidt, Susanne V., Sander, J., Draffehn, A., Krebs, W., Quester, I., De Nardo, D., Gohel, Trupti D., Emde, M., Schmidleithner, L., Ganesan, H., Nino-Castro, A., Mallmann, Michael R., Labzin, L., Theis, H., Kraut, M., Beyer, M., Latz, E., Freeman, Tom C., ... and Schultze, Joachim L. 2014. Transcriptome-Based Network Analysis Reveals a Spectrum Model of Human Macrophage Activation. *Immunity.* **40**(2), pp.274-288.

Xue, Q., Lu, Y., Eisele, M.R., Sulistijo, E.S., Khan, N., Fan, R. and Miller-Jensen, K. 2015. Analysis of single-cell cytokine secretion reveals a role for paracrine signaling in coordinating macrophage responses to TLR4 stimulation. *Sci Signal.* **8**(381), pra59.

Yadav, S., Dalai, P., Gowda, S., Nivsarkar, M. and Agrawal- Rajput, R. 2023. Azithromycin alters Colony Stimulating Factor-1R (CSF-1R) expression and functional output of murine bone marrow-derived macrophages: A novel report. *International Immunopharmacology.* **123**, p110688.

Yadav, V., Sahoo, S., Malhotra, N., Mishra, R., Rajmani, R.S., Shanmugam, S., Shandil, R.K., Narayanan, S., Thacker, V.V., Jolly, M., Seshasayee, A.S.N. and Singh, A. 2025. Bioenergetic reprogramming of macrophages reduces drug tolerance in Mycobacterium tuberculosis. *bioRxiv.* p2025.2001.2024.634842.

Yamada, K.J., Heim, C.E., Aldrich, A.L., Gries, C.M., Staudacher, A.G. and Kielian, T. 2018. Arginase-1 Expression in Myeloid Cells Regulates Staphylococcus aureus Planktonic but Not Biofilm Infection. *Infect Immun.* **86**(7).

Yang, K., Wu, Y., Xie, H., Li, M., Ming, S., Li, L., Li, M., Wu, M., Gong, S. and Huang, X. 2016. Macrophage-mediated inflammatory response decreases mycobacterial survival in mouse MSCs by augmenting NO production. *Scientific Reports.* **6**(1), p27326.

Yang, L., Rojas, A.M. and Shiau, C.E. 2021. Liposomal Clodronate-mediated Macrophage Depletion in the Zebrafish Model. *Bio Protoc.* **11**(6), pe3951.

Yang, M., Birnbaum, M.J., MacKay, C.A., Mason-Savas, A., Thompson, B. and Odgren, P.R. 2008. Osteoclast stimulatory transmembrane protein (OC-STAMP), a novel protein induced by RANKL that promotes osteoclast differentiation. *J Cell Physiol.* **215**(2), pp.497-505.

Yang, R., Chen, Y. and Chen, D. 2018. Biological functions and role of CCN1/Cyr61 in embryogenesis and tumorigenesis in the female reproductive system (Review). *Mol Med Rep.* **17**(1), pp.3-10.

Yang, X., Wang, Q., Shao, F., Zhuang, Z., Wei, Y., Zhang, Y., Zhang, L., Ren, C. and Wang, H. 2024. Cell volume regulation modulates macrophage-related inflammatory responses via JAK/STAT signaling pathways. *Acta Biomaterialia.* **186**, pp.286-299.

Yao, Y., Jeyanathan, M., Haddadi, S., Barra, N.G., Vaseghi-Shanjani, M., Damjanovic, D., Lai, R., Afkhami, S., Chen, Y., Dvorkin-Gheva, A., Robbins, C.S., Schertzer, J.D. and Xing, Z. 2018. Induction of Autonomous Memory Alveolar Macrophages Requires T Cell Help and Is Critical to Trained Immunity. *Cell.* **175**(6), pp.1634-1650.e1617.

Yao, Y., Li, Q. and Yan, Q. 2024. Distribution and response strategies of non-specific cytotoxic cell receptor protein 1 in large yellow croaker. *Fish & Shellfish Immunology.* **151**, p109728.

Yarilina, A., Park-Min, K.H., Antoniv, T., Hu, X. and Ivashkiv, L.B. 2008. TNF activates an IRF1-dependent autocrine loop leading to sustained expression of chemokines and STAT1-dependent type I interferon-response genes. *Nat Immunol.* **9**(4), pp.378-387.

Yedgarian, N., Agopian, J., Flaig, B., Hajjar, F., Karapetyan, A., Murthy, K., Patrikyan, A., Tomas, K., Tumanyan, K., Nasiri, M.J., Subbian, S. and Venketaraman, V. 2025. The Intricate Process of Calcification in Granuloma Formation and the Complications Following M. tuberculosis Infection. *Biomolecules.* **15**(7).

Yellanki, Y.C., Patil, M.M. and Raghu, A.V. 2024. Macrophage polarization and future perspectives: a comprehensive review. *Discover Materials.* **4**(1), p61.

Yin, C., Cai, J., Gou, Y., Li, D., Tang, H., Wang, L., Liu, H. and Luo, B. 2023. Dynamic changes in human THP-1-derived M1-to-M2 macrophage polarization during Thelazia callipaeda MIF induction. *Frontiers in Immunology.* **Volume 13 - 2022**.

Yona, S., Kim, K.-W., Wolf, Y., Mildner, A., Varol, D., Breker, M., Strauss-Ayali, D., Viukov, S., Guilliams, M., Misharin, A., Hume, David A., Perlman, H., Malissen, B., Zelzer, E. and Jung, S. 2013. Fate Mapping Reveals Origins and Dynamics of Monocytes and Tissue Macrophages under Homeostasis. *Immunity.* **38**(1), pp.79-91.

Young, C., Walzl, G. and Du Plessis, N. 2020. Therapeutic host-directed strategies to improve outcome in tuberculosis. *Mucosal Immunology.* **13**(2), pp.190-204.

Yuan, H., He, J., Zhang, G., Zhang, D., Kong, X. and Chen, F. 2017. Osteoclast stimulatory transmembrane protein induces a phenotypic switch in macrophage polarization suppressing an M1 pro-inflammatory state. *Acta Biochim Biophys Sin (Shanghai).* **49**(10), pp.935-944.

Yurdagul, A., Subramanian, M., Wang, X., Crown, S.B., Ilkayeva, O.R., Darville, L., Kolluru, G.K., Rymond, C.C., Gerlach, B.D., Zheng, Z., Kuriakose, G., Kevil, C.G., Koomen, J.M., Cleveland, J.L., Muoio, D.M. and Tabas, I. 2020. Macrophage Metabolism of Apoptotic Cell-Derived Arginine Promotes Continual Efferocytosis and Resolution of Injury. *Cell Metabolism.* **31**(3), pp.518-533.e510.

Zavašnik-Bergant, T. and Turk, B. 2007. Cysteine proteases: destruction ability versus immunomodulation capacity in immune cells. **388**(11), pp.1141-1149.

Zenk, S.F., Hauck, S., Mayer, D., Grieshober, M. and Stenger, S. 2021. Stabilization of Hypoxia-Inducible Factor Promotes Antimicrobial Activity of Human Macrophages Against Mycobacterium tuberculosis. *Front Immunol.* **12**, p678354.

Zhai, W., Wu, F., Zhang, Y., Fu, Y. and Liu, Z. 2019. The Immune Escape Mechanisms of Mycobacterium Tuberculosis. *Int J Mol Sci.* **20**(2).

Zhang, F., Liang, J., Lu, Y., Tang, Y., Liu, S., Wu, K., Liu, Z. and Wang, X. 2022. Macrophage-Specific Cathepsin as a Marker Correlated with Prognosis and Tumor Microenvironmental Characteristics of Clear Cell Renal Cell Carcinoma. *J Inflamm Res.* **15**, pp.6275-6292.

Zhang, H., Chen, Y., Chen, R., Ning, Y. and Dai, Y. 2025. Hemophagocytic lymphohistiocytosis is associated with disseminated tuberculosis in patients with advanced HIV infection. *Journal of Infection.* **90**(1).

Zhang, H., Ishii, K., Shibata, T., Ishii, S., Hirao, M., Lu, Z., Takamura, R., Kitano, S., Miyachi, H., Kageyama, R., Itakura, E. and Kobayashi, T. 2024. Fluctuation of lysosomal protein degradation in neural stem cells of the postnatal mouse brain. *Development.* **151**(4), pdev202231.

Zhang, J., He, Z., Xiong, C., Yao, Y., Zhang, C., Yao, W., Yang, S., Li, X. and Han, Y. 2024. SHH induces macrophage oxidative phosphorylation and efferocytosis to promote scar formation. *Cell Commun Signal.* **22**(1), p336.

Zhang, J., Li, Y., Duan, Z., Kang, J., Chen, K., Li, G., Weng, C., Zhang, D., Zhang, L., Wang, J. and Li, B. 2020. The effects of the M2a macrophage-induced axonal regeneration of neurons by arginase 1. *Bioscience Reports.* **40**(2), pBSR20193031.

Zhang, J., Liu, X., Wan, C., Liu, Y., Wang, Y., Meng, C., Zhang, Y. and Jiang, C. 2020. NLRP3 inflammasome mediates M1 macrophage polarization and IL-1β production in inflammatory root resorption. *J Clin Periodontol.* **47**(4), pp.451-460.

Zhang, J., Yuan, Z., Li, X., Wang, F., Wei, X., Kang, Y., Mo, C., Jiang, J., Liang, H. and Ye, L. 2023. Activation of the JNK/COX-2/HIF-1α axis promotes M1 macrophage via glycolytic shift in HIV-1 infection. *Life Science Alliance.* **6**(12), pe202302148.

Zhang, L., Chen, C., Fu, J., Lilley, B., Berlinicke, C., Hansen, B., Ding, D., Wang, G., Wang, T., Shou, D., Ye, Y., Mulligan, T., Emmerich, K., Saxena, M.T., Hall, K.R., Sharrock, A.V., Brandon, C., Park, H., Kam, T.-I., ... and Mumm, J.S. 2021. Large-scale phenotypic drug screen identifies neuroprotectants in zebrafish and mouse models of retinitis pigmentosa. *eLife.* **10**, pe57245.

Zhang, M., Gong, J., Lin, Y. and Barnes, P.F. 1998. Growth of virulent and avirulent Mycobacterium tuberculosis strains in human macrophages. *Infect Immun.* **66**(2), pp.794-799.

Zhang, P., Yao, Q., Lu, L., Li, Y., Chen, P.-J. and Duan, C. 2014. Hypoxia-Inducible Factor 3 Is an Oxygen-Dependent Transcription Activator and Regulates a Distinct Transcriptional Response to Hypoxia. *Cell Reports.* **6**(6), pp.1110-1121.

Zhang, Y., Marshall-Phelps, K. and de Almeida, R.G. 2023. Fast, precise and cloning-free knock-in of reporter sequences *in vivo* with high efficiency. *Development.* **150**(12).

Zhang, Y., Shi, W., Zhang, W. and Mitchison, D. 2013. Mechanisms of Pyrazinamide Action and Resistance. *Microbiol Spectr.* **2**(4), pp.1-12.

Zhang, Z., Fan, W., Yang, G., Xu, Z., Wang, J., Cheng, Q. and Yu, M. 2017. Risk of tuberculosis in patients treated with TNF-α antagonists: a systematic review and meta-analysis of randomised controlled trials. *BMJ Open.* **7**(3), pe012567.

Zheng, J., Dong, C. and Xiong, S. 2024. Mycobacterial Rv1804c binds to the PEST domain of IκBα and activates macrophage-mediated proinflammatory responses. *iScience.* **27**(3).

Zhou, Q., Zhao, C., Yang, Z., Qu, R., Li, Y., Fan, Y., Tang, J., Xie, T. and Wen, Z. 2023. Cross-organ single-cell transcriptome profiling reveals macrophage and dendritic cell heterogeneity in zebrafish. *Cell Rep.* **42**(7), p112793.

Zlatar, L., Knopf, J., Singh, J., Wang, H., Muñoz-Becerra, M., Herrmann, I., Chukwuanukwu, R.C., Eckstein, M., Eichhorn, P., Rieker, R.J., Naschberger, E., Burkovski, A., Krenn, V., Bilyy, R., Butova, T., Liskina, I., Kalabukha, I., Khmel, O., Boettcher, M., ... and Herrmann, M. 2024. Neutrophil extracellular traps characterize caseating granulomas. *Cell Death & Disease.* **15**(7), p548.

Zohaib Ali, M., Dutt, T.S., MacNeill, A., Walz, A., Pearce, C., Lam, H., Philp, J.S., Patterson, J., Henao-Tamayo, M., Lee, R., Liu, J., Robertson, G.T., Hickey, A.J., Meibohm, B. and Gonzalez Juarrero, M. 2024. A modified BPaL regimen for tuberculosis treatment replaces linezolid with inhaled spectinamides. *Elife.* **13**.

Zou, X., Wang, K., Deng, Y., Guan, P., Pu, Q., Wang, Y., Mou, J., Du, Y., Lou, X., Wang, S., Jiang, N., Zhou, S., Wang, H., Du, D., Liu, X., Hu, H. and Zhang, H. 2024. Hypoxia-inducible factor 2α promotes pathogenic polarization of stem-like Th2 cells via modulation of phospholipid metabolism. *Immunity.* **57**(12), pp.2808-2826.e2808.

Zou, Y.-x., Xiang, T.-n., Xu, L.-r., Zhang, H., Ma, Y.-h., Zhang, L., Zhou, C.-x., Wu, X., Huang, Q.-l., Lei, B., Mu, J.-w., Qin, X.-y., Jiang, X. and Zheng, Y.-j. 2024. Dehydrozaluzanin C- derivative protects septic mice by alleviating over-activated inflammatory response and promoting the phagocytosis of macrophages. *International Immunopharmacology.* **132**, p111889.